

Quantification of the effects of small organic molecules on actinide(III/IV) retention by cement-based materials

Dissertation
zur Erlangung des Grades

"Doktorin der Naturwissenschaften"

im Promotionsfach Chemie

am Fachbereich 09 - Chemie, Pharmazie, Geografie und Geowissenschaften
der Johannes Gutenberg-Universität Mainz

Janina Stietz

geb. in Memmingen

Mainz, 2023

1. Gutachter: [REDACTED]

2. Gutachter: [REDACTED]

Datum der mündlichen Prüfung: 18.01.2024

Erklärung

Ich bestätige hiermit, dass ich die vorliegende Arbeit eigenständig verfasst habe und ausschließlich die angegebenen Quellen und Hilfsmittel verwendet habe. Ferner versichere ich, dass alle Passagen in der Arbeit, die wortwörtlich oder sinngemäß aus anderen Quellen übernommen wurden, entsprechend gekennzeichnet sind. Die elektronische Version der Arbeit stimmt mit der schriftlichen Fassung überein, und die Arbeit wurde in gleicher oder ähnlicher Form noch keiner anderen Prüfungsbehörde vorgelegt.

Datum, Ort

Unterschrift

Danksagung

Ich möchte allen Personen meinen aufrichtigen Dank aussprechen, die mich während meines Studiums und der Promotion unterstützt und begleitet haben.

[Redacted text block]

[Redacted text block]

[Redacted text block]

[Redacted text block]

[Redacted text block]

[Redacted text block]



Zusammenfassung

In sämtlichen internationalen Konzepten zur Entsorgung von radioaktiven Abfällen in tiefen geologischen Endlagern ist das vorrangige Ziel eines Multibarrierensystems, die Ausbreitung von Actiniden (An) in die Umwelt zu vermeiden. Nuklearer Abfall soll in geeigneten Gesteinsformationen in einem tiefegeologischen Endlager eingebettet werden. Die gegenwärtig verwendeten zementhaltigen Materialien, die häufig für Bau- und Abfallkonditionierungszwecke eingesetzt werden, werden den pH-Wert des eindringenden Grundwassers im alkalischen Bereich ($10 \leq \text{pH} \leq 13,3$) über einen sehr langen Zeitraum stabilisieren. Schwach- oder mittelradioaktive Abfälle enthalten organische Stoffe in unterschiedlichen Formen, wie beispielsweise Papier, Handschuhe, Flaschen, Filter, Ionenaustauscherharze usw. Darüber hinaus können organische Stoffe auch Bestandteil der Zementmatrix sein, beispielsweise in Form von *Superplasticier*. Aufgrund der anaeroben Korrosionsprozesse von Stahl und verwandten Materialien werden stark reduzierende Bedingungen in einem Endlager erwartet. Plutonium im radioaktiven Abfall trägt potenziell zum langfristigen radiologischen Risiko bei, was aufgrund der langen Halbwertszeit von ^{239}Pu ($t_{1/2} = 2,41 \times 10^4$ a) entsteht. In reduzierenden, wässrigen Umgebungen ist die Bildung von Pu(III) und Pu(IV) zu erwarten. Als redoxstabile Analoge werden in dieser Arbeit $^{241}\text{Am(III)}$ und $^{232/234}\text{Th(IV)}$ verwendet.

Es wurden ausführlich die eingesetzten Materialien charakterisiert: *hardened cement paste* (HCP) entsprechend für frischen Zement ($\text{pH} > 13$), Calcium-Silikat-Hydrat (C-S-H) Phasen entsprechend für gealterten Zement ($C/S = 0,8$, $\text{pH} \sim 10$), sowie die organischen Liganden Gluconat (GLU), Ethylendiamintetraessigsäure (EDTA) und Isosaccharinsäure (ISA). Auf Grundlage dessen wurden Untersuchungen im binären System gemacht, um den Einfluss der organischen Liganden auf die Festphase (HCP, C-S-H Phase) zu bestimmen. Um ein besseres Verständnis für Transportprozesse im Zement wie Sorption oder Diffusion zu erlangen, wurden Experimente mit verschiedenen Actiniden in unterschiedlichen Oxidationsstufen (Am(III), Th(IV) und Pu(IV)) durchgeführt. Zusätzlich wurden Speziationsrechnungen durchgeführt und CE-ICP-MS-Messungen (Kapillarelektrophorese mit induktiv gekoppeltem Plasma) verwendet, um die Komplexierung der Actiniden mit den organischen Liganden und dem umgebenden Porenwasser zu untersuchen.

Ein deutlicher Einfluss auf den Rückhalt von Pu(IV) und Th(IV) konnte bei den Untersuchungen mit GLU und ISA an frischem Zement bei $\text{pH} > 13$ festgestellt werden. Bei der Diffusion mit $^{238}\text{Pu(IV)}$ (verwendet aufgrund der hohen spezifischen Aktivität) konnte durch zwei parallellaufende Diffusionsexperimente gezeigt werden, dass in Gegenwart von ISA Pu(IV) deutlich tiefer in den Zementkern eindringt. Keinen Einfluss auf die Sorption von An(III/IV) hat EDTA an frischem Zement ($\text{pH} > 13$) und GLU an gealterten Zement (C-S-H Phasen, $C/S = 0,8$) bei $\text{pH} = 10$. Durch die CE-ICP-MS Messungen konnte gezeigt werden, dass Th(IV) und Pu(IV) mit den organischen Liganden (OL) komplexieren und sich mit Ca(II), was im Porenwasser enthalten ist, Ca-An(IV)-OH-OL-Komplexe bilden.

Abstract

In all international concepts for the disposal of radioactive waste, including deep geological repositories, the primary goal of a multibarrier system is to prevent the spread of actinides (An) into the environment. Radioactive waste is planned to be embedded in suitable rock formations within a deep geological repository. Over time, groundwater can infiltrate from the surrounding rock and saturate the repository. The currently used cementitious materials, commonly employed for construction and waste conditioning purposes, will stabilize the pH in the alkaline range ($10 \leq \text{pH} \leq 13.3$) over a very long period. Low- or intermediate-level radioactive waste contains organic materials in various forms, such as paper, gloves, bottles, filters, ion exchange resins, etc. Strongly reducing conditions are expected in the system due to the anaerobic corrosion processes of steel and related materials. Plutonium in the radioactive waste potentially contributes to the long-term radiological risk, attributed to the long half-life of ^{239}Pu ($t_{1/2} = 2.41 \times 10^4$ years). In reducing, aqueous environments, the formation of Pu(III) and Pu(IV) is expected. As stable redox analogs, ^{241}Am (III) and $^{232/234}\text{Th}$ (IV) are used in this study.

The materials used were characterized in detail: Cement paste (HCP) corresponding to fresh cement ($\text{pH} > 13$), calcium silicate hydrate (C-S-H) phases corresponding to aged cement ($\text{C/S} = 0.8$, $\text{pH} \sim 10$) and the organic ligands gluconate (GLU), ethylenediaminetetraacetic acid (EDTA) and isosaccharinic acid (ISA). On this basis, investigations were conducted in the binary system to determine the influence of the organic ligands on the solid phase (HCP, C-S-H phase). To gain a better understanding of transport processes in cement, such as sorption or diffusion, experiments were conducted with actinides in different oxidation states (Am(III), Th(IV) and Pu(IV)). Additionally, speciation calculations were performed, and CE-ICP-MS (capillary electrophoresis with inductively coupled plasma mass spectrometry) measurements were utilized to investigate and understand the complexation of actinides with organic ligands, as well as with the surrounding pore water.

Considerable influence on the retention of Pu(IV) and Th(IV) was observed in the investigations with GLU and ISA on fresh cement at $\text{pH} > 13$. Diffusion experiments with ^{238}Pu (IV) (used due to high specific activity) performed in parallel demonstrated that in the presence of ISA, Pu(IV) penetrates deeper into the cement core. EDTA on fresh cement ($\text{pH} > 13$) and GLU on aged cement (C-S-H phases, $\text{C/S} = 0.8$) at $\text{pH} = 10$ have no influence on the uptake of An(III/IV). The speciation calculations and the CE-ICP-MS measurements showed that Th(IV) and Pu(IV) complex with the organic ligands (OL) and probably form Ca-An(IV)-OH-OL complexes with Ca(II) contained in the pore water.

Table of content

Zusammenfassung	i
Abstract.....	ii
1 Introduction.....	1
1.1 General.....	2
1.2 Sorption.....	5
1.3 Diffusion	7
1.4 Speciation.....	8
1.4.1 Organic ligands.....	9
1.4.2 Actinides.....	14
1.5 Literature overview	22
2 Manuscripts.....	29
2.1 Publication: Uptake of actinides by hardened cement paste in high-salinity pore water	30
2.2 Investigation on cementitious materials with GLU.....	45
2.2.1 Publication: Uptake of Pu(IV) by hardened cement paste in the presence of gluconate at high and low ionic strengths	45
2.2.2 Publication: Influence of gluconate on the retention of Eu(III), Am(III), Th(IV), Pu(IV), and U(VI) by C-S-H (C/S = 0.8).....	57
2.2.3 Further investigations with GLU.....	73
2.2.3.1 Semiquantitative analysis mode.....	73
2.2.3.2 Effect of GLU and ISA on HCP.....	75
2.2.3.3 Leaching effect of ²³² Th from HCP in the presence of GLU	76
2.2.3.4 Batch sorption experiment C-S-H / Th(IV) / GLU (C/S = 1.0).....	78
2.2.3.5 CE-ICP-MS measurement of Ca-Th(IV)-OH-GLU.....	79
2.3 Manuscript: Investigation on cementitious materials with EDTA	82
2.4 Manuscript: Sorption and diffusion experiments with HCP under the influence of ISA	117
2.4.1 Screening experiments.....	152
3 Summary and conclusion	154
References	156
Appendix A1 SI “The Uptake of Actinides by Hardened Cement Paste in High-Salinity Pore Water”.....	163
Appendix A2 SM ”Uptake of Pu(IV) by hardened cement paste in the presence of gluconate at high and low ionic strengths”	167
Appendix A3 SM “Influence of gluconate on the retention of Eu(III), Am(III), Th(IV), Pu(IV), and U(VI) by C-S-H (C/S = 0.8)”	174
Appendix A4 Tables of measured values and calculated parameters	183
Appendix A5 Figures of experiments.....	220
Appendix A6 Error calculation.....	234
List of Abbreviation.....	237
List of Chemicals.....	239
List of Units.....	241
List of Variables and Constants	243
List of Figures.....	245
List of Tables.....	247

1 Introduction

One of tod's greatest challenges is the safe disposal of radioactive waste. Countries around the world have accumulated a significant amount of radioactive waste from the use of nuclear energy to generate electricity (high level waste, HLW). Other sources of radioactive waste can originate from the decommissioning, nuclear research, as well as from the industrial and medical use of various radionuclides (low and intermediate level waste, L-/ILW). This must be stored safely over a long period of time to protect the environment and people. A final repository for radioactive waste is a highly complex technical, scientific and political issue [1-4]. The final storage of high radioactive waste is a controversial issue in many countries, as it raises both technical and ethical questions. Various expert committees and authorities have addressed this problem and make recommendations for the final disposal of HLW. The European Union has agreed, among other things, that each member state that generates radioactive waste is also responsible for the safe disposal or permanent safe storage of this waste [5]. The following examples are just a few of many projects and developments around the world. Finland is leading the development of a deep geological repository for HLW. The "Onkalo" project was approved in 2020 and construction is underway [6,7]. It is expected that the repository will be operational in this decade. Sweden has been operating the repository for L-/ILW "SFR" (Final Repository for Short-lived Radioactive Waste) since the 1980s. The construction of a deep geological repository for HLW is currently in the licensing procedure [8]. France has also had a repository for L-/ILW since the 1990s ("Centre de l'Aube"). The construction of a deep geological repository for HLW is being planned, but the exact location and timetable have not yet been determined [9,10]. There is currently no central repository for HLW in the United States. The Yucca Mountain project in Nevada was considered as a possible site in the past, but there was considerable legal and political controversy that led to a temporary suspension of the project. Alternative sites and concepts are currently being investigated [11,12]. Germany decided in 2011 to phase out the use of nuclear energy [13]. On 15 April 2023, the last three nuclear power plants were shut down [14]. The site for a deep geological repository for HLW is currently being identified in a multi-stage selection procedure under the "Standortauswahlgesetz" of 2017 [15]. A special aspect of the region in Northern Germany is that suitable areas consist of clay rocks, but it is a region with pore and formation waters of medium and high ionic strength [16,17]. At the depths required for a repository, ionic strengths of 1 M to 4 M are found [18]. These values are significantly higher than in other areas that could be considered for a nuclear waste repository.

Ultimately, deep geological disposal of HLW is the safest method according to current knowledge. In a multi-barrier concept, salt rock, clay rock and crystalline rock are considered as host rock and geological barrier. Furthermore, cement (usually Ordinary Portland cement) is used as construction material and can be used to seal boreholes or shafts. L-/ILW is often super compacted in steel drums to reduce volume. The containers are then filled with cement to encapsulate and immobilize the waste and placed in the engineered concrete vaults of a designated repository. It can also be used for stabilization and

immobilization, the latter minimizing the release and migration of radionuclides into the biosphere. Cementitious materials are thus not only used as a construction material, but also provide a physical and chemical barrier (technical barriers) preventing the release of radionuclides [19-21].

1.1 General

Cementitious material mainly consists of various calcium silicates. By adding around 2% of gypsum, ordinary Portland cement (OPC) is obtained, which is the most common type of cementitious material [22]. Furthermore, OPC consists of approximately 50 - 70% alite (Ca_3SiO_5 , C_3S), 20 - 30% belite ($\beta\text{-Ca}_2\text{SiO}_4$, C_2S), 5-12% aluminate ($\text{Ca}_3\text{Al}_2\text{O}_6$, C_3A), and 5 - 12% ferrite ($\text{C}_2(\text{F,A})_5$) [23]. In contact with water, a hydration reaction occurs, leading to the formation of four main phases: C-S-H (calcium silicate hydrate) phases, which are the main components, portlandite ($\text{Ca}(\text{OH})_2$), AFt (aluminoferrite trisulfates such as ettringite), and AFm (aluminoferrite monosulfates) [22]. Possible infiltration of groundwater into the repository is prevented with the cementitious materials and with the steel components and containers in the repository. As a result, the pH of the groundwater medium will be buffered in the alkaline to hyperalkaline range, while the anoxic corrosion of the steel will cause strongly reducing conditions in the system [24]. The inflowing groundwater can degrade the cement, which is divided into four stages. Stage I is characterized by hyperalkaline conditions ($13.5 > \text{pH} > 12.5$) due to the dissolution of alkali metal sulfates, which leads to the formation of hydroxide ions for charge balance. The composition of the cement pore water is determined by Na^+ , K^+ , and OH^- ions. As the number of pore water exchange cycles increases, the pH decreases to 12.5. At this point, stage II begins, where the dissolution of portlandite dominates and influences the composition of the pore water with $\text{Ca}(\text{OH})_2$ [22]. After the dissolution of portlandite, stage III starts, where the pH is determined by the C-S-H phases. The C-S-H phases have a structure similar to tobermorite ($\text{Ca}_5\text{Si}_6\text{O}_{16}(\text{OH})_2$) and possess a large surface area of $148 \text{ m}^2 \text{ g}^{-1}$ [25]. They consist of CaO layers and a triple chain formation of SiO_4 tetrahedra [26]. In the beginning of stage III, the C-S-H phases have a C/S ratio > 1.5 , similar to the first two stages. However, with further pore water exchange cycles, this ratio decreases to 0.6, resulting in a decreasing pH up to 10 [22]. The structures of the C-S-H phases can be seen in Figure 1. With a C/S ratio of 1.5, there are no bridging SiO_4 tetrahedra. The resulting negative charges are compensated by Ca(II) ions in the interlayer. With a C/S ratio of 0.67, a non-bridged SiO_4 tetrahedron connects two bridged SiO_4 tetrahedra. This leaves unshared oxygen atoms in the bridged tetrahedra and at the end groups, which are neutralized via H^+ and form silanol groups. The investigations in this work are limited to the first stage, which corresponds to fresh cement at approx. $\text{pH} = 13$, and to the third stage, which begins after the dissolution of the portlandite, and the pH value is determined by the C-S-H phase (C/S = 0.8) and is approx. 10, this is aged cement.

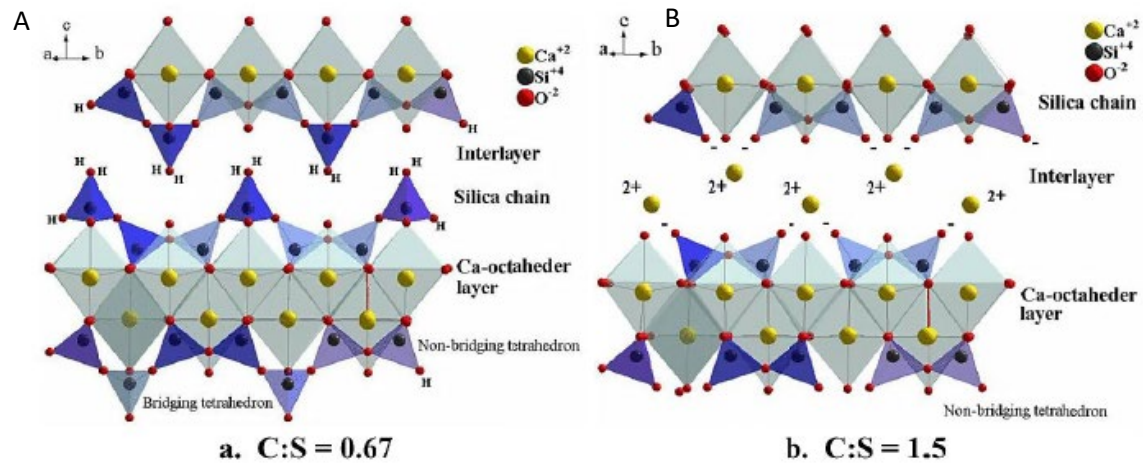


Figure 1: Tobermorite-based structure of the C-S-H phases at C/S ratios of 1.5 (A) and 0.67 (B) due to ageing of the cement [27].

L/ILW contains, in particular, organic molecules that are formed by radiolysis or hydrolysis of polymers or are added to the cement as additives (e.g., superplasticizers). Examples of organic wastes are paper, gloves, flasks, over-clothing, seals, cables, filters, ion exchange resins, etc. Due the degradation of cement, organic ligands present in the form of cement additives (0.1 – 2 % wt. [28-30]) or as waste components could possibly influence the migration behavior of actinides in the host rock of the repository. In more detail, they can complex and mobilize them or sorb them themselves to cement, thereby reducing the uptake of actinides [31]. At the alkaline pH values in the disposal system, organic ligands are deprotonated and can form stable complexes with trivalent and tetravalent actinides. This complex formation can increase the solubility and thus has an influence on the sorption behavior [32]. In this work, investigations are mainly conducted with gluconate, ethylenediaminetetraacetic acid and isosaccharinic acid, less consideration is given to the ligand's phthalate, oxalate, and citrate. Gluconate (GLU) is often used as a plasticizer in cement admixtures to improve its workability [33-35]. When the cement corrodes over time, gluconate is released. In addition to its use as a cement additive, gluconate can also enter the disposal system through waste from medicine and research as decontamination and cleaning agents [27,32,36]. However, for the Swedish repository for L-/ILW "SFR", it is reported that the sorption of gluconate onto hydrated cement in the waste packaging process leads in a decrease in gluconate concentrations in all cement-conditioned waste packages, resulting in a range of 10^{-10} – 10^{-8} M. While the packaging material itself does not reduce the gluconate concentration, during migration into the relevant compartments, dilution, and sorption to the hydrated cement in the construction concrete are anticipated to lower the concentration to at least 10^{-9} M [37]. Ethylenediaminetetraacetic acid (EDTA) is used as a decontamination reagent in radioactive waste reprocessing for its ability to form stable complexes with a wide range of cations, including actinides and was therefore chosen as a model organic ligand system. As an example, according to the findings in Fanger et al. [38], it is estimated that

a total of 10 kg of EDTA has been deposited at the SFR in waste packages generated by 1998, which resulted in a maximum concentration of 6×10^{-3} M. Similar to previous assumptions, it is assumed that this EDTA was used evenly across the four nuclear power plants [37]. Another example: The Waste Isolation Pilot Plant (WIPP) in Carlsbad, New Mexico, is currently the only operational deep geologic repository in the United States of America. Situated 655 meters (2,150 feet) below ground level in the Salado Formation, the WIPP is specifically designed for the disposal of defense transuranic (TRU) waste. As of 2019, the WIPP inventory includes the co-disposal of approximately 400 kg of EDTA, corresponding to concentrations of up to approximately 8×10^{-5} M [39]. EDTA is a potent chelating ligand known for forming stable aqueous complexes with plutonium in various oxidation states, including +III, +IV, and +V, as well as with several other metal cations. The complexation of plutonium with EDTA can have significant effects on the solubility and retention of plutonium, ultimately influencing the environmental mobility of this radionuclide [39]. The main component of tissues found in the waste is cellulose and isosaccharinic acid (ISA) is the main degradation product (~80%) of cellulose in hyperalkaline solutions [33,37]. As a result, the calcium phases present in the cementitious materials may dissolve, potentially significantly impacting the sorption of radionuclides [40,41]. For example, the disposal of materials such as contaminated paper, textiles, and wood has resulted in the presence of substantial amounts of cellulose in SFR. The mass of cellulose in the relevant waste packages can reach up to 150 kg per package [37]. Considering additional sorption processes of isosaccharinate in different compartments, the dissolved concentrations are reduced to a maximum of 1.2×10^{-2} M [42]. At high pH values, ISA forms stable complexes with trivalent and tetravalent metal cations such as Am(III), Pu(III), Th(IV), and Pu(IV), thereby influencing the sorption behavior of radionuclides onto cement [43,44].

The transport of actinides from a nuclear waste repository is primarily governed by sorption and diffusion processes. Under the reducing conditions anticipated in such repositories, the trivalent and tetravalent species of actinides are expected to dominate [22]. Therefore, in this work, the actinides Am(III) and Th(IV) were used as analogues to redox-sensitive actinides such as Pu. Understanding the behavior of the actinides in the presence of other components is crucial for evaluating their transport and possible interactions. The competitive and synergistic effects were studied in detail in both binary systems with cement and organic materials and ternary systems with cement, organic materials, and actinides. By studying these complex systems, it is expected that insights will be gained into the interplay of the different components and an assessment of their impact on the overall transport mechanisms of actinides in nuclear waste repositories. An overview of the different retention mechanisms on a solid phase is shown schematically in Figure 2.

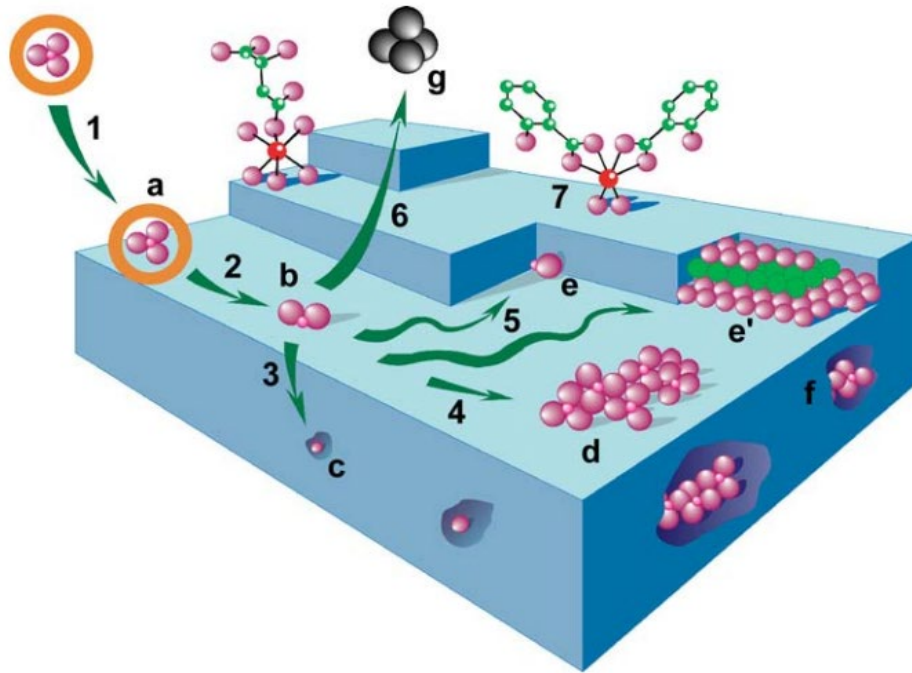


Figure 2: The different retention mechanisms; according to Charlet and Manceau [45]. Adsorption (1) in the form of an outer-sphere complex (a); loss of hydration sphere (2) and formation of an inner-sphere complex (b); diffusion into the crystal lattice (3) and isomorphous substitution (c); rapid lateral diffusion (4,5) and formation of a surface polymer (d); adsorption on a mineral growth front (e and e'); formation of surface polymer and incorporation into the host matrix after crystal growth (f). The adsorbed ion can eventually return to solution, for example, due to surface redox reactions or dynamic equilibrium (g). (7) Organic-mineral complexation [46].

1.2 Sorption

The sorption of actinides in a repository for radioactive waste is of significant importance because it makes a significant contribution to the immobilization of radioactive substances. Through sorption, actinides can be transferred from the liquid phase to solid materials, e.g., the host rock or cementitious materials, thereby reducing their mobility. This is important for ensuring that they remain in the repository during the emplacement period and are not released into the environment.

Sorption generally refers to a process in which a dissolved or gaseous substance (sorbate) adheres to a solid or liquid phase (sorbent). The reverse process, in which the sorbate detaches from the sorbent, is desorption. If the sorbate remains on the surface of the sorbent, it is referred to as adsorption. Adsorption involves the accumulation of molecules or ions on the surface of a solid or liquid, forming a thin layer. This process occurs due to attractive forces between the sorbate and the sorbent surface. The extent of adsorption depends on factors such as the surface area, porosity, and chemical properties of the sorbent

material. It is based on various mechanisms, with a broad distinction between physisorption and chemisorption. Physisorption is an unspecific interaction mediated by London forces, in which the hydration shell of the adsorbate remains intact, classifying it as an outer-sphere sorption. On the other hand, chemisorption relies on the formation of bonds between the adsorbate and sorbent. Since the hydration shell is lost during this process, chemisorption is categorized as inner-sphere sorption. Absorption involves the uptake or incorporation of the sorbate into the bulk or sorbent. It typically occurs when a liquid or gas permeates into a porous solid material. The absorbed substance becomes uniformly distributed within the sorbent, often undergoing physical or chemical changes in the process. Sorption processes are influenced by several factors, including temperature, pressure, concentration gradients, and the chemical nature of the sorbates and sorbents. Additionally, the kinetics of sorption can vary, ranging from fast, reversible processes to slower, irreversible reactions [47]. Sorption isotherms can be used to describe the sorption behavior of a sorbent in equilibrium at constant temperature. There are various models that consider a variety of factors. In the simplest case, the correlation between concentration and loading is linear, which is represented by the Henry isotherm. In this model, it is assumed that sorbates attach to the sorbent independently of each other, leading to no interaction and no saturation. However, due to increasing interactions at higher concentrations, the Henry isotherm is applicable only for small concentrations [48]. The Freundlich isotherm considers the increasing interaction between sorbate molecules as the loading increases. This results in more challenging sorption at higher loading, leading to a flattened curve in the Freundlich isotherm [49]. Langmuir isotherm describes sorption under the assumption that it occurs only in a monolayer. Interactions with other sorption sites, which are considered equivalent, are not considered. This also leads to a flattened curve in the Langmuir isotherm [50]. Figure 3 shows a schematic representation of the sorption isotherms mentioned, although the individual isotherms will be discussed in more detail later. Here, q stands for the loading of the sorbent (mass of sorbate in relation to the mass of sorbent) and $[C]$ for the concentration of sorbate in solution.

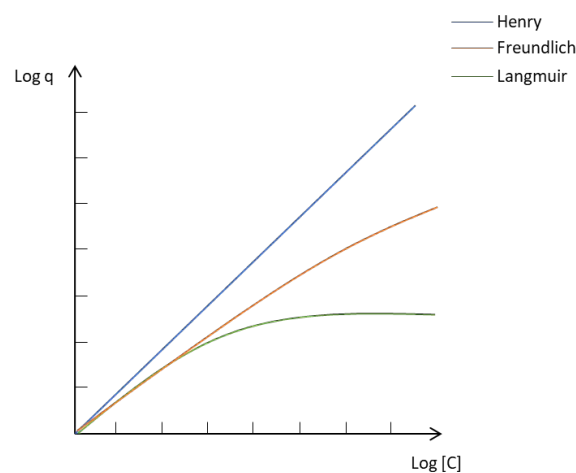


Figure 3: Schematic representation of the sorption isotherms with the loading of the sorbent $\log(q)$ and concentration of the sorbate in solution $\log([C])$ adopted according to [48].

Understanding sorption processes is crucial for assessing the long-term stability of a repository and predicting the behavior of actinides over a long period of time. It is important to know how strong sorption is, how it is influenced by organic ligands and how it changes over time. Therefore, in this work, the sorption of actinides under repository relevant conditions is studied in more detail. Experimental and theoretical approaches are used to analyze the sorption behavior and assess the impact on the safety of the repository. The aim is to develop a better understanding of the sorption processes and to provide a basis for the development of effective safety measures for repositories.

1.3 Diffusion

To better understand the mechanisms promoting the mobility of radionuclides and radionuclides in the form of organic complexes, it is important to investigate their diffusion behavior. During the storage period in geological formations or other barriers, such as cement, actinides can migrate from the waste into the environment, and diffusion is one of the most important mechanisms for this transport. It is a passive transport mechanism that takes place without external influence and is based on the random movement of particles in a liquid, gas or solid. The movement occurs along a concentration gradient, i.e., the particles diffuse from areas of high concentration to areas of low concentration in order to establish equilibrium. The rate of diffusion is influenced by several factors, including the physical properties of the medium in which diffusion takes place and the properties of the diffusing material itself. Parameters such as porosity, permeability, temperature, viscosity of the medium, the size and shape of the diffusing particles, and the interactions between the particles and the medium can influence the diffusion. In liquids and gases, diffusion occurs mainly through the movement of particles along their concentration gradient. In solid materials, diffusion occurs through the cracks or pores between particles. In this process, particles can diffuse either through the cracks between the particles (interstitial diffusion) or through the particle surfaces (surface-driven diffusion). Diffusion is described by Fick's law (equation (1)) and is a basic mathematical relationship that states that the flow of particles through a material is proportional to the concentration gradient.

$$J = -D_e \cdot \frac{\partial c}{\partial x}. \quad (1)$$

J is the diffusion current flux, D_e the diffusion coefficient, c for the concentration of the diffusing material and x for the spatial coordinate. The negative sign in the equation means that the diffusion flow is always along the concentration gradient, i.e., from the higher concentration to the lower concentration. The diffusion coefficient D_e is a material- and temperature-dependent constant that indicates the mobility of the particles in the medium. Fick's law describes the idealized case of Fick's diffusion, where the concentration of the diffusing substance varies continuously over time and space. It is important to

note that Fick's law presupposes certain assumptions, e.g., an isotropic structure of the material and a negligible interaction between the particles. It forms the basis for mathematical modelling of diffusion in different systems to analyze and understand the transport of particles and substances in different materials [51].

Knowledge of the diffusion processes is of significant importance for assessing the long-term stability of a repository and for predicting the behavior of actinides over a long period of time. Modelling and analysis of diffusion experiments can provide insight into how actinides move through barriers and how effectively they can be retained. In this work, therefore, the diffusion of actinide in a repository is studied experimental and theoretical approaches. The aim is to improve the understanding of diffusion processes and to provide a basis for the development of effective safety measures for repositories.

1.4 Speciation

A comprehensive understanding of the aquatic chemistry of actinides is essential for a wide range of processes and research efforts. It plays a significant role in various areas, such as the extraction of nuclear fuel from ores, the reprocessing of spent nuclear fuel, the development of secure long-term disposal methods for radioactive waste, and the study of actinide behavior in the environment. In the context of radioactive waste repository, understanding the solution chemistry of actinides is crucial for predicting their potential migration from the repository to the biosphere [52]. To fully comprehend the main retention processes, identify mobilization pathways, and assess the kinetics of relevant processes, a comprehensive and quantitative understanding is needed of the competing (geo)chemical processes that govern actinide concentrations in solution. The actinides include thirteen elements with atomic numbers 90 to 103, which are listed after actinium in the periodic table. In the context of nuclear waste management, uranium (U), plutonium (Pu), neptunium (Np), americium (Am) and curium (Cm) are particularly important actinide elements. Thorium (Th) is a naturally occurring element and may be present in certain types of L-/ILW, waste originating, for example, from research. However, it is mainly used as a redox-stable analogue for Pu(IV). In this work, investigations are conducted with Am(III), Th(IV) and Pu(IV) since the reducing conditions mainly lead to the oxidation states +III and +IV. By means of speciation calculations, statements can be made about the species present in solution depending on the pH value. This, in turn, can provide insights into whether the uptake on a mineral surface is expected for the respective complexes of the organic ligands and the actinides. The speciation calculations were conducted for the investigated systems in the binary system of background electrolyte and organics and in the ternary system with the influence of actinides. For the calculations carried out in May/June 2023, the program PhreePlot (version 1.0 [53]) using PHREEQC and the ThermoChimie database 11a, 2022 [54], which was current at that time, was used. If additional complexation constants from the literature were used for the calculations, this is noted at the appropriate place. The

concentrations of the elements contained in the solution used are given for each calculation. The ionic strength is corrected in the calculations by program PhreePlot (version 1.0 [53]).

1.4.1 Organic ligands

The calculations were conducted with a Ca concentration of 2×10^{-3} M in the binary system with the organic ligands GLU, EDTA and ISA ($[\text{OL}]_0/\text{M} = 1.0 \times 10^{-2}$). The Ca concentration refer to the concentration in the background electrolytes of the experiments with values from the literature [22,55]. Only in the case of EDTA do the calculations of the two background electrolytes C-S-H supernatant and Artificial Cement Porewater (ACW) lead to different speciation diagrams, which are discussed in the corresponding part of this Section.

GLU

D-gluconic acid ((2R,3S,4R,5R)-2,3,4,5,6-pentahydroxyhexanoic acid (HGLU)) is a polyhydroxy carboxylic acid. It is used in the cement industry, among others, mainly due to its weakly acidic character and the strong complexing ability of its deprotonated forms, including the D-gluconate anion (GLU^-) forming under near-neutral to hyperalkaline ($\text{pH} > 12$) conditions [35,56]. This is also shown in the speciation calculations in Figure 4. The chemical formula of D-gluconic acid is $\text{C}_6\text{H}_{12}\text{O}_7$, referred to as HGLU, or in its deprotonated state, known as alpha-D-gluconate, denoted as GLU. HGLU exhibits the ability to coordinate with metal ions by either coordinating the deprotonated carboxyl group in acidic solutions or adopting a bidentate mode by coordinating both the carboxylate and hydroxyl group(s) in more alkaline environments or with metal ions of high positive charge. The enhanced stability of gluconate complexes, compared to other monocarboxylic acids/salts, can be attributed to the presence of adjacent hydroxyl groups to the carboxylate anchor group, facilitating the formation of five-membered chelate rings. The formation of chelate rings has been observed in the literature for various metal ions, including actinides [57-59] and Ca(II) [35,56,60,61], and various others like transition metals, lanthanides, Al(III) and Pb(II).

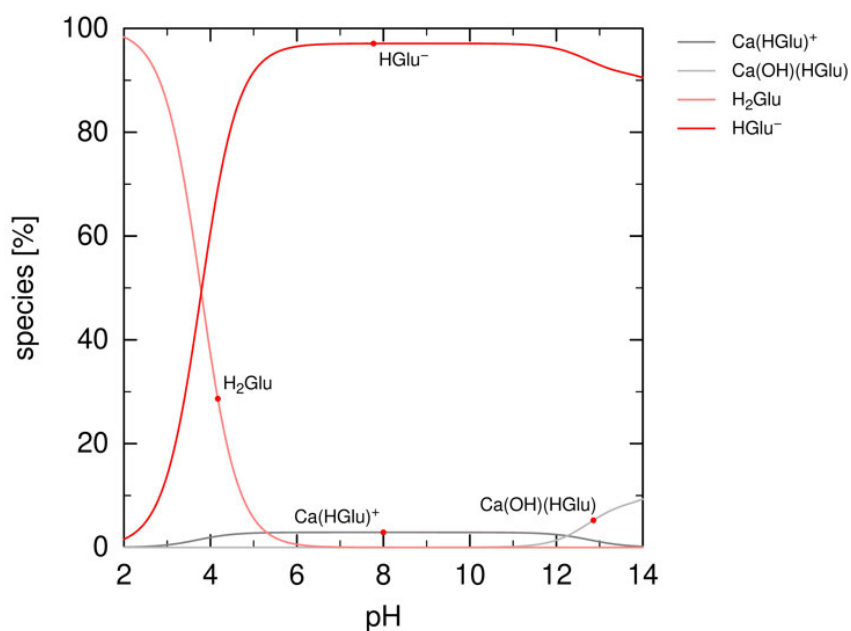


Figure 4: Speciation calculation of $1 \times 10^{-2} \text{ M GLU}$ and $2 \times 10^{-3} \text{ M Ca}$ (Graphic generated by PhreePlot (version 1.0 [53]) using PHREEQC and the ThermoChimie database 11a, 2022 [54]).

Sodium gluconate is commonly used in the cement industry as a retarding additive that slows down the curing process. The incorporation of gluconate into cementitious materials allows for high workability and plasticity, even with reduced water content, while also enhancing stability upon setting [62-64]. The presence of gluconate in cement and concrete, as well as its potential use in certain radioactive waste disposal concepts such as repositories for low- and intermediate-level waste, has raised concerns regarding the complexation of gluconate with radionuclides and the potential mobilization of these complexes from the repository into the biosphere. Numerous studies have demonstrated the strong complexation of gluconate with actinides and fission products [33,44,65-67]. In the case of An(III) and An(IV), these complexes exhibit further stability in the presence of calcium, with the proposed formation of ternary Ca(II)/An(III/IV) gluconate species observed in studies involving Nd(III)/Cm(III) [68] and Th(IV) [66]. Additionally, HGLU can also be considered as an analogous compound to ISA, a degradation product of cellulose, which is also a topic of investigation in this study.

EDTA

Ethylenediaminetetraacetic acid ($\text{C}_{10}\text{H}_{16}\text{N}_2\text{O}_8$) is a versatile chemical compound widely known for its chelating properties. It possesses a complex molecular structure with four carboxylic acid groups and two amine groups. The ethylenediaminetetraacetic acid anion can provide complexation through both the two free electron pairs of the nitrogen atoms and the four carboxyl groups, enabling it to bind to a

cation in a 6-fold manner. This capability allows it to create highly stable complexes, even with cations that typically exhibit low affinity for complex formation, such as Ca. The speciation calculation for EDTA shows differences due to its strong tendency to form complexes, especially when considering the different background electrolytes used in this study. The difference at high pH values can be attributed to the composition of the background electrolytes used in this work. The ACW used in the experiments comprises a mixture of 1.14×10^{-1} M NaOH and 1.8×10^{-1} M KOH, which explains the presence of both $\text{Na}(\text{EDTA})^{3-}$ and $\text{K}(\text{EDTA})^{3-}$ in Figure 5A. Consequently, since the Na-EDTA salt ($[\text{EDTA}]/\text{M} = 1.0 \times 10^{-2}$) was used in the experiments, $\text{Na}(\text{EDTA})^{3-}$ was calculated for the speciation in the C-S-H supernatant solution in Figure 5B.

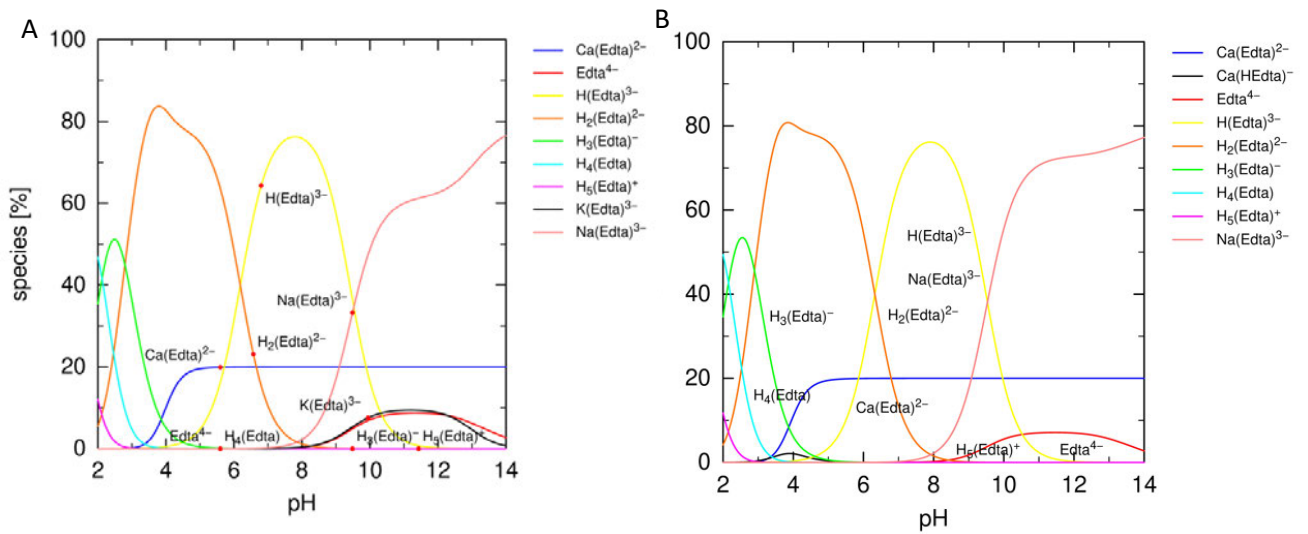


Figure 5: Speciation calculation of 1×10^{-2} M EDTA and (A): for the system HCP / ACW calculated with 1.14×10^{-1} M Na, 2×10^{-3} M Ca, 1.8×10^{-1} M K and (B): for the system C-S-H / Milli-Q calculated with 1×10^{-2} M Na, 2×10^{-3} M Ca (Graphic generated by PhreePlot (version 1.0 [53]) using PHREEQC and the ThermoChimie database 11a, 2022 [54]).

Furthermore, this property makes EDTA useful in various industrial and scientific processes. In the context of a repository for radioactive waste, EDTA's chelating properties make it potentially useful for binding and immobilizing radionuclides [69]. For instance, it could be incorporated into backfill materials or grouts used to encapsulate the waste to enhance their immobilization capabilities. Additionally, EDTA has found extensive use in the nuclear industry for various purposes. It has been employed in the processing of plutonium-containing wastes, the defense production of plutonium, and as a decontamination agent. The properties of EDTA make it a valuable tool in these applications, allowing for effective treatment and management of radioactive materials. Recent studies have revealed that the coexistence of EDTA with Pu has the potential to enhance the solubility and transport of Pu. This phenomenon is commonly attributed to the complexation of Pu(IV) with EDTA, which facilitates

its mobility in geologic environments. However, the mobilization of Pu(IV) by EDTA in such environments is influenced by several factors. These factors include the complexation constants between Pu and EDTA, the dominant oxidation state of Pu, the nature of Pu solids, and the presence of other environmentally significant metal ions such as Fe, Al, Ca, and Mg. It is important to note that these metal ions may compete with Pu for EDTA, thereby affecting its ability to form complexes with Pu. Moreover, the interactions between EDTA and the surrounding geologic media should also be taken into consideration [70]. The complexation of Pu with EDTA can have profound implications for the environmental mobility of this radionuclide. Under specific conditions, the formation of Pu-EDTA complexes may increase the solubility of plutonium and reduce its retention, thus influencing its potential mobility in the environment [39,70-72].

ISA

In calcium-rich alkaline solutions, it has been observed that the primary degradation product of cellulose is isosaccharinic acid ((2S,4S)-2,4,5-Trihydroxy-2-(hydroxymethyl)pentanoic acid), with an estimated overall yield of approximately 80% and therefore is expected to be one of the most abundant complexing agents in a repository [73-76]. The mechanism is shown in Figure 6.

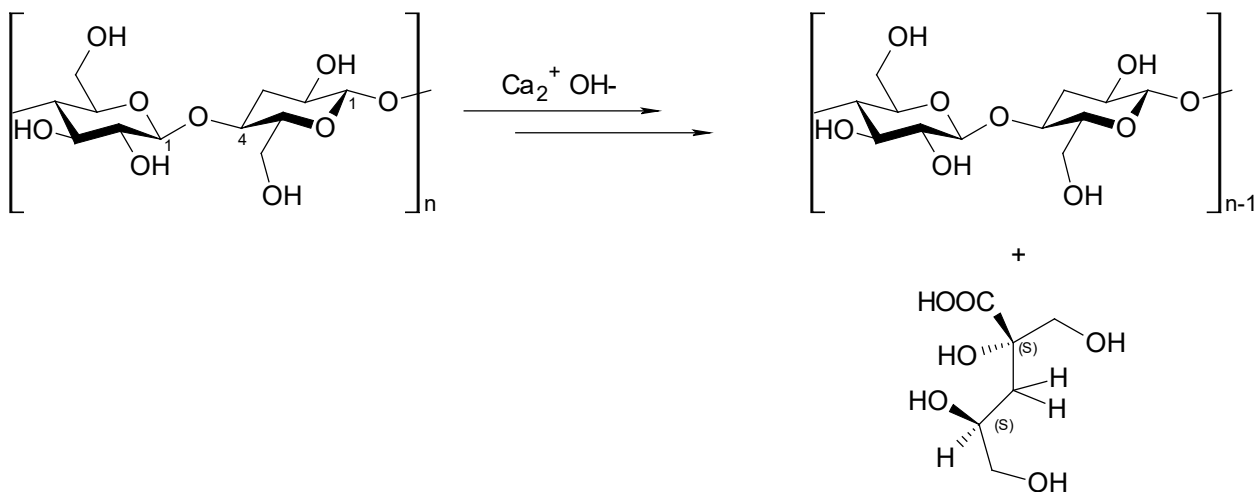


Figure 6: Repository-related decomposition of cellulose by $\text{Ca}(\text{OH})_2$ by benzylic acid rearrangement to *alpha*-D-isosaccharinic acid (2S,4S) [77].

The chemical formula is $\text{C}_6\text{H}_{12}\text{O}_6$, referred to as HISA, or in its deprotonated state, known as *alpha*-D-isosaccharinate, denoted as ISA. Two diastereomers can occur: *alpha*-D-isosaccharinic acid (2S,4S) and *beta*-D-isosaccharinic acid (2R,4S). The *alpha* (α)- and *beta* (β)-diastereomer forms of isosaccharinic acid were found to be present in equal proportions [77]. The degree of cellulose degradation over time was estimated in a recent study [37] using the kinetic model of Glaus et al. [73].

This model was based on a 12-year degradation experiment of four different cellulosic materials under artificial cement porewater conditions, was extrapolated to repository conditions and timescales (> 5000 years) using the reported reaction rate constants. The calculations indicate that the cellulose content of tissue and paper will be completely degraded (~99%) after 5000 years. However, in the case of cotton, the simulation suggests a lower degradation rate, with virtual completion expected only after 25,000 years. The study also estimated the concentrations of alpha-D-isosaccharinic acid, with and without considering the sorption of the ligand onto the available hydrated cement. The results indicate that in most of the relevant waste packages, the amount of HISA produced exceeds the capacity of the hydrated cement to remove it, suggesting that sorption processes do not significantly affect the concentrations of the free ligand in solution [37]. Further studies have indicated that alpha-D-isosaccharinate exhibits stronger complexing abilities towards metal ions compared to the beta-form. This observation was supported by the finding that the stability of the beta-isosaccharinate-Eu(III) complex was determined to be two orders of magnitude lower than that of the analogous species with the alpha-form. In further studies with Eu(III) and Th(IV), the alpha form was found to have stronger complexation properties [78,79] and is therefore of great importance because of its potential ability to mobilize radionuclides [74,80-82]. Like alpha-D-gluconic acid it belongs to the polyhydroxy carboxylic acids and could form complexes with metal ions. According to upper limit calculations, the concentrations of alpha-D-isosaccharinic acid reach the solubility limit of $\text{Ca}(\text{ISA})_2(\text{s})$ (2×10^{-2} M) in the pore and void volume inside the majority of the waste packages after 1000 years of cellulose degradation, specifically during the degradation stage II of cement. Even considering additional sorption processes of isosaccharinate in different compartments, the dissolved concentrations are only reduced to a maximum of 1.2×10^{-2} M, encompassing both the alpha- and beta-forms. If the ISA concentration is below 0.1 M, the aqueous ISA species dominates at a calcium concentration of < 0.01 M due to the deprotonated HISA species in the alkaline to hyperalkaline pH range [83]. The speciation calculations, which is shown in Figure 7, agree well with observations in the literature of Garcia et al. [42].

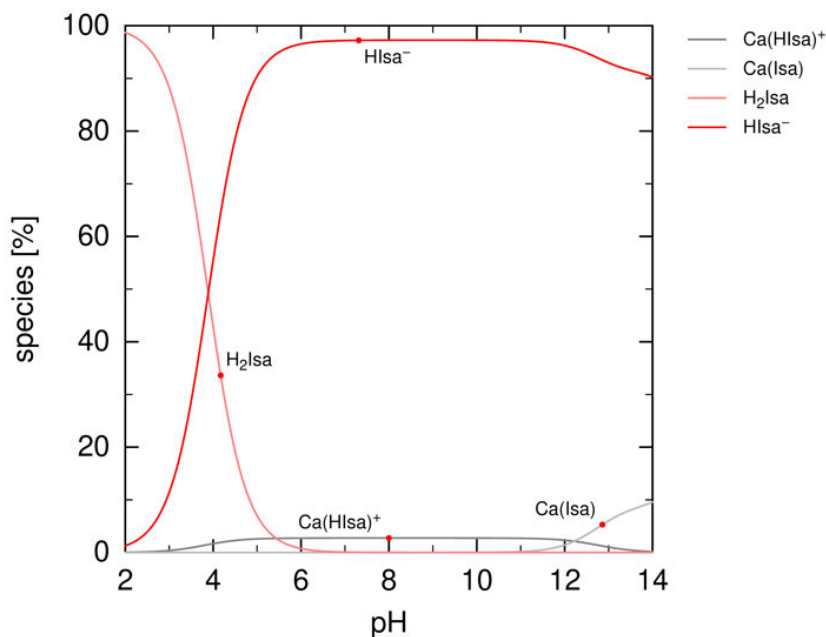


Figure 7: Speciation calculation of 1×10^{-2} M ISA and 2×10^{-3} M Ca (Graphic generated by PhreePlot (version 1.0 [53]) using PHREEQC and the ThermoChimie database 11a, 2022 [54]).

1.4.2 Actinides

To gain a better understanding of the An(III/IV) species ($[An]_0/M = 1 \times 10^{-8}$) in solution, speciation calculations were performed in the ternary system with the organic ligands ($[OL]_0/M = 1 \times 10^{-2}$) and the background ligands ($[Ca]_0/M = 2 \times 10^{-3}$) used in the experiment of this work. Disparities were partly observed in the calculations involving values from the ThermoChimie database (11a, 2022; [54]) and the complexation constants sourced from literature. This discrepancy can be partially addressed by considering recent studies that have provided additional complexation constants for systems involving organic ligands. If a complex has been reported by multiple sources, it is included in the database. However, further studies on these systems are still needed. A comprehensive discussion on this topic is provided in the relevant Sections of this Chapter. Understanding the speciation behavior of the actinides in the presence of different organic ligands, is crucial for the comprehension of the experiments performed, which are then applied to gain a better understanding in the processes of radioactive waste repository.

Americium

Americium was first produced in 1944 by Glenn T. Seaborg, Ralph A. James, Leon O. Morgan, and Albert Ghiorso using the 60-inch cyclotron at the University of California, Berkeley, as well as at the Metallurgical Laboratory of the University of Chicago [84]. Americium has various isotopes, but the most used ones are ^{241}Am ($t_{1/2} = 432.2$ years) and ^{243}Am ($t_{1/2} = 7370$ years) due to their long half-lives. Artificial production is the primary method for obtaining americium, typically in small quantities dedicated to research purposes. Approximately 100 grams of various americium isotopes, primarily ^{241}Am and ^{243}Am , can be found in one ton of spent nuclear fuel [85]. ^{241}Am is also used in industrial radiography, where it serves as a gamma-ray source for non-destructive testing of materials [86]. The main oxidation state of americium is +III. The other oxidation states +II, +IV, +V and +VI can also exist, but these are less common compared to the predominant +III state. The speciation calculations in Figure 8 provide insights into the behavior of americium in the presence of EDTA. It is observed that under the influence of EDTA, the complex $\text{Am}(\text{EDTA})^-$ forms and becomes the dominant species within a pH range up to 13. At higher pH values, the hydroxospecies $\text{Am}(\text{OH})_3$ begins to form, indicating the hydrolysis of americium ions in the alkaline conditions. The influence of EDTA decreases, as the $\text{Am}(\text{OH})_3$ species becomes dominant and EDTA no longer seems to have a significant impact on the speciation of Am.

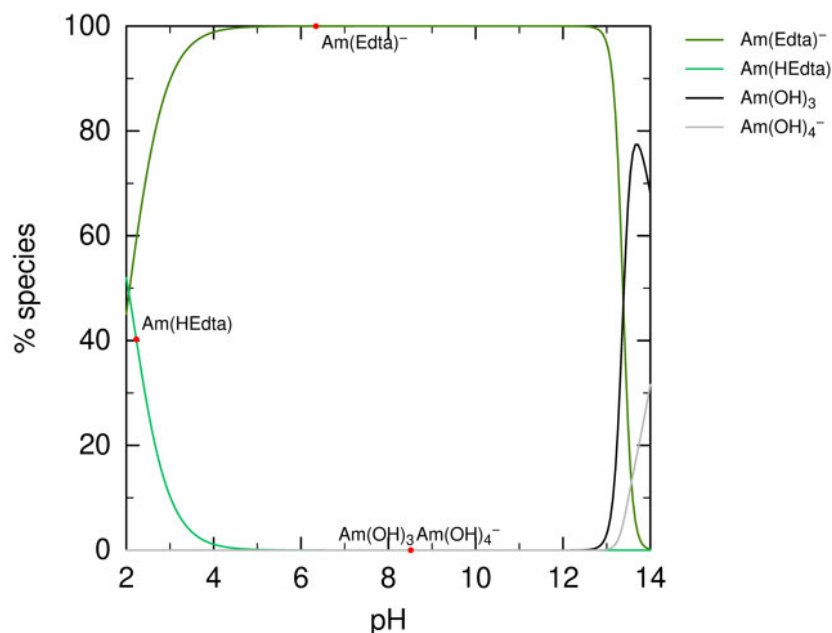


Figure 8: Speciation calculation of 1×10^{-8} M Am, 1×10^{-2} M EDTA and 2×10^{-3} M Ca (Graphic generated by PhreePlot (version 1.0 [53]) using PHREEQC and the ThermoChimie database 11a, 2022 [54]).

Thorium

Thorium is a naturally occurring radioactive element, which is relatively abundant in the Earth's crust. It is found in lesser amounts in various minerals, including monazite, thorite, and thorianite. It is also present in some granites and soils. Its most stable isotope is ^{232}Th with $t_{1/2} = 1.4 \times 10^{10}$ years and the thorium chemistry is dominated by the +IV oxidation state [87]. Thorium has been used as a fuel in nuclear reactors, particularly in certain experimental and research reactors. It can be used as a fertile material to breed the fissile isotope ^{233}U , which is capable of sustaining a nuclear chain reaction [88]. Furthermore, it has gained attention as a potential alternative to conventional nuclear power due to its abundance and potential for reduced waste production. It has certain advantages over uranium in terms of safety and waste management [89,90]. In the field of research, radioactive waste containing Th could be generated. Therefore, it is important to consider the behavior of Th(IV) in a radioactive waste repository. Additionally, Th(IV) is often used as a redox analogue for Pu(IV). This means that studying the behavior of Th(IV) can provide valuable insights into the behavior of Pu(IV) in similar environments. The calculations with GLU shown in Figure 9 indicate that at $\text{pH} > 6$, the following complexes are formed: $\text{Th}(\text{OH})_4(\text{HGLU})^-$, $\text{Th}(\text{OH})_4(\text{HGLU})_2^{2-}$ and $\text{CaTh}(\text{OH})_4(\text{HGLU})^+$. As the concentration of Ca in the solution increases, the proportion of Ca complex also increases. However, according to references [32,33] in the literature, a neutral $\text{CaTh}(\text{OH})_4(\text{HGLU})_2$ complex is described to form with a stability constant $\log^*\beta^0 = -0.8 \pm 0.1$ under alkaline to hyperalkaline conditions, which is not included in the ThermoChimie database (see graphic in the Appendix Figure A1).

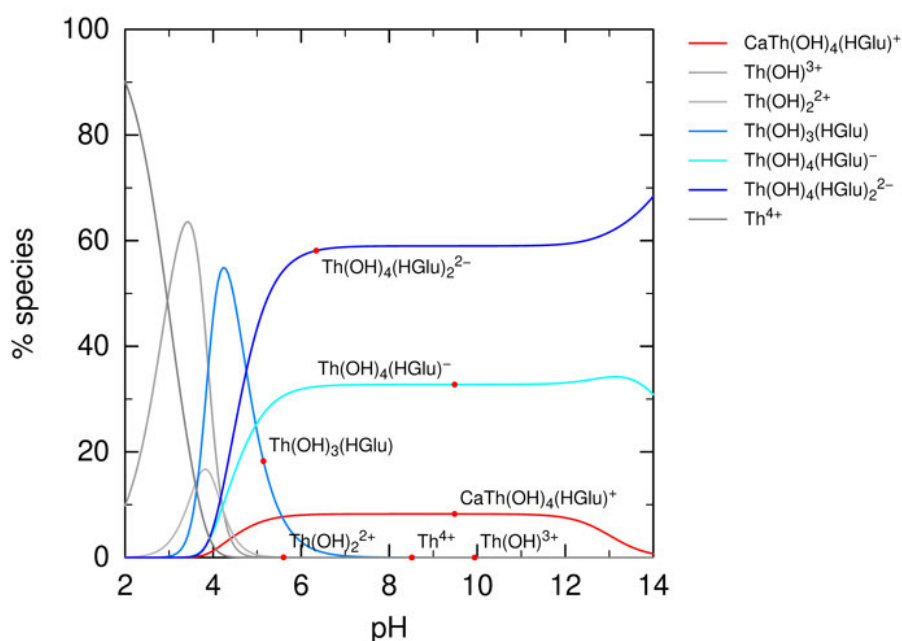


Figure 9: Speciation calculation of $1 \times 10^{-8} \text{ M Th}$, $1 \times 10^{-2} \text{ M GLU}$ and $2 \times 10^{-3} \text{ M Ca}$ (Graphic generated by PhreePlot (version 1.0 [53]) using PHREEQC and the ThermoChimie database 11a, 2022 [54]).

In Figure 10, the calculations with EDTA are shown. In the alkaline pH range (pH 7-11) $\text{Th}(\text{OH})_4(\text{EDTA})^-$ is the dominating species. Above pH 10, $\text{Th}(\text{OH})_4$ is the predominant species and EDTA no longer seems to form a complex with Th(IV). According to experiments of Xia et al. [91], the thermodynamic analyses indicating that monomeric mixed Th-OH-EDTA complexes dominate under basic conditions (pH > 9). Equilibrium constants were calculated for $\text{Th}(\text{OH})_2\text{EDTA}^{2-}$ ($\log K = 39.5$) and $\text{Th}(\text{OH})_3\text{EDTA}^{3-}$ ($\log K \sim 38.0$) species (see graphic in the Appendix Figure A2). The study also noted limitations of the solubility method due to EDTA chelator adsorption by the $\text{ThO}_2(\text{am})$ precipitate, requiring higher aqueous EDTA concentrations relative to the amount of precipitate for accurate examination of complexation with tetravalent actinides [91]. No literature has been found regarding the formation of a Ca-Th-OH-EDTA complex.

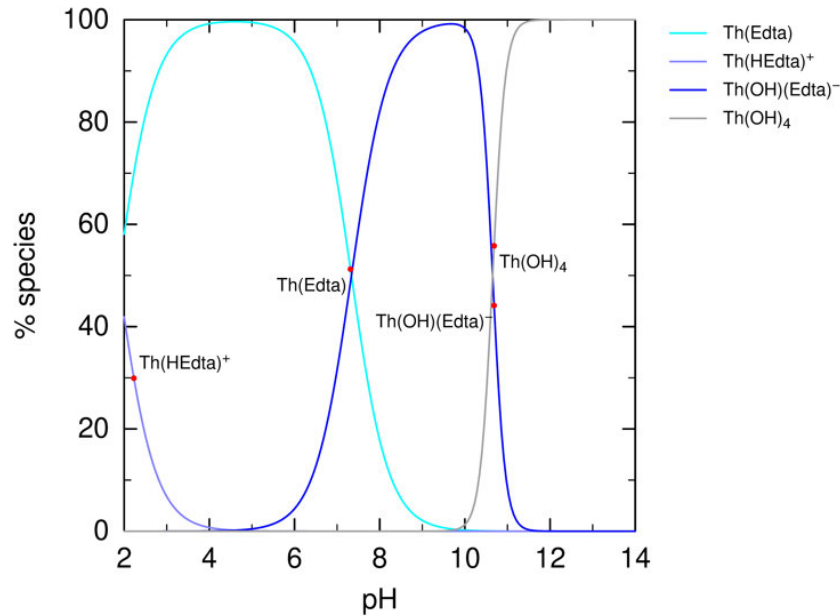


Figure 10: Speciation calculation of $1 \times 10^{-8} \text{ M Th}$, $1 \times 10^{-2} \text{ M EDTA}$ and $2 \times 10^{-3} \text{ M Ca}$ (Graphic generated by PhreePlot (version 1.0 [53]) using PHREEQC and the ThermoChimie database 11a, 2022 [54]).

The calculations with ISA as shown in in Figure 11 reveal a complex similar to the calculations with GLU. However, in the case of ISA, the $\text{Th}(\text{OH})_4(\text{HISA})_2^{2-}$ -complex is significantly more dominant, while the $\text{Th}(\text{OH})_4(\text{HISA})^-$ -complex is present to a lesser extent. Additionally, a positively charged Ca complex, $\text{CaTh}(\text{OH})_4(\text{HISA})^+$, is formed. It is worth noting that in the literature, the formation of a neutral complex, $\text{CaTh}(\text{OH})_4(\text{HISA})_2$, is also described with a stability constant $\log^* \beta^0 = -4.0 \pm 0.4$ under alkaline to hyperalkaline conditions [32,33,92], which is not included in the ThermoChimie database.

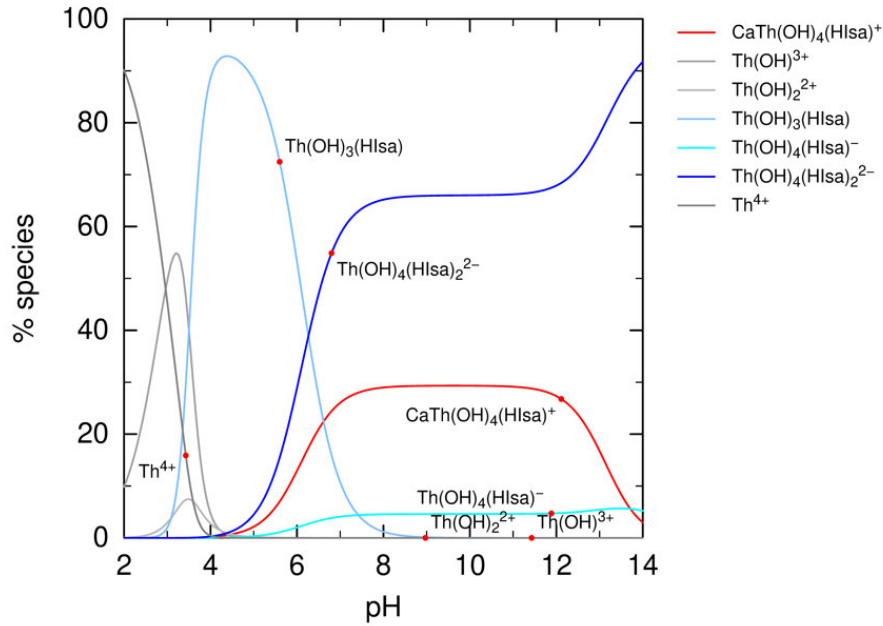


Figure 11: Speciation calculation of $1 \times 10^{-8} \text{ M Th}$, $1 \times 10^{-2} \text{ M ISA}$ and $2 \times 10^{-3} \text{ M Ca}$ (Graphic generated by PhreePlot (version 1.0 [53]) using PHREEQC and the ThermoChimie database 11a, 2022 [54]).

The speciation calculations for Th(IV) in the presence of the organic ligands oxalates and citrates are provided in Appendix (Figure A3 and Figure A4). Based on these calculations, it was determined that Th(OH)_4 is present in the hyperalkaline pH range. However, it is important to note that there are no complexation constants available in the literature for the formation of a complex of Th(IV)-phthalate. No calculations were performed for the speciation of Th(IV) in the presence of phthalate.

Plutonium

Only three years after its discovery and isolation in 1940 through the bombardment of ^{238}U with deuterons in a cyclotron facility at the University of California, Berkeley, the first production reactor for generating the ^{239}Pu isotope was established in Oak Ridge. The primary objective of this reactor was to develop the first nuclear bomb. ^{239}Pu ($t_{1/2} = 2.4 \times 10^4$ years) is a fissile isotope with a relatively high thermal neutron cross-section. It is formed in nuclear reactors through the conversion of ^{238}U and can also be intentionally added to fresh nuclear fuel, such as in mixed oxide fuels (MOX). When considering spent nuclear fuel and nuclear waste in general, it is crucial to take into account not only the presence of ^{239}Pu but also other isotopes of plutonium that hold significant importance, such as ^{241}Pu and the even-mass fertile isotopes (^{240}Pu and ^{242}Pu). These fertile isotopes are generated through sequential neutron captures of ^{238}U in the presence of thermal neutrons [84]. Pu exhibits the most intricate chemical behavior

among all metallic elements listed in the periodic table. Considering its electronic configuration, there are five stable oxidation states that can exist in aqueous conditions: Pu(III), Pu(IV), Pu(V), Pu(VI), and Pu(VII) [21]. These oxidation states have closely similar standard redox potentials, allowing for the possibility of up to four of them (+III to +VI) coexisting in the same aqueous solution. [87].

Limited information is available in the literature regarding the complexation of Pu(IV) with GLU. The calculations, which are shown in Figure 12 indicate the formation of two complexes, with $\text{Pu}(\text{OH})_4(\text{HGLU})^-$ being the predominant species in the alkaline pH range >7 . However, there is a lack of literature regarding the formation of a quaternary complex formation of Ca-Pu-OH-GLU. Additionally, the calculations for Pu(IV)-GLU system are not comparable to the behavior of Th(IV), which suggests less investigations specifically focused on the Pu(IV)-GLU system. Further research and investigation are necessary to understand the complexation behavior of Pu(IV) with GLU and the potential formation of quaternary complexes with Ca and to gain a better understanding to its similarities or differences with Th(IV) complexation. The discrepancies observed between the complexation behavior of Pu(IV) and Th(IV) with GLU can be attributed, at least in part, to differences in their solution chemistry. Pu(IV) has a smaller ionic radius ($r = 1.01 \pm 0.02 \text{ \AA}$) compared to Th(IV) ($r = 1.08 \pm 0.02 \text{ \AA}$). These differences in ionic radii could significantly affect their interactions with ligands such as GLU. Therefore, caution should be exercised when considering Pu(IV) and Th(IV) as redox analogues, as their distinct solution chemistries can lead to variations in their complexation behavior.

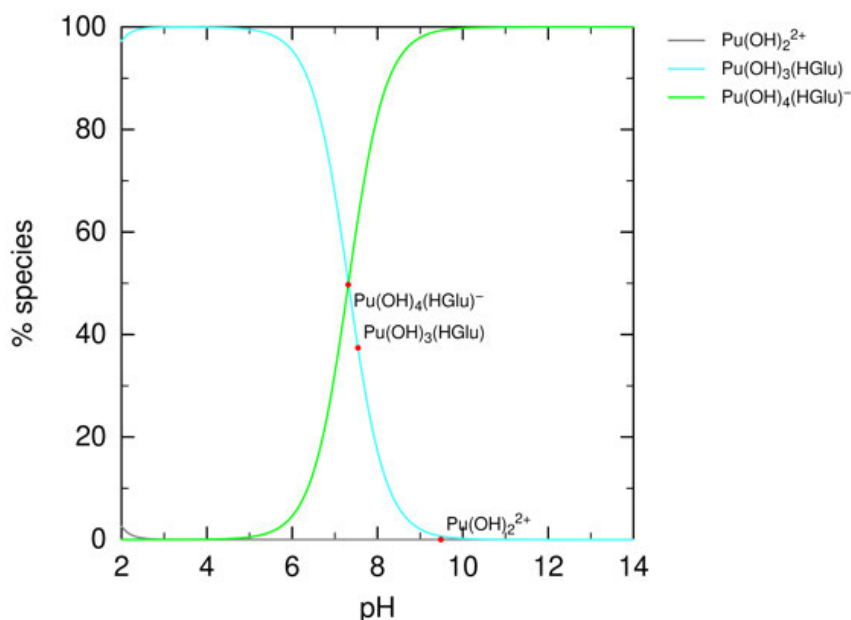


Figure 12: Speciation calculation of $1 \times 10^{-8} \text{ M}$ Pu(IV), $1 \times 10^{-2} \text{ M}$ GLU and $2 \times 10^{-3} \text{ M}$ Ca (Graphic generated by PhreePlot (version 1.0 [53]) using PHREEQC and the ThermoChimie database 11a, 2022 [54]).

Figure 13A shows the speciation calculations for EDTA. However, the current ThermoChimie database selection does not account for the formation of hydroxospecies in any of the An(IV)-EDTA systems. Nevertheless, recent literature provides evidence that these hydroxocomplexes play a dominant role in the aqueous speciation of An(IV) in the presence of EDTA under weakly acidic to hyperalkaline pH conditions. The calculations indicate that $\text{Pu}(\text{OH})_4$ is formed starting from pH 8, suggesting that Pu(IV) does not form complexes with EDTA in the alkaline pH range. Recent research by DiBlasi et al. [39] reports the influence of Ca(II) on the aqueous speciation of Pu(IV) in the presence of EDTA. An updated thermodynamic model has been developed, which includes the complexes $\text{Pu}(\text{OH})(\text{EDTA})^-$, $\text{Pu}(\text{OH})_2(\text{EDTA})^{2-}$, and $\text{Pu}(\text{OH})_3(\text{EDTA})^{3-}$. Solubility experiments conducted across a wide range of total calcium concentrations ($1 \text{ mM} < [\text{Ca}(\text{II})] < 3.5 \text{ M}$) strongly support the formation of quaternary $\text{CaPu}(\text{OH})_4(\text{EDTA})^{2-}$ complex. Additional calculations were performed considering the complexation constants of DiBlasi et al. [39], and the results are presented in Figure 13B. As a result of the stabilization effect of Ca(II) on the Pu(IV)-OH-EDTA system, the previously established redox boundary for Pu(III)/Pu(IV) aqueous species experiences a significant shift towards lower pH values. This shift expands the stability region of Pu(IV) species under conditions relevant to nuclear waste disposal. Similar to the calculations with Th(IV), differences are also evident in the calculations with Pu(IV), especially because no Ca complex is included in the calculation for Th(IV).

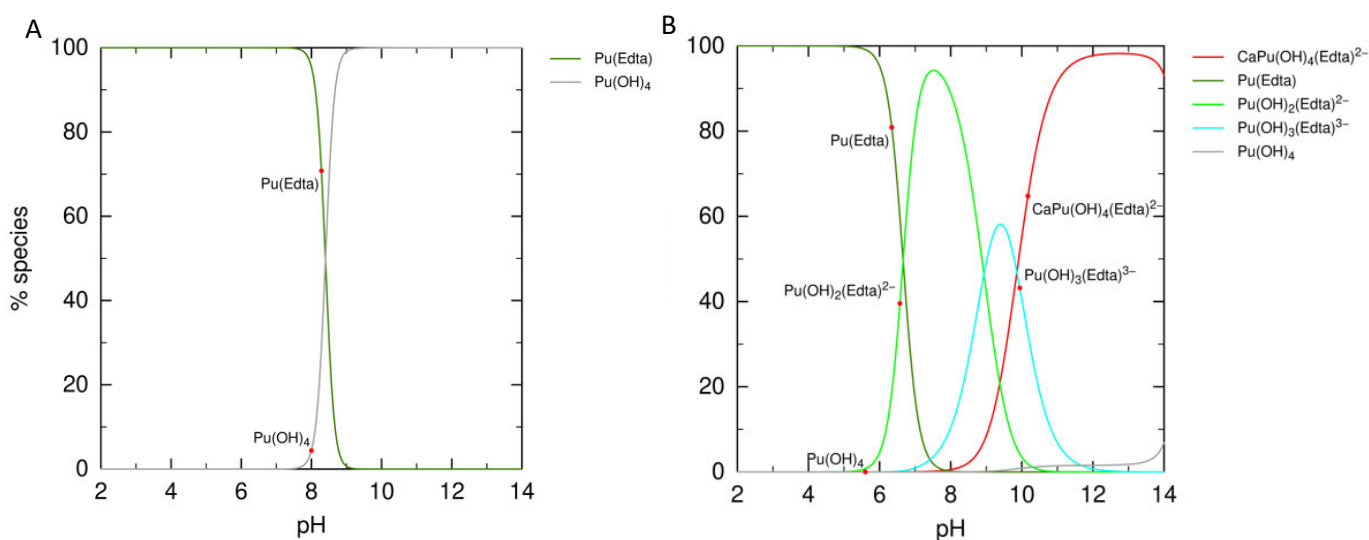


Figure 13: Speciation calculation of $1 \times 10^{-8} \text{ M Pu(IV)}$, $1 \times 10^{-2} \text{ M EDTA}$ and $2 \times 10^{-3} \text{ M Ca}$ (Graphic generated by PhreePlot (version 1.0 [53]) using PHREEQC and (A): the ThermoChimie database 11a, 2022 [54] and (B): complex formation constants determined by DiBlasi et al.[39]).

The speciation calculations for the Pu(IV)-ISA system are shown in Figure 14. In the ThermoChimie database, hydroxocomplexes for Pu(IV)-ISA are included, but there are no listed complexes with Ca(II). The calculations for the Pu(IV)-ISA system can be observed in Figure 14A. Similar to the calculations with EDTA, there are discrepancies of the ThermoChimie database and the literature. However, Tasi et al. have provided a comprehensive thermodynamic dataset for the Pu-OH-ISA [93] and Ca-Pu-OH-ISA [94] system, which was then utilized in the calculations presented in Figure 14B. Tasi et al. reported that ISA has a considerable influence on the solubility of Pu under alkaline to hyperalkaline pH conditions, particularly at higher total ISA concentrations ($m(\text{ISA}) \geq 10^{-3.5} \text{ M}$). The observed effect is pH-dependent, indicating the formation of Pu(IV)-ISA aqueous complexes with varying Pu-OH ratios. Additionally, in the presence of Ca(II), the formation of complexes such as $\text{CaPu}(\text{OH})_4\text{ISA}^+$ and $\text{CaPu}(\text{OH})_5\text{ISA}$ in the aqueous phase becomes possible. The calculations indicate that $\text{Pu}(\text{OH})_5\text{ISA}^{2-}$ species are present at pH values greater than 13. The differences between the calculations with ISA for Th(IV) and Pu(IV) are relatively small compared to other systems, mainly due to more extensive investigations conducted on the An(IV)-ISA system. However, the presence of different complexes in solution indicates that Th(IV) and Pu(IV) exhibit distinct behaviors.

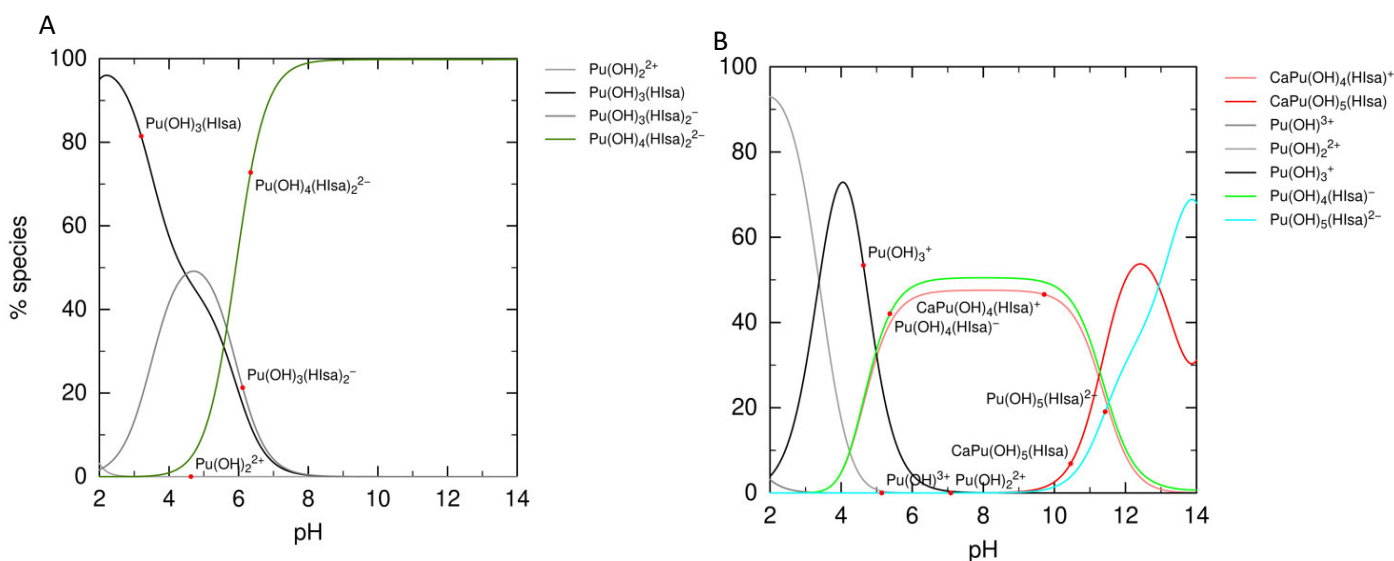


Figure 14: Speciation calculation of $1 \times 10^{-8} \text{ M}$ Pu(IV), $1 \times 10^{-2} \text{ M}$ ISA and $2 \times 10^{-3} \text{ M}$ Ca (Graphic generated by PhreePlot (version 1.0 [53]) using PHREEQC and (A): the ThermoChimie database 11a, 2022 [54] and (B): complex formation constants determined by Tasi et al. [93,94]).

1.5 Literature overview

This Chapter aims to provide an overview of the literature data available on the binary system of cement and the organic ligands, as well as the ternary system with An(III/IV). A briefly discussion is also presented on the available data for the binary system cement-An(III/IV), along with the recommended distribution ratios. Emphasis is placed on the experimental details of the studies discussed, as this information is valuable for the development of the experimental program in this PhD thesis.

Cement/organic

Limited information exists regarding the sorption of organic molecules on cement-based materials. However, it is important to consider this effect as an integral part of a comprehensive description of sorption phenomena. The substantial quantity and volume of cement-based materials present in a repository indicate that, even if the sorption of a particular organic molecule may be relatively low per unit mass, their presence can still have a significant impact on the behavior of organic molecules overall. Androniuk et al. conducted a study to investigate the interaction between gluconate and C-S-H phases with varying C/S ratios (0.83, 1.0, 1.4) [95]. The sorption behavior of gluconate on C-S-H phases has been investigated using a combination of wet chemistry and computational molecular modeling techniques. The findings regarding the sorption and desorption of gluconate at very low concentrations ($[GLU]/M = 10^{-8} - 10^{-5}$) on C-S-H have been obtained. The study revealed that sorption is a rapid process, while desorption is not fully reversible. The adsorption of gluconate is influenced by the Ca/Si ratio of C-S-H phases, with higher ratios exhibiting enhanced sorption ability, consistent with findings reported in previous literature [36,96]. Notably, the Ca/Si ratio has a significant impact on gluconate sorption on C-S-H phases, with stronger sorption observed at higher Ca/Si ratios. The sorption of organic anions on C-S-H phases are mediated by the presence of Ca(II) at the interface and strongly depends on the surface charge and Ca(II) concentration. Concurrently, the molecular-level structural properties of C-S-H interfaces have been examined, and specific adsorption environments have been identified using classical molecular dynamics (MD) simulations for Ca/Si ratios from 0.83 to 1.4. Gluconate sorbs onto the C-S-H phases through the formation of cation bridging inner-sphere and outer-sphere surface complexes [95]. Moreover, Nalet et al.[96] observed that GLU is influenced by the calcium counterions located on the surface of C-S-H when the Ca/Si ratio exceeds 1. They also described a linear correlation between the molecules' affinity for these C-S-H particles and their ability to form complexes with calcium. Glaus et al. [36] determined the distribution between hardened cement paste (HCP) and cement pore water of selected concrete admixtures (BZM), such as a plasticizer containing gluconate, which is used for waste conditioning at the Paul Scherrer Institute (PSI). A two-site Langmuir sorption model was employed to accurately fit the data. The sorption parameters, the affinity constant K and a sorption capacity factor q , for gluconate were determined as follows: $K_1 = (2 \pm 1) \times 10^6 \text{ dm}^3 \text{ mol}^{-1}$ and $q_1 = (0.04 \pm 0.02) \text{ mol kg}^{-1}$ for the stronger binding site, and $K_2 = (2.6 \pm 1.1) \times 10^3 \text{ dm}^3 \text{ mol}^{-1}$ and $q_2 = (0.7 \pm 0.3) \text{ mol kg}^{-1}$ for the weaker binding site [36]. Sorption data for GLU and ISA on hardened

cement pastes at degradation stages I (pH = 13.2) and III (pH = 11.9) over time are presented in Pointeau et al. [67]. The results demonstrate a kinetic evolution of sorption for both GLU and ISA. Initially, the sorbed content increased during the early ds (3 ds for stage I and 10 ds for stage III), but then a subsequent decrease was observed, eventually leading to near-complete desorption. The authors propose that this desorption process may be attributed to carbonation of the HCP grains. Cement-based materials are highly susceptible to carbonation, and sorption tests of GLU and ISA on calcite (CaCO_3) under pH 13.3 conditions showed no sorption. It is suggested that the formation of calcite on the surface of HCP grains could hinder the sorption of ISA and gluconate. This assumption is significant because the waters in the host rock contain carbonate ions, which could facilitate the degradation of cement pastes into stage IV, commonly referred to as the carbonated state [67]. Moreover, the interactions of ISA with cement-based materials have been investigated by several authors. Van Loon and Glaus [97] conducted a study on the sorption of ISA on cement pastes and C-S-H / C-A-S-H (calcium aluminosilicate hydrate) phases, which are the primary hydration products of cement pastes. The focus of the study was on α -ISA, which has been extensively investigated due to its well-known synthesis process and higher anticipated sorption and complexation capacities compared to β -ISA [98]. The sorption isotherm of α -ISA on Portland cement at pH 13.3 exhibited a good fit using a two-site model with Langmuir adsorption behavior. The parameters for the stronger binding site were $q_1 = 0.1 \pm 0.01 \text{ mol kg}^{-1}$ and $K_1 = 1730 \pm 385 \text{ L mol}^{-1}$, while for the weaker binding site, $q_2 = 0.17 \pm 0.02 \text{ mol kg}^{-1}$ and $K_2 = 12 \pm 4 \text{ L mol}^{-1}$ [41]. A recent study conducted by Tasi et al. [43] investigated the sorption of ISA onto cement in degradation stage II at pH 12.5. The modeling approach employed in the study provided insights into the sorption capacities and affinity constants, revealing $q_1 = 0.18 \pm 0.02 \text{ mol kg}^{-1}$ and $K_1 = 2510 \pm 500 \text{ L mol}^{-1}$ and $q_2 = 0.17 \pm 0.02 \text{ mol kg}^{-1}$ and $K_2 = 12 \pm 4 \text{ L mol}^{-1}$. It is noteworthy that ISA exhibits specific adsorption on C-A-S-H phases, as previously observed by Van Loon and Glaus [97]. Consequently, the derived sorption capacities are closely linked to the surface density of aluminate-like groups present in this solid phase. Moreover, the study highlights that the uptake of ISA by cement is considerable. As the relevant sorption sites on the hydrated cement paste approach saturation, there is a noticeable reduction in the zeta potential values of the suspended cement particles. This change occurs when the total ISA concentration $[\text{ISA}]_{\text{tot}}/M \geq -3.5$ at a solid-to-liquid ratio of 4 g L^{-1} . The observed transition from positive to negative surface charges on the HCP indicates a gradual alteration in the surface properties, particularly when the ISA coverage reaches around 25% [43]. Furthermore, the sorption of ISA on cement pastes at degradation stage II has been investigated by several researchers. Pointeau et al. [99] focused on CEM I cement pastes, while García et al. [42] examined CEM-V. The findings indicate that the sorption affinity of ISA is comparable between the two types of cement, except for the lowest concentration of ISA that was investigated. Limited information is available in the literature regarding the uptake of EDTA in cementitious materials. Pointeau et al. [99] conducted an investigation on the uptake of both ISA and EDTA on cement. The results suggest that the affinity of EDTA follows a similar trend to that of ISA, although only two R_d

values (distribution coefficient) were measured. For pH values of 13.2 and 11.9, the R_d values for EDTA were found to be 0.172 ± 0.04 and $11 \pm 6 \text{ mL g}^{-1}$, respectively. These values indicate a lower affinity compared to ISA, which exhibited R_d values of 5 ± 2 and $61 \pm 21 \text{ mL g}^{-1}$, respectively. Quantitatively, the sorption process is expressed by demonstrating the organic ligand and radionuclide loss from solution in terms of (solid-to-liquid) distribution ratios (R_d values in L kg^{-1} or in m^3kg^{-1}), respectively.

Cement/actinide

Significantly more investigations have been conducted on the interaction between actinides and cement, revealing a strong sorption of these elements by hydrated cementitious phases. In this work, as the investigation focuses on the influence of organic ligands on the sorption of An(III/IV), a literature comparison for the binary system An(III/IV) on cement is also conducted. In sorption studies focusing on cement-An systems, the determination of R_d values is influenced by various equilibria. These include precipitation processes, solid-solution formation, and adsorption onto available surfaces. Precipitation processes involve the formation of An as a separate solid phase through precipitation or surface precipitation, as well as co-precipitation with other metal ions. Solid-solution formation refers to the incorporation of An into the lattice structure of existing solid phases through diffusion or lattice incorporation. Adsorption onto available surfaces encompasses both physisorption (physical adsorption) and chemisorption (chemical adsorption) onto the surfaces of the cementitious materials. Experimental findings can help exclude precipitation and solid-solution formation processes, in which case the distribution ratio (R_d) is equivalent to the distribution coefficient (K_d). In this case, R_d represents the adsorption equilibrium between the solid and liquid phases of the system. The sorption process's evolution is influenced by the hydrated cement phases, as metal cations can undergo fast adsorption onto surface sites and, in part, be incorporated into the structure of the C-S-H phases through solid phase re-crystallization processes. Recent studies have provided clear evidence that trivalent (Eu(III)) [100] and tetravalent (Np(IV)) [101] actinides are incorporated into the C-S-H phases by structural incorporation, with the amorphous C-S-H phase identified as the primary solid phase responsible for the incorporation of An(III/IV) [22,102,103]. Trivalent actinides (Am(III)) and tetravalent actinides (Th(IV), Np(IV)) exhibit strong sorption behavior, as indicated by R_d values ranging from 10^5 L kg^{-1} to 10^7 L kg^{-1} . The uptake process for these actinides is rapid, occurring within 1-3 ds [103]. In the case of Pu(IV), the expected similar sorption behavior to Th(IV) across the pH range of interest (pH $\sim 8 - 13.5$) was not supported by the available data summarized by Ochs et al [22]. The data shows that the reported R_d values [104,105] for Pu(IV) uptake by the hydrated cement phases in state I (pH $\sim 13.5 - 12.6$) are consistently lower than those for states II and III. Considering the work conducted by Ochs et al. [22], a conservative R_d value of $5 \times 10^3 \text{ L kg}^{-1}$ was chosen for the sorption of Pu(IV) during this phase of cement degradation.

Cement/actinide/organic

Complexing ligands can have both positive and negative effects on the sorption of radionuclides onto hydrated cement phases. These effects can occur separately or simultaneously, influencing the overall sorption behavior. Complexes can form between the ligand and radionuclides in the solution, altering their speciation and potentially reducing their sorption onto cement surfaces. The presence of ligands can lead to the formation of complex structures involving both the radionuclide and the cement surface. These complexes may have different sorption characteristics compared to individual species. The ligand molecules can adsorb onto the available surface sites of the cement without competing with radionuclides, potentially affecting the overall sorption capacity. Ligands can compete with radionuclides for the available sorption sites on the cement surface, leading to a reduction in radionuclide sorption. The ligand may undergo surface precipitation, forming a solid phase on the cement surface. This can further influence the sorption behavior of radionuclides. In some cases, the ligand and radionuclide can form precipitates together, altering their mobility and sorption characteristics. Based on the current literature, the impact of the organic ligands on radionuclide uptake by cementitious materials is primarily attributed to complex formation with cationic radionuclides in the aqueous phase. This complex formation can result in a reduction in the associated R_d values, indicating a decrease in radionuclide sorption onto cement surfaces. To gain a comprehensive understanding of retention processes in complex materials such as cement, a mechanistic approach is necessary. An approach focuses on the behavior of the primary sorbing minerals, such as the C-S-H phases. To further explore the mechanisms of interaction between radionuclides, organic compounds, and cement, molecular dynamic simulation has emerged as a valuable and modern technique. In particular, the works of Androniuk et al. [95] and Androniuk and Kalinichev [106] have delved into the analysis of U(VI) and GLU interactions with C-S-H phases. By employing molecular dynamic simulation, these studies have contributed to an increased understanding of the underlying mechanisms governing these interactions. The formation of ternary surface complexes between uranyl hydroxides, Ca(II) cations, and the C-S-H phase at aqueous interfaces plays a significant role in the sorption process. When GLU is present, it facilitates the sorption of U(VI) on the C-S-H phase by weakening the binding of Ca(II) to the surface. Furthermore, the presence of Na^+ ions is found to compete for specific surface sorption sites, potentially impacting the equilibrium properties of the interface. These findings highlight the complex interplay between uranyl hydroxides, Ca(II) cations, gluconate, and Na^+ ions in the sorption process on the C-S-H phase. No additional literature regarding the uptake of An(III) or An(IV) in the presence of GLU at cement phases was found. In the absence of experimental data, Bradbury and Van Loon [76] made estimations for the sorption reduction factors of Ni(II) and its chemical analogues in hydrated cement. They assigned a reduction factor of 50 when in the porewater concentration was 4.6×10^{-2} M EDTA. Experimental evidence has also demonstrated that EDTA can have a temporary impact on radionuclide sorption. For instance, the sorption of Am(III) to hydrated cement was initially reduced in the presence of an EDTA concentration of 1.5×10^{-3} M reported by Allard and Andersson [107]. However, over a

period of weeks to months, the sorption increased to a point where the EDTA no longer affected the Am(III) concentration. Slower sorption kinetics were observed with a higher EDTA concentration of 3×10^{-2} M, but after one year, the Am(III) concentration reached the same level as in the absence of EDTA. Further and more recent studies have demonstrated their strong chelation capabilities towards trivalent and tetravalent actinides, leading to enhanced mobility of these radionuclides in different substrates [108,109]. However, Reinoso-Maset et al. [110] have shown that the impact of EDTA varies among different organic-radionuclide systems. For instance, the presence of EDTA did not affect the mobility of Cs in silica/sand matrices. Furthermore, the migration of U is only moderately influenced by EDTA, likely due to the presence of other cations in solution (e.g., Mg, Ca) that can form stronger complexes with EDTA than U. No literature references were found regarding the retention of An(IV) in the presence of EDTA on cementitious materials. In contrast, ISA, which is widely studied in the context of radioactive waste disposal, has demonstrated a high affinity for complexing radionuclides, particularly actinides [111,112]. In a study conducted by Diesen et al. [113], the impact of cellulose degradation products on cement was investigated. The researchers examined an artificial cement pore water with a pH of 12.5, containing a mixture of cellulose degradation products. Freshly precipitated solid europium hydroxide (Eu(III)) was introduced in varying amounts into the mixture. The solutions were then filtered, and Portland cement was added. Based on their measurements, the authors concluded that, under the given experimental conditions, the adsorption of the resulting organic europium complexes onto the cement was relatively low, with a maximum value of $< 9 \mu\text{mol Eu g}^{-1}$ of cement. This finding contrasted with previous literature reports on the adsorption of europium onto cement in the absence of organic degradation products. Holgersson et al. [114] conducted an early study on the cement-Th(IV)-ISA system, investigating the impact of ISA on the sorption and diffusion of Cs(I), Ni(II), Pm(III), and Th(IV) onto hydrated cement pastes. The experiments utilized synthetic fresh concrete porewater (NaOH, KOH in Milli-Q water) with a constant Ca(II) concentration of 4×10^{-2} M (saturated with portlandite). The cement pastes were pre-equilibrated for 3 months with the porewater before being exposed to porewater solutions containing radionuclides and organic additives. The concentrations of ISA varied at different pH levels. The porewater solutions used in the study contained different concentrations of ISA: 3×10^{-3} M at pH = 13.40, 5×10^{-3} M at pH = 13.42, and 3×10^{-2} M at pH = 12.67. The results showed high R_d values for Th(IV) uptake in the absence of ISA, while the presence of ISA significantly reduced Th(IV) sorption onto the hydrated cement pastes, with R_d values in the range of 10-20 L kg⁻¹. The Th(IV) concentration in solution remained high throughout the sampling period. Multiple studies conducted by PSI have reported on the uptake of Th(IV) by HCP and different C-S-H phases in the presence of ISA at the degradation state I at pH = 13.3 [40,82,97,102]. Prior to conducting the Th(IV) uptake studies, Wieland et al. investigated the stability of HCP (S/L ratio 0.1 – 5 g L⁻¹) in the presence of ISA ($10^{-5} < [\text{ISA}]/\text{M} < 0.3$). Their aim was to evaluate the dissolution of Ca-bearing hydrated cementitious phases based on the total concentration of the ligand in solution [40]. They demonstrated the impact of ISA on the chemical composition of the porewater in contact with

ordinary Portland cement paste can be described by assuming equilibrium solubility of portlandite and the formation of Ca(II)-ISA-OH species in solution. The total concentration of Ca(II) ranged from 1.6×10^{-3} to 2.8×10^{-3} M for ISA concentrations ranging from 10^{-5} M to 10^{-2} M. To ensure a maximum weight reduction limit for HCP ($\Delta_{\max} = 5$ w/w%), the authors determined the maximum “allowable” total ISA concentrations for the sorption experiments. These concentrations were set at 10^{-3} M and a S/L ratio of 0.1 g L^{-1} and 5×10^{-2} M and an S/L ratio of 5 g L^{-1} . The sorption data obtained in the HCP systems were comparable to those obtained with synthetic C-S-H phases, highlighting the significant involvement of C-S-H phases in the uptake of tetravalent actinides. Th(IV) concentrations significantly increased when $[\text{ISA}] > 10^{-4}$ M in the porewater. This concentration was identified as the “no effect concentration” for ISA in relation to An(IV) uptake by HCP during cement degradation states I and II [102]. The sorption data obtained by Holgersson et al. aligned well with the findings of Wieland et al., particularly at high ISA concentrations (2.7×10^{-2} M, pH = 12.67, $[\text{Ca(II)}] < 10^{-5}$ M, S/L = 50 g L^{-1}). However, the diminishing impact of ISA on Th(IV) sorption over time at lower ligand concentrations (3×10^{-3} M at pH = 13.40, 5×10^{-3} M at pH = 13.42) did not fit the overall trend observed by Wieland et al., possibly due to the higher limit of detection used in the measurements by Holgersson et al. The kinetics of the sorption process were found to be fast, reaching steady-state Th(IV) concentrations within 2 ds, indicating surface equilibria as the primary mechanism. The uptake of Th(IV), its complexation with ISA, and Ca(II) in solution were observed to be competing reactions. They assumed the $\text{CaTh(OH)}_4(\text{ISA})_2$ complex as the only predominating species in solution [40,102]. Baston et al. [115] investigated the sorption of Pu(IV) onto hydrated concrete and mortar powders at alkaline pH and different S/L ratios (20 and 200 g L^{-1}). They also conducted similar experiments in the presence of ISA at a total ligand concentration of 2×10^{-3} M to examine the ligand's impact on Pu(IV) uptake. The observed R_d values on concrete showed a significant decrease in the presence of the ligand, ranging from $R_d = 68$ to 190 L kg^{-1} under hyperalkaline conditions (pH ~ 12.4) [115]. In a recent study, Tasi et al. [43] investigated the uptake of plutonium by Portland cement in degradation stage II (pH ~ 12.5) in the presence of ISA under reducing conditions. Sorption experiments were conducted at various Pu ($\log[\text{Pu}]_{\text{in}} = -6$ to -9) and ISA ($\log[\text{ISA}]_{\text{in}} = -6$ to -2) concentrations and solid-to-liquid ratios (S/L = $0.1 - 50 \text{ g L}^{-1}$). The strong sorption of ISA onto cement particles resulted in a significant decrease in their ζ potentials when $\log[\text{ISA}]_{\text{in}} \geq -3.5$ at $\text{S/L} \leq 4 \text{ g L}^{-1}$. The sorption of Pu decreased notably when $\log[\text{ISA}]_{\text{in}} \geq -4.5$ due to the formation of aqueous Ca(II)-Pu(IV)-ISA complexes. Above approximately 25% surface coverage by ISA, there was an increased retention of Pu attributed to co-adsorption with ISA. The order of addition of individual components had a significant impact on the sorption kinetics of Pu, potentially spanning several years [43].

Diffusion

Although diffusion processes in HCP, concrete, and mortars have been studied in recent years, there is a scarcity of data available in the literature. The limited availability of diffusion data in cement-based materials can be attributed, in part, to the experimental challenges associated with working with these materials. The chemical conditions created by cement often lead to high adsorption and/or low solubility of many elements, making diffusion tests with moderately and highly sorbing species time-consuming (months to years). As a result, in through-diffusion experiments, the radioactive nuclide may not appear in the outlet deposit even after several months. Similarly, in in-diffusion experiments, the diffusion profile may be too short (only a few micrometers) to be adequately analyzed. In such cases, only the upper limit of diffusion coefficients can be estimated, and the true value remains unknown. Most of the existing data focus on the diffusion of conservative tracers such as tritiated water (HTO) or low-sorbing species like Cl^- and I^- [116-120]. A compilation of diffusion coefficients from safety analyses studies can be found in literature [102,121,122], which are typically associated with specific materials and/or chemical conditions relevant to each repository design. Different cement formulations exhibit notably different diffusion behaviors [123], making it challenging to draw definitive general conclusions. However, for a given formulation, it can be observed that the diffusion coefficient (D_e) decreases as the water-to-cement ratio decreases, indicating a less porous material [124]. A single study conducted by Yamaguchi et al. [125] focused on in-diffusion experiments with Pu in the presence of fulvic acid. The experiments were performed using compacted sand-bentonite mixtures under anaerobic conditions. The observed diffusive transport of Pu was significantly lower compared to that of HTO, Cs^+ , I^- , and $\text{Np}(\text{CO}_3)_2(\text{OH})_2^{2-}$. This difference is likely attributed to Pu being present in colloidal forms and the limited pore space in the compacted sand-bentonite mixtures, which restricts the diffusive transport of colloidal plutonium [125]. Additionally, regarding the influence of organics on radionuclide diffusion, Holgersson et al. [114] conducted through diffusion experiments to examine the impact of gluco-isosaccharinate on the diffusion of Cs, Ni, Pm, and Th in Portland cement. They observed breakthrough only for HTO and Cs, while no breakthrough was observed for Ni, Pm, or Th. The effect of the organic on Cs diffusion was considered negligible. Felipe-Sotelo et al. [126] investigated the migration of selenium in cementitious backfill (specifically Nirex reference vault backfill and OPC) in the presence of cellulose degradation products. After one year, no breakthrough was detected for either of the solids, which is consistent with the low solubility of selenium under alkaline conditions and the presence of calcium. Further, Felipe-Sotelo et al. [127] studied the diffusion of U and Th through intact cylinders of Nirex reference vault backfill using in-diffusion experiments and found no breakthrough for either U or Th, regardless of the presence of cellulose degradation products.

2 Manuscripts

3.1. Publication: Uptake of actinides by hardened cement paste in high-salinity pore water

Janina Stietz *, Samer Amayri, Verena Häußler, Raphael Scholze and Tobias Reich *

Minerals **2023**, 13(11), 1380; <https://doi.org/10.3390/min13111380> (published on 28th October 2023)

3.2.1 Publication: Uptake of Pu(IV) by hardened cement paste in the presence of gluconate at high and low ionic strengths

Janina Stietz *, Samer Amayri, Tobias Reich *, Verena Häußler and Damien Prieur

Front. Nucl. Eng., Sec. Radioactive Waste Management **2023**, Volume 2

doi: 10.3389/fnuen.2023.1268767 (published on 02nd November 2023)

3.2.2 Publication: Influence of gluconate on the retention of Eu(III), Am(III), Th(IV), Pu(IV), and U(VI) by C-S-H (C/S = 0.8)

Sophie Dettmann, Nina M. Huittinen, Nicolas Jahn, Jerome Kretzschmar, Michael U. Kumke*, Tamara Kutyma, Janik Lohmann, Tobias Reich*, Katja Schmeide*, Salim Shams Aldin Azzam, Leon Spittler and Janina Stietz

Front. Nucl. Eng., Sec. Radioactive Waste Management **2023**, Volume 2

doi: 10.3389/fnuen.2023.1124856 (published on 01st March 2023)

3.3 Manuscript: Investigation on cementitious materials with EDTA

Janina Stietz *, [REDACTED] *

In preparation for submission.

3.4 Manuscript: Sorption and diffusion experiments with HCP under the influence of ISA

Janina Stietz *, [REDACTED] *

In preparation for submission.

2.1 Publication: Uptake of actinides by hardened cement paste in high-salinity pore water

Author Contribution

The retention of An at HCP at high ionic strength was conducted as part of the GRaZ I project. Sample preparation and ICP-MS measurements for the batch sorption experiments were carried out by S. Amayri, R. Scholze, V. Häußler and J. Stietz. The CE-ICP-MS measurements were performed by J. Stietz and S. Leidich as part of J. Stietz's master's thesis under the supervision of V. Häußler and T. Reich [128]. The XAFS investigations were conducted by V. Häußler, S. Amayri and T. Reich. The conceptual planning of these investigations was accomplished by T. Reich. The manuscript was written by J. Stietz with contributions from S. Amayri and T. Reich. Further details can be found in the acknowledgements in the publication.


Summary

In the specific scenario of a prospective radioactive waste repository situated in Northern Germany with an argillaceous host rock, the aim of this study was to explore how ionic strength affects the retention of actinides by HCP during degradation stages II and III. The results show a strong interaction between actinides in oxidation states III/VI and HCP in diluted caprock solution (VGL, $I = 2.5$ M) within a pH range of 10–12.5. An actinide retention of over 99% was observed. This observation aligns with prior research conducted at low ionic strengths ($I = 0.1$ M). In connection with the analysis of the safety of a repository for radioactive waste, it can be concluded that the rate and extent of actinide uptake by HCP does not depend significantly on the ionic strength of the cement pore water. Regarding plutonium, a critical element in determining the long-term radiotoxicity of nuclear waste, XAFS measurements suggest that the primary mechanism of HCP's actinide retention at pH 12.5 involves the incorporation of Pu(IV) into the C-S-H phase. This study shows that data obtained at low ionic strengths can serve as a proxy for missing data associated with high ionic strengths.

© 2023 by the authors. Licensee MDPI, Basel, Switzerland. This article is an open access article distributed under the terms and conditions of the Creative Commons Attribution (CC BY) license (<https://creativecommons.org/licenses/by/4.0/>).

Article

The Uptake of Actinides by Hardened Cement Paste in High-Salinity Pore Water

Janina Stietz *, Samer Amayri, Verena Häußler, Raphael Scholze and Tobias Reich * 

Department of Chemistry, Johannes Gutenberg-Universität Mainz, 55099 Mainz, Germany; amayri@uni-mainz.de (S.A.)

* Correspondence: jastietz@uni-mainz.de (J.S.); treich@uni-mainz.de (T.R.); Tel.: +49-6131-39-36184 (J.S.); +49-6131-39-25250 (T.R.)

Abstract: The interaction of the actinides Pu(III), Am(III), Np(V), Np(VI), and U(VI) with hardened cement paste (HCP) prepared from ordinary Portland cement was investigated by batch experiments in a diluted caprock solution ($I = 2.5$ M) as a function of the solid-to-liquid (S/L) ratio (0.5–20.0 g L⁻¹) and pH (10–13). Independent of the oxidation state of the actinides, strong sorption was observed with R_d values between 10^4 and 5×10^5 L kg⁻¹. For the hexavalent actinides U(VI) and Np(VI), a decrease in sorption was observed with increasing pH, which could be due to the formation of the $\text{AnO}_2(\text{OH})_4^{2-}$ species. CE-ICP-MS measurements of the supernatant solution from the U(VI) batch sorption experiment at $\text{pH} \geq 10$ indicate that $\text{UO}_2(\text{OH})_3^-$ and $\text{UO}_2(\text{OH})_4^{2-}$ dominate the speciation. Pu L_{III}-edge XANES and EXAFS measurements showed oxidation of Pu(III) to Pu(IV) when interacting with HCP. Calcium silicate hydrate (C-S-H) phases effectively immobilize Pu(IV) by incorporating it into the CaO layer. This was observed in a C-S-H sample with C/S = 1.65 and HCP at pH 12.7. Compared to data published in the literature on the retention of actinides on HCP at low ionic strength, the influence of high ionic strength ($I = 2.5$ M) on the sorption behavior was insignificant.

Keywords: sorption; speciation; actinides; cement; high ionic strength; XANES; EXAFS; CE-ICP-MS



Citation: Stietz, J.; Amayri, S.; Häußler, V.; Scholze, R.; Reich, T. The Uptake of Actinides by Hardened Cement Paste in High-Salinity Pore Water. *Minerals* **2023**, *13*, 1380. <https://doi.org/10.3390/min13111380>

Academic Editors: Katharina Müller and Norbert Jordan

Received: 7 July 2023

Revised: 23 October 2023

Accepted: 24 October 2023

Published: 28 October 2023



Copyright: © 2023 by the authors. Licensee MDPI, Basel, Switzerland. This article is an open access article distributed under the terms and conditions of the Creative Commons Attribution (CC BY) license (<https://creativecommons.org/licenses/by/4.0/>).

1. Introduction

In many countries, a repository for high-level radioactive waste is to be constructed in a deep geological formation with several protective barriers. In Germany, possible host rocks for such a repository are clay rock, salt rock, or granite as natural barriers. Suitable clay formations can be found, for example, in Northern Germany, a region with pore and formation waters of medium and high ionic strength [1,2], which is well above 1 M and even up to 4 M at appropriate depths [3]. These values are significantly higher than in other clay formations (e.g., Switzerland, France, Belgium) considered as host rocks for nuclear waste repositories. In addition to the natural barrier of the host rock, the technical components of the repository also have an influence on the confinement of the emplaced radiotoxic waste. Cementitious materials are used widely as construction materials and engineered barriers in high-level waste (HLW) repositories and possess a high capacity for actinide retention [4–6]. Hydrated cement consists of different phases, such as portlandite, calcium aluminate/ferrite phases, and calcium silicate hydrate (C-S-H) phases, the latter having a mass fraction of 50–70% [4,7]. Actinides can be retarded by these phases due to their large surface area, microcrystalline structure with defect sites, and the presence of binding sites. The actinides can be adsorbed on the surface or incorporated into their structure, where the C-S-H phases play an important part in the sorption process of actinides (or radionuclides) on hardened cement paste (HCP) [8–13]. Potential contact with aqueous solutions, such as the inflowing saline groundwater, can lead to degradation of the cement, where the pH of the inflowing water increases. Furthermore, corrosion of the solid containers with the

radioactive waste leads to the release of actinides into the near field of the emplacement spaces [14–16]. For the corresponding safety assessment, studies on the retention of actinides by cementitious materials with regard to the high ionic strength of the pore water and its alkalinity (pH 10–13) in a cementitious environment are essential. It is important to know to what extent the findings obtained for low ionic strengths also apply to the description of actinide retention at high ionic strengths. Of particular interest are actinides with long half-lives that have a high contribution to the radiotoxicity of the waste, such as ^{239}Pu ($t_{1/2} = 2.411 \times 10^4$ yr), as well as ^{238}U ($t_{1/2} = 4.468 \times 10^9$ yr), ^{237}Np ($t_{1/2} = 2.144 \times 10^6$ yr), and ^{241}Am ($t_{1/2} = 432.2$ yr). Plutonium is very redox-sensitive and can occur in all oxidation states from +III to +VI in aqueous media. The low oxidation states +III and +IV are of particular interest due to reducing conditions in the repository, but the study of the higher oxidation states must also be included to gain a comprehensive insight into the chemical processes in a nuclear waste repository. The current literature contains mainly results of studies of actinide retention on cement at low ionic strength [14,17]. For tri-(Am(III)), tetra-(Th(IV), Np(IV)), and pentavalent (Np(V), Pu(V)) actinides, a strong sorption was reported with distribution ratios, R_d , between 10^5 L kg $^{-1}$ and 10^7 L kg $^{-1}$, as well as a fast (1–3 d) uptake kinetics. Also, for the hexavalent actinides (U(VI), Np(VI)), a strong sorption was observed with R_d values in the range of $\sim 5 \times 10^2$ L kg $^{-1}$ – $\sim 3 \times 10^6$ L kg $^{-1}$, but decreasing R_d values were observed with an increasing calcium-to-silicon (C/S) ratio of C–S–H phases in alkali-free conditions, as well as slower sorption kinetics onto cement pastes within ~ 30 d [17]. It was further observed that the hydrolysis of the actinides has a major influence on their retention in cementitious materials. The associated affinity of the different actinides for cement paste and C–S–H phases was explained by the concept of electrostatic inter-ligand repulsion [18]. In this concept, it is predicted that for each actinide in each oxidation state, the number of OH $^{-}$ groups in the first coordination sphere is limited [19]. The literature presents the following maximal number of hydroxyl groups for the investigated actinides: four (An(III)), four (An(IV)), two (An(V)), and four (An(VI)) [19]. Consequently, the actinide species An(III)(OH) $_4^{-}$, An(V)O $_2$ (OH) $_2^{-}$, and An(VI)(OH) $_4^{2-}$ are unable to form surface complexes with the silanol or silandiol groups of C–S–H phases. Therefore, these species are also described as non-sorbing species [18]. To our knowledge, there are only a few sorption investigations that have been performed at high ionic strength, e.g., on clay minerals, in the current literature. Stockmann et al. found no significant effect of ionic strength on the sorption of U(VI) onto montmorillonite [20].

In this work, the retention of Pu(III), Am(III), Np(V), Np(VI), and U(VI) on HCP prepared from ordinary Portland cement (OPC) was investigated by batch sorption experiments. The electrolyte was chosen to simulate the conditions expected for a nuclear waste repository in claystone formations of Northern Germany according to the “Standortmodell NORD” [1]. These pore waters are characterized by high salinity and an ionic strength of up to 2.5 M [1]. To identify the main processes involved in actinide retention and to obtain a molecular-level understanding, selected speciation measurements of the aqueous and solid phases were performed using CE-ICP-MS (capillary electrophoresis coupled to inductively coupled plasma mass spectrometry) and XANES/EXAFS spectroscopy (X-ray absorption near-edge structure/extended X-ray absorption fine-structure), respectively. The results obtained at 2.5 M ionic strength are compared with results at low ionic strength.

2. Materials and Methods

2.1. Materials

Experiments were performed in a glovebox under Ar atmosphere (Ar $\geq 99.99\%$, O $_2$ < 0.1 ppm). Solutions were prepared in Milli-Q water (18.2 M Ω cm, SynergyTM Millipore water system, Millipore GmbH, Germany) previously degassed with Ar. All chemicals used were from p.a. (pro analysis) quality grade. As a background electrolyte, a diluted caprock solution (VGL, German acronym for Verdünnte Gipshuttlösung) was chosen as a model solution for high saline pore water at the interface between clay and salt formations in Northern Germany [21]. It contains mainly 2.523 M NaCl (VWR Chemicals BDH

Prolabo[®], VWR Int., USA), 0.010 M CaCl₂ (CaCl₂ × 6H₂O, Merck, Germany), 0.008 M Na₂SO₄ (Merck, Germany) and 0.005 M KCl (Merck, Germany) with a pH of 8.0. Furthermore, the preparation of HCP powder (particle size of Ø < 63 µm) as the solid phase was based on DIN EN 196–3 [22], which has been slightly modified. Briefly, Portland cement (PZ Doppel N CEM 1 42.5 N, Dyckerhoff, Germany) was mixed with Milli-Q water to achieve a water-to-cement ratio (w/c) of 0.5. The paste was used to fill cylindrical molds and hardened for 48 h before the blocks were demolded and further stored in Milli-Q water for at least 28 d. The obtained HCP was crushed with a vibrating disk mill and sieved to a particle size with a diameter of Ø < 63 µm. The HCP powder was characterized by XRF, XRD, XPS, N₂-BET, and CEC measurements. A detailed description of these measurements and of the results can be found in the Supplementary Materials, Sections S1–S5.

2.2. Stock Solutions

A 1×10^{-5} M ²³⁹Pu(III) solution and a 6×10^{-6} M ²⁴¹Am(III) solution, each in 1 M HClO₄ (VWR Chemicals BDH, VWR Int., USA), were used for the Pu and Am sorption experiments, respectively. The preparation of these stock solutions is described in [23].

For sorption experiments with Np, ²³⁹Np was used as tracer in combination with a 6×10^{-4} M ²³⁷Np stock solution. The isotope ²³⁹Np was obtained by neutron irradiation of ²³⁸U (UO₂(NO₃)₂ × 6 H₂O diluted in Milli-Q water) at the research reactor TRIGA Mainz and separation of the ²³⁹Np from uranium and its fission products via anion exchange chromatography, as described in [24]. Hexavalent Np was prepared from the respective ²³⁷Np and ²³⁹Np stock solutions by fuming several times with 1 M HClO₄ (not to complete dryness). This oxidation state was stabilized by the addition of aliquots of 2 M NaClO (VWR Chemicals BDH Prolabo[®], VWR Int., USA) [25]. By adding NaNO₂ to the Np(VI) solution after fuming with HClO₄, Np(V) was obtained [24]. The stock solution of 4×10^{-5} M uranium was prepared by diluting an ICP-MS standard solution of ²³⁸U (Peak Performance, CPI International, USA) in 2% HNO₃.

2.3. Batch Sorption Experiments

Batch sorption experiments were conducted to investigate the influence of various contact times and solid-to-liquid (S/L) ratios, as well as to comprehensively evaluate degradation stages I–III [14] of hardened cement paste (pH 10–13) and their impact on actinide immobilization. For all sorption samples, HCP powder was weighed into 40-mL polycarbonate centrifuge tubes (Beckman Coulter, USA) and filled with VGL (prepared from its chemicals dissolved in Milli-Q water as described in 2.1) to achieve the required S/L ratio. Samples were preconditioned by shaking in an end-over-end rotator (Stuart Rotator SB3, UK) for 72 h. During this time, the pH increased from 8.0 to ~12.2–12.8. Before the addition of the actinides to the HCP suspensions, the pH was adjusted for eight days until the desired pH (10–13) was stable. Adjustments of pH were made with freshly prepared solutions of NaOH (CO₂-free; VWR Chemicals BDH Prolabo[®], VWR Int., USA) and HCl (Fisher Scientific, UK) ranging from 0.01 M to 5 M. Subsequently, aliquots of the respective actinide stock solution were added to obtain the following initial concentrations: 1×10^{-8} M Am(III), 1×10^{-8} M Pu(III), 8×10^{-6} M and 1×10^{-8} M Np(V), 1×10^{-8} M Np(VI), and 1×10^{-6} M U(VI). The samples were again rotated in the end-over-end rotator for 72 h and afterward centrifuged for 15 min at $3770 \times g$ (SIGMA 3K30, SIGMA Laborzentrifugen GmbH, Germany) and ultracentrifuged for 1 h at $108,800 \times g$ (Avanti J30I, Beckman-Coulter, USA). Finally, the pH value was again measured in all samples immediately after centrifugation. The equilibrium concentrations of the analyte in the supernatant $[An]_{eq}$ [M] and the initial analyte concentration in the sample $[An]_0$ [M] were determined as described in Section 2.4 and used to calculate the distribution ratio R_d

[L kg⁻¹] between the solid and liquid phases according to Equation (1), where V [L] is the sample volume and m [kg] is the total mass of the sorbent.

$$R_d = \frac{V}{m} \cdot \left(\frac{[An]_0 - [An]_{eq}}{[An]_{eq}} \right) \quad (1)$$

It should be noted that the phase composition of HCP changed during the course of the batch experiments. Due to contact with VGL, which is not in equilibrium with HCP pore fluid in stage I, HCP degraded to stage II, which is characterized by portlandite dissolution [14]. The C/S ratio of HCP powder before and after contact with VGL (S/L = 5 g L⁻¹ for 72 h, final pH = 12.8) was determined by X-ray photoelectron spectroscopy (XPS) (see Supplementary Materials for details). The XPS data show that the C/S ratio decreased from 3.4 to 2.6 due to the degradation of hydrated cement in VGL solution. During the subsequent pH adjustments in the preconditioned suspensions and after addition of the actinide tracer solution, the cement phase might have degraded further. In the pH range of 10–12.5, degradation stage III is reached, which is controlled by soluble C-S-H phases [14]. The pH values of electrolytes in equilibrium with synthetic C-S-H phases with C/S of 1.65 and 0.8 were reported as 12.5 and 10, respectively [26].

2.4. Analytical Methods

To quantify the concentrations of ²³⁹Np and ²⁴¹Am, γ -ray spectrometry was performed with an HPGe (GMX–13180-S, EG & G ORTEC, USA) coaxial γ -ray detector, Canberra InSpector 2000 (model IN2K, Canberra Industries, Inc., USA), in combination with the Genie 2000 Gamma acquisition and analysis software (Canberra Industries, Inc., USA). Calibration of the spectrometric system was carried out with a mixed radionuclide- γ -ray standard reference solution No: 7601 (Eckert und Ziegler, Germany). The resulting limits of detection (LOD) were 3×10^{-16} M for ²³⁹Np and 1×10^{-11} M for ²⁴¹Am, respectively.

Inductively coupled plasma mass spectrometry (ICP-MS) was performed with a 7500ce Series ICP-MS (Agilent Technologies, USA) to quantify ²³⁸U, ²³⁷Np, and ²³⁹Pu. For ICP-MS measurements, aliquots of the samples were diluted in 2% HNO₃ (VWR Chemicals BDH Prolabo®, VWR Int., USA), and 200 ppt ¹⁹³Ir was added as internal standard. The LOD of ICP-MS measurements of ²³⁸U and ²³⁹Pu were 1×10^{-11} M and 2×10^{-10} M, respectively.

To determine the pH values, a pH meter (WTW ino Lab. pH Level 1, WTW GmbH, Germany) with a BlueLine 16 pH electrode (Schott Instruments GmbH, Germany) was used, calibrated with the certified commercial DIN buffers at pH 4.01, 6.87, and 9.18 (Schott Instruments GmbH, Germany). High pH values above this calibration range were checked with a certified DIN buffer at pH 13.00 (Hanna Instruments, USA), where the resulting pH value was 12.89, indicating an uncertainty of $\Delta\text{pH} = 0.11$ by using this calibration. At high ionic strengths ($I > 0.1$ M), as in the VGL solution, the measured pH values must be corrected since deviations are caused by the activities of the ions in the electrolyte solution of the electrode and in the sample solution [27]. A correction parameter ($A = 0.41$) was empirically derived by using NaCl solutions with known H⁺ concentrations at different ionic strengths. This parameter was subsequently added to the experimentally measured pH (pH_{exp}), resulting in the corrected pH (pH_C), i.e., $pH_C = pH_{exp} + A$. In the following, pH will be used as a representative for pH_C .

Redox potentials were measured by connecting a redox electrode (BlueLine 31 RX, reference system: Ag/AgCl, Schott Instruments GmbH, Germany) to the pH meter, which was checked with standard solutions of known potential (+220, +470, and +640 mV; Schott Instruments GmbH, Germany). The Eh values reported here were converted to the standard hydrogen electrode (SHE) by adding 210 mV to the measured redox potential.

2.5. CE-ICP-MS Measurements

To determine the speciation of $\sim 1 \times 10^{-8}$ M U(VI) in the aqueous phase at pH values between 10 and 13, the electrophoretic mobility of U(VI) in the supernatant of the batch

sorption experiments was measured by capillary electrophoresis (CE). This technique allows conclusions to be made regarding charge distribution and, thus, the complexation of uranium in solution. The CE (Agilent 7100, Agilent Technologies, USA) was coupled with the high sensitivity of ICP-MS (Agilent 7500ce, Agilent Technologies, USA) using a MiraMist CE nebulizer (Burgener Research, Canada), which led into a Scott-type spray chamber (AHF Analysentechnik, Germany). CE-ICP-MS experiments were performed as described in [28]. The high voltage U applied to the fused silica capillary (id. = 50 μm , $l = 76$ cm, Polymicro Technologies, USA) for the separation was set to 25 kV. To each sample, 2-bromopropane (Merck, Germany) was added as a marker for the electro-osmotic flow (EOF). To match the background electrolyte for CE as close as possible to that of the batch experiments, the electrolyte was prepared by contacting HCP (S/L = 10 g L⁻¹) in VGL for at least one week. Due to the high salt content in this background electrolyte, it had to be diluted 1:100 in Milli-Q water for ICP-MS measurements. This resulted in an ionic strength of $I \sim 0.025$ M and a pH of 10.8. The sample (~16 nL) was introduced by hydrodynamic injection (100 mbar for 8 s) without prior dilution. The retention times in the electropherograms were obtained using MassHunter Workstation software (G7200B, Agilent Technologies, USA). The electrophoretic mobility μ_e of ²³⁸U was calculated from the retention times t and t_{EOF} of the uranium species and the EOF, respectively, according to Equation (2).

$$\mu_e = \frac{l^2}{U} \left(\frac{1}{t} - \frac{1}{t_{EOF}} \right) \quad (2)$$

2.6. XAFS Measurements

To obtain information on the speciation of Pu after uptake by HCP, Pu L_{III}-edge X-ray absorption fine-structure (XAFS) spectroscopy was used. Two HCP samples were prepared by batch experiments following the procedure described in Section 2.3. For the spectroscopic measurements, the Pu uptake by HCP had to be increased by using a higher initial Pu concentration (5×10^{-6} M ²³⁹Pu(III)) and a lower S/L ratio (2.5 g L⁻¹). The pH values of the HCP samples were 10.4, corresponding to aged cement (degradation stage III) and 12.7 for cement at stage II, respectively. Since C-S-H is the main constituent of HCP, one additional sample representative for cement degradation state II was prepared by contacting 5×10^{-6} M ²³⁹Pu(III) with a C-S-H (C/S = 1.65) suspension (S/L = 2.5 g L⁻¹) at pH 12.5 under Ar atmosphere. The C-S-H phase was synthesized by the reaction of appropriate amounts of SiO₂ (Aerosil 300, Evonik Industries AG, Germany) and CaO (ThermoFisher GmbH, Germany) in Milli-Q water for two weeks. For all samples, solid and liquid phases were separated by centrifugation, as described before. Afterward, the solids were dried under an Ar atmosphere at room temperature and placed as a homogenized powder into double-confinement oblong plastic holders transparent to X-rays. The samples were transported under a liquid nitrogen atmosphere to the European Synchrotron Radiation Facility (ESRF) in Grenoble (France). The Pu L_{III}-edge XAFS spectra were recorded at the Rossendorf Beamline (ROBL BM20) [29]. The ESRF storage ring was operated in 7/8 bunch mode. Samples were positioned in a closed-cycle He cryostat (CRYOVAC, Germany) and kept at 15 K during the entire measurement to prevent beam damage to the samples and to increase signal intensity. The tuneable synchrotron radiation beam was delivered by a Si(111) double-crystal monochromator (DCM). Two Rh-coated mirrors located before and after the DCM suppressed higher harmonic radiation. Multiple scans of Pu L_{III}-edge (18,057 eV) XAFS spectra were recorded in fluorescence mode using a 13-element Ge detector (Canberra, USA). For each scan, energy calibration was achieved by simultaneously recording the transmission spectrum of a Zr metal foil at the Zr K-edge (17,998 eV). The X-ray absorption near-edge structure (XANES) part of the XAFS spectrum was recorded with energy steps of 0.5 eV. The region of the extended X-ray absorption fine-structure (EXAFS) was recorded in k -space with 0.05 Å⁻¹ steps and gradually increasing counting time (2–20 s).

To determine the Pu oxidation state in the samples, the XANES spectra were analyzed by two methods: (i) The energy of the Pu L_{III}-edge, defined as the first inflection point of the absorption spectrum, was determined from the zero-crossing of the second derivative of the XANES. (ii) The module ATHENA of the software package Demeter (version 0.9.25) [30] was used to analyze the Pu L_{III}-edge XANES spectra by least-squares fitting. After energy calibration, the averaged Pu L_{III}-edge XANES spectra were modeled using published reference spectra of Pu(III) [31] and Pu(IV) [32] to determine the fractions of these oxidation states in the samples.

The software packages EXAFSPAK [33] and FEFF9 (version 9.6) [34] were used to analyze the EXAFS data. To calculate FEFF scattering amplitudes and phases, a structural model based on density functional calculations of the sorption modes of U(IV) in the C-S-H phase was used [35], where U in the CaO layer of the C-S-H was substituted by Pu.

2.7. Speciation Calculations

The speciation of U, Np, Pu, and Am in VGL in the pH range 10–13 was calculated using PHREEQC [36] in combination with thermodynamic data of the ThermoChimie database 12a, version 7 August 2023 [37]. The high ionic strength of VGL was taken into account by using the specific ion interaction theory (SIT) as implemented in ThermoChimie. Since Si can be released into VGL due to HCP degradation, the influence of Si on the actinide speciation was considered by adding 4×10^{-3} M Si to the composition of VGL, as provided in Section 2.1. It should be noted that VGL (pH = 8.0) contains 0.01 M Ca²⁺. Therefore, the possible formation of ternary actinide complexes with Ca²⁺ was also included in the speciation calculations based on the available thermodynamic data.

3. Results and Discussion

3.1. Batch Sorption Experiments

Sorption kinetics were studied using 1×10^{-6} M U(VI) and a S/L ratio of 1.0 g L⁻¹ in VGL at pH 11.9. The experiments were performed over a period of 5 min to 28 d. As shown in Figure 1a, the R_d values increased from 3×10^3 L kg⁻¹ at 5 min contact time to 6×10^4 L kg⁻¹ at 24 h, after which the uptake remained > 99%. Note that the sorption equilibrium was reached after only three days of contact. Results from the literature for C-S-H phases (C/S = 1.65, pH = 11.4–12.5) at low ionic strength are about one order of magnitude higher, with R_d values between 5×10^4 and 5×10^5 L kg⁻¹ [17]. It has been further described that the sorption proceeds in two steps [17]. After a very rapid initial uptake during about one day, R_d values continue to increase slightly until equilibrium is reached after about 30 days. For the C-S-H phases, the sorption kinetics is relatively fast, and a steady state is reached within about three days [17]. A similar observation was also made in previous studies of U(VI) uptake onto degraded cement pastes and C-S-H phases by Pointeau et al., which suggest that the initial uptake mechanism includes a surface sorption process, followed by a slow incorporation into the structure [38]. In addition, the literature reports that the sorption kinetics of U(VI) is very similar to that of pentavalent actinides but different from that of tri- and tetravalent actinides [17]. For the latter actinides, equilibrium was achieved within one day without a second slow sorption step [17]. Therefore, a contact time of three days was chosen for further experiments in this study.

The sorption of Am(III), Np(V), Np(VI), and U(VI) was studied at different S/L ratios from 0.5 to 15 g L⁻¹. In all cases, the actinide uptake exceeded 85% (see Figure 1b). In this experiment, a quantitative uptake of Am(III) by HCP was observed, even at a low S/L ratio of 0.5 g L⁻¹. Furthermore, both the pentavalent and hexavalent actinides show a similar sorption behavior after a contact time of three days.

In the sorption experiments at different pH values, an S/L ratio of 5.0 g L⁻¹ was used for Pu(III), Am(III), and Np(V) and 1.0 g L⁻¹ for U(VI), Np(VI), respectively. As can be seen in Figure 2a, pH has no effect on the uptake of Pu(III), Am(III), and Np(V). Independent of the actinide and its oxidation state, a high uptake of 99%, corresponding

to R_d values in the range between 1×10^4 and $2 \times 10^5 \text{ L kg}^{-1}$, was observed. Note that for the experimental conditions of the batch experiments, the following upper limits for the determination of sorption values apply: Trivalent actinides— $R_{d,max} = 2 \times 10^4 \text{ L kg}^{-1}$; Np(V)— $R_{d,max} = 2 \times 10^6 \text{ L kg}^{-1}$.

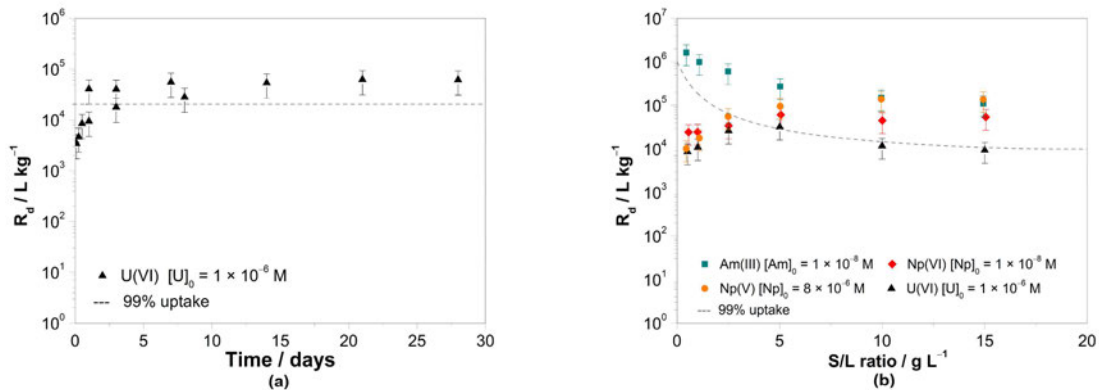


Figure 1. (a) Distribution coefficients R_d for the sorption of U(VI) on HCP in VGL for $S/L = 1.0 \text{ g L}^{-1}$ and $\text{pH} = 11.9$ after contact times of 5 min to 28 d and (b) for the sorption of Am(III), Np(V), Np(VI), and U(VI) on HCP in VGL for S/L ratios between 0.5 and 15.0 g L^{-1} at $\text{pH} \sim 10$ after three days of contact. A calculated actinide uptake of 99% is represented by the dashed line.

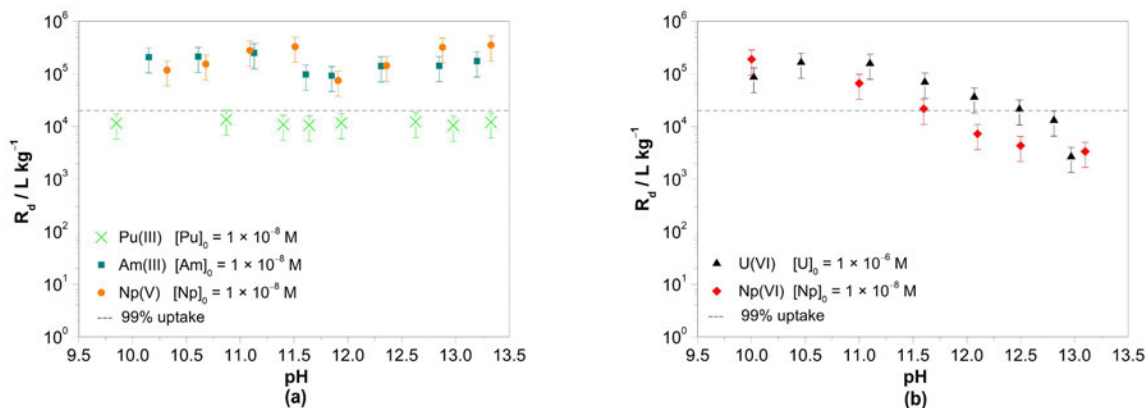


Figure 2. Distribution coefficients R_d for the sorption of (a) Pu(III), Am(III), and Np(V) at $S/L = 5 \text{ g L}^{-1}$ and (b) of U(VI) and Np(VI) at $S/L = 1 \text{ g L}^{-1}$ on HCP in VGL. A calculated actinide uptake of 99% is represented by the dashed line.

A significant influence of pH on the uptake of the hexavalent actinides, especially at high pH values, was observed (Figure 2b). A steady decrease in R_d values at $\text{pH} \geq 11$ from 1×10^5 to $1 \times 10^3 \text{ L kg}^{-1}$ (U(VI)— $R_{d,max} = 5 \times 10^6 \text{ L kg}^{-1}$; Np(VI)— $R_{d,max} = 1 \times 10^7 \text{ L kg}^{-1}$) is observed for both U(VI) and Np(VI), respectively. This observation at high ionic strength agrees well with the observations from the literature at low ionic strength [17].

The distribution coefficients for Am(III) ($R_d(av) = 2 \times 10^5 \text{ L kg}^{-1}$) determined in this study confirm the data known from the literature for the uptake of Am(III) by HCP at different degradation levels in the pH range 10–12 with R_d values between $2 \times 10^4 \text{ L kg}^{-1}$ and $2 \times 10^5 \text{ L kg}^{-1}$ [39]. Strong sorption of Am(III) on HCP at pH values of 12.5 and 13.3 was reported by Tits and Wieland, with R_d values between 10^5 and 10^6 L kg^{-1} [17]. Speciation calculations show that the dihydroxy species $\text{Am}(\text{OH})_2^+$ dominates in the pH range between 10 and 11, and the trihydroxy species $\text{Am}(\text{OH})_3(\text{aq})$ dominates above pH 11 [36,37], as well as in calculations at high ionic strength. The theory of electrostatic inter-ligand repulsion predicts that the limited number (n_{limit}) of OH^- groups that fit into the first coordination sphere of trivalent actinides is four and that the formation constants for adding a third or fourth OH^- group into the first coordination sphere of the metal

cation are similar [19]. This implies that the sorption of aquatic dihydroxy and trihydroxy Am(III) species is similar, agreeing with the observations shown in Figure 2a. The sorption of Am(III) on HCP at pH 10–13 is the same in all samples. For the redox-sensitive species Pu(III), values of R_d ($av = 1 \times 10^4 \text{ L kg}^{-1}$) were determined, which are about one order of magnitude lower than those for Am(III). However, the redox sensitivity of Pu required further considerations, so Eh and pH measurements of the supernatant solutions were performed. The Eh values obtained indicate that Pu(III) should be oxidized to Pu(IV) during the batch sorption experiment at pH 10–13, as can be seen in the predominance diagram in Figure 3a. This observation is discussed further in the following section using XAFS spectroscopy of Pu uptake on HCP.

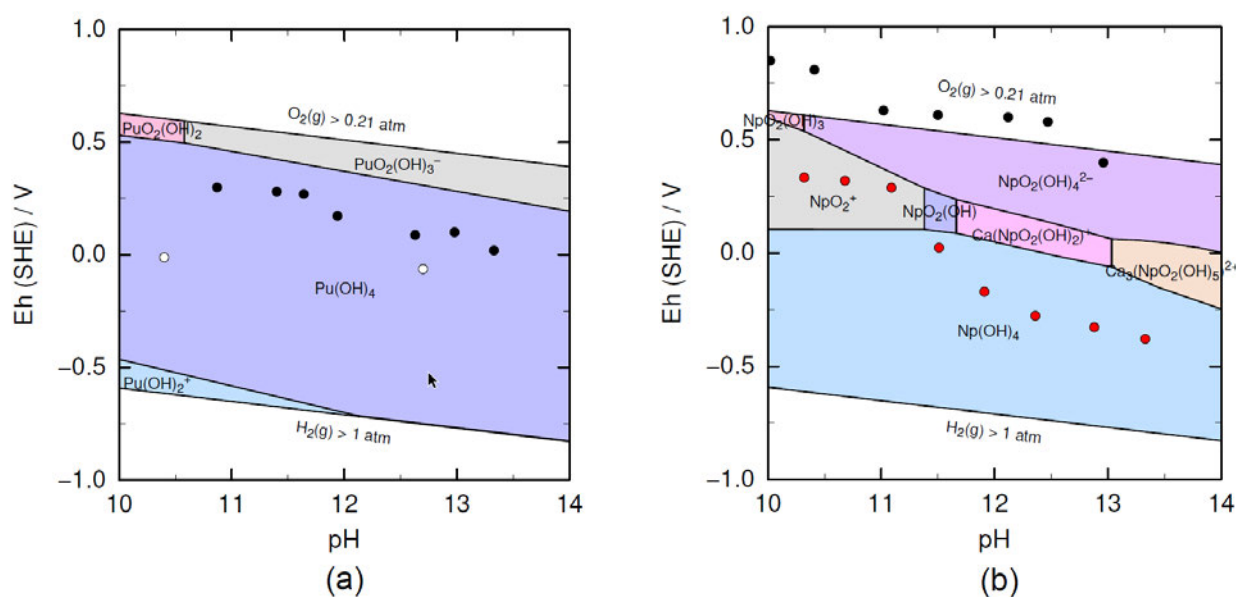


Figure 3. (a) Predominance diagram for $1 \times 10^{-8} \text{ M}$ Pu in VGL. The dots mark the measured Eh and pH values of the batch sorption samples (black dots) and of EXAFS samples (white dots). (b) Predominance diagram for $1 \times 10^{-8} \text{ M}$ Np in VGL. The dots mark the measured Eh and pH values of the batch sorption samples of Np(V) (red dots) and Np(VI) (black dots) in presence of $5 \times 10^{-3} \text{ M}$ NaClO. (Graphic generated by PhreePlot (version 1.0) using PHREEQC [36] and the ThermoChimie database 12a, 2023 [37]).

The R_d values determined for Np(V) are shown in Figure 2a. Between pH 10 and pH 13, the R_d values range between $1 \times 10^5 \text{ L kg}^{-1}$ and $4 \times 10^5 \text{ L kg}^{-1}$. The measured Eh-pH values (red dots in Figure 3b) and the thermodynamic calculations indicate that the redox state of Np in VGL changed from Np(V) to Np(IV) with increasing pH, i.e., from NpO_2^+ at pH 10–11 to $\text{Np(OH)}_{4(\text{aq})}$ at pH ≥ 11.5 (Figure 3b). However, the Np uptake by HCP does not seem to be affected by this change in speciation (Figure 2a). This agrees with the observation that the sorption of both Np(IV) and Np(V) on cementitious phases is very strong, with R_d values ranging from 10^5 L kg^{-1} to 10^7 L kg^{-1} [17]. To confirm the uptake of Np(IV) by HCP, XAFS measurements should be performed in the future.

The sorption of U(VI) and Np(VI) on HCP in VGL was also studied in the pH range 10–13 (Figure 2b). A pronounced effect of pH on actinide uptake by HCP can be seen for U(VI) and Np(VI), where the R_d values decrease in the pH range 11–13 by more than one order of magnitude (Figure 2b). For the discussion of these results, the speciation of both actinides should be considered.

Due to the addition of $5 \times 10^{-3} \text{ M}$ NaClO to the HCP suspensions, the measured Eh and pH values (black dots in Figure 3b) were outside the stability range of water, and the hexavalent Np oxidation state was stabilized in the pH range 10–13. This agrees with similar experiments performed by Gaona et al. [25].

In the case of uranium, the measured Eh and pH values (dots in Figure 4a) are in the stability field of U(VI). The dominating species are $\text{UO}_2(\text{OH})_3^-$ and $\text{UO}_2(\text{OH})_4^{2-}$ with nearly equal contributions at pH 12 (Figure 4a,b). The calculated speciation could be confirmed by CE-ICP-MS measurements. In Figure 4b, the measured electrophoretic mobilities μ_{eff} of U(VI) for the batch samples in the pH range 10–13 are shown and compared with the average ionic charge derived from the calculated speciation of U(VI) [36,37]. The measured mobilities of U(VI) follow the trend of the average charge of all U(VI) species (Figure 4b). For example, at pH 13, the average ionic charge is approx. -1.95 since $\text{UO}_2(\text{OH})_4^{2-}$ is the dominating species at this pH. Consequently, the largest negative electrophoretic mobility of approx. $-5.6 \times 10^{-4} \text{ cm}^2(\text{Vs})^{-1}$ was measured in the corresponding supernatant.

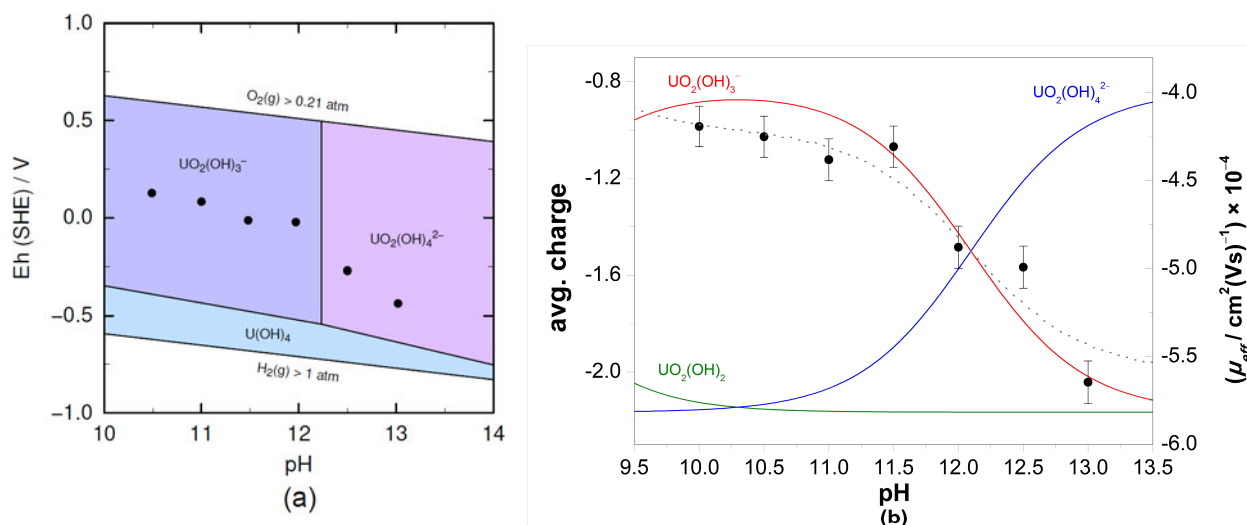


Figure 4. (a) Predominance diagrams for $1 \times 10^{-6} \text{ M U}$ in VGL. The dots mark the measured Eh and pH values of the batch sorption samples. (Graphic generated by PhreePlot (version 1.0) using PHREEQC [36] and the ThermoChimie database 12a, 2023 [37]). (b) Measured effective electrophoretic mobilities μ_{eff} of ^{238}U (black points) in the supernatant of the U(VI) batch samples. The calculated speciation of U(VI) (colored lines) was used to derive the average ionic charge of uranium complexes in dependence on pH (dotted grey line).

Several studies for the sorption of hexavalent actinides, especially U(VI) on cementitious phases, have been performed in the past. The R_d values for U(VI) sorption on different cement types in different degradation stages are relatively independent of salinity, pH, stage of degradation, and temperature and range from $\sim 2 \times 10^3 \text{ L kg}^{-1}$ to 10^4 L kg^{-1} [14,38,40]. In addition, the same effect observed in this study at high ionic strength was also observed in studies of U(VI) and Np(VI) on C-S-H phases at low ionic strength [17,18]. A decreasing R_d value with increasing pH is largely explained in the literature by hydrolysis effects, assuming that the species $\text{NpO}_2(\text{OH})_4^{2-}$ and $\text{UO}_2(\text{OH})_4^{2-}$ are non-sorbing species [18] (see Section 1). However, the observed sorption behavior could also be rationalized by the increase of electrostatic repulsion between the negatively charged U(VI)/Np(VI) species and the negative surface charge of HCP. Only for U(VI) and Np(VI) are species with a high negative charge formed by hydrolysis. For the other actinide oxidation states III–V, the hydrolysis species are positively charged or neutral (see Figure 3a,b). Therefore, the electrostatic repulsion from surface functional groups is less, and the sorption does not decrease with pH.

3.2. XAFS Measurements

Based on the Eh-pH measurements of the supernatant solution in the batch sorption experiments with Pu(III) (Figure 3a), its oxidation to Pu(IV) was expected. The Pu L_{III}-edge XANES was analyzed to obtain the Pu oxidation state after uptake from $5 \times 10^{-6} \text{ M Pu(III)}$ solution by HCP ($S/L = 2.5 \text{ g/L}$, $S_{\%} = 99\%$) in VGL at pH 10.4 and 12.7. In Table 1, the

energies of the absorption edge for the samples and of reference spectra of Pu(III)_(aq) and Pu(IV)_(aq) are summarized [41]. The corresponding Pu L_{III}-edge XANES spectra are shown in Figure S3. Both the Pu L_{III}-edge energies and the least-squares fits (Figure S3) show the presence of Pu(IV) as the dominant species, indicating that the initial Pu(III) was oxidized to Pu(IV) during the uptake of HCP. The same results were observed for the uptake of Pu by C-S-H with C/S = 1.65 at pH 12.5 (Table 1) and previously also for C-S-H with C/S = 0.8 at pH 10 [42].

Table 1. Pu L_{III}-edge energies derived from the inflection points of the XANES spectra of the studied samples in comparison to that of the Pu(III)_(aq) and Pu(IV)_(aq) aquo ions [41].

Sample	Energy/eV
HCP/Pu/VGL (pH 10.4)	18,062.0
HCP/Pu/VGL (pH 12.7)	18,062.1
C-S-H (C/S 1.65)/Pu/Milli-Q (pH 12.5)	18,062.0
Pu(III) _(aq)	18,060.0
Pu(IV) _(aq)	18,063.2

In addition, Pu L_{III}-edge k^3 -weighted EXAFS was analyzed to obtain structural and chemical information about the plutonium coordination environment after the uptake on HCP, including the identities and coordination numbers of the neighboring atoms and the bond distances to them. The EXAFS modeling was performed in k -space (2.1–10.9 Å⁻¹) without a window function. The maximum number of independent fit parameters was ten. Figure 5 shows the Pu L_{III}-edge k^3 -weighted EXAFS spectra with applied fit and the corresponding Fourier transform magnitudes. Note a monochromator-induced glitch in the EXAFS data at $k = 7.8$ Å⁻¹. In Table 2, the structural parameters are summarized. The raw EXAFS data could be best modeled with two coordination shells for the samples HCP/Pu/VGL (pH 10.4) and with three coordination shells for the samples of HCP/Pu/VGL (pH 12.7) and C-S-H (C/S 1.65)/Pu/Milli-Q (pH = 12.5). A Pu-Pu interaction indicative of polynuclear Pu species or precipitates was not observed in any sample. In all samples, the Pu-O distance ranges from 2.24 to 2.27 Å, indicating the tetravalent oxidation state of Pu, as reported previously [43]. This result agrees with the interpretation of the corresponding XANES analysis mentioned above. The sample of HCP/Pu/VGL at pH 12.7 could be modeled with two silicon atoms at 3.13 Å and four calcium atoms with an average Pu-Ca distance of 4.19 Å. This result fits well with the reference sample C-S-H (C/S 1.65)/Pu/Milli-Q (pH = 12.5) modeled with one silicon atom at 3.13 Å and five calcium atoms with an average distance of 4.17 Å. It is also consistent with the literature describing the incorporation of Pu(IV) into the CaO layer of the C-S-H phases by two Si atoms at 3.15 Å, five Si atoms at a larger distance of 3.54 Å, and six Ca atoms with 4.12 Å [42]. The observed Si and Ca coordination numbers of the samples HCP/Pu/VGL (pH 12.7) and C-S-H (C/S 1.65)/Pu/Milli-Q (pH = 12.5) agree well with the structural parameters obtained by density functional calculations for the incorporation of U(IV) into the CaO layer [35]. Furthermore, Gaona et al. [11] describe the uptake mechanism as the incorporation of Np(IV) into C-S-H phases based on the observed short distances for the Np-Si shell in combination with high coordination numbers of Si and Ca shells. The evaluation of the EXAFS measurements and the agreement of the spectra for HCP (pH = 12.7) with the spectra of the C-S-H phases also demonstrate that the C-S-H phase is the primary sorption phase of hardened cement paste, independent of ionic strength.

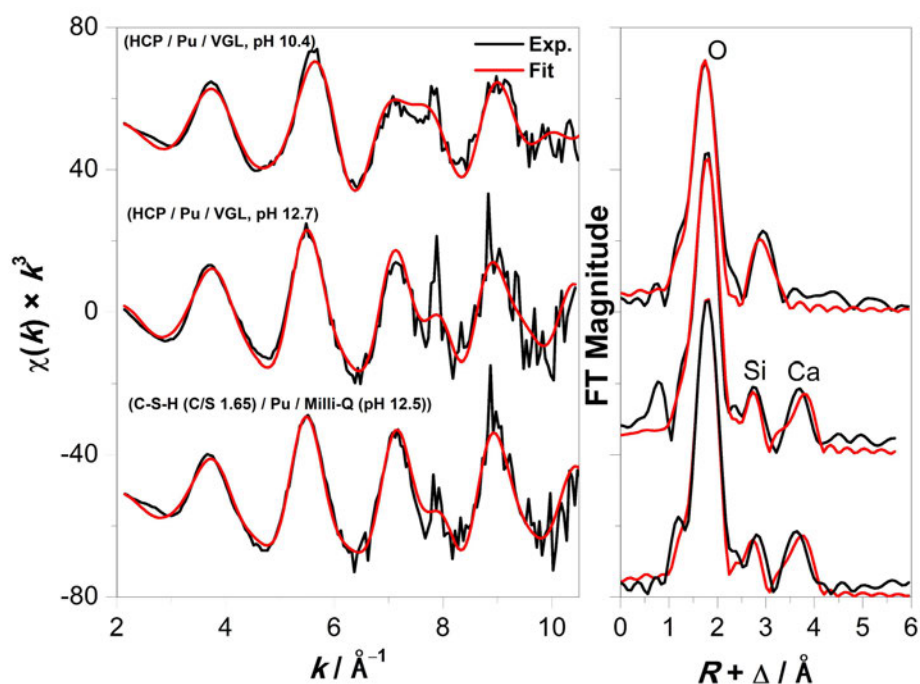


Figure 5. Pu L_{III} -edge k^3 -weighted EXAFS spectra (left) of Pu uptake on HCP and on C-S-H phases (C/S = 1.65) and the corresponding Fourier transform magnitudes (right). Black line: experimental; red line: best model.

Table 2. Structural parameters of Pu of the measured samples determined by Pu L_{III} -edge EXAFS spectroscopy with N —coordination number; R —distance; and σ^2 —Debye–Waller factor ($S_0^2 = 0.9$) and data from the literature for C-S-H with C/S = 0.8 [42]. * Linked to the Pu-O shell during the fit.

Sample	Shell	N	$R/\text{Å}$	$\sigma^2/\text{Å}^2$
HCP/Pu/VGL (pH 10.4) (norm. error = 0.2, $\Delta E_0 = 0.46$ eV)	Pu-O	$6.0 (\pm 0.2)$	$2.24 (\pm 0.01)$	$0.011 (\pm 0.001)$
	Pu-Ca	$2.1 (\pm 0.4)$	$3.41 (\pm 0.01)$	$0.008 (\pm 0.002)$
HCP/Pu/VGL (pH 12.7) (norm. error = 0.4, $\Delta E_0 = 2.11$ eV)	Pu-O	$7.4 (\pm 0.4)$	$2.27 (\pm 0.01)$	$0.011 (\pm 0.001)$
	Pu-Si	$1.7 (\pm 0.5)$	$3.13 (\pm 0.01)$	$0.008 (\pm 0.003)$
	Pu-Ca	$4.2 (\pm 1.3)$	$4.19 (\pm 0.01)$	$0.009 (\pm 0.003)$
C-S-H (C/S 1.65)/Pu/Milli-Q (pH = 12.5) (norm. error = 0.3, $\Delta E_0 = 1.31$ eV)	Pu-O	$6.0 (\pm 0.3)$	$2.27 (\pm 0.01)$	$0.008 (\pm 0.001)$
	Pu-Si	$1.2 (\pm 0.4)$	$3.13 (\pm 0.01)$	$0.006 (\pm 0.002)$
	Pu-Ca	$5.0 (\pm 1.3)$	$4.17 (\pm 0.01)$	$0.011 (\pm 0.002)$
C-S-H (C/S 0.8)/Pu/Milli-Q (pH = 10) (norm. error = 0.9, $\Delta E_0 = 0.26$ eV)	Pu-O	6.8 ± 0.3	$2.25 (\pm 0.02)$	$0.0119 (\pm 0.0004)$
	Pu-Si ₁	2.0 ± 0.3	$3.15 (\pm 0.02)$	0.0119 *
	Pu-Si ₂	4.6 ± 0.5	$3.54 (\pm 0.02)$	0.0119 *
	Pu-Ca	6.3 ± 1.0	$4.12 (\pm 0.02)$	0.0179 *

A considerable deviation was observed for sample HCP/Pu/VGL at pH 10.4, as no Pu-Si interaction could be modeled. In addition to the Pu-O shell, a Pu-Ca shell with two calcium atoms with an average Pu-Ca distance of 3.41 Å had to be included in the fit. An incorporation into the intermediate layers of the C-S-H phases, as observed for the other samples, seems unlikely here. This observation should be confirmed by additional EXAFS measurements.

4. Conclusions

The main objective of this work was the investigation of the influence of diluted caprock solution (VGL, $I = 2.5$ M) on the retention of actinides by HCP in degradation stages II and III. It was observed that actinides in oxidation states III–VI strongly interact with HCP in the pH range of 10–12.5. The corresponding R_d values determined after a contact time of three days range from 1×10^4 – 5×10^5 L kg⁻¹. This corresponds to an actinide retention of $\geq 99\%$. This general observation agrees with published results obtained at lower ionic strengths in the range of 0.1 M. Regarding the safety analysis of a nuclear waste repository, one can conclude that the kinetics and the degree of actinide uptake by HCP are not significantly dependent on ionic strength of the cement pore water. For the specific situation of a future nuclear waste repository in Northern Germany with an argillaceous host rock, sorption data obtained at low ionic strengths might be used as an estimate for missing data for high ionic strength.

For plutonium, which determines the long-term radiotoxicity of the nuclear waste, XAFS measurements indicate that the incorporation of Pu(IV) into the C-S-H phase is the main retention mechanism of HCP at pH 12.5. The result obtained for degradation stage II of HCP should also be verified for stage III at pH < 12.5.

Supplementary Materials: The following supporting information can be downloaded at <https://www.mdpi.com/article/10.3390/min13111380/s1>. Figure S1: XRD pattern of the HCP sample with $w/c = 0.5$ (size fraction <63 μm) and assignment of the reflections to portlandite, alite, calcite, and ettringite. The tobermorite could show the theoretical position of the most significant reflexes of C-S-H phases; Figure S2: Result of the XPS measurements of HCP powder ($w/c = 0.5$) before and after contact with VGL at pH 12.8 for 72 h. Ca-LMM and O-KLL denote Auger transitions. The other signals were assigned to the XPS lines of the contained elements; Figure S3: Normalized Pu L_{III}-edge XANES spectra of the samples HCP/Pu at pH 10.4 and 12.7 and C-S-H (C/S 1.65)/Pu at pH 12.5. The largest residual of all fits is shown as blue line. The raw data for the reference spectrum of PuO₂ were provided by P. Martin [32]; Table S1: Results of the XRF measurements for the main components of OPC and HCP in w%; Table S2: Results of the XRF measurements for the trace elements of OPC and HCP in ppm; Table S3: Atomic Ca/Si ratios of HCP before and after contact with VGL determined by XPS (the estimated uncertainty is about $\pm 10\%$); Table S4: N₂-BET specific surface areas of the HCP powder ($w/c = 0.5$ and size fraction <63 μm); Table S5: pH values, distribution coefficients R_d , percentage of sorption, CEC_{Na} with ²²Na⁺, and HCP (S/L = 67 g L⁻¹) in VGL and Milli-Q after 72 h contact time. The calculated site density for the surface areas is also listed. References [32,44–46] are cited in the supplementary materials.

Author Contributions: Conceptualization, S.A. and T.R.; investigations, S.A., V.H., R.S., J.S. and T.R.; formal analysis, J.S., S.A., V.H., R.S. and T.R.; writing—original draft preparation, J.S.; writing—review and editing, J.S., S.A. and T.R.; visualization, J.S., S.A. and T.R.; supervision, T.R. All authors have read and agreed to the published version of the manuscript.

Funding: This work was financially supported within the GRaZ project by the Federal Ministry for Economic Affairs and Energy (BMWi) under contract No. 02E11415A and the Federal Ministry for Environment, Nature Conservation, Nuclear Safety and Consumer Protection (BMUV) under contract No. 02E11860A.

Data Availability Statement: The data is available upon request to the corresponding author due to privacy reason.

Acknowledgments: We thank the anonymous reviewers for their helpful comments for improving the manuscript. We acknowledge the ESRF for the provision of synchrotron beam time and thank Damien Prieur as a local contact from the Helmholtz-Zentrum Dresden-Rossendorf, Germany, for the experimental support during the XAFS measurements at ROBL. The authors would like to thank Jakob Drebert (Department of Chemistry, Mainz) for the XPS measurements, Regina Walter (Institute of Geosciences, Mainz) for the BET measurements, and Ralf Meffert (Institute of Geosciences, Mainz) for the XRD measurements; Gianna Köhn for the support of the HCP characterization; Saskia Leidich and Janik Lohmann for CE-ICP-MS measurements; and Felix Berg for his support by speciation calculations.

Conflicts of Interest: The authors declare no conflict of interest.

References

1. Lommerzheim, A.; Jobmann, M. *Projekt ANSICHT-Endlagerkonzept sowie Verfüll- und Verschlusskonzept für das Standortmodell NORD*; TEC-14-2015-TB; DBE Technology GmbH: Peine, Germany, 2015.
2. Jobmann, M.; Bebiolka, A.; Burlaka, V.; Herold, P.; Jahn, S.; Lommerzheim, A.; Maßmann, J.; Meleshyn, A.; Mrugalla, S.; Reinhold, K.; et al. Safety assessment methodology for a German high-level waste repository in clay formations. *J. Rock Mech. Geotech. Eng.* **2017**, *9*, 856–876. [[CrossRef](#)]
3. Brewitz, W. *Eignungsprüfung der Schachtanlage Konrad für die Endlagerung radioaktiver Abfälle: Abschlussbericht (GSF-T 136)*; GSF: Neuherberg, Germany, 1982.
4. Pointeau, I.; Piriou, B.; Fedoroff, M.; Barthes, M.G.; Marmier, N.; Fromage, F. Sorption mechanisms of Eu³⁺ on CSH phases of hydrated cements. *J. Colloid Interface Sci.* **2001**, *236*, 252–259. [[CrossRef](#)]
5. Almendros-Ginestà, O.; Missana, T.; García-Gutiérrez, M.; Alonso, U. Analysis of radionuclide retention by the cement hydrate phase portlandite: A novel modelling approach. *Prog. Nucl. Energy* **2023**, *159*, 104636. [[CrossRef](#)]
6. Wieland, E. *Sorption Data Base for the Cementitious Near Field of L/ILW and ILW Repositories for Provisional Safety Analyses for SGT-E2*; Technical Report 14-08; NAGRA: Wetingen, Switzerland, 2014.
7. Taylor, H.F.W. *Cement Chemistry*; Springer International Publishing: London, UK, 1997.
8. Schlegel, M.L.; Pointeau, I.; Coreau, N.; Reiller, P. Mechanism of europium retention by calcium silicate hydrates: An EXAFS study. *Environ. Sci. Technol.* **2004**, *38*, 4423–4431. [[CrossRef](#)]
9. Stumpf, T.; Tits, J.; Walther, C.; Wieland, E.; Fanghänel, T. Uptake of trivalent actinides (curium(III)) by hardened cement paste: A time-resolved laser fluorescence spectroscopy study. *J. Colloid Interface Sci.* **2004**, *276*, 118–124. [[CrossRef](#)] [[PubMed](#)]
10. Tits, J.; Stumpf, T.; Rabung, T.; Wieland, E.; Fanghänel, T. Uptake of Cm(III) and Eu(III) by calcium silicate hydrates: A solution chemistry and time-resolved laser fluorescence spectroscopy study. *Environ. Sci. Technol.* **2003**, *37*, 3568–3573. [[CrossRef](#)]
11. Gaona, X.; Dähn, R.; Tits, J.; Scheinost, A.C.; Wieland, E. Uptake of Np(IV) by C-S-H phases and cement paste: An EXAFS study. *Environ. Sci. Technol.* **2011**, *45*, 8765–8771. [[CrossRef](#)]
12. Macé, N.; Wieland, E.; Dähn, R.; Tits, J.; Scheinost, A.C. EXAFS investigation on U(VI) immobilization in hardened cement paste: Influence of experimental conditions on speciation. *Radiochim. Acta* **2013**, *101*, 379–389. [[CrossRef](#)]
13. Häußler, V.; Amayri, S.; Beck, A.; Platte, T.; Stern, T.A.; Vitova, T.; Reich, T. Uptake of actinides by calcium silicate hydrate (C-S-H) phases. *Appl. Geochem.* **2018**, *98*, 426–434. [[CrossRef](#)]
14. Ochs, M.; Mallants, D.; Wang, L. *Radionuclide and Metal Sorption on Cement and Concrete*; Gheorghe, A.V., Ed.; Springer: Berlin/Heidelberg, Germany, 2016.
15. Guo, X.; Gin, S.; Frankel, G.S. Review of corrosion interactions between different materials relevant to disposal of high-level nuclear waste. *npj Mat. Degrad.* **2020**, *4*, 34. [[CrossRef](#)]
16. Duquette, D.J.; Latanision, R.M.; Di Bella, C.A.; Kirstein, B.E. Corrosion issues related to disposal of high-level nuclear waste in the Yucca Mountain repository—Peer reviewers’ perspective. *Corrosion* **2009**, *65*, 272–280. [[CrossRef](#)]
17. Tits, J.; Wieland, E. *Actinide Sorption by Cementitious Materials*; Bericht Nr. 18-02; PSI: Villigen, Switzerland, 2018.
18. Tits, J.; Gaona, X.; Laube, A.; Wieland, E. Influence of the redox state on the neptunium sorption under alkaline conditions: Batch sorption studies on titanium dioxide and calcium silicate hydrates. *Radiochim. Acta* **2014**, *102*, 385–400. [[CrossRef](#)]
19. Fanghänel, T.; Neck, V. Aquatic chemistry and solubility phenomena of actinide oxides/hydroxides. *Pure Appl. Chem.* **2002**, *74*, 1895–1907. [[CrossRef](#)]
20. Stockmann, M.; Fritsch, K.; Bok, F.; Fernandes, M.M.; Baeyens, B.; Steudtner, R.; Müller, K.; Nebelung, C.; Brendler, V.; Stumpf, T. New insights into U(VI) sorption onto montmorillonite from batch sorption and spectroscopic studies at increased ionic strength. *Sci. Total Environ.* **2022**, *806*, 150653. [[CrossRef](#)]
21. Meleshyn, A. *Mechanisms of Transformation of Bentonite Barriers—Testing a New Experimental Concept*; Gesellschaft für Anlagen- und Reaktorsicherheit: Cologne, Germany, 2015; GRS-A-3844.
22. *DIN EN 196-3:2005+A1:2008*; Prüfverfahren für Zement in Teil 3: Bestimmung der Erstarrungszeiten und der Raumbeständigkeit. Deutsche Fassung EN: Berlin, Germany, 2009.
23. Amayri, S.; Fröhlich, D.R.; Kaplan, U.; Trautmann, N.; Reich, T. Distribution coefficients for the sorption of Th, U, Np, Pu, and Am on Opalinus Clay. *Radiochim. Acta* **2016**, *104*, 33–40. [[CrossRef](#)]
24. Amayri, S.; Jermolajev, A.; Reich, T. Neptunium(V) sorption on kaolinite. *Radiochim. Acta* **2011**, *99*, 349–357. [[CrossRef](#)]
25. Gaona, X.; Wieland, E.; Tits, J.; Scheinost, A.C.; Dähn, R. Np(V/VI) redox chemistry in cementitious systems: XAFS investigations on the speciation under anoxic and oxidizing conditions. *Appl. Geochem.* **2013**, *28*, 109–118. [[CrossRef](#)]
26. Tits, J.; Fujita, T.; Tsukamoto, M.; Wieland, E. Uranium(VI) uptake by synthetic calcium silicate hydrates. *MRS Online Proc. Libr.* **2008**, *1107*, 467. [[CrossRef](#)]
27. Fanghänel, T.; Neck, V.; Kim, J.I. The ion product of H₂O, dissociation constants of H₂CO₃ and Pitzer parameters in the system Na⁺/H⁺/OH⁻/HCO₃⁻/CO₃²⁻/ClO₄⁻/H₂O at 25 °C. *J. Solut. Chem.* **1996**, *25*, 327–343. [[CrossRef](#)]
28. Willberger, C.; Amayri, S.; Häußler, V.; Scholze, R.; Reich, T. Investigation of the electrophoretic mobility of the actinides Th, U, Np, Pu, and Am in different oxidation states. *Anal. Chem.* **2019**, *91*, 11537–11543. [[CrossRef](#)]

29. Scheinost, A.C.; Claussner, J.; Exner, J.; Feig, M.; Findeisen, S.; Hennig, C.; Kvashnina, K.O.; Naudet, D.; Prieur, D.; Rossberg, A. ROBL-II at ESRF: A synchrotron toolbox for actinide research. *J. Synchrotron Radiat.* **2021**, *28*, 333–349. [[CrossRef](#)]
30. Ravel, B.; Newville, M. ATHENA, ARTEMIS, HEPHAESTUS: Data analysis for X-ray absorption spectroscopy using IFEFFIT. *J. Synchrotron Radiat.* **2005**, *12*, 537–541. [[CrossRef](#)]
31. Schmeide, K.; Reich, T.; Sachs, S.; Bernhard, G. Plutonium(III) complexation by humic substances studied by X-ray absorption fine structure spectroscopy. *Inorg. Chim. Acta* **2006**, *359*, 237–242. [[CrossRef](#)]
32. Martin, P.; Grandjean, S.; Valot, C.; Carlot, G.; Ripert, M.; Blanc, P.; Hennig, C. XAS study of (U_{1-y}Pu_y)O₂ solid solutions. *J. Alloys Compd.* **2007**, *444*, 410–414. [[CrossRef](#)]
33. George, G.N.; Pickering, I.J. EXAFSPAK—A Suite of Computer Programs for Analysis of X-ray Absorption Spectra; Stanford Synchrotron Radiation Lightsource: Menlo Park, CA, USA, 2000.
34. Rehr, J.J.; Kas, J.J.; Vila, F.D.; Prange, M.P.; Jorissen, K. Parameter-free calculations of X-ray spectra with FEFF9. *Phys. Chem. Chem. Phys.* **2010**, *12*, 5503–5513. [[CrossRef](#)] [[PubMed](#)]
35. Chiorescu, I.; Kremleva, A.; Krüger, S. On the sorption mode of U(IV) at calcium silicate hydrate: A comparison of adsorption, absorption in the interlayer, and incorporation by means of density functional calculations. *Minerals* **2022**, *12*, 1541. [[CrossRef](#)]
36. Parkhurst, D.L.; Appelo, C.A.J. PHREEQC (Version 3.3.5)—A Computer Program for Speciation, Batch-Reaction, One-Dimensional Transport, and Inverse Geochemical Calculations. Available online: http://wwwbrr.cr.usgs.gov/projects/GWC_coupled/phreeqc/index.html (accessed on 12 October 2023).
37. Giffaut, E.; Grivé, M.; Blanc, P.; Vieillard, P.; Colàs, E.; Gailhanou, H.; Gaboreau, S.; Marty, N.; Madé, B.; Duro, L. Andra thermodynamic database for performance assessment: ThermoChimie. *Appl. Geochem.* **2014**, *49*, 225–236. [[CrossRef](#)]
38. Pointeau, I.; Landesman, C.; Giffaut, E.; Reiller, P. Reproducibility of the uptake of U(VI) onto degraded cement pastes and calcium silicate hydrate phases. *Radiochim. Acta* **2004**, *92*, 645–650. [[CrossRef](#)]
39. Pointeau, I.; Landesman, C.; Coreau, N.; Moisan, C.; Reiller, P. *Am(III), Zr(IV), Pu(IV), Nb(V), U(VI) et Tc(IV) par les Matériaux Cimentaires Dégradés*; CEA Report; Commissariat à l'énergie atomique: Gif sur Yvette, France, 2004; pp. 3–37.
40. Wieland, E.; Lothenbach, B.; Glaus, M.A.; Thoenen, T.; Schwyn, B. Influence of superplasticizers on the long-term properties of cement pastes and possible impact on radionuclide uptake in a cement-based repository for radioactive waste. *Appl. Geochem.* **2014**, *49*, 126–142. [[CrossRef](#)]
41. Conradson, S.D.; Abney, K.D.; Begg, B.D.; Brady, E.D.; Clark, D.L.; Den Auwer, C.; Ding, M.; Dorhout, P.K.; Espinosa-Faller, F.J.; Gordon, P.L. Higher order speciation effects on plutonium L₃ X-ray absorption near edge spectra. *Inorg. Chem.* **2004**, *43*, 116–131. [[CrossRef](#)]
42. Dettmann, S.; Huittinen, N.M.; Jahn, N.; Kretzschmar, J.; Kumke, M.U.; Kutyma, T.; Lohmann, J.; Reich, T.; Schmeide, K.; Shams Aldin Azzam, S.; et al. Influence of gluconate on the retention of Eu(III), Am(III), Th(IV), Pu(IV), and U(VI) by CSH (C/S = 0.8). *Front. Nucl. Eng.* **2023**, *2*, 4. [[CrossRef](#)]
43. Reich, T.; Reich, T.Y.; Amayri, S.; Drebert, J.; Banik, N.L.; Buda, R.A.; Kratz, J.V.; Trautmann, N. Application of XAFS spectroscopy to actinide environmental science. *AIP Conf. Proc.* **2007**, *882*, 179–183. [[CrossRef](#)]
44. Wedler, G.; Freund, H.-J. *Lehrbuch der Physikalischen Chemie*; Wiley-VCH: Weinheim, Germany, 2012.
45. Odler, I. The BET-specific surface area of hydrated Portland cement and related materials. *Cem. Concr. Res.* **2003**, *33*, 2049–2056. [[CrossRef](#)]
46. Hong, S.-Y.; Glasser, F.P. Alkali binding in cement pastes: Part I. The C-S-H phase. *Cem. Concr. Res.* **1999**, *29*, 1893–1903. [[CrossRef](#)]

Disclaimer/Publisher's Note: The statements, opinions and data contained in all publications are solely those of the individual author(s) and contributor(s) and not of MDPI and/or the editor(s). MDPI and/or the editor(s) disclaim responsibility for any injury to people or property resulting from any ideas, methods, instructions or products referred to in the content.

2.2 Investigation on cementitious materials with GLU

2.2.1 Publication: Uptake of Pu(IV) by hardened cement paste in the presence of gluconate at high and low ionic strengths

Author Contribution

J. Stietz contributed to the formal analysis and investigation of the batch experiments at low ionic strength, wrote the original draft and the visualization, and participated in drafting, reviewing and editing the manuscript. S. Amayri contributed to the design, formal analysis and investigation at high ionic strength and wrote, reviewed, visualized and edited the manuscript. The XAFS studies were carried out by V. Häußler, S. Amayri and T. Reich under the supervision of D. Prieur. T. Reich was responsible for the formal analysis, review and editing of the manuscript as well as the supervision of the entire project. Further details can be found in the acknowledgements in the publication.

Summary

The findings in this publication enhance the understanding of Pu(IV) behavior on HCP in low to intermediate level waste repositories in the presence of GLU, regardless of groundwater ionic strength. GLU uptake by HCP may saturate sorption sites, consistent with known data for C-S-H phases (C/S = 1.4). High GLU concentration ($[GLU]_0/M = 1 \times 10^{-2}$) notably impacts Pu(IV) uptake, independent of groundwater ionic strength. The order of addition of Pu(IV) and GLU in batch sorption experiments with HCP affects Pu(IV) uptake, with significantly reduced sorption. This suggests a potential competitive reaction between Pu(IV) and GLU, possibly leading to GLU's desorbing effect on Pu(IV) or the formation of $Pu(OH)_4(GLU)^-$ complexes. The Ca^{2+} concentration in the background electrolyte influences GLU experiments and subsequently Pu(IV) uptake on HCP. XAFS evaluations indicate Pu(IV) incorporation into C-S-H phases, the main sorption phase of HCP. Importantly, ionic strength has no discernible effect on Pu uptake by HCP, even in the presence of GLU.

© 2023 Stietz, Amayri, Reich, Haeussler and Prieur. This is an open-access article distributed under the terms of the Creative Commons Attribution License (CC BY). The use, distribution or reproduction in other forums is permitted, provided the original author(s) or licensor are credited and that the original publication in this journal is cited, in accordance with accepted academic practice. No use, distribution or reproduction is permitted which does not comply with these terms.



OPEN ACCESS

EDITED BY

Xavier Gaona,
Karlsruhe Institute of Technology (KIT),
Germany

REVIEWED BY

Tiziana Missana,
Medioambientales y Tecnológicas, Spain
Sarah Saslow,
Pacific Northwest National Laboratory
(DOE), United States
Erich Wieland,
Paul Scherrer Institut (PSI), Switzerland

*CORRESPONDENCE

J. Stietz,
✉ jastietz@uni-mainz.de
T. Reich,
✉ treich@uni-mainz.de

RECEIVED 28 July 2023

ACCEPTED 06 October 2023

PUBLISHED 02 November 2023

CITATION

Stietz J, Amayri S, Häußler V, Prieur D and Reich T (2023), Uptake of Pu(IV) by hardened cement paste in the presence of gluconate at high and low ionic strengths.
Front. Nucl. Eng. 2:1268767.
doi: 10.3389/fnuen.2023.1268767

COPYRIGHT

© 2023 Stietz, Amayri, Häußler, Prieur and Reich. This is an open-access article distributed under the terms of the [Creative Commons Attribution License \(CC BY\)](https://creativecommons.org/licenses/by/4.0/). The use, distribution or reproduction in other forums is permitted, provided the original author(s) and the copyright owner(s) are credited and that the original publication in this journal is cited, in accordance with accepted academic practice. No use, distribution or reproduction is permitted which does not comply with these terms.

Uptake of Pu(IV) by hardened cement paste in the presence of gluconate at high and low ionic strengths

J. Stietz^{1*}, S. Amayri¹, V. Häußler¹, D. Prieur² and T. Reich^{1*}

¹Department of Chemistry, Johannes Gutenberg-Universität Mainz, Mainz, Germany, ²Institute of Resource Ecology, Helmholtz-Zentrum Dresden-Rossendorf e.V., Dresden, Germany

The uptake of Pu(IV) by hardened cement paste (HCP) at degradation state I was investigated in the absence and presence of gluconate (GLU). Furthermore, the influence of the ionic strength was examined in different background electrolytes. Artificial cement pore water (ACW, pH = 13) was used for low ionic strength ($I = 0.3$ M), and cement pore water based on the diluted caprock solution (ACW-VGL, pH = 12.5) was used for high ionic strength ($I = 2.5$ M). Sorption experiments were performed under an Ar atmosphere using HCP in the HCP/GLU binary system ($[GLU]_0 = 1 \times 10^{-1} - 1 \times 10^{-8}$ M) and the HCP/Pu(IV)/GLU ternary system ($[^{239}\text{Pu(IV)}]_0 = 1 \times 10^{-8}$ M, $[GLU]_0 = 1 \times 10^{-2}$ M) with solid-to-liquid (S/L) ratios of 0.5–50 g L⁻¹ within a contact time of 72 h. GLU sorbs strongly on HCP; a saturation of the sorption sites of HCP with GLU was observed at $[GLU] \geq 1 \times 10^{-4}$ M at S/L = 5 g L⁻¹. The effects of the order of addition of the components Pu(IV) and GLU on the sorption of Pu(IV) on HCP were investigated. In the absence of GLU, a quantitative uptake ($S\% \geq 99\%$) of Pu(IV) by HCP was observed, independent of the ionic strength of the background electrolytes. In the presence of 1×10^{-2} M GLU, the sorption of Pu(IV) on HCP was significantly lower. For X-ray absorption fine structure (XAFS) measurements, powder samples with Pu ($[^{239}\text{Pu(III)}]_0 = 5 \times 10^{-6}$ M) sorbed on HCP (S/L = 2.5 g L⁻¹) were prepared at pH ≈ 13 in ACW and ACW-VGL, respectively. One additional sample was prepared in the presence of GLU ($[GLU]_0 = 1 \times 10^{-2}$ M) with ACW-VGL as the electrolyte for comparison. Pu L_{III}-edge X-ray absorption near-edge structure (XANES) spectra show that Pu is in the tetravalent oxidation state after being taken up by the HCP. The structural parameters obtained from extended X-ray absorption fine structure (EXAFS) analysis and comparison with literature indicate incorporation of Pu(IV) into the calcium-silicate-hydrate (C-S-H) phases of HCP. The different ionic strengths and the presence of GLU had no influence on the near-neighbor environment of Pu in HCP.

KEYWORDS

sorption, ionic strength, plutonium, ordinary Portland cement, gluconate, extended X-ray absorption fine structure, X-ray absorption near-edge structure

1 Introduction

The assessment of environmental issues regarding the long-term disposal of radioactive waste is essential in nuclear waste management. In a deep geological nuclear waste repository, cement-based materials will be used not only as a building material but also as a part of the engineered barrier, including waste containers and surrounding backfill

materials (Duro et al., 2020; Tyupina et al., 2023). Hydrated cement is the main component of concrete used in the repository. In this context, hydrated cement phases buffer the pH value, and thus three main states of cement degradation are described by the interaction with inflowing groundwater or pore water from the host rock of the repository. In the first state, the cement pore water evolves from a solution dominated by NaOH and KOH ($[Na] \approx 0.1$ M, $[K] \approx 0.2$ M, $pH \approx 13.3$) to a solution saturated with portlandite ($Ca(OH)_2$) with a pH of 12.5 (state II). After leaching of the portlandite, cement degradation achieves a third state characterized by the noncongruent dissolution of the calcium-silicate-hydrate (C-S-H) phases and a decrease of pH in the cement pore water to ≈ 10 (Ochs et al., 2016). Changes in cement chemistry, such as pH shifts or dissolution of cement phases, can affect radionuclide mobility and interactions and must, therefore, be included in risk assessments.

This investigation deals with degradation state I, where the cement is largely fresh ($pH > 12.5$). The composition of incoming groundwater varies in terms of ionic strength, depending on the specific location of the repository. For instance, in the clay formations of Northern Germany, a high ionic strength ($I = 2.5$ M) is expected due to the significant salt content, as described by the “Standortmodell NORD” (Lommerzheim and Jobmann, 2015; Jobmann et al., 2017). On the other hand, pore water in clay formations in Southern Germany typically exhibits a lower ionic strength ($I = 0.3$ M) (Jobmann and Lommerzheim, 2015). If the cement comes into contact with the pore water of the clay formation, degradation of cementitious materials can occur, potentially leading to significant changes in the geochemical environment in the near field of the repository (Duquette et al., 2009; Guo et al., 2020).

The present investigation on the influence of ionic strength on actinide retention is intended to provide information on the extent to which the findings obtained for low ionic strength also apply to the description of actinide retention at higher ionic strength. Furthermore, to be able to make statements about the safety of such a repository, it is necessary to investigate processes such as sorption of the actinides on cementitious materials. The radioactive waste will contain long-lived actinides, such as plutonium ($t_{1/2}^{(239}Pu) = 2.41 \times 10^4$ a). The isotope ^{239}Pu is present as a component of spent nuclear fuel and highly relevant in the long-term safety assessment of a deep geological radioactive waste repository. Strongly reducing conditions are expected in the repository in the case of anaerobic iron corrosion (e.g., steel containers) and hydrogen formation. Therefore, the actinides will be predominantly in oxidation states +III and +IV (Duro et al., 2014). In aqueous solutions, plutonium can be present in different oxidation states simultaneously. Under the reducing and hyperalkaline environment as a result of cement degradation, Pu(IV) is expected as the dominant species (Stietz et al., 2023). Only a few studies have examined the uptake of Pu(III/IV) on hardened cement paste (HCP), including Wieland (2014) and Ochs et al. (2016). Distribution ratios, R_d , up to 1×10^4 L kg⁻¹ were reported for cement by Ochs et al. (2016). Wieland et al. (2014) reported an R_d value of 10^5 L kg⁻¹ for An(IV) in the degradation states I–III. Tasi et al. (2021) reported an R_d value of 2×10^6 L kg⁻¹ for Pu(IV) uptake by HCP at degradation state II ($pH = 12.6$). Experiments by Häußler et al. (2018) with Pu(III) and C-S-H phases ($S/L = 5$ g L⁻¹; calcium-to-silicon ratio (Ca/Si) = 0.7–1.8) have shown an R_d value of 2×10^5 L kg⁻¹ but also showed that Pu(III) was oxidized to Pu(IV) during the uptake by C-S-H.

In addition, due to cement degradation, organic ligands present in the form of cement additives or degradation products of cellulose and other organic waste materials could affect the migration behavior of actinides in a cement-based repository (Altmaier et al., 2021). Some studies have examined the complexation of actinides with such organic ligands like EDTA, isosaccharinic acid (ISA), and gluconate (GLU) and their effect on the sorption of actinides on cementitious phases as well as changes of the structure and chemical composition of the C-S-H phases (Taylor, 1997; Tits et al., 2005; Dario et al., 2006; Glaus et al., 2006; Gaona et al., 2008; Altmaier et al., 2021; Ochs et al., 2022).

GLU is used as an organic additive in concrete formulations, and its interaction with cementitious phases was investigated, for example, by Androniuk et al. (2017). In the concentration range of 1×10^{-9} – 1×10^{-2} M GLU, an R_d value of 285 L kg⁻¹ was determined for the sorption of GLU on the C-S-H phase with Ca/Si = 1.4. This study also showed that GLU sorption is a fast process. The equilibrium was reached after only 1 day, which is also in agreement with results of Glaus et al. (2006). Furthermore, GLU forms stable complexes with Ca(II) occurring in cementitious systems (Kutus et al., 2020) and with a variety of radionuclides, due to its carboxyl group and hydroxyl groups, which can participate in complexation processes (Tits et al., 2005; Gaona et al., 2008; Colàs et al., 2013; Adam et al., 2021). The formation of aqueous ternary complexes with GLU and Ca(II) is reported for tri- and tetravalent actinides (Colàs et al., 2013; Böszörményi et al., 2020; Rojo et al., 2021).

In the HCP/Pu(IV)/GLU ternary system, Gaona et al. (2008) described a possible formation of a $Pu(IV)(OH)_4(GLU)^-$ complex as the predominant species observed under alkaline to hyperalkaline conditions in solution. Tits et al. (2005) determined an R_d value of 3×10^4 L kg⁻¹ for the sorption of Th(IV) on calcite in the presence of GLU. Tasi et al. (2021) investigated the interaction of Pu with cement at degradation state II in the presence of ISA as another representative of polyhydroxy carboxylic acids likely to be present in cementitious repositories. In the presence of ISA ($[ISA]_{tot} \geq 10^{-4.5}$ M) low uptake of Pu(IV) on cement was observed, which decreased with increasing ISA concentration.

To the best of our knowledge, no previous literature has been reported on sorption experiments and spectroscopic investigations specifically examining the Pu-GLU system in relation to cementitious materials. Consequently, the primary objective of this study was to explore the sorption behavior of Pu on HCP, in both the absence and presence of GLU. In addition, the influence of ionic strength was assessed by using two different electrolytes: artificial cement pore water (ACW, $I = 0.3$ M) and a diluted caprock solution based on artificial cement pore water (VGL, German acronym for *Verdünnte Gipshuttlösung*, ACW-VGL; $I = 2.5$ M). The third aim was to determine the oxidation state of Pu sorbed on HCP and to obtain molecular-level information about the effects of GLU and ionic strength on the Pu sorption using X-ray absorption fine structure (XAFS) spectroscopy.

2 Materials and methods

All experiments were performed under anaerobic conditions in a glove box under an Ar atmosphere ($Ar \geq 99.99\%$, $O_2 < 0.1$ ppm) to exclude oxidation processes by O_2 and to eliminate carbonate

complexation by dissolved CO₂. Solutions were prepared using Milli-Q water (18.2 MΩ cm, Synergy™ Millipore water system, Millipore GmbH, Germany) previously degassed with Ar. All chemicals used for the solutions were p. a. (pro analysis) quality grade or better. Furthermore, the production of HCP powder (particle size of $\varnothing < 63 \mu\text{m}$) from ordinary Portland cement (Dyckerhoff, Germany) with a water-to-cement ratio (w/c) of 0.5 was based on DIN EN 196-3 (DIN, 2009), which has been slightly modified as described in Stietz et al. (2023).

2.1 Stock solutions

2.1.1 Gluconate

For the experiments in the HCP/GLU binary system, a stock solution of 3.7 MBq mL⁻¹ ¹⁴C-GLU (Hartmann Analytic, Germany) was diluted to the desired concentration in Milli-Q water. Furthermore, an inactive GLU stock solution ([GLU] = 0.3 M) was prepared from sodium gluconate (Sigma-Aldrich, United States) in Milli-Q water.

2.1.2 Plutonium

After purification from its decay products and ²⁴¹Am using anion exchange chromatography, ²³⁹Pu(VI) stock solution was obtained by fuming it several times with 1 M HClO₄ (Riedel-de Haën, Germany) (not to complete dryness) (Amayri et al., 2016). The tri- and tetravalent oxidation states of Pu were obtained from the purified Pu(VI) stock solution by potentiostatic electrolysis using a potentiostat (Wenking POS 2, Bank Elektronik-Intelligent Controls GmbH, Germany) in 1 M HClO₄ using a three-electrode cell consisting of a Pt-mesh as a working electrode, a Pt counter-electrode separated from the cell by a Vycor frit, and an Ag/AgCl reference electrode following the methods described by Cohen (1961). The oxidation state was verified by UV-vis spectroscopy: (Tidas 100, J & M Analytik AG, Germany) using the characteristic absorption bands at 601 nm for Pu(III), 470 nm for Pu(IV), 569 nm for Pu(V), and 830 nm for Pu(VI) (Cohen, 1961). The concentration of the ²³⁹Pu stock solutions was determined by liquid scintillation counting (LSC; Hidex 300 SL, Hidex, Finland) and α -spectroscopy (Si surface barrier detector, CR-SNA-450-100, AMETEK, USA). An aliquot of the ²³⁹Pu stock solution was diluted in 1 M HClO₄ to achieve initial concentrations of 1×10^{-8} M Pu(IV) for batch experiments and 5×10^{-6} M Pu(III) for XAFS investigations, respectively.

2.2 Background electrolytes

2.2.1 Artificial cement pore water

Sorption batch experiments at low ionic strength were carried out using ACW with a composition of 0.18 M KOH (Merck, Germany) and 0.114 M NaOH (Merck, Germany), yielding a pH value of 13.3. This composition corresponds to the experimental results obtained according to Wieland et al. (2006). An ICP-MS SemiQuant analysis: (7900 Series ICP-MS, Agilent Technologies, United States) was performed to determine the chemical composition of ACW after a 72 h contact time with HCP (S/L = 5 g L⁻¹). The results of the measurement are summarized in Table 1. For more information, please refer to Supplementary Material S1.

2.2.2 Cement pore water based on diluted caprock solution

The diluted caprock solution (VGL) was chosen as a reference solution for the high ionic strength to simulate the prevailing conditions at the interface between neighboring claystone and salt formations in Northern Germany. ACW based on VGL (Meleshyn, 2015) was prepared via leaching of HCP powder in a VGL solution under an Ar atmosphere. For this, HCP powder (grain size < 63 μm , w/c = 0.5) was suspended in VGL (S/L = 10 g L⁻¹) and shaken for at least 1 week in an overhead shaker (Reax 20, Heidolph Instruments GmbH & Co. KG, Germany) at 16 rpm. To separate the solid and liquid phases, the wide-mouth bottles (Beckman Coulter, United States) were first centrifuged for 15 min at 7,000 rpm (7,519 g) with an Avanti J-30I (Beckman Coulter, United States). Subsequently, the supernatant was filtrated using a 50-mL syringe with a disposable syringe filter (CHROMAFIL® Xtra PVDF-20/25, pore size: 0.2 μm , filter- ϕ : 25 mm, Macherey-Nagel GmbH & Co. KG, Germany). The pH value of the ACW-VGL solution was 12.8. The individual constituents of VGL (Meleshyn, 2015) and ACW-VGL (determined with XRF) are listed in Table 1. The XRF measurement is given in Supplementary Material S2.

2.3 Batch experiments

The HCP powder was mixed with the related ACW or ACW-VGL background electrolyte to achieve suspensions with S/L ratios between 0.5 and 50.0 g L⁻¹. The samples were turned in an end-over-end rotator (Stuart Rotator SB3, United Kingdom) for a preconditioning period of 72 h. The individual experiments are described in more detail in Section 2.3.2. For phase separation, the samples were precentrifuged at 3,770 g (SIGMA 3K30, SIGMA Laborzentrifugen GmbH, Germany) for 15 min and ultracentrifuged at 108,800 g (Avanti J-30I, Beckman Coulter; United States) for 1 h. The pH value was measured in all samples immediately after centrifugation. The pH values in both electrolytes remained constant after a contact time of 72 h.

2.3.1 pH and Eh measurements

A pH meter (WTW inoLab. pH Level 1, WTW GmbH, Germany) equipped with a pH electrode (BlueLine 16 pH, Schott Instruments GmbH, Germany) was used for the measurement of the pH of the supernatant solutions. The electrode was calibrated regularly using certificated buffer solutions of pH 4.01, 6.87, and 9.18 (Schott Instruments GmbH, Germany). Samples at pH values in the high alkaline range were controlled with certificated buffer solutions of pH 13.00 (Hanna Instruments, Inc., United States). The measured pH value for this buffer was 12.89, giving an uncertainty of $\Delta\text{pH} = 0.11$ when using this calibration. It is necessary to correct the measured pH values obtained at higher ionic strengths because of the discrepancies between the activities of the ions in the electrolyte solution of the electrode and the sample solution (Fanghänel et al., 1996). An empirically derived correction parameter ($A = 0.41$) was used to accurately account for these differences according to the following equation (Fanghänel et al., 1996):

TABLE 1 Composition of the background electrolyte ACW (Wieland et al., 2006) and the result of the semiquantitative analysis made in ICP-MS of ACW after 72 h contact time with HCP (S/L = 5 g L⁻¹). For the preparation of the background electrolyte with high ionic strength, the composition of VGL (Meleshyn, 2015) and the results from the XRF analysis of ACW-VGL after 10 days of contact time with HCP (S/L = 10 g L⁻¹) are summarized.

	Concentration/M			
	ACW (Wieland et al., 2006)	ACW ^a	VGL (Meleshyn, 2015)	ACW-VGL ^b
Na ⁺	0.11	0.14	2.52	2.40
K ⁺	0.18	0.22	5.0 × 10 ⁻³	3.6 × 10 ⁻³
Ca ²⁺	-	2.8 × 10 ⁻³	1.00 × 10 ⁻²	2.03 × 10 ⁻²
Cl ⁻	-	-	2.52	1.86
SO ₄ ²⁻	-	2.0 × 10 ⁻³	8.0 × 10 ⁻³	3.8 × 10 ⁻⁴
Si ⁴⁺	-	4.3 × 10 ⁻⁴	-	1.2 × 10 ⁻³
pH	13.3	13.3	8.0	12.8
IS/M	0.3	0.3	2.6	2.5

^aObtained from ICP-MS SemiQuant analysis, Supplementary Table S1.

^bObtained from XRF analysis, Supplementary Table S2.

$$pH = pH_{exp} + A. \quad (1)$$

The redox potentials were determined using a pH meter connected with a redox electrode (BlueLine 31 RX, reference system: Ag/AgCl, Schott Instruments GmbH, Germany). To ensure the accuracy and reliability of the setup, the functionality was verified using standard solutions of known potentials (+220 mV, +470 mV, and +640 mV; Schott Instruments GmbH, Germany). All values were converted to the standard hydrogen electrode (SHE) by adding 210 mV to the measured values.

2.3.2 Sorption experiments

2.3.2.1 HCP/GLU

The uptake of GLU by HCP was investigated in two different series of batch experiments after a contact time of 72 h. The contact time of 72 h was considered sufficient because a rapid uptake process of GLU was shown in the literature, where the equilibrium was reached after only 1 day (Glaus et al., 2006; Androniuk et al., 2017). One batch experiment was performed as a function of the S/L ratio ([GLU]₀ = 1 × 10⁻² M; S/L = 0.5–50 g L⁻¹) and the other as sorption isotherm of GLU (S/L = 5 g L⁻¹; [GLU]₀ = 1 × 10⁻⁹–1 × 10⁻¹ M). In both experiments, ¹⁴C-labelled GLU (2.5–200 Bq ¹⁴C-GLU) was used as a tracer and analyzed by LSC. A 1–2 mL sample was added to 10 mL LSC cocktail Ultima Gold™ XR (PerkinElmer LAS GmbH, Germany) without acidifying. Samples were measured until a 2σ error of 2% was achieved. The resulting limit of detection (LOD) for ¹⁴C-GLU was 1 × 10⁻⁹ M.

2.3.2.2 HCP/Pu(IV)

Sorption batch experiments in the HCP/Pu(IV) binary system after a contact time of 72 h aimed to provide a basis for interpreting the Pu uptake in the presence of GLU at high and low ionic strengths using different approaches. Each sample was prepared in duplicate. In the first batch experiment, the sorption of Pu(IV) ([²³⁹Pu(IV)]₀ = 1 × 10⁻⁸ M) on HCP was determined with ICP-MS analysis (7900 Series ICP-MS, Agilent Technologies, United States).

After phase separation, the supernatant was diluted in 2% HNO₃. ¹⁹³Ir ([Ir] = 100 ppt) in 2% HNO₃ was added as an internal standard. The LOD for ICP-MS measurements of ²³⁹Pu was 2 × 10⁻¹⁰ M.

The measured concentration [Pu]_{eq} [M] of the analyte in the supernatant and its initial concentration [Pu]₀ [M], respectively, were used to calculate the sorption:

$$\text{Sorption\%} = \left(1 - \frac{[Pu]_{eq}}{[Pu]_0}\right) \cdot 100\%. \quad (2)$$

The distribution ratio R_d [L kg⁻¹] between the solid and the liquid phases was calculated using Eq. (3), with the sample volume V [L] and the total mass of the solids m [kg]:

$$R_d = \frac{V}{m} \cdot \left(\frac{[Pu]_0 - [Pu]_{eq}}{[Pu]_{eq}}\right). \quad (3)$$

2.3.2.3 HCP/Pu(IV)/GLU

In order to study the influence of GLU as an organic additive on the sorption behavior, experiments in the HCP/Pu(IV)/GLU ternary system were performed. The order of addition of Pu(IV) ([Pu]₀ = 1 × 10⁻⁸ M) and GLU ([GLU]₀ = 1 × 10⁻² M) on HCP (S/L = 5 g L⁻¹) was varied in three combinations: (i) (HCP + Pu(IV)) + GLU, Pu(IV) was equilibrated with HCP for 72 h, followed by the addition of GLU, also with a contact time of 72 h. In variation (ii), described as (HCP + GLU) + Pu(IV), GLU was equilibrated with HCP for 72 h before the addition of Pu(IV) and subsequently equilibrated for 72 h. In variation (iii), (HCP + Pu(IV) + GLU), GLU and Pu(IV) were added simultaneously and equilibrated for 72 h. Each sample was prepared in duplicate.

2.3.3 XAFS measurements of ²³⁹Pu

To examine the sorbed Pu species after the uptake by HCP at different ionic strengths, samples were prepared in the background electrolytes ACW and ACW-VGL with an initial concentration of 5 × 10⁻⁶ M ²³⁹Pu(III) as described in Section 2.3.2.2 (HCP/Pu(IV)).

TABLE 2 Samples of the Pu/HCP binary and the Pu/HCP/GLU ternary systems prepared for Pu L_{III}-edge XAFS measurements with S/L = 2.5 g L⁻¹ and an initial concentration of 5 × 10⁻⁶ M Pu(III).

Sample	[GLU] ₀ /M	pH	Pu/ppm
Pu/HCP in ACW	-	13.4	493
Pu/HCP in ACW-VGL	-	12.3	493
Pu/HCP/GLU in ACW-VGL	0.01	12.7	479

The influence of 1 × 10⁻² M GLU was investigated by preparing one additional sample in ACW-VGL, where aliquots of Pu(III) and GLU stock solutions were added simultaneously to the pre-equilibrated HCP suspension. To increase the uptake of Pu by HCP for the spectroscopic measurements, the S/L ratio during sample preparation was reduced to 2.5 g L⁻¹. A description of the samples can be found in Table 2. The samples were prepared using Pu(III) because its hydrolysis is less and its solubility is higher than Pu(IV) (Grenthe et al., 2020). Therefore, the initial concentration could be increased, which was necessary to perform these spectroscopic investigations. In addition, the use of Pu(III) prevented the formation of Pu(IV) colloids and solid phases (PuO_{2(hyd,aged)}) at the high pH. After centrifugation of the samples, the solid phase was dried under an Ar atmosphere at room temperature, homogenized, and transferred into double-confinement oblong plastic holders transparent to X-rays. The samples were transported under a liquid nitrogen atmosphere to the European Synchrotron Radiation Facility (ESRF), Grenoble, France. Synchrotron radiation XAFS measurements of the batch samples were performed in 7/8 bunch mode at the BM20 Rossendorf Beamline (ROBL) (Matz et al., 1999; Scheinost et al., 2021) using the Si(111) double-crystal monochromator. Higher harmonic radiation was rejected by Rh-coated mirrors positioned in front of and behind the monochromator. During the measurements, the samples were cooled to 15 K with a closed-cycle He cryostat (CryoVac, Germany). A 13-element Ge-detector (Canberra, United States) was used to record multiple scans of the Pu L_{III}-edge XAFS spectrum in fluorescence mode. During each scan, the Zr K-edge spectrum of a Zr foil was measured simultaneously in transmission mode. The corresponding ionization chambers were filled with a gas mixture of 82% N₂ and 18% Ar. The X-ray absorption near-edge structure (XANES) spectra of the Zr K-edge (17,998 eV) and the Pu L_{III}-edge (18,057 eV) were recorded with a step size of 0.5 eV. The extended X-ray absorption fine structure (EXAFS) part of the Pu spectrum was recorded in *k*-space with a step size of 0.05 Å⁻¹ and a gradually increasing counting time from 2 s to 20 s per data point. The programs EXAFSPAK (George and Pickering, 2000) and FEFF9 (version 9.6) (Rehr et al., 2010) were used to analyze the EXAFS spectra. A structural model based on density functional calculations of the sorption modes of U(IV) at the C-S-H phase (Chiorescu et al., 2022), where the U in the CaO layer of C-S-H was replaced by Pu, was used for the calculation of the FEFF scattering amplitudes and phases.

The recorded XANES spectra were analyzed using the software package Demeter, Athena, v. 0.9.025 (Ravel and Newville, 2005). After energy calibration using the Zr K-edge energy at 17,998 eV, the

spectra were averaged and modeled using least-squares fitting and the reference spectra of Pu(III) aquo ion (Schmeide et al., 2006) and PuO₂ (Martin et al., 2007). In addition, the energy of the Pu L_{III} edge in the XANES spectra of the HCP samples was determined based on the first inflection point, which is defined as the zero-crossing of the second derivative of the XANES.

3 Results and discussion

3.1 Sorption experiments

3.1.1 HCP/GLU

As described in Section 2.3.2.1, the uptake of GLU by HCP at degradation state I was investigated with ¹⁴C-labelled GLU as the sorption isotherm (Figure 1A) and as a function of the S/L ratio (Figure 1B). In Figure 1A, the values flatten at [GLU]₀ ≥ 1 × 10⁻⁴ M, indicating saturation of the HCP sorption sites. Below this concentration, that is, the range relevant for the waste repository, the sorption isotherm is linear and has a slope of 1. The *R_d* value equals (4.9 ± 0.4) × 10³ L kg⁻¹. All data of the GLU/HCP system were modeled using the two-site Langmuir isotherm given in Eq. (4):

$$[\text{GLU}]_{\text{sorbed}} = \frac{K_1 q_1 [\text{GLU}]_{\text{eq}}}{1 + K_1 [\text{GLU}]_{\text{eq}}} + \frac{K_2 q_2 [\text{GLU}]_{\text{eq}}}{1 + K_2 [\text{GLU}]_{\text{eq}}}, \quad (4)$$

where *K*_{1,2} [L mol⁻¹] is the adsorption affinity constant, *q*_{1,2} [mol kg⁻¹] is the sorption capacity of HCP for GLU for two distinct sorption sites, and [GLU]_{eq} is the equilibrium concentration. The Langmuir isotherm parameters for both background electrolytes are summarized in Table 3. These parameters were used to calculate the equilibrium concentration [GLU]_{eq} as a function of S/L for [GLU]₀ = 1 × 10⁻² M using Eq. (5). The calculated concentrations [GLU]_{eq} agree well with the experimental data as shown in Figure 1B.

$$[\text{GLU}]_{\text{sorbed}} = ([\text{GLU}]_0 - [\text{GLU}]_{\text{eq}}) \times \frac{V}{m}. \quad (5)$$

In general, as the amount of HCP in solution increased to 50 g L⁻¹, the equilibrium concentration of GLU in solution decreased for both electrolytes. Particularly in the range between 5 and 20 g L⁻¹, the equilibrium concentration differs regarding the ionic strength of the background electrolytes. The exact distribution of the ligand on the sorption sites cannot be deduced. One possibility would be the uptake of GLU into the interlayer of the C-S-H phase. Due to the high affinity of GLU to Ca²⁺ and its H-bonding ability, a strong interaction of GLU with the cement surface is expected (Pallagi et al., 2014; Kutus et al., 2020). According to the calculated speciation (see Supplementary Material S3, Supplementary Figure S1), Ca-GLU complexes are formed under the experimental conditions. Due to a higher Ca²⁺ concentration in ACW-VGL (Table 1), proportionally more [Ca(OH)(GLU)]_{aq} is formed, which may not sorb onto the HCP surface. This could lead to a lower uptake of GLU by HCP in ACW-VGL and a higher GLU concentration in solution, as seen in Figure 1B, respectively. At low S/L ratios (S/L ≤ 2 g L⁻¹), the amount of GLU is probably so high that the influence of the background electrolyte is not significant. At an S/L ratio of

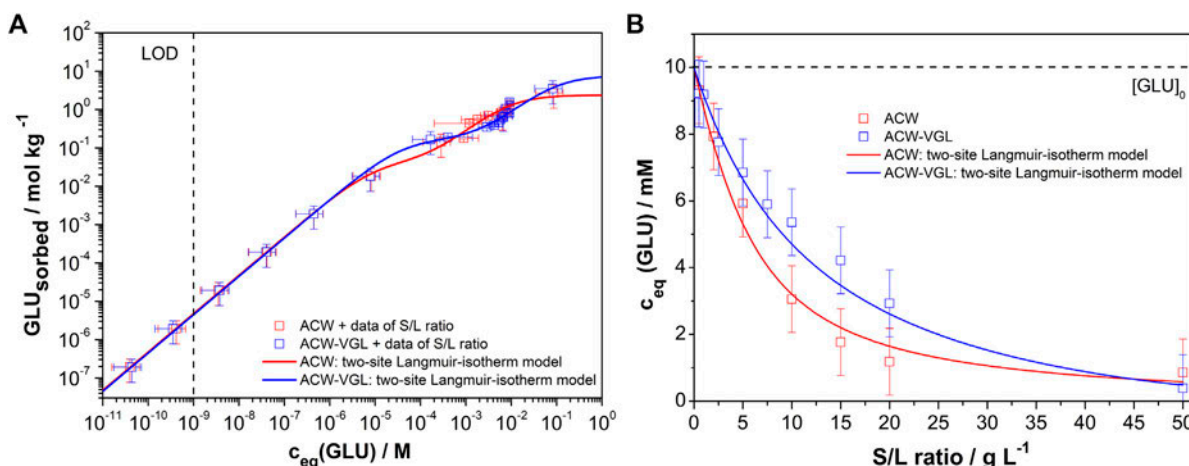


FIGURE 1 Batch sorption experiments of GLU at HCP with ACW (red, pH = 13.3) and ACW-VGL (blue, pH = 12.8) and a contact time of 72 h: (A) sorption isotherm with initial GLU concentrations from 1 × 10⁻⁹ M to 1 × 10⁻¹ M at S/L = 5 g L⁻¹. The dashed black line shows the limit of detection (LOD); (B) at constant GLU concentration ([GLU]₀ = 1 × 10⁻² M) and varying S/L ratio (S/L = 0.5–50 g L⁻¹). The dashed black line marks the initial concentration of 1 × 10⁻² M GLU. The solid red and blue lines in (A) represent the best fit using two-site Langmuir sorption isotherms. The colored lines in B are the equilibrium concentrations of GLU calculated using Eq. 5 with the parameters in Table 3.

TABLE 3 Sorption affinity constants K_1 and K_2 and sorption capacities q_1 and q_2 for two distinct sorption sites determined by fitting the GLU sorption data using a two-site Langmuir sorption isotherm.

Langmuir-isotherm parameter	GLU/HCP in ACW	GLU/HCP in ACW-VGL
K_1/mol^{-1}	$(1.1 \pm 0.6) \times 10^5$	$(2.7 \pm 0.7) \times 10^4$
$q_1/\text{mol kg}^{-1}$	0.04 ± 0.02	0.16 ± 0.04
$K_2/\text{L mol}^{-1}$	116 ± 39	11 ± 8
$q_2/\text{mol kg}^{-1}$	2.4 ± 0.5	7.5 ± 4.5

50 g L⁻¹, the concentration values converge again. The high uptake of GLU in both experiments is in good agreement with Androniuk et al. (2017) for C-S-H phases at a Ca/Si ratio of 1.4, which is representative of the Ca/Si ratio of C-S-H phases in unaltered HCP. Based on these results compared with the results from the literature (Androniuk et al., 2017), a blocking of sorption sites by GLU on HCP can be assumed.

3.1.2 HCP/Pu(IV)

First, the sorption of 1 × 10⁻⁸ M Pu(IV) on HCP (S/L = 5 g L⁻¹) was studied in both background electrolytes. For the experiments, values of $R_{d,min} = 30 \text{ L kg}^{-1}$, $R_{d,max} = 8.5 \times 10^4 \text{ L kg}^{-1}$ (ACW), and $R_{d,max} = 2.4 \times 10^5 \text{ L kg}^{-1}$ (ACW-VGL) were determined as described in Tits et al. (2002). The results of the batch experiments show a high uptake of Pu by HCP independent of the ionic strength (see Table 4; R_d (ACW) = 1.3 × 10⁷ L kg⁻¹ (S/L = 1 g L⁻¹) and 2.2 × 10⁶ L kg⁻¹ (S/L = 5 g L⁻¹); R_d (ACW-VGL) = 2.6 × 10⁶ L kg⁻¹ (S/L = 5 g L⁻¹)), which is in good agreement with the literature ($R_d > 10^4 \text{ L kg}^{-1}$ (Ochs et al., 2016) and 2.0 (+7.9/-0.5) × 10⁶ L kg⁻¹ (Tasi et al., 2021)). Furthermore, the speciation calculations for Pu indicate the species of Pu(OH)₄ to be present over a wide pH range. Figure 2A shows the predominance diagram of Pu calculated

for an equilibrium concentration of [Pu]_{eq} = 5 × 10⁻⁸ M for both background electrolytes using the “Thermodynamic database ThermoChimie 9b0, 2015” (used complex formation constants are in SM-4). The measured Eh and pH values of the batch sorption samples, including those for the XAFS experiments, show that the samples are in the stability range of Pu(IV) (see Figure 2). Therefore, we assume that Pu(IV) is the species sorbed on the cement.

3.1.3 HCP/Pu(IV)/GLU

To our knowledge, no data are available for the uptake of Pu(IV) by HCP in the HCP/Pu(IV)/GLU ternary system. Table 4 summarizes the R_d values obtained from batch experiments where the order of addition was varied. These values are up to five orders of magnitude lower than those observed for the HCP/Pu(IV) binary system. The order of addition of Pu(IV) and GLU has a significant influence on the Pu uptake. When Pu(IV) was added first ((HCP + Pu(IV)) + GLU), the corresponding distribution ratios are R_d (ACW) = 1.1 (±0.1) × 10³ L kg⁻¹ and R_d (ACW-VGL) = 2.7 (±0.4) × 10³ L kg⁻¹. In this case, GLU was added to the HCP suspension 72 h after the addition of Pu(IV). We assume that part of the Pu initially sorbed on HCP (compared with the binary system) was desorbed due to a mobilizing effect of

TABLE 4 Values for R_d , $R_{d,max}$ and $R_{d,min}$ in the experiments of the Pu(IV)/HCP binary system and the Pu(IV)/HCP/GLU ternary system under alkaline conditions (pH = 12.5–13) at high and low ionic strengths. Other parameters were $S/L = 5 \text{ g L}^{-1}$, $[Pu(IV)]_0 = 1 \times 10^{-8} \text{ M}$, $[GLU]_0 = 1 \times 10^{-2} \text{ M}$, and 72 h contact time.

Medium	Experiment	$R_d/L \text{ kg}^{-1}$	$R_{d,max}/L \text{ kg}^{-1}$	$R_{d,min}/L \text{ kg}^{-1}$
ACW	HCP + Pu(IV)	2.2×10^6	8.5×10^4	
		1.3×10^{7a}	4.2×10^{5a}	
ACW-VGL	HCP + Pu(IV)	2.6×10^6	2.4×10^5	
Tasi et al. (2021)	HCP + Pu(IV)	$2.0 (+7.9/-0.5) \times 10^6$		
Ochs et al. (2016)	HCP + Pu(IV)	$> 10^4$		
ACW	(HCP + Pu(IV)) + GLU	$1.1 (\pm 0.1) \times 10^3$	6.3×10^5	
	(HCP + GLU) + Pu(IV)	0		30
	(HCP + Pu(IV) + GLU)	0		30
ACW-VGL	(HCP + Pu(IV)) + GLU	$2.7 (\pm 0.4) \times 10^3$	2.4×10^5	
	(HCP + GLU) + Pu(IV)	11 ± 6		30
	(HCP + Pu(IV) + GLU)	64 ± 30		30

^a) In this batch experiment, S/L was 1 g L^{-1} .

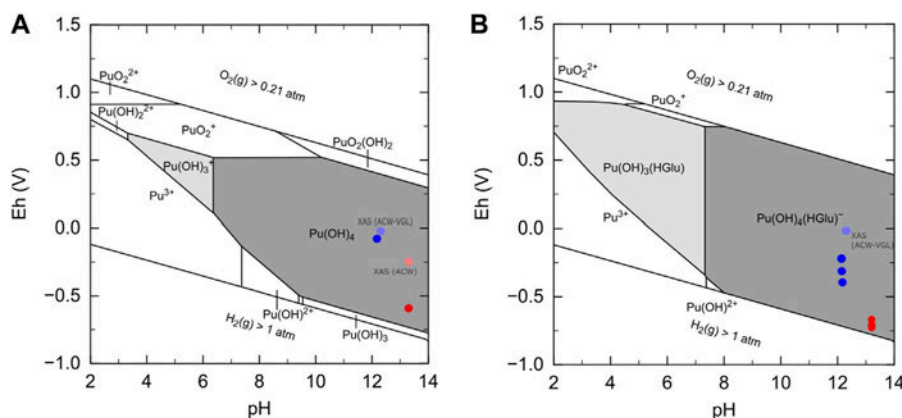


FIGURE 2

Speciation calculation for $5 \times 10^{-8} \text{ M}$ Pu in the absence (A) and the presence (B) of $1 \times 10^{-2} \text{ M}$ GLU. The dots mark the measured Eh (SHE) and pH values of the samples of the ACW-VGL (blue) and ACW (red) experiments. (Graphic generated by PhreePlot (version 1.0 (Parkhurst and Appelo, 2016)) using PHREEQC and the ThermoChimie database 9b0, 2015 (Giffaut et al., 2014)).

GLU. The desorption of Pu by GLU may be due to GLU being strongly taken up by HCP or to the complexation of Pu(IV) with dissolved GLU, as can be seen in the predominance diagram in Figure 2B. The measured Eh and pH values of all samples are in the predominance region of $Pu(OH)_4(GLU)^-$ complex formation. Furthermore, no Pu uptake ($R_{d,min} = 30 \text{ L kg}^{-1}$) was observed when GLU was added first or simultaneously with Pu(IV) at low ionic strength (ACW). Also, small R_d values were determined (Table 4) at high ionic strength (ACW-VGL). In the second variant ((HCP + GLU) + Pu(IV)), GLU, which could be taken up at the HCP, was added first, so relevant sorption sites could be occupied, and Pu(IV) is not taken up at the HCP. Both components were added simultaneously in the third variant (HCP + Pu(IV) + GLU). Two effects could be important: first, the strong sorption of GLU on the HCP surface, and second, the formation of the $Pu(OH)_4(GLU)^-$ complex that could remain in

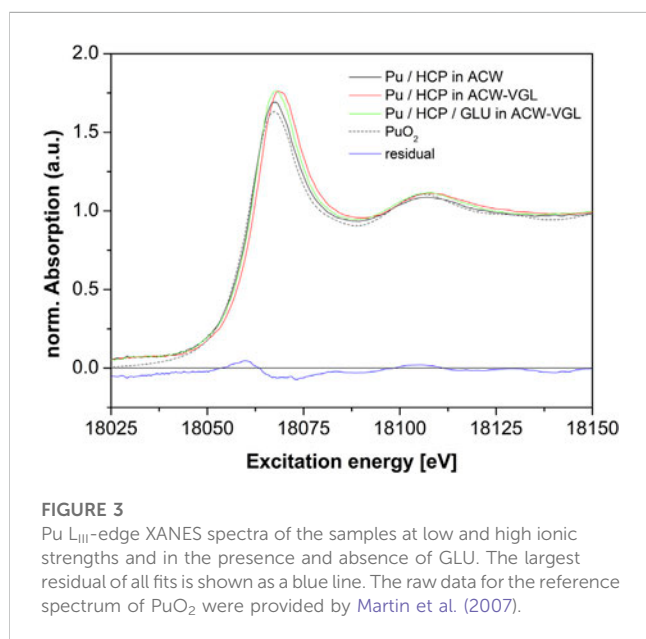
solution. The higher proportion of Ca^{2+} in ACW-VGL may be the reason for a slightly higher Pu uptake in ACW-VGL ($R_d = 64 \pm 30 \text{ L kg}^{-1}$) compared to the uptake in ACW (Table 4). Moreover, the comparison of the results for variant (i) with the other two variants indicates: (1) the sorption of Pu(IV) on HCP (variant (i)) may be partially irreversible. (2) The kinetics of Pu desorption from HCP by GLU are slower than its contact time of 72 h.

3.2 XAFS measurements (XANES and EXAFS)

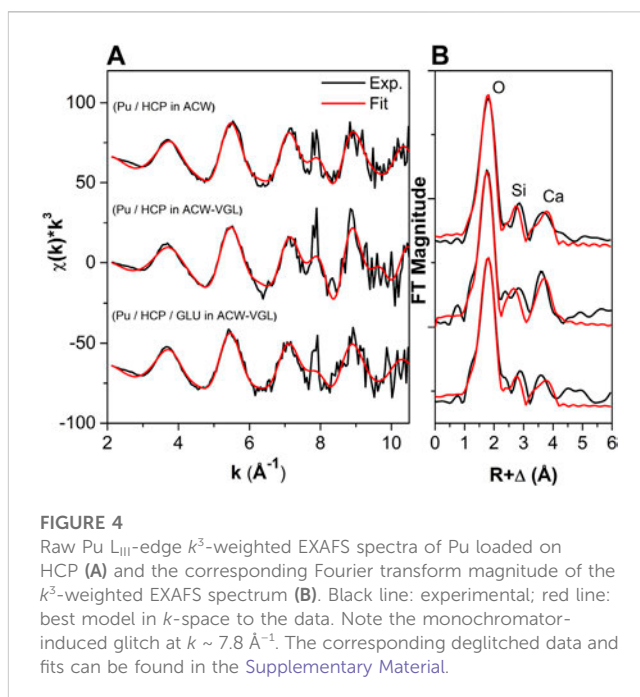
EXAFS measurements provide element-specific, short-range structural and chemical information on the Pu coordination environment, including identities and coordination numbers of the neighboring atoms and bond distances. We used this technique to obtain the local coordination environment of $5 \times$

TABLE 5 The Pu L_{III}-edge energies were determined by analyzing the inflection points of the XANES spectra of the samples studied. A comparison was made with the Pu(III)_(aq) and Pu(IV)_(aq) aquo ions (Conradson et al., 2004).

Absorption edges of Pu L _{III} -edge XANES	Energy/eV
Pu/HCP in ACW	18,062.8 (±0.6)
Pu/HCP in ACW-VGL	18,062.8 (±0.6)
Pu/HCP/GLU in ACW-VGL	18,062.6 (±0.7)
Pu(III) _(aq)	18,060.0
Pu(IV) _(aq)	18,063.2



10⁻⁶ M Pu after being taken up by HCP (S% = 99%, S/L = 2.5 g L⁻¹) in the investigated samples at high pH and in different electrolytes. The higher uptake of Pu in the presence of GLU (S% = 97%; [GLU]₀ = 1 × 10⁻² M) in this experiment can probably be attributed to the higher initial Pu concentration used. All samples were measured at approximately 15 K to reduce thermal vibrations and to enhance the corresponding contribution of these atoms to the EXAFS amplitude. Furthermore, the oxidation state of Pu retained on the HCP was investigated with Pu L_{III}-edge XANES spectroscopy. The energies of the absorption edges for the measured samples and of Pu(III)_(aq) and Pu(IV)_(aq) reference spectra (Conradson et al., 2004) are listed in Table 5. Additionally, a linear combination fit was performed using a subroutine in the program Athena (Ravel and Newville, 2005) to determine the fractions of different Pu oxidation states. This determination was achieved by fitting the measured XANES spectrum with reference spectra of Pu(III) aquo ion (Schneide et al., 2006) and PuO₂ (Martin et al., 2007) in the energy range between 18,012 and 18,212 eV. The Pu L_{III}-edge XANES spectra (Figure 3) demonstrate that Pu(IV) exclusively dominates as the oxidation state (100%) in the absence and presence of GLU. The relative uncertainty of the XANES fits with Pu(III) and Pu(IV) was less than 3%. The initial Pu(III) was oxidized to Pu(IV) after being taken up by the HCP. This solid phase characterization result



confirms the conclusion derived from the measured Eh and pH values of the supernatant solutions and the calculated predominance diagrams (Figure 2).

Figure 4 shows the raw Pu L_{III}-edge k³-weighted EXAFS spectra together with the best model to the data and the corresponding Fourier transform magnitudes for the samples Pu/HCP in the different background electrolytes and in the presence of GLU. The EXAFS spectra of the samples show similar oscillations, indicating similar Pu near-neighbor surroundings. Unfortunately, a monochromator-induced glitch between 18,284.6 eV and 18,299.9 eV (five measurement points) led to a distortion at k ~ 7.8 Å⁻¹ in the EXAFS spectra. An attempt to remove this glitch and to model the modified data can be found in Supplementary Material SM-7. The raw EXAFS data (Figure 4) were analyzed in k-space (2.1–10.9 Å⁻¹) without a window function and could be best modeled with three coordination shells. The total number of independent fit parameters was 10. The EXAFS structural parameters are summarized in Table 6. In the samples, Pu is surrounded by 6.0–6.7 (±0.4) oxygen atoms with Pu-O distances between 2.25 and 2.28 (±0.02) Å. These average Pu-O bond lengths agree with literature data for tetravalent Pu (Reich et al., 2007) and support the conclusion derived from the XANES measurements mentioned before. The second Pu coordination shell was modeled with Si. The average Pu-Si distance is between 3.15 and 3.16 (±0.02) Å, with Si coordination numbers between 1.1 and 1.8 (±0.6). The third coordination shell could be modeled as a Pu-Ca interaction with an average distance of 4.16–4.19 (±0.02) Å. For this coordination shell, a strong correlation between coordination number N and the Debye–Waller factor σ² was observed. For the samples Pu/HCP in ACW and Pu/HCP/GLU in ACW-VGL, the Ca coordination numbers are 5.2 ± 1.4 and 6.0 ± 2.3, respectively. For the Pu/HCP in the ACW-VGL sample, the Ca coordination number is lower, that is, 2.9 ± 0.9. Note that the corresponding σ² = 0.003 ± 0.002 is very small for such a distant shell. It should further

TABLE 6 Structural parameters of the Pu samples determined by Pu L_{III}-edge EXAFS spectroscopy with *N* - coordination number, *R* - distance, and σ^2 - Debye–Waller factor ($S_0^2 = 0.9$) and data from the literature for comparison.

Sample	Shell	<i>N</i>	<i>R</i> /Å	$\sigma^2/\text{Å}^2$
Pu/HCP/ACW (norm. error = 0.3, $\Delta E_0 = 1.5 \pm 0.4$ eV)	Pu-O	6.4 ± 0.3	2.27 ± 0.01	0.010 ± 0.001
	Pu-Si	1.4 ± 0.4	3.15 ± 0.01	0.005 ± 0.002
	Pu-Ca	5.2 ± 1.4	4.19 ± 0.01	0.011 ± 0.003
Pu/HCP/ACW-VGL (norm. error = 0.5, $\Delta E_0 = -1.1 \pm 0.7$ eV)	Pu-O	6.0 ± 0.4	2.25 ± 0.01	0.009 ± 0.001
	Pu-Si	1.8 ± 0.6	3.15 ± 0.01	0.007 ± 0.002
	Pu-Ca	2.9 ± 0.9	4.16 ± 0.01	0.003 ± 0.002
Pu/HCP/GLU/ACW-VGL (norm. error = 0.4, $\Delta E_0 = 1.1 \pm 0.5$ eV)	Pu-O	6.7 ± 0.4	2.28 ± 0.01	0.011 ± 0.001
	Pu-Si	1.1 ± 0.5	3.16 ± 0.01	0.006 ± 0.003
	Pu-Ca	6.0 ± 2.3	4.18 ± 0.01	0.015 ± 0.004
C-S-H (Ca/Si 1.65)/Pu/Milli-Q (pH = 12.5) (Stietz et al., 2023) (norm. error = 0.3, $\Delta E_0 = 1.31 \pm 0.4$ eV)	Pu-O	6.0 ± 0.3	2.27 ± 0.01	0.008 ± 0.001
	Pu-Si	1.2 ± 0.4	3.13 ± 0.01	0.006 ± 0.002
	Pu-Ca	5.0 ± 1.3	4.17 ± 0.01	0.011 ± 0.002

be noted that similar EXAFS structural parameters were obtained using the deglitched, k^3 -weighted EXAFS spectra (see Supplementary Table S4), with only one exception for sample Pu/HCP/GLU in ACW-VGL. Here, both *N* and σ^2 are strongly correlated and increased to 11.7 ± 5 atoms and $0.027 \pm 0.006 \text{ Å}^2$, respectively. In addition, no Pu–Pu interaction could be modeled, indicating the absence of Pu clusters or precipitates at the HCP surface. Because both the atomic distances between Pu and its neighboring O, Si, and Ca atoms and the corresponding coordination numbers are almost identical for the three samples, one can conclude that neither ionic strength nor GLU affects the Pu uptake mechanism. No formation of ternary Pu(IV) complexes on HCP involving GLU was observed.

The obtained EXAFS structural parameters can be compared with previous EXAFS studies of Pu(IV) interaction with C-S-H (Ca/Si = 1.65, pH 12.5) (Stietz et al., 2023) and of Np(IV) interaction with HCP in ACW at pH 13.3 and with C-S-H (Ca/Si = 1.65, pH 12.5) (Gaona et al., 2011). For Pu/C-S-H, the following interatomic distances with coordination numbers in parentheses were reported: Pu-O 2.27 Å (6), Pu-Si 3.13 Å (1), and Pu-Ca 4.17 Å (5) (see Table 6). These EXAFS structural parameters are very similar to those of the HCP samples of this study, indicating that C-S-H is the main phase responsible for the uptake of Pu(IV) by HCP.

Gaona et al. (2011) obtained the following interatomic distances with coordination numbers in parentheses for Np/C-S-H: Np-O 2.31 Å (8.3), Np-Si 3.60 Å (2.9), and Np-Ca 4.18 Å (12.7). These results show some agreement and some differences compared to our Pu/HCP samples, that is, a longer Np-Si distance and a higher Ca coordination number. Based on a detailed discussion of the results, Gaona et al. concluded that “Np(IV) is incorporated in the interlayer of the C-S-H structure”.

The uptake of U(IV) by 14 Å tobermorite (Ca/Si = 1.0) was investigated in a recent density functional calculation (Chiorescu et al., 2022). The quantum mechanical calculations of geometry

parameters and relative energies included U(IV) adsorption on the (001) surface, absorption in the interlayer, and incorporation into the CaO layer of tobermorite that served as a structural model for C-S-H. The results show that the structural parameters of the U-O coordination shell are insensitive to the different sorption mechanisms. Furthermore, the wide scatter of calculated U-Si distances between 3.0 and 4.2 Å for all sorption modes makes it difficult to distinguish between them. The most promising parameter is the number of Ca atoms below 5.0 Å. *N* is in the range of 2–4 for the thermodynamically most stable U(IV) complexes at the (001) surface and in the interlayer. For U(IV) incorporation into the CaO layer, the calculations yielded six Ca atoms between 3.7–4.2 Å. Based on the close match between this DFT result and previous EXAFS measurements for Pu(IV)/C-S-H (Ca/Si = 0.8), it was concluded that incorporation of Pu(IV) into the CaO layer of C-S-H is the most probable uptake mechanism (Chiorescu et al., 2022; Dettmann et al., 2023). Compared to these quantum mechanical and spectroscopic results and taking into account the large uncertainty of coordination numbers determined by EXAFS, the uptake into the CaO layer of HCP might be the dominant but not the only uptake mechanism.

4 Conclusion

The results provide an improved basis for predicting the behavior of Pu in radioactive waste repositories under reducing conditions, independent of the ionic strength of the groundwater. The sorption experiments in the binary system show a quantitative uptake of Pu(IV) by HCP that is in good agreement with the sorption data available in the literature. The uptake of GLU by HCP could lead to saturation of the sorption sites and is also consistent with the sorption data available in the literature for C-S-H phases (Ca/Si = 1.4) (Androniuk et al., 2017).

The XANES measurements show that Pu(IV) is the predominant species after being taken up by HCP. The evaluation of the EXAFS measurements suggests that Pu is incorporated into the C-S-H phases, which are the main sorption phase of the HCP. Furthermore, the influence of the ionic strength was investigated, and neither it nor the presence of GLU showed an effect on the uptake of Pu by HCP.

The results show a significant influence of high GLU concentration ($[GLU]_0 = 1 \times 10^{-2} \text{ M}$) on the uptake of Pu(IV), independent of the ionic strength of the groundwater. The impact of the order of addition of Pu and GLU to HCP was investigated. The uptake of Pu by HCP in the presence of GLU decreases. Significant differences in the uptake are found in the experiments of (ii) (HCP + GLU) + Pu(IV) and (iii) (HCP + Pu(IV) + GLU), where (almost) no sorption occurred. This might be a competitive reaction of Pu(IV) and GLU, where GLU may have a desorbing effect or a complex of $\text{Pu}(\text{OH})_4(\text{GLU})^-$ might be formed. In addition, the amount of Ca^{2+} in the background electrolyte is crucial for the results of the experiments with GLU and, consequently, in the uptake of Pu by HCP. However, a significantly lower GLU concentration ($[GLU]_0 = 1 \times 10^{-8} \text{ M}$) is to be expected in a repository. A speciation calculation (see SM-5, Supplementary Figure S2) for this concentration shows that $\text{Pu}(\text{OH})_{4(\text{aq})}$ is the dominant species in the alkaline-to-hyperalkaline pH range. Further studies with lower GLU concentrations are needed to gain a better understanding of the processes controlling the effect of the order of addition in cement radionuclide-organic systems. Experiments over a significantly longer period of time are planned to increase the relevance of these assessments for use in repository planning. In addition, experiments should be performed in the other degradation stages of HCP to understand the impact of GLU on the long-term safety of a radioactive waste repository.

Data availability statement

The original contributions presented in the study are included in the article/Supplementary Material; further inquiries can be directed to the corresponding authors.

Author contributions

JS: formal analysis, investigation, visualization, writing—original draft, and writing—review & editing. SA: conceptualization, formal analysis, writing—review & editing, investigation, and visualization. VH: investigation. DP: investigation. TR: conceptualization, formal analysis, writing—review & editing, and supervision.

References

Adam, N., Hinz, K., Gaona, X., Panak, P. J., and Altmaier, M. (2021). Impact of selected cement additives and model compounds on the solubility of Nd(III), Th(IV) and U(VI): screening experiments in alkaline NaCl, MgCl_2 and CaCl_2 solutions at elevated ionic strength. *Radiochim. Acta* 109, 431–443. doi:10.1515/ract-2021-1010

Funding

The authors declare financial support was received for the research, authorship, and/or publication of this article. This work was financially supported within the EURAD project—WP CORI, which receives funding from the EU Horizon 2020 Research and Innovation Programme under grant agreement no. 847593 and the GRaZ project by the Federal Ministry for Economic Affairs and Energy (BMWi) under contract no. 02E11415A and the Federal Ministry for the Environment, Nature Conservation, Nuclear Safety and Consumer Protection (BMUV) under contract no. 02E11860A.

Acknowledgments

The authors thank three reviewers for their helpful comments for improving the manuscript. The authors are grateful to the ESRF for granting access to synchrotron beam time. Additionally, they thank the ROBL Group from the Helmholtz-Zentrum Dresden-Rossendorf (Germany) for providing experimental support during the XANES and EXAFS measurements. The authors thank Carl-Christian Meyer and Daniel Hagenlocher for their support with the XAFS measurements, Nora Groschopf (Institute of Geosciences, Mainz) for the XRF measurements, Janik Lohmann for ICP-MS SemiQuant analysis, and Markus Breckheimer for sorption modeling.

Conflict of interest

The authors declare that the research was conducted in the absence of any commercial or financial relationships that could be construed as a potential conflict of interest.

Publisher's note

All claims expressed in this article are solely those of the authors and do not necessarily represent those of their affiliated organizations, or those of the publisher, the editors, and the reviewers. Any product that may be evaluated in this article, or claim that may be made by its manufacturer, is not guaranteed or endorsed by the publisher.

Supplementary material

The Supplementary Material for this article can be found online at: <https://www.frontiersin.org/articles/10.3389/fnuen.2023.1268767/full#supplementary-material>

Altmaier, M., Blin, V., Garcia, D., Henocq, P., Missana, T., and Ricard, D. (2021). Final version as of 19.05.2021 of deliverable D3.1 of the HORIZON 2020 project EURAD. EC Grant agreement no: 847593. State-of-the art report on cement-organic-radionuclide interactions.

- Amayri, S., Fröhlich, D. R., Kaplan, U., Trautmann, N., and Reich, T. (2016). Distribution coefficients for the sorption of Th, U, Np, Pu, and Am on Opalinus Clay. *Radiochim. Acta* 104, 33–40. doi:10.1515/ract-2015-2409
- Androniuk, I., Landesman, C., Henocq, P., and Kalinichev, A. G. (2017). Adsorption of gluconate and uranyl on C-S-H phases: combination of wet chemistry experiments and molecular dynamics simulations for the binary systems. *Phys. Chem. Earth* 99, 194–203. doi:10.1016/j.pce.2017.05.005
- Böszörményi, É., Lado, J., Dudás, C., Kutus, B., Szabados, M., Varga, G., et al. (2020). The structure and composition of solid complexes comprising of Nd(III), Ca(II) and D-gluconate isolated from solutions relevant to radioactive waste disposal. *Pure Appl. Chem.* 92, 1709–1715. doi:10.1515/pac-2019-1010
- Chiorescu, I., Kremleva, A., and Krüger, S. (2022). On the sorption mode of U(IV) at calcium silicate hydrate: a comparison of adsorption, absorption in the interlayer, and incorporation by means of density functional calculations. *Minerals* 12, 1541. doi:10.3390/min12121541
- Cohen, D. (1961). The absorption spectra of plutonium ions in perchloric acid solutions. *J. Inorg. Nucl. Chem.* 18, 211–218. doi:10.1016/0022-1902(61)80390-4
- Colàs, E., Grivé, M., Rojo, I., and Duro, L. (2013). The effect of gluconate and EDTA on thorium solubility under simulated cement porewater conditions. *J. Solut. Chem.* 42, 1680–1690. doi:10.1007/s10953-013-0054-2
- Conradson, S. D., Abney, K. D., Begg, B. D., Brady, E. D., Clark, D. L., Den Auwer, C., et al. (2004). Higher order speciation effects on plutonium L_{2,3} X-ray absorption near edge spectra. *Inorg. Chem.* 43, 116–131. doi:10.1021/ic0346477
- Dario, M., Molera, M., and Allard, B. (2006). Sorption of europium on TiO₂ and cement at high pH in the presence of organic ligands. *J. Radioanal. Nucl. Chem.* 270, 495–505. doi:10.1007/s10967-006-0455-4
- Dettmann, S., Huittinen, N. M., Jahn, N., Kretzschmar, J., Kumke, M. U., Kutyma, T., et al. (2023). Influence of gluconate on the retention of Eu(III), Am(III), Th(IV), Pu(IV), and U(VI) by C-S-H (C/S = 0.8). *Front. Nucl. Eng.* 2. doi:10.3389/fnuen.2023.1124856
- DIN, (2009). Prüfverfahren für Zement in Teil 3: Bestimmung der Erstarrungszeiten und der Raumbeständigkeit, *Deutsche Fassung EN 196-3:2005+a1:2008*. Dtsch. Fass. EN DIN EN 196-3.
- Duquette, D. J., Latanision, R. M., Di Bella, C. A., and Kirstein, B. E. (2009). Corrosion issues related to disposal of high-level nuclear waste in the Yucca Mountain repository—peer reviewers' perspective. *Corrosion* 65, 272–280. doi:10.5006/1.3319133
- Duro, L., Altmaier, M., Holt, E., Mäder, U., Claret, F., Grambow, B., et al. (2020). Contribution of the results of the CEBAMA project to decrease uncertainties in the Safety Case and Performance Assessment of radioactive waste repositories. *Appl. Geochem.* 112, 104479. doi:10.1016/j.apgeochem.2019.104479
- Duro, L., Domènech, C., Grivé, M., Roman-Ross, G., Bruno, J., and Källström, K. (2014). Assessment of the evolution of the redox conditions in a low and intermediate level nuclear waste repository (SFR1, Sweden). *Appl. Geochem.* 49, 192–205. doi:10.1016/j.apgeochem.2014.04.015
- Fanghänel, T., Neck, V., and Kim, J. I. (1996). The ion product of H₂O, dissociation constants of H₂CO₃ and Pitzer parameters in the system Na⁺/H⁺/OH⁻/HCO₃⁻/CO₃²⁻/ClO₄⁻/H₂O at 25°C. *J. Solut. Chem.* 25, 327–343. doi:10.1007/bf00972890
- Gaona, X., Dähn, R., Tits, J., Scheinost, A. C., and Wieland, E. (2011). Uptake of Np(IV) by C-S-H phases and cement paste: an EXAFS study. *Environ. Sci. Technol.* 45, 8765–8771. doi:10.1021/es2012897
- Gaona, X., Montoya, V., Colàs, E., Grivé, M., and Duro, L. (2008). Review of the complexation of tetravalent actinides by ISA and gluconate under alkaline to hyperalkaline conditions. *J. Contam. Hydrol.* 102, 217–227. doi:10.1016/j.jconhyd.2008.09.017
- George, G. N., and Pickering, I. J. (2000). *EXAFSPAK - a suite of computer programs for analysis of X-ray absorption spectra*. Stanford Synchrotron Radiation Lightsource.
- Giffaut, E., Grivé, M., Blanc, P., Vieillard, P., Colàs, E., Gailhanou, H., et al. (2014). Andra thermodynamic database for performance assessment: ThermoChimie. *Appl. Geochem.* 49, 225–236. doi:10.1016/j.apgeochem.2014.05.007
- Glaus, M. A., Laube, A., and Van Loon, L. R. (2006). Solid-liquid distribution of selected concrete admixtures in hardened cement pastes. *Waste Manag.* 26, 741–751. doi:10.1016/j.wasman.2006.01.019
- Grenthe, I., Gaona, X., Rao, L., Plyasunov, A., Runde, W., Grambow, B., et al. (2020). *Second update on the chemical thermodynamics of uranium, neptunium, plutonium, americium and technetium*. Paris: OECD Publishing.
- Guo, X., Gin, S., and Frankel, G. S. (2020). Review of corrosion interactions between different materials relevant to disposal of high-level nuclear waste. *npj Mat. Degrad.* 4, 34. doi:10.1038/s41529-020-00140-7
- Häußler, V., Amayri, S., Beck, A., Platte, T., Stern, T. A., Vitova, T., et al. (2018). Uptake of actinides by calcium silicate hydrate (C-S-H) phases. *Appl. Geochem.* 98, 426–434. doi:10.1016/j.apgeochem.2018.08.021
- Jobmann, M., Bebiolka, A., Burlaka, V., Herold, P., Jahn, S., Lommerzheim, A., et al. (2017). Safety assessment methodology for a German high-level waste repository in clay formations. *J. Rock Mech. Geotech. Eng.* 9, 856–876. doi:10.1016/j.jrmge.2017.05.007
- Jobmann, M., and Lommerzheim, A. (2015). *Projekt ANSICHT - Endlagerkonzept sowie Verfüll- und Verschlusskonzept für das Endlagerstandortmodell SÜD*. DBE Technology GmbH.
- Kutus, B., Gaona, X., Pallagi, A., Pálíncó, I., Altmaier, M., and Sipos, P. (2020). Recent advances in the aqueous chemistry of the calcium(II)-gluconate system – equilibria, structure and composition of the complexes forming in neutral and in alkaline solutions. *Coord. Chem. Rev.* 417, 213337. doi:10.1016/j.ccr.2020.213337
- Lommerzheim, A., and Jobmann, M. (2015). *Projekt ANSICHT - Endlagerkonzept sowie Verfüll- und Verschlusskonzept für das Standortmodell NORD*. DBE Technology GmbH.
- Martin, P., Grandjean, S., Valot, C., Carlot, G., Ripert, M., Blanc, P., et al. (2007). XAS study of (U_{1-x}Pu_x)O₂ solid solutions. *J. Alloys Compd.* 444, 410–414. doi:10.1016/j.jallcom.2007.01.032
- Matz, W., Schell, N., Bernhard, G., Prokert, F., Reich, T., Claußner, J., et al. (1999). ROBL—a CRG beamline for radiochemistry and materials research at the ESRF. *J. Synchrotron Radiat.* 6, 1076–1085. doi:10.1107/s0909049599010663
- Meleshyn, A. (2015). Gesellschaft für Anlagen-und Reaktorsicherheit (GRS) GmbH GRS-A-3844. Mechanisms of transformation of bentonite barriers – testing a new experimental concept
- Ochs, M., Dolder, F., and Tachi, Y. (2022). Decrease of radionuclide sorption in hydrated cement systems by organic ligands: comparative evaluation using experimental data and thermodynamic calculations for ISA/EDTA-actinide-cement systems. *Appl. Geochem.* 136, 105161. doi:10.1016/j.apgeochem.2021.105161
- Ochs, M., Mallants, D., and Wang, L. (2016). *Radionuclide and metal sorption on cement and concrete*. Springer International Publishing Switzerland.
- Pallagi, A., Bajnóczy, É. G., Canton, S. E., Bolin, T., Peintler, G., Kutus, B., et al. (2014). Multinuclear complex formation between Ca(II) and gluconate ions in hyperalkaline solutions. *Environ. Sci. Technol.* 48, 6604–6611. doi:10.1021/es501067w
- Parkhurst, D. L., and Appelo, C. A. J. (2016). PHREEQC (Version 3.3.5) - a computer program for speciation, batch-reaction, one-dimensional transport, and inverse geochemical calculations. Available: http://www.brr.cr.usgs.gov/projects/GWC_coupled/phreeqc/index.html, Accessed, 2023).
- Ravel, B., and Newville, M. (2005). ATHENA, ARTEMIS, HEPHAESTUS: data analysis for X-ray absorption spectroscopy using IFEFFIT. *J. Synchrotron Radiat.* 12, 537–541. doi:10.1107/s0909049505012719
- Rehr, J. J., Kas, J. J., Vila, F. D., Prange, M. P., and Jorissen, K. (2010). Parameter-free calculations of X-ray spectra with FEFF9. *Phys. Chem. Chem. Phys.* 12, 5503–5513. doi:10.1039/b926434e
- Reich, T., Reich, T. Y., Amayri, S., Drebert, J., Banik, N. L., Buda, R. A., et al. (2007). Application of XAFS spectroscopy to actinide environmental science. *AIP Conf. Proc.* 882, 179–183.
- Rojo, H., Gaona, X., Rabung, T., Polly, R., García-Gutiérrez, M., Missana, T., et al. (2021). Complexation of Nd(III)/Cm(III) with gluconate in alkaline NaCl and CaCl₂ solutions: solubility, TRLFS and DFT studies. *Appl. Geochem.* 126, 104864. doi:10.1016/j.apgeochem.2020.104864
- Scheinost, A. C., Claussner, J., Exner, J., Feig, M., Findeisen, S., Hennig, C., et al. (2021). ROBL-II at ESRF: a synchrotron toolbox for actinide research. *J. Synchrotron Radiat.* 28, 333–349. doi:10.1107/s1600577520014265
- Schmeide, K., Reich, T., Sachs, S., and Bernhard, G. (2006). Plutonium(III) complexation by humic substances studied by X-ray absorption fine structure spectroscopy. *Inorg. Chim. Acta* 359, 237–242. doi:10.1016/j.ica.2005.10.037
- Stietz, J., Amayri, S., Häußler, V., Scholze, R., and Reich, T. (2023). Uptake of actinides by hardened cement paste in high-salinity pore water. *Minerals* 2023, 13, 1380. doi:10.1016/j.ica.2005.10.037
- Tasi, A., Gaona, X., Rabung, T., Fellhauer, D., Rothe, J., Dardenne, K., et al. (2021). Plutonium retention in the isosaccharinate – cement system. *Appl. Geochem.* 126, 104862. doi:10.1016/j.apgeochem.2020.104862
- Taylor, H. F. W. (1997). *Cement chemistry*. Thomas Telford Publishing.
- Tits, J., Wieland, E., Bradbury, M. H., Eckert, P., and Schaible, A. (2002). *The uptake of Eu(III) and Th(IV) by calcite under hyperalkaline conditions*. PSI Bericht 02-03.
- Tits, J., Wieland, E., and Bradbury, M. H. (2005). The effect of isosaccharinic acid and gluconic acid on the retention of Eu(III), Am(III) and Th(IV) by calcite. *Appl. Geochem.* 20, 2082–2096. doi:10.1016/j.apgeochem.2005.07.004
- Tyupina, E. A., Kozlov, P. P., and Krupskaya, V. V. (2023). Application of cement-based materials as a component of an engineered barrier system at geological disposal facilities for radioactive waste—a review. *Energies* 16, 605. doi:10.3390/en16020605
- Wieland, E. (2014). Sorption data base for the cementitious near field of L/ILW and ILW repositories for provisional safety analyses for SGT-E2. *NAGRA Tech. Rep.*, 14–08.
- Wieland, E., Tits, J., Ulrich, A., and Bradbury, M. H. (2006). Experimental evidence for solubility limitation of the aqueous Ni(II) concentration and isotopic exchange of ⁶³Ni in cementitious systems. *Radiochim. Acta* 94, 29–36. doi:10.1524/ract.2006.94.1.29

2.2.2 Publication: Influence of gluconate on the retention of Eu(III), Am(III), Th(IV), Pu(IV), and U(VI) by C-S-H (C/S = 0.8)

Author Contribution

The publication was produced in collaboration with the University of Potsdam and the HZDR – Helmholtz-Zentrum Dresden-Rossendorf as part of the CORI project. The batch sorption investigations in the binary system (C-S-H / GLU) and ternary system (C-S-H / An(III/IV) / GLU) were carried out as part of the master thesis of L. Spittler under the supervision of J. Stietz and T. Reich [129]. Sample preparation and measurements were performed by L. Spittler and J. Stietz. The analysis, the text and the visualization presented here was conducted by J. Stietz. XAFS investigations were carried out by V. Häußler, S. Amayri and T. Reich. Further details can be found in the acknowledgements in the publication.

Summary

In the study, the effects of GLU on actinide retention were investigated using the C-S-H phase (C/S = 0.8), which is representative of degraded cement in stage III of alteration. It explored various oxidation states of actinides, including Am(III), Th(IV), Pu(IV), U(VI), and analogues such as Eu(III) and Cm(III). The results indicate low GLU sorption on the C-S-H phases, which is limited to the surface without blocking the sorption sites at stage III of cement degradation. Analysis revealed no alteration in C-S-H structure due to GLU or An(X) sorption. A high retention of An(X) was obtained unaffected by GLU presence. Further measurements suggested Th(IV)-GLU-OH complex formation in the presence of GLU and Ca(II), possibly leading to Ca-Th(IV)-GLU-OH formation. Leaching experiments showed no remobilization of sorbed Eu(III) or U(VI) with GLU. However, GLU notably affected the Eu(III) coordination environment, potentially via Ca(II)-GLU complex formation, altering the coprecipitate's stoichiometry and structure. Interestingly, the study's findings, indicating a minor effect of GLU on An(X) retention (C/S 0.8), contrast with prior literature findings at higher pH and Ca(II) concentrations. This discrepancy may underscore the significance of Ca(II) ions and potential heterobimetallic Ca(II)-An(X)-GLU complex formation in An(X) mobilization by GLU.

© 2023 Dettmann, Huittinen, Jahn, Kretschmar, Kumke, Kutyma, Lohmann, Reich, Schmeide, Shams Aldin Azzam, Spittler and Stietz. This is an open-access article distributed under the terms of the Creative Commons Attribution License (CC BY). The use, distribution or reproduction in other forums is permitted, provided the original author(s) and the copyright owner(s) are credited and that the original publication in this journal is cited, in accordance with accepted academic practice. No use, distribution or reproduction is permitted which does not comply with these terms.



OPEN ACCESS

EDITED BY

Pierre Henocq,
Agence Nationale Pour la Gestion des
Déchets Radioactifs, France

REVIEWED BY

Mavrik Zavarin,
Lawrence Livermore National Laboratory
(DOE), United States
Tiziana Missana,
Medioambientales y Tecnológicas, Spain

*CORRESPONDENCE

Michael U. Kumke,
✉ kumke@uni-potsdam.de
Tobias Reich,
✉ treich@uni-mainz.de
Katja Schmeide,
✉ k.schmeide@hzdr.de

SPECIALTY SECTION

This article was submitted
to Radioactive Waste Management,
a section of the journal
Frontiers in Nuclear Engineering

RECEIVED 15 December 2022

ACCEPTED 10 February 2023

PUBLISHED 01 March 2023

CITATION

Dettmann S, Huittinen NM, Jahn N,
Kretzschmar J, Kumke MU, Kutyma T,
Lohmann J, Reich T, Schmeide K,
Shams Aldin Azzam S, Spittler L and
Stietz J (2023), Influence of gluconate on
the retention of Eu(III), Am(III), Th(IV),
Pu(IV), and U(VI) by C-S-H (C/S = 0.8).
Front. Nucl. Eng. 2:1124856.
doi: 10.3389/fnuen.2023.1124856

COPYRIGHT

© 2023 Dettmann, Huittinen, Jahn,
Kretzschmar, Kumke, Kutyma,
Lohmann, Reich, Schmeide, Shams Aldin Azzam,
Spittler and Stietz. This is an open-access
article distributed under the terms of the
[Creative Commons Attribution License
\(CC BY\)](https://creativecommons.org/licenses/by/4.0/). The use, distribution or
reproduction in other forums is
permitted, provided the original author(s)
and the copyright owner(s) are credited
and that the original publication in this
journal is cited, in accordance with
accepted academic practice. No use,
distribution or reproduction is permitted
which does not comply with these terms.

Influence of gluconate on the retention of Eu(III), Am(III), Th(IV), Pu(IV), and U(VI) by C-S-H (C/S = 0.8)

Sophie Dettmann¹, Nina M. Huittinen², Nicolas Jahn¹,
Jerome Kretzschmar², Michael U. Kumke^{1*}, Tamara Kutyma³,
Janik Lohmann³, Tobias Reich^{3*}, Katja Schmeide^{2*},
Salim Shams Aldin Azzam², Leon Spittler³ and Janina Stietz³

¹Institute of Chemistry, Universität Potsdam, Potsdam, Germany, ²Helmholtz-Zentrum Dresden-Rossendorf, Institute of Resource Ecology, Dresden, Germany, ³Department of Chemistry, Johannes Gutenberg-Universität Mainz, Mainz, Germany

The retention of actinides in different oxidation states (An(X), X = III, IV, VI) by a calcium-silicate-hydrate (C-S-H) phase with a Ca/Si (C/S) ratio of 0.8 was investigated in the presence of gluconate (GLU). The actinides considered were Am(III), Th(IV), Pu(IV), and U(VI). Eu(III) was investigated as chemical analogue for Am(III) and Cm(III). In addition to the ternary systems An(X)/GLU/C-S-H, also binary systems An(X)/C-S-H, GLU/C-S-H, and An(X)/GLU were studied. Complementary analytical techniques were applied to address the different specific aspects of the binary and ternary systems. Time-resolved laser-induced luminescence spectroscopy (TRLFS) was applied in combination with parallel factor analysis (PARAFAC) to identify retained species and to monitor species-selective sorption kinetics. ¹³C and ²⁹Si magic-angle-spinning (MAS) nuclear magnetic resonance (NMR) spectroscopy and X-ray photoelectron spectroscopy (XPS) were applied to determine the bulk structure and the composition of the C-S-H surface, respectively, in the absence and presence of GLU. The interaction of Th(IV) with GLU in different electrolytes was studied by capillary electrophoresis-inductively coupled plasma mass spectrometry (CE-ICP-MS). The influence of GLU on An(X) retention was investigated for a large concentration range up to 10⁻² M. The results showed that GLU had little to no effect on the overall An(X) retention by C-S-H with C/S of 0.8, regardless of the oxidation state of the actinides. For Eu(III), the TRLFS investigations additionally implied the formation of a Eu(III)-bearing precipitate with dissolved constituents of the C-S-H phase, which becomes structurally altered by the presence of GLU. For U(VI) sorption on the C-S-H phase, only a small influence of GLU could be established in the luminescence spectroscopic investigations, and no precipitation of U(VI)-containing secondary phases could be identified.

KEYWORDS

actinide, organic ligand, sorption, cementitious material, concrete, luminescence

1 Introduction

Concepts of deep geological repositories for nuclear waste typically include the use of cementitious materials, for example, for construction, for backfill purposes, or for conditioning of the waste. Due to their high sorption affinity towards many radionuclides and the high pH of the cement pore water, cementitious materials can act as an efficient technical barrier for the retention of radionuclides in the repository (Tits and Wieland, 2018). Calcium-silicate-hydrates (C-S-H) are major constituents of hardened cement paste and have been shown to be the most important cement phases for the retention of tri- to hexavalent actinides (Atkins and Glasser, 1992; Pointeau et al., 2004; Stumpf et al., 2004; Gaona et al., 2011; Gaona et al., 2012; Tits et al., 2015; Häußler et al., 2018; Wolter et al., 2019b). C-S-H phases are nanocrystalline and their structure is dependent on the aging stage of the cement, as the pore water chemistry (e.g., Ca(II) concentration and pH) changes over time. In the first degradation stage (I) of cement, the pore water is rich in NaOH and KOH and has a high pH of ~ 13.3 (Tits and Wieland, 2018). As the degradation progresses, portlandite is dissolved in a degradation stage II, leading to a pH of ~ 12.5 in the pore water. In degradation stage III, leaching of the C-S-H phases occurs, during which the C/S ratio of the C-S-H decreases from approximately 1.7 to ~ 0.7 , while the pH of the pore water decreases to ~ 10 (Tits and Wieland, 2018). The crystalline domains of the C-S-H phases have a tobermorite-like structure and consist of CaO sheets that are enclosed by silica tetrahedra and interlayers (Papatzani et al., 2015; Tits and Wieland, 2018). Immobilization of actinides can occur *via* sorption on the silanol groups at the surface of C-S-H phases, sorption into the interlayers, or *via* the incorporation into the CaO layers by exchange for Ca(II) ions (Pointeau et al., 2001; Tits et al., 2003; Tits et al., 2015; Wieland, 2014). Additionally, coprecipitation with ions from the pore water is possible, leading to the formation of new phases (Schlegel et al., 2004; Altmaier et al., 2005; Wieland et al., 2010).

Organic complexing agents that may be present in the radioactive waste include, e.g., cleaning agents, degradation products of cellulose materials, or additives of the cement. They may alter the retention of actinides by influencing complexation, by blocking sorption sites at the C-S-H surface, or by altering the structure and the chemical composition of the C-S-H phases (Dario et al., 2004; Gaona et al., 2008; Altmaier et al., 2021; Keith Roach and Shahkarami, 2021; Ochs et al., 2022). Gluconate (GLU) is widely used as a plasticizer in cement admixtures and it may also be present in the waste from the use in decontamination and cleaning agents (Taylor, 1997; Tits et al., 2005; Glaus et al., 2006; Keith Roach and Shahkarami, 2021). It can also be viewed as an analogue for the cellulose degradation product isosaccharinic acid (ISA), which is expected to be one of the most abundant complexing agents in a repository (Wieland, 2014). Owing to its carboxylic group as well as the hydroxyl groups, which can participate in complexation processes, GLU forms stable chelate complexes with a variety of radionuclides (Warwick et al., 2004; Tits et al., 2005; Gaona et al., 2008; Colàs et al., 2013; Adam et al., 2021). GLU also forms complexes with Ca(II) occurring in cementitious systems (Kutus et al., 2020). For tri- and tetravalent actinides, the formation of

ternary complexes with Ca(II) was reported (Colàs et al., 2013; Böszörményi et al., 2020; Rojo et al., 2021). Sorption experiments and molecular dynamics (MD) simulations showed an increasing GLU sorption on C-S-H with increasing Ca(II) concentration, which was attributed to a mediating effect of Ca(II) at the interface (Androniuk et al., 2017). It was shown that GLU could reduce the retention of Eu(III) by hardened cement paste (HCP) with a pH of 12.5 at GLU concentrations as low as 1×10^{-6} M (Dario et al., 2004). Norden (1994) observed a reduction of Eu(III) retention by HCP (pH 12.5) at 3×10^{-5} M GLU. On calcite (pH 13.3), Eu(III) retention was reduced at 1×10^{-7} M GLU (Tits et al., 2005). In contrast, Tits et al. (1998) found no effect of GLU on the retention of Eu(III) and Th(IV) by C-S-H phases (pH 13.3) at $[GLU] \leq 1 \times 10^{-4}$ M. In a recent study of the Pu-ISA-cement system by Tasi et al. (2021), a low uptake of Pu(IV) on cement at degradation stage II in the presence of ISA ($[ISA]_{\text{tot}} \geq 3.2 \times 10^{-5}$ M) was observed. However, to date, not much has been reported for the interactions between An(X), GLU, and cementitious materials at lower pH values expected in aged cement.

This study aims at extending the knowledge of the interactions between GLU, cement phases, and a number of actinides (An(X)) with different oxidation states (Am(III), Th(IV), Pu(IV), U(VI) as well as Eu(III) as a chemical analogue for Am(III) and Cm(III)) under conditions relevant for a nuclear waste repository. Here, C-S-H with a C/S ratio of 0.8 and a pH of ~ 10 was chosen to represent aged cement of the degradation stage III.

The present study is a collaboration between three different institutions, covering both a broad spectrum of actinides in various oxidation states and a large variety of state-of-the-art analytical techniques. Therefore, experimental conditions of sorption experiments and the spectroscopic methods applied for sample characterization are not exactly identical for each actinide, but have been adapted with respect to the applied experimental technique. The retention of the An(X) was qualitatively and quantitatively studied in the absence and presence of GLU to elucidate the mechanisms by which GLU may influence the retention processes. Batch sorption experiments were performed to quantify the retention of the An(X) and GLU on a macroscopic scale. For the luminescent cations Eu(III) and U(VI), time-resolved laser-induced luminescence spectroscopy (TRLFS) was used to differentiate between different sorption complexes and to determine species-selective sorption kinetics. The uptake of Pu by C-S-H was probed by EXAFS spectroscopy. To analyze the complexation of Th(IV) and GLU in C-S-H pore water, capillary electrophoresis-inductively coupled plasma mass spectrometry (CE-ICP-MS) measurements were conducted. ^{13}C and ^{29}Si magic-angle-spinning (MAS) nuclear magnetic resonance (NMR) spectroscopy, X-ray photoelectron spectroscopy (XPS), and X-ray diffraction (XRD) were applied to characterize composition and structure of the C-S-H phases before and after the sorption experiments. In addition, also the binary systems An(X)/GLU, An(X)/C-S-H, and GLU/C-S-H were investigated as references to further analyze the interactions between the individual components. Finally, after sorption experiments, GLU concentrations in the remaining supernatants were determined by means of quantitative ^1H NMR spectroscopy or liquid scintillation counting (LSC) from ^{14}C -GLU spiked samples.

2 Materials and methods

Amorphous C-S-H phases ($C/S = 0.8$) were prepared using the “direct reaction method” described by Atkins et al. (1992). In short, appropriate amounts of CaO and SiO₂ were mixed with water or NaCl solution and shaken in an end-over-end rotator to allow the formation of the C-S-H phases. The S/L ratios, equilibration times, and materials used for the different experiments are summarized in Supplementary Table S1 (Supplementary Material). To avoid the formation of carbonates, the syntheses and retention experiments were performed in glove boxes under N₂ or Ar atmosphere using deionized water (18.2 MΩcm; Millipore), which had been decarbonated by purging with Ar over night or boiling for at least 2 h, prior to use.

2.1 GLU experiments

2.1.1 Preparation of GLU samples

The C-S-H phases were prepared in 10 mL polycarbonate centrifuge tubes (Beckman Coulter, United States). The S/L ratio achieved in the samples was determined from the dry weight of the solids formed. After a two-week synthesis period, during which the centrifuge tubes were rotated in an end-over-end rotator (Stuart Rotator SB3, United Kingdom), aliquots of the respective GLU stock solutions were added. A non-radioactive GLU stock solution was prepared by weighing the appropriate amount of sodium gluconate (Sigma-Aldrich, United States) and dissolving it in deionized water at various concentrations for the batch sorption experiments. Additionally, a ¹⁴C-GLU tracer solution was added by diluting a stock solution of 3.7 MBq/mL ¹⁴C-GLU (Hartmann Analytic, Germany) in deionized water. The contact time of GLU with the C-S-H phases was 72 h.

A first batch sorption experiment was performed as a sorption isotherm of GLU ($S/L = 5$ g/L) over a concentration range of 1×10^{-9} to 1×10^{-1} M. In the second experiment, the S/L ratio was varied ($S/L = 0.5$ – 50 g/L) at a constant initial GLU concentration of 1×10^{-2} M. Finally, the samples were pre-centrifuged at $3,770 \times g$ (SIGMA 3K30, SIGMA Laborzentrifugen, Germany) for 5 min and ultracentrifuged at $108,800 \times g$ (Avanti J-30I, Beckman-Coulter, United States) for 1 h. The final pH of each suspension was determined using an inoLab pH/Cond 720 (WTW, Germany) pH-meter, which was connected to a BlueLine 16 pH electrode (Schott Instruments, Schott AG, Germany), with 3 M KCl (Mettler-Toledo AG, Switzerland) as filling solution. A three-point calibration was carried out using reference buffer solutions with the pH values 6.87 (SI Analytics, Germany), 4.01 and 9.18 (Merck, Germany). LSC (Hidex 300 SL, Hidex, Finland) was used to analyze the supernatants of the batch sorption samples containing ¹⁴C-GLU. To 10 mL LSC cocktail Ultima Gold™ XR (PerkinElmer LAS GmbH, Germany), 1–2 mL of the sample solutions was added. The samples were measured until a 2σ error of 2% was attained and with a resulting limit of detection (LOD) of 1×10^{-9} M for ¹⁴C.

2.1.2 XPS measurements

XPS measurements were performed to determine the surface composition of the solids in presence and absence of GLU. After

separation by ultracentrifugation, the C-S-H phases were dried under Ar atmosphere in a glove box at room temperature (RT) for at least 72 h. The sample powders were milled in an agate mortar and a small amount was pressed into an indium foil on a copper sample holder. The measurements were performed with a custom-built XPS system (SPECS GmbH, Germany) at RT and under a vacuum of 7×10^{-9} mbar. For photoelectron excitation, a non-monochromatic Mg Kα radiation (1,253.6 eV) from a high intensity double anode X-ray source (Al/Mg) XR-50 was used. Photoelectron detection was conducted with a constant analyzer pass energy of 13 eV using the PHOIBOS 100 hemispherical energy analyzer. The analysis of the spectra was carried out using CasaXPS (version 2.3.15). To calculate the corresponding atomic ratio n_{Ca}/n_{Si} , the intensities I_i of the Ca 2p and Si 2p signals were used (Eq. 1). The XPS measurement of a CaSiO₃ (Sigma-Aldrich, United States) standard resulted in the experimental sensitivity factor of $S = 0.24$.

$$\frac{n_{Ca}}{n_{Si}} = \frac{I_{Ca}}{I_{Si}} \cdot S \quad (1)$$

2.2 Eu(III) experiments

2.2.1 Preparation of Eu(III) samples

The Eu(III) samples were prepared in quartz tubes (Neubert-Glas GbR, Germany). For the retention experiments, different concentrations of EuCl₃·6H₂O (Sigma-Aldrich, United States) and sodium gluconate (meets USP testing specifications, Sigma-Aldrich, United States) solutions were mixed at a neutral pH to form Eu(III)-GLU complexes. Afterwards, 1 mL of the mixtures was added to the C-S-H samples (after an initial formation time of 14 days) to yield a final S/L ratio of 33.3 g/L. The Eu(III) concentration in each sample was adjusted to 1×10^{-6} M or 5×10^{-5} M, along with eight different GLU concentrations between 5×10^{-6} M and 5×10^{-3} M. After preparation, the samples were equilibrated in an end-over-end rotator (REAX 20/4, Heidolph Instruments, Germany) for a contact time of 211 days. During that time, TRLFS measurements (cf. Section 2.2.2) at fixed time intervals were carried out to monitor the retention processes. Finally, six exemplary supernatants were subjected to GLU quantification by solution NMR spectroscopy (cf. Section 2.5).

As a reference experiment, 1×10^{-6} M Eu(III) was added at the very beginning of the C-S-H preparation process to foster the incorporation of Eu(III) into the C-S-H structure. After 14 days, GLU (5×10^{-6} M to 1×10^{-2} M) was added and the samples were shaken for additional 4 weeks. Additional reference experiments were carried out in the C-S-H pore water. For this, the C-S-H phases were separated by filtration (Whatman 540, Cytiva, United States) after a formation time of 14 days. The liquid phase was mixed with stock solutions of GLU and Eu(III) to obtain samples with a Eu(III) concentration of 5×10^{-5} M and GLU concentrations between 2.5×10^{-6} M and 1×10^{-2} M. The pH, which had decreased due to the presence of GLU, was adjusted to the intrinsic pH of the C-S-H pore water of 9.8 with approximately 3 μL of 7 M NaOH (Sigma-Aldrich, United States). The samples were equilibrated for 8 days before the measurements.

2.2.2 Eu(III) luminescence spectroscopy

The Eu(III) samples were analyzed using TRFLS. The Eu(III) in the C-S-H samples was excited with a pulsed Nd:YAG laser (20 Hz, Quanta Ray, Spectra Physics, United States) combined with an OPO (GWU-Lasertechnik, Germany) set to 394 nm (using the $^5L_6 \leftarrow ^7F_0$ transition of Eu(III) for excitation). A spectrograph (Shamrock 303i, Andor Technology, Oxford Instruments, United Kingdom) equipped with a 600 lines/mm grating (blaze: 1,000 nm) and an ICCD camera (iStar DH720-18V-73, Andor Technology, Oxford Instruments, United Kingdom) were used to detect the emitted light in the spectral range of the $^5D_0 \rightarrow ^7F_0$ to $^5D_0 \rightarrow ^7F_4$ emission bands (574 nm $\leq \lambda_{em} \leq$ 711 nm).

The pore water samples were measured with a Nd:YAG/OPO system operating at 10 Hz (Quanta Ray, Spectra Physics, Germany and GWU-Lasertechnik, Germany), a spectrograph (Kymera 328i, Andor Technology, Oxford Instruments, United Kingdom) with a 300 lines/mm grating (blaze: 760 nm) and an ICCD camera (iStar sCMOS, Andor Technology, Oxford Instruments, United Kingdom). Measurements of all samples were carried out using the box-car technique with an initial delay of 10 μ s, a gate width of 1,000 μ s and 100 different delays scaling with a linear increasing gate step. The C-S-H samples, equilibrated in an end-over-end shaker, rested for at least 60 min before measurements to allow the solid phase to settle. Both the solid and liquid phases were examined. The pore water samples were measured under constant stirring (PTFE stirring rods: Rotilabo, Carl Roth GmbH + Co. KG, Germany; stirring unit: CuV-O-Stir 333, HELMA GmbH & Co. KG, Germany) to whirl up the precipitated solid into the light path. The limit of detection of the TRFLS setup used was approximately 5×10^{-8} M Eu(III).

The luminescence spectra were corrected for the spectral sensitivity of the grating and the ICCD camera. Parallel factor analysis (PARAFAC (Bro, 1997; Drobot et al., 2015) executed in Matlab 2019b (MATLAB, 2019, The MathWorks, Inc., Natick, MA, 2019.) with a monoexponential constraint in the time dimension and non-negativity in all other dimensions) was employed to deconvolute the time-resolved luminescence spectra at different GLU concentrations and contact times in order to obtain the emission spectrum, luminescence decay kinetics, and luminescence intensity of each Eu(III) species. From the deconvoluted spectra and the luminescence decay times, the Judd-Ofelt parameters and luminescence quantum yields of each species were determined. Assuming that all Eu(III) species are detectable and have similar extinction coefficients at 394 nm, the concentration c_i of the different species can be calculated from the luminescence intensities I_i obtained by the PARAFAC analysis and the luminescence quantum yields Φ_i according to Eq. 2:

$$c_i = \frac{I_i}{\phi_i \cdot \sum_{j=1}^n \left(\frac{I_j}{\phi_j} \right)} \cdot c_{Eu(III)total} \quad (2)$$

Since the Eu(III) luminescence is quenched in the presence of O-H oscillators due to a radiationless energy transfer to O-H vibrations, the number of water molecules $n(H_2O)$ in the first coordination sphere of the Eu(III) ions can be estimated from the luminescence decay time τ (Eq. 3), offering additional information about the coordination environment of the Eu(III) species (Marmodée et al., 2010):

$$n(H_2O) \approx \frac{1.09}{\tau [\text{ms}]} - 0.75 \quad (3)$$

2.3 Am(III), Th(IV), Pu(IV) experiments

2.3.1 Preparation of Am(III), Th(IV), Pu(IV) samples

For these experiments, the C-S-H phases were prepared as described in Supplementary Table S1 (Supplementary Material). Stock solutions of $^{241}\text{Am(III)}$, $^{232}\text{Th(IV)}$, and $^{239}\text{Pu(IV)}$ were diluted to achieve the initial concentration of 1×10^{-8} M in the batch sorption experiments. A ^{232}Th ICP-MS standard (SPS Science, Canada) was diluted in 2% HNO_3 . The $^{241}\text{Am(III)}$ and $^{239}\text{Pu(IV)}$ stock solutions were prepared as described elsewhere (Amayri et al., 2016) and subsequently diluted in 1 M HClO_4 . A Na-GLU solution was also added in the experiments with an initial concentration of 1×10^{-2} M, where the order of reactant addition was varied: i) An(X) was equilibrated with the C-S-H phase for 72 h before the addition of GLU to the suspension and subsequent equilibration for another 72 h, referred to as (C-S-H + An(X)) + GLU in the following text, ii) GLU was equilibrated with the C-S-H phase for 72 h before the addition of An(X) to the suspension and subsequent equilibration for another 72 h, (C-S-H + GLU) + An(X), and iii) simultaneous addition of An(X) and GLU to the C-S-H suspension followed by equilibration for 72 h, (C-S-H + An(X) + GLU). The phase separation was performed as described in Section 2.1.1. For Am(III) and Th(IV), also the influence of time was investigated, and further separations took place after 59 and 71 days, respectively.

The analysis of $^{241}\text{Am(III)}$, $^{232}\text{Th(IV)}$ and $^{239}\text{Pu(IV)}$ was performed with ICP-MS (Agilent 7900ce, Agilent Technologies, United States). For this, the samples were diluted in 2% HNO_3 . As an internal standard an aliquot of ^{193}Ir in 2% HNO_3 was added ([Ir] = 100 ppt). The LOD for ICP-MS measurements of $^{241}\text{Am(III)}$, $^{232}\text{Th(IV)}$, and $^{239}\text{Pu(IV)}$ were 1×10^{-11} M, 3×10^{-11} M and 2×10^{-11} M, respectively. The distribution coefficients R_d [L/kg] were determined by Eq. 4 using the sample volume V [L], the total mass of the solids m [kg], the initial concentration $[\text{An(X)}]_0$, and the equilibrium concentration $[\text{An(X)}]_{eq}$ of the actinides.

$$R_d = \frac{V}{m} \cdot \left(\frac{[\text{An(X)}]_0 - [\text{An(X)}]_{eq}}{[\text{An(X)}]_{eq}} \right) \quad (4)$$

2.3.2 Pu EXAFS measurement

One additional ^{239}Pu batch sample was prepared for extended X-ray absorption fine structure (EXAFS) measurements using the same experimental procedure as described before with two exceptions: First, the total Pu concentration in the batch sample was increased to 5×10^{-6} M to make the detection of an EXAFS spectrum feasible. With a S/L ratio of 2.5 g/L, this resulted in a sample loading of 494 ppm Pu on C-S-H (C/S = 0.8). Second, to avoid the precipitation of Pu(IV) colloids at pH 10.6 at the C-S-H phase, the initial Pu oxidation state was +III. As the Pu L_3 -edge X-ray absorption near edge structure (XANES) spectrum showed, the initial Pu(III) was completely oxidized to Pu(IV). This also agrees with the redox conditions during the contact time of Pu in the C-S-H suspension with an E_h value of +29 mV (SHE). The Pu L_3 -edge EXAFS measurement was performed at the BM20 Rossendorf

Beamline (ROBL) (Matz et al., 1999; Scheinost et al., 2021) at the European Synchrotron Radiation Facility (ESRF), Grenoble, France. Details of this measurement and the EXAFS data analysis are given in the [Supplementary Material](#).

2.3.3 CE-ICP-MS measurements of Th(IV) samples

The complexation behavior of Th(IV) with GLU at pH 10 and the influence of Ca(II) were investigated by capillary electrophoresis (CE) coupled to ICP-MS. Four samples with 4×10^{-7} M Th(IV) were investigated at pH 10 and 0.1 M ionic strength. The pH and the ionic strength were adjusted using NaOH (VWR Chemicals, United States), HClO₄ (VWR Chemicals, United States), and NaClO₄ (Fluka Analytical, Germany), respectively. Solution 1 contained only Th(IV) and no GLU and no Ca(II). Solution 2 consisted of Th(IV) and 1×10^{-2} M GLU. Sample 3 was prepared the same as sample 2 but in C-S-H pore water, i.e., with [Ca(II)] = 1.7×10^{-3} M (Häußler et al., 2018). To emphasize the influence of Ca(II) on the Th(IV)-GLU complexation, the Ca(II) concentration was increased. Therefore, solution 4 had the following composition: 4×10^{-7} M Th(IV), 1×10^{-2} M GLU, and 1×10^{-2} M Ca(II).

The experimental setup consisted of CE (Agilent 7,100, Agilent Technologies, United States) coupled to ICP-MS (Agilent 7900 ce, Agilent Technologies, United States) with a MiraMist CE nebulizer (Burgener Research, United Kingdom) leading into a Scott-type spray chamber (AHS Analysentechnik, Germany). The fused silica capillary (id. = 50 μ m, Polymicro Technologies, LLC, United States) had length l of 50 cm. The applied voltage U was 10 kV. To each sample 2-bromopropane (Merck, Germany) was added as EOF marker. Measurements and data evaluation were performed as described by Willberger et al. (2019). The electrophoretic mobility μ_e was calculated according to Eq. 5 using the retention times of ²³²Th (t_{Th}) and ⁷⁹Br of the EOF marker (t_{EOF}), respectively:

$$\mu_e = \frac{l^2}{U} \cdot \left(\frac{1}{t_{Th}} - \frac{1}{t_{EOF}} \right) \quad (5)$$

2.4 U(VI) experiments

2.4.1 Preparation of U(VI) samples

A C-S-H phase was prepared as described in [Supplementary Table S1 \(Supplementary Material\)](#) in a 50 mL centrifuge tube (polypropylene, Greiner bio-one, Austria) and equilibrated using an end-over-end rotator (Stuart Rotator SB3, United Kingdom). The final pH value was 10.9. For phase separation, the suspension was centrifuged at $6,800 \times g$ for 30 min (mod. Avanti J-20 XP, Beckman Coulter, United States), and the solid phase isolated. The powder was left to dry to constant weight under N₂ atmosphere at RT and stored inside the glove box. This U(VI)-free C-S-H phase was used together with the respective supernatant solution for U(VI) retention experiments in absence and presence of GLU. Using stock solutions of U_{nat} (1×10^{-3} M UO₂Cl₂ in 5×10^{-3} M HCl) and GLU (1 M, sodium gluconate (Sigma-Aldrich, United States)), samples for solid-state NMR ([U(VI)] = 5×10^{-6} M, [GLU] = 1×10^{-2} M, S/L = 10 g/L) and TRLFS ([U(VI)] = 5×10^{-7} M, [GLU] = 1×10^{-2} M, S/L = 1 g/L) measurements were prepared. For this, the order of reactant additions was varied (cf. [Table 1](#)).

A further C-S-H phase was prepared by using the same procedure as described above, however, immediately after mixing the reactants with deionized water, an aliquot of the U(VI) stock solution was added to the suspension. The initial U(VI) concentration was 2×10^{-5} M. During the equilibration time of 67 days, a U(VI)-doped C-S-H phase formed. The final pH value and U(VI) loading were 10.8 and 198 ppm, respectively. To study the influence of GLU on U(VI) leaching, aliquots of the GLU stock solution were added to the suspension of U(VI)-doped C-S-H (S/L = 10 g/L) to obtain 1×10^{-3} M or 1×10^{-2} M GLU. The samples were equilibrated for 160 days.

After equilibrating the retention and leaching samples by shaking end-over-end, solid and liquid phases were separated by centrifugation, and aliquots were taken from the supernatant solutions for U(VI) concentration determination by ICP-MS (NexION 350X/Elan 9,000, PerkinElmer, United States) and for GLU quantification by solution NMR spectroscopy (cf. [Section 2.5](#)). Uranyl uptake by C-S-H is given in terms of a distribution ratio (R_d) according to Eq. 4.

2.4.2 U(VI) luminescence spectroscopy

For TRLFS measurements of U(VI)-containing C-S-H prepared in absence or presence of GLU, the samples were transferred as wet pastes into copper sample holders with sealable quartz glass lids and measured with a tunable diode pumped solid state (DPSS) laser (Ekspla, NT230, Lithuania) at 10 K. The emitted luminescence light was directed into a spectrograph (Shamrock 303i Andor Oxford Instruments, United Kingdom) equipped with a polychromator with 300, 600 and 1,200 lines/mm gratings, and the emission was monitored with an intensified CCD camera (Andor iStar, Oxford Instruments) 10 μ s after the exciting laser pulse in a time window of 10 ms. The U(VI) associated with the C-S-H phase was excited at selected wavelengths (330–335 nm, 342 nm, 357 nm). Spectra were collected at varying delay times (up to 1,200 μ s) between the laser pulse and camera gating to obtain luminescence decay kinetics and to extract pure component spectra of individual U(VI) species in the samples. More specifically, the decomposition of the spectra using the measured U(VI) emission data recorded at varying delay times was done with the Origin 2019b software (OriginLab Corporation, United States). The emission spectra recorded after long delay times were taken as pure components for U(VI) species with long luminescence lifetimes. The pure component spectrum was thereafter subtracted from the recorded emission data at shorter delays, yielding pure components of the U(VI) species with shorter luminescence lifetimes. Luminescence decay kinetics were obtained by integrating the collected emission spectra using MATLAB (R2019b) (Natick, Massachusetts: The MathWorks Inc., United States). Biexponential decay functions were thereafter fitted to the decay curves to obtain luminescence lifetimes of the present species in the samples.

2.4.3 Solid-state NMR spectroscopy

²⁹Si and ¹³C cross-polarization (CP) and ²⁹Si single-pulse (SP) MAS NMR spectra were recorded on a Bruker AvanceTM 400 MHz WB spectrometer operating at a field strength of 9.4 T, with corresponding ¹³C, ²⁹Si and ¹H resonance frequencies of 100.7,

TABLE 1 Characterization of U(VI)- and/or GLU-containing C-S-H samples with C/S = 0.8 and distribution coefficients (R_d in L/kg) determined for U(VI) uptake.

Sample	Sample preparation	[U(VI)] ₀ /M	[GLU] ₀ /M	S/L/g/L	Equil. Time/d	pH _{End}	log R_d
U1	C-S-H/U (directly synthesized)	2×10^{-5}	–	24	67	10.8	5.6
U2	C-S-H + GLU	–	1×10^{-2}	10	26	11.0	–
U3	C-S-H + (U/GLU) ^a	5×10^{-6}	1×10^{-2}	10	26	11.0	4.7
U4	C-S-H + U	5×10^{-7}	–	1	20	10.9	5.1
U5	(C-S-H + U) + GLU	5×10^{-7}	1×10^{-2}	1	7 + 13	10.8	4.9
U6	(C-S-H + GLU) + U	5×10^{-7}	1×10^{-2}	1	7 + 13	10.9	4.7
U7	C-S-H + (U/GLU) ^a	5×10^{-7}	1×10^{-2}	1	20	11.0	4.9

^aU(VI) and GLU were pre-equilibrated for 2 days before addition to the C-S-H suspension.

79.5 and 400.3 MHz, respectively, equipped with a CP/MAS DVT probe. Samples were packed in 7 mm zirconia rotors and spun at 5 kHz rotational frequency. ²⁹Si CP spectra were acquired with 5 ms contact time, using a 80% ramp, by accumulating 2048 spectra recorded for 25 ms applying a relaxation delay of 3 s. ¹³C CP spectra were acquired with 1 ms contact time, using a 70% ramp, accumulating 16 k spectra recorded for 25 ms applying a relaxation delay of 3 s. 200 ²⁹Si SP spectra were accumulated by respectively applying 5.6 μs (30°) excitation pulse, 25 ms acquisition time, and a relaxation delay of 360 s allowing for quantitative measurements. Chemical shifts are reported in ppm relative to external tetramethylsilane (TMS).

2.4.4 XRD measurements

X-ray diffractograms of a U(VI)-free and a U(VI)-containing C-S-H sample with C/S of 0.8 were collected with a MiniFlex 600 diffractometer (Rigaku, Japan) equipped with a Cu Kα X-ray source (40 keV/15 mA operation for X-ray generation) and the D/teX Ultra 1D silicon strip detector in the Bragg-Brentano θ -2 θ geometry at a scanning speed of 2° per minute. The samples were mounted on a low-Si-background sample holder.

2.5 GLU quantification in aqueous phase by solution NMR spectroscopy

For the quantification of remaining GLU in supernatant solutions after retention experiments in the Eu(III) and U(VI) systems, 1 mL of the supernatant was lyophilized, redissolved in 750 μL D₂O solution containing 1.492 mM of internal standard TMSP-*d*₄ (sodium 3-(trimethylsilyl)-2,2,3,3-tetra-deuteropropionate) and ¹H NMR spectra were recorded. In order to achieve quantitative acquisition conditions, an excitation pulse of 2.67 μs (30°) and a relaxation delay of 60 s were used upon accumulation of 16–256 spectra, depending on [GLU], with an acquisition time of 3 s, recorded on an Agilent DD2-600 system operating at 14.1 T with a corresponding ¹H resonance frequency of 599.82 MHz using a 5 mm oneNMR™ probe. The GLU concentration was determined according to Eq. 6:

$$c_{\text{GLU}} = \frac{I_{\text{GLU}}}{I_{\text{TMSP}}} \cdot \frac{N_{\text{TMSP}}}{N_{\text{GLU}}} \cdot c_{\text{TMSP}} \cdot 0.75 \quad (6)$$

where c , I , and N denote concentrations, ¹H NMR signal integrals, and number of ¹H nuclei contributing to the integrated signal(s), respectively, with $N_{\text{TMSP}} = 9$ (integrated region ± 90 Hz of TMSP signal center), $c_{\text{TMSP}} = 1.492$ mM, and accounting for strengthening upon re-dissolution in only 75% of the initial volume.

3 Results and discussion

3.1 GLU/C-S-H

Initially, the binary GLU/C-S-H system was investigated in two types of batch sorption experiments. In the first experiment, shown in Figure 1A, the sorption isotherm of GLU on C-S-H phases was determined by varying the concentration over eight orders of magnitude ([GLU]₀ = 1×10^{-9} – 1×10^{-1} M; S/L = 5 g/L). A linear fit with a slope of one was used to determine the log R_d value of 0.31 ± 0.11 ($R_d = 2.02 \pm 1.3$ L/kg), which is slightly lower compared to the value ($R_d = 4.5$ L/kg) from the study of Androniuk et al. (2017). In the second experiment, shown in Figure 1B, the S/L ratio was varied between 0.5 and 50 g/L at a constant GLU concentration of 1×10^{-2} M. The R_d value calculated from the fit shown in Figure 1A was used to calculate [GLU]_{eq} for different S/L ratios. As can be seen from Figure 1B, the measured and calculated equilibrium concentrations of GLU are consistent. Both the experimental and the calculated data show a slight decrease in concentration to a value [GLU]_{eq} = 9×10^{-3} M at a S/L ratio of 50 g/L. The determined GLU concentration after 72 h of contact is consistent with the calculated concentration. The results of the two batch sorption experiments confirm the very low sorption of GLU on the C-S-H phase at the C/S ratio of 0.8 and no blocking of sorption sites by GLU on C-S-H can be assumed.

Furthermore, XPS measurements of C-S-H samples were performed for an analysis of the C-S-H surfaces in presence and absence of GLU. Both spectra of the C-S-H samples showed identical signals of calcium, oxygen, and silicon, but no C 1s signal. Since there is no C 1s signal in the spectrum of the sample with GLU, it can be assumed that a sorption of GLU on the C-S-H phase is unlikely under the experimental conditions. Thus, the

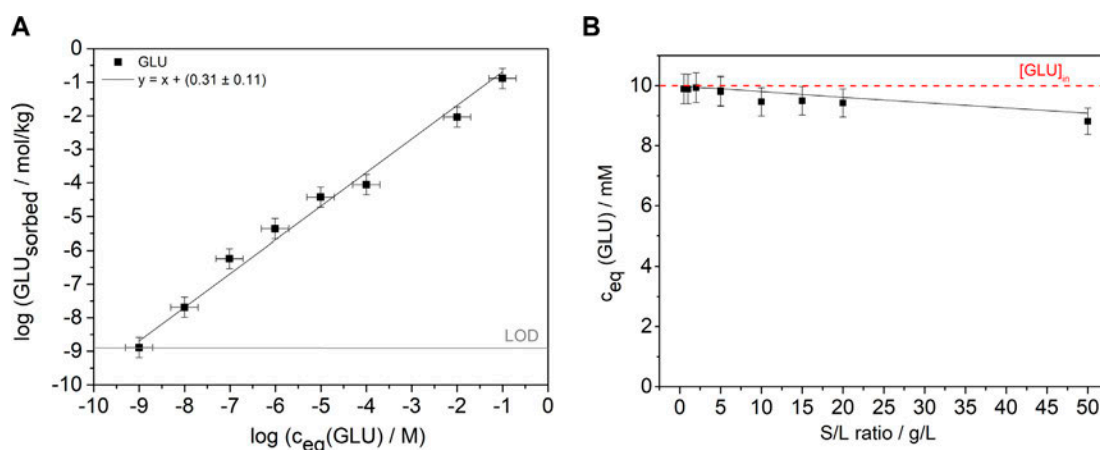


FIGURE 1

(A) Sorption isotherm with constant S/L ratio of 5 g/L and initial GLU concentrations from 1×10^{-9} M to 1×10^{-1} M (pH 9.8) after a contact time of 72 h. The gray line shows the LOD. The black line is a linear fit with a slope of one to the data. (B) Batch sorption experiments at varying S/L ratios and constant GLU concentration (S/L = 0.5–50 g/L, $[\text{GLU}]_0 = 1 \times 10^{-2}$ M, pH 9.8) and a contact time of 72 h. The black line represents the calculated concentrations using the R_d value from the fit in (A) and the red line marks the initial concentration of 1×10^{-2} M of GLU.

results for the solid phases confirm the liquid phase results of the experiments given above. In addition, the C/S ratio at the surface of the C-S-H powders is lower than the C/S ratio of 0.8 in the bulk, as seen in Supplementary Table S2 (Supplementary Material). Häußler et al. (2018) had also observed a lower Ca(II) content at the surface than the C/S ratio used in the C-S-H synthesis.

3.2 Eu(III)/GLU/C-S-H

3.2.1 Reference experiments: Eu(III) addition during C-S-H formation

An initial Eu(III) reference experiment using TRLFS was performed in an attempt to approximate a plausible endpoint for the retention of Eu(III) in C-S-H phases. Therefore, Eu(III) was already added in the very beginning of the C-S-H formation assuming that it will enter the interlayer and the CaO layer faster. In these experiments, using the PARAFAC algorithm for the evaluation of the TRLFS data, two different Eu(III) species could be identified after a contact time of one, two, and 6 weeks, respectively. Both were located in the solid phase. The Eu(III) concentration in the liquid phase was below the limit of detection in all samples, thus indicating a high degree of retention. The two species, whose luminescence spectra are shown in comparison to the raw data in Supplementary Figure S1 (Supplementary Material), had luminescence decay times of (520 ± 40) μs and $(2,100 \pm 200)$ μs , respectively. According to Eq. 3, the shorter decay time corresponds to a sorption complex with approximately one or two water molecules in the coordination sphere of Eu(III), which may indicate sorption of Eu(III) into the interlayer of the C-S-H structure. The decay time of the second species relates to an environment without water molecules in the first coordination sphere of Eu(III), which implies substitution for Ca(II) positions in the CaO layer of the C-S-H phases. Similar results

have been reported in the literature (Pointeau et al., 2001; Tits et al., 2003; Mandaliev et al., 2011). However, a third species, possibly corresponding to a surface complex was observed by Pointeau et al. (2001) and Mandaliev et al. (2011), which occurred only when Eu(III) was added after the C-S-H formation or at higher Eu(III) loadings than in the present experiments, respectively.

The PARAFAC analysis suggests that after a contact time of 6 weeks approximately (90 ± 3) % of the Eu(III) ions were sorbed into the interlayers of the C-S-H phases, while (10 ± 3) % were incorporated into the CaO layers in all samples. The addition of GLU (5×10^{-6} M– 5×10^{-3} M) after a contact time of 14 days had no effect on the Eu(III) speciation, implying that GLU did not cause the desorption of Eu(III), even at the highest GLU concentration of 1×10^{-2} M.

3.2.2 Reference experiments: Eu(III) in C-S-H pore water

In the reference experiments with aqueous phases previously equilibrated with C-S-H phases (referred to as pore water samples), a white precipitate was formed upon the addition of Eu(III) (5×10^{-5} M) in the absence and presence of GLU. Consequently, the Eu(III) concentration in the solution dropped below the limit of detection of the used TRLFS setup of approximately 5×10^{-8} M. Similar findings have also been reported by Schlegel et al. (2004), who observed the formation of a C-S-H-like precipitate upon the addition of Eu(III) (3.5×10^{-5} M) to pore water equilibrated previously with C-S-H phases with a C/S ratio of 1.3.

In the pore water precipitate, a total of four Eu(III) species were identified at different GLU concentrations. Their emission spectra and luminescence decay times obtained using PARAFAC are shown in Figure 2A. The shortest observed decay time of (64 ± 5) μs cannot be explained solely by quenching due to O-H oscillators in the coordination sphere, suggesting that this Eu(III) species may (additionally) have neighboring Eu(III) ions adding self-quenching through a Eu(III)-Eu(III) energy transfer (cross-

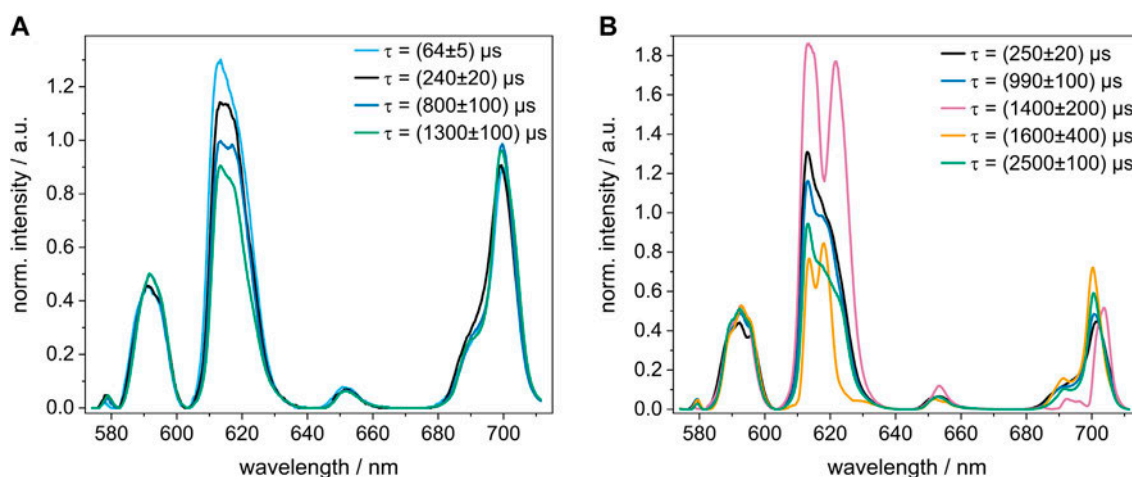


FIGURE 2

Normalized luminescence spectrum of each Eu(III) species with its respective decay time τ calculated with PARAFAC. (A) pore water samples and (B) C-S-H retention samples, in which Eu(III) and GLU were added 14 days after the preparation of the C-S-H phases. The Eu(III) concentration was 5×10^{-5} M in all samples and the GLU concentration was varied between 5×10^{-6} M and 5×10^{-3} M. Note that both sample sets were measured with different detection systems, as described in the experimental section.

relaxation) to the overall radiationless deactivation (Buijs et al., 1987). This would be in accordance with the findings by Schlegel et al. (2004), who observed a high Eu(III) content in their precipitate with a bulk composition of $\text{Si}_{0.99}\text{Ca}_{1.87}\text{Eu}_{4.77}\text{O}_{11} \cdot 48\text{H}_2\text{O}$ and confirmed the presence of neighboring Eu(III) shells using Eu L₃-edge EXAFS. The luminescence decay time of the second species (240 ± 20 μs) may correspond to three or four water molecules in the coordination environment of Eu(III) or likewise to the presence of other Eu(III) ions. The other observed species with luminescence decay times of (800 ± 100) μs and $(1,300 \pm 100)$ μs are likely not surrounded by any neighboring Eu(III) ions or water molecules in the first coordination sphere.

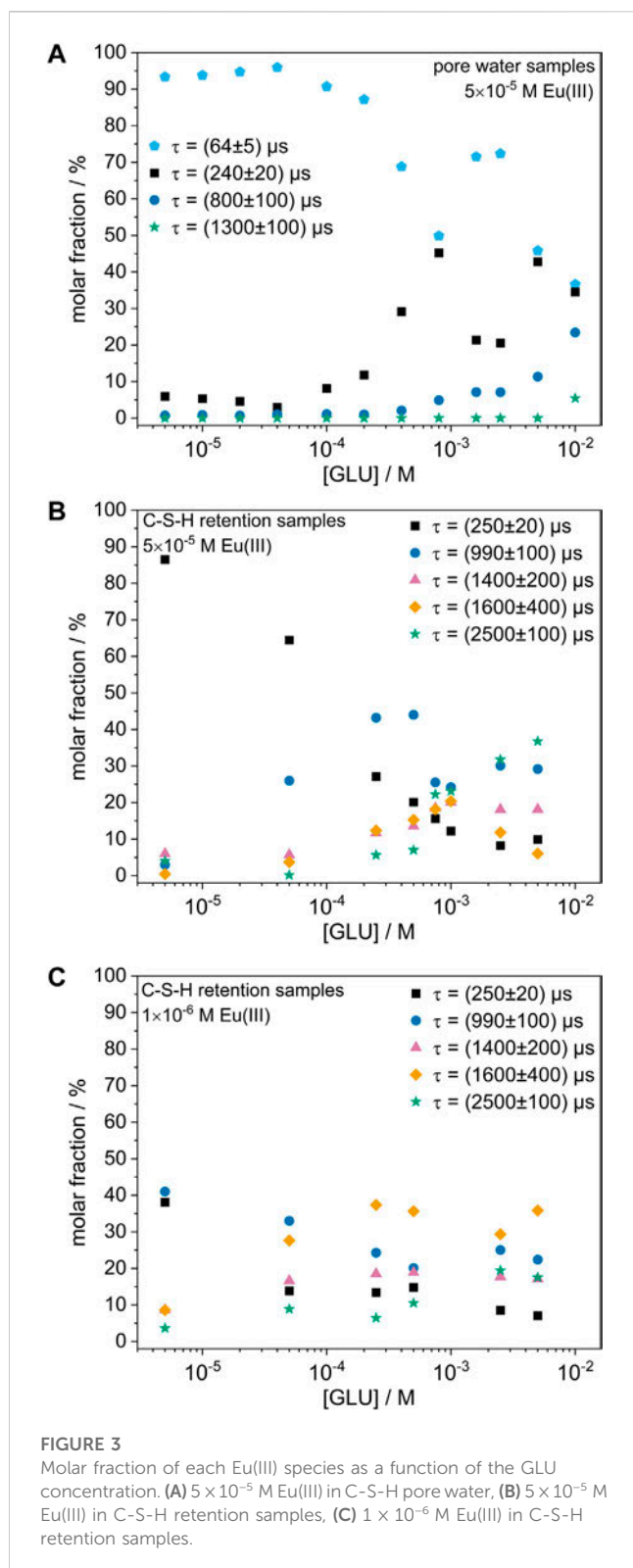
The molar fractions of each Eu(III) species at varying GLU concentrations are shown in Figure 3A. It is notable that in the absence of GLU and at low GLU concentrations mainly the species with the shortest luminescence decay time (64 ± 5 μs) was formed. However, at GLU concentrations above 1×10^{-4} M, additional species with higher decay times were present, which will be discussed in more detail in the following section. Nonetheless, the Eu(III) signal in the liquid phase remained below the limit of detection at all GLU concentrations, thus indicating that Eu(III) was effectively immobilized in the solid phase even in the presence of up to 1×10^{-2} M GLU.

In further reference experiments in which NaCl solution (1×10^{-2} M) was used instead of C-S-H pore water, the precipitation of Eu(III) hydroxide (at low GLU concentrations) and the formation of soluble Eu(III)-GLU complexes (at $[\text{GLU}] \geq 2 \times 10^{-4}$ M) were observed. The luminescence spectra and decay times of these species are different from the Eu(III) species in the pore water samples, thus corroborating the hypothesis that a coprecipitation of Eu(III) with the pore water constituents (i.e., Ca(II) and Si(IV)) occurred in the pore water experiments, where the Ca(II) and Si(IV) concentrations are expected to be 1.0×10^{-3} M and 1.3×10^{-3} M at C/S 0.8, respectively (Lothenbach and Nonat, 2015).

3.2.3 C-S-H retention experiments: Eu(III) addition after C-S-H formation

In the C-S-H retention experiments, Eu(III) and GLU were added to prepared C-S-H phases (time for formation: 14 days). The TRFLS measurements were carried out on the solid as well as on the supernatant solution. Over a contact time of 1–211 days, a total of five different Eu(III) species could be identified in the presence of GLU in the solid phases, while similarly to the reference experiments (cf. Section 3.2.1; Section 3.2.2) no Eu(III) signal was detectable in the liquid phase. Hence, high log R_d values above 4.5 were obtained, even at the highest GLU concentration of 1×10^{-2} M. Luminescence spectra of the solid phases at different GLU concentrations are shown in Supplementary Figure S2 (Supplementary Material). Interestingly, the two species found in the reference experiments, in which Eu(III) was present during the C-S-H formation, were not found when Eu(III) was added later, therefore suggesting that the Eu(III) in these C-S-H retention samples might have been immobilized through a different mechanism than the sorption into the interlayers and incorporation into the C-S-H structure. In fact, three of the observed species have similar luminescence spectra and decay times as the species observed in the pore water samples (cf. Figures 2A, B), thus implying that Eu(III) added to the C-S-H phases after their formation appeared to be immobilized mainly by coprecipitation with the C-S-H pore water constituents rather than *via* sorption or incorporation into the C-S-H phases.

However, in the presence of C-S-H phases, a lower Eu(III) content and thus fewer neighboring Eu(III) ions may be expected for the formation of a precipitate compared to the pore water samples, as the C-S-H phase might act as a reservoir for the possible dissolution of additional Ca(II) and Si(IV) (as well as a potential competing phase for the sorption of Eu(III)).

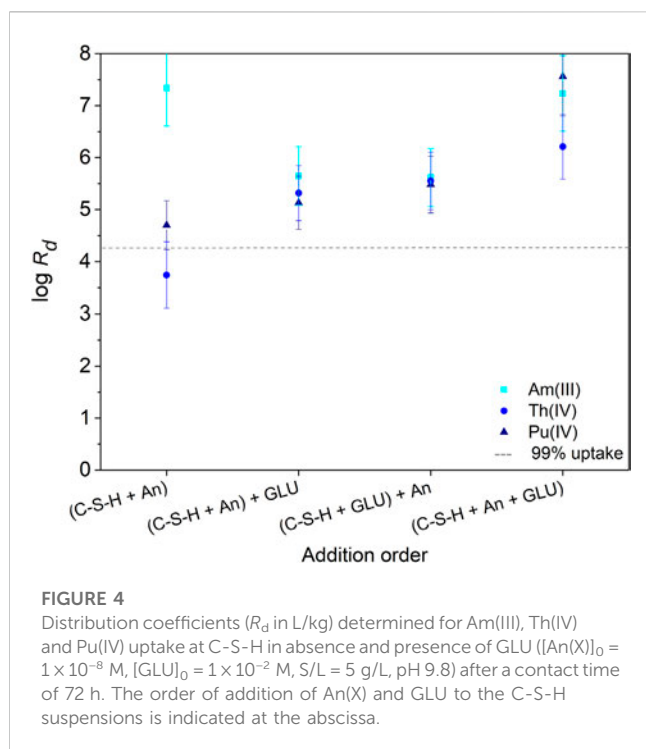


This idea is supported by the observation that the species with the lowest luminescence decay time and therefore lowest number in neighboring Eu(III) ions only occurred in the precipitate found in the pore water samples, but not in the precipitate formed when C-S-H phases were present. Moreover,

the pore water samples generally showed a higher molar fraction of Eu(III) species that might experience cross relaxation due to neighboring Eu(III) ions than the C-S-H retention samples, as can be seen in Figures 3A, B. Furthermore, two additional Eu(III) species were observed in the C-S-H retention samples with GLU that neither appeared in the reference experiments in the C-S-H pore water nor when Eu(III) was present during the C-S-H phase formation. They might correspond to a different chemical composition of the precipitate due to the presence of GLU (and greater amounts of Ca(II) and Si(IV) compared to the pore water samples), however this cannot be verified based on the present information yet.

Supplementary Figure S3 (Supplementary Material) shows the obtained speciation for the C-S-H retention samples with 5×10^{-5} M Eu(III) and different GLU concentrations in dependence of the contact time. It can be seen that the changes with contact time were small and the equilibrium appeared to be reached after <14 days in all samples. However, large differences in speciation were obtained with increasing GLU concentration, indicating that, although GLU did not measurably increase the Eu(III) concentration in solution, it appeared to strongly influence the Eu(III) speciation in the solid phase. While in the absence of GLU mainly the species with a short luminescence decay time of (250 ± 20) μ s was present, GLU appeared to promote the formation of species with higher luminescence decay times and thus likely smaller numbers in neighboring Eu(III) ions and/or O-H-oscillators in the coordination sphere of Eu(III). This trend was observed both in the pore water samples and the C-S-H retention samples, as shown in Figures 3A, B. In analogous experiments with nitrilotriacetic acid (NTA) instead of GLU (not shown here), a similar behavior and identical species were found, ruling out that those species could be attributed to “simple” Eu(III)-GLU complexes. Instead, GLU might alter the composition of the precipitate *via* complexation of Ca(II) ions, which might lead to a lower Ca(II) content in the precipitate and thus to changes in the Eu(III) coordination environment. This hypothesis is supported by the findings by Bouzouaid et al. (2022), who investigated the influence of GLU on the Ca(II) and Si(IV) concentration in C-S-H pore waters at different C/S ratios. Through wet chemistry experiments and theoretical modelling, they proposed that in the presence of 2×10^{-1} M GLU, free H_3SiO_4^- and CaGLU^+ dominate the pore water speciation at a C/S ratio of 0.8, thus indicating that under these conditions the majority of dissolved Ca(II) ions is complexed by GLU (Bouzouaid et al., 2021; Bouzouaid et al., 2022). However, it must be noted that the GLU concentration in this calculation is 20 times larger than the highest concentration used here. Additionally, some of the species, whose formation seems to be promoted by GLU, also appeared in samples without GLU to a small extent. Thus, further analysis of the Ca(II) and Si(IV) concentration in the liquid phase and of the composition of the precipitate is necessary to fully understand the influence of GLU on the Eu(III) speciation.

To investigate whether these results are also representative for lower Eu(III) concentrations, similar C-S-H retention experiments were performed with a Eu(III) concentration of 1×10^{-6} M. The Eu(III) speciation for these samples at different GLU concentrations is shown in Figure 3C. Similarly to the experiments at higher Eu(III) concentration, no Eu(III) signal was measurable in the liquid phase at all GLU



concentrations. Furthermore, the observed species were the same as at higher Eu(III) concentration, indicating that Eu(III) was immobilized by the same coprecipitation processes. However, a smaller molar fraction of species with short decay times was observed at lower Eu(III) concentration, which may support the cross-relaxation hypothesis, as a lower Eu(III) content in the precipitate and therefore less cross-relaxation is expected at lower Eu(III) concentration.

Analyses were complemented by GLU concentration determination in the supernatants after the full retention period (211 days) by quantitative ^1H NMR spectroscopy (spectra not shown). A summary of the calculated figures is given in Supplementary Table S3 (Supplementary Material), revealing GLU quantities sorbed to the C-S-H phase comparable to those determined in the U(VI)/GLU/C-S-H experiments (cf. Section 3.4).

3.3 Am(III), Th(IV), Pu(IV)/GLU/C-S-H

The influence of GLU ($[GLU]_0 = 1 \times 10^{-2}$ M) on the retention of Am(III), Th(IV), and Pu(IV) ($[An(X)]_0 = 1 \times 10^{-8}$ M) by C-S-H phases (S/L = 5 g/L) was investigated as a function of addition order: i) (C-S-H + An(X)) + GLU, ii) (C-S-H + GLU) + An(X), and (iii) (C-S-H + An(X) + GLU). The calculated $\log R_d$ values are shown in Figure 4. For comparison, the $\log R_d$ values obtained in the binary An(X)/C-S-H systems without addition of GLU are added. The order of reactant addition, as well as the presence of GLU, had no influence on the retention of the An(X) by the C-S-H phase after a contact time of 72 h to 71 days. A quantitative uptake of An(X) on the C-S-H phase was observed. The $\log R_d$ values are in the range of 4.5–7 and are thus in the same order of magnitude as reported in the literature by Häußler et al. (2018) in the absence of GLU. In the

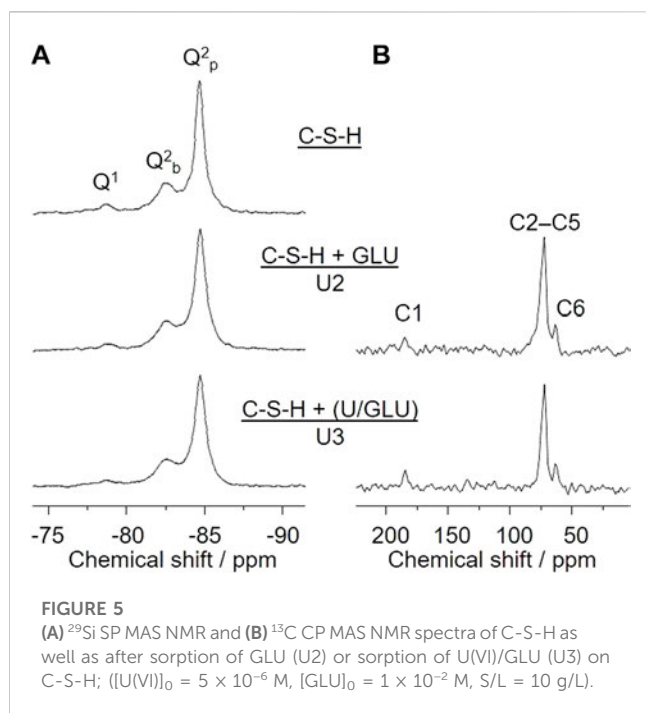
binary system Th(IV)/C-S-H, the measured value $\log R_d = 3.8$ was slightly lower.

The near-neighbor environment of 5×10^{-6} M Pu interacting with C-S-H (C/S = 0.8) at pH 10.6 was probed by Pu $L_{3\text{-edge}}$ EXAFS spectroscopy. The experimental EXAFS data (Supplementary Figure S4; Supplementary Material) could be best modelled with four coordination shells, i.e., seven oxygen atoms at an average distance of 2.25 ± 0.02 Å, two silicon atoms at 3.15 ± 0.02 Å, five silicon atoms at 3.54 ± 0.02 Å, and six calcium atoms with an average Pu–Ca distance of 4.12 ± 0.02 Å. For experimental uncertainties of these values and Debye-Waller factors refer to Supplementary Table S4 (Supplementary Material). A Pu–Pu interaction could not be detected in the EXAFS signal, indicating the absence of Pu clusters at C-S-H. The measured average Pu–O distance is indicative of Pu(IV). The observed Si and Ca coordination numbers (Supplementary Table S4; Supplementary Material) agree favorably with the structural parameters obtained by DFT calculations (Chiorescu et al., 2022) for the incorporation of U(IV) in the CaO layer. For example, six U–Ca distances in the range of 3.7–4.2 Å have been obtained in the density functional calculation. As observed by EXAFS analysis, the tetravalent actinide incorporated in the CaO layer is surrounded by one Si atom at 3.2 Å and four Si atoms at a larger distance of 3.4–3.7 Å (Chiorescu et al., 2022).

The electrophoretic mobilities μ_e of the Th(IV) species measured by CE-ICP-MS are summarized in Supplementary Table S5 (Supplementary Material). In the solution where no Ca(II) and GLU were added, the electrophoretic mobility of Th(IV) was nearly zero ($\mu_e = (0.03 \pm 0.03) \times 10^{-4}$ cm²/(Vs)). This indicates that the average effective charge of Th(IV) species in solution is zero. This is in good agreement with the expected predominant neutral Th(OH)₄ complex at pH 10 (Rand et al., 2009). In presence of GLU, a negative mobility of $-(2.72 \pm 0.09) \times 10^{-4}$ cm²/(Vs) was measured for Th(IV). This change in mobility indicates that Th(IV) forms complexes with GLU leading to a negatively charged species, suggesting the formation of anionic complexes such as Th(OH)₄(HGLU)[−] and Th(OH)₄(HGLU)₂^{2−} previously proposed by Colàs et al. (2013). For analog samples of Th(IV)-GLU with C-S-H pore water as electrolyte, a less negative mobility of $-(2.02 \pm 0.08) \times 10^{-4}$ cm²/(Vs) was measured. This slight decrease in the negative mobility compared to $\mu_e = -2.72 \times 10^{-4}$ cm²/(Vs) could be attributed to the presence of Ca(II) ($[Ca(II)] = 1.7 \times 10^{-3}$ M) in the C-S-H pore water (Häußler et al., 2018), leading to the formation of quaternary complexes CaTh(OH)₄(HGLU)⁺ (Colàs et al., 2013) and CaTh(OH)₄(HGLU)₂ (Gaona et al., 2008), respectively. To amplify the influence of Ca(II), its concentration in solution was increased ($[Ca(II)] = 1 \times 10^{-2}$ M). The measured electrophoretic mobility was $-(0.65 \pm 0.04) \times 10^{-4}$ cm²/(Vs), indicating a less negative average charge of the Th(IV) species due to the influence of Ca(II) on the Th(IV)-OH-GLU system. The observed trend of the electrophoretic mobilities confirms that Ca(II) is associated to Th(IV)-OH-GLU complex species.

3.4 U(VI)/GLU/C-S-H

The characteristics of the different U(VI)- and/or GLU-containing C-S-H samples are listed in Table 1, highlighting the



sequence of U(VI) and GLU additions to the C-S-H suspensions during the sorption experiments (samples U2–U7).

The X-ray diffractograms of the U(VI)-free C-S-H phase and of the directly synthesized U(VI)-containing C-S-H phase U1 (198 ppm U(VI)) are given in [Supplementary Figure S5 \(Supplementary Material\)](#). The diffractograms are characteristic for C-S-H phases, with U(VI) showing no effect on the C-S-H structure (long-range order).

The log R_d values determined for the U(VI) uptake in the absence of GLU amount to 5.6 and 5.1 for the directly synthesized sample U1 and the sorption sample U4, respectively. These values are well within the range of data reported in the literature ([Pointeau et al., 2004](#); [Tits et al., 2011](#)). To study the influence of GLU on U(VI) retention by C-S-H, a leaching experiment was performed with the directly synthesized sample U1 by adding aliquots of the GLU stock solution to the suspension of U(VI)-doped C-S-H (S/L = 10 g/L) to adjust $1 \times 10^{-3} \text{ M}$ or $1 \times 10^{-2} \text{ M}$ GLU. Less than 0.1% of the previously retained U(VI) is remobilized in the presence of GLU. Similar results were obtained by U(VI) sorption experiments. In the presence of $1 \times 10^{-2} \text{ M}$ GLU, the log R_d only slightly decreases to 4.8 ± 0.1 . Regarding the U(VI) uptake, no clear trend can be seen in the tests with different addition sequences of U(VI) and GLU. That means, the organic ligand GLU has only a very small influence on the U(VI) retention by C-S-H under these conditions. To identify U(VI) and GLU species on the solid phase and in the supernatant, the samples were studied by TRLFS and NMR, respectively.

^{29}Si SP MAS NMR spectra in principle allow for discrimination and quantification of $\text{Si}(\text{OH})_4$ tetrahedra degree of condensation, denoted as Q^n groups. In this notation, n refers to the number of O-Si bonds of a considered $\text{Si}(\text{IV})$ site, according to $\text{Si}(\text{OH})_{4-n}(\text{OSi})_n$ with $n = 1$ through 4. Accordingly, the mean chain length (MCL) of

the C-S-H dreierketten units can be determined. Upon increasing C/S the $Q^1:Q^2$ ratio also increases, according to a decreasing mean chain length. Varying C/S between 0.6 and 1.6 almost inverts the $Q^1:Q^2$ ratio from 0.09 to 7.33, associated with MCL of about 24 and 2.3, respectively ([Roosz et al., 2018](#)). [Figure 5A](#) shows ^{29}Si SP MAS NMR spectra of the C-S-H phase with C/S = 0.8 (top) as well as of the same phase after the sorption experiments with $1 \times 10^{-2} \text{ M}$ GLU (middle, U2) or $5 \times 10^{-6} \text{ M}$ U(VI) and $1 \times 10^{-2} \text{ M}$ GLU, where U(VI) and GLU were pre-equilibrated before addition to the C-S-H suspension (bottom, U3). These spectra reveal two major results. First, the degree of silicate condensation is high. Based on the integral of the signals associated with Q^1 and Q^2 groups, respectively, their corresponding ratio is almost exactly 1:10. According to [Richardson \(2014\)](#), the MCL is about 20. Second, no notable spectral changes upon sorption of either GLU or U(VI)/GLU on the C-S-H phase can be detected. Hence, the short-range order of the C-S-H phase remains unaffected by U(VI) and/or GLU.

In addition, ^{13}C CP MAS NMR spectra of the GLU containing samples U2 and U3 ([Figure 5B](#)), i.e., C-S-H + GLU (top) and C-S-H + (U(VI)/GLU) (bottom), reveal the presence of GLU in the sorption samples. The quite low signal-to-noise ratio implies that only a fraction of the initial $1 \times 10^{-2} \text{ M}$ GLU is associated with the C-S-H phase. This observation is in full agreement with the findings from both GLU sorption experiments (cf. [Figure 1B](#)) and GLU quantification in the remaining supernatants ([Supplementary Figure S6](#); [Supplementary Table S6](#); [Supplementary Material](#)), where the amount of sorbed GLU is determined to be about 10% or 14% of $[\text{GLU}]_0$ in case of S/L = 1 g/L (U5–U7) or 10 g/L (U2, U3), respectively. The solid-state NMR signals of the CH(OH) carbons C2–C5 overlap as a broad signal centered at δ_C 72.3 ppm, whereas the signals of the carboxyl carbon C1 and of the CH_2OH carbon C6 can be well resolved at δ_C 184.4 and 63.4 ppm, respectively. The carboxyl carbon's observed chemical shift is remarkably downfield from that of both free GLU (δ_C 176.4 ppm) and the Ca(II)-GLU-complex (δ_C 179.6 ppm) determined in D_2O solution ([Tajmir-Riahi, 1990](#)). We therefore conclude that GLU is exclusively associated with surface Ca(II), i.e., “cation bridging complexation” instead of, e.g., GLU being taken up into the C-S-H phase (interlayer) or being precipitated as a separate calcium gluconate phase. See also the discussion of GLU's influence on relative concentrations of the different C-S-H-associated Eu(III) species, above.

The luminescence spectra of samples U1 and U4–U7 obtained at two different excitation wavelengths (335 and 342 nm) are shown in [Supplementary Figure S7 \(Supplementary Material\)](#). It is obvious that the luminescence spectra of these five U(VI)-loaded C-S-H samples are comparable to luminescence spectra measured for U(VI)-loaded C-S-H phases before ([Philipp et al., 2022](#)), and moreover, the spectra are very similar to each other and independent of the presence or absence of GLU. The luminescence spectra of samples U1 and U4 resemble one another at all collected excitation wavelengths. Samples U5 and U6 are comparable and have a slightly more intense shoulder at around 500 nm in comparison to U4. Sample U7 shows the strongest deviation from the samples U1 and U4. The overall intensity of the luminescence spectrum of sample U4 is much better than of the other sorption samples U5–U7, although an identical U(VI) concentration of $5 \times 10^{-7} \text{ M}$ was applied. Sample

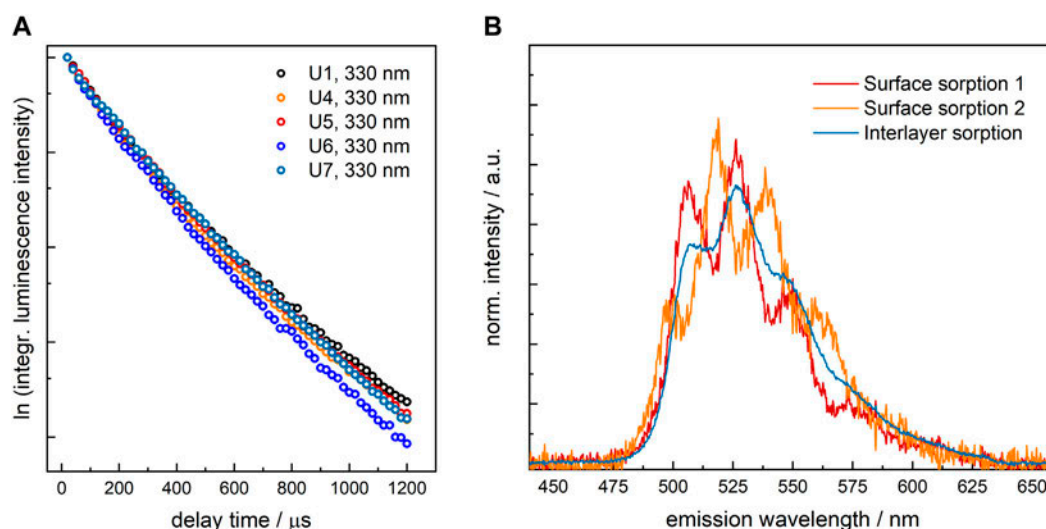


FIGURE 6

(A) Luminescence decay kinetics obtained from U(VI)-loaded C-S-H phases U1 and U4–U7 at $\lambda_{\text{ex}} = 330$ nm; (B) Emission spectra of extracted pure components from the decomposition of the measured U(VI) luminescence spectra obtained from U(VI)-loaded C-S-H phases.

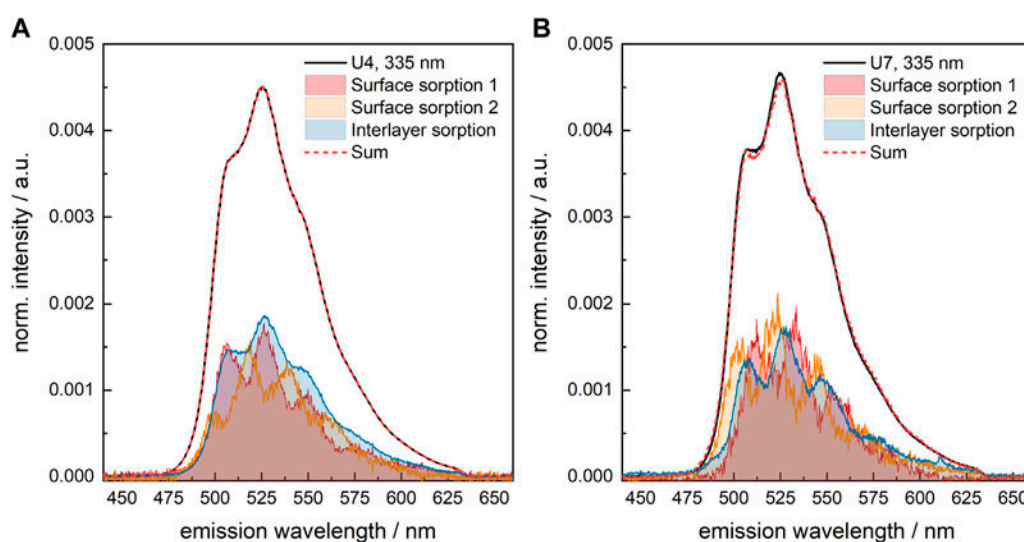


FIGURE 7

Results of spectral decomposition of the measured U(VI) luminescence spectra of U(VI)-loaded C-S-H phases (A) U4 (absence of GLU) and (B) U7 (presence of 1×10^{-2} M GLU); $\lambda_{\text{ex}} = 335$ nm.

U7 has the poorest overall intensity. This points toward U(VI) luminescence quenching by GLU, since total U(VI) uptake is similar for all samples.

The luminescence decay kinetics obtained for the five U(VI)-loaded C-S-H samples (Figure 6A) can all be fitted biexponentially. The longer lifetime is very similar for all samples (U1, U4–U7) with an average value of $\tau_2 = (387 \pm 40)$ μs . The shorter lifetime is identical for samples U4 and U6 with $\tau_1 = (143 \pm 18)$ μs and slightly longer for samples U5 and U7 with $\tau_1 = (176 \pm 31)$ μs . These

differences, however, are too small to clearly distinguish the components with shorter lifetimes.

Three pure components can be extracted from each measured spectrum. Two of them have almost identical lifetimes and are assigned to U(VI) sorption complexes on C-S-H surfaces. The third one has a clearly longer lifetime, and is assigned to U(VI) sorbed into the interlayer region of C-S-H. The spectra of the three extracted pure components are presented in Figure 6B as they were obtained. Similar U(VI) species were identified in previous studies of U(VI)-loaded C-S-H

phases with varying C/S ratios (Tits et al., 2011; Tits et al., 2015; Wolter et al., 2019a).

The pure component spectra extracted from the measured data for sample U7 are slightly narrower than those from, e.g., sample U4, see Figure 7. This is indicative of a more ordered environment, either influenced by the crystallinity of the solid phase or a more rigid structure of the U(VI) sorption complexes. Otherwise, the spectra are identical. Thus, to allow for a comparison of the U(VI) speciation in the various samples, the same set of pure components (shown in Figure 6B) was used to deconvolute the measured luminescence spectra.

The species distribution, determined for the various U(VI)-containing C-S-H samples by TRLFS, is summarized in Supplementary Table S7 (Supplementary Material). Despite the different U(VI) concentrations applied for preparation of these samples (2×10^{-5} M for U1 compared to 5×10^{-7} for U4–U7, corresponding to U(VI) loadings of about 198 and 119 ppm, respectively), precipitates are not detectable in any of these samples.

Moreover, despite the longer equilibration time for sample U1 (67 days compared to 20 days for samples U4–U7) and the different preparation procedure of U1, where U(VI) was already present at the beginning of C-S-H formation, the fraction of U(VI) sorbed into the interlayer is only slightly larger in the directly synthesized U(VI)-containing C-S-H sample than in the U(VI) sorption samples. This shows that both synthesis routes lead to the same U(VI) species in C-S-H. Generally, the results confirm that interlayer sorption contributes to a considerable extent to the U(VI) uptake by C-S-H as proposed by Harfouche et al. (2006) and Kremleva et al. (2020).

The effect of GLU on the fraction of the various species (surface sorption 1, surface sorption 2, sorption into the interlayer) in the differently prepared U(VI)-containing C-S-H samples is very small (Supplementary Table S7, Supplementary Material). Only when a pre-equilibrated U(VI)-GLU solution is added to the C-S-H phase, as is the case of U7, the fraction of U(VI) sorbed into the interlayer is somewhat lower, which benefits the surface sorption 1 species. Steric hindrance due to the organic ligand in the equatorial plane of UO_2^{2+} might be the cause for this.

The identity of the two different surface sorption species cannot be clarified by TRLFS. The aqueous speciation of U(VI) was calculated with the geochemical modelling software PHREEQC (Parkhurst and Appelo, 2013), based on thermodynamic data of the PSI/Nagra Chemical Thermodynamic Database 12/07 (Thoenen et al., 2014). The results for 5×10^{-7} M U(VI) (0.1 M NaCl, N_2 atmosphere) showed that at pH ~ 10.9 , which is the equilibrium pH value of the C-S-H suspension in this study, the aqueous U(VI) speciation is dominated by $\text{UO}_2(\text{OH})_3^-$ with increasing amounts of $\text{UO}_2(\text{OH})_4^{2-}$ only at increasing pH values (cf. Philipp et al. (2022)); Please note: Since ternary calcium uranyl hydroxo complexes are not yet part of current data bases (THEREDA, ThermoChimie, PSI/Nagra Chemical TDB, NEA-TDB, JAEA-TDB, JESS, Lawrence-Livermore-National-Lab (LLNL) TDB), the U(VI) speciation at hyperalkaline conditions cannot be calculated for Ca-containing background electrolytes. For the retention of the negatively charged U(VI) and/or GLU species on the negatively charged C-S-H phase at hyperalkaline conditions, previous sorption experiments combined with spectroscopic studies as well as

molecular dynamics (MD) simulations showed the effect of Ca(II) mediating between mineral surface and U(VI) as well as GLU species (Androniuk et al., 2017; Androniuk and Kalinichev, 2020; Philipp et al., 2022). For GLU sorption, this is corroborated by our ^{13}C CP MAS NMR spectroscopic results. In addition, direct binding of U(VI) species to unoccupied deprotonated silanol groups is described in the literature by Harfouche et al. (2006) and Kremleva et al. (2020).

4 Summary and conclusion

The influence of gluconate (GLU) on the retention of actinides in different oxidation states (An(X): Am(III), Th(IV), Pu(IV), U(VI), as well as Eu(III) as an analogue for Am(III) and Cm(III)) was examined in the context of a deep geological radioactive waste repository. A C-S-H phase with a C/S ratio of 0.8 was used, representing degraded cement in the alteration stage III. In addition, binary systems of GLU/C-S-H, An(X)/C-S-H, and An(X)/GLU were investigated.

Sorption of GLU on C-S-H was low and occurred only at the C-S-H surface, confirming previous results of the literature (Androniuk et al., 2017) and therefore, no blocking of sorption sites by GLU is expected at the cement degradation stage III. XRD and ^{29}Si SP MAS NMR investigations showed that no alteration of the C-S-H short and long range orders, microcrystallinity, and degree of condensation occurs due to sorption of GLU, of An(X), or both. EXAFS measurements of a Pu(IV)/C-S-H sample showed that Pu(IV) can be immobilized by incorporation into the CaO layer. Accordingly, a high retention of all An(X) by the C-S-H phase was obtained with $\log R_d$ values between $4.5 < \log R_d < 7$, which remained unaffected by the presence of GLU and the order of addition of the reactants. Leaching experiments showed no remobilization of sorbed Eu(III) or U(VI) upon the addition of GLU, and no GLU complexes were found for the ternary Eu(III) or U(VI)/GLU/C-S-H systems. In case of Eu(III), a strong influence of GLU on the Eu(III) coordination environment in the precipitate was observed by TRLFS. It can be assumed that coprecipitation of Eu(III) with pore water constituents Ca(II) and Si(IV) occurred and that the effect of GLU on the Eu(III) speciation might be explained by the formation of Ca(II)-GLU complexes, leading to a change in the stoichiometry and structure of the formed coprecipitate. The influence of GLU on the proportion of the three U(VI) sorption complexes on C-S-H is small. The observed trend of the electrophoretic mobilities of Th(IV), determined with CE-ICP-MS measurements of the ternary system Th(IV)/GLU/C-S-H, indicates a complex formation of Th(IV)-GLU-OH. In the presence of Ca(II), formation of Ca-Th(IV)-GLU-OH is conceivable.

The small effect of GLU on the An(X) retention on C-S-H (C/S 0.8) observed in this study differs from the results reported in literature for higher pH values and Ca(II) concentrations (Norden, 1994; Dario et al., 2004; Tits et al., 2005; Tasi et al., 2021). This may indicate the importance of Ca(II) ions and the formation of heterobimetallic Ca(II)-An(X)-GLU complexes for the possible mobilization of An(X) by GLU. It emphasizes the necessity to investigate the effect of GLU further, also for other cement degradation stages, which are relevant to deep geological radioactive waste repositories.

Data availability statement

The raw data supporting the conclusions of this article will be made available by the authors, without undue reservation.

Author contributions

All authors listed have made a substantial, direct, and intellectual contribution to the work and approved it for publication.

Funding

This work was partly funded by the European Union's Horizon 2020 Research and Innovation Programme (CORI project, no. 847593), partly funded by the German Federal Ministry for Economic Affairs and Energy (BMWi) within the GRaZ II projects (nos. 02E11860A, 02E11860B, 02E11860F) and partly funded by the Deutsche Forschungsgemeinschaft (DFG, German Research Foundation, no. 491466077). SD and MUK are also thankful to the Christa-Paulus-Pinus-TH foundation for financial support.

Acknowledgments

The authors would like to thank Erica Brendler (TU Bergakademie Freiberg) for solid-state NMR measurements, Sabrina Beutner (HZDR), Samer Amayri (JGU Mainz) for ICP-MS measurements, and Jürgern Hübner (JGU Mainz)

References

- Adam, N., Hinz, K., Gaona, X., Panak, P. J., and Altmaier, M. (2021). Impact of selected cement additives and model compounds on the solubility of Nd(III), Th(IV) and U(VI): Screening experiments in alkaline NaCl, MgCl₂ and CaCl₂ solutions at elevated ionic strength. *Radiochim. Acta* 109, 431–443. doi:10.1515/ract-2021-1010
- Altmaier, M., Blin, V., García, D., Henocq, P., Missana, T., Ricard, D., et al. (2021). SOTA on cement-organic-radionuclide interactions. In final version as of 19.05.2021 of deliverable D3.1 of the HORIZON 2020 project EURAD. EC grant agreement no: 847593. Available at: <https://www.ejp-eurad.eu/publications/eurad-deliverable-31-cori-sota-cement-organic-radionuclide-interactions-content-lilw>.
- Altmaier, M., Neck, V., Mueller, R., and Fanghaenel, T. (2005). "Solubility of U(VI) and formation of CaU₂O₇ · 3H₂O(cr) in alkaline CaCl₂ solutions," in MIGRATION 2005, 10 international conference on chemistry and migration behaviour of actinides and fission products in the geosphere (France), Washington, 20 - 25 September 2009 (MIGRATION).
- Amayri, S., Fröhlich, D. R., Kaplan, U., Trautmann, N., and Reich, T. (2016). Distribution coefficients for the sorption of Th, U, Np, Pu, and Am on Opalinus Clay. *Radiochim. Acta* 104, 33–40. doi:10.1515/ract-2015-2409
- Androniuk, I., and Kalinichev, A. G. (2020). Molecular dynamics simulation of the interaction of uranium (VI) with the C–S–H phase of cement in the presence of gluconate. *Appl. Geochem.* 113, 104496. doi:10.1016/J.APGEOCHEM.2019.104496
- Androniuk, I., Landesman, C., Henocq, P., and Kalinichev, A. G. (2017). Adsorption of gluconate and uranyl on C–S–H phases: Combination of wet chemistry experiments and molecular dynamics simulations for the binary systems. *Phys. Chem. Earth* 99, 194–203. doi:10.1016/j.pce.2017.05.005
- Atkins, M., and Glasser, F. P. (1992). Application of portland cement-based materials to radioactive waste immobilization. *Waste Manag.* 12, 105–131. doi:10.1016/0956-053X(92)90044-J
- Atkins, M., Glasser, F. P., and Kindness, A. (1992). Cement hydrate phase: Solubility at 25°C. *Cem. Concr. Res.* 22, 241–246. doi:10.1016/0008-8846(92)90062-Z
- Böszörményi, É., Lado, J., Dudás, C., Kutus, B., Szabados, M., Varga, G., et al. (2020). The structure and composition of solid complexes comprising of Nd(III),

for XPS measurements. The EXAFS investigation was supported by Samer Amayri, Verena Häußler (JGU Mainz), and Damien Prieur (HZDR) and was performed at the BM20 Rossendorf Beamline (ROBL) at the European Synchrotron Radiation Facility (ESRF), Grenoble, France. Furthermore, Aerosil 300 was provided by Evonik Industries AG.

Conflict of interest

The authors declare that the research was conducted in the absence of any commercial or financial relationships that could be construed as a potential conflict of interest.

Publisher's note

All claims expressed in this article are solely those of the authors and do not necessarily represent those of their affiliated organizations, or those of the publisher, the editors and the reviewers. Any product that may be evaluated in this article, or claim that may be made by its manufacturer, is not guaranteed or endorsed by the publisher.

Supplementary material

The Supplementary Material for this article can be found online at: <https://www.frontiersin.org/articles/10.3389/fnuen.2023.1124856/full#supplementary-material>

- Ca(II) and D-gluconate isolated from solutions relevant to radioactive waste disposal. *Pure Appl. Chem.* 92, 1709–1715. doi:10.1515/pac-2019-1010
- Bouzouaid, L., Lothenbach, B., Fernandez-Martinez, A., and Labbez, C. (2022). Gluconate and hexitols effects on C–S–H solubility. *Cem. Concr. Res.* 160, 106894. doi:10.1016/j.cemconres.2022.106894
- Bouzouaid, L., Lothenbach, B., Fernandez-Martinez, A., and Labbez, C. (2021). Portlandite solubility and Ca²⁺ activity in presence of gluconate and hexitols. *Cem. Concr. Res.* 149, 106563. doi:10.1016/j.cemconres.2021.106563
- Bro, R. (1997). Parafac: Tutorial & applications. *Chemom. Intell. Lab. Syst.* 38, 149–171. doi:10.1016/S0169-7439(97)00032-4
- Buijs, M., Meyerink, A., and Blasse, G. (1987). Energy transfer between Eu³⁺ ions in a lattice with two different crystallographic sites: Y₂O₃:Eu³⁺, Gd₂O₃:Eu³⁺ and Eu₂O₃. *J. Lumin.* 37, 9–20. doi:10.1016/0022-2313(87)90177-3
- Chiorescu, I., Kremleva, A., and Krüger, S. (2022). On the sorption mode of U(IV) at calcium silicate hydrate: A comparison of adsorption, absorption in the interlayer, and incorporation by means of density functional calculations. *Minerals* 12, 1541. doi:10.3390/min12121541
- Colàs, E., Grivé, M., Rojo, I., and Duro, L. (2013). The effect of gluconate and EDTA on thorium solubility under simulated cement porewater conditions. *J. Solut. Chem.* 42, 1680–1690. doi:10.1007/s10953-013-0054-2
- Dario, M., Molera, M., and Allard, B. (2004). *Effect of organic ligands on the sorption of europium on TiO₂ and cement at high pH*. Stockholm: SKB. Technical Report TR-04-04. doi:10.1007/s10967-006-0455-4
- Drobot, B., Steudtner, R., Raff, J., Geipel, G., Brendler, V., and Tsushima, S. (2015). Combining luminescence spectroscopy, parallel factor analysis and quantum chemistry to reveal metal speciation – A case study of uranyl(VI) hydrolysis. *Chem. Sci.* 6, 964–972. doi:10.1039/c4sc02022g
- Gaona, X., Dähn, R., Tits, J., Scheinost, A. C., and Wieland, E. (2011). Uptake of Np(IV) by C–S–H phases and cement paste: An EXAFS study. *Environ. Sci. Technol.* 45, 8765–8771. doi:10.1021/es2012897

- Gaona, X., Kulik, D. A., Macé, N., and Wieland, E. (2012). Aqueous–solid solution thermodynamic model of U(VI) uptake in C–S–H phases. *Appl. Geochem.* 27, 81–95. doi:10.1016/j.apgeochem.2011.09.005
- Gaona, X., Montoya, V., Colàs, E., Grivé, M., and Duro, L. (2008). Review of the complexation of tetravalent actinides by ISA and gluconate under alkaline to hyperalkaline conditions. *J. Contam. Hydrol.* 102, 217–227. doi:10.1016/j.jconhyd.2008.09.017
- Glaus, M. A., Laube, A., and Van Loon, L. R. (2006). Solid-liquid distribution of selected concrete admixtures in hardened cement pastes. *Waste Manag.* 26, 741–751. doi:10.1016/j.wasman.2006.01.019
- Harfouche, M., Wieland, E., Dähn, R., Fujita, T., Tits, J., Kunz, D., et al. (2006). EXAFS study of U(VI) uptake by calcium silicate hydrates. *J. Colloid Interface Sci.* 303, 195–204. doi:10.1016/j.jcis.2006.07.019
- Häufli, V., Amayri, S., Beck, A., Platte, T., Stern, T. A., Vitova, T., et al. (2018). Uptake of actinides by calcium silicate hydrate (C–S–H) phases. *Appl. Geochem.* 98, 426–434. doi:10.1016/j.apgeochem.2018.08.021
- Keith Roach, M., and Shakhkarami, P. (2021). *Organic materials with the potential for complexation in SFR, the final repository for short-lived radioactive waste*. Stockholm, Sweden: SKB. Report R-21-03.
- Kremleva, A., Krüger, S., and Rösch, N. (2020). Uranyl(VI) sorption in calcium silicate hydrate phases. A quantum chemical study of tobermorite models. *Appl. Geochem.* 113, 104463. doi:10.1016/j.apgeochem.2019.104463
- Kutus, B., Gaona, X., Pallagi, A., Pálkó, I., Altmair, M., and Sipos, P. (2020). Recent advances in the aqueous chemistry of the calcium(II)-gluconate system – equilibria, structure and composition of the complexes forming in neutral and in alkaline solutions. *Coord. Chem. Rev.* 417, 213337. doi:10.1016/j.ccr.2020.213337
- Lothenbach, B., and Nonat, A. (2015). Calcium silicate hydrates: Solid and liquid phase composition. *Cem. Concr. Res.* 78, 57–70. doi:10.1016/j.cemconres.2015.03.019
- Mandaliev, P. N., Stumpf, T., Tits, J., Dähn, R., Walther, C., and Wieland, E. (2011). Uptake of Eu(III) by 11 Å tobermorite and xonotlite: A TRLFS and EXAFS study. *Geochim. Cosmochim. Acta* 75, 2017–2029. doi:10.1016/j.gca.2010.10.028
- Marmodé, B., Jahn, K., Ariese, F., Gooijer, C., and Kumke, M. U. (2010). Direct spectroscopic evidence of 8- and 9-fold coordinated europium(III) species in H₂O and D₂O. *J. Phys. Chem. A* 114, 13050–13054. doi:10.1021/jp1094036
- MATLAB (2019). *MATLAB and optimization toolbox 2019b*. Natick, MA: The MathWorks, Inc.
- Matz, W., Schell, N., Bernhard, G., Prokert, F., Reich, T., Claußner, J., et al. (1999). ROBL - a CRG beamline for radiochemistry and materials research at the ESRF. *J. Synchrotron Radiat.* 6, 1076–1085. doi:10.1107/S0909049599010663
- Norden, M. (1994). *The influence of cellulose and its degradation products on the adsorption of europium on cement* (Sweden: University of Linköping). PhD thesis.
- Ochs, M., Dolder, F., and Tachi, Y. (2022). Decrease of radionuclide sorption in hydrated cement systems by organic ligands: Comparative evaluation using experimental data and thermodynamic calculations for ISA/EDTA-actinide-cement systems. *Appl. Geochem.* 136, 105161. doi:10.1016/j.apgeochem.2021.105161
- Papatzani, S., Paine, K., and Calabria-Holley, J. (2015). A comprehensive review of the models on the nanostructure of calcium silicate hydrates. *Constr. Build. Mat.* 74, 219–234. doi:10.1016/j.conbuildmat.2014.10.029
- Parkhurst, L., and Appelo, C. (2013). *Description of input and examples for PHREEQC version 3: A computer program for speciation, batch-reaction, one-dimensional transport, and inverse geochemical calculations Techniques and methods*. Denver, USA. book 6, chap. A43. Available at: <https://pubs.usgs.gov/tm/06/a43/>.
- Philipp, T., Huittinen, N., Shams Aldin Azzam, S., Stohr, R., Stietz, J., Reich, T., et al. (2022). Effect of Ca(II) on U(VI) and Np(VI) retention on Ca-bentonite and clay minerals at hyperalkaline conditions - new insights from batch sorption experiments and luminescence spectroscopy. *Sci. Total Environ.* 842, 156837. doi:10.1016/j.scitotenv.2022.156837
- Pointeau, I., Landesman, C., Giffaut, E., and Reiller, P. (2004). Reproducibility of the uptake of U(VI) onto degraded cement pastes and calcium silicate hydrate phases. *Radiochim. Acta* 92, 645–650. doi:10.1524/ract.92.9.645.55008
- Pointeau, I., Piriou, B., Fedoroff, M., Barthes, M. G., Marmier, N., and Fromage, F. (2001). Sorption mechanisms of Eu³⁺ on CSH phases of hydrated cements. *J. Colloid Interface Sci.* 236, 252–259. doi:10.1006/jcis.2000.7411
- Rand, M., Fuger, J., Grenthe, I., Neck, V., and Rai, D. (2009). *Chemical thermodynamics 11: Chemical thermodynamics of thorium*. Amsterdam, The Netherlands: NEA North Holland Elsevier Science Publishers B. V.
- Richardson, I. G. (2014). Model structures for C-(A)-S-H(I). *Acta Crystallogr. Sect. B* 70, 903–923. doi:10.1107/S2052520614021982
- Rojo, H., Gaona, X., Rabung, T., Polly, R., García-Gutiérrez, M., Missana, T., et al. (2021). Complexation of Nd(III)/Cm(III) with gluconate in alkaline NaCl and CaCl₂ solutions: Solubility, TRLFS and DFT studies. *Appl. Geochem.* 126, 104864. doi:10.1016/j.apgeochem.2020.104864
- Roosz, C., Vieillard, P., Blanc, P., Gaboreau, S., Gailhanou, H., Braithwaite, D., et al. (2018). Thermodynamic properties of C-S-H, C-A-S-H and M-S-H phases: Results from direct measurements and predictive modelling. *Appl. Geochem.* 92, 140–156. doi:10.1016/j.apgeochem.2018.03.004
- Scheinost, A. C., Claussner, J., Exner, J., Feig, M., Findeisen, S., Hennig, C., et al. (2021). ROBL-II at ESRF: A synchrotron toolbox for actinide research. *J. Synchrotron Radiat.* 28, 333–349. doi:10.1107/S1600577520014265
- Schlegel, M. L., Pointeau, I., Coreau, N., and Reiller, P. E. (2004). Mechanism of europium retention by calcium silicate hydrates: An EXAFS study. *Environ. Sci. Technol.* 38, 4423–4431. doi:10.1021/es0498989
- Stumpf, T., Tits, J., Walther, C., Wieland, E., and Fanghänel, T. (2004). Uptake of trivalent actinides (curium(III)) by hardened cement paste: A time-resolved laser fluorescence spectroscopy study. *J. Colloid Interface Sci.* 276, 118–124. doi:10.1016/j.jcis.2004.03.014
- Tajmir-Riahi, H. A. (1990). Carbohydrate complexes with alkaline Earth metal ions. Interaction of D-glucono-1,5-lactone with the Mg(II), Ca(II), Sr(II), and Ba(II) cations in the crystalline solid and aqueous solution. *J. Inorg. Biochem.* 39, 33–41. doi:10.1016/0162-0134(90)80013-N
- Tasi, A., Gaona, X., Rabung, T., Fellhauer, D., Rothe, J., Dardenne, K., et al. (2021). Plutonium retention in the isosaccharinate – cement system. *Appl. Geochem.* 126, 104862. doi:10.1016/j.apgeochem.2020.104862
- Taylor, H. F. W. (1997). *Cement chemistry*. 2nd Ed. London, UK: Thomas Telford Publishing.
- Thoenen, T., Hummel, W., Berner, U., and Curti, E. (2014). *The PSI/nagra chemical thermodynamic Database 12/07. PSI report 14-04*. Switzerland: Villigen.
- Tits, J., Bradbury, M. H., Wieland, E., and Mantovani, M. (1998). *The uptake of Cs, Sr, Ni, Eu and Th by CSH phases under high pH cement pore water conditions*. Switzerland: Villigen. PSI Internal Report TM-44-98-01.
- Tits, J., Geipel, G., Macé, N., Eilzer, M., and Wieland, E. (2011). Determination of uranium(VI) sorbed species in calcium silicate hydrate phases: A laser-induced luminescence spectroscopy and batch sorption study. *J. Colloid Interface Sci.* 359, 248–256. doi:10.1016/j.jcis.2011.03.046
- Tits, J., Stumpf, T., Rabung, T., Wieland, E., and Fanghänel, T. (2003). Uptake of Cm(III) and Eu(III) by calcium silicate hydrates: A solution chemistry and time-resolved laser fluorescence spectroscopy study. *Environ. Sci. Technol.* 37, 3568–3573. doi:10.1021/es030020b
- Tits, J., Walther, C., Stumpf, T., Macé, N., and Wieland, E. (2015). A luminescence line-narrowing spectroscopic study of the uranium(VI) interaction with cementitious materials and titanium dioxide. *Dalt. Trans.* 44, 966–976. doi:10.1039/C4DT02172J
- Tits, J., and Wieland, E. (2018). *Actinide sorption by cementitious materials*, 18–02. Switzerland: Villigen. PSI Report.
- Tits, J., Wieland, E., and Bradbury, M. H. (2005). The effect of isosaccharinic acid and gluconic acid on the retention of Eu(III), Am(III) and Th(IV) by calcite. *Appl. Geochem.* 20, 2082–2096. doi:10.1016/j.apgeochem.2005.07.004
- Warwick, P., Evans, N., Hall, T., and Vines, S. (2004). Stability constants of uranium(IV)-α-isosaccharinic acid and gluconic acid complexes. *Radiochim. Acta* 92, 897–902. doi:10.1524/ract.92.12.897.55106
- Wieland, E., Macé, N., Dähn, R., Kunz, D., and Tits, J. (2010). Macro- and micro-scale studies on U(VI) immobilization in hardened cement paste. *J. Radioanal. Nucl. Chem.* 286, 793–800. doi:10.1007/s10967-010-0742-y
- Wieland, E. (2014). *Sorption data base for the cementitious near field of L/ILW and ILW repositories for provisional safety analyses for SGT-E2. PSI technical report 14-08*. Switzerland: Villigen.
- Willberger, C., Amayri, S., Häufli, V., Scholze, R., and Reich, T. (2019). Investigation of the electrophoretic mobility of the actinides Th, U, Np, Pu, and Am in different oxidation states. *Anal. Chem.* 91, 11537–11543. doi:10.1021/acs.analchem.9b00997
- Wolter, J.-M., Schmeide, K., Weiss, S., Bok, F., Brendler, V., and Stumpf, T. (2019a). Stability of U(VI) doped calcium silicate hydrate gel in repository-relevant brines studied by leaching experiments and spectroscopy. *Chemosphere* 218, 241–251. doi:10.1016/j.chemosphere.2018.11.074
- Wolter, J. M., Schmeide, K., Huittinen, N., and Stumpf, T. (2019b). Cm(III) retention by calcium silicate hydrate (C-S-H) gel and secondary alteration phases in carbonate solutions with high ionic strength: A site-selective TRLFS study. *Sci. Rep.* 9, 14255. doi:10.1038/s41598-019-50402-x

2.2.3 Further investigations with GLU

In addition to the work published in the paper of Stietz et al. (Chapter 2.2.1; [130]) and Dettmann et al. (Chapter 2.2.2; [34]), a characterization of the liquid phase was carried out using a semi-quantitative analysis mode of ICP-MS. In addition, batch sorption experiments on HCP and C-S-H phases in the presence and absence of GLU are discussed. Additional CE-ICP-MS measurements were performed to get a better understanding of the complexation behavior of Th(IV) with GLU and Ca(II) at different pH values.

2.2.3.1 Semiquantitative analysis mode

A semiquantitative analysis mode was employed in ICP-MS for rapid screening of the background electrolytes [131], in the absence and presence of EDTA. An ICP-MS 7900, Model No. G8409A (Agilent Technologies, USA) with an SPS4 Autosampler (Agilent Technologies, USA) and a CGC MicroMist 0.5 mL min⁻¹ nebulizer (AHF Analysetechnik GmbH, Germany) was used, operating in *Collisions mode*. In this mode, a non-reactive gas (He) and kinetic energy discrimination were utilized to selectively attenuate polyatomic interferences based on their size. As polyatomic ions are larger than the analyte mass ions, they experience more frequent collisions with the cell gas as they traverse the cell, resulting in a lower residual energy upon exit. At the cell exit, ions with low energy are excluded from the ion beam using a bias voltage. Here, the measurement and evaluation program MassHunter 5.1 D.01.01 (Agilent Technologies, USA) was used. Each sample was measured using a calibration solution containing 10 ppb of Li, Mg, Co, Y, Ce, and Tl. This mode also allowed for the determination of elements not included in the calibration solution. The accuracy of this method, within 30% (specified by the manufacturer) for the matrices used in this study, is acceptable for obtaining an overview of the elements that may contribute to the speciation in solution. For clarity, only the relevant elements that exhibited significant changes after the contact time and in the presence of organic ligands are listed. The reported values are in units ranging from ng L⁻¹ to mg L⁻¹. By considering the molar mass of the respective element, the results were then converted to M for further analysis.

ACW

To determine the chemical composition of ACW before and after the contact time of 72 h with HCP, ICP-MS measurements were performed in semiquantitative analyze mode. For a comprehensive overview and comparison, the composition of the background electrolyte with organic ligands (GLU, EDTA, ISA) is presented and listed in Table 1. The contact time of HCP / ACW with the organic ligands was 124 d.

Table 1: Results of the semiquantitative analysis mode in ICP-MS for ACW and after leaching of HCP in absence in presence of the organic ligands GLU, EDTA and ISA. All values are given in M and the comparison to the literature at the cement degradation state I [22].

Element	ACW	HCP / ACW	Lit. Degradation State I [22]	HCP / ACW / GLU	HCP / ACW / EDTA	HCP / ACW / ISA
²³ Na	1.21×10^{-1}	1.42×10^{-1}	6.0×10^{-2}	1.99×10^{-1}	7.85×10^{-2}	1.64×10^{-1}
²⁴ Mg	$< 2.61 \times 10^{-6}$	$< 2.61 \times 10^{-6}$	2.0×10^{-9}	1.04×10^{-3}	$< 2.61 \times 10^{-6}$	$< 2.61 \times 10^{-6}$
²⁷ Al	$< 9.53 \times 10^{-6}$	1.18×10^{-4}	1.5×10^{-5}	4.69×10^{-4}	1.26×10^{-4}	3.66×10^{-4}
²⁸ Si	3.31×10^{-4}	4.32×10^{-4}	3.5×10^{-5}	3.74×10^{-5}	$< 1.35 \times 10^{-5}$	5.16×10^{-5}
³⁴ S	$< 1.30 \times 10^{-3}$	1.99×10^{-3}	3.0×10^{-4}	3.85×10^{-3}	3.23×10^{-3}	3.60×10^{-3}
³⁹ K	1.39×10^{-1}	2.23×10^{-1}	1.7×10^{-1}	2.64×10^{-1}	1.25×10^{-1}	2.71×10^{-1}
⁴³ Ca	$< 6.60 \times 10^{-4}$	2.83×10^{-3}	1.7×10^{-3}	5.53×10^{-3}	1.82×10^{-2}	3.65×10^{-3}
⁵⁶ Fe	2.77×10^{-7}	2.14×10^{-6}	-	5.16×10^{-4}	$< 7.27 \times 10^{-8}$	8.18×10^{-6}
²³² Th	$< 1.83 \times 10^{-9}$	$< 1.83 \times 10^{-9}$	-	1.32×10^{-8}	$< 1.83 \times 10^{-9}$	5.57×10^{-9}

In general, the values for ACW (prepared from 0.11 M NaOH and 0.18 KOH) agree well with the measured values within the 30% error range of the semiquantitative analysis mode. However, the detection of Si and Fe in the ACW could indicate contamination from the chemicals used. Regarding the background electrolyte measurement results for the HCP / ACW sample, the values for K and Ca agree well with the degradation stage I values reported in the literature by Ochs et al.[22]. However, for Na, Al, Si, and S, the determined values are an order of magnitude higher than the literature values. No literature values are available for Fe and Th [22]. In that study, 1000 cm³ of concrete was leached with typical soil water, where 21% of the concrete is composed of cement and 67% of concrete aggregates [22]. It is important to note that only Portland cement was used for the HCPs employed in this work, which may explain the observed differences. In the presence of GLU and ISA, significant leaching of Fe and Th is observed. Additionally, the presence of GLU leads to substantial leaching of Mg, while in the case of EDTA, the most significant difference is observed in Ca.

C-S-H solution

ICP-MS measurements were also performed for the C-S-H solution in the semiquantitative analysis mode after a two-week equilibration period, both in the absence and presence of the organic ligands GLU, EDTA, and ISA (after 6 d of contact time). The results are presented in Table 2. It should be noted that the values obtained for Al and Ca in the C-S-H solution are below the limit of quantification, indicating lower concentrations compared to those reported in the literature [22]. A wide range of values

is reported for Al, Si, and Ca in the literature [22] at degradation state III, thus a range is provided here. It is important to mention that in this work, the C-S-H phase is synthesized from CaO and SiO₂, whereas the literature primarily focuses on the degradation of concrete. This disparity could potentially explain the observed deviations. The increased Na signal in the presence of the organic ligands can be attributed to the use of Na salts for all the salts employed. Similarly, the heightened Fe signal might be explained by the presence of Fe impurities in the chemicals used for the organic ligands. In the case of EDTA, a noticeable increase in the concentration of Ca is observed, suggesting that EDTA has the capability to leach Ca from the C-S-H phases.

Table 2: Results of the semiquantitative analysis mode in ICP-MS for the Milli-Q water after leaching of C-S-H phases (C/S = 0.8) in absence in presence of the organic ligands GLU, EDTA and ISA. All values are given in M and the comparison to the literature at the cement degradation state III [22].

Element	C-S-H / MQ	Lit. Degradation State I [22]	C-S-H / MQ / GLU	C-S-H / MQ / EDTA	C-S-H / MQ / ISA
²³ Na	2.66×10^{-5}	2.0×10^{-4}	2.99×10^{-3}	6.89×10^{-3}	74.12×10^{-3}
²⁷ Al	$< 9.53 \times 10^{-6}$	$10^{-6} - 10^{-3}$	$< 9.53 \times 10^{-6}$	$< 9.53 \times 10^{-6}$	$< 9.53 \times 10^{-6}$
²⁸ Si	9.41×10^{-4}	$10^{-5} - 10^{-3}$	1.54×10^{-3}	1.32×10^{-3}	1.99×10^{-3}
⁴³ Ca	$< 6.60 \times 10^{-4}$	$10^{-3} - 10^{-2}$	6.91×10^{-4}	4.15×10^{-3}	$< 6.60 \times 10^{-4}$
⁵⁶ Fe	8.94×10^{-7}	-	1.28×10^{-6}	1.63×10^{-6}	1.29×10^{-6}

2.2.3.2 Effect of GLU and ISA on HCP

During the experiments with HCP, an interesting observation was made regarding the change in color of the cement when ISA and GLU were added. To further investigate this phenomenon, an additional batch experiment was conducted using HCP and the organic ligands ISA and GLU, with a contact time of 124 d. The color change can be clearly seen in Figure 15. However, no noticeable differences were observed when EDTA was added. The HCP powder after contact time was dried in a glovebox under Ar atmosphere for several d after separating the liquid phase. The resulting powder was subjected to XRD measurements to preserve the different phases present in the HCP. A comparison of the XRD spectra in the presence and absence of ISA and GLU can be found in Figure A10, where no change could be observed. Cement primarily consists of four mineral phases: two calcium silicates, one calcium aluminate, and calcium aluminate ferrite. The first three phases appear white as pure minerals, whereas pure C₄AF exhibits a brown color due to its iron content. Most of the iron oxide and some of the aluminum oxides present in the clinker are bound in the calcium aluminate ferrite phase. This phase is a solid solution compound in which Al₂O₃ and Fe₂O₃ can substitute for each other. In cement clinker, its composition is approximately represented by the formula 4 CaO - Al₂O₃ - Fe₂O₃. The calcium

aluminate ferrite can incorporate up to around 2 wt.% MgO into its crystal lattice, leading to a color change from brown to grey [132]. The semiquantitative analysis mode of the ICP-MS measurements (refer to Table 1), revealed that relatively high amounts of Mg and Fe were dissolved in the presence of GLU, which likely explains the observed whitening of the cement compared to its original color.

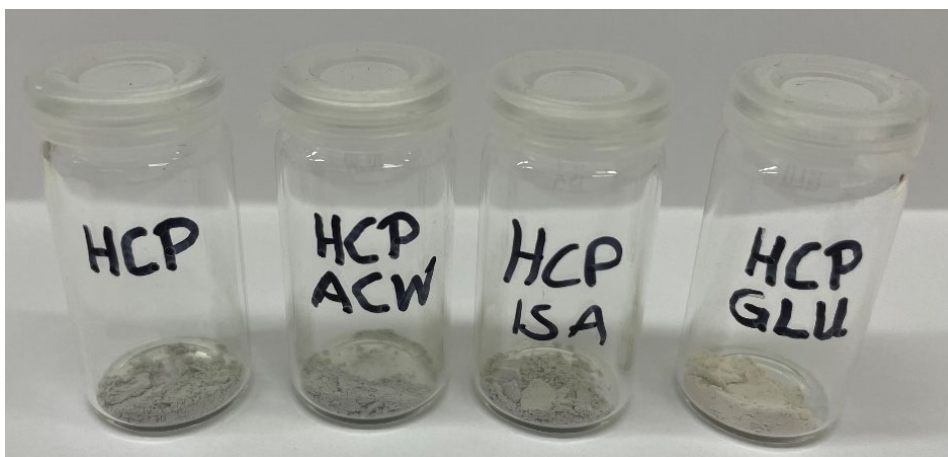


Figure 15: Change in color of HCP after batch experiments with ISA and GLU after a contact time of 124 d, with the effect being more evident with GLU.

2.2.3.3 Leaching effect of ^{232}Th from HCP in the presence of GLU

Findings of a semiquantitative analysis of HCP in presence of GLU, revealed that Th was leached from HCP in the presence of GLU. To further investigate this observation and determine the order of addition, batch sorption experiments were conducted on the HCP / Th(IV) / GLU system. A similar experiment was performed as the one described in Chapter 2.2.1 [130], for the ternary system of HCP / Pu(IV) / GLU. In this experiment, $^{232}\text{Th(IV)}$ was used with an initial concentration of 1×10^{-8} and an initial GLU concentration of 1×10^{-2} at a pH of 13.3 and an S/L ratio of 5 g L^{-1} . The calibration and measured values can be found in Table A14 and Table A15. The ICP-MS measurements indicated a higher concentration of ^{232}Th than what was initially added in the blank samples after a 72 h of contact time. Table 3 presents the calculated concentrations as mean values obtained from the double determination in the batch sorption experiment of HCP / Th(IV) / GLU, along with the values for the binary systems of HCP / Th(IV) and HCP / GLU. In the absence of GLU, the concentration of ^{232}Th is very low due to the high uptake of Th(IV) on HCP (> 99%, as shown in Table A71). The semiquantitative analysis of the HCP / GLU sample, as described in Section 2.2.3.1 revealed a concentration of $1.43 (\pm 0.1) \times 10^{-8} \text{ M}$. In this experiment, it is possible that an additive effect of the determined concentrations occurred due to the leaching of ^{232}Th . This could explain the higher concentration of ^{232}Th observed compared to the initial amount added in the blank samples. In the (HCP+Th(IV)) + GLU sample, it is conceivable that

^{232}Th was initially sorbed onto the HCP, followed by partial leaching by the HCP after addition of GLU, which is why the concentration is somewhat lower.

Table 3: Determined concentrations as a mean value from the double determination of ^{232}Th in the samples of the batch sorption experiment HCP / Th(IV) / GLU after a contact time of 72 h along the values of the binary system HCP / Th(IV) and HCP / GLU determined with ICP-MS measurements.

Sample	$[\text{}^{232}\text{Th}]_{\text{eq}} / \text{M}$
HCP + Th(IV) (Table A71)	$3.89 (\pm 0.1) \times 10^{-11}$
(HCP+Th(IV)) + GLU	$7.70 (\pm 0.3) \times 10^{-9}$
(HCP+GLU) + Th(IV)	$1.75 (\pm 0.1) \times 10^{-8}$
(HCP+Th(IV)) + GLU	$1.73 (\pm 0.1) \times 10^{-8}$
HCP + GLU (Section 0)	$1.43 (\pm 0.1) \times 10^{-8}$

Following the observation of this effect in the ternary system, the samples from the batch sorption experiment in the binary system HCP / GLU [130] varying the S/L ratio ($S/L = 0.5 - 50 \text{ g L}^{-1}$, $[\text{GLU}]_0/\text{M} = \text{const.} = 1 \times 10^{-2}$) were further analyzed by ICP-MS. The calibration and measured values are listed in Table A16 and Table A17. Table 4 summarizes the determined ^{232}Th concentration in these samples, along with the calculated concentration of how much ^{232}Th should be present in the HCP. According to a XRF analysis of ordinary Portland cement, approximately 2.8 ppm of Th should be present (refer to Appendix A1). It should be noted that the solubility limit of Th(IV) at high pH values (> 13) is in the range of 10^{-7} M [133]. Indeed, GLU exhibits a strong mobilizing effect on ^{232}Th in HCP, confirming the leaching of ^{232}Th from HCP in the presence of GLU. The leaching phenomenon suggests a dynamic interaction between the HCP, ^{232}Th , and GLU, where sorption and desorption processes are taking place concurrently. Further investigations and analysis would be necessary to fully understand the mechanisms involved in the leaching behavior and the complex interactions between the components in the system.

Table 4: The determined values from the ICP-MS measurement of the batch sorption experiment HCP / GLU after a contact time of 72 h and the calculated concentrations of ^{232}Th when the ordinary Portland cement contains 2.8 ppm ^{232}Th .

Sample S/L / g L^{-1}	$[\text{}^{232}\text{Th}]_{\text{eq}} / \text{M}$	$[\text{}^{232}\text{Th}]_{\text{calc}} / \text{M}$
0.5	2.41×10^{-9}	6.03×10^{-9}
2	7.46×10^{-9}	2.41×10^{-8}
5	1.44×10^{-8}	6.03×10^{-8}
10	6.95×10^{-9}	1.21×10^{-7}
15	4.68×10^{-9}	1.81×10^{-7}
20	2.84×10^{-9}	2.41×10^{-7}
50	1.77×10^{-9}	6.03×10^{-7}

2.2.3.4 Batch sorption experiment C-S-H / Th(IV) / GLU (C/S = 1.0)

In addition to the experiments in the ternary system described in the previous Chapter 2.2.2 [34], a batch sorption experiment was performed to investigate the order of addition with an C/S ratio of 1.0. The experiment ($[Th(IV)]_0/M = 1 \times 10^{-8}$; $[GLU]_0/M = 1 \times 10^{-2}$; $pH = 11.4$; $S/L = 5 \text{ g L}^{-1}$) involved three different scenarios: (i) (C-S-H+Th(VI)) + GLU, (ii) (C-S-H+GLU) + Th(IV), and (iii) (C-S-H+Th(IV)+GLU). The results from the ICP-MS measurements, along with the corresponding calculated values, can be found in Table A19. Figure 16 shows the calculated R_d values for $^{232}Th(IV)$ uptake on the C-S-H phases after 72 h of contact time, representing the average values from double determinations in the presence and absence of GLU. The R_d values range around 10^3 L kg^{-1} , with slight variations depending on the order of addition.

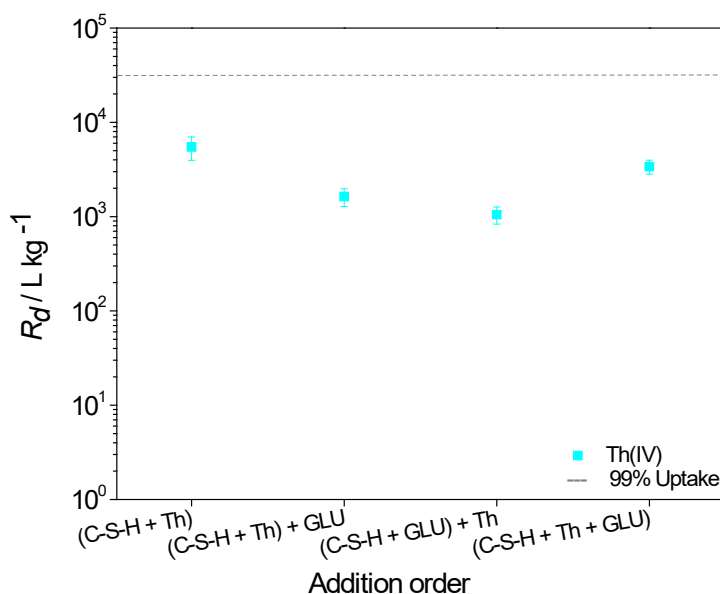


Figure 16: Average value from a double determination of the distribution coefficients R_d (L kg^{-1}) determined for Th(IV) uptake on C-S-H phase ($C/S = 1.0$) in presence and absence of GLU ($[Th(IV)]_0/M = 1 \times 10^{-8}$, $[GLU]_0/M = 1 \times 10^{-2}$, $S/L = 5 \text{ g L}^{-1}$, $pH 11.4$) after a contact time of 72 h. The dashed line represents an uptake of 99%.

According to the findings of Androniuk et al.[95], the sorption of GLU onto C-S-H phases occurs at a C/S ratio of 1.0, primarily due to the presence of more Ca(II) on the surface of the C-S-H phases (refer to Chapter 1.1). Consequently, the sorption of GLU onto the C-S-H phases can lead to a reduction in available sorption sites for Th(IV) species, which can limit the complete sorption of Th(IV) species. Additional investigations are required to further examine the binary system of C-S-H phases with higher C/S ratios and GLU to confirm the sorption of GLU. Section 2.2.3.5 provides evidence for the formation of Ca-Th-OH-GLU complexes in solution, which probably co-adsorb Th(VI) onto the C-S-H phases.

This competition arises from the strong hydrolysis occurring on the silanol groups of the C-S-H phase. It is likely that both processes, the blocking of sorption sites of GLU on C-S-H phases and the formation of Ca-Th-OH-GLU complexes, contribute to the overall sorption behavior of Th(IV) on the C-S-H phases. Solid phase studies can provide valuable insights into the sorption behavior of Th(IV) on the C-S-H phases at different C/S ratios, allowing for a better understanding of the underlying sorption mechanisms. Moreover, the results suggest that the system has not yet reached thermodynamic equilibrium, even after a contact time of 72 h.

Remarks

The investigations of Th(IV) on C-S-H phases in the presence of GLU described above were carried out as part of the master thesis of [REDACTED] under the supervision of J. Stietz and [REDACTED] [129]. Sample preparation and measurements were performed by [REDACTED] and J. Stietz, the analysis presented here was conducted by J. Stietz.

2.2.3.5 CE-ICP-MS measurement of Ca-Th(IV)-OH-GLU

To gain a better understanding of actinide retention processes in solution, it is important to investigate the actinide species present at different pH values and their complexation behavior. Speciation calculations presented in Section 1.4.2 revealed a discrepancy between the complexation constants obtained from the Thermochemie database [54] and those reported in the literature [33]. Figure 17 shows the charge distributions of Th(IV) in the presence and absence of Ca(II) and GLU, along with the experimentally determined electrophoretic mobilities μ_{eff} of Th(IV) species (electropherogram of each measurement can be found in the Appendix). The electrophoretic mobility is influenced by the analyte's charge, thus the trends in mobilities at different pH values should mirror the charge distribution. In CE-ICP-MS measurements, the exchange between the species occurs rapidly, resulting in a single peak representing the average mobility of all species. At a pH of 4, the electrophoretic mobility becomes negative, indicating the formation of complexes between Th(IV) and GLU. Colàs et al. [66] proposed the formation of anionic complexes such as $\text{Th}(\text{OH})_4(\text{HGLU})^-$ and $\text{Th}(\text{OH})_4(\text{HGLU})_2^{2-}$. Additionally, the influence of Ca(II) can be observed, suggesting the formation of quaternary complexes of $\text{CaTh}(\text{OH})_4(\text{HGLU})_2$ [33] and $\text{CaTh}(\text{OH})_4(\text{HGLU})^+$ [66], respectively. Both of these complex formations are discussed in Chapter 2.2.2 [34]. However, considering the charge distribution depicted in Figure 17 and the measured values at different pH values, the complete formation of the complex $\text{CaTh}(\text{OH})_4(\text{HGLU})_2$, as calculated based on the speciation calculation (see Figure A1) using the complex formation constants described by Gaona et al. [33], appears to be rather unlikely. It seems more likely that the calculation using the Thermochemie database [54] is consistent with the experimental values.

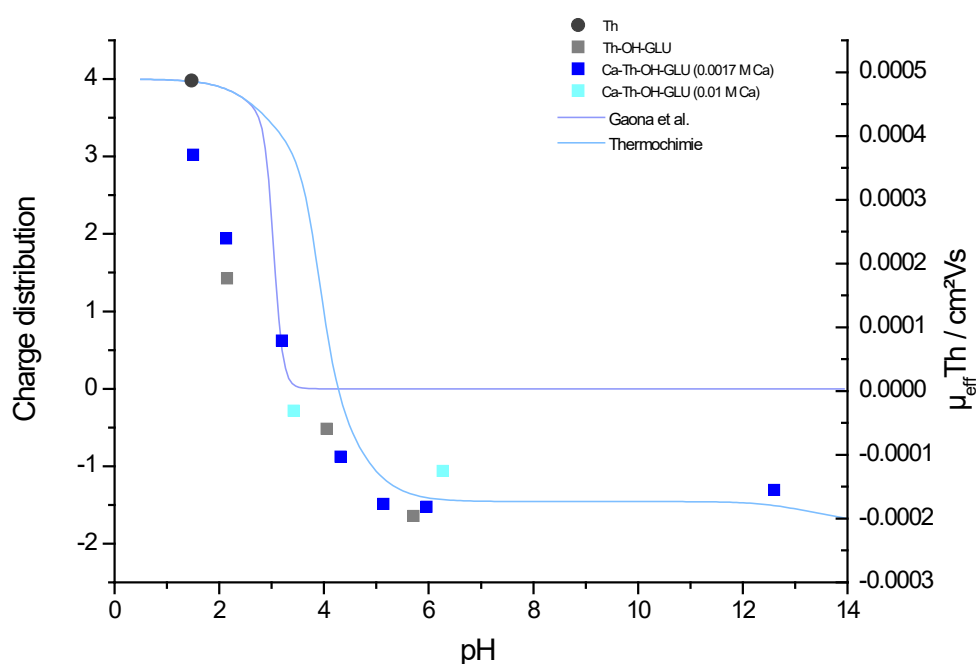


Figure 17: Results of the CE-ICP-MS measurement in the system Ca-Th(IV)-OH-GLU. Charge distribution determined from speciation calculations (solid lines) described in Section 1.4.2 and the electrophoretic mobilities μ_{eff} of Th(IV) ($[\text{Th(IV)}]_0 = 4 \times 10^{-7}$) in absence and presence of GLU ($[\text{GLU}]_0/M = 1 \times 10^{-2}$) and Ca(II) ($[\text{Ca(II)}]/M = 1.7 \times 10^{-3}$ and 1×10^{-2}) at different pH values ($I = 0.1 \text{ M}$).

In the master thesis of [redacted] [129], the system was further investigated, focusing on the determination of complex formation constants for the Th-OH-GLU / Ca-Th-OH-GLU and Pu-OH-GLU / Ca-Pu-OH-GLU systems. Table 5 provides a summary of the determined values and their comparison with literature values [33,66]. The investigations revealed that the formation of the doubly negatively charged complex $\text{Th(OH)}_4(\text{HGLU})_2^{2-}$ is more likely than the singly negatively charged $\text{Th(OH)}_4(\text{HGLU})^-$ complex. In contrast, for Pu(IV), complexation constants were determined for both $\text{Pu(OH)}_4(\text{HGLU})^-$ and $\text{Pu(OH)}_4(\text{HGLU})_2^{2-}$ complexes. Additionally, the influence of Ca(II) was investigated, leading to the determination of complex formation constants for the neutral complexes $\text{CaTh(OH)}_4(\text{HGLU})_2$ and $\text{CaPu(OH)}_4(\text{HGLU})_2$. The determined complexation constants tended to be smaller than those reported in the literature, suggesting that the complexation of Th(IV) and Pu(IV) with GLU is weaker than previously expected [33,66]. Comparing Th(IV) and Pu(IV) reveals that Pu(IV) exhibits a higher affinity for complexation with GLU. These measurements also indicating that Pu(IV) has a higher tendency for complexation with GLU.

Table 5: Summary of complexation constants from the master's thesis of [redacted] [129] and values from the literature [33,66].

Complex	$\log\beta^*_0$ [129]	$\log\beta^*_{Lit.}$
Th(OH)₄(HGLU)₂²⁻ [66]	-15.56 ± 0.06	-9.90 ± 0.60
CaTh(OH)₄(HGLU)₂ [66]	-10.72 ± 0.27	-0.80 ± 0.10
Pu(OH)₄(HGLU)⁻ [33]	-5.46 ± 0.50	-2.80 ± 1.50
Pu(OH)₄(HGLU)₂²⁻	-3.17 ± 0.08	-
CaPu(OH)₄(HGLU)₂	-0.77 ± 0.80	-

GLU sorbs strongly onto HCP (pH > 13), but not onto C-S-H phases (C/S = 0.8, pH ≈ 10). Furthermore, GLU at high concentrations appears to have such a strong effect on Th(IV) on HCP that it leaches or mobilizes it. The experiments of the order of addition of Pu(IV) and GLU has a significant impact on the uptake of Pu(IV) on HCP. Reasons for this could be the sorption of GLU on HCP or the formation of Ca-Pu-OH-GLU complexes in solution, which probably sorb onto HCP. The formation of such complexes could be demonstrated by CE-ICP-MS measurement. How these complexes sorb at the surface cannot be determined. Also, in the presence of GLU, Pu(IV) was shown to be incorporated into the CaO interlayer of the C-S-H phase [130]. GLU has no effect on the quantitative uptake of Th(IV), Am(III) and Pu(IV) on C-S-H phases with a C/S ratio of 0.8. At an increased C/S ratio of 1.0, the uptake of Th(IV) is lower, which could be due to the fact that possible sorption sites are occupied by GLU due to the changed surface of the solid phase. In addition, the experimental results and the speciation calculations highlight the different behavior of Th(IV) and Pu(IV) in the presence of GLU and emphasize the importance of considering individual actinide-ligand interactions for understanding their retention processes.

2.3 Manuscript: Investigation on cementitious materials with EDTA

Author Contribution

The investigations were carried out as part of the bachelor thesis of [REDACTED] (HCP / EDTA) [134] and the “Forschungsmodul” by [REDACTED] (C-S-H / EDTA) [135] under the supervision of J. Stietz and [REDACTED]. Sample preparation and measurements were performed by [REDACTED] and J. Stietz. J. Stietz carried out the CE-ICP-MS measurements with [REDACTED] and the XPS measurements with [REDACTED]. The analysis and the visualization presented here were performed by J. Stietz. The visualization and the manuscript were conducted by J. Stietz. It refers to Chapters from this work (especially the introduction) to avoid repetition.

Summary

In order to better understand the behavior of An(III/IV) in a repository for radioactive waste in the presence of organic material, investigations were carried out with EDTA on HCP and C-S-H phases (C/S = 0.8). For this purpose, the materials used were first examined and characterized in detail at low ionic strength. Additional investigations revealed no evidence of EDTA sorption on the solid phases, indicating that EDTA does not block the sorption sites. Furthermore, under the experimental conditions (with fresh cement and a pH of 13) and a contact time of 72 hours, EDTA showed no discernible effect on the uptake of An(III/IV) at HCP. Interestingly, the observed trend of electrophoretic mobilities indicated the possible formation of An(IV)-OH-EDTA and Ca-An(IV)-OH-EDTA complexes in solution. Together with calculations from the dominance diagram for Pu(IV), it was hypothesized that the formation of Ca-An(IV)-OH-EDTA complexes could quantitatively sorb to HCP. Although EDTA may not interact directly with the solid phases under the reported experimental conditions or affect the uptake of An(III/IV) on HCP, the formation of complexes in solution could indicate a possible role in sorption processes. Further experiments with EDTA are required to confirm and improve the results. Also, to improve and substantiate the findings of this manuscript.

Investigation on cementitious materials with EDTA

Janina Stietz *, [REDACTED] *

Johannes Gutenberg-Universität Mainz, Department of Chemistry, Mainz, Germany

*Correspondence:

Janina Stietz: jastietz@uni-mainz.de

[REDACTED]

1. Introduction

Cementitious materials serve a dual purpose: they are used extensively for the disposal of radioactive waste and play a crucial role in technical applications in underground repositories for low and intermediate level radioactive waste (L/ILW) and high-level radioactive waste (HLW). In the post-closure phase of these facilities, however, the ingress of water can trigger various degradation processes. The hydrated phases of the cement act as a buffer for the pH value and the concentrations of certain metal ions (such as Ca^{2+} , Al^{3+} etc.) in the presence of penetrating groundwater. The interaction between cement and inflowing groundwater is characterized by three primary degradation stages. In the first stage (Stage I), the composition of the pore water is buffered by the dissolution of Na and K oxides/hydroxides. This leads to increased alkali concentrations ($[\text{Na}] \approx 0.1 \text{ M}$, $[\text{K}] \approx 0.2 \text{ M}$) and a high pH value (≈ 13.3). Stage II is mainly influenced by the dissolution of portlandite, $\text{Ca}(\text{OH})_2$, which stabilizes the pH (≈ 12.5) and regulates the calcium concentration ($[\text{Ca}] \approx 0.02 \text{ M}$) in the pore water. During the transition to stage III, after the complete dissolution of Portlandite, the composition of the pore water is regulated by the non-congruent dissolution of calcium silicate hydrate phases (C-S-H), which leads to a gradual decrease in pH (from 12.5 to 10).

In the field of radioactive waste disposal, compounds such as ethylenediaminetetraacetic acid (EDTA) have proven useful due to their chelating properties, which can potentially bind and immobilize radionuclides [1]. In this context, EDTA could be integrated into backfill materials or grouts used to encapsulate radioactive waste, effectively enhancing their immobilization capabilities. The nuclear industry has used EDTA for various purposes, including the reprocessing of plutonium-containing waste, the production of defense articles containing plutonium, and as a decontamination agent. Studies have shown an interaction of EDTA with Pu, where the coexistence of EDTA with Pu decreases solubility. This phenomenon usually results from the complexation of Pu(IV) with EDTA, which could facilitate the mobility of Pu in geologic environments [2-5].

In this study, the effect of inflowing water with low ionic strength ($I = 0.1 \text{ M}$) and the associated leaching of cement in a repository for radioactive waste is investigated. Furthermore, the influence of EDTA on the retention of actinides is determined. There are still few studies in the current literature on the influence of EDTA on the retention of actinides in cementitious materials. This study provides initial findings.

2. Experimental description and characterization of the initial conditions

All experiments were performed in a glove box (UNIlab, mBraun, Germany) under Argon (Ar) atmosphere ($\text{O}_2 < 1 \text{ ppm}$, Argon 4.6, Westfahlen AG, Germany) under the exclusion of CO_2 . If not mentioned, sample preparation was done outside the glovebox. The solutions used were prepared with Milli-Q water ($18.2 \text{ M } \Omega \text{ cm}$; Synergy™ Millipore water system, Millipore GmbH, Germany), which was degassed by boiling and introducing Ar before use in the glove box. A list of the chemicals used with details of the manufacturer can be found in the Appendix.

Preparation of HCP

Based on the modified DIN EN 196-3 [6] standard, the hardened cement paste was produced with Portland cement (PZ Doppel N CEM I 42.5 N, Dyckerhoff, Germany) to achieve a water to cement ratio (w/c) of 0.5. The cement was mixed with Milli-Q water and stirred as described in the DIN standard. The paste was cured in cylindrical molds for 48 h, after which the blocks were stored in Milli-Q water for at least 28 d. The cement stone was dried and subsequently crushed using a vibrating disk mill at the Institute of Geosciences at the Johannes Gutenberg-University Mainz. The crushed cement was then sieved to achieve a particle size of $\varnothing < 63 \mu\text{m}$, and this powder was utilized for all batch sorption experiments. To characterize the solid phase, the resulting powder was analyzed by X-ray powder diffraction (XRD) and X-ray photoelectron spectroscopy (XPS).

Preparation of C-S-H phases

By using the "direct reaction method" [7] amorphous C-S-H phases were prepared. Appropriate amounts of CaO (Thermo Fisher GmbH, Germany) and SiO_2 (Aerosil 300, Evonik Industries, Germany) were mixed with decarbonized Milli-Q water in 10 mL polycarbonate centrifuge tubes (Beckman Coulter, USA). C/S ratios of 0.8 and 1.0 were synthesized for the batch sorption experiments. The mixture was shaken in an end-over-end rotator (Stuart Rotator SB3, Bibby Scientific Limited, UK) within a glove box under Ar atmosphere for 14 d. For the analysis of the C-S-H phase by XPS measurements, it was dried under Ar atmosphere before measurement.

Artificial Cement Pore Water

The composition of Artificial Cement Pore Water (ACW) was determined based on experimental findings reported by Wieland and Tits [8]. The decarbonated Milli-Q water was mixed with 0.114 M NaOH (Merck, Germany) and 0.18 M KOH (Merck, Germany) in the glove box under Ar atmosphere. The pH value of this solution was regularly monitored during the experiments and consistently measured within the range of $\text{pH} > 13$. pH values were determined using an inoLab pH/Cond 720 (WTW; Weilheim, Germany) pH meter, which was connected to a BlueLine 16 pH electrode (Schott Instruments GmbH, Germany). The electrode was filled with 3 M KCl (Mettler-Toledo AG, Switzerland) and 3 M NaCl (Merck, Germany), respectively. Prior to each pH measurement, a three-point calibration was performed using reference buffer solutions with pH values of 4.01, 6.87 and 9.18 (Schott Instruments GmbH, Germany). A buffer solution in the high pH range of $\text{pH} = 13$ (Hanna Instruments, USA) was used as a control solution for measuring high pH values, resulting in $\Delta\text{pH} = 0.2$.

Stock Solutions

The stock solutions were applied in a diluted form for the conducted experiments. The specific dilution procedures are provided for each solution accordingly. The characterization of the stock solutions and their dilutions followed the respective methods described in each case.

Iridium

To perform ICP-MS measurements, ^{193}Ir was added to each sample as an internal standard. For this purpose, a 1000 ppm ^{193}Ir -ICP-MS standard (Accu Trace™, Accu Standard, USA) was diluted to 10 ppb in 2% HNO_3 (Merck, Germany).

Americium

The $^{241}\text{Am(III)}$ stock solution was obtained from an in-house standard of the isotope repository of TRIGA Mainz. The concentration of the stock solution was determined by γ -spectroscopy. An HPGe detector (high-purity Ge detector; GMX-13180-S, EG & G ORTEC, USA with Genie 2000 Gamma acquisition and analysis software: V. 3.0, Apr. 05, 2004; Canberra Industries, Inc., USA) was used for this measurement. For evaluation, the γ -line with an energy of 59.5 keV was used, and the following equations were applied for analysis (t_{det} is the detection time):

$$A_{det} = \frac{\text{Peak area}}{t_{det} \cdot \text{Peak efficiency} \cdot \text{Emission probability}} \quad (1)$$

The concentration c was calculated using the measured activity A_{det} , the specific activity A_{spec} , the volume V , and the molar mass M in the following equation:

$$c = \frac{A_{det}}{A_{spec} \cdot V \cdot M} \quad (2)$$

An $^{241}\text{Am(III)}$ concentration of 2.7×10^{-5} M was determined by using equation (2). To achieve a concentration of 1.0×10^{-8} M in the batch sorption experiment, this stock solution was diluted in 1 M HClO_4 . Since americium has the most stable oxidation state +III in aqueous solution, this was assumed without further investigation.

Thorium

The $^{232}\text{Th(IV)}$ stock solution, a Thorium-ICP-standard from Peak Performance, CPI International, USA, comes at a concentration of 4.3×10^{-3} M, dissolved in 2% HNO_3 . For the batch sorption experiments, it was diluted further to reach a concentration of 1.0×10^{-8} M in 2% HNO_3 , while for the CE-ICP-MS measurements, its concentration was adjusted to 4.0×10^{-7} M in 1 M HClO_4 . Given the stable oxidation state of +IV for thorium in this study's experimental conditions, no additional investigation into its state was deemed necessary.

Plutonium

For the batch sorption experiments a $^{239}\text{Pu(IV)}$ stock solution was used, which was obtained from the isotope repository of TRIGA Mainz and was already electrolyzed for previous experiments. To ensure the presence of the +IV oxidation state in all experiments, the stock solutions were electrolyzed in 1 M HClO_4 prior to each experiment. In the initial step, Pu(VI) was obtained by evaporating the Pu solution nearly to dryness, followed by dissolution of the remaining residue with 1 M HClO_4 . This process was repeated 2-3 times. Subsequently, Pu(VI) was reduced to Pu(III) and then oxidized to Pu(IV) using an electrolysis cell, illustrated schematically in Figure 1. An inert atmosphere was generated by introducing Ar purge gas through a glass pipette. As this setup employed potentiostatic control, the voltage had to be periodically readjusted to maintain continuous reduction or oxidation processes.

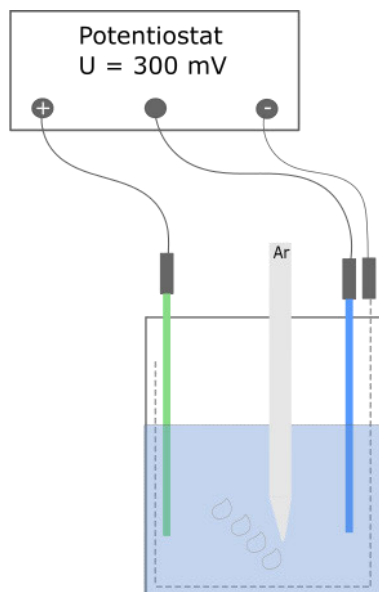


Figure 1: Schematic structure of the electrolysis cell for the preparation of $^{239}\text{Pu(IV)}$ stock solution in 1M HClO_4 . Electrolysis was performed in a glass vessel equipped with an Ag counter electrode (green), an Ag/AgCl counter electrode (blue), and a Pt working electrode (grey) placed in a net shape on the rim of the vessel. During electrolysis, Ar was induced via a glass pipette.

The oxidation states of each step were monitored using UV-Vis spectroscopy. As an example, from one of the experiments, Figure 2 shows the UV-Vis spectra for the three different oxidation states [9].

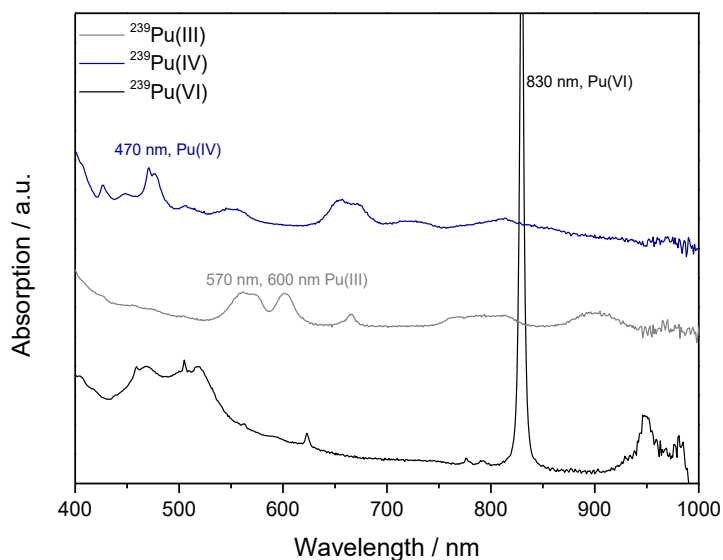


Figure 2: Summarized UV-Vis spectra of the oxidation states of ^{239}Pu achieved before and after the different steps of the electrolysis. For a better overview, an offset was introduced in the spectra (+0.2 for the spectrum of Pu(III) (grey), +0.4 for the spectrum of Pu(IV) (blue) compared to the spectrum of Pu(VI) (black))[9].

The concentration of the $^{239}\text{Pu(IV)}$ stock solution was determined by LSC in conjunction with equation (2). A concentration of $[\text{}^{239}\text{Pu(IV)}]_0/\text{M} = 1.0 \times 10^{-8}$ was utilized for the batch sorption experiments, while a concentration of $[\text{}^{239}\text{Pu(IV)}]_0/\text{M} = 1.0 \times 10^{-7}$ M was used for the CE-ICP-MS measurements.

To determine the oxidation state of Pu after the designated contact time, the redox potential of the solution was measured. The inoLab pH/Cond 720 instrument, equipped with an Ag/AgCl₂ redox electrode (Blue Line 31 RX, Schott Instruments GmbH, Germany), was employed for this purpose. A +470 mV redox standard (Schott Instruments GmbH, Germany) was utilized as a reference and measured prior to each measurement. All values were adjusted based on the deviation from the reference value and then referenced to the standard hydrogen electrode (SHE) by adding 210 mV using equation (3):

$$E_{h,SHE}(V) = E_{h,exp} - (E_{h,ref} - 470 \text{ mV}) + 210 \text{ mV}. \quad (3)$$

EDTA

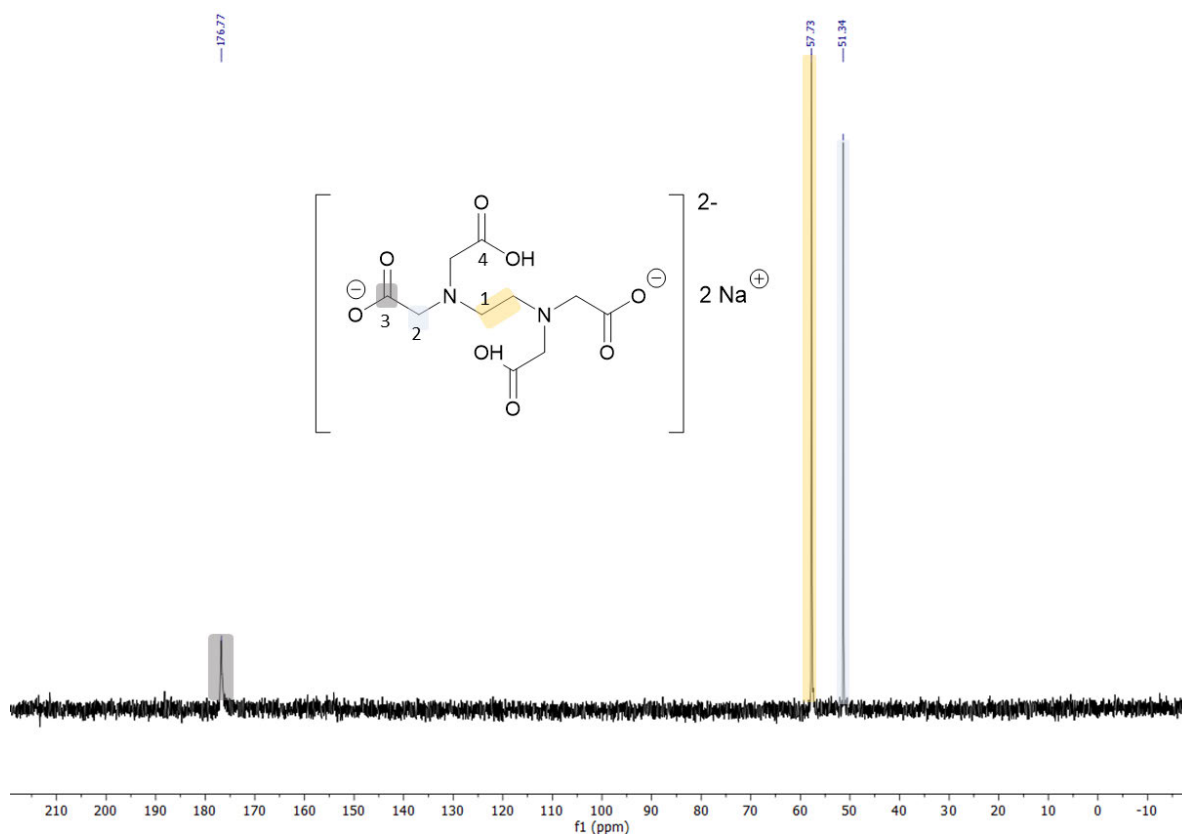
For the experiments with EDTA, an EDTA stock solution was prepared. An appropriate amount of Na₄EDTA × 2 H₂O (VWR International GmbH, Germany) was weighed and diluted with ACW and decarbonized Milli-Q water, respectively. The concentrations of the stock solution ranged from $[\text{EDTA}]_0/\text{M} = 0.1 - 0.4$, as specified in the experiments. Additionally, in the batch sorption experiments conducted in the binary systems (HCP / EDTA and C-S-H / EDTA), a ^{14}C -EDTA tracer solution was included by diluting a stock solution of 3.7 MBq mL⁻¹ ^{14}C -EDTA (Hartmann Analytic, Germany) in decarbonated water.

NMR measurement

EDTA was investigated and characterized. Nuclear magnetic resonance (NMR) spectroscopy was conducted in ACW at a high pH of 13 to assess any potential influence of the alkaline conditions. The NMR spectroscopic analyses were performed using multicore resonance spectrometers, namely Avance III HD 300, Avance II 400, and Avance III 600 (Bruker Analytical Instruments, Germany). These measurements were conducted in the central analytical laboratories of the Department of Chemistry at the Johannes Gutenberg-University Mainz. D₂O (deuterium oxide) was utilized as the solvent for the NMR measurements. The assignment of ^1H and ^{13}C signals was partially accomplished through the analysis of H,H-COSY, H,C HSQC, and H,C-HMBC spectra. Chemical shifts are reported as δ -values in parts per million (ppm). The following abbreviations describe the multiplicities of the NMR signals: s (singlet), bs (broad singlet), d (doublet), t (triplet), q (quartet), m (multiplet), dd (doublet of doublet),

dt (doublet of triplet), and tt (triplet of triplet). All coupling constants $J_{x,y}$ were expressed in Hertz (Hz), indicating the number of bonds included. The acquired spectra were analyzed using MestReNova software version 14.1.2-25024.

$\text{Na}_4\text{EDTA} \times 2 \text{H}_2\text{O}$ was also subjected to NMR spectroscopy for characterization in ACW at $\text{pH} > 13$. Figure 3 shows the ^{13}C -NMR spectrum of $\text{Na}_4\text{EDTA} \times 2 \text{H}_2\text{O}$, along with the assigned signals. The ^1H spectrum can be found in the Appendix (Figure A5). Similar to NaGLU, the high pH does not affect the chemical shifts of $\text{Na}_4\text{EDTA} \times 2 \text{H}_2\text{O}$, as the shifts determined from the NMR measurement align with the literature [10].



^{13}C -NMR (100,6 MHz, D_2O , HMBC, HSQC): δ (ppm): 51.34 (s, C_2), 57.73 (s, C_1), 176.77 (s, C_3)

Figure 3: ^{13}C -NMR spectrum of $\text{Na}_4\text{EDTA} \times 2 \text{H}_2\text{O}$ diluted in ACW ($\text{pH} > 13$) with D_2O , and assignment of signals based on structural formula.

XPS measurement

In addition, XPS (X-ray photoelectron spectroscopy) measurements were conducted on the respective organic salts employed for the preparation of the stock solutions. Prior to the measurements, the salts were milled briefly in an agate mortar, and a small amount was pressed onto an indium foil mounted on a copper sample holder. The measurements were conducted at room temperature (RT) under a vacuum of 7×10^{-9} mbar using a XPS system (SPECS GmbH, Germany). Excitation of photoelectrons was

achieved using non-monochromatic Mg K_{α} (1253.6 eV) and Al K_{α} (1486.6 eV) radiations emitted by a high-intensity double anode X-ray source (Al/Mg) XR-50. Photoelectron detection was performed using the PHOIBOS 100 hemispherical energy analyzer (SPECS Surface Nano Analysis GmbH, Germany), with a constant analyzer pass energy of 13 eV. The data analysis was conducted using CasaXPS version 2.3.24PR1.0 (Casa Software Ltd, UK).

XPS measurements were performed for the $\text{Na}_4\text{EDTA} \times 2 \text{H}_2\text{O}$ salt, and the overview spectrum is presented in Figure 4. The spectrum exhibits several distinct signals, which were assigned based on their chemical nature and comparisons to literature values [10]. The assigned signals are summarized in Table A6. A notable aspect of the XPS spectrum of $\text{Na}_4\text{EDTA} \times 2 \text{H}_2\text{O}$ is the signal observed in the N 1s region. This signal indicates the presence of nitrogen in the compound and distinguishes it from the spectra of, e.g., GLU and ISA.

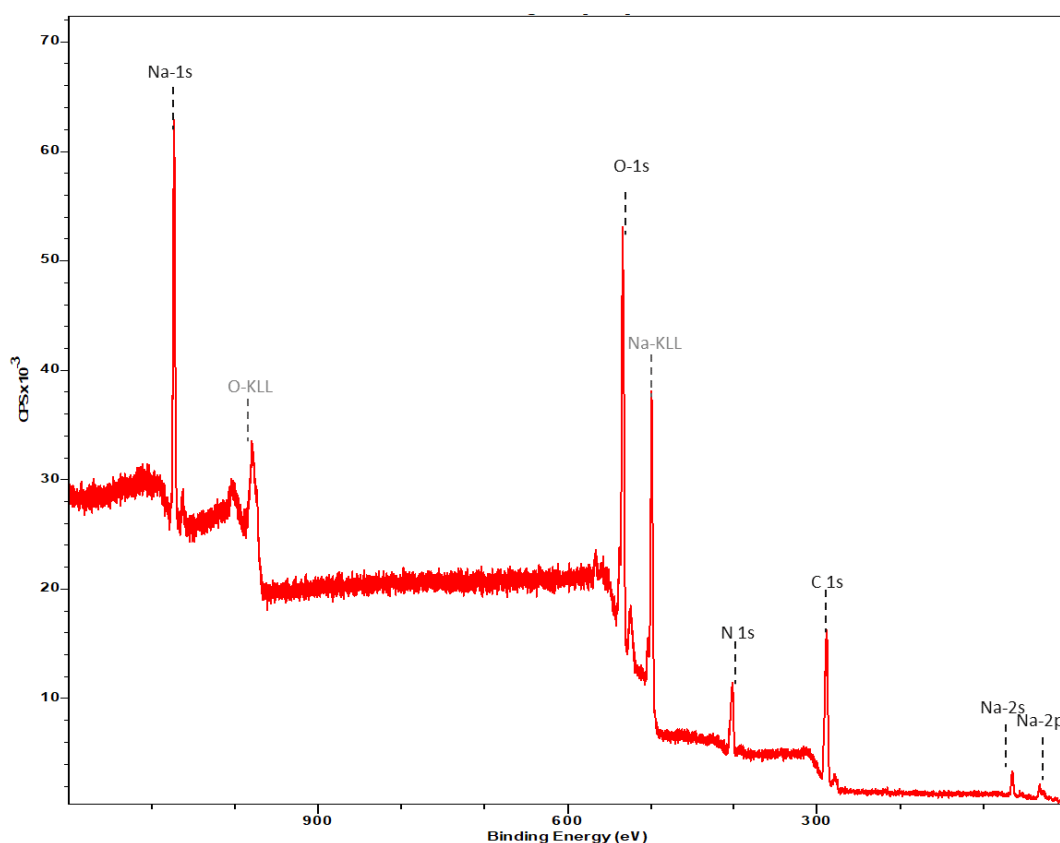


Figure 4: XPS overview spectra of $\text{Na}_4\text{EDTA} \times 2 \text{H}_2\text{O}$ with Al K_{α} at an anode excitation energy of 1486.6 eV after surface admittance correction of 1.0 eV (Na 1s signal). O-KLL and Na-KLL denote Auger transitions and can be assigned the signals of the Auger electrons of O and Na. The other signals were assigned to the photoelectrons of the contained elements.

Na_4EDTA consists of four different carbon atoms, each exhibiting different shifts in the C 1s signal due to their respective substituents. The structure, including the numbering of the carbon atoms, is illustrated in Figure 3. In the case of electronegative substituents, electron density is pulled away from the carbon

atom, resulting in ionization occurring at higher energies. Consequently, the binding energy is higher in these cases. By employing an additive scheme [11], the shifts can be calculated in comparison to aliphatic carbon. For this, the binding energy of a standard (e.g. C 1s with 284.8 eV in graphite [12]), is used as a reference, and the shifts caused by neighboring atoms/groups B are considered in the following equation (6) and are presented in Table 2 [11]. Here, ΔE_B represents the shift in the binding energy of carbon atom C, B_j corresponds to the shift contribution factor for the neighboring atom/group B.

$$\Delta E_B = \sum_j E_B(C + B_j). \quad (4)$$

Considering that bond energy differences smaller than 1 eV cannot be distinguished from each other due to the resolution of the measurement. Generally, the -COO- group exhibits the highest shift in binding energy due to the strong electronegativity of the two oxygen atoms, while the CH₂-group has the lowest shift owing to the absence of oxygen atoms. As a result, two distinct signals can be expected for C₁/C₄ and C₂/C₃, which are also depicted in the selected range of the spectrum in Figure 5.

Table 1: Shift of the binding energy of carbon atoms in Na₄EDTA × 2 H₂O calculated according to the additive scheme [11] and equation (6).

C-atoms	ΔE_B [eV]	E_B [eV]
1,4	3.6	288.4
2	1.1	285.9
3	0.8	285.6

As can be seen in Figure 5, the peak exhibits asymmetry, indicating that it is composed of multiple components. To deconvolute the peak into its constituent components, two fits were performed. A 60:40 combination of Gaussian and Lorentzian functions was employed as the peak shape. The Shirley background correction method [13] was utilized to correct for the background, and the half-widths of the individual components were set to be equal. Two fits were performed in Figure 5, which demonstrate good agreement with the binding energies provided in Table 1. The intensities of the two fits indicate a ratio of approximately 3:2, which corresponds well to the ratio of carbon atoms contributing to the signal (refer to Table A6). Thus, the additive scheme not only provides a reliable means to determine the bond energy locations but also reflects the atomic ratios contributing to the signal.

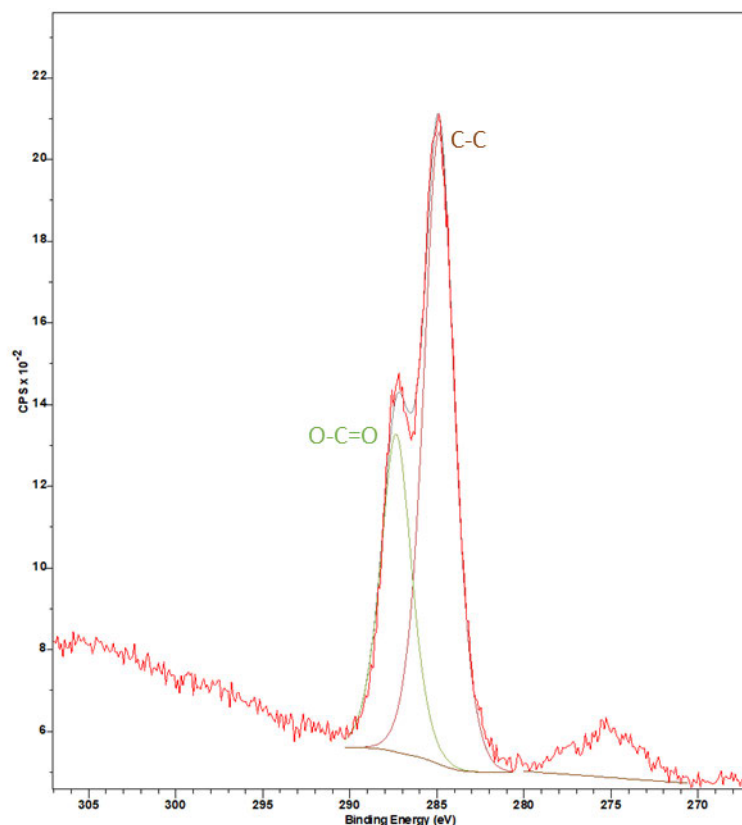


Figure 5: XPS overview spectra of $\text{Na}_4\text{EDTA} \times 2 \text{H}_2\text{O}$ with Al K_α at an anode excitation energy of 1486.6 eV after surface admittance correction of 1.0 eV (Na 1s signal). The magnification shows the range of 310 - 260 keV.

2.1. Batch sorption experiments

The batch sorption experiments were conducted as illustrated in Figure 6. The solid phase (HCP powder or CaO/SiO_2) was weighed and filled with the appropriate background electrolyte (ACW or Milli-Q water) to achieve suspensions with solid-to-liquid (S/L) ratios ranging from 0.5 to 50.0 g L^{-1} . Centrifuge tubes with volumes of 15 mL (VWR Int., USA), 10 mL or 40 mL (Beckman Coulter, USA) were used for the different batch experiments. This suspension was then preconditioned for min. 3 d in an end-over-end rotator. Pre-conditioning was followed by the addition of EDTA or actinide with a contact time of 72 h (binary system). The experiments in the ternary systems, where the order of reactant addition of the organic ligand (OL) ($[\text{EDTA}]_0/\text{M} = 1 \times 10^{-2}$) and actinides (An(X) , ($[\text{An}]_0/\text{M} = 1 \times 10^{-8}$)) was varied, consistently followed the same principle:

- (i) An(X) was equilibrated with the suspension (S) for 72 h before EDTA was added, followed by an additional 72 h of equilibration time, referred to as (S + An(X)) + EDTA.
- (ii) EDTA was equilibrated with the suspension for 72 h before An(X) was added, and another 72 h of contact time was allowed, denoted as (S + EDTA) + An(X) .

- (iii) Simultaneous addition of An(X) and EDTA to the suspension with an equilibration time of 72 h, denoted as (S + An(X) + EDTA).

For preparing the blank samples (without solid phase), which served as a reference for 0% sorption, the background electrolyte was prepared in a centrifuge tube with the appropriate concentration of the organic or the An(X) and adjusted to a pH > 1 with concentrated HNO₃ to prevent wall sorption on the vessels. In kinetic experiments, the contact time was extended by several weeks after complete addition. The specific time for each corresponding experiment is provided. Finally, the samples were centrifuged at 3,770×g (SIGMA 3K30, SIGMA Laborzentrifugen GmbH, Germany) for 15 min and ultracentrifuged at 108,800×g (Avanti J 30I, Beckman-Coulter, USA) for 1 h to separate the phases. The pH of each suspension was measured for all samples during the contact time and immediately after centrifugation.

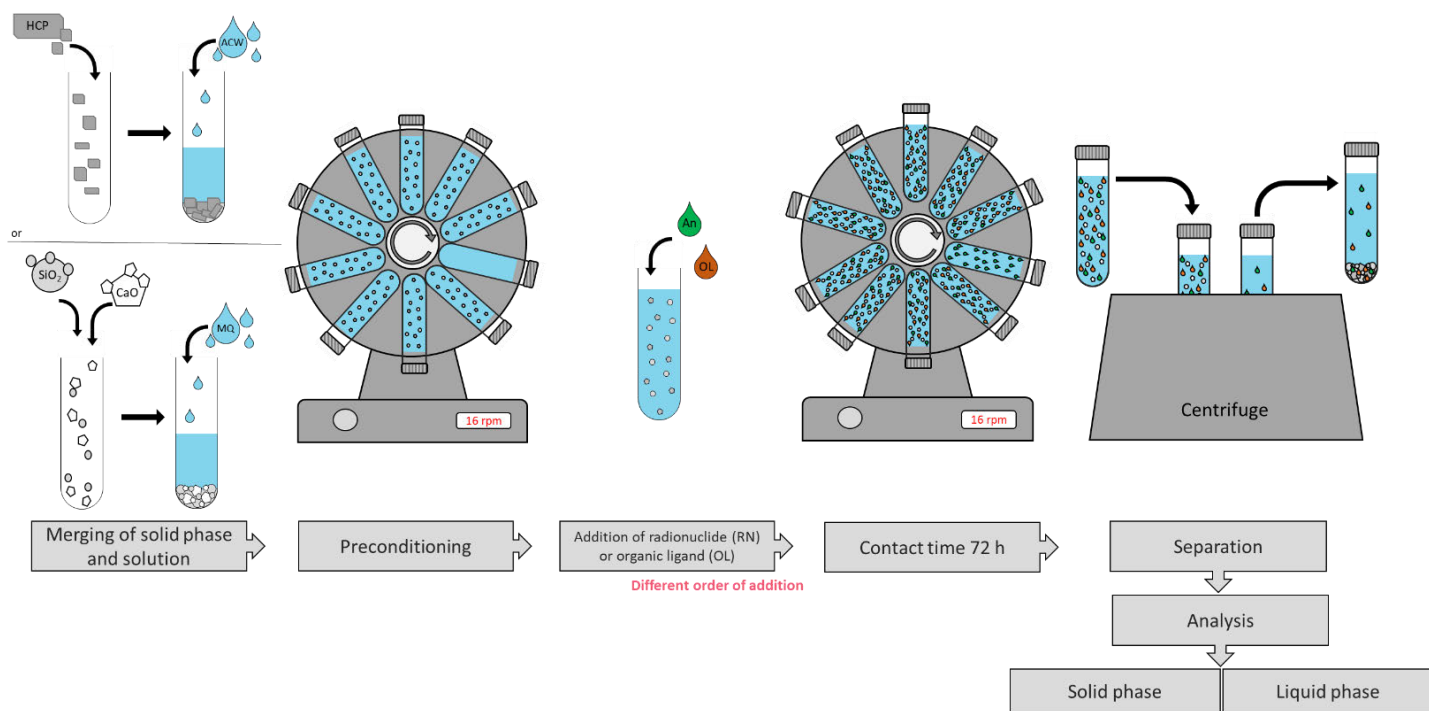


Figure 6: Schematic illustration for the preparation of the samples for the batch sorption experiments.

2.2. ICP-MS measurements

Inductively coupled plasma mass spectrometry (ICP-MS) is used for characterizing the liquid phase of the batch sorption experiments. The measurements were conducted using an ICP-MS 7500ce instrument (Agilent Technologies, USA) equipped with a CGC MicroMist 0.5 mL min⁻¹ nebulizer (AHF Analysetechnik GmbH, Germany). This measurement was performed using the ICP-MS MassHunter measurement software (G7200B, Agilent Technologies, USA), and the analysis was performed using the MassHunter Workstation Software for ICP-MS Ver. B.01.01 (Agilent Technologies, USA). Prior to each measurement, the instruments were optimized for sensitivity (Li, Y, Tl), level of oxide (Ce), and doubly charged ion (Ce). A tuning solution containing 10 µg L⁻¹ of Li, Y, Tl, Ce, and Co in 2% HNO₃ was used for the optimization process. The operating conditions are summarized in Table 2.

Table 2: Overview of the parameters for the ICP-MS measurements.

Parameter	Values
RF Power	1550 W
Nebulizer Pump	0,1 rps
Uptake PeriPump	90 s
Stabilize PeriPump	30 s
Integration Time	0,1 s
Measurements per sample	6
Carrier Gas	0,85 L min ⁻¹
Makeup Gas	0,41 L min ⁻¹
Rinse with Milli-Q water	2 min
Rinse with 2% HNO₃	2 min

To provide a reliable assessment of the measured signals, the limit of detection (LOD) and the limit of quantification (LOQ) were determined. The LOD, as described in equation (5), indicates whether the signal of an analyte is detectable at a qualitative level in a sample. On the other hand, the LOQ, described in equation (6), represents the minimum signal strength required for a quantitative determination of the analyte. Both LOD and LOQ are determined based on the mean value of the analyte signal μ in a background sample (BG) and the corresponding standard deviation σ .

$$LOD = \mu + 3\sigma . \quad (5)$$

$$LOQ = \mu + 6\sigma . \quad (6)$$

The corrected ratio R_{corr} was determined by the ratio of the signal of the analyte in the sample $S_{A,Sample}$ and the signal of the internal standard $S_{ISTD,Sample}$ minus this ratio of the background sample with the signal $S_{A,BG}$ and the signal of the internal standard $S_{ISTD,BG}$ of the background sample. Some samples were diluted, which is considered in the dilution factor f_{dil} .

$$R_{corr} = f_{dil} \cdot \left(\frac{S_{A,Sample}}{S_{ISTD,Sample}} - \frac{S_{A,BG}}{S_{ISTD,BG}} \right) . \quad (7)$$

With the corrected ratio R_{corr} , the sorption $S_{\%}$ in the batch sorption experiments could be calculated. Since two blank samples were used per batch sorption experiment, the averaged corrected rate $\bar{R}_{corr,Blank}$ was used for the calculation.

$$S_{\%} = 100 \% \cdot \left(1 - \frac{R_{corr,Sample}}{\bar{R}_{corr,Blank}} \right) . \quad (8)$$

The corrected ratio R_{corr} , together with the volume of the sample V and the mass m of the solid phase, allowed the calculation of the distribution coefficient R_d .

$$R_d = \frac{V}{m} \cdot \left(\frac{\bar{R}_{corr,Blank} - R_{corr,Sample}}{R_{corr,Sample}} \right) . \quad (9)$$

Using the corrected ratio R_{corr} and the parameters of the calibration (slope m and intercept b), the equilibrium concentration c_{eq} remaining in the solution was determined.

$$c_{eq} = \frac{R_{corr,Sample} - b}{m} . \quad (10)$$

2.3. Speciation measurements using CE-ICP-MS

To gain a better understanding of processes such as actinide sorption, it is important to study the actinide species present in solution and their complexation behavior. In the literature, one commonly used method for this purpose is solubility experiments conducted at relatively high concentrations, which exceed the expected environmental concentration when actinides are released into a repository [4,5,14,15]. Another method employed is the coupling of capillary electrophoresis (CE) with inductively coupled plasma mass spectrometry (CE-ICP-MS), which allows for the investigation of actinide complexation behavior at trace environmental concentrations. This analytical technique offers several advantages, including high separation efficiency, small sample volume requirements and short analysis times. The separation of species in the sample is based on the charge-radius ratio. This exploits the different migration velocities of charged particles in an electric field, resulting from their distinct electrophoretic mobilities μ of the different species [16]. The effective mobility μ_{eff} depends on the charge distribution, which can be compared to speciation diagrams. In capillary electrophoresis, the electrophoretic migration of ions is accompanied by the electroosmotic flow (EOF). The EOF is the movement of the electrolyte solution through the capillary driven by the electric field and depends on the charge distribution near the capillary surface. Consequently, it causes the co-migration of positively charged, neutral, and negatively charged particles in the electrolyte solution. When a voltage is applied in electrophoresis, the electric field affects the movement of charged particles. Cations experience additional acceleration, anions are slowed down, and neutral species are unaffected by the electric field. As a result, cations move faster, anions move slower, and neutral particles migrate through the capillary at the speed of the EOF.

In this study, 2-bromopropane (Merck, Germany) was added as an EOF marker to each sample, and its detection was utilized to determine the migration time of the EOF (t_{EOF}). The electroosmotic flow causes the EOF marker to migrate towards the cathodic end of the capillary. The electrophoretic mobility μ_{eff} can be expressed using equation (11), when detected with ICP-MS. Here, l represents the capillary length in centimeters, U denotes the voltage in volts, and t refers to the migration time in seconds. The error for equation (11) was calculated using Gaussian error propagation and can be found in the Appendix (equation (33)).

$$\mu_{eff} = \frac{l^2}{U} \left(\frac{1}{t} - \frac{1}{t_{EOF}} \right). \quad (11)$$

The experimental setup employed in this study consisted of an Agilent 7100 capillary electrophoresis system (Agilent Technologies, USA) coupled to an Agilent 7900 ICP-MS (Agilent Technologies, USA) through a MiraMist CE nebulizer (Burgener Research, UK) and a Scott-type spray chamber (AHS Analysentechnik, Germany). A fused silica capillary was utilized, featuring inner capillary walls coated with silanol groups that possess a negative surface charge resulting from the partial dissociation of these

groups at $\text{pH} > 4$ [17]. The CE system was controlled by the 3D-CE ChemStation software (Agilent Technologies, USA). Data acquisition and analysis were conducted using the MassHunter Workstation Software for ICP-MS Ver. 5.1. A summary of the measurement parameters is provided in Table 3.

Table 3: Parameters for the performed CE-ICP-MS measurements.

	parameters	values
CE - system	Voltage	10 kV
	Amperage	10 – 50 μA
	Capillary	fused silica; $\text{Ø} = 50 \mu\text{m}$, $l = 50 \text{ cm}$
Make-up solution	Make-up electrolyte	1.25% HNO_3 + 10% ethanol + 5 ppb of ^{89}Y , ^{107}Rh , ^{140}Ce and ^{209}Bi
	Flow rate	ca. 15 $\mu\text{L min}^{-1}$
ICP-MS	Plasma Power	1550 W

3. Results and discussion

3.1. Characterization of the solid phase

The characterization of crushed HCP, HCP with ACW after a preconditioning time of 72 h and the C-S-H phases ($C/S = 0.8$) in Milli-Q water after two weeks of synthesis are discussed. To characterize these samples, XPS measurements were performed. Additionally, the effect of ACW on HCP was investigated using SEM/EDX and XRD measurements. The samples were prepared as previously described, separated from the liquid phase, and the solid phase was dried under an Ar atmosphere at room temperature.

HCP

XPS measurements

To investigate the possible influence of ACW on the surface of HCP, measurements and evaluations were performed on both HCP powder (red) and HCP in contact with ACW (green). Figure 7 show the overview spectra, along with the assignment of the peaks to their corresponding elements. In the Appendix, Table A9 (HCP) and Table A10 (HCP / ACW) compares the experimentally determined peaks of the samples with literature values [10].

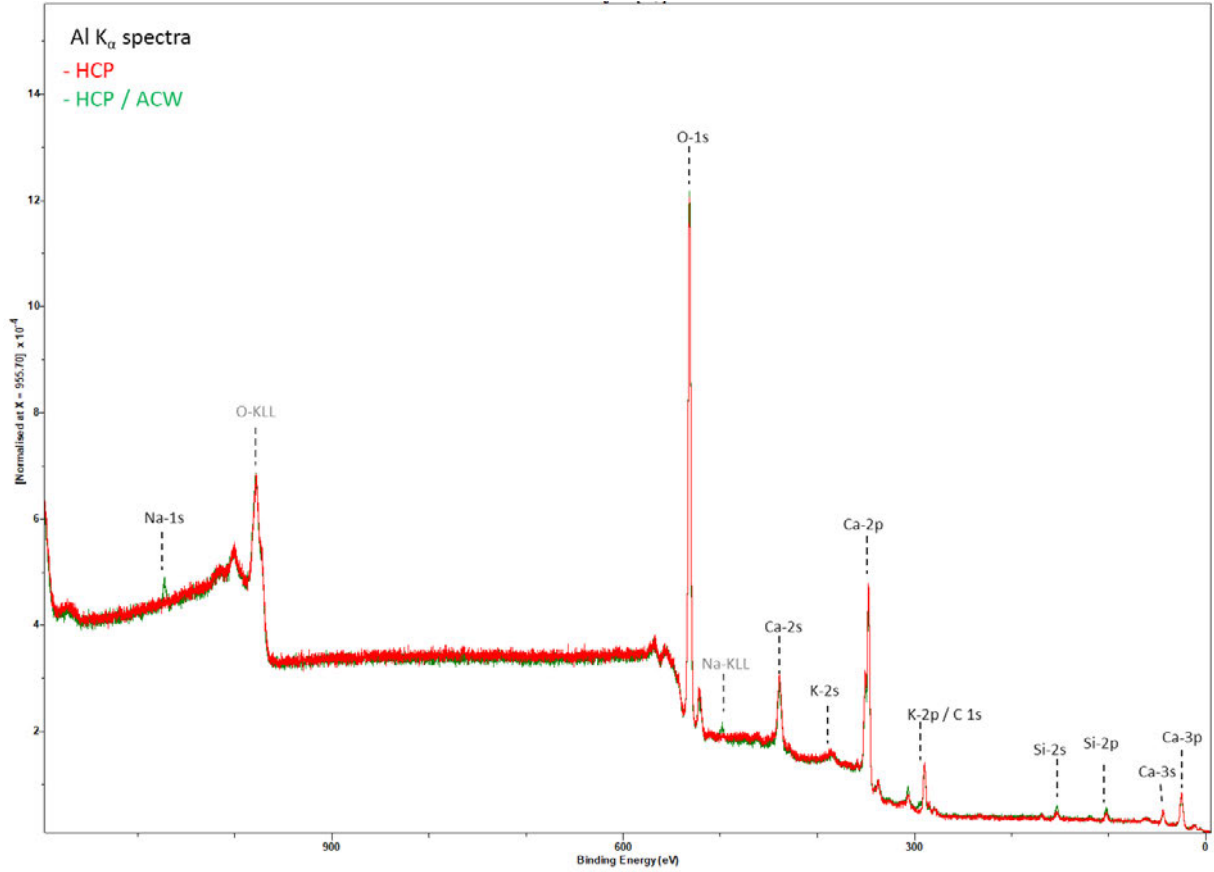


Figure 7: XPS overview spectra of crushed HCP (red) and HCP (w/c 0.5) in ACW (green) after a contact time of 72 h measured with Al K_{α} at an anode excitation energy of 1486.6 eV after surface admittance correction of 4.1 eV (Ca 2p signal). O-KLL and Na-KLL denote Auger transitions and can be assigned the signals of the Auger electrons of O and Na. The other signals were assigned to the photoelectrons of the contained elements.

The ratio $\frac{n_{Ca}}{n_{Si}}$ of the two elements in the spectrum was determined by calculating the peak areas using the corresponding photoionization cross-sections σ , as per equation (12). The peak areas $I_{Ca\ 2p}$ and $I_{Si\ 2p}$ represent the intensities of the respective elements, which can be composed of several sublevels within the shell.

$$\frac{n_{Ca}}{n_{Si}} = \frac{I_{Ca\ 2p}}{I_{Si\ 2p}} \cdot \frac{\sigma_{Si}}{\sigma_{Ca}} \quad (12)$$

This enables a quantitative determination of the stoichiometric ratio of the elements present, allowing the C/S ratio to be derived from the obtained peak averages. Based on the peak areas (Table A10) and equation (12), a C/S ratio of 2.7 is calculated for the HCP / ACW sample using the Ca 2p ($\sigma = 0.068$ barn) and Si 2p ($\sigma = 0.011$ barn) peaks. This value is significantly higher than the theoretical value for fresh cement (C/S = 1.8) [15]. Further evaluation with other peaks yields an even higher C/S ratio, but those results are not included here. The deviation from the theory can be attributed to the method of

surface analysis. As shown in Figure 7, the two spectra do not differ significantly in terms of the obtained peaks, only an additional peak for Na 1s in the HCP / ACW sample can be observed. Furthermore, a K 2s peak at 378 eV is observed, corresponding to dried ACW (0.114 M Na and 0.18 M K). Further K 2p peaks (K 2p 1/2 at 296 eV; 2p 3/2 at 293 eV) can potentially be confused with C 1s (285 eV) [18]. However, by identifying the spin-orbit components expected for K 2p, it is possible to distinguish between the K 2p and C 1s features. This area of analysis is essential for further research as it involves comparing the results of the liquid phase with those of the solid phase in the binary system (HCP / OL).

As depicted in Figure 8, the most notable difference between the two spectra is observed in this particular region. There is a discernible change in the intensities of the C species. One possible explanation for this observation is the surface carbonation of the HCP powder, which occurs during its production and storage in air. When the HCP comes into contact with ACW, the carbonate present on the surface may dissolve, leading to a decrease in the intensity of the corresponding O-C=O component. Additionally, the intensity of the C-C species peak increases. If one compares the C range under consideration with a literature spectrum of adventitious carbon [19], also shown in Figure 8, the peaks appearing in the spectrum can probably be assigned to this type of carbon. The C1s spectrum for impurities normally has C-C, C-O-C and O-C=O components. The C-C component can be set to a binding energy of 284.8 eV as standard. It is worth noting that the samples were prepared for the XPS measurement and stored in holders exposed to air, which could result in the accumulation of adventitious carbon from the environment. This accumulation may account for the observed peak intensity [20]. In future experiments, it is advisable to freshly mortar and prepare the samples shortly before the measurement to minimize the accumulation of adventitious carbon.

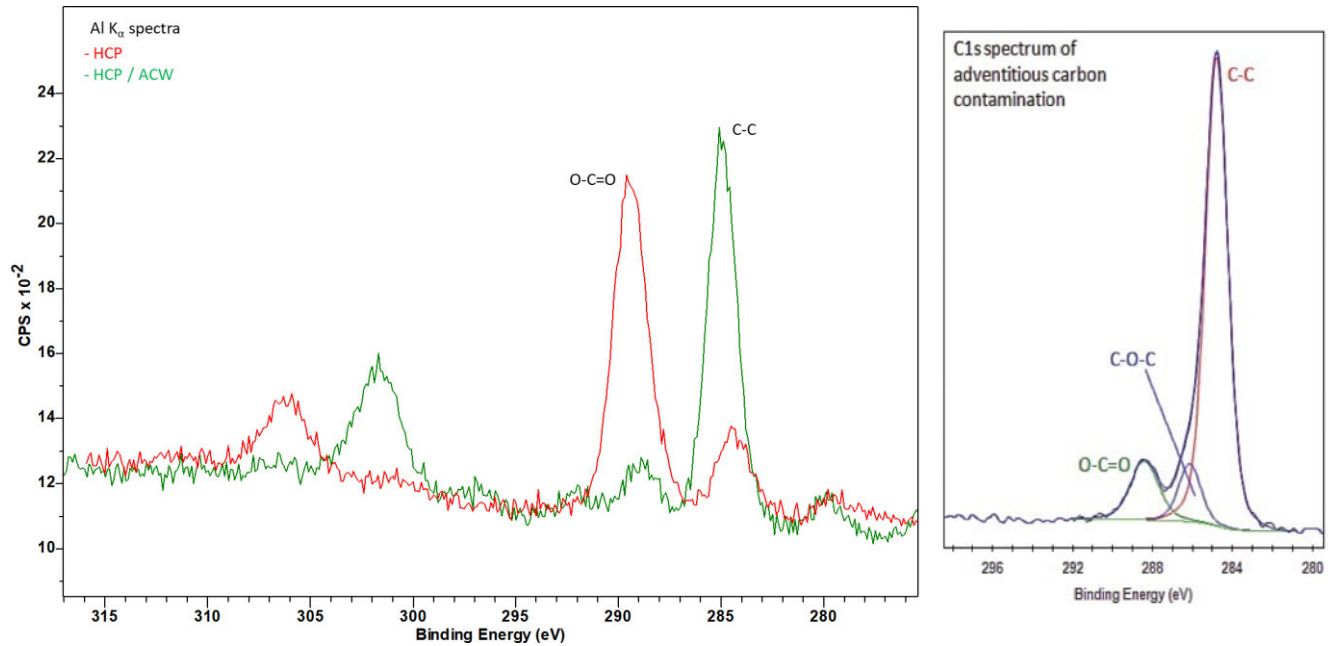


Figure 8: Superposition of two XPS spectra magnified in the region around C 1s (315 - 275 eV), HCP (red) and HCP preconditioned in ACW (green) measured with Al K_{α} at an anode excitation energy of 1486.6 eV after surface admittance correction of 4.1 eV (Ca 2p signal) (left) and a literature spectrum of adventitious carbon (right) [19].

XRD measurements

The XRD measurements were performed using a Seifert XRD3000 TT diffractometer (Eigenmann GmbH, Germany) with an automatic divergence slit (ADS) using Cu K_{α} radiation (40 kV, 30 mA, 257 Hz) at the Institute of Geosciences at the Johannes Gutenberg-University Mainz. A step counting time of 2 s and a step width of $0.03^{\circ} 2\theta$ were selected for the analysis. The diffractograms are shown in Figure 9 present the main signals that have been identified. Both samples exhibit signals corresponding to Portlandite, Ettringite, Calcite, and Alite. No evidence of an obvious phase dissolution can be observed after a contact time of 124 d with ACW.

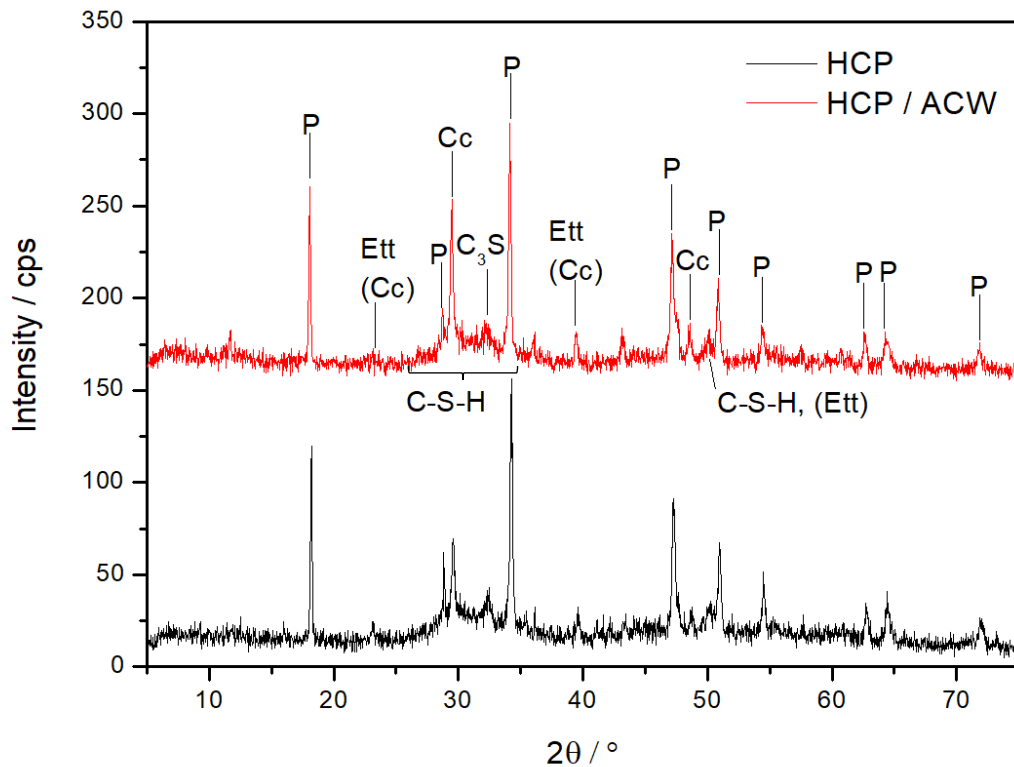


Figure 9: XRD patterns of crushed HCP (black) and HCP / ACW (red) after a contact time of 124 d. The main signals are identified: P – Portlandite, Ett – Ettringite, Cc – Calcite, C₃S – Alite, C-S-H phases.

SEM measurements

To study the effect of ACW on the surface, SEM (scanning electron microscopy) imaging technique was used to make measurements to visualize the changes on the surface. Information acquisition in electron microscopy is based on the interaction of an accelerated electron beam, focused by scanning methods, with the sample surface, which is registered by various detectors. Electrons emitted from the surface are divided into two categories in terms of their energy. Backscattered electrons (BSE) remerge at the surface after a path of predominantly elastic interactions and exhibit an energy distribution significantly dependent on the nuclear charge number Z of the scattering partners close to the primary energy. They emerge from deeper locations within the sample surface. The BSE image mainly exhibits elemental contrast. Secondary electrons (SE) show after a large number of dissipation processes have energies of only a few electron volts and have a small average exit depth, SEs escape only from the top few nanometers of the surface of a sample. Topographic information is well obtained with this type of detection. Consequently, the resolution of SE images (~ 1 nm) is better than that of BSE images (~ 100 nm) [21,22]. Since the change of the individual phases in the HCP is to be investigated, the generation of BSE images is suitable. A Philips XL30 scanning electron microscope (Philips, Netherland) was used for the measurements. The resolution limit is 2 nm at 30 kV. The external image acquisition system

(remX GmbH, DISS5, Germany) made it possible to adjust the image resolution, allowing the high-resolution BSE images to be acquired.

Polished sections of HCP were prepared to facilitate the identification of individual phases and evaluate any changes in the microstructure of HCP after a 6-d contact time with ACW. In Figure 10 (top), the main phases in HCP including Alite, Belite, C-S-H phases, Ferrite, and Portlandite, were clearly identified [23]. In Figure 10 (bottom), significant alterations in the microstructure were observed. The dissolution of Portlandite and Alite after contact with ACW can be observed. Upon closer inspection, fine precipitates or crystals on the surface were detected, which may indicate the presence of dried ACW components (such as NaOH or KOH). The SEM images show changes on the surface of the HCP, indicating that only small part of the portlandite and alite dissolves, while a significant part probably remains within the HCP structure, as indicated by the XRD measurements of the pulverized samples, where no obvious dissolution of portlandite and alite signals was observed.

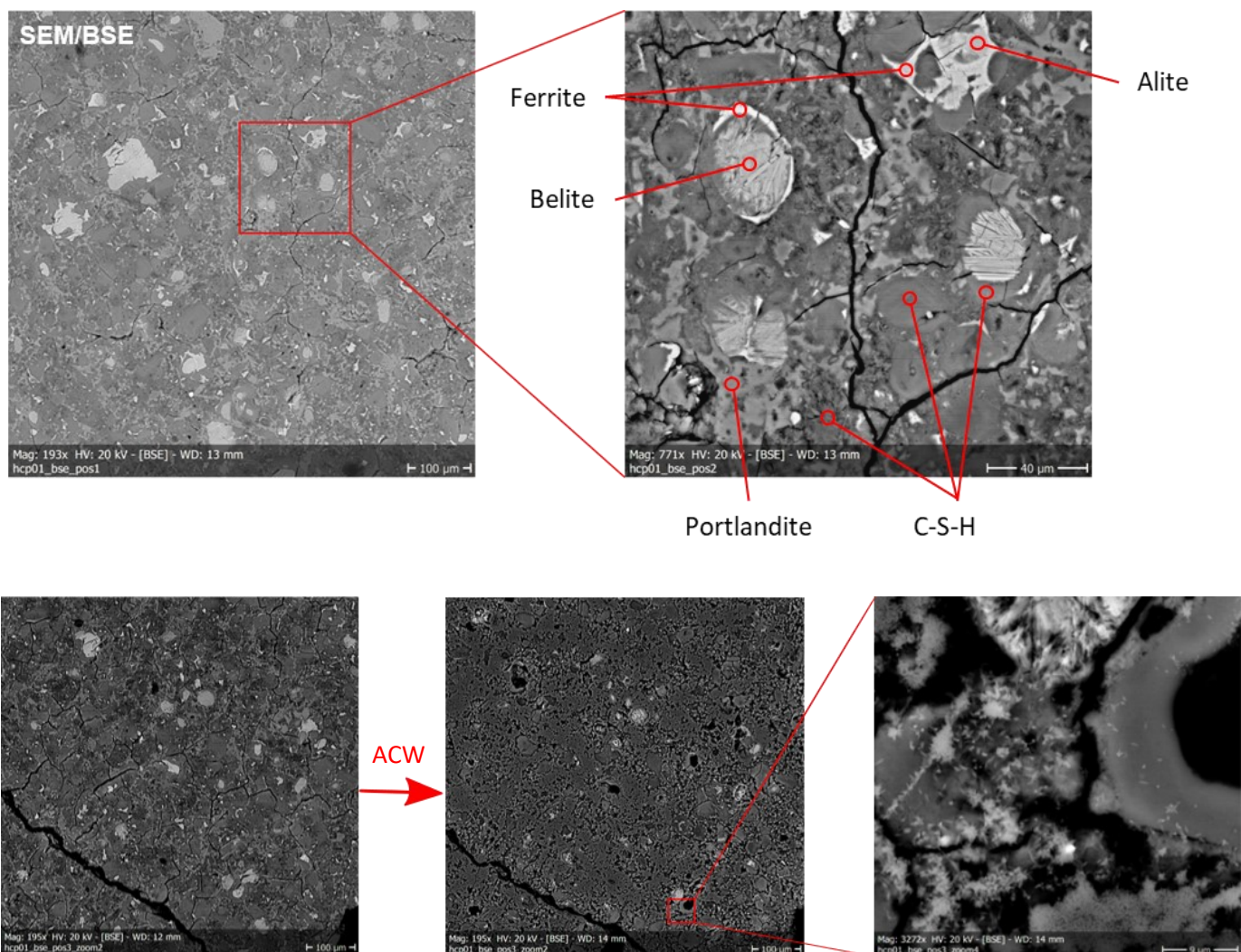


Figure 10: BSE images of a polished HCP section before (top) and after 6 d of contact with ACW (bottom). The different phases in the HCP could be assigned.

C-S-H phases (C/S = 0.8)

XPS measurements

To characterize the C-S-H phases after two weeks of synthesis, XPS measurements were performed. An alternative approach to determine the atomic ratio is by measuring a sample with a known atomic ratio. In this case, a sample of CaSiO₃ (Sigma-Aldrich, USA) was measured, where the C/S ratio is defined as 1. The overview spectrum is presented in Figure A9, and a comparison of identified signals with literature values can be found in Table A11. The overview spectrum of a C-S-H sample (C/S = 0.8) is shown in Figure 11 and the list of the identified signals with comparison to literature values is summarized Table A12.

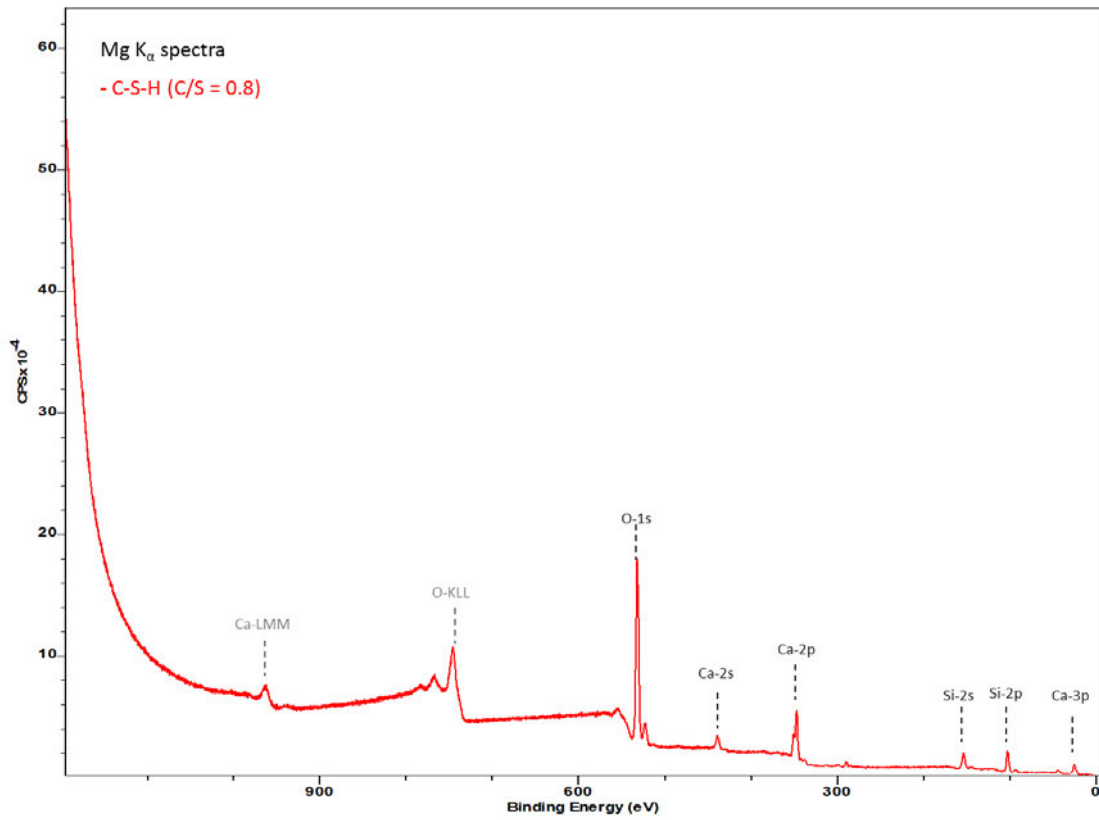


Figure 11: XPS overview spectra of C-S-H phases (C/S = 0.8) measured with Mg K α at an anode excitation energy of 1253.6 eV. The surface charge was corrected with 1.1 eV by normalizing the Ca 2p peak. Ca-LMM and O-KLL denote Auger transitions and can be assigned the signals of the Auger electrons of Ca and O. The other signals were assigned to the photoelectrons from the different layers of the contained elements.

The peak areas of the Ca 2p_{1/2}, Ca 2p_{3/2}, and Si 2p peaks were determined using the fitting parameters described above. By applying equation (13), the sensitivity factor S can be calculated:

$$S = \frac{n_{Ca}}{n_{Si}} \cdot \frac{I_{Si\ 2p}}{I_{Ca\ 2p}} \quad (13)$$

Using the sensitivity factor, the C/S ratio of the C-S-H samples can thus be calculated according to equation (14):

$$\frac{n_{Ca}}{n_{Si}} = S \cdot \frac{I_{Ca\ 2p}}{I_{Si\ 2p}} \quad (14)$$

For this sample, the C/S ratio was determined to be 0.56 [24]. This result indicates a significantly lower C/S ratio than the initial weight ratio, which was also confirmed by pH measurements [25]. The observation of lower C/S ratios is consistent with findings in the literature. Häußler et al. [25] also reported a lower Ca(II) content at the surface compared to the C/S ratio used in C-S-H synthesis, suggesting that the C/S ratio at the surface of C-S-H powders is lower than the bulk C/S ratio of 0.8. Similarly, Tits et al. [26] found a lower C/S ratio through ICP-OES measurements.

In contrast to HCP, no adventitious carbon was observed in the C-S-H phase samples. It appears that C-S-H phases have a low affinity for sorption of adventitious carbon. Additionally, previous observations have shown that (alumo)-silicate surfaces often do not exhibit a C 1s signal from adventitious carbon.

3.2. Binary system

3.2.1. Batch sorption experiments

The uptake of EDTA on HCP and C-S-H phases (C/S = 0.8) was studied using ^{14}C -labelled EDTA as a tracer solution in two types of batch sorption experiments: as a sorption isotherm of EDTA ($[\text{EDTA}]_0/M = 1 \times 10^{-9} - 1 \times 10^{-1}$; S/L = 5 g L $^{-1}$) and as a function of S/L ratio (S/L = 0.5 – 50 g L $^{-1}$; $[\text{EDTA}]_0/M = 1 \times 10^{-2}$) within a contact time of 72 h.

HCP / EDTA

The results of the sorption isotherm in terms of $[\text{EDTA}]_{\text{sorbed}}$, calculated using equation (2) as a function of the equilibrium concentrations of EDTA, is shown in Figure 12A. A $\log R_d$ value of 0.86 ± 0.12 ($R_d = 7.24 \pm 1.32 \text{ L kg}^{-1}$) was determined using a linear fit with a slope of one. This value is slightly lower than the R_d value reported in the literature of $11 \pm 6 \text{ mL g}^{-1}$ (pH > 13, S/L = 1-7 g L $^{-1}$) [27]. Figure 12B shows the quantified $[\text{EDTA}]_{\text{eq}}$ concentrations within the series of experiment with $[\text{EDTA}]_0 = 1.0 \times 10^{-2} \text{ M}$ as a function of S/L ratios ranging from 0.5 - 20 g L $^{-1}$. $[\text{EDTA}]_{\text{calc}}$, calculated using the R_d value determined in Figure 12A, is shown as a function of different S/L ratios.

The concentrations of EDTA determined and calculated agree within the error bars, except for the values at 20 g L $^{-1}$, where a slightly higher concentration was obtained compared to the calculated concentration. The calculated data exhibit a decrease in concentration, reaching $[\text{EDTA}]_{\text{calc}} = 9 \times 10^{-3} \text{ M}$ at an S/L ratio

of 20 g L^{-1} , with $[\text{EDTA}]_{\text{eq}}$ at 20 g L^{-1} being in the range of $[\text{EDTA}]_0$. The results indicate a very low uptake ($S_{\%} \leq 7\%$) of EDTA on HCP in both batch sorption experiments, suggesting that there is no significant blocking of sorption sites by EDTA on HCP. This behavior distinguishes EDTA from GLU, which exhibits strong sorption on HCP. The speciation calculations (refer to Chapter 1.5) reveals that at alkaline pH values, EDTA exists as the deprotonated species EDTA^{4-} or as complex $\text{Na}(\text{EDTA})^{3-}$, $\text{K}(\text{EDTA})^{3-}$ and $\text{Ca}(\text{EDTA})^{2-}$, all of which carry a negative charge. Steric effects could be a possible explanation for the absence of EDTA sorption on HCP. Alternatively, Ca(II) could be leached out from the interlayer through complexation with EDTA, as supported by the semiquantitative analysis mode of the ICP-MS of the C-S-H phases (refer to Chapter 2.2.3.1). Increased Ca(II) ($[\text{Ca}(\text{II})]_0/M = 4 \times 10^{-3}$) concentration was observed in the presence of EDTA. The dissolution of Ca(II) may reduce the C/S ratio, resulting in a neutral or negatively charged surface ($C/S < 1.3$ [28,29]), thereby repelling the remaining negatively charged EDTA species and minimizing the uptake.

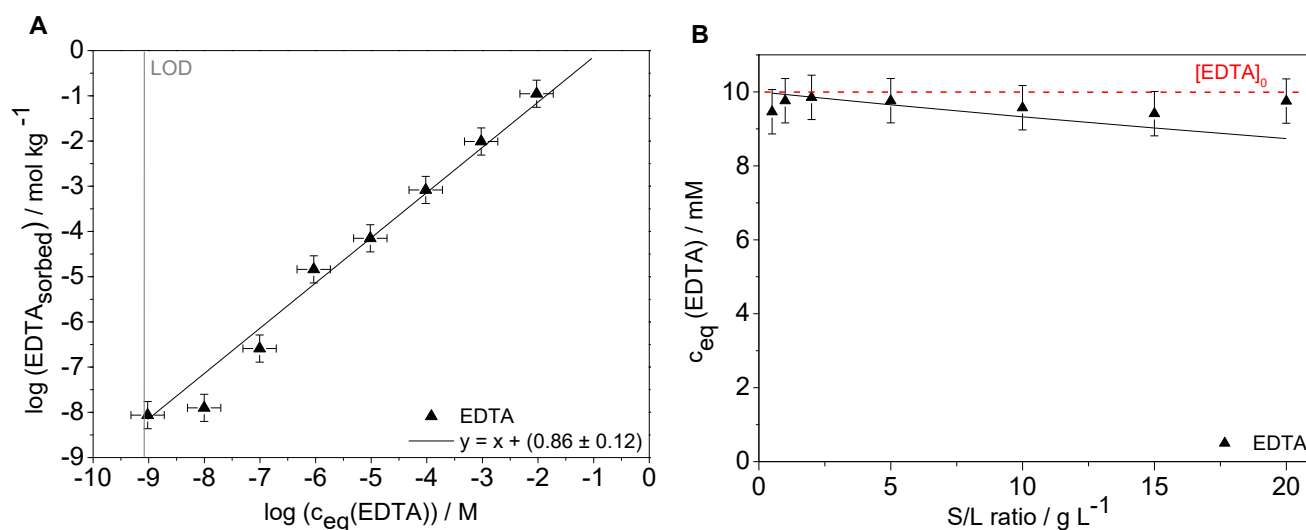


Figure 12: A) Sorption isotherm of the binary system HCP / EDTA with initial EDTA concentrations from $1 \times 10^{-9} \text{ M}$ to $1 \times 10^{-1} \text{ M}$ ($\text{pH} > 13$) and a constant S/L ratio of 5 g/L after a contact time of 72 h. The black line is the linear fit of the data with a slope of one, and the grey line represents the LOD. B) Batch sorption experiments at constant EDTA concentration of $[\text{EDTA}]_0/M = 1 \times 10^{-2}$ (red line) with varying S/L ratios of $0.5 - 20 \text{ g L}^{-1}$ within a contact time of 72 h ($\text{pH} > 13$), while the black line represents the calculated concentration $[\text{EDTA}]_{\text{calc}}$ using the R_d value from the fit in (A).

C-S-H / EDTA

Analogous experiments and analysis were performed with C-S-H phases with a C/S ratio of 0.8 (pH = 9.8), as presented in Figure 13. The sorption isotherm data in Figure 13A were fitted using a linear fit with a slope of 1, yielding a $\log R_d$ value of 0.76 ± 0.19 ($R_d = 5.75 \pm 1.55 \text{ L kg}^{-1}$). The sample with an EDTA concentration of $1.0 \times 10^{-9} \text{ M}$ had an activity below the LOD, thus it was excluded from the calculations and not shown in Figure 13A. Figure 13B shows the equilibrium concentration $[\text{EDTA}]_{\text{eq}}$ plotted against the S/L ratio. Interestingly, no sorption of EDTA on C-S-H phases at a C/S ratio of 0.8 was observed, as the measured concentrations is within the range of the initial concentration $[\text{EDTA}]_0$. The calculated concentrations $[\text{EDTA}]_{\text{calc}}$, based on the determined R_d value, decreased with increasing S/L ratio, and did not align with the measured concentrations $[\text{EDTA}]_{\text{eq}}$. Further experiments are necessary to confirm these results or whether it is may a preparation error. This would help clarify the discrepancy between the calculated concentrations $[\text{EDTA}]_{\text{calc}}$ and the measured concentrations $[\text{EDTA}]_{\text{eq}}$. The literature suggests that EDTA does not adsorb on C-S-H phases under their experimental conditions ($\text{S/L} = 1 \text{ g L}^{-1}$, $\text{C/S} = 0.6 - 1.3$, 1 M NaCl or 0.1 M CaCl_2). They further report that the surface is negatively charged for $\text{C/S} < 1.3$ and therefore the negatively charged species of EDTA in the alkaline pH range are repelled from the surface [29]. This observation aligns with the experimental findings and speciation calculations. Similarly, in the binary system of GLU / C-S-H, low sorption on C-S-H phases was observed under similar experimental conditions [24].

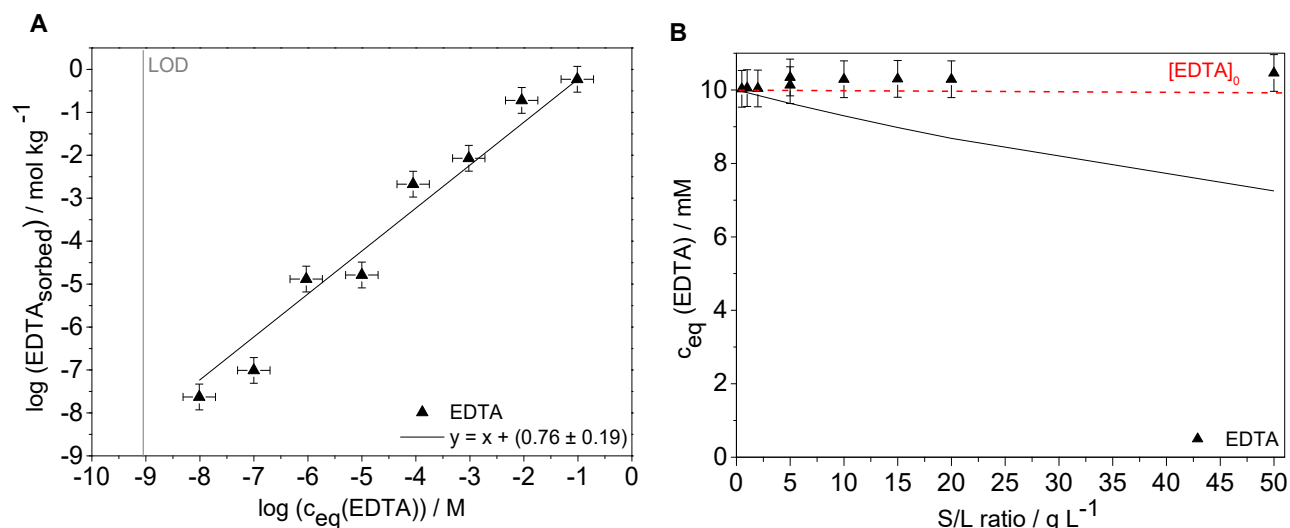


Figure 13: A) Sorption isotherm of the binary system C-S-H / EDTA with initial EDTA concentrations from $1 \times 10^{-9} \text{ M}$ to $1 \times 10^{-1} \text{ M}$ (pH = 9.8) and a constant S/L ratio of 5 g/L ($\text{C/S} = 0.8$) after a contact time of 72 h. The black line is the linear fit of the data with a slope of one, and the grey line represents the LOD. B) Batch sorption experiments at constant EDTA concentration of $[\text{EDTA}]_0 / \text{M} = 1 \times 10^{-2}$ (red line) with varying S/L ratios of $0.5 - 20 \text{ g L}^{-1}$ ($\text{C/S} = 0.8$) within a contact time of 72 h (pH = 9.8).

3.2.2. XPS measurements

In addition to the investigation of the liquid phase, XPS measurements were performed on HCP and C-S-H samples in the binary system to analyze the surface in the presence of EDTA. Figure 14 shows the Al K_{α} spectrum of HCP in ACW (green) and HCP / EDTA in ACW (red) after a contact time of 72 h. Both spectra exhibit signals of calcium, oxygen, silicon, and potassium. A signal for C 1s, potentially originating from adventitious carbon, is also observed. The magnification of this area $E_b = 320\text{-}200\text{ keV}$ with the fitted peaks is shown in the Appendix. Since the samples were not freshly mortared prior to measurement and accordingly prepared and stored in air, adventitious carbon could accumulate on the sample with time, which has already been discussed. However, no nitrogen signal characteristic of EDTA is detected, which was observed in the measurement of $\text{Na}_4(\text{EDTA}) \times 2 \text{H}_2\text{O}$. While no definitive conclusion can be drawn from this measurement, the absence of a nitrogen signal supports the results of liquid phase, indicating that no EDTA sorbs on the surface of HCP. It is worth noting that the presence of adventitious carbon and the accumulation of potassium signal from ACW drying on the HCP surface should be considered.

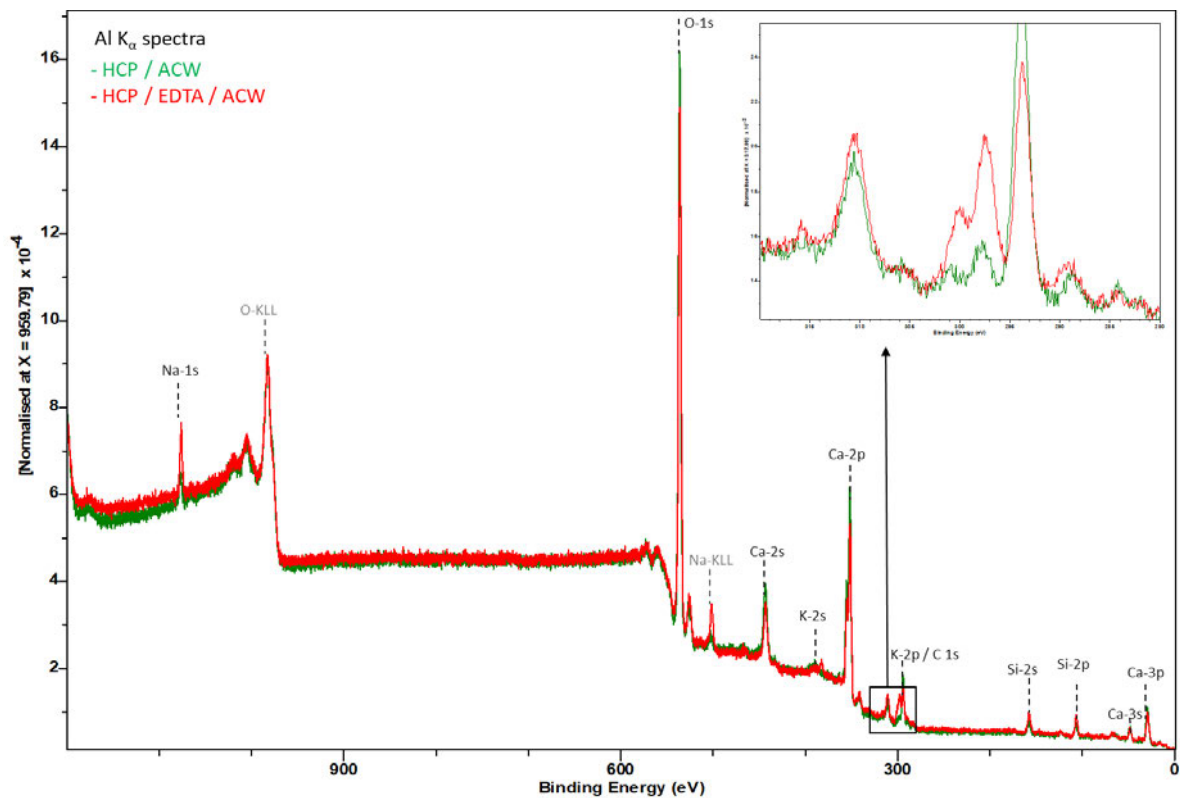


Figure 14: XPS overview spectra of HCP (w/c 0.5) in ACW (green) and HCP in presence of EDTA in ACW (red) after a contact time of 72 h measured with Al K_{α} at an anode excitation energy of 1486.6 eV after surface admittance correction of 4.2 eV (Ca 2p signal). The magnification shows the range of 320-200 keV. O-KLL and Na-KLL denote Auger transitions and can be assigned the signals of the Auger electrons of O and Na. The other signals were assigned to the photoelectrons of the contained elements.

Table A25 shows the assigned peaks with literature comparison [18]. The experimentally determined binding energies are in good agreement with the literature values. According to equation (12), the C/S ratio can be determined from the peak areas obtained. It was determined to be 1.6, which is slightly lower than the value of 1.8 given in the literature for fresh cement [30].

The XPS spectra of the solid phase of C-S-H phases ($C/S = 0.8$) in the presence (red) and absence (green) of EDTA are shown in Figure 15. The magnification of the area from 340-220 eV reveals no C 1s signal for the C-S-H / EDTA sample. This suggests that EDTA sorption on the C-S-H phase is unlikely under the experimental conditions, and the results from the solid phases support the findings from the liquid phase experiments described earlier. Additionally, the low affinity of the C-S-H phases for adventitious carbon is evident, considering the samples were stored in air. The elements (Ca, Si, O) in the C-S-H phases were clearly identified, and Table A26 presents the assigned peaks along with literature comparisons, which are in good agreement with literature values [18]. The calculation of the C/S ratio using the sensitivity factor according to equation (14) yields a value of $C/S = 0.54$. A similar value of 0.57 was reported in the literature by Dettmann et al. [24] in the presence of GLU.

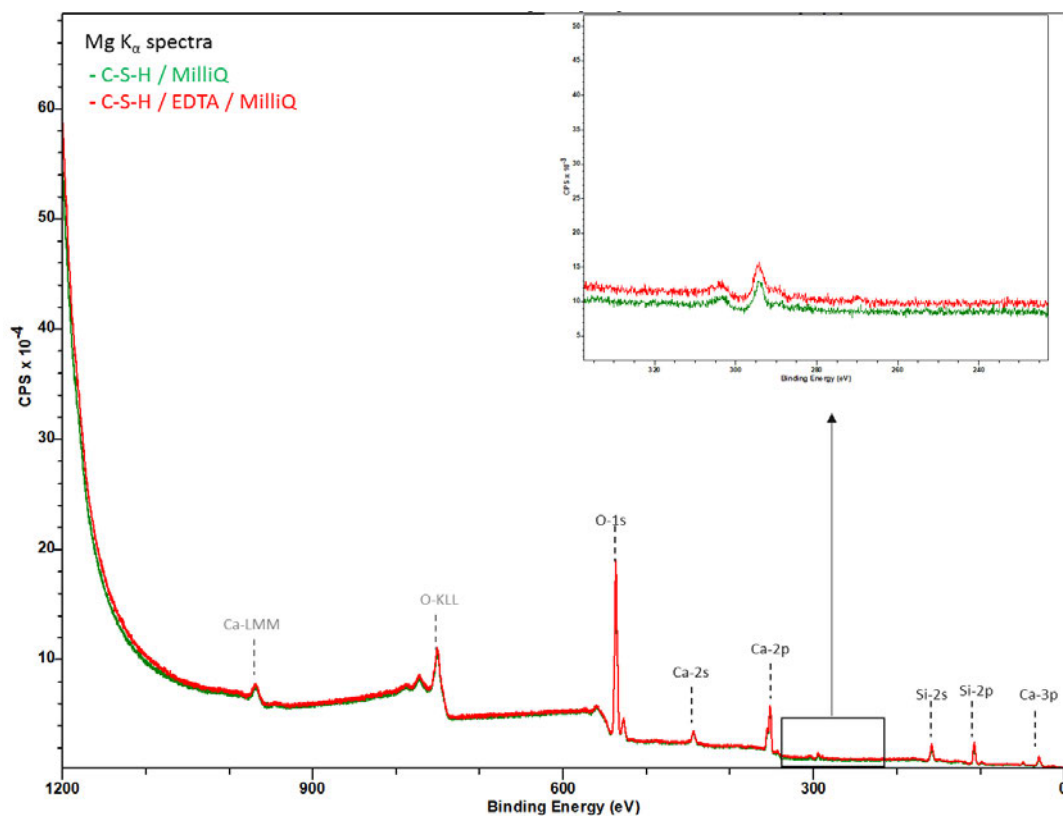


Figure 15: XPS overview spectra of C-S-H phases ($C/S = 0.8$) in Milli-Q in absence and presence of EDTA after a contact time of 72 h measured with Mg K_{α} at an anode excitation energy of 1253.6 eV. The surface charge was corrected by normalizing the Ca 2p peak ($\Delta E_b = + 1.2$ eV). The magnification shows the range of 340-220 keV. Ca-LMM and O-KLL denote Auger transitions and can be assigned the signals of the Auger electrons of Ca and O. The other signals were assigned to the photoelectrons of the contained elements.

3.3. Ternary system

The influence of EDTA on the sorption of An(III/IV) on HCP was investigated by batch sorption experiments ($[An]_0/M = 1 \times 10^{-8}$; $[EDTA]_0/M = 1 \times 10^{-2}$; $pH > 13$; $S/L = 5 \text{ g L}^{-1}$) considering different addition orders: (i) (HCP+An(X)) + EDTA, (ii) (HCP+EDTA) + An(X), and (iii) (HCP+An(X)+EDTA). Figure 16 shows the calculated R_d values for Am(III), Th(IV) and Pu(IV) uptake on HCP, obtained from an average of double determinations in the presence and absence of EDTA after 72 h of contact time. These values show a quantitative uptake and are in the range of $10^4 - 10^6 \text{ L kg}^{-1}$. For the experiments values of $R_{d,max}$ ($R_{d,max}(Th(IV)) = 1.65 \times 10^5 \text{ L kg}^{-1}$, $R_{d,max}(Pu(IV)) = 4.51 \times 10^5 \text{ L kg}^{-1}$, $R_{d,max}(Am(III)) = 2.82 \times 10^6 \text{ L kg}^{-1}$) were calculated as described in Tits et al. [31].

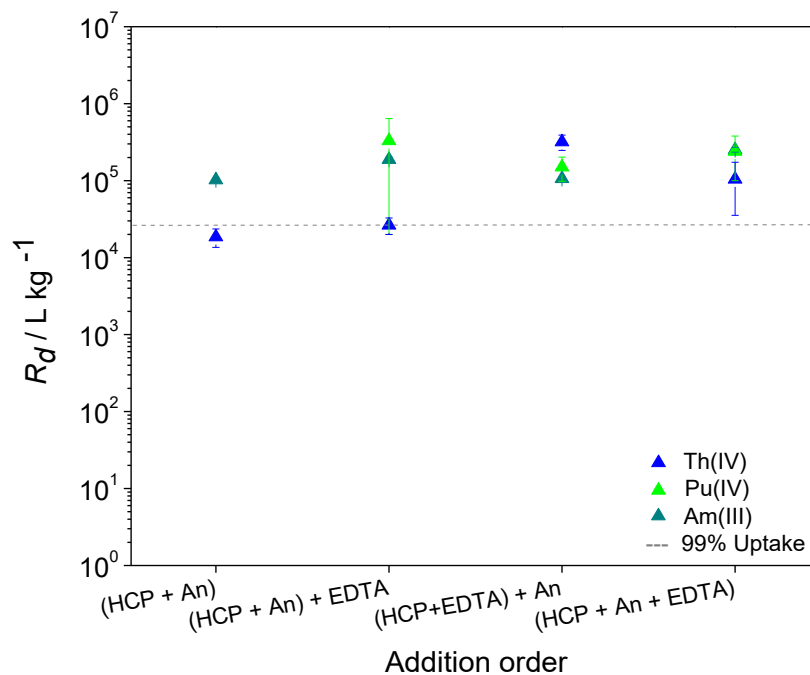


Figure 16: Average value from a double determination of the distribution coefficients R_d (L kg^{-1}) determined for Am(III), Th(IV) and Pu(IV) uptake on HCP in presence and absence of EDTA ($[An(X)]_0/M = 1 \times 10^{-8}$, $[EDTA]_0/M = 1 \times 10^{-2}$, $S/L = 5 \text{ g L}^{-1}$, $pH > 13$) after a contact time of 72 h. The dashed line represents an uptake of 99%.

Thus, the determined uptake values for Th(IV), Pu(IV) and Am(III) on HCP, in the presence of EDTA, are consistent with literature reports by Tits et al. [30] and Ochs et al. [32] in the absence of EDTA. The quantitative uptake of An(III/IV) on HCP observed in this study suggests that the order of reactant addition and the presence of EDTA did not influence the retention of An(III/IV) by HCP after 72 h of contact time. Speciation calculations (discussed in 1.5), indicate the presence of negatively charged $Am(EDTA)^-$ complexes in solution alongside $Am(OH)_3$, which may sorb quantitatively onto the HCP

surface. The speciation calculation (Chapter 1.5) demonstrate the complexation behavior of EDTA with Th(IV). The dominant species for Th(IV) in the alkaline pH range is $\text{Th}(\text{OH})_4(\text{EDTA})^-$. However, at pH levels above 10, $\text{Th}(\text{OH})_4$ becomes the predominant species, and EDTA no longer forms a complex with Th(IV). Xia et al. [33] have observed a linear decrease in Th concentrations with increasing pH beyond pH 9, which is not accurately predicted by current thermodynamic models. The results in that study indicate that monomeric mixed Th-OH-EDTA complexes prevail under basic conditions. Equilibrium constants were calculated for $\text{Th}(\text{OH})_2\text{EDTA}^{2-}$ ($\log K = 39.5$) and $\text{Th}(\text{OH})_3\text{EDTA}^{3-}$ ($\log K \sim 38.0$) species [33] (see graphic in the Appendix Figure A2). No definitive statement can be made regarding the specific complex present in the solution. For Pu(IV), more conclusive data will be described below. There is no available literature data on the uptake of trivalent and tetravalent An on cementitious materials under the influence of EDTA. In Sebastian Herz's master's thesis, the Th(IV) / HCP / EDTA experiment was conducted under the same experimental conditions. It was also observed that Th(IV) had no effect on the quantitative sorption of Th(IV) to HCP after 72 h of contact time [34].

Ph and Eh measurements of the batch sorption experiment HCP / Pu(IV) / EDTA

The pH and Eh values measured during the batch sorption experiment of HCP / Pu(IV) / EDTA are provided in Table A31. These values are plotted in the Pu predominance diagram shown in Figure 17. Thermodynamic calculations for constructing the diagram were performed using the program PhreePlot, incorporating complexation constants from DiBlasi et al. [4] to the Thermochemie database (11a; 2022) [35]. The measured pH and Eh values are within the predominance region of the quaternary complexes' formation of $\text{CaPu}(\text{OH})_4(\text{EDTA})^{2-}$. This complex could potentially be the prevailing species in solution. If the complexes are strong, they may also be reflected in the surface speciation, suggesting that similar complexes could form at the Ca-complexed surface sites of HCP. However, considering that previous results indicate no sorption of EDTA on HCP, one possibility is that the $\text{CaPu}(\text{OH})_4(\text{EDTA})^{2-}$ complex co-adsorbs EDTA. Drawing a definitive conclusion on the co-adsorption of EDTA during Pu(IV) uptake on HCP and whether the complex sorbs to the HCP surface is not possible without further investigations, such as using ^{14}C -labelled EDTA or examining the solid phase. To verify the formation of a complex with Pu(IV) and EDTA, particularly in the presence of Ca, CE-ICP-MS measurements were conducted and will be discussed below.

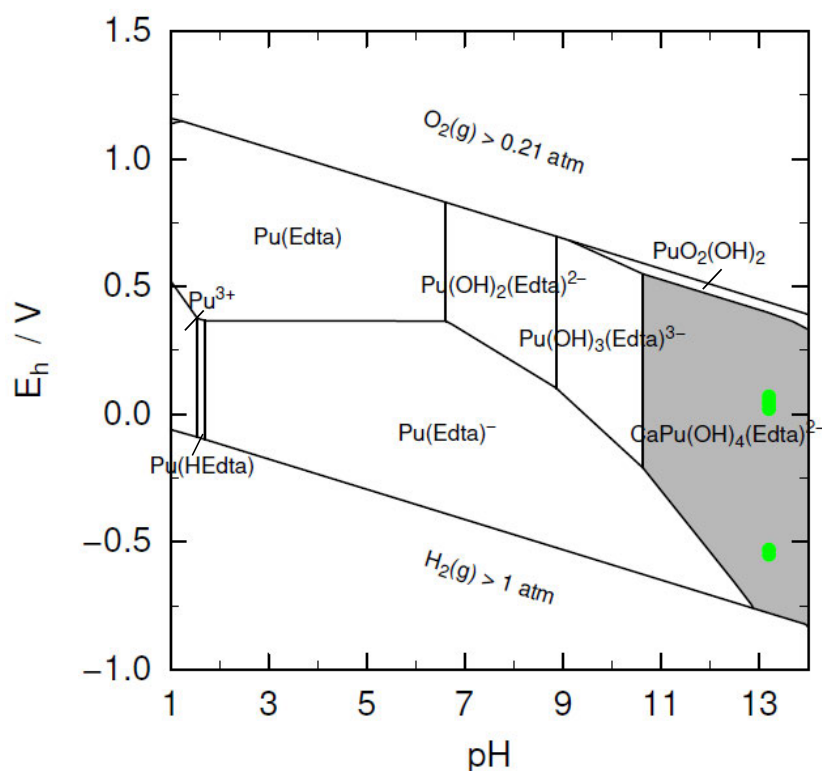


Figure 17: Predominance diagram of Pu calculated for $[Pu(IV)]_0/M = 1 \times 10^{-8}$ and $[EDTA]_0/M = 1 \times 10^{-2}$ M in the system HCP / ACW. The graphic was generated by PhreePlot (version 1.0 [36]) using PHREEQC and the ThermoChimie database 11a, 2022 [35] with complex formation constants determined by DiBlasi et al.[4]. The green dots mark the experimental pH and Eh values of the batch sorption samples for the HCP / Pu(IV) / EDTA experiment.

CE-ICP-MS measurements

The complexation behavior of Th(IV) and Pu(IV) in the presence of EDTA at pH 10 and an ionic strength of 0.1 M was investigated using CE-ICP-MS measurements. The influence of Ca was also examined. Three samples were prepared with 4×10^{-7} M Th(IV) and 1.0×10^{-8} M Pu(IV), respectively. Sample 1 contained only Th(IV) or Pu(IV), while in sample 2 amounts of EDTA ($[EDTA]/M = 1.0 \times 10^{-2}$), and further in sample 3 Ca(II) ($[Ca(II)]/M = 1.0 \times 10^{-2}$) was added. The pH and ionic strength were adjusted using NaOH, HClO₄, and NaClO₄ as needed.

Table 4 summarized the electrophoretic mobilities (μ_{eff}) of Th(IV) and Pu(IV) species and the electropherograms are shown in the Appendix. In the absence of Ca(II) and EDTA, the electrophoretic mobility of Th(IV) was nearly zero ($\mu_{eff} = (-0.03 \pm 0.07) \times 10^{-4}$ cm² (Vs)⁻¹), indicating that Th(IV) species in solution have an average effective charge of zero. This aligns with the expected dominant neutral Th(OH)₄ complex at pH 10 [37]. A similar electrophoretic mobility of Th(IV) was observed in analogues measurements in [24] ($\mu_{eff} = (0.03 \pm 0.03) \times 10^{-4}$ cm² (Vs)⁻¹). Pu(IV) complex was not detected in the solution due to its low solubility at pH 10 (1.0×10^{-11} M). In the presence of EDTA, negative mobilities of $-(3.22 \pm 0.14) \times 10^{-4}$ cm² (Vs)⁻¹ for Th(IV) and $-(3.43 \pm 0.13) \times 10^{-4}$ cm² (Vs)⁻¹ for Pu(IV),

were observed. This change in mobility indicates that An(IV) forms complexes with EDTA leading to a negatively charged species and suggesting the formation of anionic complexes such as $\text{Th}(\text{OH})_3(\text{EDTA})^{3-}$ as previously proposed by Xia et al. [33]. For Pu(IV), Rai et al. [38] described a $\text{Pu}(\text{OH})_2(\text{EDTA})^{2-}$, whereby a $\text{Pu}(\text{OH})_3(\text{EDTA})^{3-}$ complex is also described in the current literature by DiBlasi et al. [4]. The similar mobilities of Th(IV) and Pu(IV) also indicate the formation of similar complexes. In the samples of Th(IV)-GLU with Ca(II), a less negative mobility of $-(2.44 \pm 0.14) \times 10^{-4} \text{ cm}^2 (\text{Vs})^{-1}$ was determined for Th(IV) and $-(2.73 \pm 0.14) \times 10^{-4} \text{ cm}^2 (\text{Vs})^{-1}$ for Pu(IV). This decrease in negative mobility suggests the formation of quaternary complexes. For Th(IV) no complexes with Ca and EDTA could be found in the literature. A $\text{CaPu}(\text{OH})_4(\text{EDTA})^{2-}$ was described by DiBlasi et al. Similar mobilities of Th(IV) and Pu(IV) also occur here, so that the formation of a $\text{CaTh}(\text{OH})_4(\text{EDTA})^{2-}$ complex is possible.

Table 4: The electrophoretic mobilities (μ_{eff}) of Th(IV) ($[\text{Th}(\text{IV})]_0/M = 4 \times 10^{-7}$) and Pu(IV) ($[\text{Pu}(\text{IV})]_0/M = 1 \times 10^{-8} \text{ M}$) were measured in three different conditions: in the absence of EDTA, in the presence of EDTA ($[\text{EDTA}]_0/M = 1 \times 10^{-2}$) and in the presence of Ca(II) ($[\text{Ca}(\text{II})]_0/M = 1 \times 10^{-2}$) at pH 10 and an ionic strength of 0.1 M.

Complex	Th(IV)	Pu(IV)
An(IV)	-0.03 ± 0.07	-
An(IV) + EDTA	-3.22 ± 0.14	-3.43 ± 0.13
An(IV) + EDTA + Ca(II)	-2.44 ± 0.14	-2.73 ± 0.14

4. Summary

The cementitious materials used could be characterized well. The investigations with EDTA on HCP and C-S-H phases demonstrate that there is no sorption of EDTA on the solid phases and therefore no blocking of sorption sites by EDTA. EDTA does not influence the uptake of An(III/IV) on HCP under the experimental conditions (fresh cement, $\text{pH} > 13$) within a contact time of 72 h. The observed trend in electrophoretic mobilities supports the formation of An(IV)-OH-EDTA and Ca-An(IV)-OH-EDTA complex species in solution. In combination with the calculation in the predominance diagram for Pu(IV), a Ca-An(IV)-OH-EDTA complex formation may quantitatively sorb on HCP. Further investigations are necessary in both the solid and the liquid phase in order to be able to make statements about the influence of EDTA on the sorption behavior of actinides on cement.

5. References

1. McFadden, K. *Organic components of nuclear wastes and their potential for altering radionuclide distribution when released to soil*; Battelle Pacific Northwest Labs.: 1980.
2. Rai, D.; Moore, D.; Rosso, K.; Felmy, A.; Bolton, H. Environmental Mobility of Pu(IV) in the Presence of Ethylenediaminetetraacetic Acid: Myth or Reality? *Journal of Solution Chemistry* **2008**, *37*, 957-986.
3. Meyer, M.; Burgat, R.; Faure, S.; Batifol, B.; Hubinois, J.-C.; Chollet, H.; Guillard, R. Thermodynamic studies of actinide complexes. 1. A reappraisal of the solution equilibria between plutonium (IV) and ethylenediaminetetraacetic acid (EDTAH₄) in nitric media. *Comptes Rendus Chimie* **2007**, *10*, 929-947.
4. DiBlasi, N.A.; Tasi, A.G.; Gaona, X.; Fellhauer, D.; Dardenne, K.; Rothe, J.; Reed, D.T.; Hixon, A.E.; Altmaier, M. Impact of Ca(II) on the aqueous speciation, redox behavior, and environmental mobility of Pu(IV) in the presence of EDTA. *Science of The Total Environment* **2021**, *783*, 146993.
5. DiBlasi, N.A.; Tasi, A.; Trumm, M.; Schnurr, A.; Gaona, X.; Fellhauer, D.; Dardenne, K.; Rothe, J.; Reed, D.T.; Hixon, A.E.; et al. Pu(III) and Cm(III) in the presence of EDTA: aqueous speciation, redox behavior, and the impact of Ca(II). *Royal Society of Chemistry* **2022**, *12*, 9478-9493.
6. Prüfverfahren für Zement. Teil 3: Bestimmung der Erstarrungszeiten und der Raumbeständigkeit; Deutsche Fassung EN 196-3:2005+A1:2008 **2009**, DIN EN 196-3.
7. Atkins, M.; Glasser, F.P.; Kindness, A. Cement hydrate phases: solubility at 25°C. *Cement and Concrete Research* **1992**, *22*, 241-246.
8. Wieland, E.; Tits, J.; Ulrich, A.; Bradbury, M.H. Experimental evidence for solubility limitation of the aqueous Ni(II) concentration and isotopic exchange of ⁶³Ni in cementitious systems. *Radiochim. Acta* **2006**, *94*.
9. Cohen, D. The absorption spectra of plutonium in perchloric acid solutions. *J. inorg. nucl. chem.* **1961**, 211-218.
10. SDBS. https://sdb.sdb.aist.go.jp/sdb/cgi-bin/cre_index.cgi. Available online: (accessed on 12.04.2023).
11. Gelius, U.; Heden, P.; Hedman, J.; Lindberg, B.; Manne, R.; Nordberg, R.; Nordling, C.; Siegbahn, K. Molecular spectroscopy by means of ESCA III. Carbon compounds. *Physica Scripta* **1970**, *2*, 70.
12. Chastain, J.; King Jr, R.C. Handbook of X-ray photoelectron spectroscopy. *Perkin-Elmer Corporation* **1992**, *40*, 221.
13. Shirley, D.A. High-resolution X-ray photoemission spectrum of the valence bands of gold. *Physical Review B* **1972**, *5*, 4709.
14. Tasi, A.; Gaona, X.; Fellhauer, D.; Böttle, M.; Rothe, J.; Dardenne, K.; Polly, R.; Grivé, M.; Colàs, E.; Bruno, J.; et al. Thermodynamic description of the plutonium – α -D-isosaccharinic acid system I: Solubility, complexation and redox behavior. *Applied Geochemistry* **2018**, *98*, 247-264.
15. Goudarzi, R. *Prototype Repository – Sensor data report; Period 2001-09-17 to 2022-01-01; Report No 33*; 33; SKB: 2023.
16. Engelhardt, H.; Beck, W.; Kohr, J.; Schmitt, T. *Kapillarelektrophorese: Methoden und Möglichkeiten*; Angewandte Chemie, 1993.
17. Heiger, D. *High Performance Capillary Electrophoresis: A Primer*; Agilent Technologies, 2010.
18. A., T. *X-Ray Data Booklet, Center for X-ray optics advanced light source, X-Ray Data Booklet, second edition*; 2001; Volume LBNL/PUB-490 Rev.2.
19. Carbon | XPS Periodic Table | Thermo Fisher Scientific - DE. Available online: <https://www.thermofisher.com/de/de/home/materials-science/learning-center/periodic-table/non-metal/carbon.html> (accessed on 16.11.2023).
20. DE, C.X.P.T.T.F.S.-. <https://www.thermofisher.com/de/de/home/materials-science/learning-center/periodic-table/non-metal/carbon.html>. Available online: (accessed on 19.04.2023).
21. Reed, S.J.B. *Electron microprobe analysis and scanning electron microscopy in geology*; Cambridge university press: 2005.

22. Goldstein, J.I.; Newbury, D.E.; Michael, J.R.; Ritchie, N.W.; Scott, J.H.J.; Joy, D.C. *Scanning electron microscopy and X-ray microanalysis*; Springer: 2017.
23. Scrivener, K.; Snellings, R.; Lothenbach, B. *A Practical Guide to Microstructural Analysis of Cementitious Materials*; 2015.
24. Dettmann, S.; Huittinen, N.M.; Jahn, N.; Kretzschmar, J.; Kumke, M.U.; Kutyma, T.; Lohmann, J.; Reich, T.; Schmeide, K.; Shams Aldin Azzam, S.; et al. Influence of gluconate on the retention of Eu(III), Am(III), Th(IV), Pu(IV), and U(VI) by CSH (C/S= 0.8). *Front. Nucl. Eng.* **2023**, *2*.
25. Häußler, V.; Amayri, S.; Beck, A.; Platte, T.; Stern, T.A.; Vitova, T.; Reich, T. Uptake of actinides by calcium silicate hydrate (C-S-H) phases. *Appl. Geochem.* **2018**, 426-434.
26. Tits, J.; Wieland, E.; Mueller, C.J.; Landesman, C.; Bradbury, M.H. Strontium binding by calcium silicate hydrates. *J. Colloid Interface Sci.* **2006**, *300*, 78-87.
27. Pointeau, I.; Coreau, N.; Reiller, P. Uptake of anionic radionuclides onto degraded cement pastes and competing effect of organic ligands. *Radiochimica Acta* **2008**, 367.
28. Iwaida, T.; Nagasaki, S.; Tanaka, S. Sorption study of strontium onto hydrated cement phases using a sequential desorption method. *Radiochimica Acta* **2000**, *88*, 483-487.
29. Geckeis, H.; Altmaier, M.; Fanghaenel, S. *Annual Report 2020/21-Institute for Nuclear Waste Disposal*; INE: Karlsruher Institut für Technologie (KIT), 2022.
30. Kaden, M.; Degering, D. *JAHRESBERICHT STRAHLENSCHUTZ 2019*; Bericht Nr. 18-2; VKTA - Strahlenschutz, Analytik & Entsorgung Rossendorf e. V. Helmholtz-Zentrums Dresden - Rossendorf e. V: 2020.
31. Tits, J.; Wieland, E.; Bradbury, M.H.; Eckert, P.; Schaible, A. *The uptake of Eu(III) and Th(IV) by calcite under hyperalkaline conditions*; 1019-0643; Laboratory for Waste Management (LES): 2002; pp. i-xii, 1-78, A71-A14.
32. Ochs, M.; Mallants, D.; Wang, L. *Radionuclide and Metal Sorption on Cement and Concrete*; Springer: 2016.
33. Xia, Y.X.; Felmy, A.; Rao, L.; Wang, Z.; Hess, N. Thermodynamic model for the solubility of ThO₂(am) in the aqueous Na⁺-H⁺-OH⁻-NO₃⁻-H₂O-EDTA system. *Radiochimica Acta* **2003**, *91*, 751-760.
34. Herz, S.C. Rückhaltung von Th(IV) an Zementstein in Gegenwart von EDTA bei hohen pH-Werten. Masterarbeit, Johannes Gutenberg-Universität Mainz, Mainz, 2020.
35. Giffaut, E.; Grivé, M.; Blanc, P.; Vieillard, P.; Colàs, E.; Gailhanou, H.; Gaboreau, S.; Marty, N.; Madé, B.; Duro, L. Andra thermodynamic database for performance assessment: ThermoChimie. *Appl. Geochem.* **2014**, *49*, 225-236.
36. Parkhurst, D.; Appelo, C.; 3.3.5), C.A.J.P.V. A Computer Program for Speciation, Batch-Reaction, One-Dimensional Transport, and Inverse Geochemical Calculations. Available online: http://wwwbrr.cr.usgs.gov/projects/GWC_coupled/phreeqc/index.html (accessed on 15 June 2023).
37. Rand, M.; Fuger, J.; Grenthe, I.; Neck, V.; Rai, D. Chemical thermodynamics 11: Chemical thermodynamics of Thorium. Amsterdam, The Netherlands: NEA North Holland Elsevier Science Publishers B. V. **2009**.
38. Rai, D.; Kitamura, A. Thermodynamic equilibrium constants for important isosaccharinate reactions: A review. *The Journal of Chemical Thermodynamics* **2017**, *114*, 135-143.

2.4 Manuscript: Sorption and diffusion experiments with HCP under the influence of ISA

Author Contribution

The batch sorption experiments are part of the bachelor thesis of [REDACTED] [136] and the master thesis of [REDACTED] [137]. The investigations were carried out under the supervision of J. Stietz and [REDACTED]. Sample preparation and measurements were performed by [REDACTED] and J. Stietz. J. Stietz carried out the CE-ICP-MS measurements with [REDACTED] and the XPS measurements with [REDACTED]. Diffusion experiments were performed by J. Stietz, as was the evaluation of the HTO through-diffusion. The HCP / Pu(IV) diffusion experiment was modeled by [REDACTED]. The visualization and the manuscript were conducted by J. Stietz. It refers to Chapters from this work (especially the introduction) to avoid repetition.

Summary

The presence of ISA has a notable effect on the sorption mechanisms of Th(IV) and Pu(IV) onto HCP at $\text{pH} > 13$, resulting in lower uptake of these elements. One reason for this could be that ISA has a strong affinity for sorption onto HCP. Despite a slight leaching effect observed for Th from HCP in the presence of ISA, this effect remains relatively insignificant compared to the high sorption affinity of ISA itself. The results of the batch sorption experiments indicate a competitive interaction between An(IV) and ISA, possibly leading to desorption or the formation of complex species such as $\text{Th}(\text{OH})_4(\text{ISA})_2^{2-}$ and $\text{Pu}(\text{OH})_5(\text{ISA})_2^{2-}$. The observed results are consistent with the values published in the literature. Furthermore, the study demonstrated the formation of An(IV)-OH-ISA and Ca(II)-An(IV)-OH-ISA complexes, which could underline the complexation behavior in this particular system. However, the main focus is on the diffusion experiments with Pu(IV), which were carried out under similar experimental conditions and also show that Pu(IV) penetrates significantly deeper into an HCP core in the presence of ISA.

Sorption and diffusion experiments with HCP under the influence of ISA

Janina Stietz ^{1*}, [REDACTED] ^{1*}

¹Johannes Gutenberg-Universität Mainz, Department of Chemistry, Mainz, Germany

²Paul Scherrer Institut, Villingen, Switzerland

*Correspondence:

Janina Stietz: jastietz@uni-mainz.de

[REDACTED]

1. Introduction

Due to its high sorption capacity, cement is well suited as an engineered barrier for radioactive waste repositories [1,2]. The migration behavior of radionuclides is of crucial importance and is often evaluated by parameters such as the distribution coefficient (K_d), which is essential for understanding radionuclide movement in cement. It is assumed that diffusion is an important process for radionuclide transport. However, accurate simulation of this migration behavior requires difficult control of chemical parameters such as pH, Eh and ion composition, especially in diffusion experiments with porous material. In previous studies, it was difficult to reconcile K_d values from batch experiments with those from diffusion experiments in, e.g. clay rock [3].

Plutonium has a very high radiotoxicity and a long half-life [4]. Understanding its migration behavior, especially in the predominant oxidation state (IV) at high pH values due to reducing conditions, is crucial for the disposal of radioactive waste [5,6]. While the current literature mainly contains sorption experiments of Pu, there are no studies on the diffusion behavior in cementitious materials. Isosaccharinic acid (ISA), a polyhydroxycarboxylic acid, is the primary degradation product of cellulose when exposed to Ca-rich hyperalkaline solutions in cementitious systems. The concentration of free ISA in the pore water of these systems is strongly influenced by the initial amount of cellulose and the sorption of the ISA ligand onto cement phases. This sorption process is significantly influenced by various factors such as pH, calcium concentration ($[Ca]$), solid-liquid ratio (S/L), average surface charge and coverage [7-9]. Studies have shown that ISA tends to form stable complexes with the elements An(III)/Ln(III) and An(IV) under hyperalkaline conditions [9-12].

The main objective of this study was to investigate the sorption and diffusion behavior of Pu(IV) in HCP in presence and absence of ISA. In order to verify the reliability of the diffusion techniques and to determine the properties of Hardened Cement Paste (HCP), a two-step experimental approach was chosen, including various diffusion experiments with different radionuclides such as tritiated water (HTO) and Pu(IV). The K_d value for the sorption of Pu(IV) on HCP in presence and absence of ISA derived from both batch experiments and in-diffusion experiments, while maintaining experimental conditions.

2. Experimental description and characterization of the initial conditions

The experimental conditions and the characterization of the starting materials as well as the framework conditions for carrying out the batch sorption experiments (HCP , $\text{S/L} = 0.1 - 50 \text{ g L}^{-1}$, $([\text{An(IV)}]/\text{M}) = 1.0 \times 10^{-6} - 1.0 \times 10^{-13}$, $[\text{ISA}]_0/\text{M} = 3.0 \times 10^{-4} - 1.0 \times 10^{-2}$) are described analogously to the methods described in chapter 2.3 (Manuscript EDTA). The diffusion experiments are described in more detail below.

2.1. Stock solutions

Synthesis and characterization of ISA

ISA was synthesized specifically as part of this work. The synthesis of NaISA involved a two-step process starting from lactose. In the second step, CaISA was converted into the Na form using a cation exchange resin. This step was necessary because CaISA has low solubility in water (1.2 g L^{-1}) and is therefore unsuitable for the experiments. These synthesis steps are shown in Figure 1.

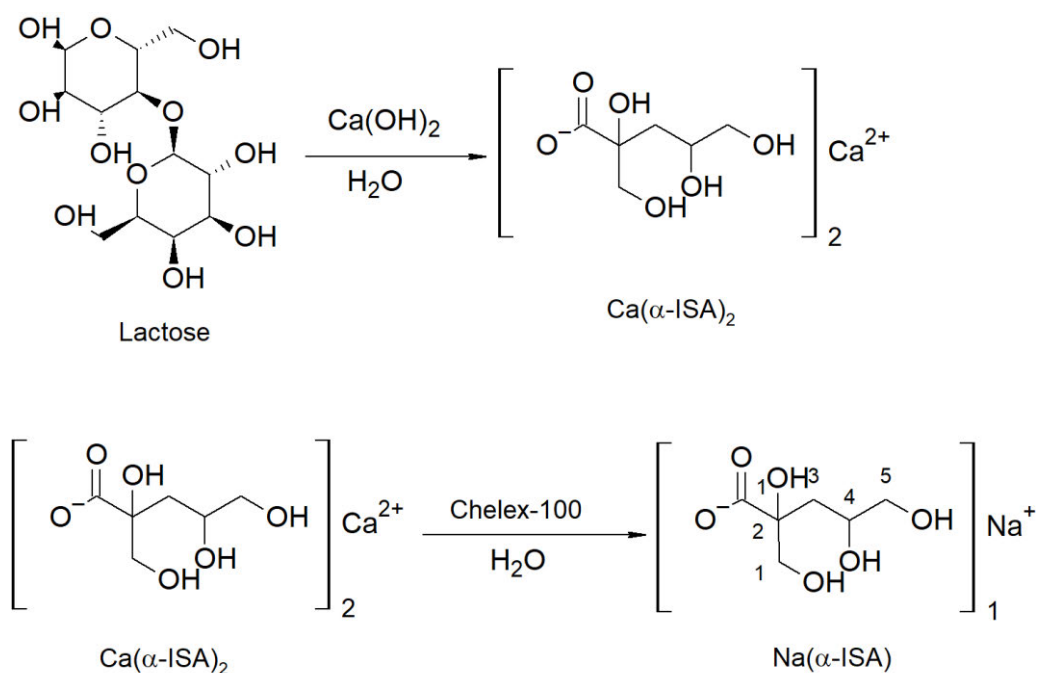


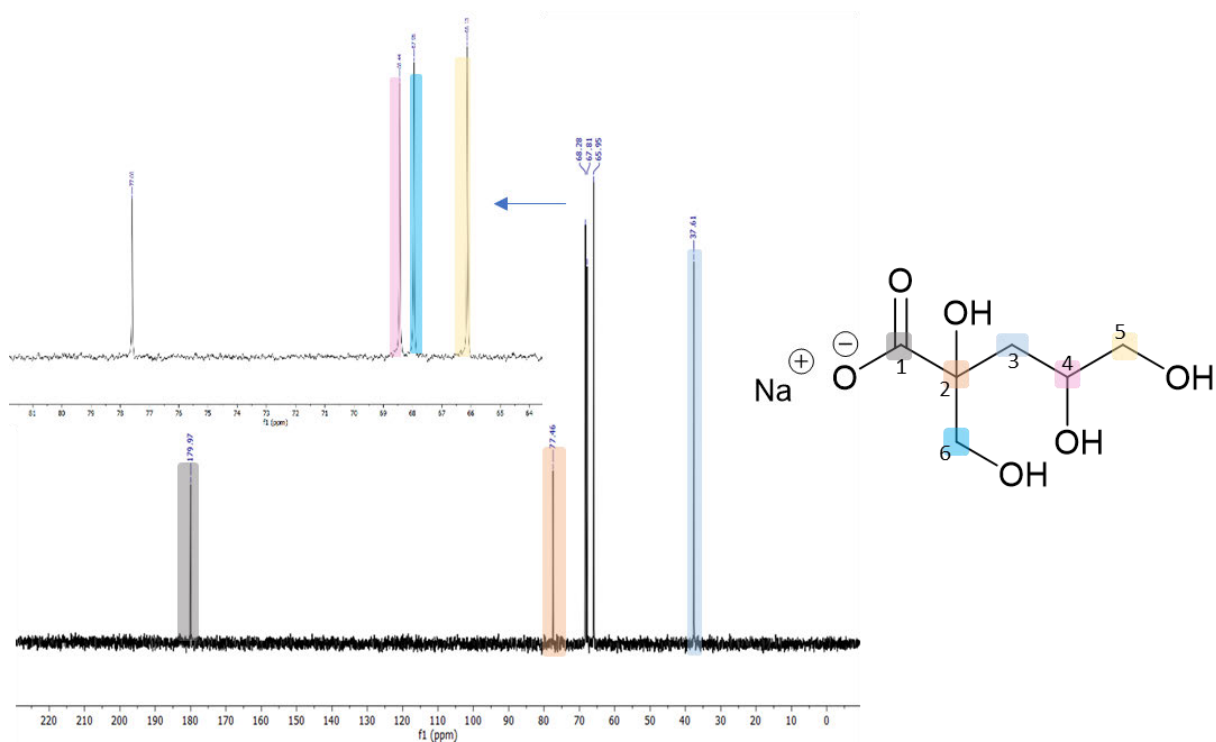
Figure 1: Synthesis steps of Na(α -ISA) starting from lactose monohydrate and with Ca(α -ISA) as intermediate.

The synthetic route was based on the findings of Whistler and BeMiller [13]. Lactose monohydrate (VWR International GmbH, Germany; 101.2 g, 0.28 mol, 1 eq.) and Ca(OH)_2 (VWR International GmbH, Germany; 27.0 g, 0.36 mol, 1.3 eq.) were suspended with Ar decarbonized Milli-Q water (220 mL) and sealed. The mixture was allowed to stand for 3 d. The suspension was then boiled under

reflux for 6 h, followed by hot filtration. The resulting solution was evaporated to approximately 10% of its initial volume and stored overnight at 4 °C. The precipitate was aspirated, washed with ethanol (Merck, Germany), and dried in a drying oven at 60 °C for 3 d. To further purify the solid, recrystallization was carried out in hot Milli-Q water (1.2 g / 100 mL). The resulting colorless precipitate was aspirated and dried again in a drying oven at 60 °C for 3 d. The colorless solid (yield: 15.9 g) was characterized by mass spectrometry. The experimental value obtained from the mass spectrometry (6545 QTOF-MS, ESI-Tof, Agilent Technologies, USA) was 399.08 g mol⁻¹, which matched the literature value of 399.00 g mol⁻¹ ([CaC₁₂H₂₃O₁₂]⁺) [14]. This confirmed that the colorless solid was CaISA and could be further converted to the Na form. In this synthesis step, a cation exchange resin, BioRad Chelex 100 Resin® (100-200 mesh, (BioRad Chelex 100 Resin®, USA), was used [15]. Ca(ISA)₂ (8.2 g) was suspended with the Na resin (200 g) in Ar decarbonized Milli-Q water (400 mL) and stirred for 3 h. The solution changed from milky to brown and clear. The resin was filtered through a glass frit, and the supernatant was slowly evaporated. The resulting viscous liquid was dried in a drying oven at 60 °C for 3 d to complete crystallization. Mass spectrometry showed an experimental value of 180.81 g mol⁻¹, matching with the literature value of 179.06 g mol⁻¹ ([C₆H₁₁O₆+H]⁺) [14]. To confirm that it was not the lactoform of ISA, the pH of a 0.06 M NaISA solution in Milli-Q water was measured, resulting in a pH of 10.1. The lactoform would lead to an acidic pH value.

NMR measurement

For further characterization of the obtained Na(ISA) diluted in Milli-Q water, NMR spectroscopy was performed. Figure 2 shows the ¹³C-NMR of NaISA with assignment of the signals, and the ¹H spectrum can be found in Figure A6. The shifts determined from the NMR spectra are consistent with the literature [16]. The stock solution of Na(ISA) in ACW at pH > 13, which was used for the experiments, was also analyzed by NMR spectroscopy. No significant changes in the signals of ISA were observed, indicating that the high pH had no effect on the compound. A comparison of both spectra can be found in Figure A6 and Figure A7.



^{13}C -NMR (100,6 MHz, D_2O , HMBC, HSQC, 3): δ (ppm): 37.61 (s, C_3), 65.96 (s, C_5), 67.813 (s, C_6), 68.28 (s, C_4), 77.46 (s, C_2), 179.97 (s, C_1)

Figure 2: ^{13}C -NMR spectrum of NaISA in Milli-Q ($\text{pH} = 10.1$) with D_2O , and assignment of signals based on structural formula.

XPS measurement

In addition, XPS measurements were performed to characterize the self-synthesized NaISA. Spectra of CaISA (Sigma Aldrich, USA) and NaISA were recorded for this purpose. The overview spectra of both salts can be seen in Figure 3. The peaks were compared with literature data [16], and the table containing the values can be found in Table A7 and A8. The experimentally determined binding energies of the peaks in both spectra show good agreement with the literature values, confirming the successful synthesis of NaISA.

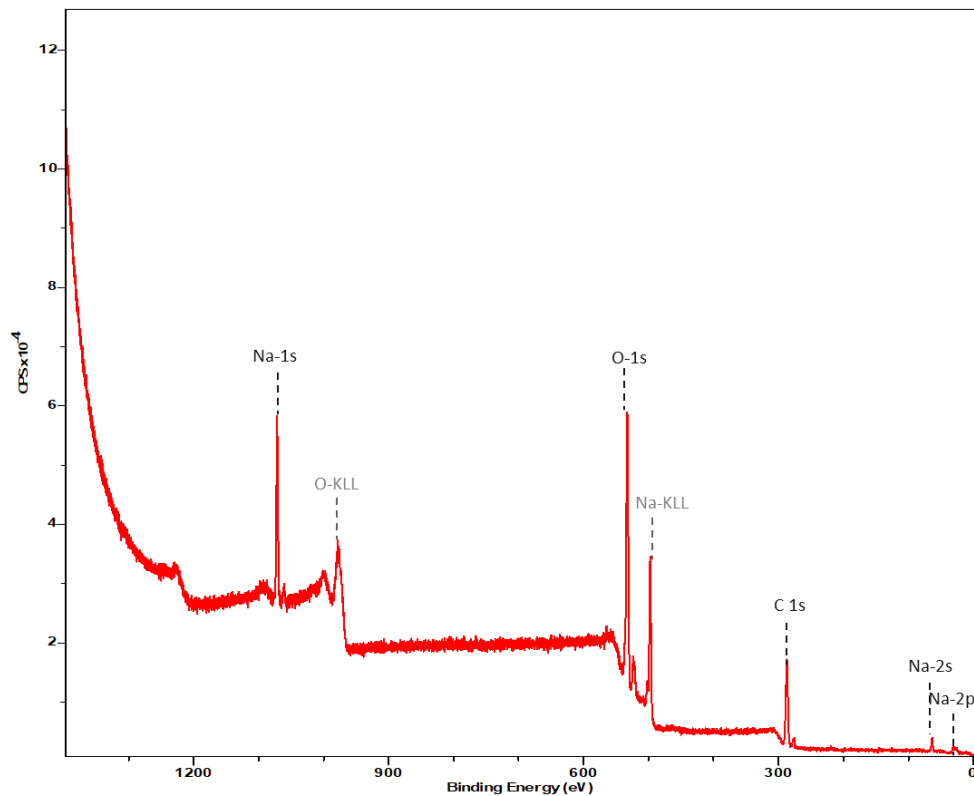
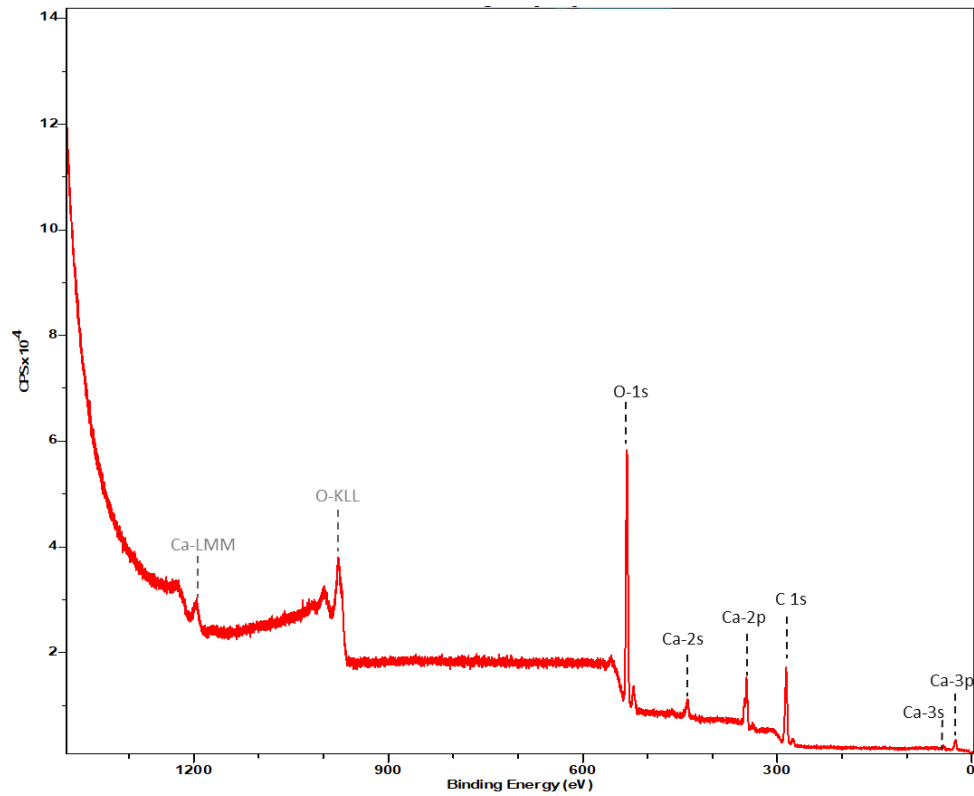


Figure 3: XPS overview spectra of CaISA (top) and NaISA (bottom) with Al K_{α} at an anode excitation energy of 1486.6 eV. Surface admittance correction of 2.7 eV (corrected to Ca 2p for the CaISA spectra) and 2.0 eV (corrected to Na 1s for the NaISA spectra) was applied. O-KLL and Na-KLL denote Auger transitions and can be assigned the signals of the Auger electrons of O and Na. The other signals were assigned to the photoelectrons of the contained elements.

The chemical environment of the individual carbon atoms was compared using the additive scheme [17], with a focus on the C 1s region. ISA consists of six different carbon atoms, which have different shifts in the C 1s signal due to their respective substituents. The structure, including the numbering of the carbon atoms, is shown in Figure 2. The calculated shifts relative to the aliphatic carbon atom were determined according to Chapter 2.3 (Manuscript EDTA) and are listed in Table 1. Due to the resolution limitations of the measurement, binding energy differences smaller than 1 eV cannot be distinguished, resulting in three distinguishable signals: C₁, C₃, and C₂/C₄/C₅/C₆. The spectrum of CaISA was fitted using three components with the same full width at half maximum (FWHM). The calculated relative proportions of the carbon atoms in CaISA align very well with the theoretical values. The relative intensities and peak spacings obtained from the fitting of the C 1s spectrum of CaISA were applied to fit the NaISA sample using the "CaISA" model. The C 1s region, depicted in Figure 4 for CaISA (A) and NaISA (B), shows the fitting results. The modeling of the C 1s spectrum of NaISA essentially corresponds to the purchased CaISA, which is further supported by the determined residual standard deviation (STD) of 2.318. Therefore, it can be concluded again that the synthesis of NaISA was successful. Slight deviations in the fits may be attributed to impurities, likely Ca(OH)₂ from the synthesis, which was converted to NaOH using Chelex.

Table 1: Shift of the binding energy of carbon atoms in CaISA and NaISA calculated according to the additive scheme [17].

C-atoms	ΔE_B [eV] CaISA	E_B [eV] CaISA	ΔE_B [eV] NaISA	E_B [eV] NaISA
1	3.3	288.0	3.9	288.7
2, 4, 5,6	1.0	285.8	1.7	286.5
3	-0.6	284.2	0.2	285.0

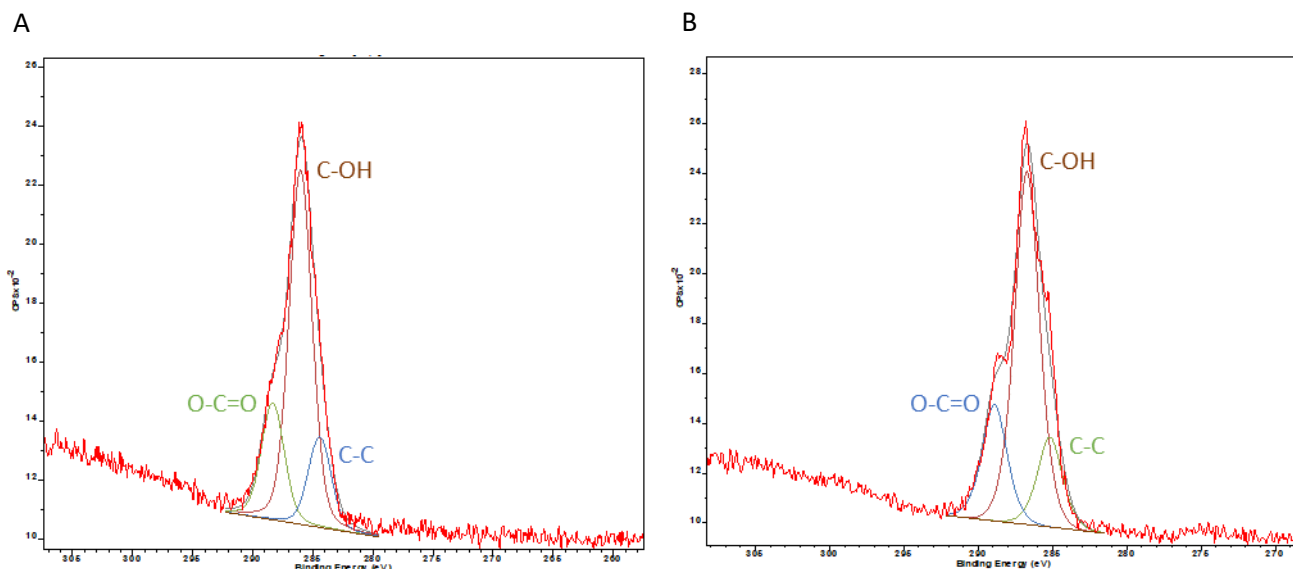


Figure 4: XPS overview spectra of CaISA (A) and NaISA (B) with Al K_{α} at an anode excitation energy of 1486.6 eV after surface admittance correction of 2.7 eV (corrected to Ca 2p for the CaISA spectra) and 2.0 eV (corrected to Na 1s for the NaISA spectra). The magnification shows the range of 310 - 270 keV.

The three fits performed in Figure 4 for both components are in good agreement with the binding energies from Table 1. The intensities exhibit a ratio of approximately 1:4:1, which corresponds well to the ratio of carbon atoms contributing to the signal (refer to Appendix Table A7 and Table A8).

Thorium

The $^{232}\text{Th(IV)}$ stock solution is a Thorium-ICP-standard (Peak Performance, CPI International, USA), provided by the manufacturer with a concentration of 4.3×10^{-3} M, and it is dissolved in 2% HNO_3 . The standard was further diluted to obtain a concentration of 1.0×10^{-8} M (in 2% HNO_3) in the batch sorption experiments and 4.0×10^{-7} M (in 1 M HClO_4) for the CE-ICP-MS measurements. Since thorium maintains a stable oxidation state of +IV under the experimental conditions of this study, no additional investigation was performed.

In addition, $^{234}\text{Th(IV)}$ was utilized as a tracer in batch sorption experiments to perform a sorption isotherm experiment. The stock solution of $^{234}\text{Th(IV)}$ was prepared via anion exchange chromatography. The ion exchange resin DOWEX® 1X8 (Alfa Aesar, USA) served as the stationary phase and was pre-conditioned with Milli-Q water and methanol (Acros Organics, Thermo Fisher Scientific, USA). Interactions of various strengths, predominantly adsorption, of an analyte dissolved in the mobile phase led to the separation of substance mixtures. The column (300×6 mm) was maintained at a temperature of 60 °C. When HCl (Fisher Scientific, UK) was used as a solvent for the separation of Th and U from a uranyl nitrate solution ($[\text{UO}_2(\text{NO}_3)_2]/\text{M} = 1.4$; isotope repository, TRIGA Mainz, Germany), chloride complexes form in the solution, depending on the HCl concentration. The capacitance factors of these

complexes on the column material varied depending on their concentration. These factors were inversely proportional to the migration rate of a species within the column. By utilizing 8 M HCl, significant differences in the capacity factors were achieved, allowing for the elution of Th while U continued to adsorb on the stationary phase. Subsequently, 0.5 M HCl was used to remove the remaining U. Multiple fractions of Th were obtained, evaporated, and diluted again in 8 M HCl. For further purification, the resulting stock solution was similarly loaded onto a second column (150 × 4 mm). The activity of individual fractions was determined with γ -spectroscopy. The γ -line with an energy of 63.3 keV was used for the evaluation of A_{det} with the time t_{det} , and the efficiency of the detector by using equation (1), considering that the measured activity was calculated back to the initial activity A_0 using the decay constant λ ($\lambda(^{234}\text{Th}) = 3.33 \times 10^{-8} \text{ s}^{-1}$) and the time from the sample preparation to the measurement t :

$$A_{det} = \frac{\frac{\text{Peak area}}{t_{det}}}{\text{Efficiency}} \quad (1)$$

$$A_0 = \frac{A_{det}}{e^{(-\lambda \cdot t)}} \quad (2)$$

These fractions were combined and diluted with 2% HNO₃. Since ²³⁴Th(IV) was used as a tracer, and ²³²Th(IV) was added to the samples as a carrier, the concentration of ²³²Th in the stock solution was also determined using ICP-MS (Inductively Coupled Plasma - Mass Spectrometry). Additionally, the concentration of ²³⁸U was also measured by ICP-MS to confirm the effectiveness of the separation achieved by the column. For this purpose, a calibration containing ²³²Th and ²³⁸U was done (Table A1 and Table A3). The values obtained from the ICP-MS measurements are listed in Table A2 and Table A4. Table 2 presents the calculated concentrations obtained from two column chromatography separations for the HCP / Th and HCP / Th / ISA batch sorption experiments.

Table 2: Concentrations of ²³²Th, ²³⁴Th, and ²³⁸U in the stock solutions used for the HCP / Th and HCP / Th / ISA experiments.

Isotopes	HCP / Th	HCP / Th / ISA
[²³² Th] / M	1.30 (± 0.33) $\times 10^{-8}$	3.90 (± 0.33) $\times 10^{-8}$
[²³⁴ Th] / M	1.76 (± 0.33) $\times 10^{-10}$	7.67 (± 0.22) $\times 10^{-11}$
[²³⁸ U] / M	1.63 (± 0.33) $\times 10^{-7}$	3.29 (± 0.15) $\times 10^{-8}$

Since ²³²Th cannot be separated from ²³⁴Th during the chromatographic separation process, there is a possibility of small amounts of ²³²Th present in the chemicals used, such as HCl and Milli-Q water, which could lead to an increased concentration. The presence of ²³⁸U may also be attributed to minimal contamination in the chemicals employed, which was also measured using ICP-MS. The measurement

results of the used chemicals for both ^{232}Th and ^{238}U can be found in Table A2 and Table A4, respectively.

2.2. Diffusion experiments

In this study, two diffusion cells were utilized in parallel to investigate the diffusion behavior of Pu(IV) in HCP in the presence and absence of ISA ($[\text{Pu(IV)}]/\text{M} = 7 \times 10^{-10}$, ($[\text{ISA}]/\text{M} = 1.0 \times 10^{-2}$) in ACW at pH 13.3. The experimental procedure, setup, and analysis for the diffusion experiments were identical for both cells.

2.2.1. Experimental description

HTO

For the characterization of the cement cores in the diffusion experiments, a stock solution of HTO (tritiated water, ^3H ; Perkin Elmer, USA) with a concentration of $37 \times 10^9 \text{ Bq L}^{-1}$ was used and appropriately diluted in 1 M HClO_4 (Riedel-de Haën, Germany) to give an initial activity of $1.7 \times 10^9 \text{ Bq L}^{-1}$ ($[\text{HTO}]/\text{M} = 1.6 \times 10^{-9}$) in the diffusion experiments. One advantage of using HTO to characterize the cement cores in the diffusion experiments is that it allows for tracking the movement or diffusion in an aqueous system without significantly altering the chemical properties of the system [18]. The concentration of HTO was determined with Liquid Scintillation Counting (LSC) measurement. For the concentration measurements of the HTO stock solution in this work, the Hidex 300 SL instrument (Hidex, Finland) and the Ultima GoldTM® XR scintillator cocktail (PerkinElmer LAS GmbH, Germany) were used.

To conduct comprehensive diffusion experiments, a filter-free and tubeless diffusion cell made of Perspex was designed based on the setup described by Tits et al. [19]. This design was further refined by V. Häußler in previous work. Two identical cells were subsequently manufactured in the "Mechanische Werkstatt" of TRIGA Mainz. This setup addresses issues related to precipitation, which can arise due to the high pH (>13) of the cement degradation stage I. As depicted in Figure 5, the two compartments of the cell are situated directly adjacent to the HCP core. The larger primary compartment (210 mL) is located on the left, while the smaller secondary compartment (20 mL) is on the right.

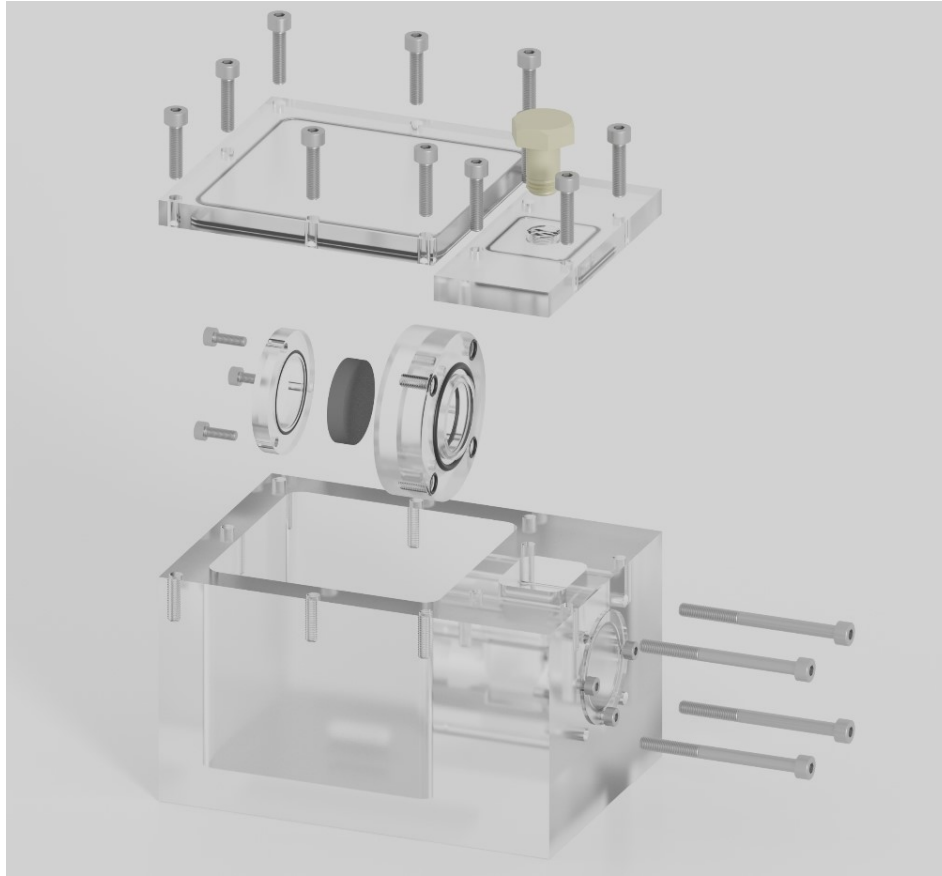


Figure 5: 3D representation of the diffusion cell used and the respective components with the primary compartment ($V = 210$ ml, left), the HCP core (middle) and the secondary compartment ($V = 20$ ml, right). A magnetic stirrer is placed in the primary compartment. (Graphic created by [REDACTED] with Blender).

The entire setup is placed inside a glove box under Ar atmosphere and placed on a magnetic stirring plate at a temperature of approximately 25 °C. A magnetic stirrer ensures continuous mixing of the solution in the primary compartment. From the cylindrical samples of the HCP preparation (refer to 2.3, EDTA Manuscript), cement cores ($h = 6$ mm; $\text{Ø} = 25.3$ mm) were bored in the “Mechanische Werkstatt” of TRIGA Mainz. To ensure a tight seal between the cells and the HCP cores, the outer surface of the cores was wrapped with Teflon tape. ACW served as the background electrolyte, supplemented with 0.003 M NaN_3 to prevent the growth of bacteria or algae during the diffusion process. Prior to characterizing the HCP cores, they were pre-equilibrated with ACW for one week. It was ensured that the solution levels in both the primary and secondary compartments were maintained at the same level to prevent any pressure gradient.

HTO through- and out-diffusion tests

Preliminary tests confirmed that HTO does not exhibit sorption onto the walls of the diffusion cell or onto the HCP material. After the preconditioning period, the primary compartment was filled with a stock solution of HTO ($[\text{HTO}]/\text{Bq L}^{-1} = 1.7 \times 10^9$; $[\text{HTO}]/\text{M} = 1.6 \times 10^{-9}$). The initial concentration was

determined by directly sampling 100 μl from the primary compartment approximately 5 min after addition and measuring it with LSC. The corresponding data can be found in Table A13. No additional HTO was added to the secondary compartment. The purpose of this diffusion experiment was to characterize the HCP cores by allowing HTO to pass through them. During the diffusion experiments, samples from the secondary compartments were regularly collected and analyzed for HTO activity using LSC. Immediately after each sampling, the secondary compartments were refilled with HTO-free ACW. The HTO through-diffusion tests were conducted for a period of 38 d for both cells. In the subsequent out-diffusion tests, the solutions in both compartments were completely exchanged at regular intervals, and the HTO activity was determined by LSC. The contents of the primary compartment were completely replaced every 10 d, while the contents of the secondary compartment were replaced every 3 d. This allowed for the completion of the out-diffusion process within 90 d.

Pu in-diffusion

Once the characterization of the HCP cores was completed and the HTO was completely removed from the cells, the actual diffusion experiment commenced. Cell I was designated for the experiment conducted in the absence of ISA, while cell II was designated for the experiment HCP / Pu(IV) / ISA ($[\text{ISA}]/M = 1 \times 10^{-2}$). A $^{238}\text{Pu(IV)}$ stock solution was acquired from the isotope magazine at TRIGA Mainz, chosen for its high specific activity ($A_{\text{spec}} = 633.73 \times 10^{12} \text{ Bq kg}^{-1}$). In the primary compartment of each cell, an aliquot of the $^{238}\text{Pu(IV)}$ stock solution was added, resulting in an initial concentration of $7.0 \times 10^{-10} \text{ M}$, which was determined using α -spectroscopy. However, due to the low concentration of the ^{238}Pu stock solution ($[\text{Pu(IV)}]/M = 1.1 \times 10^{-6}$), UV-Vis measurements were not feasible. In such case, electrolysis was conducted based on voltage control. The electrochemical reduction of $^{238}\text{Pu(VI)}$ to $^{238}\text{Pu(III)}$ was conducted until a voltage of -550 mV was reached. The polarity of the potentiostat was then reversed. Additionally, the oxidation of $^{238}\text{Pu(III)}$ to $^{238}\text{Pu(IV)}$ was accomplished by increasing the voltage to -1000 mV. To determine the concentration of $^{238}\text{Pu(IV)}$, 10 μl was dropped onto a tantalum plate, evaporated to dryness, and then measured by α -spectroscopy. The activity of the sample was determined by analyzing the peak area at 5.6 MeV using equation (1) and (2). In the diffusion experiments, a concentration of $[\text{Pu(IV)}]_0/M = 7 \times 10^{-10}$ was used.

However, due to the salt content of the background electrolyte, slight salt crusts formed when the solution dried, leading to signal broadening in the α -spectrum. Since it was assumed that only ^{238}Pu was present, the entire energy range of 4429 – 5576 keV in the α -spectrum was accumulated for evaluation. pH and Eh values were measured at regular intervals throughout the experiment. After a diffusion period of 118 d, the HCP core was removed from the cells and stored in the glove box under Ar atmosphere to allow for drying over several days. Before fixation, the core was characterized using Imager and SEM images. Subsequently, the core was fixed to a sample holder with the back side, i.e., the side facing the secondary compartment, using the fast-drying resin Cementit® (Merz+Benteli AG, Switzerland).

Abrasive peeling technique

The abrasive peeling technique offers the advantage of ablating thin layers of a sample by abrasively grinding the HCP core on sandpaper. This technique was originally described by Van Loon and Eikenberg [20] and further adapted from previous investigations in the group, specifically with Opalinus Clay, as performed and described by Wu et al. [3]. Considering diffusion experiments previously conducted with cement by V. Häußler, it was assumed that the diffusion of actinides into cement solids is significantly lower than that within clay. Hence, the optimization focused solely on the grinding process through a series of tests using fine sandpaper (P240, P320, P400 Vitex silicon carbide, VSM AG, Germany) and an inactive HCP core. The choice of sandpaper grit size is crucial as it determines the thickness of the removed layers and ensures a finer-meshed diffusion profile of Pu into cement. Additionally, factors such as grinding force and material hardness can affect the sandpaper's performance [21]. Based on the test trials, it was determined that sandpaper with a grit size of P320 is most suitable for the HCP core. The sandpaper was punched and securely attached to plastic specimen holders (Ø33x16 mm; Semadeni AG, Germany), and the weight of each specimen holder was measured using an analytical balance (Serie 320XT, Precisa Instruments AG, Switzerland) with an accuracy of 0.01%.

The dried HCP core was glued onto sample holders. After the resin had hardened overnight, a central cavity of approximately 400 µm in diameter was drilled in the center of the HCP core. This was done because the abrasion process is minimal in the center of the sample, as the movement in the center of a rotating object is almost negligible. Following each grinding step, the thickness of the HCP core was measured at four different lines using a digital caliper (IP 67, DIN 862, Messwelt, Germany), as shown in Figure 6. The weight of the plastic specimen holders with the removed HCP material was determined using the same analytical balance. The radionuclide associated with the abraded material could be directly detected using α -spectroscopy. Based on the distance removed and the activity measured on the sandpaper, the diffusion profile could be established.



Figure 6: Picture of the sample holder with the four different lines for measuring the thickness of the HCP cores.

2.2.2. Evaluation and modelling

HTO through-diffusion tests using Wolfram Mathematica

The equation used for modelling the diffusion experiments can be derived from the literature, as described by Van Loon et al. [22,23]. In terms of transport properties, the HCP cores are assumed to be homogeneous and isotropic, allowing for a well-described 1D model for a single porous medium to be applied to HTO diffusion. The diffusion coefficient is considered constant in both time and space, and independent of the HTO concentration, neglecting sorption ($K_d = 0$). To perform the calculations, the data obtained from the LSC measurements (Table 55 and Table 56) are utilized, along with the parameters listed in Table 3 were used.

Table 3: Experimental parameters of HTO diffusion through both cells used for modeling.

Parameter	Cell I	Cell II
V_{sample}	2.0 ± 0.1 ml	2.0 ± 0.1 ml
V_L	20.0 ± 0.1 ml	20.0 ± 0.1 ml
c_0	1.7×10^9 Bq L ⁻¹	1.8×10^9 Bq L ⁻¹
l	6.0 mm	6.0 mm
d	25.3 mm	25.5 mm

In the table, V_{sample} represents the volume of the LSC measurement sample, V_L denotes the volume of the secondary compartment, c_0 represents the initial HTO concentration in the primary compartment, while l and d represent the height and diameter of the HCP cores, respectively.

The porosity ε and the diffusion coefficient D_e of the HCP cores can be determined according to equation (3) which involves the accumulated time t_A and the accumulated activity A_{cum} obtained from the LSC measurement of HTO in the secondary compartment. The porosity ε is equivalent to the capacity factor α of the material for non-absorbing nuclides like HTO. The base area of the core S is calculated based on its diameter, and L represents the thickness of the HCP core. To determine the values of ε and D_e , a computer code and Wolfram Mathematica 12.2 (Wolfram Research Inc., UK) were employed. The code aims to fit the parameters of a theoretical plot to the experimental data, minimizing any deviation between them.

$$A_{cum} = S \cdot L \cdot c_0 \cdot \left(\frac{D_e \cdot t}{L^2} - \frac{\alpha}{6} - \frac{2 \cdot \alpha}{\pi^2} \cdot \sum_{n=1}^{\infty} \frac{(-1)^n}{n^2} \cdot e^{-\frac{D_e \cdot n^2 \cdot \pi^2 \cdot t}{L^2 \cdot \alpha}} \right). \quad (3)$$

In addition, the parameters ε and D_e are used to calculate the averaged flux J_L^t according to equation (4).

$$J_L^t = \frac{1}{100^2 \cdot S} \cdot \frac{\partial A_{dif}^t}{\partial t}. \quad (4)$$

Pu in-diffusion

To derive the diffusion coefficient D_e and the distribution coefficient K_d based on the data obtained from the Pu in-diffusion experiment, equation (6) and (7) can be used. The equation allows for determining the theoretical course of the activity of $^{238}\text{Pu(IV)}$ in the HCP core AC_r and the time course of the $^{238}\text{Pu(IV)}$ concentration in the primary compartment c_t by minimizing the deviation from the experimental data. V_{pw} represents the volume of the pore spaces, m_{corr} the mass of the HCP core corrected for the mass of the hole, H_f the capacity of the primary reservoir, d the diameter and x the abraded section of the HCP core. The calculations are summarized in equation (5). Otherwise, the values from Table 3 were used. A derivation of the equation can be found in [24].

$$V_{pw} = \varepsilon \cdot \pi \cdot \frac{d^2}{4} \cdot l; H_f = \frac{V_0}{\pi \cdot \frac{d^2}{4}}; \alpha = \varepsilon + \frac{m}{\pi \cdot \frac{d^2}{4} \cdot l} \cdot K_d; \quad (5)$$

$$m_{corr} = \frac{m}{\pi \cdot \frac{d^2}{4} \cdot l} \cdot \pi \left(\frac{d^2}{4} - \frac{d_h^2}{4} \right) \cdot l.$$

$$AC_r = \frac{V_{pw} + m_{corr} \cdot K_d}{m_{corr}} \cdot c_0 \cdot e^{\alpha \frac{x}{H_f} + \frac{D_e \alpha}{H_f^2} t} \cdot \operatorname{erfc} \left(\frac{x}{2 \cdot \sqrt{\frac{D_e t}{\alpha}}} + \sqrt{\frac{D_e \alpha}{H_f}} \right). \quad (6)$$

$$c_t = c_0 \cdot 10^{12} \cdot e^{\alpha \frac{x}{H_f} + \frac{D_e \alpha}{H_f^2} t} \cdot \operatorname{erfc} \left(\frac{x}{2 \cdot \sqrt{\frac{D_e t}{\alpha}}} + \sqrt{\frac{D_e \alpha}{H_f}} \right). \quad (7)$$

3. Results and discussion

The results of the investigations with ISA under alkaline conditions can be divided into two main parts. First, the batch sorption experiments (3.1) in the binary system HCP / ISA and ternary system HCP / An(IV) / ISA were investigated. Measurements in the binary system were performed using TOC (total organic carbon) in collaboration with the ‘‘Karlsruher Institut für Technologie (KIT) - Institut für Nukleare Entsorgung (INE)’’ (KIT-INE, Germany). In the second Chapter (3.2) diffusion experiments of $^{238}\text{Pu(IV)}$ in HCP in absence and presence of ISA were discussed.

3.1. Batch sorption experiments

3.1.1. Binary system

NPOC measurements

NPOC (non-purgeable organic carbon) is a method used to measure the total organic carbon in a sample. In this study, a Multi N/C 2100s instrument (Analytik Jena, Germany) was utilized for NPOC measurements. Two sets of experiments were conducted to investigate the relationship between ISA concentration and S/L ratio on the sorption behavior. In the first experiment, the concentration of ISA was varied while maintaining a constant S/L ratio ($[ISA]_0/M = 3 \times 10^{-4} - 1 \times 10^{-2}$; $S/L = 5 \text{ g L}^{-1}$). Duplicate determinations were performed to ensure accuracy. To accurately determine the NPOC in the sample with different S/L ratios, a corresponding background sample containing only HCP in ACW (without ISA) was used for comparison. In the second experiment, the S/L ratio was varied while keeping the ISA concentration constant ($S/L = 0.5 - 50 \text{ g L}^{-1}$; $[ISA]_0/M = 1 \times 10^{-3}$). The purpose of this experiment was to determine the remaining NPOC in the sorption isotherm by calculating the ppm of ISA using the background sample from the first experiment. The experimental range was chosen because the concentration of ISA in the solution after sorption is otherwise below the detection limit (2 ppm) for NPOC measurement.

The measured concentrations of NPOC in ppm, as well as the calculated sorption $S\%$ and equilibrium concentrations c_{eq} after a contact time of 72 h, are summarized in Table A32 and Table A34. The results are shown in Figure 7. Considering the fact that ISA sorption is known to be a fast process [25-27], usually occurring within 2 d of contact time with cement pastes, both data sets were evaluated and adjusted. Figure 7A shows the sorption isotherm with varying ISA concentration, including the results from the literature of Tasi et al. (orange) [9]. In this study, the obtained data (represented in black) were plotted using the Langmuir isotherm model with one adsorption side given in equation (8):

$$[GLU]_{sorbed} = \frac{Kq(GLU)_{eq}}{1 + K(GLU)_{eq}}. \quad (8)$$

The fitting resulted in an affinity constant of $K_l = 5051 \pm 1644 \text{ L mol}^{-1}$ and a sorption capacity factor of $q_l = 0.25 \pm 0.03 \text{ mol kg}^{-1}$. The sorption model developed for the Langmuir isotherm at $\text{pH} > 13$ is used for the calculation of $[ISA]_{eq}$ as a function of $S:L$ and $[ISA]_{in}$ in the second batch experiments using equation (9). This explains well the experimental observations shown in Figure 7B.

$$[GLU]_{sorbed} = ([GLU]_{in} - [GLU]_{eq}) \cdot V \cdot m^{-1}. \quad (9)$$

Tasi et al. [9] reported their values using a two-site Langmuir isotherm model, with $K_1 = 2510 \pm 500 \text{ L mol}^{-1}$, $q_1 = 0.18 \pm 0.02 \text{ mol kg}^{-1}$, for the first site, and $K_2 = 12 \pm 2 \text{ L mol}^{-1}$, $q_2 = 0.17 \pm 0.02 \text{ mol kg}^{-1}$ for the second site, resulting in a total sorption capacity of $q_{1+2} = 0.35 \text{ mol kg}^{-1}$. Similarly, Van Loon et al. [25,26] employed a two-site model with Langmuir adsorption behavior and calculated their results with $K_1 = 1730 \pm 385 \text{ L mol}^{-1}$, $q_1 = 0.1 \pm 0.01 \text{ mol kg}^{-1}$ for the first site, and $K_2 = 12 \pm 4 \text{ L mol}^{-1}$, $q_2 = 0.17 \pm 0.02 \text{ mol kg}^{-1}$ for the second site, resulting in $q_{1+2} = 0.27 \text{ mol kg}^{-1}$. The values obtained in this work are slightly higher than those reported in the literature. This difference could be attributed to variations in experimental conditions. Tasi et al. conducted their experiments during degradation stage II, with a pH of 12.5 and a contact time of 14 d. Van Loon et al. reported contact times ranging from a few days to 9 months. Additionally, there is a difference in grain size, with HCP grain sizes of 100 - 400 μm in the literature, while this study used a grain size $< 63 \mu\text{m}$ [25,26]. Despite these differences, both curves exhibit a similar trend, flattening towards higher ISA concentrations ($[\text{ISA}]_0/M > 1 \times 10^{-3}$), indicating saturation of sorption sites of HCP.

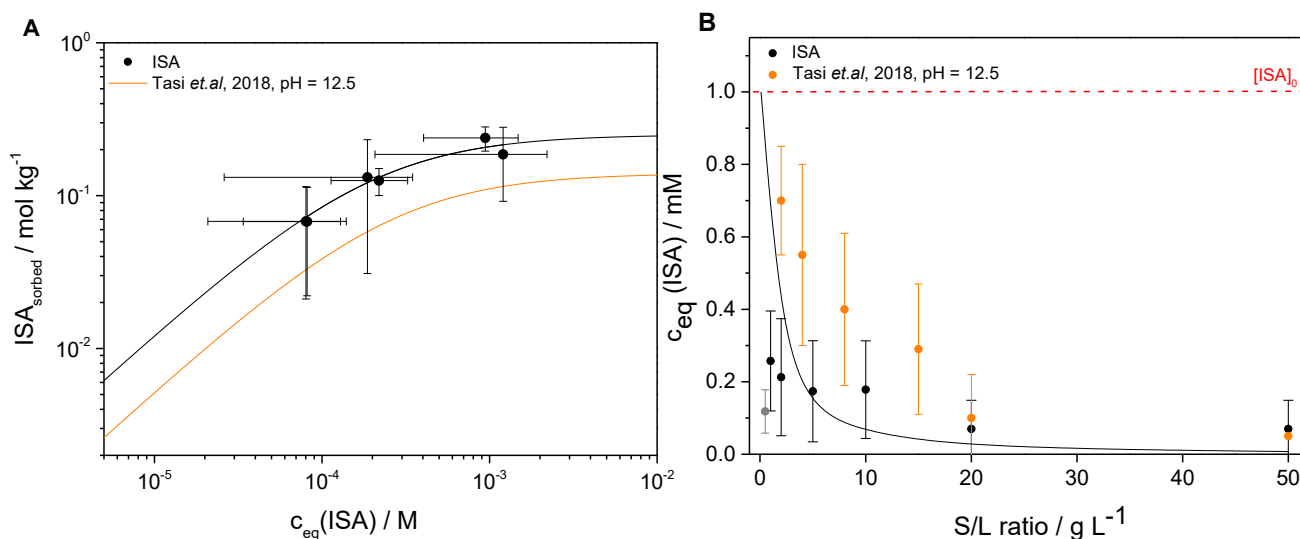


Figure 7: Batch sorption experiments of the binary system at HCP / ISA in ACE after a contact time of 72 h ($\text{pH} > 13$): A) sorption isotherm with initial ISA concentrations from $3 \times 10^{-4} - 1 \times 10^{-2}$ at $S/L = 5 \text{ g L}^{-1}$, solid lines represent the calculated Langmuir-isotherms, from the model reported by Tasi et al. [6](two-site Langmuir isotherm, orange) and the results from the fitting performed in the present work (one-site Langmuir isotherm, black); B) at constant ISA concentration ($[\text{ISA}]_0/M = 1 \times 10^{-3}$) and varying S/L ratio ($S/L = 0.5 - 50 \text{ g L}^{-1}$). The solid line represents the calculated concentration using the Langmuir isotherm based on the results of (A), where the grey data point was not included in the calculation of the fit. The orange values are reported in the literature by Tasi et al. [9]. The red line marks the initial concentration of $1 \times 10^{-3} \text{ M}$ ISA.

Figure 7B demonstrates that the equilibrium concentration c_{eq} decreases with increasing S/L ratio in both the current experiments and the literature data [6,9]. This observation can be attributed to the increasing number of sorption sites available with a higher amount of HCP. Under the experimental

conditions with a high pH >13, ISA exists as a deprotonated species. Considering the complexation constants, the formation of the HISA^- complex is favored [9,29]. In fresh cement, there exists a Ca(II) interlayer situated between two of these Si-O tetrahedral layers. Consequently, it could be assumed that ISA sorb onto the Ca(II) within the interlayer. The slight deviation from the literature data may once again be attributed to the differing experimental conditions. The experimental data available in the literature indicate that pH, total ISA concentration, calcium concentration, and S/L ratio significantly influence the uptake of ISA by cement [9,26,27]. According to Pointeau et al. [27], it is suggested that the sorption of the ligand occurs through the formation of a ternary species that includes Ca, such as $>\text{SOCaISA}$. However, it should be noted that there is currently no experimental evidence to confirm this hypothesis. Comparable results are obtained in the experiments with GLU, indicating a comparable sorption behavior [28]. Since ISA and GLU are structurally analogous, this similarity is plausible.

Leaching effect of ^{232}Th from HCP in the presence of ISA

In the semiquantitative analysis mode of ICP-MS (refer to Chapter 2.2.3.1), it was observed that ^{232}Th leaches in the presence of ISA, although to a lesser extent compared to GLU (as discussed in Chapter 2.3, Manuscript EDTA). To further investigate this effect, a sorption isotherm was conducted with a constant S/L ratio of 5 g L^{-1} and varying ISA concentration ($[\text{ISA}]_0/\text{M} = 1 \times 10^{-3} - 1 \times 10^{-2}$) at pH > 13. ICP-MS measurements were taken after 3, 30, 50, and 80 d. The calibration and results from the individual measurements can be found in the Appendix. Figure 8 shows the results of the leaching experiment. It was found that ^{232}Th leaches from HCP in the presence of ISA. In samples of HCP / ISA with an ISA concentration of $1 \times 10^{-3} \text{ M}$, no significant leaching effect was observed after 30 d, with a ^{232}Th concentration in the range of samples without ISA at a concentration of $\sim 5 \times 10^{-11} \text{ M}$. However, at higher ISA concentrations ($[\text{ISA}]_0/\text{M} > 3.16 \times 10^{-3}$), a significant leaching effect was observed after only 3 d of contact time. These samples reached an equilibrium concentration of $^{232}\text{Th} \sim 5 \times 10^{-9} \text{ M}$ after a contact time of 53 d, which corresponds well to the value obtained in the semiquantitative analysis mode for the HCP / ISA sample ($[\text{ISA}]_0/\text{M} = 1 \times 10^{-2}$) after 118 d, determined to be $6 \times 10^{-9} \text{ M}$. This leaching affects the results in the following batch sorption experiments less, as a concentration of Th(IV) of $1.0 \times 10^{-8} \text{ M}$ was used there.

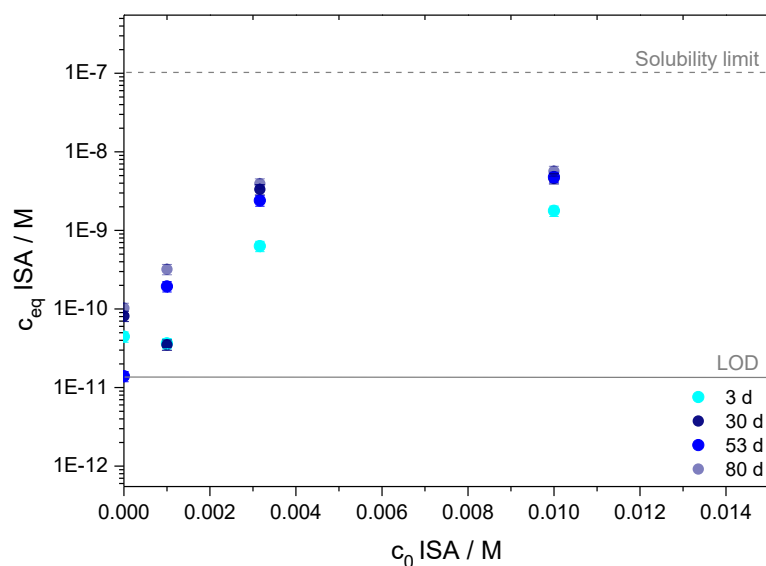


Figure 8: Determined concentration of ^{232}Th in the leaching batch experiments of HCP / ISA after a contact time of 3 d, 30 d, 53 d and 80 d. The dashed line shows the solubility limit of Th(IV) at $\text{pH} > 13$, the solid line represents the limit of detection of ^{232}Th from the ICP-MS measurement.

XPS measurements

Further experiments were performed to investigate the binary system of HCP / ISA on the solid phase. XPS measurements were performed to verify the findings from the liquid phase experiments, specifically regarding the sorption of ISA onto HCP. Figure 9 shows the Al K_{α} spectra of HCP in ACW (green) as well as HCP / ISA in ACW (red) after a contact time of 72 h, revealing characteristic signals of calcium, oxygen, silicon, sodium, and potassium. A magnified view of the spectrum in the 330-280 keV range highlights a signal for C 1s, which may be attributed to adventitious carbon, as already discussed in Chapter 2.3 (Manuscript EDTA). The fitted peaks in this range are depicted in Figure A18. Table A34 presents all the assigned peaks, which align well with literature values [30]. The determination of the C/S ratio was calculated according to Chapter 2.3 (Manuscript EDTA) based on the obtained peak areas. The calculated C/S ratio was found to be 1.9, slightly higher than the literature value of 1.8 reported for fresh cement [18]. It is worth noting that the sodium signal may have been augmented by dried ACW on the sample surface. Again, it should be mentioned that the samples were not freshly prepared prior to measurement, which may have resulted in the accumulation of adventitious carbon on the sample surface. Consequently, it is challenging to definitively determine whether ISA sorbed onto the HCP surface.

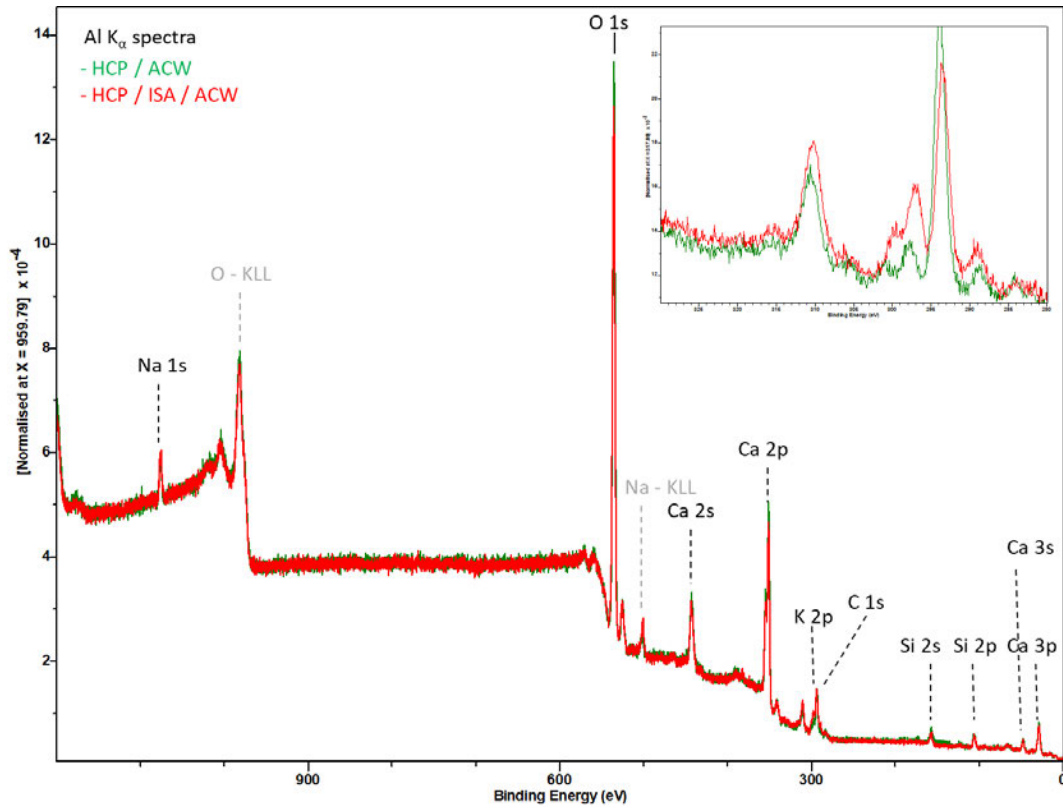


Figure 9: XPS overview spectra of HCP (w/c 0.5) in ACW (green) and HCP in presence of ISA in ACW (red) after a contact time of 72 h measured with Al K_{α} at an anode excitation energy of 1486.6 eV after surface admittance correction of 4.1 eV (Ca 2p signal). The magnification shows the range of 330-280 keV. O-KLL and Na-KLL denote Auger transitions and can be assigned the signals of the Auger electrons of O and Na. The other signals were assigned to the photoelectrons from the different layers of the contained elements.

In addition, further measurements were performed on C-S-H phases (C/S = 0.8) in the presence (red) and absence (green) of ISA. The corresponding spectra are presented in Figure 10. Upon closer examination of the magnified area from 340 - 200 eV, no C 1s signal is observed, indicating that the sorption of ISA onto the C-S-H phase is unlikely under the given experimental conditions. Also, in the presence of ISA the C-S-H phases are shown to have a low affinity for adventitious carbon, since the samples were also stored in air. The elements (Ca, Si, O) present in the C-S-H phases could be clearly identified. Table A35 shows the assigned peaks with literature comparison [30], which agree well. The C/S ratio was calculated using the sensitivity factor according to Chapter 2.3 (Manuscript EDTA) and gives a value of C/S = 0.59. A similar value of C/S = 0.57 was determined in the literature in the presence of GLU by Dettmann et al. [31] and C/S = 0.54 for the measurements with EDTA.

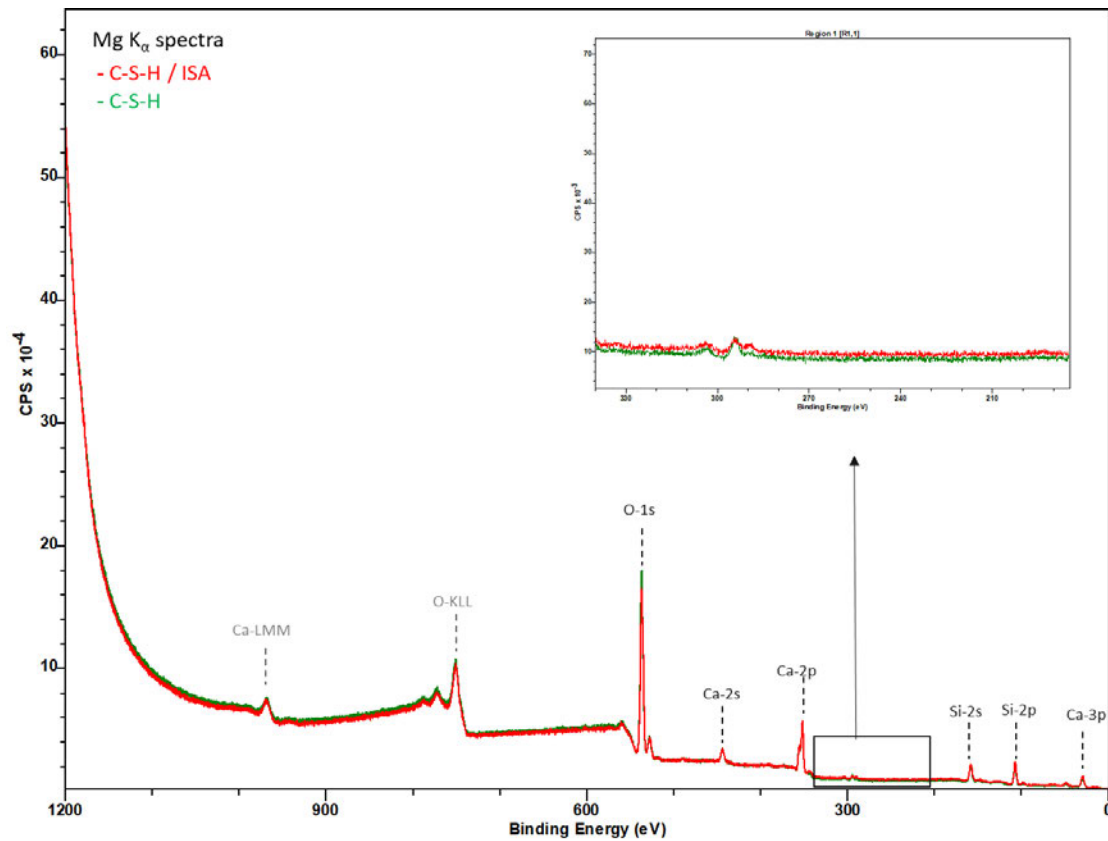


Figure 10: XPS overview spectra of C-S-H phases ($C/S = 0.8$) in Milli-Q presence (red) and absence (green) of ISA after a contact time of 72 h measured with Mg K_{α} at an anode excitation energy of 1253.6 eV. The surface charge was corrected by normalizing the Ca 2p peak ($\Delta E_b = + 1.0$ eV). The magnification shows the range of 340-200 keV. Ca-LMM and O-KLL denote Auger transitions and can be assigned the signals of the Auger electrons of Ca and O. The other signals were assigned to the photoelectrons from the different layers of the contained elements.

3.1.2. Ternary system

To investigate the influence of ISA on An(IV) uptake by HCP in batch sorption experiments ($[An(IV)]_0/M = 1 \times 10^{-8}$; $[ISA]_0/M = 1 \times 10^{-2}$; $pH > 13$; $S/L = 5$ g L $^{-1}$), three different addition were studied: (i) (HCP+An(IV)) + ISA, (ii) (HCP+ISA) + An(IV), and (iii) (HCP+An(IV)+ISA). The ICP-MS measurements for $^{232}Th(IV)$ along with the calculated values can be found in the Appendix. The results are shown in Figure 11A. It was observed that ISA and the order of addition significantly influenced the sorption behavior of $^{232}Th(IV)$ on HCP. The obtained K_d values were two orders of magnitude smaller compared to samples without organic influence. After a contact time of 194 d, it appeared that equilibrium could be reached at $K_d \approx 10^2$ L kg $^{-1}$. The order of addition of Th(IV) and ISA determined the extent of Th(IV) sorption or desorption after a longer contact time. Wieland et al. [29] also observed a reduced uptake of Th(IV) by HCP ($S/L = 1.25 \times 10^{-2}$ kg L $^{-1}$) at ISA concentrations above 10^{-4} M. The

K_d values obtained ($10^2 - 10^3 \text{ m}^3 \text{ kg}^{-1}$) were in the same order of magnitude for an S/L ratio of 5 g L^{-1} . The decrease in sorption due to the presence of ISA can be attributed to the blocking of sorption sites of ISA onto HCP or to the formation of Ca-Th(IV)-OH-ISA complexes in solution at high pH values, as determined by speciation calculations (see Chapter 1.4.2). This phenomenon is also described in the literature [11,12,32]. Similar to the experiments with GLU [28], ISA was found to sorb onto HCP, thereby blocking the sorption sites.

The influence of ISA on the sorption of $^{232/234}\text{Th(IV)}$ becomes even more significant, as observed in the sorption isotherm experiments ($[\text{Th(IV)}]_0/M = 1 \times 10^{-6} - 1 \times 10^{-13}$; S/L = 0.1 g L^{-1} ; pH > 13) in absence and presence of ISA ($[\text{ISA}]_0/M = 1 \times 10^{-2}$). Th(IV) and ISA were added simultaneously with a contact time of 72 h.

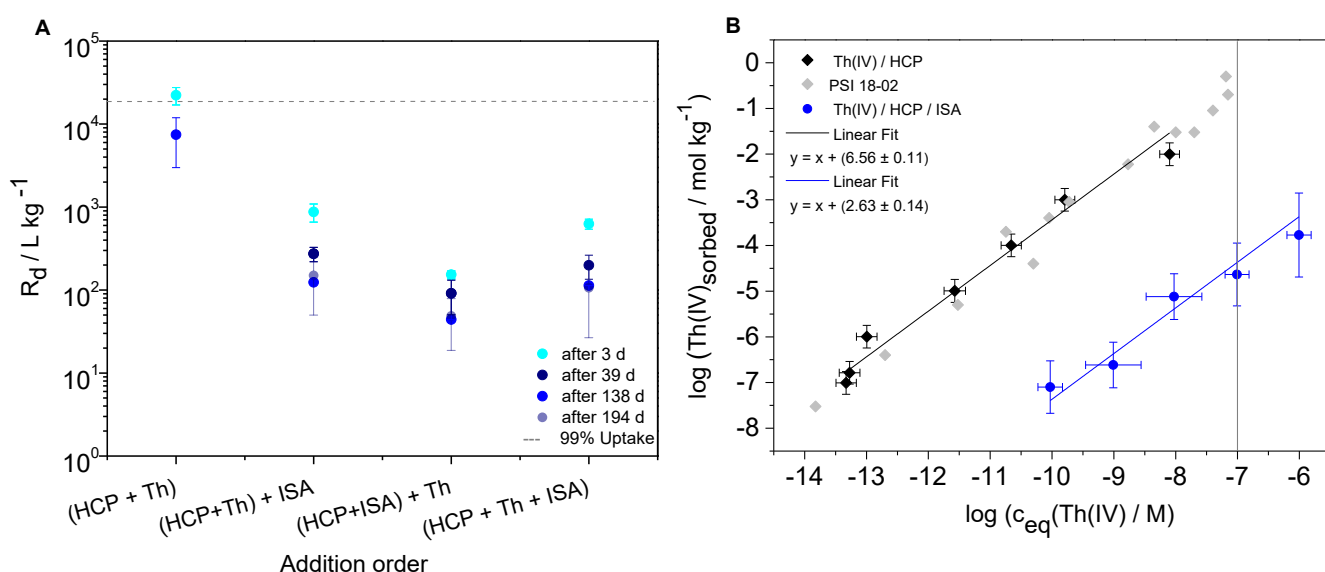


Figure 11: A) Average value from a double determination of the distribution coefficients K_d (L kg^{-1}) determined for Th(IV) uptake on HCP in presence and absence of ISA ($[\text{Th(IV)}]_0/M = 1 \times 10^{-8}$, $[\text{ISA}]_0/M = 1 \times 10^{-2}$, S/L = 5 g L^{-1} , pH > 13) after a contact time of 3 d, 39 d, 138 d and 194 d. The dashed line represents an uptake of 99%. B) Sorption isotherm of HCP / $^{232/234}\text{Th(IV)}$ ($[\text{Th(IV)}]_0/M = 1 \times 10^{-6} - 1 \times 10^{-13}$; S/L = 0.1 g L^{-1} ; pH = 13.3) in the absence (black) and presence (blue) of ISA ($[\text{ISA}]_0/M = 1 \times 10^{-2}$) with corresponding fits. The grey dots are values from the literature [33]. The solubility limit of Th(IV) at high pH values of > 13 is shown by the grey line [34].

The results of both experiments can be found in the Appendix and are presented in Figure 11B. In the absence of ISA, a $\log K_d$ value of 6.57 ± 0.11 ($K_d = 3.72 (\pm 1.29) \times 10^6 \text{ L kg}^{-1}$) was determined using a linear fit with a slope of one. This indicates an uptake of > 99%, which is consistent with values reported in the literature [33] and the results of the (HCP + Th(IV)) experiment of Figure 11A without ISA. In the presence of ISA, $\log K_d$ value of 2.63 ± 0.14 ($K_d = 4.72 (\pm 1.39) \times 10^2 \text{ L kg}^{-1}$) was determined using

the same linear fit. This value is in the same order of magnitude ($K_d \sim 5 \times \text{L kg}^{-1}$) as the value obtained in the experiment with different addition orders in Figure 11A. As described in Tits et al. [32], values of $K_{d,min} = 36 \text{ L kg}^{-1}$ and $K_{d,max} = 7.60 \times 10^4 \text{ L kg}^{-1}$ were determined. It is worth noting that the solubility behavior of Th(IV) is significantly increased in the presence of ISA. The solubility of Th(IV) is represented by the grey line in Figure 11B. A value below the solubility limit could be measured in the presence of ISA. Literature reports describe the formation of Th-OH-ISA [11,12,35] and Ca-Th-OH-ISA [11,12,32] complexes, which have a significant influence on the solubility of Th at $[\text{ISA}]_0/M \geq 1 \times 10^{-3.5}$ under hyperalkaline pH conditions ($\text{pH} > 13$). The possible formation of Th-OH-ISA and Ca-Th-OH-ISA complexes will be discussed further. Similar effects on the solubility of Pu have been described by Tasi et al. [7,8].

Furthermore, analogous experiments were conducted to investigate the influence of the order of addition on Pu(IV) sorption. The calculated K_d values are shown in Figure 12 revealing a significant impact of the order of addition of Pu(IV) and ISA on the sorption behavior of Pu(IV) on HCP after 72 h and 119 d of contact time. Values of $K_{d,min} = 10 \text{ L kg}^{-1}$ and $K_{d,max} = 8.51 \times 10^4 \text{ L kg}^{-1}$ were calculated according to [32]. In the absence of ISA and during the cement degradation state I, the uptake of Pu(IV) on HCP is $> 99\%$ ($K_d = 5.91 \times 10^4 \text{ L kg}^{-1}$), consistent with existing literature [9,28,36]. When ISA is added first ($K_d = 11 \text{ L kg}^{-1}$) or simultaneously ($K_d = 22 \text{ L kg}^{-1}$), the uptake of Pu(IV) is significantly reduced, similar to the results obtained in the HCP / Th(IV) / ISA and HCP / Pu(IV) / GLU experiments [28]. The strong affinity of ISA for the HCP surface may hinder the sorption of Pu(IV) on HCP. After 119 d of contact time, the uptake of Pu(IV) in the presence of ISA decreased in all cases. The effect is particularly pronounced for the addition sequence (HCP + Pu) + ISA, where the K_d value is 534 L kg^{-1} and two orders of magnitude lower. It appears that the sorption of ISA on HCP is more dominant, leading to the desorption of Pu(IV) from HCP. In the case of (HCP + ISA) + Pu, a concentration of $1.07 \times 10^{-8} \text{ M}$ was measured, which mathematically yields a negative K_d value. Hence, this value is not included in Figure 12. The observed effect of the order of addition can be supported by the findings of Tasi et al. [9], where higher K_d values were obtained in the sequences (Pu + Cement) + ISA compared to (Pu + ISA) + Cement. Tasi et al. [9] reported values of $\log([\text{Pu}]_{eq}/M) \approx \log([\text{Pu}]_{in}/M)$ for a systems with $S:L \leq 8 \text{ g L}^{-1}$ at the degradation state II ($\text{pH} \approx 12$) even after 490 d of contact time. Furthermore, it is worth noting that the formation of complexes involving ISA, such as Pu-OH-ISA and Ca-Pu-OH-ISA, is significant and can have a notable influence on the sorption of Pu on HCP. In the study by Tasi et al. [9] a simplified sorption model was proposed, which suggests that the decrease in Pu uptake by HCP at pH 9-12 is primarily attributed to the formation of Ca(II)-Pu(IV)-OH-ISA aqueous complexes in the solution. The predictions of this model align qualitatively well with the observed trend in the experimental data.

On one hand, desorption of ISA may occur in the presence of An(IV), or An(IV) could be partially co-adsorbed as Ca-An(IV)-OH-ISA complexes, which could potentially account for the observed K_d values. To gain a more comprehensive understanding of the sorption mechanism of An(VI) on HCP, further investigations involving solid phase studies would be necessary.

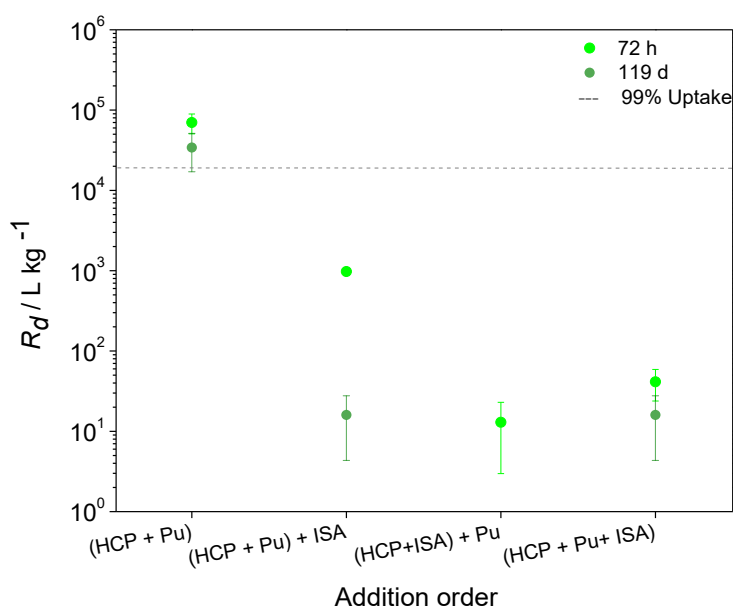


Figure 12: Average value from a double determination of the distribution coefficients K_d ($L\ kg^{-1}$) determined for Pu(IV) uptake on HCP in presence and absence of ISA ($[Pu(IV)]_0/M = 1 \times 10^{-8}$, $[ISA]_0/M = 1 \times 10^{-2}$, $S/L = 5\ g\ L^{-1}$, $pH > 13$) after a contact time of 72 h and 119 d. The dashed line represents an uptake of 99%.

The experimental pH and Eh values obtained from the batch sorption experiment HCP / Pu(IV) / ISA are presented in Figure 13 in the predominance diagram of Pu. In accordance with the speciation outlined in Chapter 1.4, thermodynamic calculations were conducted using the PhreePlot with the ThermoChimie database 11a (2022) [37], and complexation formation constants from the literature, provided by Tasi et al. [7,8]. The measured Eh values of the samples are within the predominant region of $Pu(OH)_5(HISA)^{2-}$, suggesting its formation as a significant speciation in solution at $pH > 13$. In order to verify the complexation of An(IV) with ISA, also in the presence of Ca, CE-ICP-MS measurements were carried out.

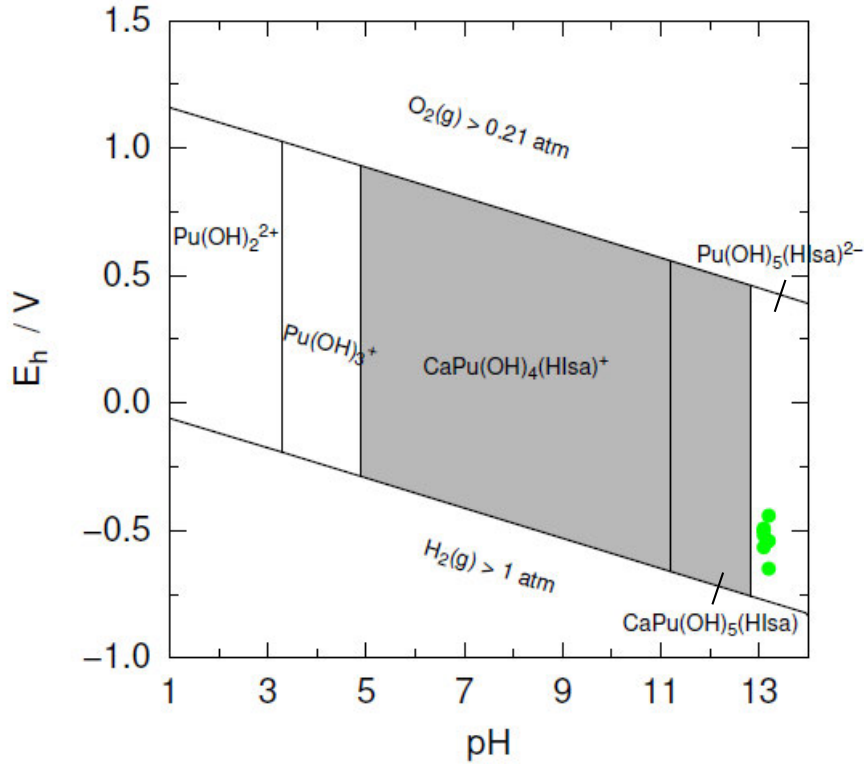


Figure 13: Predominance diagram of Pu calculated for $[Pu(IV)]_0/M = 1 \times 10^{-8}$, $[ISA]_0/M = 1 \times 10^{-2}$ M, and $[Ca]_0/M = 2 \times 10^{-3}$ M in the system HCP / ACW. The graphic was generated by PhreePlot (version 1.0 [38]) using PHREEQC and the ThermoChimie database 11a, 2022 [37] with complex formation constants determined by Tasi et al. [7,8]. The green dots mark the experimental pH and Eh values of the batch sorption samples for the HCP / Pu(IV) / ISA experiment. The values of the second Eh measurement after 119 ds of contact time is in the same range and can be found in the Appendix (Table A54).

CE-ICP-MS measurements

Furthermore, additional measurements (refer to Chapter 2.3, Manuscript EDTA) were conducted to investigate the influence of ISA ($[ISA]_0/M = 1 \times 10^{-2}$) and Ca ($[Ca(II)]_0/M = 1 \times 10^{-2}$) on the electrophoretic mobilities of Th(IV) ($[Th(IV)]_0/M = 4 \times 10^{-7}$) and Pu(IV) ($[Pu(IV)]_0/M = 1 \times 10^{-8}$ M) species at pH = 10 and an ionic strength of 0.1 M. For the experiments with Pu(IV), an additional measurement with a higher concentration of Ca ($[Ca(II)]_0/M = 3 \times 10^{-2}$) was used to highlight its impact more clearly. The results are summarized in Table 4, the speciation calculations from Chapter 1.5 (Introduction) were used for the discussion. In the presence of ISA, both Th(IV) and Pu(IV) species exhibited negative μ_{eff} , with values of $-(2.73 \pm 0.14) \times 10^{-4} \text{ cm}^2(\text{Vs})^{-1}$ and $-(2.36 \pm 0.13) \times 10^{-4} \text{ cm}^2(\text{Vs})^{-1}$, respectively. This change in mobility in comparison to the neutral value already discussed in Chapter 2.2.2 [31] and 3.2 ($\mu_{eff} = (0.03 \pm 0.03) \times 10^{-4} \text{ cm}^2 (\text{Vs})^{-1}$) for $\text{Th}(\text{OH})_4$ indicates the formation of complexes between An(IV) and ISA, resulting in negatively charged species. Previous studies by Vercammen et al. [12] and Tits et al. [11,32] proposed $\text{Th}(\text{OH})_4(\text{ISA})^-$ as the main species in solution, while Colàs et al. [35] the existence of an anionic complex, such as $\text{Th}(\text{OH})_4(\text{ISA})_2^{2-}$ described at high

ISA concentrations $> 10^{-3}$ M. Based on the measured mobility, the formation of the latter complex is more likely. Similarly, Tasi et al. [8] described the complex formation of $\text{Pu}(\text{OH})_4(\text{ISA})^-$ up to pH 11.5 with the formation of $\text{Pu}(\text{OH})_5(\text{ISA})^{2-}$ being described at higher pH values. Since the measured mobilities of Th(IV) and Pu(IV) are similar, the formation of an $\text{Pu}(\text{OH})_4(\text{ISA})_2^{2-}$ complex would also be conceivable.

In the presence of Ca(II) in the An(IV)-ISA samples, both Th(IV) and Pu(IV) exhibited neutral mobilities of $-(0.80 \pm 0.08) \times 10^{-4} \text{ cm}^2(\text{Vs})^{-1}$ for Th(IV) and $-(0.02 \pm 0.08) \times 10^{-4} \text{ cm}^2(\text{Vs})^{-1}$ for Pu(IV). This suggests the possible formation of quaternary complexes involving Ca(II). Vercammen et al. [12] and Tits et al. [11,32] have described the formation of a neutral complex, $\text{CaTh}(\text{OH})_4(\text{ISA})_2$ at pH 9, while Tasi et al. [7] reported the formation of $\text{CaPu}(\text{OH})_4(\text{ISA})^+$ (and $\text{Pu}(\text{OH})_4(\text{ISA})^-$ at pH 9). Since both complexes are present in similar proportions, this also could be the explanation for the neutral mobility. It is important to note that while the mobilities are similar, the species present in solution for Th(IV) and Pu(IV) may be different, as indicated by the speciation calculations in Chapter 1.4. The measurements conducted with a Ca concentration of 3×10^{-2} M yielded comparable mobilities, further supporting the presence of the aforementioned complexes in the system.

Table 4: The electrophoretic mobilities (μ_{eff}) of Th(IV) ($[\text{Th(IV)}]_0/M = 4 \times 10^{-7}$) and Pu(IV) ($[\text{Pu(IV)}]_0/M = 1 \times 10^{-8}$ M) in the presence of ISA ($[\text{ISA}]_0/M = 1 \times 10^{-2}$) and additionally in the presence of (a) 1×10^{-2} M and (b) 3×10^{-2} M Ca(II) at pH 10 and an ionic strength of 0.1 M calculated according equation (13) from Chapter 2.3 (Manuscript EDTA).

Complex	Th(IV)	Pu(IV) (a)	Pu(IV) (b)
An(IV) + ISA	-2.73 ± 0.14	-2.36 ± 0.13	-2.63 ± 0.13
An(IV) + ISA + Ca(II)	-0.80 ± 0.08	-0.02 ± 0.08	-0.12 ± 0.07

3.2. Diffusion experiments

Diffusion studies are a critical component in the long-term safety analysis for a repository as they provide valuable insights into the mobility of actinides in cement systems. In this study, the in-diffusion of $^{238}\text{Pu}(\text{IV})$ ($[\text{Pu}]_0/\text{M} = 7 \times 10^{-10}$) into HCP at degradation stage I ($\text{pH} > 13$) in absence and presence of ISA ($[\text{ISA}]_0/\text{M} = 1 \times 10^{-2}$) was investigated, considering previous literature studies [3,19,22-24] and the research conducted by Verena Häußler. The experiment starts with the characterization of the cement cores in two cells using through-diffusion of HTO ($[\text{HTO}]_0/\text{M} = 1.6 \times 10^{-9}$), allowing the determination of diffusion parameters. Subsequently, the HTO was removed, and the in-diffusion experiment with $^{238}\text{Pu}(\text{IV})$ commenced, lasting for a period of 118 d. After the cores were dried, they were subjected to the abrasive peeling technique to remove surface layers, and α -spectroscopy was employed to quantify the amount of $^{238}\text{Pu}(\text{IV})$ present in HCP. This approach enabled the establishment of an in-diffusion profile, providing insights into the behavior of $^{238}\text{Pu}(\text{IV})$ in HCP.

HTO through- and out-diffusion

The activity obtained from the LSC measurements, including their efficiencies, sampling time, accumulated activity, and calculated flux according to equations (3) and (4) can be found in the Appendix. Figure 14 presents the experimental data of accumulated diffused activity and flux, along with the corresponding theoretical curves derived from the fitted diffusion parameters.

The through-diffusion data were fitted using an 1D diffusion/linear sorption model that neglected sorption entirely. The theoretical curve closely matched the experimental data within the specified error limits for both cells. Furthermore, the breakthrough of HTO at an early stage, as mentioned in the literature [19], could be reproduced. This successful fit allowed for the determination of the diffusion parameters, porosity ε and the diffusion coefficient D_e , which are presented in Table 5 alongside a literature comparison [19,39]. The porosity ε represents the material's capacitance factor α for non-absorbing nuclides like HTO ($K_d = 0 \text{ L kg}^{-1}$). The results from the master thesis of Johanna Bott [39], conducted under parallel experimental conditions to the two cells in this study, agree well. It is important to note that Tits et al. [19] used a different water-cement ratio of 0.33 and a core thickness of 1 cm. Drawing definitive and unambiguous conclusions is challenging due to the specific characteristics of individual cementitious materials. However, existing literature suggests that D_e tends to decrease with decreasing water-cement ratio, indicating reduced porosity [40-42]. These findings could not be confirmed by the results obtained in this study. Additionally, different cement formulations exhibit distinct diffusion behaviors, as observed in current literature [42,43]. Consequently, it is crucial to compare experiments conducted under identical conditions for meaningful comparisons.

Table 5: Diffusion parameters of HTO through-diffusion test of both cells compared with literature [19].

	Cell I	Cell II	Master thesis J. Bott [39]	Tits et al. [19]
$D_e / \text{m}^2 \text{s}^{-1}$	$(1.73 \pm 0.005) \times 10^{-11}$	$(1.66 \pm 0.005) \times 10^{-11}$	$(1.3 \pm 0.2) \times 10^{-11}$	2.72×10^{-10}
ε	0.65 (± 0.02)	0.68 (± 0.02)	0.68 (± 0.01)	0.63

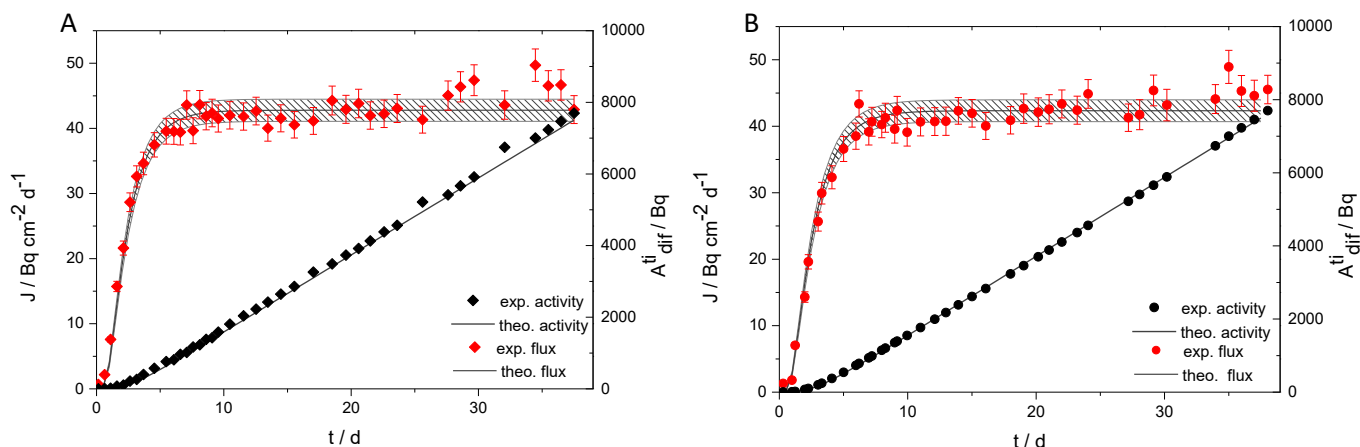


Figure 14: Experimental and theoretical representation of accumulated activity and flux with time course of HTO through-diffusion in cell I (A) and cell II (B) with $[\text{HTO}]_0/M = 1.6 \times 10^{-9}$ at $\text{pH} > 13$ and $V = 210 \text{ ml}$ in the secondary compartment.

After determining the diffusion parameters, the HTO present in both cells was completely removed by periodically replacing the reservoirs of both cells with inactive ACW for a duration of 90 ds. The LSC measurements obtained during this period are documented in Table A57 to Table A60. Additionally, the distribution of the accumulated activity in both compartments is shown in Figure A22 and Figure A23.

Pu in-diffusion

In the diffusion experiment involving $^{238}\text{Pu}(\text{IV})$, ISA was introduced to cell II in addition to the primary reservoir. Regular sampling was performed from the primary reservoir, and the samples were analyzed using α -spectroscopy. The experiment was conducted for a total of 118 d, running both cells in parallel. The concentration progression in the absence and presence of ISA is shown in Figure 15. The data in Figure 16A was modeled by [redacted] using the program Comsol.

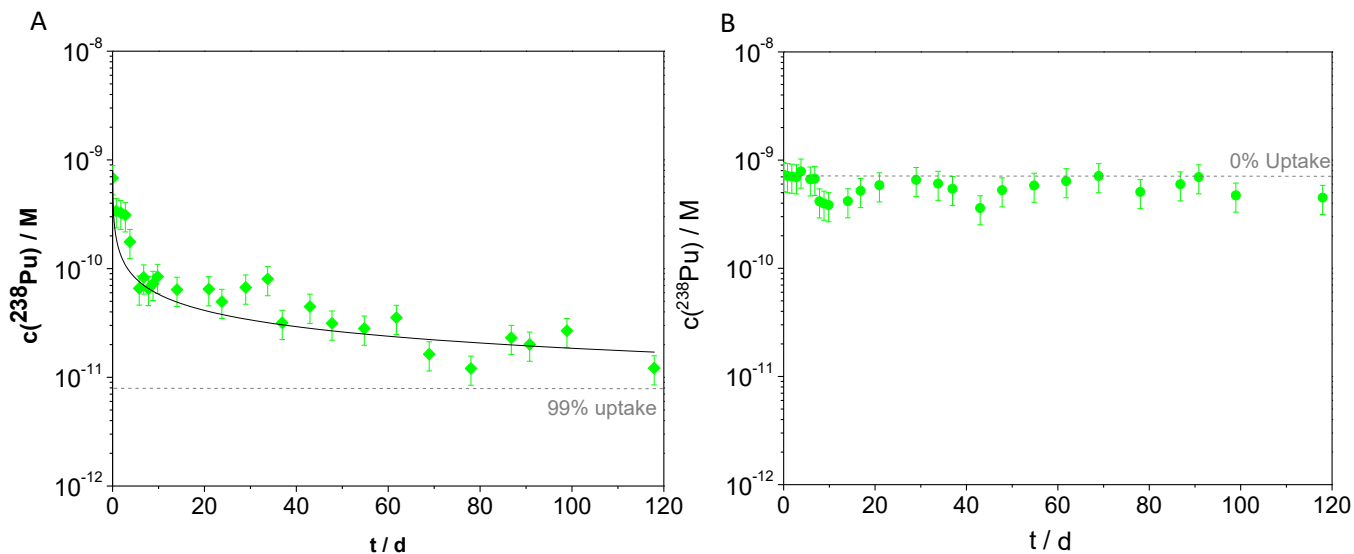


Figure 15: Concentration of $^{238}\text{Pu}(\text{IV})$ in the primary compartment ($V = 20 \text{ ml}$) determined with α -spectroscopy of the Pu in-diffusion experiments in absence (A) and presence (B) of ISA ($[\text{ISA}]_0/M = 2 \times 10^{-2}$) within 118 d.

A significant difference can be observed between the two cells. In cell I, without ISA, the concentration of Pu(IV) significantly decreases over time, with HCP already exhibiting an uptake of Pu(IV) of 90% by HCP after 6 d and at the end of the experiment after 118 d, an uptake of 98 % was obtained. Conversely, in cell II in the presence of ISA, only a low uptake of Pu(IV) by HCP is observed throughout the entire duration, with the concentration decreasing to $3.6 \times 10^{-11} \text{ M}$ and an average uptake of 21%. These findings are consistent with the results obtained from the batch sorption experiments. Simultaneous addition of Pu(IV) and ISA leads to a low uptake of around 15% after 119 d of contact time. This behavior aligns with the values reported by Tasi et al. [9], where systems with $S/L \leq 8 \text{ g L}^{-1}$ showed similar values of $[\text{Pu}_{\text{eq}}/M] \approx [\text{Pu}_{\text{in}}/M]$ even after 490 d of contact time, indicating that Pu does not sorb on HCP in the presence of ISA. Upon completion of the experiment, wall sorption of $^{238}\text{Pu}(\text{IV})$ was determined by rinsing the primary compartment with 50 ml of 2% HNO_3 . A wall sorption of 12% was determined for the cell without ISA, while the cell with ISA exhibited a wall sorption of 0.22%. This suggests that ISA also adsorbs onto the walls of the diffusion cell. The α -spectroscopy results of the wall sorption can be found in Table A61.

Additionally, the pH value was monitored and remained constant throughout the entire diffusion period. The Eh value was also measured at regular intervals. These data allowed for the construction of a predominance diagram, depicted in Figure 16. The measured values fall within the stability range of Pu(IV). In the presence of ISA, the determined values align with the range of the $\text{Pu}(\text{OH})_5(\text{HISA})_2^-$ complexes, which was already observed by the Eh measurements in the batch sorption experiment of

HCP / Pu(IV) / ISA, only one value is in the region of the $\text{CaPu}(\text{OH})_5(\text{HISA})$ complex due to the slightly lower pH value. While it is important to consider potential fluctuations in pH measurements within this high pH range.

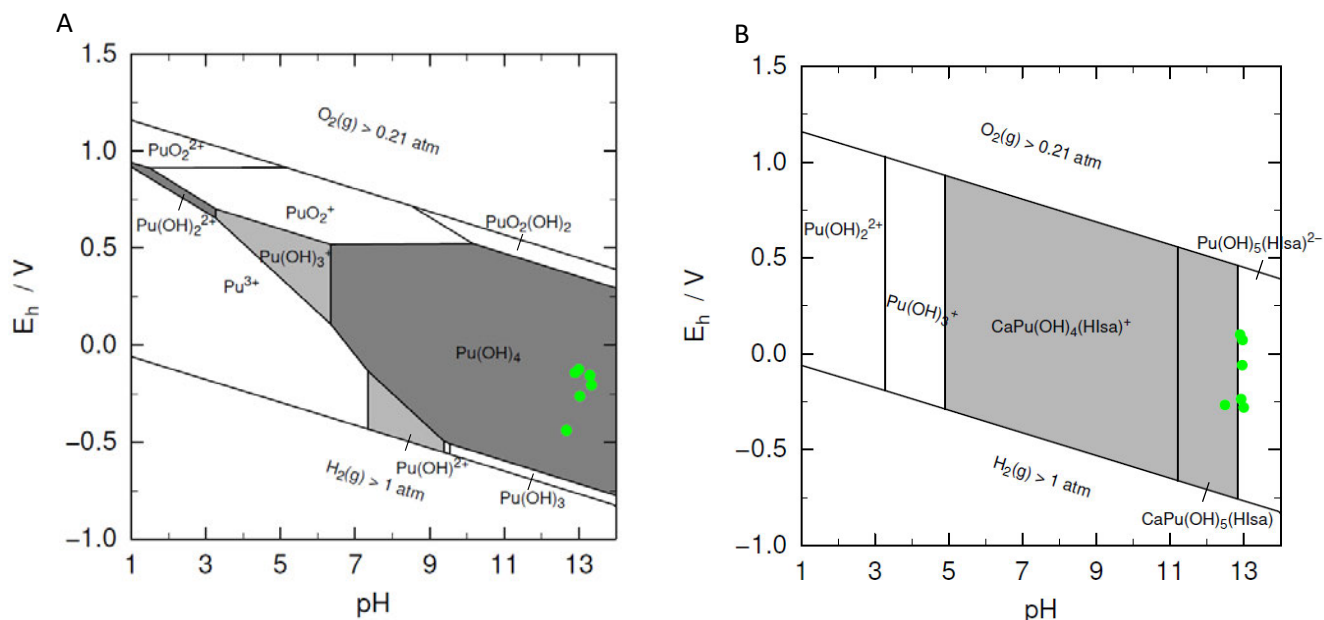


Figure 16: Predominance diagram of Pu calculated for $[\text{Pu}(\text{IV})]_0/M = 1 \times 10^{-10}$ in absence (A) and presence (B) of ISA $[\text{ISA}]_0/M = 1 \times 10^{-2}$ M in the system HCP / ACW ($[\text{Ca}]/M = 2 \times 10^{-3}$ M). The graphic was generated by PhreePlot (version 1.0 [38]) using PHREEQC and the ThermoChimie database 11a, 2022 [37] with complex formation constants determined by Tasi et al. [7,8]. The green dots mark the experimental pH and Eh values of the Pu in-diffusion experiment after different sampling times.

After the Pu in-diffusion experiment were concluded, the HCP cores were extracted from the cells and subjected to a drying process in the glovebox under Ar atmosphere for one week. Before further analysis, the cores underwent characterization using PSL (Photostimulated luminescence) imaging plate measurement (Imager) as well as microscopy or SEM imaging techniques. Subsequently, the cores were mounted with the secondary compartment side facing upwards on a sample holder. To obtain detailed information about the in-diffusion of Pu(IV), the abrasive peeling technique developed by Van Loon et al. [24] was employed to gradually remove layers of the core.

Imager

Spatially resolved images of activity were captured from both HCP cores to compare the discolorations of the core with potential Pu activity. For this purpose, an Elysia-Raytest Image Reader CR35 Bio (Dürr Medical, Germany) was utilized for measurement, and VistaEasy software was employed for image processing. The HCP core from the experiment without ISA was placed for 3 d, while the HCP core from the experiment with ISA was placed for 1 d under light rejection directly on the X-ray bearing plate. In the case of the latter core, measurements were taken after grinding off a few μm , as it was observed that Pu had diffused further into the HCP core. Figure 17 shows photos of the cores alongside the images from the Imager in the same orientation. White represents the highest activity, followed by blue, green to yellow/orange indicating lower activity levels. Red corresponds to the background with no activity. In the last photo (Figure 17(D)), the activity was very low, resulting in reduced contrast and a green background. Quantitative evaluation of the images was not possible due to varying exposure times and the absence of a calibration sample with the same nuclide and known activity taken simultaneously. Retrospective assignment of how both HCP cores were integrated into the cell was not feasible. A distinct difference can be observed in the HCP core from cell I (Figure 17(A) without ISA). No activity was detected in the notches of this core. Furthermore, a "white" or perhaps specular phase in the center right of the core photo also prevented activity assignment, as indicated by a red dot in the image. Different activity distributions on the core were discernible, but no specific assignment to individual phases could be made. The same applies to the HCP core from cell 2 (Figure 17(B) with ISA). It was noted during the measurement of grinding samples that $^{238}\text{Pu(IV)}$ diffused significantly further into the core compared to the core without ISA, prompting additional imager recordings after grinding off 578 μm and 2317 μm . Figure 17(C) displays a bright "splotch" in the photo of the core, consistent with the activity distribution depicted in the image. The discoloration of cement in the presence of ISA has already been discussed above. It can be concluded that ISA can diffuse deeper into the core in the form of a Ca-Pu-OH-ISA complex formed in solution. Even after 2317 μm , less activity is still visible on the surface of the core, but further removal of the core was not feasible as it would have also removed the sample holder.

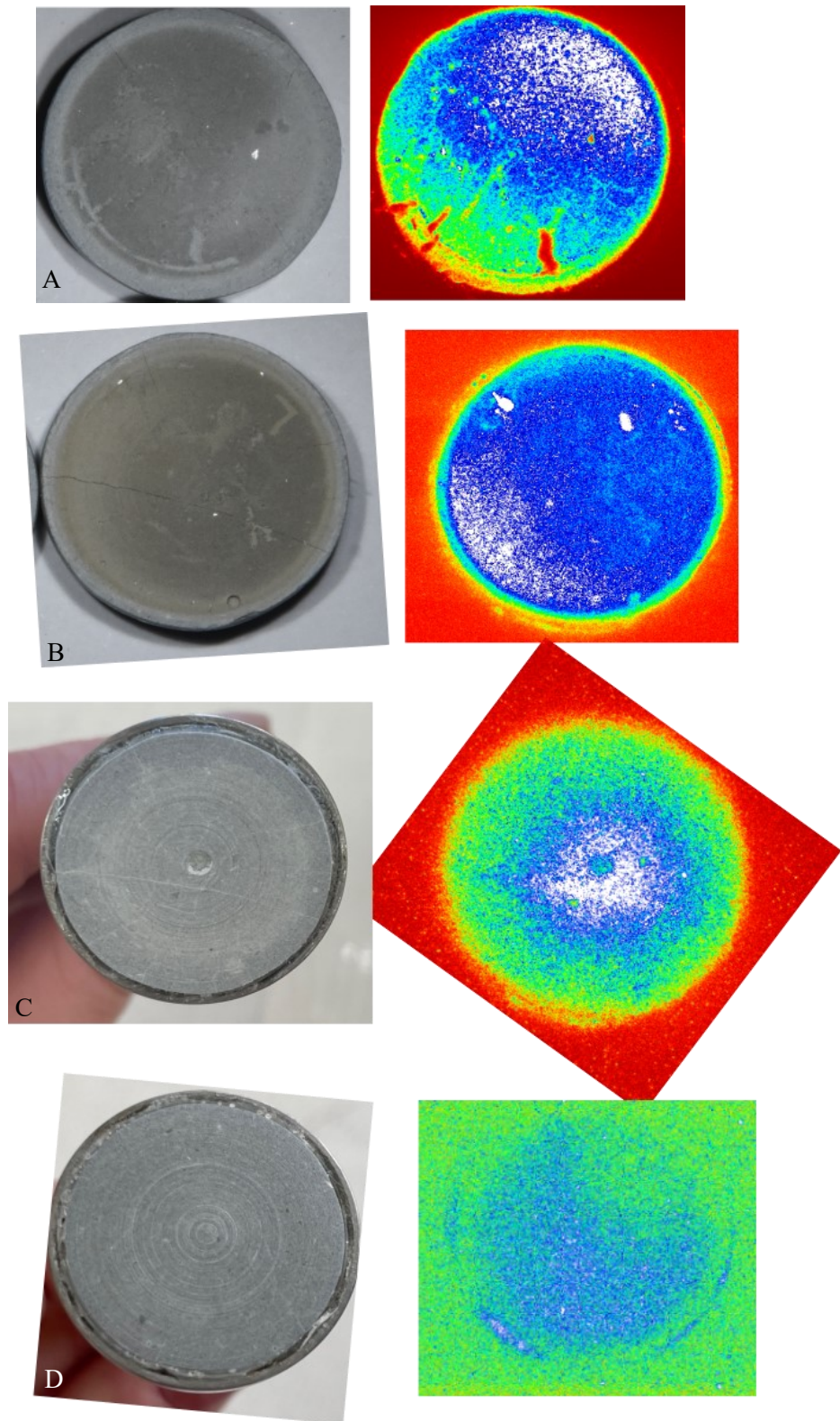


Figure 17: Photos and spatially resolved images of the activity of the HCP cores of the in-diffusion experiments in absence (A) and presence ((B) original core, (C) after 578 μm grinding, (D) after 2317 μm grinding) of ISA after the in-diffusion of $^{238}\text{Pu}(\text{IV})$. The images of the HCP cores were taken with PSL imaging plates after 1 d (B) and 3 d (A, C, D) contact time, respectively. In the color scheme used, white signifies the highest activity, followed by blue and green to yellow/orange, indicating progressively lower activity levels. The red color represents the background with no activity.

SEM

To further characterize the core, scanning electron microscope (SEM) images were captured using the Philips Inc. XL 30. Figure 18 shows backscattered electron (BSE) images of both HCP cores, taken from various areas. Clear surface changes can be observed, particularly at the edges of the cores. The location where the sealing ring was situated is clearly visible. The third image was captured from the center of the core from cell II (with ISA). It appears as if the cement has split open or that some ACW on the surface has dislodged. However, the images do not provide additional information regarding individual phases or differences between the cores with and without ISA. The surface of the cement cores could not be further characterized through energy-dispersive X-ray spectroscopy (EDX) analysis. The typical signals, including C, O, Na, Mg, Al, Si, K, Ca, Fe, and Pu, were detected (refer to Figure A25 and Figure A26). Since the core was subsequently ground off in this work, no polished sections were produced. To obtain localized information about changes in the cores, it is recommended to polish the cores.

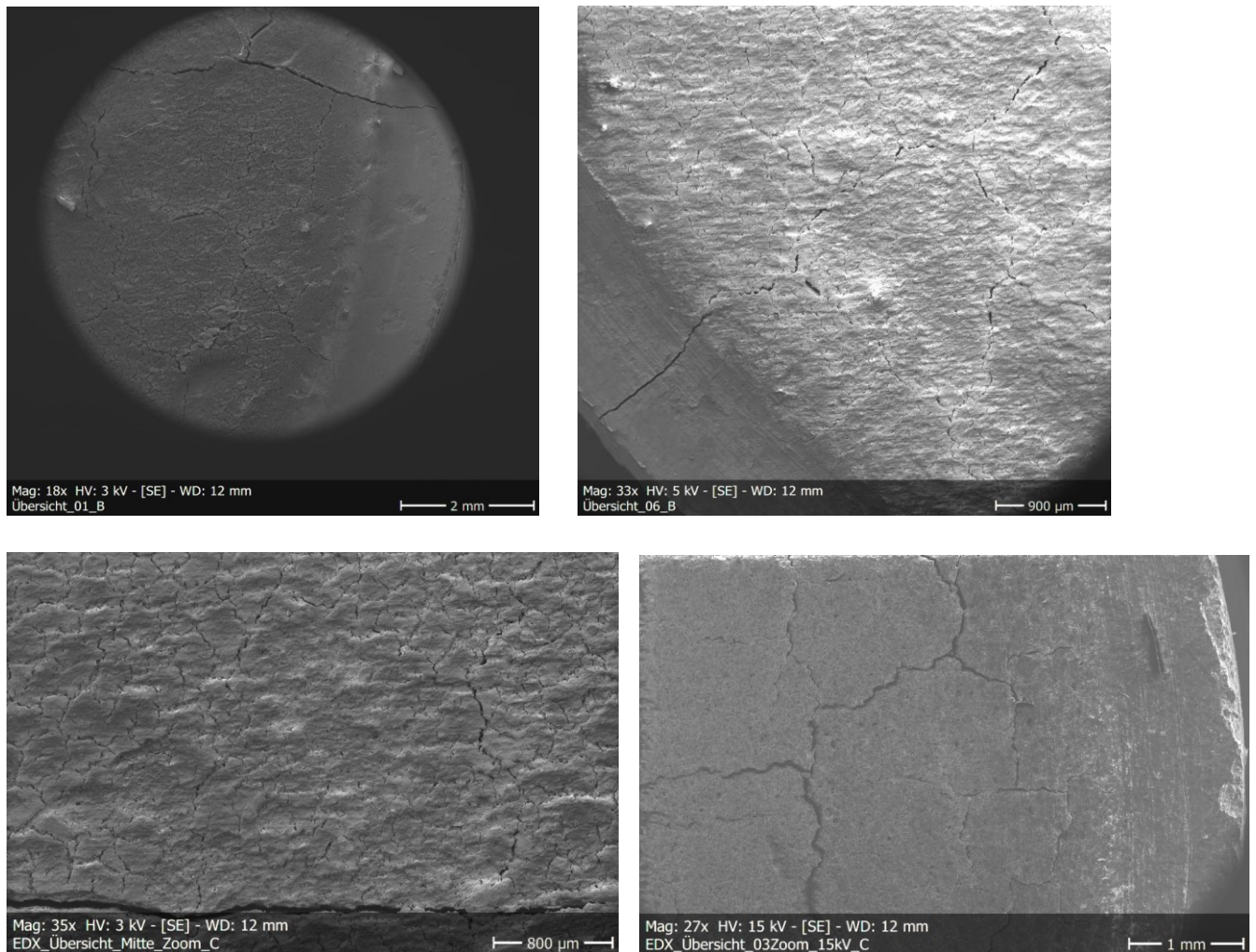


Figure 18: BSE images of the HCP cores of the in-diffusion experiments in the absence (top) and presence (bottom) of ISA after the in-diffusion of $^{238}\text{Pu(IV)}$.

Abrasive Peeling

After capturing spatially resolved images of the two cores, a hole was drilled in the center of each core to prevent protrusion during the circular grinding process. The activity of the individual grinding samples was determined using α -spectroscopy. Figure 19 show the experimental data. The diffusion profile of the core from cell I, in the absence of ISA, reveals that $^{238}\text{Pu(IV)}$ exhibits strong sorption at the HCP core, diffusing only up to a depth of 627 μm . In contrast, the diffusion profile of the HCP core from cell II, in the presence of ISA, demonstrates that Pu diffuses deeper into the core. Through α -measurements of the secondary compartment, it can be confirmed that $^{238}\text{Pu(IV)}$ did not diffuse through the HCP core, as no activity was detected in the secondary compartment. ISA appears to have a significant influence on the diffusion of $^{238}\text{Pu(IV)}$ into HCP. Firstly, there is a high uptake of ISA by HCP, leading to the blocking of sorption sites. Additionally, a Ca-Pu-OH-ISA complex forms in solution, potentially exhibiting different uptake behavior by HCP. No diffusion profiles of Pu on cement are reported in the literature. However, in J. Bott's master's thesis [39], a similar result was obtained for the Pu in-diffusion experiment in the absence of ISA, with a penetration depth of 300 μm of $^{238}\text{Pu(IV)}$ into HCP observed under high ionic strength and otherwise similar conditions, also within a contact time of 118 d. The modeling presented in Figure 20A was once again performed by [REDACTED] using the Comsol program. From this approach, specific values were obtained of $D_e = 1.70 \times 10^{-10} \text{ m}^2 \text{ s}^{-1}$ and $K_d = 1.0 \times 10^5 \text{ L kg}^{-1}$, resulting in a capacity factor $\alpha = 1.2 \times 10^5$. Initially, K_d was adjusted to fit the concentration boundary value in the first step, followed by the adjustment of D_e to match the profile depth in the second step. The reservoir curve in Figure 15A served as an independent verification check for the mass balance but was not utilized for parameter adjustment. In the batch sorption experiment of HCP / Pu(IV) after 119 days of contact time, a value of $K_d = 5.91 \times 10^4 \text{ L kg}^{-1}$ was obtained, which is in good agreement with the results from the diffusion experiments and confirms the high uptake of Pu(IV) on HCP in ACW at $\text{pH} > 13$.

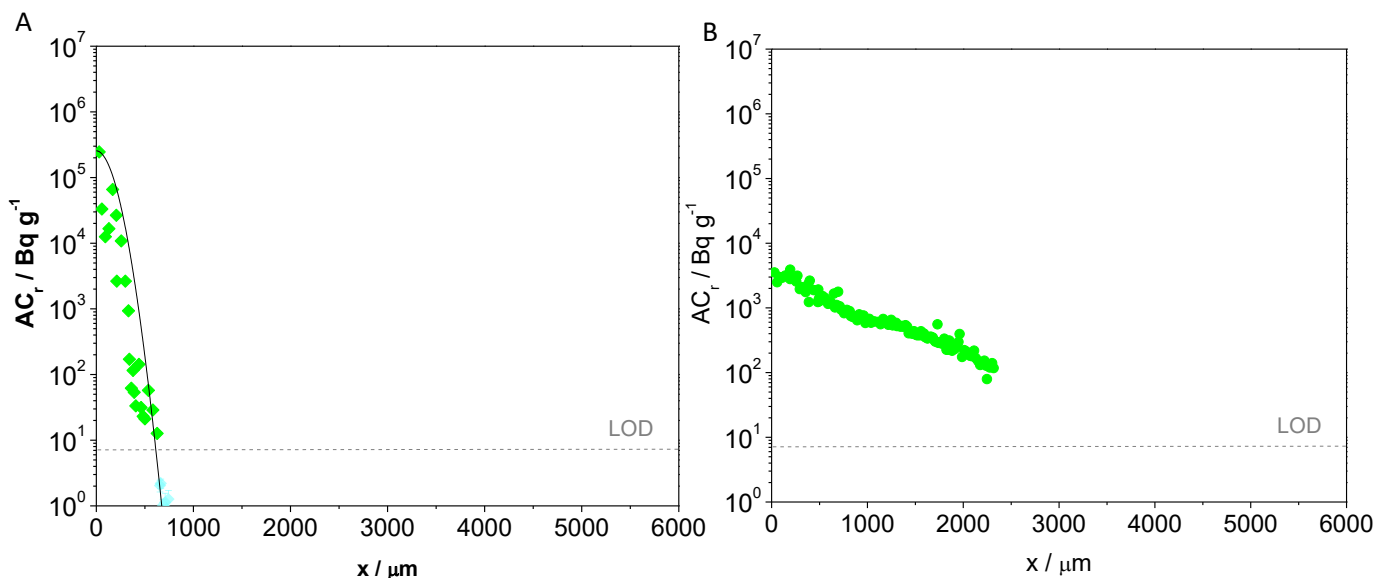


Figure 19: Experimental data of $^{238}\text{Pu(IV)}$ activity in the HCP core of the $^{238}\text{Pu(IV)}$ in-diffusion experiment in the absence (A) and presence (B) of ISA at $\text{pH} > 13$ ($[\text{Pu(IV)}]_0/M = 7 \times 10^{-10} \text{ M}$ $[\text{ISA}]_0/M = 1 \times 10^{-2} \text{ M}$). The x-axis represents the total height of the core ($h = 6 \text{ mm}$). The light blue dots are experimental data below the detection limit.

4. Summary

ISA exhibits strong sorption ($S\% = 2 - 13\%$) on HCP at a $\text{pH} > 13$. The presence of ISA has a significant impact on the sorption of Th(IV) and Pu(IV) on HCP, leading to a reduction in uptake. The findings from this study align well with values reported in literature. In addition, the formation of An(IV)-OH-ISA and Ca(II)-An(IV)-OH-ISA complexes was detected, which could also indicate complexation behavior in the batch sorption experiments. Although the measured mobilities are similar, it is not clear whether Th(IV) and Pu(IV) behave similarly upon complexation with ISA. The uptake on HCP of these two elements differ significantly, indicating that their interactions with ISA are distinct. The K_d values obtained from batch sorption and diffusion experiments for the Pu(IV) experiment on HCP in ACW at $\text{pH} > 13$ after contact times of 119 and 118 days, respectively, exhibit good agreement and confirm the high uptake of Pu(IV) on HCP. However, the diffusion experiments could not be modeled in the presence of ISA. Nevertheless, there is a clear indication that Pu(IV) diffused significantly deeper into the cement. This indicates a lower sorption of Pu(IV) on HCP, as was also observed in the batch sorption experiments. This behavior could be attributed to the high sorption affinity of ISA to HCP or the formation of Ca-Pu(IV)-ISA-OH complexes.

5. References

1. Wieland, E. *Sorption data base for the cementitious near-field of L/ILW and ILW repositories for provisional safety analyses for SGT-E2*; Paul Scherrer Institute (PSI): 2014.
2. Tits, J.; Wieland, E. *Actinide Sorption by Cementitious Materials; Technical Report*; Bericht Nr. 18-2; PSI: Villingen, Schweiz, 2018.
3. Wu, T.; Amayri, S.; Drebert, J.; Van Loon, L.R.; Reich, T. Neptunium(V) Sorption and Diffusion in Opalinus Clay. *Environ. Sci. Technol.* **2009**, *43*, 6567-6571.
4. Zhao, P.; Allen, P.G.; Sylwester, E.R.; Viani, B.E. The partitioning of uranium and neptunium onto hydrothermally altered concrete. *Radiochimica Acta* **2000**, *88*, 729-736.
5. Stietz, J.; Amayri, S.; Häußler, V.; Scholze, R.; Reich, T. Uptake of actinides by hardened cement paste in high-salinity pore water. *Minerals* **2023**.
6. Tasi, A.; Gaona, X.; Fellhauer, D.; Bottle, M.; Rothe, J.; Dardenne, K.; Schild, D.; Grive, M.; Colas, E.; Bruno, J.; et al. Redox behavior and solubility of plutonium under alkaline, reducing conditions. *Radiochimica Acta* **2018**, *106*, 259-279.
7. Tasi, A.; Gaona, X.; Fellhauer, D.; Böttle, M.; Rothe, J.; Dardenne, K.; Polly, R.; Grivé, M.; Colàs, E.; Bruno, J.; et al. Thermodynamic description of the plutonium – α -D-isosaccharinic acid system ii: Formation of quaternary Ca(II)–Pu(IV)–OH–ISA complexes. *Applied Geochemistry* **2018**, *98*, 351-366.
8. Tasi, A.; Gaona, X.; Fellhauer, D.; Böttle, M.; Rothe, J.; Dardenne, K.; Polly, R.; Grivé, M.; Colàs, E.; Bruno, J.; et al. Thermodynamic description of the plutonium – α -D-isosaccharinic acid system I: Solubility, complexation and redox behavior. *Applied Geochemistry* **2018**, *98*, 247-264.
9. Tasi, A.; Gaona, X.; Rabung, T.; Fellhauer, D.; Rothe, J.; Dardenne, K.; Lützenkirchen, J.; Grivé, M.; Colàs, E.; Bruno, J.; et al. Plutonium retention in the isosaccharinate – cement system. *Appl. Geochem.* **2021**, *126*, 104862.
10. Gaona, X.; Montoya, V.; Colàs, E.; Grivé, M.; Duro, L. Review of the complexation of tetravalent actinides by ISA and gluconate under alkaline to hyperalkaline conditions. *J. Contam. Hydrol.* **2008**, *102*, 217-227.
11. Tits, J.; Wieland, E.; Bradbury, M.H. The effect of isosaccharinic acid and gluconic acid on the retention of Eu(III), Am(III) and Th(IV) by calcite. *Appl. Geochem.* **2005**, *20*, 2082-2096.
12. Vercammen, K.; Glaus, M.; Van Loon, L.R. Complexation of Th(IV) and Eu(III) by α -isosaccharinic acid under alkaline conditions. *Radiochimica Acta* **2001**, *89*, 393-402.
13. Musso, H. Über Phenol-Oxydationen. *Angewandte Chemie* **1963**, *75*, 965-977.
14. Schwarzinger, C. Identification of methylated saccharinolactones and partially methylated saccharinic acids in the thermally assisted hydrolysis and methylation of carbohydrates. *Journal of analytical and applied pyrolysis* **2004**, *71*, 501-514.
15. Bontchev, R.P.; Moore, R.C. Crystal structure of sodium isosaccharate, NaC₆H₁₁O₆ · H₂O. *Carbohydrate research* **2004**, *339*, 801-805.
16. SDBS. https://sdb.sdb.aist.go.jp/sdb/cgi-bin/cre_index.cgi. Available online: (accessed on 12.04.2023).
17. Gelius, U.; Heden, P.; Hedman, J.; Lindberg, B.; Manne, R.; Nordberg, R.; Nordling, C.; Siegbahn, K. Molecular spectroscopy by means of ESCA III. Carbon compounds. *Physica Scripta* **1970**, *2*, 70.
18. Kaden, M.; Degering, D. *JAHRESBERICHT STRAHLENSCHUTZ 2019*; Bericht Nr. 18-2; VKTA - Strahlenschutz, Analytik & Entsorgung Rossendorf e. V. Helmholtz-Zentrums Dresden - Rossendorf e. V: 2020.
19. Tits, J.; Jakob, A.; Wieland, E.; Spieler, P. Diffusion of tritiated water and ²²Na⁺ through non-degraded hardened cement pastes. *J. Contam. Hydrol.* **2003**, *61*, 45-62.
20. Van Loon, L.; Eikenberg, J. A high-resolution abrasive method for determining diffusion profiles of sorbing radionuclides in dense argillaceous rocks. *Applied Radiation and Isotopes* **2005**, *63*, 11-21.
21. Zipperian, D. Silicon Carbide Abrasive Grinding. Pace Technologies. *Quality Matters Newsletter 1* **2002**, 1-3.

22. Van Loon, L.; Soler, J.; Jakob, A.; Bradbury, M. Effect of confining pressure on the diffusion of HTO, $^{36}\text{Cl}^-$ and $^{125}\text{I}^-$ in a layered argillaceous rock (Opalinus Clay): diffusion perpendicular to the fabric. *Applied Geochemistry* **2003**, *18*, 1653-1662.
23. Van Loon, L.R.; Soler, J.M.; Bradbury, M.H. Diffusion of HTO, $^{36}\text{Cl}^-$ and $^{125}\text{I}^-$ in Opalinus Clay samples from Mont Terri. *Journal of Contaminant Hydrology* **2003**, *61*, 73-83.
24. Van Loon, L.R.; Eikenberg, J. A high-resolution abrasive method for determining diffusion profiles of sorbing radionuclides in dense argillaceous rocks. *Applied Radiation and Isotopes* **2005**, *63*, 11-21.
25. Loon, L.R.v.; Glaus, M.A. *Experimental and Theoretical Studies on Alkaline Degradation of Cellulose and its Impact on the Sorption of Radionuclides*; 1019-0643; Switzerland, 1998; p. 156.
26. Van Loon, L.R.; Glaus, M.A.; Stallone, S.; Laube, A. Sorption of Isosaccharinic Acid, a Cellulose Degradation Product, on Cement. *Environ Sci Technol* **1997**, *31*, 1243-1245.
27. Pointeau, I.; Coreau, N.; Reiller, P. Uptake of anionic radionuclides onto degraded cement pastes and competing effect of organic ligands. *Radiochimica Acta* **2008**, 367.
28. Stietz, J.; Amayri, S.; Reich, T.; Haeussler, V.; Prieur, D. Uptake of Pu(IV) by hardened cement paste in the presence of gluconate at high and low ionic strengths. *Front. Nucl. Eng.* **2023**, *2*.
29. Wieland, E.; Tits, J.; Dobler, J.; Spieler, P. The effect of α -isosaccharinic acid on the stability of and Th(IV) uptake by hardened cement paste. *Radiochimica Acta* **2002**, *90*, 683-688.
30. A., T. *X-Ray Data Booklet, Center for X-ray optics advanced light source, X-Ray Data Booklet, second edition*; 2001; Volume LBNL/PUB-490 Rev.2.
31. Dettmann, S.; Huittinen, N.M.; Jahn, N.; Kretzschmar, J.; Kumke, M.U.; Kutyma, T.; Lohmann, J.; Reich, T.; Schmeide, K.; Shams Aldin Azzam, S.; et al. Influence of gluconate on the retention of Eu(III), Am(III), Th(IV), Pu(IV), and U(VI) by CSH (C/S= 0.8). *Front. Nucl. Eng.* **2023**, *2*.
32. Tits, J.; Wieland, E.; Bradbury, M.H.; Eckert, P.; Schaible, A. *The uptake of Eu(III) and Th(IV) by calcite under hyperalkaline conditions*; 1019-0643; Laboratory for Waste Management (LES): 2002; pp. i-xii, 1-78, A71-A14.
33. Goudarzi, R. *Prototype Repository – Sensor data report; Period 2001-09-17 to 2022-01-01; Report No 33*; 33; SKB: 2023.
34. Neck, V. Aquatic Chemistry and Solubility Phenomena of Actinoid Oxides/Hydroxides. *Pure and Applied Chemistry - PURE APPL CHEM* **2002**, *74*, 1895-1907.
35. Colàs Anguita, E. Complexation of Th(IV) and U(VI) by polyhydroxy and polyamino carboxylic acids. Universitat Politècnica de Catalunya, Barcelona, 2014.
36. Ochs, M.; Mallants, D.; Wang, L. *Radionuclide and Metal Sorption on Cement and Concrete*; Springer: 2016.
37. Giffaut, E.; Grivé, M.; Blanc, P.; Vieillard, P.; Colàs, E.; Gailhanou, H.; Gaboreau, S.; Marty, N.; Madé, B.; Duro, L. Andra thermodynamic database for performance assessment: ThermoChimie. *Appl. Geochem.* **2014**, *49*, 225-236.
38. Parkhurst, D.; Appelo, C.; 3.3.5), C.A.J.P.V. A Computer Program for Speciation, Batch-Reaction, One-Dimensional Transport, and Inverse Geochemical Calculations. Available online: http://wwwbr.cr.usgs.gov/projects/GWC_coupled/phreeqc/index.html (accessed on 15 June 2023).
39. Bott, J. Diffusion von Actiniden in Zementstein. Johannes Gutenberg-Universität Mainz, Mainz, 2022.
40. Yamaguchi, T.; Negishi, K.; Hoshino, S.; Tanaka, T. Modeling of diffusive mass transport in micropores in cement based materials. *Cement and Concrete Research* **2009**, *39*, 1149-1155.
41. Jakob, A.; Sarott, F.-A.; Spieler, P. *Diffusion and sorption on hardened cement pastes-experiments and modelling results*; Paul Scherrer Inst.: 1999.
42. Altmaier, M.; Blin, V.; Garcia, D.; Henocq, P.; Missana, T.; Ricard, D. SOTA on cement-organic-radionuclide interactions. *Final version as of 19.05.2021 of deliverable D3.1 of the HORIZON 2020 project EURAD. EC Grant agreement no: 847593* **2021**.
43. Grambow, B.; López-García, M.; Olmeda, J.; Grivé, M.; Marty, N.C.; Grangeon, S.; Claret, F.; Lange, S.; Deissmann, G.; Klinkenberg, M. Retention and diffusion of radioactive and toxic species on cementitious systems: Main outcome of the CEBAMA project. *Applied Geochemistry* **2020**, *112*, 104480.

2.4.1 Screening experiments

This Section discusses the results of a screening experiment conducted as a batch sorption experiment to investigate the order of addition of Th(IV) and the organic ligands oxalate, citrate, and phthalate on HCP. The experimental conditions were set as in the other batch sorption experiments ($[Th(IV)]_0/M = 1 \times 10^{-8}$; $[OL]_0/M = 1 \times 10^{-2}$; $pH = 13.3$; $S/L = 5 \text{ g L}^{-1}$). The measured values from the ICP-MS measurement, along with the calculated values, can be found in in the Appendix (Table A67 to Table A71). For this experiment, $R_{d,max} = 2.55 \times 10^5 \text{ L kg}^{-1}$ were calculated according to [92]. As shown in Figure 18, the order of reactant addition and the presence of citrate, oxalate, and phthalate did not influence the retention of Th(IV) on HCP after a contact time of 72 h. These observations align with the expectations based on the speciation diagram discussed in Section 1.4.2 and Figure A3 and Figure A4. At the pH levels (< 13) present in the samples, no complex is formed between Th(IV) and oxalate or citrate. The dominant species is $Th(OH)_4$, which is quantitatively present at high pH values. Furthermore, the measured values without organic ligands reported in the literature by Tits and Wieland are in the same order of magnitude, with R_d values of 10^5 L kg^{-1} [138]. This suggests that the presence of oxalate or citrate has no influence on sorption under the given experimental conditions. Regarding phthalate, no speciation diagram could be calculated due to the unavailability of data in the ThermoChimie database (version 11a (2022) [54]). No further data is available in the literature regarding the sorption of Th(IV) on cementitious materials under the influence of oxalate, citrate, and phthalate, respectively.

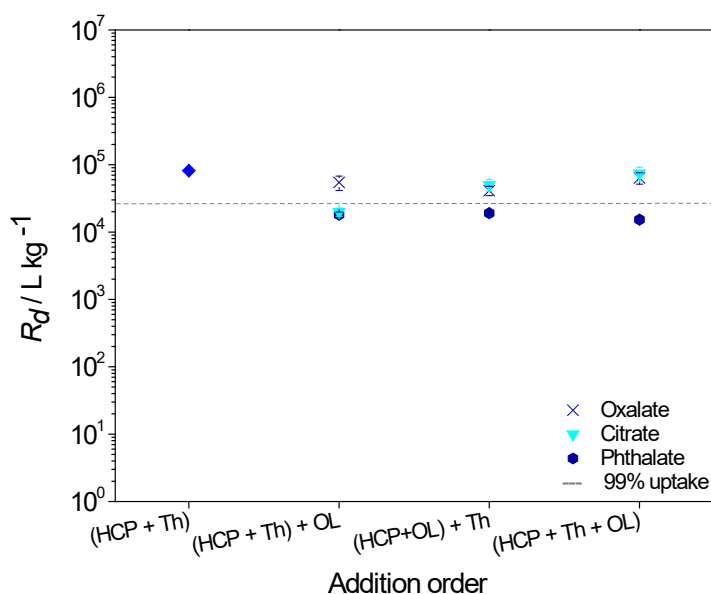


Figure 18: Average value from a double determination of the distribution coefficients R_d (L kg^{-1}) determined for Th(IV) uptake on HCP in presence of the organic ligands oxalate, citrate and phthalate ($[Th(IV)]_0/M = 1 \times 10^{-8}$, $[OL]_0/M = 1 \times 10^{-2}$, $S/L = 5 \text{ g L}^{-1}$, $pH 13.3$) after a contact time of 72 h.

Remarks

The investigations of Th(IV) on HCP in the presence the organic ligands oxalate, citrate and phthalate described above were carried out as part of a “Forschungsmodul” of [REDACTED] under the supervision of J. Stietz and [REDACTED] [137]. Sample preparation and measurements were performed by [REDACTED] and J. Stietz, the analysis presented here was conducted by J. Stietz.

3 Summary and conclusion

This study focused on investigating the influence of different organic ligands, such as GLU, EDTA, and ISA, on the retention of tri- and tetravalent actinides in the context of a deep geological radioactive waste repository. The experiments were conducted using HCP at pH = 13 representing fresh cement in the degradation state I and C-S-H phase with a C/S ratio of 0.8, representing degraded cement in the degradation stage III. An(III/IV) are strongly sorbing on cement under the reducing and hyperalkaline conditions in the absence of organic ligands. R_d values ($> 10^5 \text{ L kg}^{-1}$) determined in the present work are in good agreement with data available in the literature [22,103].

The sorption of GLU on HCP led to saturation of sorption sites and the experimental data was fitted using Langmuir-isotherm. No uptake of GLU on C-S-H phases (C/S = 0.8) were observed. Previous literature findings were confirmed [36,95], showing sorption of GLU is limited to the surface. Consequently, no blocking of sorption sites by GLU is anticipated during the cement degradation stage III and in the experiments An(III/IV) sorbs quantitatively onto the C-S-H phases (C/S = 0.8). Furthermore, the results showed that GLU had a significant impact on the uptake of Pu(IV), leading to decreased sorption on HCP at pH 13. The order of addition of Pu(IV) and GLU also affected the sorption, suggesting a competitive reaction between Pu(IV) and GLU. Lower GLU concentrations were expected in a repository, where Pu(OH)₄ was found to be the dominant species. Th(IV) showed a strong interaction with GLU, potentially leaching or mobilizing it from HCP.

EDTA did not sorb onto the solid phases of HCP and C-S-H under the experimental conditions, nor did it influence the quantitative uptake of An(III/IV) on HCP. The formation of An(IV)-OH-EDTA and Ca(II)-An(IV)-OH-EDTA complex species in solution was supported by different electrophoretic mobilities in the CE-ICP-MS measurements.

ISA exhibits similar behavior to GLU due to its similar structure. Consequently, ISA also demonstrates strong sorption onto HCP at a pH > 13 and the experimental data was modelled using the Langmuir-isotherm. Furthermore, ISA had a significant impact on the sorption of Th(IV) and Pu(IV) on HCP, leading to reduced uptake which confirm the results obtain in the literature [43]. Although there was some leaching of ²³²Th from HCP in the presence of ISA. Competitive reactions between An(IV) and ISA were observed, potentially involving desorption or the formation of complex species of An(IV)-OH-ISA and Ca(II)-An(IV)-OH-ISA. The diffusion experiments demonstrated the migration behavior of Pu(IV) within the HCP core, with deeper diffusion observed in the presence of ISA. The characterization techniques provided valuable information about the distribution and surface characteristics of the HCP cores.

Th(IV) and Pu(IV) displayed distinct behaviors and sorption mechanisms in the presence of organic ligands, underscoring the significance of acknowledging the characteristics of different actinides within complex systems. Overall, these findings contribute to the understanding of actinide behavior in a

radioactive waste repository. Optimizing containment strategies, evaluating the effectiveness of cementitious materials as engineered barriers, and ensuring the long-term safety of the repository can be informed by a comprehensive understanding of actinide-ligand interactions. Further investigations are recommended to examine the impact of other ligands that may be present in the repository setting. First, the diffusion experiments of Pu(IV) should be repeated in the presence and absence of ISA to confirm the results. In any case, also with longer contact times. Diffusion experiments in the presence and absence of EDTA would also be interesting. Since the sorption experiments showed no effect on the quantitative uptake of An(III/IV), it would be interesting to see if the complexes formed in solution with EDTA diffuse deeper into the cement core. In addition, experiments with repository-relevant concentrations, especially at GLU ($[GLU]_0/M = 1 \times 10^{-8}$) and longer contact times (several months), would be essential for a better understanding of the migration of An(III/IV) in cement. Additionally, studying the various stages of cement degradation is important for deep geological repositories and requires further research.

References

1. Saling, J. *Radioactive waste management*; CRC Press: 2001.
2. Ojovan, M.I.; Lee, W.E.; Kalmykov, S.N. *An introduction to nuclear waste immobilisation*; Elsevier: 2019.
3. Di Nucci, M.R.; Isidoro Losada, A.M. An open door for spent fuel and radioactive waste export? The international and EU framework. *Nuclear Waste Governance: An International Comparison* **2015**, 79-97.
4. Lee, W.E.; Ojovan, M.I.; Jantzen, C.M. *Radioactive waste management and contaminated site clean-up: Processes, technologies and international experience*; Elsevier: 2013.
5. Ferraro, G. *The politics of radioactive waste management: Public involvement and policy-making in the European Union*; Routledge: 2018.
6. Häikiö, J. Regulatory oversight of nuclear safety in Finland: Annual report 2021. **2022**.
7. Hämäläinen, J.; Suolainen, V. SAFIR2018-The Finnish Research Programme on Nuclear Power Plant Safety 2015-2018: Interim Report. **2017**.
8. Goudarzi, R. *Prototype Repository – Sensor data report; Period 2001-09-17 to 2022-01-01; Report No 33*; 33; SKB: 2023.
9. Pérot, B.; Jallu, F.; Passard, C.; Gueton, O.; Allinei, P.-G.; Loubet, L.; Estre, N.; Simon, E.; Carasco, C.; Roure, C. The characterization of radioactive waste: a critical review of techniques implemented or under development at CEA, France. *EPJ N-Nuclear Sciences & Technologies* **2018**, 4, 3.
10. Armand, G.; Plas, F.; Talandier, J.; Dizier, A.; Li, X.; Levasseur, S. Contribution of HADES URL to the development of the Cigéo project, the French industrial centre for geological disposal of high-level and long-lived intermediate-level radioactive waste in a deep clay formation. *Geological Society, London, Special Publications* **2023**, 536, SP536-2022-2098.
11. Richter, J.; Bernstein, M.J.; Farooque, M. The process to find a process for governance: Nuclear waste management and consent-based siting in the United States. *Energy Research & Social Science* **2022**, 87, 102473.
12. Corkhill, C.; Hyatt, N. *Nuclear waste management*; IOP Publishing: 2018.
13. Bredberg, I.; Hutter, J.; Kühn, K.; Niedzwiedz, K.; Philipczyk, F.; Thömmes, F. Statusbericht Zur Kernenergienutzung in Der Bundesrepublik Deutschland 2016. *Salzgitter: Bundesamt für kerntechnische Entsorgungssicherheit* **2017**.
14. https://www.base.bund.de/DE/themen/kt/ausstieg-atomkraft/ausstieg_node.html#:~:text=Der%20Bundestag%20hat%20am%2011.11,und%20sind%20dann%20abgeschaltet%20worden, . Available online: (accessed on 24.05.2023).
15. Gesetz zur Suche und Auswahl eines Standortes für ein Endlager für hochradioaktive Abfälle (Standortauswahlgesetz - StandAG). *StandAG* **2017**.
16. Lommerzheim, A.; Jobmann, M. *Projekt ANSICHT - Endlagerkonzept sowie Verfüll- und Verschlusskonzept für das Standortmodell NORD*; TEC-14-2015-TB; DBE Technology GmbH: 2015.
17. Jobmann, M.; Bebiolka, A.; Burlaka, V.; Herold, P.; Jahn, S.; Lommerzheim, A.; Maßmann, J.; Meleshyn, A.; Mrugalla, S.; Reinhold, K.; et al. Safety assessment methodology for a German high-level waste repository in clay formations. *J. Rock Mech. Geotech. Eng.* **2017**, 9, 856-876.
18. Brewitz, W. *Eignungsprüfung der Schachanlage Konrad für die Endlagerung radioaktiver Abfälle: Abschlussbericht (GSF - T 136)*; GSF: 1982.
19. Alexander, W.R.; McKinley, L. Deep geological disposal of radioactive waste. **2011**.
20. Tyupina, E.A.; Kozlov, P.P.; Krupskaya, V.V. Application of cement-based materials as a component of an engineered barrier system at geological disposal facilities for radioactive waste—A review. *Energies* **2023**, 16, 605.
21. Duro, L.; Altmaier, M.; Holt, E.; Mäder, U.; Claret, F.; Grambow, B.; Idiart, A.; Valls, A.; Montoya, V. Contribution of the results of the CEBAMA project to decrease uncertainties in the Safety Case and Performance Assessment of radioactive waste repositories. *Applied Geochemistry* **2020**, 112, 104479.
22. Ochs, M.; Mallants, D.; Wang, L. *Radionuclide and Metal Sorption on Cement and Concrete*; Springer: 2016.

23. Chen, Q.; Tyrer, M.; Hills, C.D.; Yang, X.; Carey, P. Immobilisation of heavy metal in cement-based solidification/stabilisation: A review. *Waste Manag* **2009**, *29*, 390-403.
24. AB, S.K. Safety analysis SFR. **2008**.
25. Tits, J.; Wieland, E.; Mueller, C.J.; Landesman, C.; Bradbury, M.H. Strontium binding by calcium silicate hydrates. *J. Colloid Interface Sci.* **2006**, *300*, 78-87.
26. Richardson, I. Tobermorite/jennite-and tobermorite/calcium hydroxide-based models for the structure of CSH: applicability to hardened pastes of tricalcium silicate, β -dicalcium silicate, Portland cement, and blends of Portland cement with blast-furnace slag, metakaolin, or silica fume. *Cement and Concrete Research* **2004**, *34*, 1733-1777.
27. Keith-Roach, M.; Shahkarami, P. *Organic materials with the potential for complexation in SFR, the final repository for short-lived radioactive waste. Investigation of new acceptance criteria* SKB R-21-03; SKB: Sweden, 2021.
28. Yamada, K.; Takahashi, T.; Hanehara, S.; Matsuhisa, M. Effects of the chemical structure on the properties of polycarboxylate-type superplasticizer. *Cement and Concrete Research* **2000**, *30*, 197-207.
29. NMR-SPEKTROSKOPIE, T.I.B.M.; PAR, D.D.A.D.B.; NUCLEAIRE, S.D.R.M. Determination of concrete admixtures in concrete by NMR spectroscopy. *Otto-Graf-Journal* **2003**, *14*, 101.
30. Winnefeld, F.; Becker, S.; Pakusch, J.; Götz, T. Effects of the molecular architecture of comb-shaped superplasticizers on their performance in cementitious systems. *Cement and Concrete Composites* **2007**, *29*, 251-262.
31. Altmaier, M.; Blin, V.; Garcia, D.; Henocq, P.; Missana, T.; Ricard, D. SOTA on cement-organic-radionuclide interactions. *Final version as of 19.05.2021 of deliverable D3.1 of the HORIZON 2020 project EURAD. EC Grant agreement no: 847593* **2021**.
32. Tits, J.; Wieland, E.; Bradbury, M.H. The effect of isosaccharinic acid and gluconic acid on the retention of Eu(III), Am(III) and Th(IV) by calcite. *Appl. Geochem.* **2005**, *20*, 2082-2096.
33. Gaona, X.; Montoya, V.; Colàs, E.; Grivé, M.; Duro, L. Review of the complexation of tetravalent actinides by ISA and gluconate under alkaline to hyperalkaline conditions. *J. Contam. Hydrol.* **2008**, *102*, 217-227.
34. Dettmann, S.; Huittinen, N.M.; Jahn, N.; Kretzschmar, J.; Kumke, M.U.; Kutyma, T.; Lohmann, J.; Reich, T.; Schmeide, K.; Shams Aldin Azzam, S.; et al. Influence of gluconate on the retention of Eu(III), Am(III), Th(IV), Pu(IV), and U(VI) by CSH (C/S= 0.8). *Front. Nucl. Eng.* **2023**, *2*.
35. Kutus, B.; Gaona, X.; Pallagi, A.; Pálincó, I.; Altmaier, M.; Sipos, P. Recent advances in the aqueous chemistry of the calcium(II)-gluconate system – Equilibria, structure and composition of the complexes forming in neutral and in alkaline solutions. *Coord. Chem. Rev.* **2020**, *417*, 213337.
36. Glaus, M.A.; Laube, A.; Van Loon, L.R. Solid-liquid distribution of selected concrete admixtures in hardened cement pastes. *Waste Manag* **2006**, *26*, 741-751.
37. Keith-Roach, M.; Lindgren, M.; Källström, K. Assessment of complexing agent concentrations in SFR. *Swedish Nuclear Fuel and Waste Management Co, Stockholm, Sweden* **2014**.
38. Fanger, G.; Skagius, K.; Wiborgh, M. *Project SAFE. Complexing agents in SFR*; Swedish Nuclear Fuel and Waste Management Co.: 2001.
39. DiBlasi, N.A.; Tasi, A.G.; Gaona, X.; Fellhauer, D.; Dardenne, K.; Rothe, J.; Reed, D.T.; Hixon, A.E.; Altmaier, M. Impact of Ca(II) on the aqueous speciation, redox behavior, and environmental mobility of Pu(IV) in the presence of EDTA. *Science of The Total Environment* **2021**, *783*, 146993.
40. Wieland, E.; Tits, J.; Dobler, J.; Spieler, P. The effect of α -isosaccharinic acid on the stability of and Th(IV) uptake by hardened cement paste. *Radiochimica Acta* **2002**, *90*, 683-688.
41. Van Loon, L.R.; Glaus, M.A.; Stallone, S.; Laube, A. Sorption of Isosaccharinic Acid, a Cellulose Degradation Product, on Cement. *Environ Sci Technol* **1997**, *31*, 1243-1245.
42. García, D.; Henocq, P.; Riba, O.; López-García, M.; Madé, B.; Robinet, J.-C. Adsorption behaviour of isosaccharinic acid onto cementitious materials. *Applied Geochemistry* **2020**, *118*, 104625.

43. Tasi, A.; Gaona, X.; Rabung, T.; Fellhauer, D.; Rothe, J.; Dardenne, K.; Lützenkirchen, J.; Grivé, M.; Colàs, E.; Bruno, J.; et al. Plutonium retention in the isosaccharinate – cement system. *Appl. Geochem.* **2021**, *126*, 104862.
44. Van Loon, L.; Glaus, M.; Vercammen, K.; Ghosh, S.; Andersson, P.; Møller, J.; Senning, A.; Yao, X.-K.; Wang, H.-G.; Tuchagues, J.P.; et al. Solubility Products of Calcium Isosaccharinate and Calcium Gluconate. *Acta Chemica Scandinavica - ACTA CHEM SCAND* **1999**, *53*, 235-240.
45. Charlet, L.; Schindler, P.; Spadini, L.; Furrer, G.; Zysset, M. Cation adsorption on oxides and clays: The aluminum case. *Aquatic sciences* **1993**, *55*, 291-303.
46. Panfili, F. Etude de l'évolution de la spéciation du zinc dans la phase solide d'un sédiment de curage contaminé, induit par phytostabilisation. Université de Provence-Aix-Marseille I, 2004.
47. Manceau, A.; Marcus, M.A.; Tamura, N. Quantitative speciation of heavy metals in soils and sediments by synchrotron X-ray techniques. *Reviews in mineralogy and geochemistry* **2002**, *49*, 341-428.
48. Dresden-Rossendorf, H.-Z. <https://www.yumpu.com/de/document/read/22401507/sorption-skript-2011-hzdr>. Available online: (accessed on 01.06.2023).
49. Freundlich, H. Über die adsorption in lösungen. *Zeitschrift für physikalische Chemie* **1907**, *57*, 385-470.
50. Langmuir, I. The constitution and fundamental properties of solids and liquids. Part I. Solids. *Journal of the American chemical society* **1916**, *38*, 2221-2295.
51. Atkins, P.; Atkins, P.W.; de Paula, J. *Atkins' physical chemistry*; Oxford university press: 2014.
52. Poinssot, C.; Geckeis, H. *Radionuclide behaviour in the natural environment: science, implications and lessons for the nuclear industry*; Elsevier: 2012.
53. Parkhurst, D.; Appelo, C.; 3.3.5), C.A.J.P.V. A Computer Program for Speciation, Batch-Reaction, One-Dimensional Transport, and Inverse Geochemical Calculations. Available online: http://wwwbrr.cr.usgs.gov/projects/GWC_coupled/phreeqc/index.html (accessed on 15 June 2023).
54. Giffaut, E.; Grivé, M.; Blanc, P.; Vieillard, P.; Colàs, E.; Gailhanou, H.; Gaboreau, S.; Marty, N.; Madé, B.; Duro, L. Andra thermodynamic database for performance assessment: ThermoChimie. *Appl. Geochem.* **2014**, *49*, 225-236.
55. Häußler, V.; Amayri, S.; Beck, A.; Platte, T.; Stern, T.A.; Vitova, T.; Reich, T. Uptake of actinides by calcium silicate hydrate (C-S-H) phases. *Appl. Geochem.* **2018**, 426-434.
56. Pallagi, A.; Bajnóczi, É.G.; Canton, S.E.; Bolin, T.; Peintler, G.; Kutus, B.; Kele, Z.; Pálinkó, I.; Sipos, P. Multinuclear complex formation between Ca(II) and gluconate ions in hyperalkaline solutions. *Environ. Sci. Technol.* **2014**, *48*, 6604-6611.
57. Nash, K.L.; Borkowski, M.; Hancock, M.; Laszak, I. Oxidative Leaching of Plutonium from Simulated Hanford Tank-Waste Sludges. *Separation science and technology* **2005**, *40*, 1497-1512.
58. Zhang, Z.; Clark, S.B.; Tian, G.; Zanonato, P.L.; Rao, L. Protonation of D-gluconate and its complexation with Np(V) in acidic to nearly neutral solutions. *Radiochimica Acta* **2006**, *94*, 531-536.
59. Zhang, Z.; Helms, G.; Clark, S.B.; Tian, G.; Zanonato, P.; Rao, L. Complexation of uranium (VI) by gluconate in acidic solutions: a thermodynamic study with structural analysis. *Inorganic Chemistry* **2009**, *48*, 3814-3824.
60. Zhang, Z.; Bottenus, B.; Clark, S.B.; Tian, G.; Zanonato, P.; Rao, L. Complexation of gluconic acid with Nd(III) in acidic solutions: A thermodynamic study. *Journal of alloys and compounds* **2007**, *444*, 470-476.
61. Böszörményi, É.; Lado, J.; Dudás, C.; Kutus, B.; Szabados, M.; Varga, G.; Pálinkó, I.; Sipos, P. The structure and composition of solid complexes comprising of Nd(III), Ca(II) and D-gluconate isolated from solutions relevant to radioactive waste disposal. *Pure Appl. Chem.* **2020**, *92*, 1709-1715.
62. Singh, N.B. Effect of gluconates on the hydration of cement. *Cement and Concrete Research* **1976**, *6*, 455-460.
63. Ramachandran, V.S.; Lowery, M.S. Conduction calorimetric investigation of the effect of retarders on the hydration of Portland cement. *Thermochimica Acta* **1992**, *195*, 373-387.

64. Jolicoeur, C.; Simard, M.-A. Chemical admixture-cement interactions: Phenomenology and physico-chemical concepts. *Cement and Concrete Composites* **1998**, *20*, 87-101.
65. Colàs, E.; Grivé, M.; Rojo, I.; Duro, L. Solubility of $\text{ThO}_2 \cdot x \text{H}_2\text{O}(\text{am})$ in the presence of gluconate. *Radiochimica Acta* **2011**, *99*, 269-273.
66. Colàs, E.; Grivé, M.; Rojo, I.; Duro, L. The effect of gluconate and EDTA on thorium solubility under simulated cement porewater conditions. *J Solution Chem* **2013**, *42*, 1680-1690.
67. Pointeau, I.; Hainos, D.; Coreau, N.; Reiller, P. Effect of organics on selenite uptake by cementitious materials. *Waste Manag* **2006**, *26*, 733-740.
68. Rojo, H.; Gaona, X.; Rabung, T.; Polly, R.; García-Gutiérrez, M.; Missana, T.; Altmaier, M. Complexation of Nd(III)/Cm(III) with gluconate in alkaline NaCl and CaCl_2 solutions: Solubility, TRLFS and DFT studies. *Appl. Geochem.* **2021**, *126*, 104864.
69. McFadden, K. *Organic components of nuclear wastes and their potential for altering radionuclide distribution when released to soil*; Battelle Pacific Northwest Labs.: 1980.
70. Rai, D.; Moore, D.; Rosso, K.; Felmy, A.; Bolton, H. Environmental Mobility of Pu(IV) in the Presence of Ethylenediaminetetraacetic Acid: Myth or Reality? *Journal of Solution Chemistry* **2008**, *37*, 957-986.
71. Meyer, M.; Burgat, R.; Faure, S.; Batifol, B.; Hubinois, J.-C.; Chollet, H.; Guilard, R. Thermodynamic studies of actinide complexes. 1. A reappraisal of the solution equilibria between plutonium(IV) and ethylenediaminetetraacetic acid (EDTAH_4) in nitric media. *Comptes Rendus Chimie* **2007**, *10*, 929-947.
72. DiBlasi, N.A.; Tasi, A.; Trumm, M.; Schnurr, A.; Gaona, X.; Fellhauer, D.; Dardenne, K.; Rothe, J.; Reed, D.T.; Hixon, A.E.; et al. Pu(III) and Cm(III) in the presence of EDTA: aqueous speciation, redox behavior, and the impact of Ca(II). *Royal Society of Chemistry* **2022**, *12*, 9478-9493.
73. Glaus, M.A.; Van Loon, L.R. Degradation of cellulose under alkaline conditions: new insights from a 12 years degradation study. *Environ Sci Technol* **2008**, *42*, 2906-2911.
74. Glaus, M.; Van Loon, L.; Achatz, S.; Chodura, A.; Fischer, K. Degradation of cellulosic materials under the alkaline conditions of a cementitious repository for low and intermediate level radioactive waste: Part I: Identification of degradation products. *Analytica Chimica Acta* **1999**, *398*, 111-122.
75. Pavasars, I.; Hagberg, J.; Borén, H.; Allard, B. Alkaline degradation of cellulose: mechanisms and kinetics. *Journal of Polymers and the Environment* **2003**, *11*, 39-47.
76. Bradbury, M.H.; Van Loon, L.R. *Cementitious near-field sorption data bases for performance assessment of a L/ILW repository in a Palfris Marl host rock*; Paul Scherrer Institut: 1997.
77. Van Loon, L.; Glaus, M.; Laube, A.; Stallone, S. Degradation of cellulosic materials under the alkaline conditions of a cementitious repository for low-and intermediate-level radioactive waste. II. Degradation kinetics. *Journal of environmental polymer degradation* **1999**, *7*, 41-51.
78. Aspinall, G.; Carter, M.E.; Los, M. 938. The degradation of xylobiose and xylotriose by alkali. *Journal of the Chemical Society (Resumed)* **1956**, 4807-4810.
79. Randall, M.; Rigby, B.; Thomson, O.; Trivedi, D. Assessment of the effects of cellulose degradation products on the behaviour of europium and thorium *National Nuclear Laboratory, Chadwick House, Warrington, UK* **2013**.
80. Van Loon, L.R.; Glaus, M.A. Experimental and theoretical studies on alkaline degradation of cellulose and its impact on the sorption of radionuclides. **1998**.
81. Pavasars, I. *Characterisation of organic substances in waste materials under alkaline conditions*. Linköping University Electronic Press, 1999.
82. Loon, L.R.V.; Glaus, M.A.; Laube, A.; Stallone, S. Degradation of Cellulosic Materials under the Alkaline Conditions of a Cementitious Repository for Low- and Intermediate Level Radioactive Waste. Part III: Effect of Degradation Products on the Sorption of Radionuclides on Feldspar. *Radiochimica Acta* **1999**, *86*, 183-190.
83. Rai, D.; Kitamura, A. Thermodynamic equilibrium constants for important isosaccharinate reactions: A review. *The Journal of Chemical Thermodynamics* **2017**, *114*, 135-143.
84. Seaborg, G.T. The Transuranium Elements. *Science* **1946**, *104*, 379-386.
85. Hoffmann, K. *Kann man Gold machen?: Gauner, Gaukler und Gelehrte: aus der Geschichte der chemischen Elemente*; Urania-Verlag: 1979.

86. Kostecka, K. Americium—from discovery to the smoke detector and beyond. *Bull. Hist. Chem* **2008**, *33*, 89-93.
87. Morss, L.R.; Edelstein, N.M.; Fuger, J.; Katz, J. *The Chemistry of the Actinide and Transactinide Elements (Volumes 1-5)*; Springer: 2006.
88. Wickleder, M.; Fourest, B.; Dorhout, P. The chemistry of The actinide and Transactinide Elements. *Springer* **2010**, *1*, 52-55.
89. MOIR, R.; Teller, E. 'Thorium Fueled Reactor Using Molten Salt Technology. *Nucl. Technol* **2005**, *151*, 334.
90. Jaradat, S.Q.M. *Impact of thorium based molten salt reactor on the closure of the nuclear fuel cycle*; Missouri University of Science and Technology: 2015.
91. Xia, Y.X.; Felmy, A.; Rao, L.; Wang, Z.; Hess, N. Thermodynamic model for the solubility of ThO₂(am) in the aqueous Na⁺-H⁺-OH⁻-NO₃⁻-H₂O-EDTA system. *Radiochimica Acta* **2003**, *91*, 751-760.
92. Tits, J.; Wieland, E.; Bradbury, M.H.; Eckert, P.; Schaible, A. *The uptake of Eu(III) and Th(IV) by calcite under hyperalkaline conditions*; 1019-0643; Laboratory for Waste Management (LES): 2002; pp. i-xii, 1-78, A71-A14.
93. Tasi, A.; Gaona, X.; Fellhauer, D.; Böttle, M.; Rothe, J.; Dardenne, K.; Polly, R.; Grivé, M.; Colàs, E.; Bruno, J.; et al. Thermodynamic description of the plutonium – α -D-isosaccharinic acid system I: Solubility, complexation and redox behavior. *Applied Geochemistry* **2018**, *98*, 247-264.
94. Tasi, A.; Gaona, X.; Fellhauer, D.; Böttle, M.; Rothe, J.; Dardenne, K.; Polly, R.; Grivé, M.; Colàs, E.; Bruno, J.; et al. Thermodynamic description of the plutonium – α -D-isosaccharinic acid system ii: Formation of quaternary Ca(II)-Pu(IV)-OH-ISA complexes. *Applied Geochemistry* **2018**, *98*, 351-366.
95. Androniuk, I. Effects of cement organic additives on the adsorption of uranyl ions on calcium silicate hydrate phases: experimental determination and computational molecular modelling. *Phys. Chem. Earth* **2017**, *99*, 194-203.
96. Nalet, C.; Nonat, A. Ionic complexation and adsorption of small organic molecules on calcium silicate hydrate: Relation with their retarding effect on the hydration of C3S. *Cement and Concrete Research* **2016**, *89*, 97-108.
97. Loon, L.R.v.; Glaus, M.A. *Experimental and Theoretical Studies on Alkaline Degradation of Cellulose and its Impact on the Sorption of Radionuclides*; 1019-0643; Switzerland, 1998; p. 156.
98. Brinkmann, H.; Patzschke, M.; Kaden, P.; Raiwa, M.; Rossberg, A.; Kloditz, R.; Heim, K.; Moll, H.; Stumpf, T. Complex formation between UO₂²⁺ and α -isocaccharinic acid: insights on a molecular level. *Dalton Trans* **2019**, *48*, 13440-13457.
99. Pointeau, I.; Coreau, N.; Reiller, P. Uptake of anionic radionuclides onto degraded cement pastes and competing effect of organic ligands. *Radiochimica Acta* **2008**, 367.
100. Mandaliev, P.; Stumpf, T.; Tits, J.; Dahn, R.; Walther, C.; Wieland, E. Uptake of Eu(III) by 11 Å tobermorite and xonotlite: A TRLFS and EXAFS study. *Geochim. Cosmochim. Acta* **2011**, *75*, 2017-2029.
101. Gaona, X.; Dähn, R.; Tits, J.; Scheinost, A.C.; Wieland, E. Uptake of Np(IV) by C-S-H phases and cement paste: An EXAFS study. *Environ. Sci. Technol.* **2011**, *45*, 8765-8771.
102. Wieland, E. *Sorption data base for the cementitious near-field of L/ILW and ILW repositories for provisional safety analyses for SGT-E2*; Paul Scherrer Institute (PSI): 2014.
103. Tits, J.; Wieland, E. *Actinide Sorption by Cementitious Materials; Technical Report*; Bericht Nr. 18-2; PSI: Villingen, Schweiz, 2018.
104. Höglund, S.; Eliasson, L.; Allard, B.; Andersson, K.; Torstenfelt, B. Sorption of some fission products and actinides in concrete systems. *MRS Online Proceedings Library (OPL)* **1985**, *50*, 683.
105. Allard, B.; Eliasson, L.; Andersson, K. *Technical Report - Sorption of Cs, I and actinides in concrete systems*; 84-15; SKB - KBS: Stockholm, Schweden, 1984.
106. Androniuk, I.; Kalinichev, A.G. Molecular dynamics simulation of the interaction of uranium (VI) with the C-S-H phase of cement in the presence of gluconate. *Applied Geochemistry* **2020**, *113*, 104496.

107. Allard, B.; Andersson, K. *Chemical properties of radionuclides in a cementitious environment*; Swedish Nuclear Fuel and Waste Management Company: 1987.
108. May, C.C.; Young, L.; Worsfold, P.J.; Heath, S.; Bryan, N.D.; Keith-Roach, M.J. The effect of EDTA on the groundwater transport of thorium through sand. *Water research* **2012**, *46*, 4870-4882.
109. Reinoso-Maset, E.; Worsfold, P.J.; Keith-Roach, M.J. The effect of EDTA, NTA and picolinic acid on Th (IV) mobility in a ternary system with natural sand. *Environmental pollution* **2012**, *162*, 399-405.
110. Reinoso-Maset, E.; Worsfold, P.J.; Keith-Roach, M.J. Effect of organic complexing agents on the interactions of Cs⁺, Sr²⁺ and UO₂²⁺ with silica and natural sand. *Chemosphere* **2013**, *91*, 948-954.
111. Humphreys, P.; Laws, A.; Dawson, J. A review of cellulose degradation and the fate of degradation products under repository conditions. **2010**.
112. Kuippers, G.; Boothman, C.; Bagshaw, H.; Ward, M.; Beard, R.; Bryan, N.; Lloyd, J.R. The biogeochemical fate of nickel during microbial ISA degradation; implications for nuclear waste disposal. *Scientific Reports* **2018**, *8*, 8753.
113. Diesen, V.; Forsberg, K.; Jonsson, M. Effects of cellulose degradation products on the mobility of Eu(III) in repositories for low and intermediate level radioactive waste. *Journal of Hazardous Materials* **2017**, *340*, 384-389.
114. Holgersson, S.; Albinsson, Y. Effects of Gluco-isosaccharinate on Cs, Ni, Pm and Th Sorption onto, and Diffusion into Cement. *Radiochim. Acta* **1998**, *82*, 393-398.
115. Baston, G.; Berry, J.; Brownsword, M.; Heath, T.; Tweed, C.; Williams, S. Sorption of plutonium and americium on repository, backfill and geological materials relevant to the JNFL low-level radioactive waste repository at Rokkasho-Mura. *MRS Online Proceedings Library (OPL)* **1994**, 353.
116. Bucur, C.; Olteanu, M.; Cristache, C.; Pavelescu, M. Radionuclide transport through cement matrices. *Revista De Chimie* **2010**, *61*, 458-461.
117. Felipe-Sotelo, M.; Hinchliff, J.; Drury, D.; Evans, N.; Williams, S.; Read, D. Radial diffusion of radiocaesium and radioiodide through cementitious backfill. *Physics and Chemistry of the Earth, Parts A/B/C* **2014**, *70*, 60-70.
118. Akagi, Y.; Kato, H.; Tachi, Y.; Sakamoto, H. Diffusion and sorption behavior of HTO, Cs, I and U in mortar. *Progress in nuclear science and technology* **2018**, *5*, 233-236.
119. Shafikhani, M.; Chidiac, S. Quantification of concrete chloride diffusion coefficient—A critical review. *Cement and Concrete Composites* **2019**, *99*, 225-250.
120. Tits, J.; Jakob, A.; Wieland, E.; Spieler, P. Diffusion of tritiated water and ²²Na⁺ through non-degraded hardened cement pastes. *J. Contam. Hydrol.* **2003**, *61*, 45-62.
121. Mattigod, S.V.; Whyatt, G.A.; Serne, R.J.; Schwab, K.E.; Wood, M.I. *Diffusion and leaching of selected radionuclides (Iodine-129, Technetium-99, and Uranium) through category 3 waste encasement concrete and soil fill material*; Pacific Northwest National Lab.(PNNL), Richland, WA (United States): 2001.
122. Albinsson, Y.; Boerjesson, S.; Andersson, K.; Allard, B. *Diffusion of radionuclides in concrete/bentonite systems*; Swedish Nuclear Fuel and Waste Management Co.: 1993.
123. Grambow, B.; López-García, M.; Olmeda, J.; Grivé, M.; Marty, N.C.; Grangeon, S.; Claret, F.; Lange, S.; Deissmann, G.; Klinkenberg, M. Retention and diffusion of radioactive and toxic species on cementitious systems: Main outcome of the CEBAMA project. *Applied Geochemistry* **2020**, *112*, 104480.
124. Jakob, A.; Sarott, F.-A.; Spieler, P. *Diffusion and sorption on hardened cement pastes-experiments and modelling results*; Paul Scherrer Inst.: 1999.
125. Yamaguchi, T.; Nagasaki, S.; Nagoa, S.; Kizaki, M. Diffusive transport of neptunium and plutonium through compactedsand-bentonite mixturesunder anaerobic conditions. *Radiochim. Acta* **2007**, 95.
126. Felipe-Sotelo, M.; Hinchliff, J.; Evans, N.; Read, D. Solubility constraints affecting the migration of selenium through the cementitious backfill of a geological disposal facility. *Journal of Hazardous Materials* **2016**, *305*, 21-29.

127. Felipe-Sotelo, M.; Hinchliff, J.; Field, L.; Milodowski, A.; Preedy, O.; Read, D. Retardation of uranium and thorium by a cementitious backfill developed for radioactive waste disposal. *Chemosphere* **2017**, *179*, 127-138.
128. Stietz, J. Batchexperimente und CE-ICP-MS-Messungen zur Sorption von U(VI) und Np(VI) an Zementstein. Johannes Gutenberg-Universität Mainz, Mainz, 2019.
129. Kutyma, T. CE-ICP-MS Untersuchungen zur Komplexierung vierwertiger Actinide mit Gluconsäure in Gegenwart von Calciumionen. Johannes Gutenberg-Universität Mainz, Mainz, 2023.
130. Stietz, J.; Amayri, S.; Reich, T.; Haeussler, V.; Prieur, D. Uptake of Pu(IV) by hardened cement paste in the presence of gluconate at high and low ionic strengths. *Front. Nucl. Eng.* **2023**, *2*.
131. Chen, H.; Dabek-Zlotorzynska, E.; Rasmussen, P.E.; Hassan, N.; Lanouette, M. Evaluation of semiquantitative analysis mode in ICP-MS. *Talanta* **2008**, *74*, 1547-1555.
132. Scrivener, K.; Snellings, R.; Lothenbach, B. *A Practical Guide to Microstructural Analysis of Cementitious Materials*; 2015.
133. Neck, V. Aquatic Chemistry and Solubility Phenomena of Actinoid Oxides/Hydroxides. *Pure and Applied Chemistry - PURE APPL CHEM* **2002**, *74*, 1895-1907.
134. Bösch, A. Sorption von Thorium(IV) an Zementstein und der Einfluss von EDTA. Johannes Gutenberg-Universität Mainz, Mainz, 2021.
135. Lohmann, A. Sorption von EDTA an C-S-H-Phasen. Johannes Gutenberg-Universität Mainz, Mainz, 2022.
136. Schröder, F. Untersuchung des Einflusses von Isosaccharinsäure auf das Sorptionsverhalten von ²³²Th(IV) und ²³⁹Pu(IV) an Zementstein im Zuge der Endlagerung von schwach- und mittelradioaktivem Abfall. Johannes Gutenberg-Universität Mainz, Mainz, 2023.
137. Kissel, S.; Spittler, L. Untersuchung des Einflusses von organischen Liganden auf das Sorptionsverhalten von ²³²Th(IV) an HCP. Johannes Gutenberg-Universität Mainz, Mainz, 2020.
138. Kaden, M.; Degering, D. *JAHRESBERICHT STRAHLENSCHUTZ 2019*; Bericht Nr. 18-2; VKTA - Strahlenschutz, Analytik & Entsorgung Rossendorf e. V. Helmholtz-Zentrums Dresden - Rossendorf e. V: 2020.
139. A., T. *X-Ray Data Booklet, Center for X-ray optics advanced light source, X-Ray Data Booklet, second edition*; 2001; Volume LBNL/PUB-490 Rev.2.

The Uptake of Actinides by Hardened Cement Paste in High-Salinity Pore Water

Janina Stietz *, Samer Amayri, Verena Häußler, Raphael Scholze and Tobias Reich *

Department of Chemistry, Johannes Gutenberg-Universität Mainz, 55099 Mainz, Germany; amayri@uni-mainz.de (S.A.)

* Correspondence: jastietz@uni-mainz.de (J.S.); treich@uni-mainz.de (T.R.); Tel.: +49-6131-39-36184 (J.S.); +49-6131-39-25250 (T.R.)

1. Supplementary Information

1.1. S1 XRF Measurements of OPC and HCP

Ordinary Portland cement (OPC) (PZ Doppel N CEM 1 42.5 N, Dyckerhoff, Germany) and hardened cement paste (HCP) ($w/c = 0.5$) were characterized using X-ray fluorescence (XRF) measurements with the routine programme using the standard calibration. The MagiXPRO XRF spectrometer (Philips, The Netherlands) was used for the sample with OPC and the Axios XRF spectrometer (Panalytical, United Kingdom) was used for the HCP sample. To determine the main elements, a melting tablet was used as an annealed sample. For the trace elements, a powder compact was prepared. Rh was utilized as the anode with an excitation power of 3.6 kW. The qualitative and quantitative determination of the elemental composition can be found in Table S1 and Table S2, respectively. The error in the determination with XRF is approximately 3%.

Table S1. Results of the XRF measurements for the main components of OPC and HCP in w%.

	CaO	SiO ₂	Al ₂ O ₃	Fe ₂ O ₃	SO ₃	MgO	K ₂ O	TiO ₂	Na ₂ O	P ₂ O ₅	MnO	LOI
OPC	65.4	22.3	3.6	2.8	2.6	1.4	0.8	0.2	0.2	0.2	0.03	2.7
HCP	66.0	22.4	3.6	2.8	2.1	1.3	0.1	0.2	0.1	0.1	0.03	26.8

Table S2. Results of the XRF measurements for the trace elements of OPC and HCP in ppm.

	Co	Cr	Cu	Nb	Ni	Pb	Rb	Sr	Th	U	V	W	Y	Zn	Zr
OPC	8.0	55.5	85.5	4.0	24.5	2.0	13.5	1182.5	2.8	3.3	28.0	30.5	8.5	363.5	68
HCP	8.0	45.2	66.3	2.4	16.6	2.5	2.1	833.4	2.0	0.0	29.9	1.9	7.0	277.7	51.0

1.2. S2 Powder XRD of HCP

The X-ray diffraction (XRD) measurements of the HCP powder ($w/c = 0.5$ and fraction $<63 \mu\text{m}$) were used to study the structure, composition, and physical properties of the materials. The measurements were performed on 10 mm of the irradiated sample surface. For these experiments a Seifert XRD3000 TT diffractometer (Eigenmann GmbH, Germany) with an automatic divergence slit (ADS) using Cu K α radiation and a secondary monochromator was used. A step width of $0.03^\circ 2\theta$ and a step counting time of 2 s were chosen. For the evaluation of the powder diffractogram the software Match! (Version 3.4.1, Crystal Impact, Germany) was used in combination with the COD (Crystallography Open Database, COD-Inorg REV189751 2017.01.03). By evaluating the diffractogram of the HCP sample, the most important phases of cement could be assigned, such as portlandite (COD ID: 7020139), alite (COD ID: 9014363), calcite (COD ID: 7022028) and ettringite (COD ID: 9011577). These are identified in Figure S1. Portlandite, calcite and ettringite belong to the main constituents of the hydrated hardened cement paste, while alite is a clinker phase of the cement. However, the most intensive signals of the diffractogram are all attributable to portlandite. Some of the signals show many small reflexes that stand out from the background, which could be identified as tobermorite. In these areas, the corresponding

intensities cannot be attributed exclusively to the phases identified but may indicate the presence of C-S-H phases in the sample, which are another main component of the hydrated hardened cement paste.

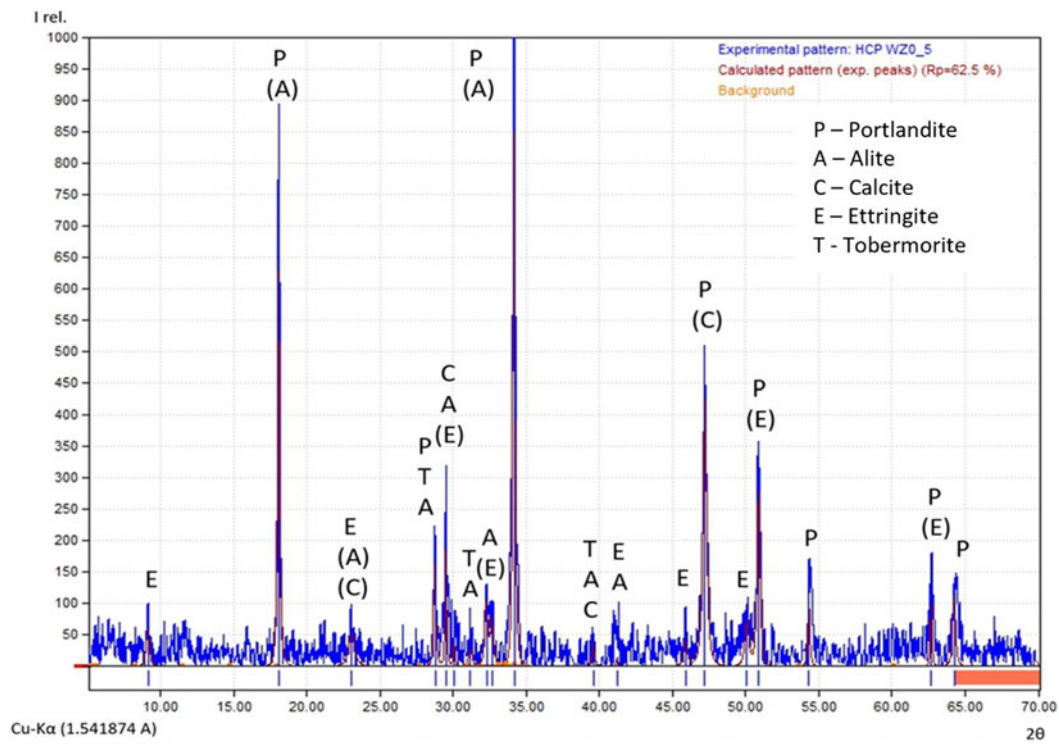


Figure S1. XRD pattern of the HCP sample with $w/c = 0.5$ (size fraction $<63 \mu\text{m}$) and assignment of the reflections to portlandite, alite, calcite and ettringite. The tobermorite could show the theoretical position of the most significant reflexes of C-S-H phases.

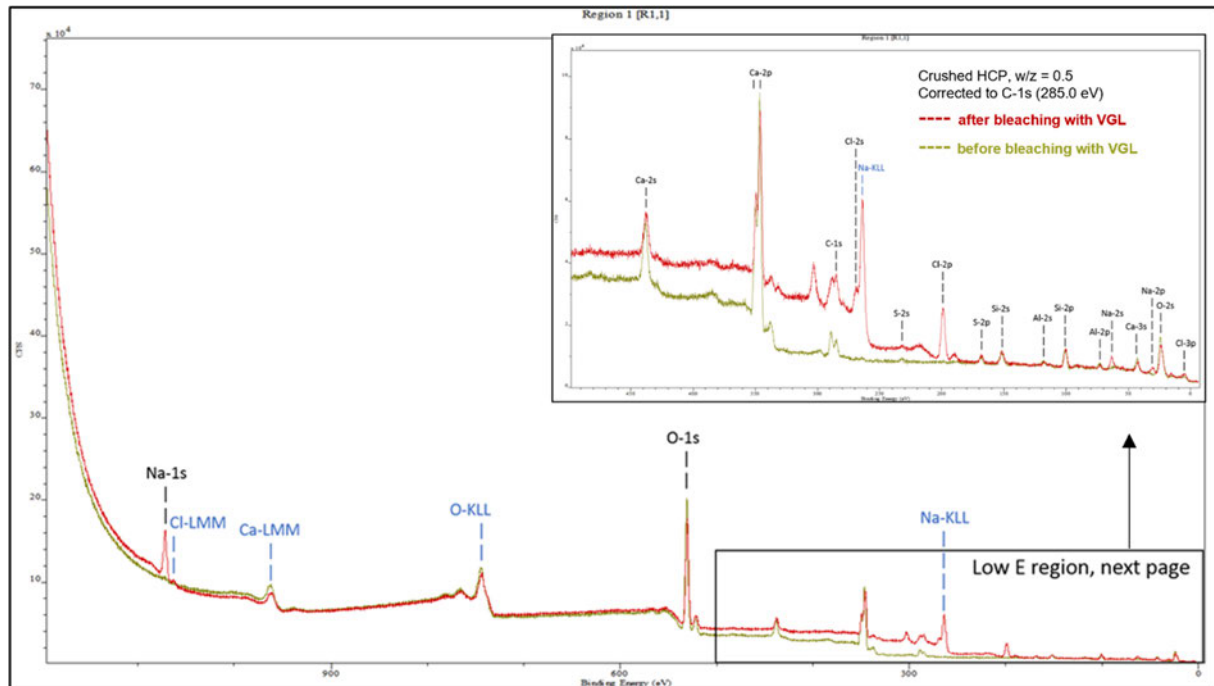
1.3. S3 XPS Analysis of HCP

The crushed and dried HCP powder ($w/c = 0.5$ and fraction $<63 \mu\text{m}$) were further analyzed by X-ray photoelectron spectroscopy (XPS) to determine the solids' surface composition. The measurements were performed with an XPS spectrometer from SPECS Surface Nano Analysis GmbH, Germany using an X-ray tube with an Al-Mg double anode and a PHOIBOS 100 MCD energy analyzer (SPECS Surface Nano Analysis GmbH, Germany). The measurement was recorded using SpecsLab measurement software (SPECS Surface Nano Analysis GmbH, Berlin, Germany). The analysis was performed using CasaXPS version 2.3.24PR1.0 (Casa Software Ltd, Teignmouth, United Kingdom). Calcium silicate powder (CaSiO_3 , Sigma-Aldrich, USA) with a known atomic ratio of calcium to silicon was used as reference sample to determine the corresponding XPS sensitivity factor $S_{\text{Si}/\text{Ca}}$. Figure S2 shows the XPS spectra of HCP samples ($S/L = 5 \text{ g L}^{-1}$) before and after contact with the background electrolyte VGL (German acronym for *Verdünnte Gipschlösung*, diluted caprock solution) at pH 12.8 for 72 h. After contact with VGL, the XPS lines of Na and Cl could be observed. The relative intensities of the Ca 2p and Si 2p XPS lines indicate that the Ca/Si ratio of the HCP surface becomes significantly smaller after contact with VGL (see Table S3). The atomic Ca/Si ratios were determined using equation S1, with $S_{\text{Si}/\text{Ca}} = 0.22$.

$$\frac{n_{\text{Ca}}}{n_{\text{Si}}} = \frac{I_{\text{Ca } 2p}}{I_{\text{Si } 2p}} \cdot S_{\text{Si}/\text{Ca}} \quad (\text{S1})$$

Table S3. Atomic Ca/Si ratios of HCP before and after contact with VGL determined by XPS (the estimated uncertainty is about $\pm 10\%$). (* = Reference sample)

Solid phase	Ca/Si-Ratio
CaSiO ₃ reference	1*
HCP (w/c 0.5)	3.45
HCP / VGL (w/c 0.5)	2.58

**Figure S2.** Result of the XPS measurements of HCP powder (w/c 0.5) before and after contact with VGL at pH 12.8 for 72 h. Ca-LMM and O-KLL denote Auger transitions. The other signals were assigned to the XPS lines of the contained elements.

1.4. S4 N₂-BET Measurement of HCP

The specific surface area of the HCP powder (w/c of 0.5; fraction < 63 μm) was determined by N₂ sorption according to the method of Brunauer, Emmett and Teller (BET) [1]. For the determination of the specific surface area a N₂-BET three-point analysis was established with a NOVA 1200 system (Quantachrome instruments, USA). The HCP powder was dried at 60 °C for 20 h. α -alumina (CRM 171, Sigma-Aldrich, USA) powder with a specific surface area of $S = 2.95 \text{ m}^2/\text{g}$ was used as reference. The determined specific surface area of the HCP powder agrees well with the literature data of Odler et al. [2] (see Table S4).

Table S4. N₂-BET specific surface areas of the HCP powder (w/c = 0.5 and size fraction <63 μm).

Samples	S(average) m ² g ⁻¹
HCP	9.91 \pm 0.66
HCP [2]	9.5

1.5. S5 CEC of HCP

To obtain an estimate for the cation exchange capacity (CEC) of the HCP powder (w/c of 0.5; fraction < 63 μm), sorption experiments ($S/L = 67 \text{ g L}^{-1}$; $V = 40 \text{ mL}$) with Na⁺ in 0.3 M NaOH, using ²²Na⁺ (195 kBq; PerkinElmer, Germany) as radioactive tracer, similar to the literature [3], were performed. The tracer content in the supernatant after centrifugation was determined by γ -ray spectroscopy using the γ -line at 1274.5 keV. The results are

shown in Table S5. From the here determined CEC and the specific surface area S_{BET} determined by the N_2 BET measurements, the sorption site density S_d was calculated using equation S2 (N_A is Avogadro constant):

$$S_d = \frac{CEC \cdot N_A}{S_{BET}} \quad (S2)$$

Table S5. pH values, distribution coefficients R_d , percentage of sorption, CEC_{Na} with $^{22}Na^+$ and HCP (S/L = 67 g L⁻¹) in VGL and Milli-Q after 72 h contact time. The calculated site density for the surface areas are also listed.

Sample	pH _{start}	pH _{end}	R_d / L kg ⁻¹	Sorption / %	CEC_{Na} / mol kg ⁻¹	Site density / sites/nm ⁻²
HCP Milli-Q	12.8	13.3	0.2	1.1	0.05	3
HCP VGL	12.7	13.2	0.2	1.1	0.05	3

1.6. S6 Pu L_{III}-edge XANES Spectra

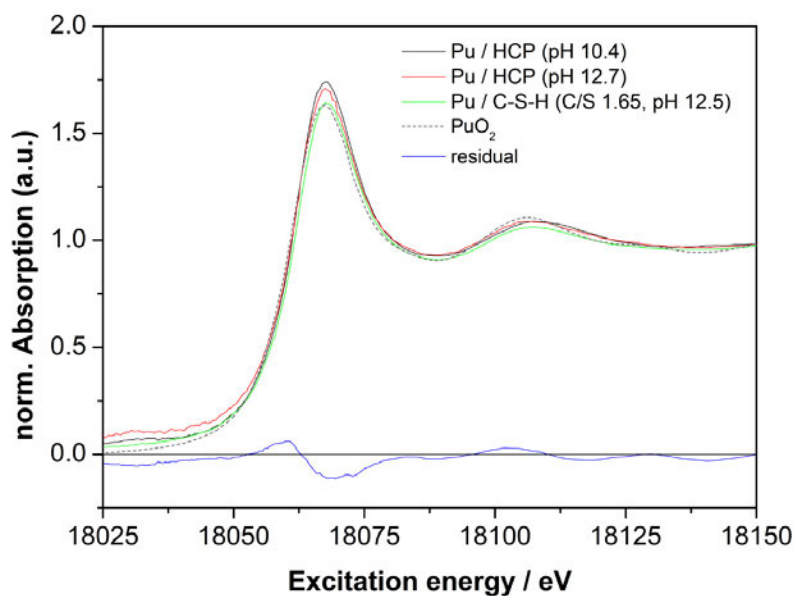


Figure S3. Normalized Pu LIII-edge XANES spectra of the samples HCP/Pu at pH 10.4 as well as at pH 12.7 and C-S-H-phase (C/S 1.65)/Pu at pH 12.5. The largest residual of all fits is shown as blue line. The raw data for the reference spectrum of PuO₂ were provided by P. Martin [4].

References

1. Wedler, G.; Freund, H.-J. *Lehrbuch der Physikalischen Chemie*; Wiley-VCH: Weinheim, Germany, 2012.
2. Odler, I. The BET-specific surface area of hydrated Portland cement and related materials. *Cem. Concr. Res.* **2003**, *33*, 2049-2056.
3. Hong, S.-Y.; Glasser, F.P. Alkali binding in cement pastes: Part I. The C-S-H phase. *Cem. Concr. Res.* **1999**, *29*, 1893-903.
4. Martin, P.; Grandjean, S.; Valot, C.; Carlot, G.; Ripert, M.; Blanc, P.; Hennig, C. XAS study of (U_{1-y}Pu_y)O₂ solid solutions. *J. Alloys Compd.* **2007**, *444*, 410-414.

Supplementary Material

Uptake of Pu(IV) by hardened cement paste in the presence of gluconate at high and low ionic strengths

J. Stietz^{1*}, S. Amayri¹, V. Häußler¹, D. Prieur², T. Reich^{1*}

¹ Department of Chemistry, Johannes Gutenberg-Universität Mainz, Mainz, Germany,

² Institute of Resource Ecology, Helmholtz-Zentrum Dresden-Rossendorf e.V., Dresden, Germany

* **Correspondence:** Janina Stietz: jastietz@uni-mainz.de

Tobias Reich: treich@uni-mainz.de

The supplementary material comprises 7 pages, including 4 tables, 4 figures, and 6 references.

Note: The order of the supplementary material is chronological, as cross references appear in the article.

SM-1. Chemical composition of ACW

The elemental concentrations in the artificial cement pore water (ACW) before and after contact with hardened cement paste (HCP) (S/L = 5 g L⁻¹) for 72 h, were identified by ICP-MS SemiQuant analysis (7900 Series ICP-MS, Agilent Technologies, United States). With the SemiQuant analysis mode of the ICP-MS (Octopol-Reaction-System), all elements of a solution can be determined by measuring a stock solution with specified concentrations of standards ([Li, Co, Y, Ce, Tl] = 1 ppb). In addition, an ¹⁹³Ir stock solution ([Ir] = 100 ppt) was used as internal standard. These stock solutions were prepared in 2% HNO₃. The uncertainty of this method is ~30%.

The measurements showed that elements are leached from HCP. Especially relevant for this work is the concentration of 3×10⁻³ M Ca²⁺, which is in good agreement with a value of the literature ([Ca] = 1×10⁻³ M (Ochs et al., 2016)). The results are summarized in Supplementary Table S1.

Supplementary Table S1. Elemental concentrations in mol L⁻¹ of ACW before and after contact with HCP.

	Na	Al	Si	S	K	Ca	Fe
ACW	1.2×10 ⁻¹	n.d.	3.3×10 ⁻⁴	n.d.	1.4×10 ⁻¹	n.d.	2.8×10 ⁻⁷
ACW*	1.4×10 ⁻¹	1.2×10 ⁻⁴	4.3×10 ⁻⁴	2.0×10 ⁻³	2.2×10 ⁻¹	2.8×10 ⁻³	2.1×10 ⁻⁶

*) ACW after contact with HCP (5 g L⁻¹, 72 h).

SM-2. Chemical composition of ACW-VGL

The Supplementary Table S2 summarizes the chemical composition in terms of weight for the oxides of ACW-VGL (for preparation see Section 2.2) determined with XRF measurements (XRF spectrometer MagiXPRO, Philips, Netherlands). Rh was utilized as the anode with an excitation power of 3.6 kW. For the measurement, 30 mL ACW-VGL was dried for 72 h at 110 °C in the drying oven. The dried salt (4.5 g) was measured as a pellet. The uncertainty for the main elements is < 3%.

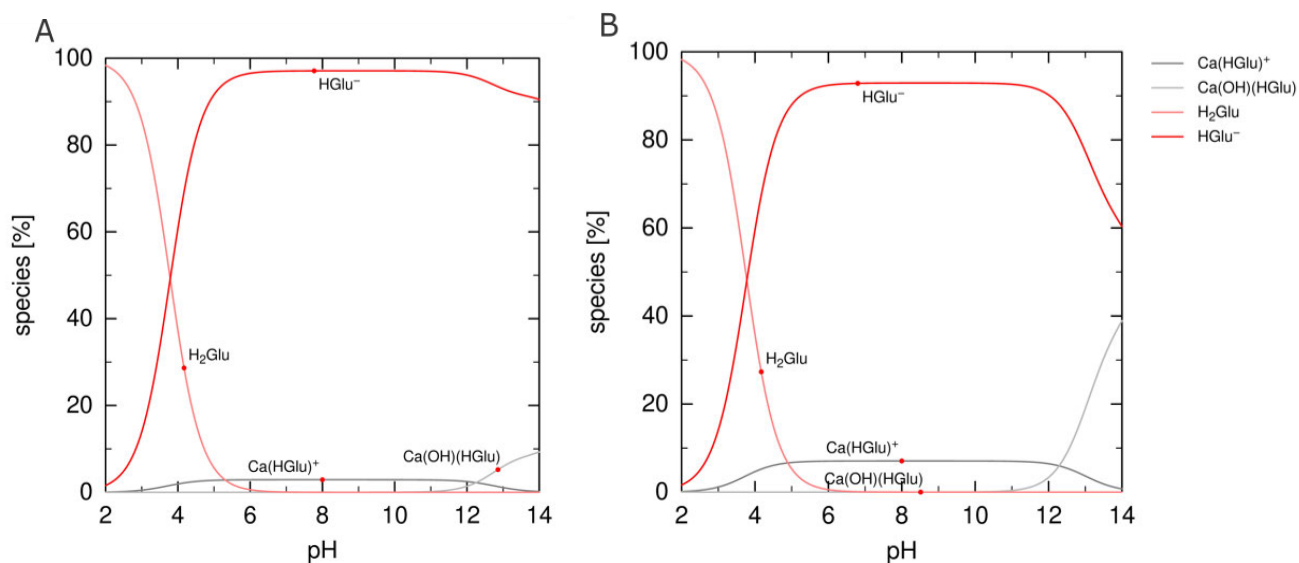
Supplementary Table S2. Chemical composition of ACW-VGL in weight-% for the oxides.

SiO ₂	Al ₂ O ₃	Fe ₂ O ₃ (t)	MnO	MgO	CaO	Na ₂ O	K ₂ O	TiO ₂	P ₂ O ₅	SO ₃	Cl
0.047	0.016	0.028	0	0	0.751	49.050	0.112	0.011	0.007	0.020	43.3

Loss on ignition at 650 °C = 0.72 weight-%

SM-3. Speciation of gluconate in ACW and ACW-VGL

Supplementary Figure S1 shows the calculated speciation of 1×10^{-2} M gluconate (GLU) in ACW (left) and ACW-VGL (right). At $\text{pH} \geq 12.5$ the concentration of the species $\text{Ca}(\text{OH})(\text{HGLU})$ is somewhat larger in ACW-VGL than in ACW due to different Ca^{2+} concentrations in both electrolytes.



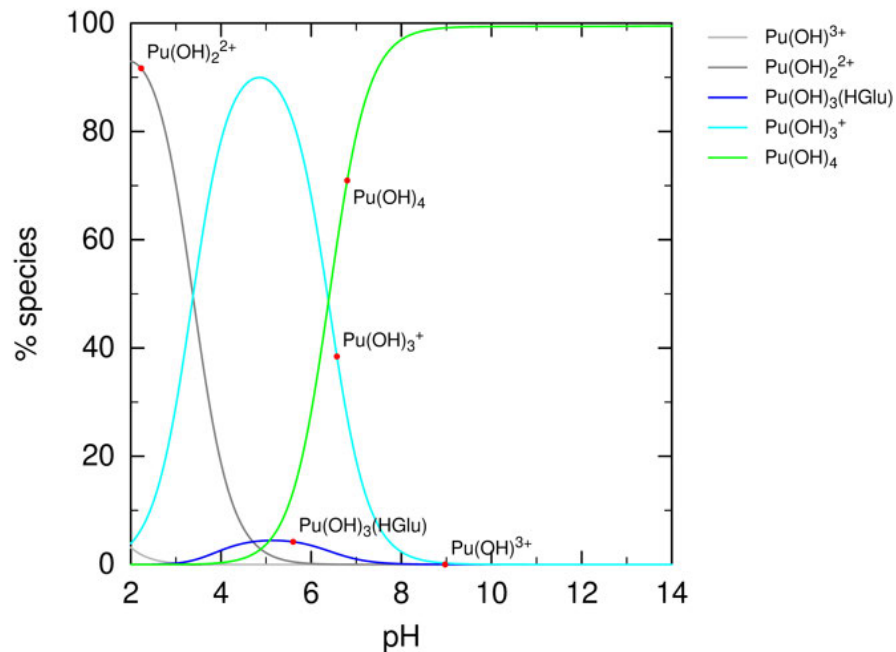
Supplementary Figure S1. Speciation calculation for 1×10^{-2} M GLU in ACW (A) and ACW-VGL (B). (Graphic generated by PhreePlot (version 1.0 (Parkhurst and Appelo, 2016)) using PHREEQC and the ThermoChimie database 9b0, 2015 (Giffaut et al., 2014)).

SM-4. Complex formation constants

Supplementary Table S3. Thermodynamic data used for the equilibria calculations of Pu(IV) in presence and absence of GLU from the ThermoChimie database 9b0, 2015 (Guillaumont et al., 2003; Gaona et al., 2008; Giffaut et al., 2014).

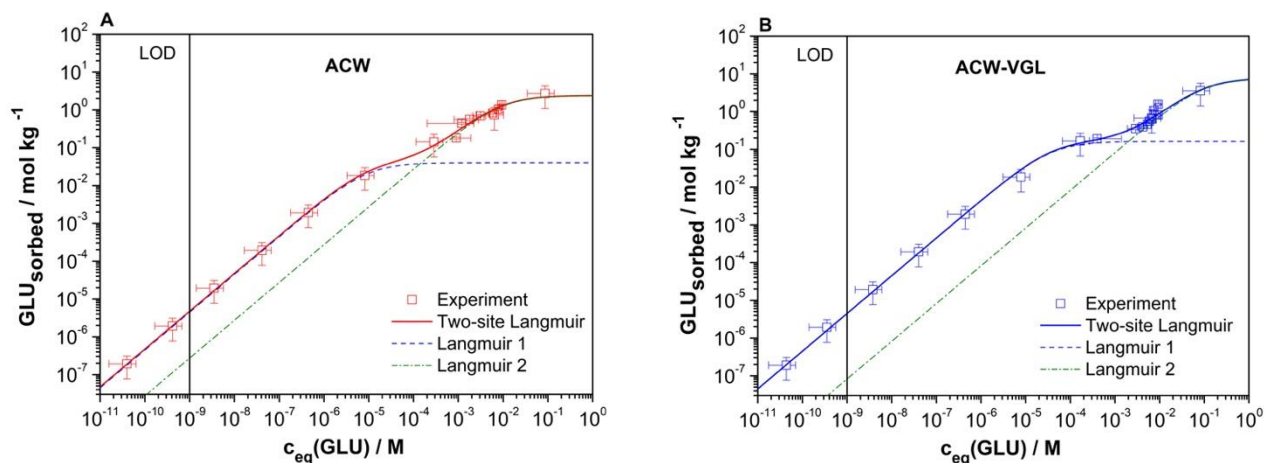
Chemical equilibrium	$\log K^0$
$\text{Pu}^{4+} + 4 \text{H}_2\text{O} \rightleftharpoons \text{Pu}(\text{OH})_4(\text{aq}) + 4\text{H}^+$	-8.50 ± 0.50
$\text{Pu}^{4+} + \text{HGlu}^- + 3 \text{H}_2\text{O} \rightleftharpoons \text{Pu}(\text{OH})_3(\text{HGlu}) + 3\text{H}^+$	4.75 ± 1.50
$\text{Pu}^{4+} + \text{HGlu}^- + 4 \text{H}_2\text{O} \rightleftharpoons \text{Pu}(\text{OH})_4(\text{HGlu})^- + 4\text{H}^+$	-2.70 ± 1.50

SM-5. Pu(IV) speciation in ACW/ACW-VGL in presence of GLU



Supplementary Figure S2. Speciation calculation for 1×10^{-8} M Pu(IV) and 1×10^{-8} M GLU in ACW. (Graphic generated by PhreePlot (version 1.0 (Parkhurst and Appelo, 2016)) using PHREEQC and the ThermoChimie database 9b0, 2015 (Giffaut et al., 2014)).

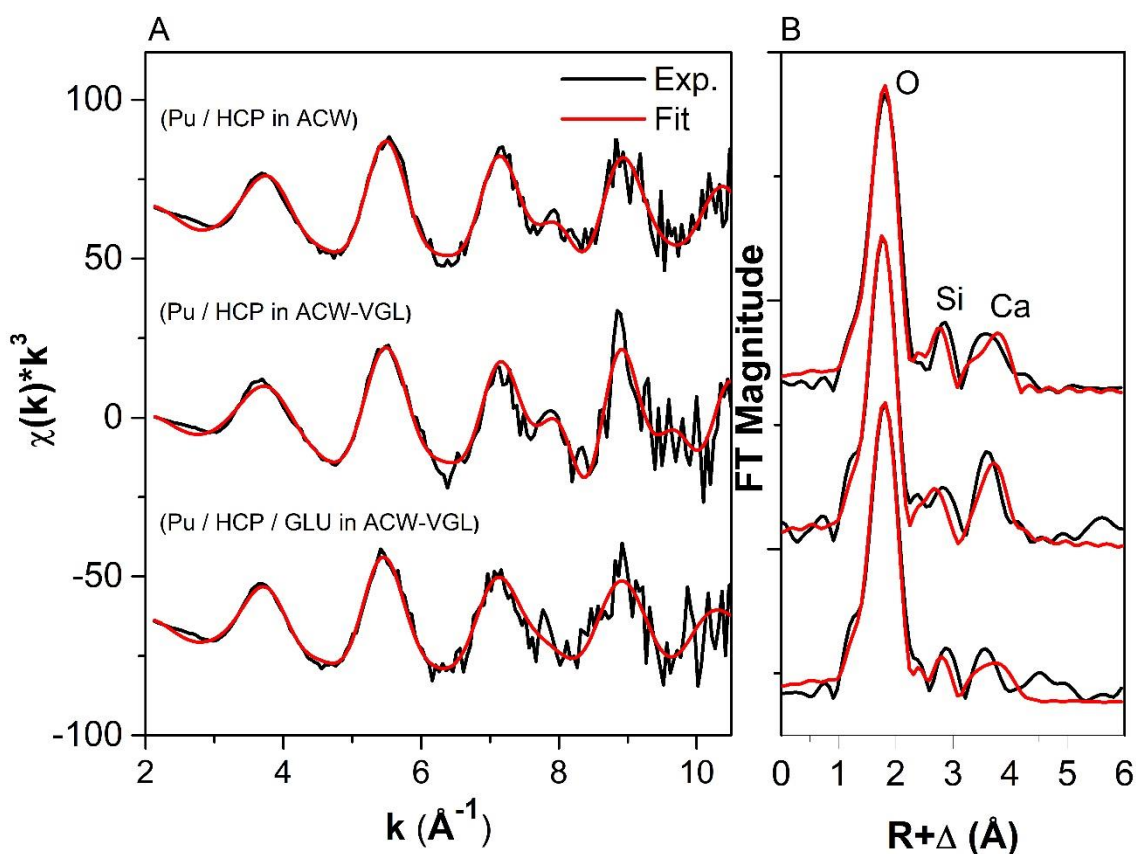
SM-6. Modelling of sorption isotherms of GLU on HCP



Supplementary Figure S3. Modelling of GLU sorption isotherms on HCP in ACW (A) and ACW-VGL (B), respectively, using a two-site Langmuir-isotherm. The dashed lines represent the components of the two-site Langmuir-isotherm. Their sums are shown as solid lines.

SM-7. Analysis of the deglitches Pu L_{III} -edge EXAFS spectra

Since all raw data showed a strong intensity variation, a so-called monochromator glitch, in the energy range from 18284.6 eV to 18299.9 eV, an attempt was made to deglitch the raw Pu L_{III} -edge XAFS data using the software package EXAFSPAK (George and Pickering, 2000). The five data points in this energy range were interpolated by a cubic through the middle of two points on either side of the glitch. The deglitched k^3 -weighted EXAFS spectra are shown in Supplementary Figure S4. Note the spectral change in the k -range from 7.7 to 7.9 \AA^{-1} compared to the raw data shown in Figure 4 of the article. The structural parameters of the best model to the deglitched EXAFS spectra are given in Supplementary Table S4 and can be compared to the corresponding model for the raw data (see Table 6 of the article). The data were fitted in the k -range from 2.1 to 10.9 \AA^{-1} . The shift in E_0 energy, ΔE_0 , was the only variable that was varied as one global parameter for all coordination shells. All other variables were allowed to vary freely.



Supplementary Figure S4. Deglitched Pu L_{III} -edge k^3 -weighted EXAFS spectra (A) of Pu loaded on HCP and the corresponding Fourier transform magnitude (B). Black line: experimental; red line: best model.

Supplementary Table S4. EXAFS structural parameters obtained from deglitched Pu L_{III}-edge k^3 -weighted EXAFS spectra. N – coordination number, R – distance in Å, and σ^2 – Debye-Waller factor in Å², $S_0^2 = 0.9$.

Sample	Shell	N	R	σ^2
Pu / HCP / ACW (norm. error = 0.2, $\Delta E_0 = 2.2 \pm 0.4$ eV)	Pu-O	6.2 ± 0.3	2.281 ± 0.004	0.009 ± 0.001
	Pu-Si	1.0 ± 0.3	3.14 ± 0.01	0.005 ± 0.002
	Pu-Ca	5.2 ± 1.4	4.18 ± 0.01	0.012 ± 0.003
Pu / HCP / ACW-VGL (norm. error = 0.4, $\Delta E_0 = 0.1 \pm 0.5$ eV)	Pu-O	6.0 ± 0.3	2.261 ± 0.004	0.009 ± 0.001
	Pu-Si	1.6 ± 0.5	3.14 ± 0.01	0.007 ± 0.003
	Pu-Ca	2.4 ± 0.7	4.16 ± 0.01	0.002 ± 0.002
Pu / HCP / GLU / ACW-VGL (norm. error = 0.3, $\Delta E_0 = 1.4 \pm 0.4$ eV)	Pu-O	6.4 ± 0.3	2.285 ± 0.004	0.010 ± 0.001
	Pu-Si	0.7 ± 0.4	3.16 ± 0.01	0.005 ± 0.004
	Pu-Ca	11.7 ± 4.7	4.18 ± 0.02	0.027 ± 0.006

References

- Gaona, X., Montoya, V., Colàs, E., Grivé, M., and Duro, L. (2008). Review of the complexation of tetravalent actinides by ISA and gluconate under alkaline to hyperalkaline conditions. *J. Contam. Hydrol.* 102, 217-227.
- George, G.N., and Pickering, I.J. (2000). EXAFSPAK - A suite of computer programs for analysis of X-ray absorption spectra. *Stanford Synchrotron Radiation Lightsource*.
- Giffaut, E., Grivé, M., Blanc, P., Vieillard, P., Colàs, E., Gailhanou, H., Gaboreau, S., Marty, N., Madé, B., and Duro, L. (2014). Andra thermodynamic database for performance assessment: ThermoChimie. *Appl. Geochem.* 49, 225-236.
- Guillaumont, R., Fanghänel, T., Fuger, J., Grenthe, I., Neck, V., Palmer, D.A., and Rand, M.H. (2003). *Update on the Chemical Thermodynamics of Uranium, Neptunium, Plutonium, Americium and Technetium*. Paris: OECD Publishing.
- Ochs, M., Mallants, D., and Wang, L. (2016). *Radionuclide and Metal Sorption on Cement and Concrete*. Springer International Publishing Switzerland.
- Parkhurst, D.L., and Appelo, C.a.J. (2016). *PHREEQC (Version 3.3.5) - A computer program for speciation, batch-reaction, one-dimensional transport, and inverse geochemical calculations* [Online]. Available: http://wwwbrr.cr.usgs.gov/projects/GWC_coupled/phreeqc/index.html [Accessed 2023].



Influence of gluconate on the retention of Eu(III), Am(III), Th(IV), Pu(IV), and U(VI) by C-S-H (C/S = 0.8)

Sophie Dettmann¹, Nina M. Huittinen², Nicolas Jahn¹, Jerome Kretzschmar², Michael U. Kumke^{1*}, Tamara Kutyma³, Janik Lohmann³, Tobias Reich^{3*}, Katja Schmeide^{2*}, Salim Shams Aldin Azzam², Leon Spittler³, Janina Stietz³

¹Universität Potsdam, Institute of Chemistry, Potsdam, Germany

²Helmholtz-Zentrum Dresden - Rossendorf, Institute of Resource Ecology, Dresden, Germany

³Johannes Gutenberg-Universität Mainz, Department of Chemistry, Mainz, Germany

Appendix A. Supplementary Material

The supplementary material comprises 9 pages, including 7 tables, 7 figures, and 6 references.

Note: The supplementary material is ordered chronologically, as cross references appear in the article.

Keywords: actinide, organic ligand, sorption, cementitious material, concrete, luminescence

Corresponding authors:

Michael U. Kumke, Tobias Reich, Katja Schmeide

kumke@uni-potsdam.de, treich@uni-mainz.de, k.schmeide@hzdr.de

Table S1: S/L ratio, equilibration time, background electrolyte and materials used for the synthesis of the C-S-H phases for sorption experiments with different An(X).

An(X)	S/L / g/L	Equil. time / d	Background electrolyte	Materials
Eu(III)	33.3	14	1×10^{-2} M NaCl	CaO: d < 160 nm, 98%, Sigma-Aldrich, USA SiO ₂ : d =10-20 nm, 99.5%, Sigma-Aldrich, USA
¹⁴ C GLU	0.5-50	14	deionized water	CaO: reagent grade, ThermoFisher GmbH, Germany SiO ₂ : Aerosil 300, Evonik Industries AG, Germany
Am(III)	5			
Th(IV)	5			
Pu(IV)	5			
U(VI)	24	67	deionized water	CaO: 99.95%, 20 mesh powder, ThermoFisher GmbH, Germany SiO ₂ : Aerosil 300, Evonik Industries AG, Germany

Table S2: C/S ratios of all samples determined by XPS measurements (the estimated errors are about $\pm 10\%$) compared to C/S target ratios and literature data.

Solid phase	C/S ratio	pH values
CaSiO ₃ reference	1*	
C-S-H phases (C/S 0.8)	0.56	10.2
C-S-H phases GLU (C/S 0.8)	0.54	10.2
C-S-H phases (C/S 0.8)**	0.70	

* This ratio was assumed to calculate the sensitivity factor $S = 0.24$.

** Häußler et. al. (2018)

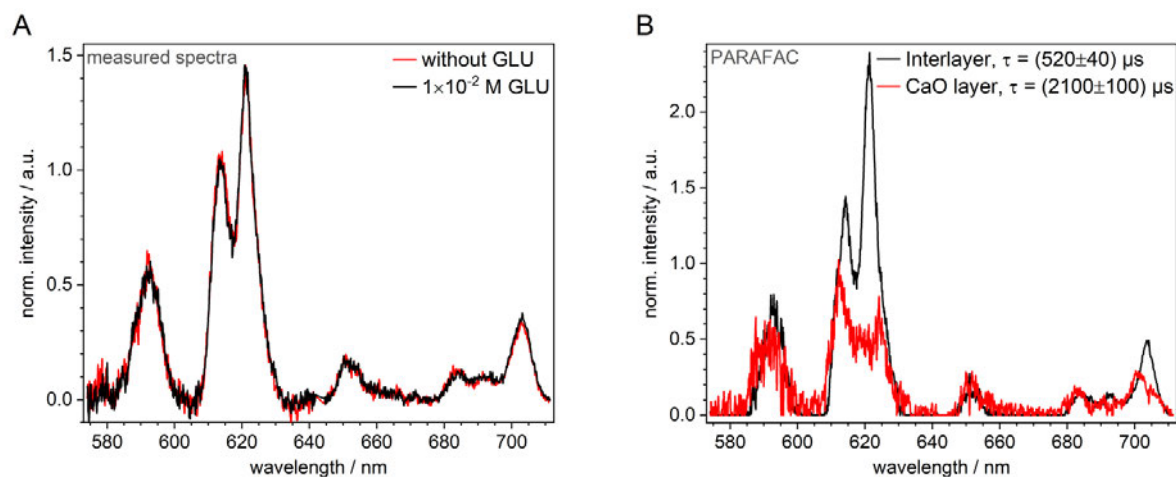


Figure S1: (A) normalized Eu(III) luminescence spectra of reference samples, in which Eu(III) was added during C-S-H formation and GLU was added 14 d later, recorded after a Eu(III) contact time of six weeks. (B) luminescence spectra of the two distinct Eu(III) species obtained with the PARAFAC analysis. Note that the peak at 683 nm corresponds to an emission from the quartz-tubes and not from Eu(III).

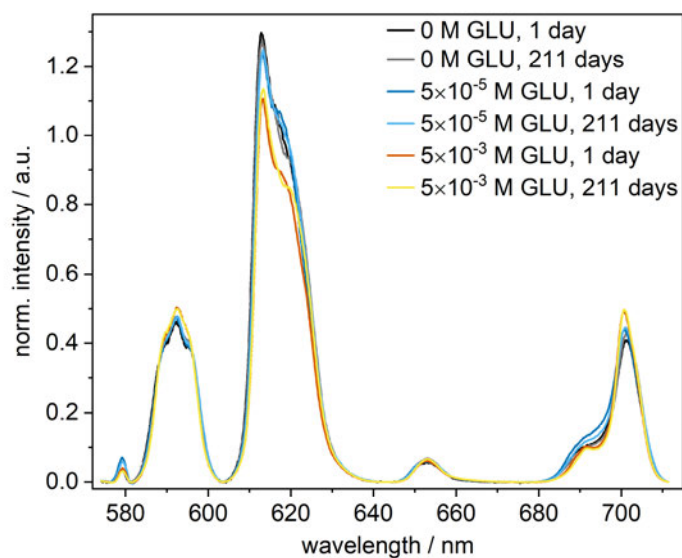


Figure S2: Normalized Eu(III) luminescence spectra measured of the C-S-H retention samples (Eu(III)+GLU addition after 14 days, [Eu(III)]= 5×10^{-5} M) at different GLU concentrations and contact times.

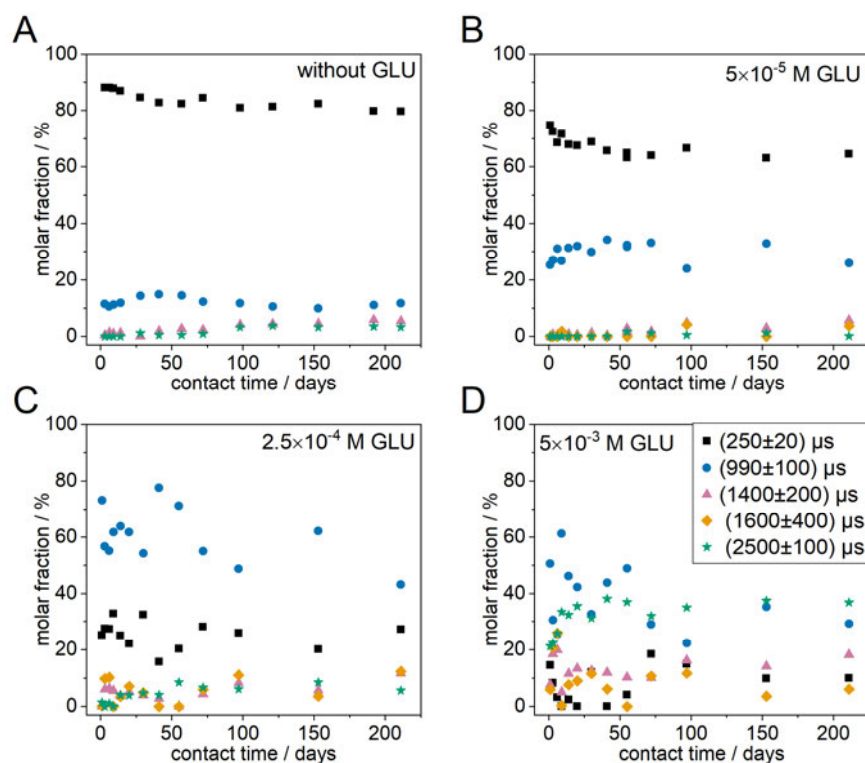


Figure S3: Molar fraction of the five Eu(III) species calculated using PARAFAC in the C-S-H retention samples with 5×10^{-5} M Eu(III) at different GLU concentrations: (A) without GLU, (B) 5×10^{-5} M GLU, (C) 2.5×10^{-4} M GLU and (D) 5×10^{-3} M GLU. The legend applies to all images.

Table S3: Determination of GLU concentration in selected supernatants after Eu(III) retention experiments by means of quantitative ^1H NMR, according to equation (6), along with calculated amounts of GLU sorbed to the solid phase relative to the initial concentration ($t = 0$).

Sample	$[\text{GLU}]_0$	$[\text{GLU}]_{\text{eq}}$	S/L / g/L	sorbed GLU / %
Eu1	5×10^{-5} M	3.8×10^{-5} M	33	24.6
Eu2	2.5×10^{-4} M	1.97×10^{-4} M	33	21.3
Eu3	5×10^{-4} M	4.25×10^{-4} M	33	15.0
Eu4	1×10^{-3} M	8.71×10^{-4} M	33	12.9
Eu5	5×10^{-3} M	4.53×10^{-3} M	33	9.4
Eu6	2.5×10^{-2} M	2.272×10^{-2} M	33	9.1

EXAFS measurement

For the EXAFS measurement the sample containing 32 kBq ^{239}Pu was dried under Ar atmosphere in the glove box, transferred into a special sample holder, and transported under liquid nitrogen atmosphere to ESRF. The EXAFS measurement was performed at the BM20 Rossendorf Beamline (ROBL) (Matz et al., 1999; Scheinost et al., 2021) at ESRF during 7/8-bunch mode using the Si(111)

double-crystal monochromator. During the measurement the sample was cooled to approx. 15 K using a closed-cycle He cryostat. Multiple scans of the Pu L₃-edge EXAFS spectrum ($E_0 = 18057$ eV) were recorded in fluorescence mode using a 13-element Ge detector. A Zr foil was measured simultaneously in transmission mode for energy calibration purposes ($E_0 = 17998$ eV).

The EXAFS data analysis was performed using EXAFSPAK (George and Pickering, 2000) and FEFF9 (version 9.6) (Rehr et al., 2010). For the calculation of FEFF scattering amplitudes and phases, a structural model based on density functional calculations of the sorption modes of U(IV) at C-S-H phase was used (Chiorescu et al., 2022). In the self-consistent FEFF calculation, U in the CaO layer of C-S-H was replaced by Pu.

The raw Pu L₃-edge k^3 -weighted EXAFS spectrum together with the fit are shown in Figure S4. The EXAFS structural parameters are summarized in Table S4.

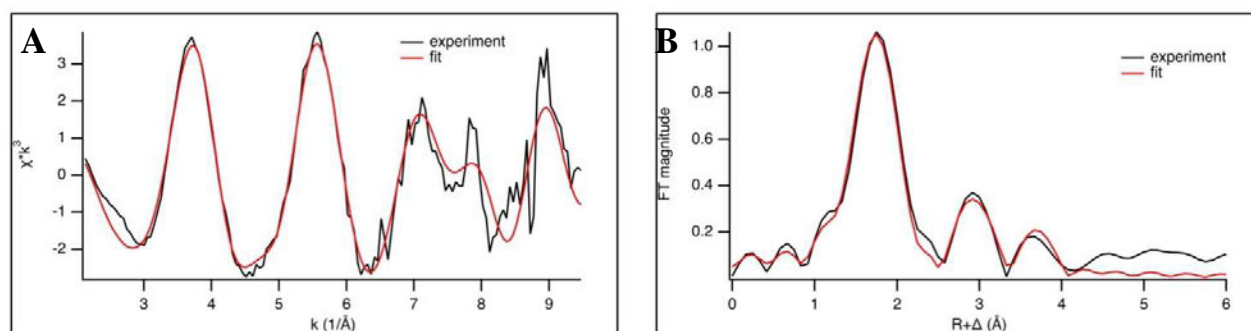


Figure S4: (A) Pu L₃-edge k^3 -weighted EXAFS spectrum of 494 ppm Pu loaded on C-S-H (C/S = 0.8). (B) Fourier transform magnitude of k^3 -weighted EXAFS spectrum. Black line: experimental; red line: calculated.

Table S4: Structural parameters of Pu in the C-S-H sample (C/S = 0.8) determined by Pu L₃-edge EXAFS spectroscopy. N – coordination number, R – distance, σ^2 – Debye-Waller factor. $S_0^2 = 0.9$, $\Delta E_0 = 0.26$ eV.

Shell	N	R (Å)	σ^2 (Å ²)
O	6.8 ± 0.3	2.25 ± 0.02	0.0119 ± 0.0004
Si	2.0 ± 0.3	3.15 ± 0.02	0.0119*
Si	4.6 ± 0.5	3.54 ± 0.02	0.0119*
Ca	6.3 ± 1.0	4.12 ± 0.02	0.0179*

* Linked to the first shell during the fit.

Table S5: Electrophoretic mobilities μ of Th(IV) ($[\text{Th(IV)}]_0 = 4 \times 10^{-7} \text{ M}$) in absence and presence of GLU ($[\text{GLU}]_0 = 1 \times 10^{-2} \text{ M}$) with C-S-H pore water ($[\text{Ca(II)}] = 1.7 \times 10^{-3} \text{ M}$) and Ca(II)-containing solution ($1 \times 10^{-2} \text{ M}$) at pH 10.

Samples	$\mu_e \text{ Th(IV)} / 10^{-4} \text{ cm}^2/(\text{Vs})$
Th(IV)	$+(0.03 \pm 0.03)$
Th(IV) + GLU	$-(2.72 \pm 0.09)$
Th(IV) + GLU in C-S-H pore water	$-(2.02 \pm 0.08)$
Th(IV) + GLU + Ca(II)	$-(0.65 \pm 0.04)$

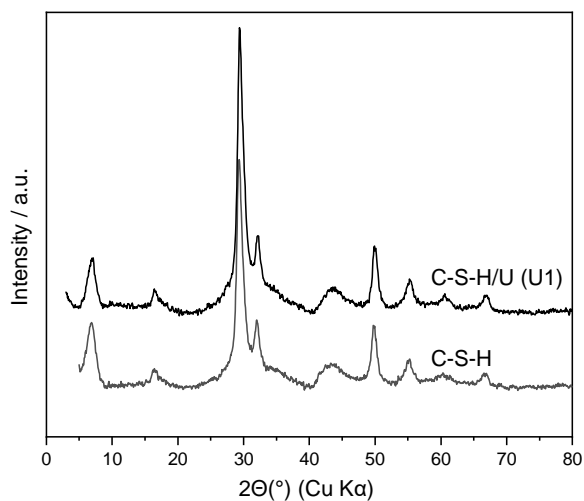


Figure S5: Powder X-ray diffractograms of C-S-H and of directly synthesized U(VI)-containing C-S-H (U1).

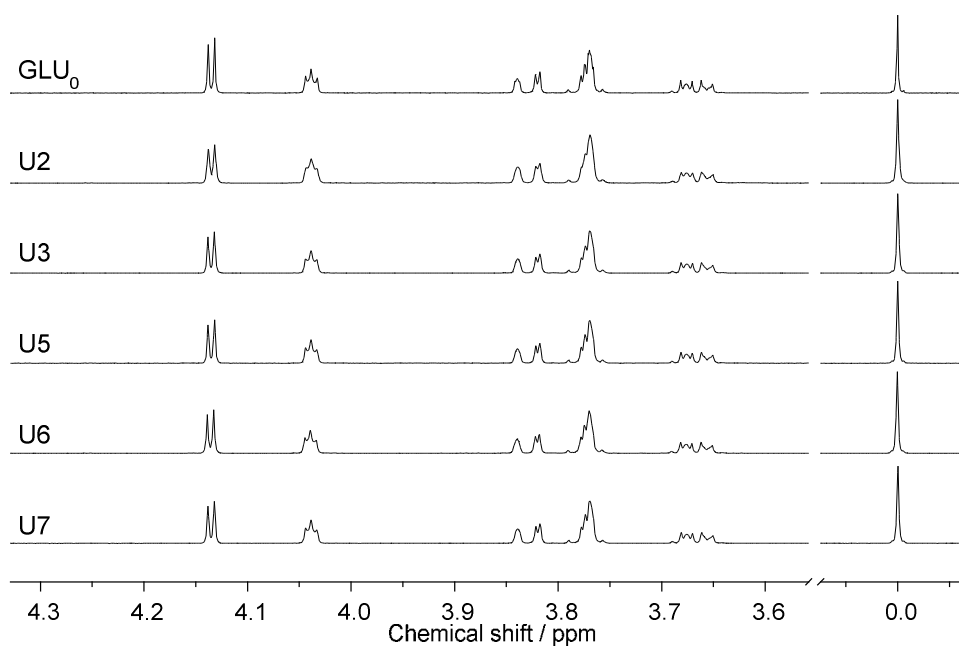


Figure S6: Quantitative ^1H NMR spectra of GLU stock solution (GLU_0) as well as of all GLU-containing supernatants in D_2O at $25\text{ }^\circ\text{C}$.

Table S6: Determination of the initial GLU concentration (GLU_0) as well as of the GLU concentration in supernatants after sorption experiments (U2–U7) by means of quantitative ^1H NMR, according to equation (6), along with calculated amounts of GLU sorbed to the solid phase relative to the initial concentration.

Sample	$[\text{GLU}] / 10^{-3} \text{ M}$	S/L / g/L	sorbed GLU / %
GLU_0	11.46	—	—
U2	9.90	10	13.7
U3	9.90	10	13.7
U5	10.14	1	11.6
U6	10.23	1	10.8
U7	10.31	1	10.1

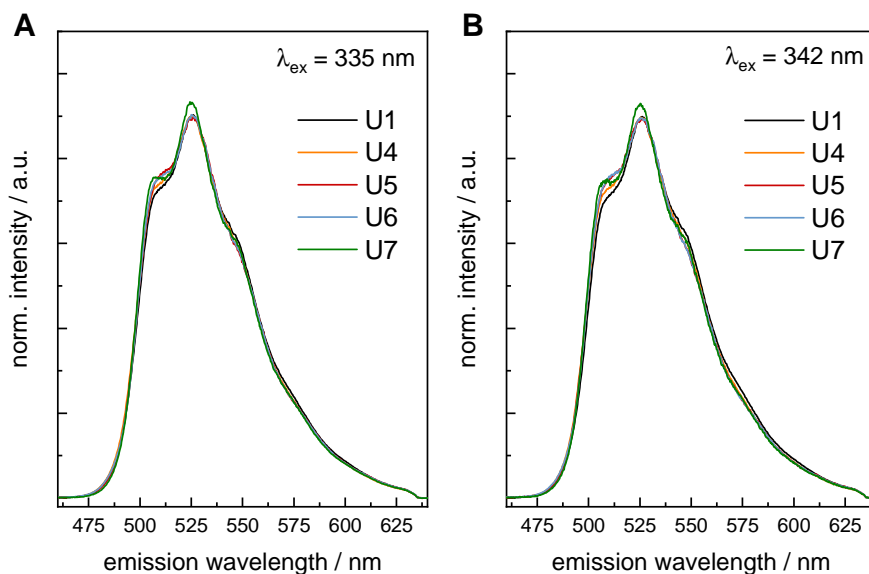


Figure S7: U(VI) luminescence spectra obtained from U(VI)-loaded C-S-H phases U1 ($[U(VI)]_0 = 2 \times 10^{-5}$ M, S/L = 24 g/L, pH 10.8) and U4 – U7 ($[U(VI)]_0 = 5 \times 10^{-7}$ M, S/L = 1 g/L, absence or presence of 1×10^{-2} M GLU, pH ~ 10.9); (A) $\lambda_{ex} = 335$ nm and (B) $\lambda_{ex} = 342$ nm.

Table S7: U(VI) species distribution of U(VI)-containing C-S-H in absence or presence of GLU determined by U(VI) luminescence spectroscopy.

Sample	Surface sorption 1 / %	Surface sorption 2 / %	Sorption into interlayer / %
U1	23	23	54
U4	30	28	42
U5	32	26	42
U6	33	25	42
U7	40	25	35

References

- Chiorescu, I., Kremleva, A., and Krüger, S. (2022). On the sorption mode of U(IV) at Calcium Silicate Hydrate: A Comparison of Adsorption, Absorption in the Interlayer, and Incorporation by Means of Density Functional Calculations. *Minerals* 12, 1541. doi: <https://doi.org/10.3390/min12121541>
- George, G. N., and Pickering, I. J. (2000). EXAFSPAK – A suite of computer programs for analysis of X-ray absorption spectra. *Stanford Synchrotron Radiat. Light. Menlo Park. CA, USA*.
- Häußler, V., Amayri, S., Beck, A., Platte, T., Stern, T. A., Vitova, T., et al. (2018). Uptake of actinides by calcium silicate hydrate (C-S-H) phases. *Appl. Geochemistry* 98, 426–434. doi: <https://doi.org/10.1016/j.apgeochem.2018.08.021>
- Matz, W., Schell, N., Bernhard, G., Prokert, F., Reich, T., Claußner, J., et al. (1999). ROBL - a CRG beamline for radiochemistry and materials research at the ESRF. *J. Synchrotron Radiat.* 6, 1076–1085. doi: 10.1107/S0909049599010663
- Rehr, J. J., Kas, J. J., Vila, F. D., Prange, M. P., and Jorissen, K. (2010). Parameter-free calculations of X-ray spectra with FEFF9. *Phys. Chem. Chem. Phys.* 12, 5503–5513. doi: 10.1039/B926434E
- Scheinost, A. C., Claussner, J., Exner, J., Feig, M., Findeisen, S., Hennig, C., et al. (2021). ROBL-II at ESRF: a synchrotron toolbox for actinide research. *J. Synchrotron Radiat.* 28, 333–349. doi: 10.1107/S1600577520014265

Appendix A4 Tables of measured values and calculated parameters

Experimental description – stock solutions

Table A1: Results of the ICP-MS measurement of the calibration with ^{232}Th and ^{238}U concentrations of 0-750 ppt in 2 % HNO_3 and ^{193}Ir as internal standard for the sorption isotherm experiment of HCP / Th(IV). The ratio was determined. The limit of detection for ^{232}Th was calculated to be $\text{LOD} = 131.29$ cps and the limit of quantitation was calculated to be $\text{LOQ} = 161.46$ cps and for ^{238}U to be $\text{LOD} = 322.95$ and $\text{LOQ} = 372.55$.

Sample	cps (^{232}Th)	Δ cps (^{232}Th)	cps (ISTD)	Δ cps (ISTD)	R_{korr}
0 ppt	101.12	33.57	5065.10	197.54	0.00
25 ppt	1861.34	169.38	4824.46	303.94	0.37
50 ppt	3532.90	254.37	4860.03	170.10	0.71
75 ppt	5346.41	181.78	4805.57	288.33	1.09
100 ppt	7122.93	477.24	4857.25	140.86	1.45
200 ppt	14509.23	783.50	4862.82	296.63	2.96
Sample	cps (^{238}U)	Δ cps (^{238}U)	cps (ISTD)	Δ cps (ISTD)	R_{korr}
0 ppt	273.35	24.33	5065.10	197.54	0.00
50 ppt	3559.00	284.72	4824.46	303.94	0.68
100 ppt	7421.98	616.02	4860.03	170.10	1.47
250 ppt	16571.84	1044.03	4805.57	288.33	3.39
500 ppt	33363.76	2902.65	4857.25	140.86	6.81
750 ppt	50936.58	3667.43	4862.82	296.63	10.42

Table A2: Results of the ICP-MS measurement and the calculated concentration determined using the calibration of Table A1 of the ^{234}Th stock solution for the sorption isotherm experiment of HCP / Th(IV). The errors were calculated using the Gaussian error propagation. The samples were diluted in 2% HNO_3 .

Sample	Dil.	cps (^{232}Th)	Δ cps (^{232}Th)	cps (ISTD)	Δ cps (ISTD)	R_{korr}	$[^{232}\text{Th}] / \text{M}$
^{234}Th stock solution	1000	2024.16	58.70	4369.27	139.82	443.31	1.29×10^{-8}
^{234}Th stock solution	1000	1937.48	81.37	4148.08	174.22	447.11	1.30×10^{-8}
8M HCl	100	138.34	58.70	4781.10	267.74	0.90	2.66×10^{-11}
Sample	Dil.	cps (^{238}U)	Δ cps (^{238}U)	cps (ISTD)	Δ cps (ISTD)	R_{korr}	$[^{238}\text{U}] / \text{M}$
^{234}Th stock solution	1000	23515.06	1434.42	4369.27	139.82	5327.95	1.62×10^{-7}
^{234}Th stock solution	1000	22465.20	988.47	4148.08	174.22	5361.84	1.63×10^{-7}
8M HCl	100	20904.20	1881.38	4781.10	267.74	431.83	1.23×10^{-8}

Table A3: Results of the ICP-MS measurement of the calibration with ^{232}Th and ^{238}U concentrations of 0-750 ppt in 2 % HNO_3 and ^{193}Ir as internal standard for the sorption isotherm experiment of HCP / Th(IV) / ISA. The ratio was determined. The limit of detection for ^{232}Th was calculated to be $\text{LOD} = 406.56$ cps and the limit of quantitation was calculated to be $\text{LOQ} = 462.71$ cps and for ^{238}U to be $\text{LOD} = 850.66$ and $\text{LOQ} = 933.78$.

Sample	cps (^{232}Th)	Δ cps (^{232}Th)	cps (ISTD)	Δ cps (ISTD)	R_{korr}
0 ppt	350.40	66.93	11299.26	338.98	0.00
25 ppt	4357.29	278.87	11456.28	217.67	0.35
50 ppt	8475.76	203.42	11381.11	386.96	0.71
75 ppt	13086.58	300.99	11434.68	548.86	1.11
100 ppt	17241.25	327.58	11322.64	452.91	1.49
200 ppt	34986.74	839.68	11307.68	361.85	3.06
Sample	cps (^{238}U)	Δ cps (^{238}U)	cps (ISTD)	Δ cps (ISTD)	R_{korr}
0 ppt	767.55	75.99	11299.26	338.98	0.00
50 ppt	9778.09	332.46	11456.28	217.67	0.79
100 ppt	18811.86	282.18	11381.11	386.96	1.58
250 ppt	46765.09	1215.89	11434.68	548.86	4.02
500 ppt	91650.48	1099.81	11322.64	452.91	8.03
750 ppt	135889.28	2446.01	11307.68	361.85	11.95

Table A4: Results of the ICP-MS measurement and the calculated concentration determined using the calibration of Table A3 of 20 ml of the ^{234}Th stock solution for the sorption isotherm experiment of HCP / Th(IV) / ISA. The volume was constrained to 2.2 ml after measurement. The errors were calculated using the Gaussian error propagation. The samples were diluted in 2% HNO_3 .

Sample	Dil.	cps (^{232}Th)	Δ cps (^{232}Th)	cps (ISTD)	Δ cps (ISTD)	R_{korr}	$[^{232}\text{Th}] / \text{M}$
^{234}Th stock solution	1000	1081.26	100.56	11736.87	469.47	61.11	1.71×10^{-8}
^{234}Th stock solution	100	2311.15	138.67	12568.65	213.67	15.29	4.29×10^{-9}
8M HCl	1000	966.12	114.97	10736.39	558.29	58.97	1.65×10^{-8}
8M HCl	100	2656.59	124.86	11745.14	164.43	19.52	5.47×10^{-9}
Sample	Dil.	cps (^{238}U)	Δ cps (^{238}U)	cps (ISTD)	Δ cps (ISTD)	R_{korr}	$[^{238}\text{U}] / \text{M}$
^{234}Th stock solution	1000	2674.94	214.00	11736.87	469.47	159.980	4.21×10^{-8}
^{234}Th stock solution	100	18126.73	743.20	12568.65	213.67	137.43	3.62×10^{-8}
8M HCl	1000	997.82	70.85	10736.39	558.29	25.009	6.58×10^{-9}
8M HCl	100	1428.36	198.54	11745.14	164.43	5.368	1.41×10^{-9}

Table A5: Overview of the parameters of the γ -spectroscopic measurement of the final ^{234}Th stock solution. The indicated activity, which was calculated according to equations (2) and (3) refers to the total volume of the stock solution.

Experiment	$V_{gem} / \mu\text{l}$	t / s	Peak area	Emission probability	Peak efficiency	V_{stock} / ml	A_0 / Bq
Th / HCP	500	401	3.67×10^4	0.045	0.1155	2.5	4.41×10^4
Th / HCP / ISA	100	3600	2.88×10^4	0.045	0.1155	2.2	3.38×10^4

Table A6: Assignment of the measured peaks of the sample of $\text{Na}_4\text{EDTA} \times 2 \text{H}_2\text{O}$ after correction of the surface charge ($\Delta E_b = + 1.0 \text{ eV}$) as well as literature comparison [139], peak area and intensity ratios I of the peaks. The surface charge correction was related to Na 1s.

Peak	E_b / eV	$E_b \text{ Lit [139]} / \text{eV}$	Peak area	I
Na 1s	1072	1072	12412	1
O 1s	532	532	9433	1
N 1s	401	400	2424	1
O-C=O	287	285	3627	0.67
C-C	284	285	1826	0.33
Na 2s	65	64	620	1
Na 2p	32	31	215	1

Table A7: Assignment of the measured peaks of the sample of CaISA after correction of the surface charge ($\Delta E_b = + 2.7 \text{ eV}$) as well as literature comparison [139], peak area and intensity ratios I of the peaks. The surface charge correction was related to Ca 2p.

Peak	E_b / eV	$E_b \text{ Lit [139]} / \text{eV}$	Peak area	I
O 1s	532	532	13421	1
Ca 2s	439	439	925	1
Ca 2p 1/2	351	350	1013	0.32
Ca 2p 3/2	347	347	2138	0.68
O-C=O	289	285	1032	0.21
C-C	284	285	795	0.16

Table A8: Assignment of the measured peaks of the sample of NaISA after correction of the surface charge ($\Delta E_b = + 2.0 \text{ eV}$) as well as literature comparison [139], peak area and intensity ratios I of the peaks. The surface charge correction was related to Na 1s.

Peak	E_b / eV	$E_b \text{ Lit [139]} / \text{eV}$	Peak area	I
Na 1s	1072	1072	10737	1
O 1s	535	532	4771	1
O-C=O	289	285	1032	0.21
C-OH	287	285	3128	0.63
C-C	285	285	798	0.16
Na 2s	64	64	505	1
Na 2p	31	31	192	1

Table A9: Assignment of the measured peaks of the sample of the HCP powder after correction of the surface charge ($\Delta E_b = + 4.1$ eV) as well as literature comparison [139], peak area and intensity ratios I of the peaks. The surface charge correction was related to Ca 2p.

Peak	E_b / eV	E_b Lit [139] / eV	Peak area	I
O 1s	532	532	24157	1
Ca 2s	439	438	4820	1
Ca 2p 1/2	351	351	9037	0.68
Ca 2p 3/2	347	347	4227	0.32
O-C=O	289	285	2328	0.77
C-C	284	285	692	0.23
Si 2s	152	150	620	1
Si 2p	102	100	215	1

Table A10: Assignment of the measured peaks of the sample of the HCP powder after the preconditioning time of 72 h with ACW and after the correction of the surface charge ($\Delta E_b = + 4.1$ eV) as well as literature comparison [139], peak area and intensity ratios I of the peaks. The surface charge correction was related to Ca 2p.

Peak	E_b / eV	E_b Lit [139] / eV	Peak area	I
Na 1s	1072	1072	2412	1
O 1s	532	532	27596	1
Ca 2s	439	438	4728	1
Ca 2p 1/2	351	351	10227	0.68
Ca 2p 3/2	347	347	4897	0.32
O-C=O	289	285	2439	0.79
C-C	284	285	633	0.21
Si 2s	152	150	583	1
Si 2p	102	100	894	1
Ca 3s	44	44	740	1
Ca 3p	25	26	2188	1

Table A11: Assignment of the measured peaks of the sample of CaSiO_3 after correction of the surface charge ($\Delta E_b = + 1.0$ eV) as well as literature comparison [139], peak area and intensity ratios I of the peaks. The surface charge correction was related to Ca 2p.

Peak	E_b / eV	E_b Lit [139] / eV	Peak area	I
O 1s	531	532	21991	1
Ca 2s	440	438	5231	1
Ca 2p 1/2	350	351	7869	0.67
Ca 2p 3/2	347	347	3823	0.33
Si 2s	153	150	2383	1
Si 2p	102	100	2709	1

Table A12: Assignment of the measured peaks of the sample C-S-H phase ($C/S = 0.8$) after correction of the surface charge ($\Delta E_b = + 1.1$ eV) as well as literature comparison [139], peak area and intensity ratios I of the peaks. The surface charge correction was related to Ca 2p.

Peak	E_b / eV	E_b Lit [139] / eV	Peak area	I
O 1s	532	532	40631	1
Ca 2s	439	438	3197	1
Ca 2p 1/2	350	351	8776	0.68
Ca 2p 3/2	347	347	4095	0.32
Si 2s	153	150	4358	1
Si 2p	102	100	5351	1

Table A13: Data for the determination of the initial concentration of HTO in both cells in the primary compartment by LSC measurement with the counts cpm, determined activity A_i and efficiency TDCR from the LSC measurement, the corrected activity $A_i(\text{korr})$.

Sample	cpm	A_i / Bq	TDCR	cpm(korr)	$A_i(\text{korr})$ / Bq
Cell I	4507.46	171.71	0.43	9465666.0	3.66×10^5
Cell II	4502.72	176.16	0.43	9455712.0	3.70×10^5

Results and discussion - GLU

Table A14: Results of the ICP-MS measurement of the calibration with ^{232}Th concentrations of 0-600 ppt in 2% HNO_3 and ^{193}Ir as internal standard for the batch sorption experiment HCP / Th(IV) / GLU. The ratio was determined. The limit of detection for ^{232}Th was calculated to be $\text{LOD} = 51.48$ cps and the limit of quantitation was calculated to be $\text{LOQ} = 102.69$ cps.

Sample	cps (^{232}Th)	Δ cps (^{232}Th)	cps (ISTD)	Δ cps (ISTD)	R_{korr}
0 ppt	294.46	35.63	2968.24	77.17	0.00
10 ppt	583.93	32.70	3063.83	165.45	0.09
50 ppt	1801.32	63.05	3202.75	124.91	0.46
100 ppt	3511.76	105.35	3243.88	123.27	0.98
200 ppt	7029.48	161.68	3299.45	72.59	2.03
400 ppt	14001.65	294.03	3311.12	105.96	4.13
600 ppt	21534.71	172.28	3346.68	73.63	6.34

Table A15: Results of the ICP-MS measurement and the calculated concentration determined using the calibration of Table A14 of the samples of the batch sorption experiment HCP / Th(IV) / GLU. The errors were calculated using the Gaussian error propagation. The samples and the blanks were diluted 1:10 in 2% HNO_3 .

Sample	cps (^{232}Th)	Δ cps (^{232}Th)	cps (ISTD)	Δ cps (ISTD)	R_{korr}	$[\text{}^{232}\text{Th(IV)}]_{\text{eq}} / \text{M}$
(HCP+Th(IV)) + GLU	6280.71	113.05	3136.06	78.40	19.04	7.76×10^{-9}
(HCP+Th(IV)) + GLU	6344.65	215.72	3222.20	103.11	18.70	7.62×10^{-9}
(HCP+GLU) + Th(IV)	13637.33	368.21	3318.35	149.33	40.10	1.63×10^{-8}
(HCP+GLU) + Th(IV)	15446.69	216.25	3310.02	105.92	45.67	1.86×10^{-8}
(HCP+ Th(IV))+GLU)	14201.35	213.02	3332.79	66.66	41.62	1.69×10^{-8}
(HCP+ Th(IV))+GLU)	14770.92	251.11	3324.45	76.46	43.44	1.77×10^{-8}
B I	7882.28	209.58	3353.92	62.46	22.51	9.17×10^{-9}
B II	7645.39	391.29	3241.10	70.14	22.60	9.21×10^{-9}

Table A16: Results of the ICP-MS measurement of the calibration with ^{232}Th concentrations of 0-600 ppt in 2% HNO_3 and ^{193}Ir as internal standard for the batch sorption experiment HCP / GLU (leaching effect). The ratio was determined. The limit of detection for ^{232}Th was calculated to be $\text{LOD} = 592.59$ cps and the limit of quantitation was calculated to be $\text{LOQ} = 661.26$ cps.

Sample	cps (^{232}Th)	Δ cps (^{232}Th)	cps (ISTD)	Δ cps (ISTD)	R_{korr}
0 ppt	523.92	6.99	3148.30	3.36	0.00
10 ppt	740.61	2.75	3013.27	6.09	0.08
50 ppt	1832.44	5.45	3102.72	2.56	0.42
100 ppt	3104.41	5.79	3087.16	5.04	0.84
200 ppt	6286.30	1.48	3216.10	2.52	1.79
400 ppt	12611.31	3.68	3258.33	3.08	3.70
600 ppt	18982.35	2.26	3241.66	4.70	5.69

Table A17: Results of the ICP-MS measurement and the calculated concentration determined using the calibration of Table A16 of the samples of the batch sorption experiment HCP / GLU (leaching effect). The errors were calculated using the Gaussian error propagation. The samples were diluted 1:10 in 2% HNO_3 .

Sample	HCP mass in batch sample / g	cps (^{232}Th)	Δ cps (^{232}Th)	cps (ISTD)	Δ cps (ISTD)	R_{korr}	$[\text{}^{232}\text{Th(IV)}]_{\text{eq}} / \text{M}$
S/L 0.5 g/L	0.02	1716.30	3.70	2488.67	3.18	5.23	2.41×10^{-9}
S/L 2 g/L	0.08	4352.61	3.27	2450.34	4.71	16.10	7.46×10^{-9}
S/L 5 g/L	0.20	7993.97	2.33	2448.12	3.51	30.99	1.44×10^{-8}
S/L 10 g/L	0.40	5436.40	1.73	3261.66	3.23	15.00	6.95×10^{-9}
S/L 15 g/L	0.60	3280.57	4.41	2786.53	5.50	10.11	4.68×10^{-9}
S/L 20 g/L	0.80	2403.67	8.59	3079.95	5.60	6.14	2.84×10^{-9}
S/L 50 g/L	2.00	1679.08	3.86	3043.82	2.85	3.85	1.77×10^{-9}

Table A18: Results of the ICP-MS measurement of the calibration with ^{232}Th concentrations of 0-600 ppt in 2% HNO_3 and ^{193}Ir as internal standard for the batch sorption experiment C-S-H / Th(IV) / GLU. The ratio was determined. The limit of detection for ^{232}Th was calculated to be $\text{LOD} = 83.24$ cps and the limit of quantitation was calculated to be $\text{LOQ} = 106.48$ cps.

Sample	cps (^{232}Th)	Δ cps (^{232}Th)	cps (ISTD)	Δ cps (ISTD)	R_{korr}
0 ppt	60.00	15.18	6656.45	1.70	0.00
10 ppt	65.56	15.73	6464.66	2.90	0.00
50 ppt	112.78	23.46	6645.33	3.30	0.01
100 ppt	192.23	22.49	6603.65	1.90	0.02
200 ppt	308.91	48.19	6532.48	2.50	0.04
400 ppt	550.59	51.76	6568.06	1.90	0.07
600 ppt	804.51	72.41	6346.83	1.60	0.12

Table A19: Results of the ICP-MS measurement and the calculated parameters $S\%$ and R_d determined using the calibration of Table A18 of the samples of the batch sorption experiment C-S-H / Th(IV) / GLU. The errors were calculated using the Gaussian error propagation. The samples were measured undiluted or 1:3 diluted, acidified with conc. HNO_3 and the blanks were diluted 1:10 in 2% HNO_3 .

Sample	cps (^{232}Th)	Δ cps (^{232}Th)	cps (ISTD)	Δ cps (ISTD)	R_{korr}	$S\% / \%$	$\Delta S\% / \%$	$R_d /$ $L\ kg^{-1}$	$\Delta R_d /$ $L\ kg^{-1}$
HCP+Th(IV)	203.90	36.70	5435.28	146.75	0.03	96.48	0.94	5.48×10^3	1.52×10^3
(C-S-H+Th(IV)) + GLU	531.32	65.35	5388.60	172.44	0.09	88.92	1.85	1.61×10^3	3.02×10^2
(C-S-H+Th(IV)) + GLU	520.69	88.52	5435.28	146.75	0.09	89.27	2.27	1.66×10^3	3.94×10^2
(C-S-H+GLU) + Th(IV)	291.13	31.44	5806.60	214.46	0.13	84.75	2.65	1.11×10^3	2.28×10^2
(C-S-H+GLU) + Th(IV)	310.02	32.55	5740.97	233.94	0.14	83.31	2.83	9.99×10^2	2.03×10^2
(C-S-H+ Th(IV)+GLU)	288.35	28.55	5393.59	118.66	0.05	94.50	0.87	3.44×10^3	5.80×10^2
(C-S-H+ Th(IV)+GLU)	295.59	29.85	5396.37	97.13	0.05	94.34	0.91	3.33×10^3	5.68×10^2
B I	507.81	50.78	6156.73	98.51					
B II	633.38	50.86	6102.82	224.68					

Table A20: Summary of the conditions for the CE-ICP-MS measurements of the system Ca-Th(IV)-OH-GLU with pH, $[GLU]_0/M$, $[Ca]_0/M$ and the electrophoretic mobilities μ_{eff} of Th(IV) ($[Th(IV)]_0 = 4 \times 10^{-7} M$) in absence and presence of GLU ($[GLU]_0 = 1 \times 10^{-2} M$) and Ca(II)-containing solutions at different pH values ($I = 0.1 M$).

Sample	pH	$[GLU]_0/M$	$[Ca]_0/M$	$\mu_{eff} Th /$ cm^2/Vs	$\Delta \mu_{eff} Th / cm^2/Vs$
Th(IV)	1.47	-	-	4.87×10^{-4}	3.74×10^{-6}
Th(IV)-OH-GLU	2.15	3.86×10^{-4}	-	1.76×10^{-4}	2.96×10^{-6}
Th(IV)-OH-GLU	4.05	7.93×10^{-3}	-	-5.92×10^{-5}	3.17×10^{-6}
Th(IV)-OH-GLU	5.71	9.93×10^{-3}	-	-1.96×10^{-4}	4.18×10^{-6}
Ca-Th(IV)-OH-GLU	1.5	7.26×10^{-5}	1.7×10^{-3}	3.70×10^{-4}	3.44×10^{-6}
Ca-Th(IV)-OH-GLU	2.13	2.96×10^{-4}	1.7×10^{-3}	2.39×10^{-4}	3.07×10^{-6}
Ca-Th(IV)-OH-GLU	3.2	2.64×10^{-3}	1.7×10^{-3}	7.90×10^{-5}	3.03×10^{-6}
Ca-Th(IV)-OH-GLU	4.32	8.25×10^{-3}	1.7×10^{-3}	-1.03×10^{-4}	3.38×10^{-6}
Ca-Th(IV)-OH-GLU	5.14	9.73×10^{-3}	1.7×10^{-3}	-1.77×10^{-4}	3.80×10^{-6}
Ca-Th(IV)-OH-GLU	5.96	9.94×10^{-3}	1.7×10^{-3}	-1.81×10^{-4}	4.44×10^{-6}
Ca-Th(IV)-OH-GLU	12.6	1.00×10^{-2}	1.7×10^{-3}	-1.55×10^{-4}	6.04×10^{-6}
Ca-Th(IV)-OH-GLU	6.27	9.98×10^{-3}	1.0×10^{-2}	-1.26×10^{-4}	4.43×10^{-6}
Ca-Th(IV)-OH-GLU	3.42	3.73×10^{-3}	1.0×10^{-2}	-3.12×10^{-5}	2.94×10^{-6}

Results and discussion - EDTA

Table A21: Overview of average of the measured activities from three LSC measurements and the calculated parameters $S\%$, R_d , $\log[EDTA]_{eq}$ and $\log[EDTA]_{sorb}$ determined for the samples of sorption isotherm from the experiment HCP / EDTA. The errors were calculated using the Gaussian error propagation. The limit of detection for ^{14}C EDTA was calculated to be $LOD = 6.57$ Bq and the limit of quantitation was calculated to be $LOQ = 10.02$ Bq.

Sample	[EDTA] ₀ / M	A / Bq	ΔA / Bq	R_{korr}	$S\%$ / %	$\Delta S\%$ / %	R_d / L kg ⁻¹	$\log [EDTA]_{eq}$	$\log [EDTA]_{sorb}$
BG		3.13	0.03						
1	1×10^{-1}	13.00	0.29	7.05	3.23	15.16	7.47	-1.03	0.15
2	1×10^{-2}	13.21	0.15	5.54	2.70	11.74	6.04	-2.02	-0.96
3	1×10^{-3}	13.30	0.21	4.87	2.91	10.24	6.44	-3.02	-2.01
4	1×10^{-4}	13.40	0.15	4.12	2.74	8.59	5.95	-4.02	-3.08
5	1×10^{-5}	13.49	0.26	3.51	3.15	7.28	6.76	-5.02	-4.15
6	1×10^{-6}	12.97	0.24	7.24	2.99	15.61	6.95	-6.03	-4.84
7	1×10^{-7}	206.15	1.52	1.28	1.59	2.60	3.27	-7.01	-6.59
8	1×10^{-8}	21.62	0.24	0.63	1.43	1.26	2.90	-8.00	-7.90
9	1×10^{-9}	4.14	0.15	4.47	5.69	9.37	3.67	-9.02	-8.05
B I to sample 1-6		13.98	0.70						
B II to sample 7		208.83	1.44						
B III to sample 8		21.76	1.09						
B IV to sample 9		2.11	0.11						

Table A22: Overview of average of the measured activities from three LSC measurements and the calculated parameters $S\%$, R_d , $[EDTA]_{eq}$ and $[EDTA]_{calc}$ determined for the samples of the batch sorption experiment HCP / EDTA. The errors were calculated using the Gaussian error propagation. The limit of detection for ^{14}C EDTA was calculated to be $LOD = 6.70$ Bq and the limit of quantitation was calculated to be $LOQ = 10.28$ Bq.

Sample	S/L / g L ⁻¹	A / Bq	ΔA / Bq	$S\%$ / %	$\Delta S\%$ / %	R_d / L kg ⁻¹	ΔR_d / L kg ⁻¹	$[EDTA]_{eq}$ / mM	$[EDTA]_{calc}$ / mM
BG		2.49	0.05						
1	0.5	12.33	0.11	5.42	1.26	114.55	28.27	9.46	9.96
2	1	12.71	0.03	2.45	1.00	25.09	10.47	9.76	9.93
3	2	12.84	0.09	1.52	1.20	7.71	6.20	9.85	9.86
4	5	12.72	0.06	2.38	1.08	4.87	2.27	9.76	9.65
5	10	12.47	0.07	4.34	1.08	4.53	1.18	9.57	9.32
6	15	12.27	0.18	5.86	1.69	4.15	1.27	9.41	9.02
7	20	12.71	0.22	2.47	1.98	1.27	1.04	9.75	8.74
B I		13.03	0.13						

Table A23: Overview of average of the measured activities from three LSC measurements and the calculated parameters $S\%$, R_d , $\log[EDTA]_{eq}$ and $\log[EDTA]_{sorb}$ determined for the samples of sorption isotherm from the experiment C-S-H / EDTA. The errors were calculated using the Gaussian error propagation. The limit of detection for ^{14}C EDTA was calculated to be $LOD = 4.42$ Bq and the limit of quantitation was calculated to be $LOQ = 7.22$ Bq.

Sample	[EDTA] ₀ /M	A / Bq	ΔA / Bq	$S\%$ / %	$\Delta S\%$ / %	R_d / L kg ⁻¹	ΔR_d / L kg ⁻¹	log [EDTA] _{eq}	log [EDTA] _{sorb}
BG		1.60	0.02						
1	1×10^{-1}	29.94	0.29	2.93	2.54	6.04	5.77	-1.01	-0.23
2	1×10^{-2}	27.93	0.24	9.44	2.35	20.85	6.13	-2.04	-0.72
3	1×10^{-3}	29.54	0.32	4.24	2.56	8.86	5.87	-3.02	-2.07
4	1×10^{-4}	27.58	0.05	10.60	2.19	23.71	5.94	-4.05	-2.67
5	1×10^{-5}	30.60	0.11	0.81	2.46	1.64	5.26	-5.00	-4.79
6	1×10^{-6}	28.83	0.18	6.53	2.36	13.97	5.75	-6.03	-4.88
7	1×10^{-7}	221.03	1.05	0.49	1.41	0.98	2.78	-7.00	-7.01
8	1×10^{-8}	23.61	0.08	1.17	0.90	2.37	1.84	-8.01	-7.63
9	1×10^{-9}	4.33	0.03	-0.70	0.86	-1.39	1.71	-	-
B I to sample 1-6		30.85	0.80						
B II to sample 7		222.12	2.92						
B III to sample 8		23.89	0.20						
B IV to sample 9		2.23	0.03						

Table A24: Overview of average of the measured activities from three LSC measurements and the calculated parameters $S\%$, R_d , $[EDTA]_{eq}$ and $[EDTA]_{calc}$ determined for the samples of the batch sorption experiment C-S-H / EDTA. The errors were calculated using the Gaussian error propagation. The limit of detection for ^{14}C EDTA was calculated to be $LOD = 4.37$ Bq and the limit of quantitation was calculated to be $LOQ = 7.16$ Bq.

Sample	S/L / g L ⁻¹	A / Bq	ΔA / Bq	$S\%$ / %	$\Delta S\%$ / %	R_d / L kg ⁻¹	ΔR_d / L kg ⁻¹	[EDTA] _{eq} / mM	[EDTA] _{calc} / mM
BG		1.61	0.02						
1	0.5	28.68	0.25	-0.28	2.04	-5.58	39.79	10.03	9.96
2	1	28.75	0.15	-0.52	1.91	-5.16	18.54	10.05	9.92
3	2	28.72	0.33	-0.40	2.18	-2.01	10.59	10.04	9.85
4	5	28.99	0.19	-1.35	1.97	-2.66	3.77	10.13	9.63
5	5	29.56	0.70	-3.36	3.12	-6.50	5.73	10.34	9.63
6	10	29.42	0.19	-2.87	2.00	-2.79	1.86	10.29	9.29
7	15	29.45	0.32	-2.97	2.20	-1.92	1.36	10.30	8.98
8	20	29.42	0.18	-2.85	1.99	-1.39	0.92	10.29	8.68
9	50	29.91	0.45	-4.58	2.49	-0.88	0.45	10.46	7.77
B I		28.33	0.51						
B II		28.87	0.32						

Table A25: Assignment of the measured peaks of the sample HCP / EDTA / ACW after correction of the surface charge ($\Delta E_b = + 4.2$ eV) as well as literature comparison [139], peak area and intensity ratios I of the peaks. The surface charge correction was related to Ca 2p.

Peak	E_b / eV	E_b Lit. [139] / eV	Peak area	I
Na 1s	1072	1072	6194	1
O 1s	531	532	32162	1
Ca 2s	439	438	4771	1
Ca 2p 1/2	347	350	4720	0.32
Ca 2p 3/2	351	346	9806	0.68
O-C=O	290	285	1924	0.80
C-C	285	285	488	0.20
K 2p 1/2	293	297	965	0.35
K 2p 3/2	296	295	1764	0.65
Si 2s	153	150	1670	1
Si 2p	102	100	1484	1

Table A26: Assignment of the measured peaks of the sample C-S-H / EDTA / Milli-Q after correction of the surface charge ($\Delta E_b = + 1.2$ eV) as well as literature comparison [139], peak area and intensity ratios I of the peaks. The surface charge correction was related to Ca 2p.

Peak	E_b / eV	E_b Lit. [139] / eV	Peak area	I
O 1s	532	532	40896	1
Ca 2s	439	438	4028	1
Ca 2p 1/2	347	350	8501	0.67
Ca 2p 3/2	351	346	3611	0.33
Si 2s	154	150	4685	1
Si 2p	102	100	5245	1

Table A27: Overview of average of the measured activities from three LSC measurements and the calculated parameters $S\%$ and R_d determined for the samples of the batch sorption experiment HCP / Am(III) / EDTA. The errors were calculated using the Gaussian error propagation.

Sample	A / Bq	ΔA / Bq	$S\%$ / %	$\Delta S\%$ / %	R_d / L kg ⁻¹	ΔR_d / L kg ⁻¹
HCP+Am(III)	1.19	5.00	99.80	0.99	1.01×10^5	5.10×10^3
HCP+ Am(III)	1.17	8.50	99.81	0.97	1.01×10^5	5.18×10^3
(HCP+ Am(III)) + EDTA	0.55	10.20	99.91	0.46	2.17×10^5	1.10×10^4
(HCP+ Am(III)) + EDTA	0.76	4.80	99.87	0.63	1.59×10^5	8.01×10^3
(HCP+EDTA) + Am(III)	1.39	8.00	99.77	1.16	8.62×10^4	4.36×10^3
(HCP+EDTA) + Am(III)	0.95	7.00	99.84	0.79	1.26×10^5	6.38×10^3
(HCP+ Am(III)+EDTA)	0.57	10.20	99.91	0.47	2.12×10^5	1.07×10^4
(HCP+ Am(III)+EDTA)	0.41	9.20	99.93	0.34	2.93×10^5	1.48×10^4
B I	600.75	6.90				
B II	602.48	4.20				

Table A28: Results of the ICP-MS measurement of the calibration with ^{232}Th concentrations of 0-400 ppt in ACW acidified with conc. HNO_3 and ^{193}Ir as internal standard for the batch sorption experiment HCP / Th(IV) / EDTA. The ratio was determined. The limit of detection for ^{232}Th was calculated to be $\text{LOD} = 607.38$ cps and the limit of quantitation was calculated to be $\text{LOQ} = 676.95$ cps.

Sample	cps (^{232}Th)	Δ cps (^{232}Th)	cps (ISTD)	Δ cps (ISTD)	R_{korr}
0 ppt	537.81	74.64	2597.04	50.63	0.00
50 ppt	2189.73	58.46	2555.36	122.85	0.65
100 ppt	4128.64	92.80	2533.68	58.05	1.42
200 ppt	7458.10	47.65	2551.47	407.94	2.72
400 ppt	15369.99	71.89	2633.16	202.37	5.63

Table A29: Results of the ICP-MS measurement and the calculated parameters $S\%$ and R_d determined the calibration of Table A28 of the samples of the batch sorption experiment HCP / Th(IV) / EDTA. The errors were calculated using the Gaussian error propagation. The samples were measured undiluted, acidified with conc. HNO_3 and the blanks were diluted 1:10 in 2% HNO_3 . Only Blank I was used to calculate $S\%$ and R_d values, as Blank II did not correspond with initial concentration of $[\text{Th(IV)}]_0 = 1 \times 10^{-8}$ M.

Sample	cps (^{232}Th)	Δ cps (^{232}Th)	cps (ISTD)	Δ cps (ISTD)	R_{korr}	$S\% / \%$	$\Delta S\% / \%$	$R_d / \text{L kg}^{-1}$	$\Delta R_d / \text{L kg}^{-1}$
HCP+Th(IV)	565.59	28.28	2494.24	189.56	0.020	99.42	14.03	3.43×10^4	8.34×10^5
HCP+Th(IV)	1073.99	91.29	2498.13	157.38	0.223	93.43	14.09	8.84×10^3	6.53×10^3
(HCP+Th(IV)) + EDTA	586.16	59.79	2348.65	70.46	0.042	98.75	14.04	1.58×10^4	1.79×10^5
(HCP+Th(IV)) + EDTA	565.04	27.12	2507.57	90.27	0.018	99.46	14.02	3.70×10^4	9.69×10^5
(HCP+EDTA) + Th(IV)	513.92	41.11	2456.45	76.15	0.002	99.94	14.03	3.19×10^5	7.13×10^5
(HCP+EDTA) + Th(IV)	510.59	35.74	2578.70	118.62	-0.009	-	-	-	-
(HCP+ Th(IV)+EDTA)	534.48	54.52	2502.57	112.62	0.006	99.81	2.20	1.04×10^4	1.20×10^6
(HCP+ Th(IV)+EDTA)	528.37	48.61	2693.72	126.60	-0.011	-	-	-	-
B I	9000.70	621.05	2501.46	155.09					
B II	18435.50	774.29	2437.56	73.13					

Table A30: Results of the ICP-MS measurement and the calculated parameters $S\%$ and R_d determined for the samples of the batch sorption experiment HCP / Pu(IV) / EDTA. The errors were calculated using the Gaussian error propagation. The samples were measured undiluted, acidified with conc. HNO_3 and the blanks were diluted 1:50 in 2% HNO_3 . The limit of detection for ^{239}Pu was calculated to be $LOD = 223.97$ cps and the limit of quantitation was calculated to be $LOQ = 264.59$ cps.

Sample	cps (^{239}Pu)	Δ cps (^{239}Pu)	cps (ISTD)	Δ cps (ISTD)	R_{korr}	$S\% / \%$	$\Delta S\% / \%$	$R_d /$ $L\ kg^{-1}$	$\Delta R_d /$ $L\ kg^{-1}$
0 ppt	183.35	16.32	2224.73	44.49	0.00				
(HCP+ Pu(IV)) + EDTA	217.79	33.54	2229.73	104.80	0.01	99.96	0.05	4.48×10^5	5.32×10^5
(HCP+ Pu(IV)) + EDTA	252.24	21.69	2224.18	91.19	0.03	99.91	0.04	2.19×10^5	9.70×10^4
(HCP+EDTA) + Pu(IV)	374.47	60.66	2164.72	90.92	0.09	99.73	0.09	7.48×10^4	2.59×10^4
(HCP+EDTA) + Pu(IV)	247.79	11.40	2189.17	96.32	0.03	99.91	0.03	2.21×10^5	7.82×10^4
(HCP+ Pu(IV)+EDTA)	236.13	29.52	2207.51	92.72	0.02	99.93	0.05	2.77×10^5	1.88×10^5
(HCP+ Pu(IV)+EDTA)	250.57	25.31	2159.16	73.41	0.03	99.90	0.04	2.02×10^5	9.06×10^4
B I	1634.62	70.29	2282.52	54.78					
B II	1711.31	41.07	2251.40	51.78					

Table A31: Measured pH and E_h values after a contact time of 72 h of the samples from the batch sorption experiment HCP / Pu(IV) / EDTA.

Sample	pH	E_h (SHE) / V
(HCP+ Pu(IV)) + EDTA	13.20	-0.55
(HCP+ Pu(IV)) + EDTA	13.20	-0.57
(HCP+EDTA) + Pu(IV)	13.20	0.07
(HCP+EDTA) + Pu(IV)	13.20	0.05
(HCP+ Pu(IV)+EDTA)	13.20	-0.58
(HCP+ Pu(IV)+EDTA)	13.20	-0.53

Results and discussion – ISA

Table A32: Overview of average of the measured activities from the NPOC measurements and the calculated parameters $S\%$, $[ISA]_{eq}$ and $[ISA]_{calc}$ determined for the samples of the batch sorption experiment HCP / ISA with varying ISA concentration. The errors were calculated using the Gaussian error propagation. The 5 g L^{-1} sample from the sorption isotherm with varying S/L ratio, which is in Table A33, was used as the background sample $\bar{c}_{NPOC,ISA} / \text{ppm}$. $\bar{c}_{NPOC,res} / \text{ppm}$ is the difference of $\bar{c}_{NPOC,ISA} / \text{ppm} - \bar{c}_{NPOC,BG} / \text{ppm}$.

$[ISA]_0 / \text{M}$	$\bar{c}_{NPOC,ISA} / \text{ppm}$	$\bar{c}_{NPOC,res} / \text{ppm}$	f_{dill}	$\bar{c}_{NPOC,korr} / \text{ppm}$	$S\% / \%$	$\Delta S\% / \%$	$[ISA]_{eq} / \text{mM}$	$[ISA]_{sorb} / \text{mM}$
1×10^{-2}	8.11	1.90	100	189.85	61.99	$\frac{10.7}{5}$	9.42×10^{-4}	3.07×10^{-1}
1×10^{-2}	8.64	2.43	100	242.69	51.42	$\frac{15.5}{7}$	1.20×10^{-3}	2.55×10^{-1}
1×10^{-3}	15.63	9.41	4	37.64	77.90	7.27	1.87×10^{-4}	1.32×10^{-1}
1×10^{-3}	17.23	11.02	4	44.07	74.13	4.08	2.19×10^{-4}	1.25×10^{-1}
$1 \times 10^{-3.5}$	22.63	16.41	1	16.41	80.98	2.35	8.15×10^{-5}	6.94×10^{-2}
$1 \times 10^{-3.5}$	22.38	16.17	1	16.17	81.26	2.98	8.03×10^{-5}	6.96×10^{-2}
I to 1×10^{-2}	5.32	1.72	250					
B II to 1×10^{-3}	11.84	9.43	20					
B III to $1 \times 10^{-3.5}$	24.89	20.04	4					

Table A33: Overview of average of the measured activities from the NPOC measurements and the calculated parameters $S\%$, $[ISA]_{eq}$ and $[ISA]_{calc}$ determined for the samples of the batch sorption experiment HCP / ISA with varying S/L ratio. The errors were calculated using the Gaussian error propagation. $\bar{c}_{NPOC,res} / \text{ppm}$ is the difference of $\bar{c}_{NPOC,ISA} / \text{ppm} - \bar{c}_{NPOC,BG} / \text{ppm}$.

$S/L / \text{g L}^{-1}$	$\bar{c}_{NPOC,BG} / \text{ppm}$	$\bar{c}_{NPOC,ISA} / \text{ppm}$	$\bar{c}_{NPOC,res} / \text{ppm}$	f_{dill}	$\bar{c}_{NPOC,korr} / \text{ppm}$	$S\% / \%$	$\Delta S\% / \%$	$[ISA]_{eq} / \text{mM}$
0.5	7.61	9.52	1.91	12	23.80	86.01	3.18	0.09
1	4.77	9.76	4.99	12	62.11	63.54	3.14	0.31
2	5.74	10.74	5.00	10	51.87	69.55	4.52	0.26
5	6.22	11.37	5.16	8	42.79	74.88	6.42	0.21
10	6.22	14.66	8.44	4	35.01	79.45	6.78	0.17
15	6.62	23.93	17.31	2	35.92	78.92	6.38	0.18
20	11.99	25.56	13.57	1	14.08	91.74	9.57	0.07

Table A34: Assignment of the measured peaks of the sample HCP / ISA / ACW after correction of the surface charge ($\Delta E_b = + 4.1$ eV) as well as literature comparison [139], peak area and intensity ratios I of the peaks. The surface charge correction was related to Ca 2p.

Peak	E_b / eV	E_b Lit [139] / eV	Peak area	I
Na 1s	1072	1072	2124	1
O 1s	531	532	27589	1
Ca 2s	439	438	4534	1
Ca 2p 1/2	351	350	4521	0.33
Ca 2p 3/2	347	346	8996	0.57
O-C=O	292	285	442	0.11
C-O-C	289	285	1230	0.32
C-C	285	285	2179	0.57
Si 2s	153	150	877	1
Si 2p	102	100	879	1

Table A35: Assignment of the measured peaks of the sample C-S-H / ISA / Milli-Q after correction of the surface charge ($\Delta E_b = + 1.0$ eV) as well as literature comparison [139], peak area and intensity ratios I of the peaks. The surface charge correction was related to Ca 2p.

Peak	E_b / eV	E_b Lit [139] / eV	Peak area	I
O 1s	538	532	38393	1
Ca 2s	443	438	3424	1
Ca 2p 1/2	347	350	9203	0.68
Ca 2p 3/2	350	346	4333	0.32
Si 2s	153	150	4318	1
Si 2p	102	100	5348	1

Table A36: Results of the ICP-MS measurement of the calibration with ^{232}Th concentrations of 0-600 ppt ACW acidified with HNO_3 and ^{193}Ir as internal standard for the batch sorption experiment HCP / ISA (leaching experiments) after 3 and 30 d of contact time. The ratio was determined. The limit of detection for ^{232}Th was calculated to be $\text{LOD} = 746.70$ cps and the limit of quantitation was calculated to be $\text{LOQ} = 824.31$ cps.

Sample	cps (^{232}Th)	Δ cps (^{232}Th)	cps (ISTD)	Δ cps (ISTD)	R_{korr}
0 ppt	669.10	99.40	4417.31	190.71	0.00
10 ppt	934.41	103.41	4021.77	155.11	0.08
50 ppt	2975.35	258.84	4208.74	254.36	0.56
100 ppt	5702.63	151.34	4998.17	136.39	0.99
200 ppt	11110.62	516.50	4701.09	132.23	2.21
400 ppt	23253.73	490.79	4872.97	277.44	4.62
600 ppt	36753.23	667.56	4782.92	209.85	7.53

Table A37: Results of the ICP-MS measurement of the samples of the batch sorption experiment HCP / ISA (leaching experiment) after 3 (top) and 30 (bottom) d of contact time. The equilibrium concentration c_{eq} was determined using the calibration of Table A36. For the measurement after 30 ds, double determinations were applied. The errors were calculated using the Gaussian error propagation. The samples were measure undiluted acidified with conc. HNO_3 .

Sample	cps (^{232}Th)	Δ cps (^{232}Th)	cps (ISTD)	Δ cps (ISTD)	R_{korr}	c_{eq} / M	$\Delta c_{eq} / M$
HCP / ACW	597.35	84.64	3970.01	119.95	0.00	4.45×10^{-11}	6.67×10^{-12}
HCP / ACW / ISA ($10^{-3} M$)	1143.00	153.73	4013.43	178.97	0.13	4.66×10^{-11}	6.99×10^{-12}
HCP / ACW / ISA ($10^{-3} M$)	964.46	101.25	4245.41	244.65	0.08	2.66×10^{-11}	3.99×10^{-12}
HCP / ACW / ISA ($10^{-2.5} M$)	7776.01	280.85	4126.95	216.78	1.73	6.02×10^{-10}	9.02×10^{-11}
HCP / ACW / ISA ($10^{-2.5} M$)	7565.68	208.26	3926.66	170.59	1.78	6.61×10^{-10}	9.91×10^{-11}
HCP / ACW / ISA ($10^{-2} M$)	21669.27	250.47	4190.33	114.83	5.02	1.74×10^{-9}	2.61×10^{-10}
HCP / ACW / ISA ($10^{-2} M$)	21867.99	250.47	4078.52	185.52	5.21	1.81×10^{-9}	2.71×10^{-10}
HCP / ACW	1074.58	93.21	4197.02	204.19	0.10	8.11×10^{-11}	1.22×10^{-11}
HCP / ACW / ISA ($10^{-3} M$)	1420.01	86.92	3978.35	260.95	0.23	3.50×10^{-11}	5.25×10^{-12}
HCP / ACW / ISA ($10^{-2.5} M$)	42209.11	585.51	4292.17	134.91	9.68	3.32×10^{-9}	4.98×10^{-10}
HCP / ACW / ISA ($10^{-2} M$)	53071.52	1348.07	3938.33	289.25	13.32	4.59×10^{-9}	6.88×10^{-10}

Table A38: Results of the ICP-MS measurement of the calibration with ^{232}Th concentrations of 0-600 ppt ACW acidified with HNO_3 and ^{193}Ir as internal standard for the batch sorption experiment HCP / ISA (leaching experiments) after 53 and 80 d of contact time. The ratio was determined. The limit of detection for ^{232}Th was calculated to be $LOD = 233.44$ cps and the limit of quantitation was calculated to be $LOQ = 274.99$ cps.

Sample	cps (^{232}Th)	Δ cps (^{232}Th)	cps (ISTD)	Δ cps (ISTD)	R_{korr}
0 ppt	191.88	23.19	4829.62	745.47	0.00
10 ppt	625.72	84.42	4726.15	476.48	0.09
50 ppt	2951.98	220.42	4701.08	117.48	0.59
100 ppt	5679.23	111.39	4767.88	230.08	1.15
200 ppt	11713.43	349.81	4727.85	953.41	2.44
400 ppt	24310.12	642.41	5320.38	845.24	4.53
600 ppt	36042.58	3291.27	5310.37	1192.38	6.75

Table A39: Results of the ICP-MS measurement of the samples of the batch sorption experiment HCP / ISA (leaching experiment) after 53 (top) and 80 (bottom) d of contact time. The equilibrium concentration c_{eq} was determined using the calibration of Table A38. For the measurement after 30 ds, double determinations were applied. The errors were calculated using the Gaussian error propagation. The samples were diluted 1:10 in 2% HNO_3 .

Sample	cps (^{232}Th)	Δ cps (^{232}Th)	cps (ISTD)	Δ cps (ISTD)	R_{korr}	c_{eq} / M	Δc_{eq} / M
HCP / ACW	468.86	41.24	10045.15	3.63	0.07	1.39×10^{-11}	2.09×10^{-12}
HCP / ACW / ISA (10^{-3} M)	1121.31	140.47	9996.59	272.81	0.72	2.51×10^{-10}	3.76×10^{-11}
HCP / ACW / ISA (10^{-3} M)	820.95	90.66	9961.55	473.54	0.43	1.37×10^{-10}	2.05×10^{-11}
HCP / ACW / ISA ($10^{-2.5}$ M)	6545.66	312.22	9868.05	703.04	6.24	2.36×10^{-9}	3.54×10^{-10}
HCP / ACW / ISA ($10^{-2.5}$ M)	6363.72	556.05	9387.26	1245.08	6.38	2.43×10^{-9}	3.64×10^{-10}
HCP / ACW / ISA (10^{-2} M)	10975.47	250.47	8929.87	2326.64	11.89	4.53×10^{-9}	6.79×10^{-10}
HCP / ACW / ISA (10^{-2} M)	13271.67	250.47	9756.15	410.55	13.21	5.03×10^{-9}	7.54×10^{-10}
HCP / ACW	687.45	94.69	9844.63	427.03	0.30	1.03×10^{-10}	1.54×10^{-11}
HCP / ACW / ISA (10^{-3} M)	1565.19	76.17	10202.07	714.73	1.14	3.20×10^{-12}	4.80×10^{-11}
HCP / ACW / ISA ($10^{-2.5}$ M)	10734.82	383.95	9777.93	292.49	10.58	3.93×10^{-9}	5.90×10^{-10}
HCP / ACW / ISA (10^{-2} M)	15509.95	547.37	9978.22	411.71	15.15	5.68×10^{-9}	8.52×10^{-10}

Table A40: Results of the ICP-MS measurement of the calibration with ^{232}Th concentrations of 0-600 ppt in 2% HNO_3 with 1:10 ACW and ^{193}Ir as internal standard for the batch sorption experiment HCP / Th(IV) / ISA after a contact time of 72 h. The ratio was determined. The limit of detection for ^{232}Th was calculated to be $LOD = 135.88$ cps and the limit of quantitation was calculated to be $LOQ = 166.63$ cps. This measurement was performed as part of S. Kissel's master's thesis [137].

Sample	cps (^{232}Th)	Δ cps (^{232}Th)	cps (ISTD)	Δ cps (ISTD)	R_{korr}
0 ppt	105.12	24.32	9836.31	187.49	0.00
10 ppt	163.52	32.08	9236.87	135.44	0.01
50 ppt	228.59	28.61	9210.16	523.10	0.01
100 ppt	288.66	57.13	9093.30	390.25	0.02
200 ppt	1084.71	104.33	9615.89	362.20	0.10
400 ppt	1171.00	360.20	9096.58	376.72	0.12
600 ppt	1828.84	120.26	8906.32	207.08	0.19

Table A41: Results of the ICP-MS measurement and the calculated parameters $S\%$ and R_d using the calibration of Table A40 of the samples of the batch sorption experiment HCP / Th(IV) / ISA after a contact time of 72 h. The errors were calculated using the Gaussian error propagation. The samples were diluted 1:10 in 2% HNO₃, the blanks were diluted 1:200 in 2% HNO₃ and the samples HCP / Th(IV) were measured undiluted acidified with conc. HNO₃. This measurement was performed as part of S. Kissel's master's thesis [137].

Sample	cps (²³² Th)	Δ cps (²³² Th)	cps (ISTD)	Δ cps (ISTD)	R_{korr}	$S\% / \%$	$\Delta S\% / \%$	$R_d / \text{L kg}^{-1}$	$\Delta R_d / \text{L kg}^{-1}$
(HCP+Th(IV)) + ISA	4601.01	197.79	9158.43	202.16	4.92	86.40	1.10	1.27×10^3	1.19×10^2
(HCP+Th(IV)) + ISA	4854.77	195.07	9076.68	279.89	5.24	85.51	1.19	1.7×10^3	1.13×10^2
(HCP+ ISA) + Th(IV)	12147.77	333.54	9126.69	227.00	13.20	63.49	2.69	3.46×10^2	4.02×10^1
(HCP+ ISA) + Th(IV)	12127.66	394.72	9128.37	299.20	13.18	63.56	2.87	3.48×10^2	4.32×10^1
(HCP+ Th(IV)+ ISA)	4811.31	298.31	9171.77	168.24	5.14	85.79	1.30	1.21×10^3	1.29×10^2
(HCP+ Th(IV)+ ISA)	4859.66	389.84	9191.82	305.63	5.18	85.68	1.56	1.19×10^3	1.52×10^2
HCP+ Th(IV)	442.81	36.31	2403.10	108.14	0.17	99.52	0.06	4.13×10^4	4.96×10^3
HCP+ Th(IV)	747.28	30.64	2467.57	93.77	0.29	99.19	0.07	2.45×10^4	2.14×10^3
B I	2379.57	129.90	11678.19	271.67					
B II	2165.95	214.26	12082.35	500.49					

Table A42: Results of the ICP-MS measurement of the calibration with ²³²Th concentrations of 0-600 ppt in 2% HNO₃ with 1:10 ACW and ¹⁹³Ir as internal standard for the batch sorption experiment HCP / Th(IV) / ISA after a contact time of 72 h. The ratio was determined. The limit of detection for ²³²Th was calculated to be LOD = 233.44 cps and the limit of quantitation was calculated to be LOQ = 274.99 cps. This measurement was performed as part of F. Schröders's bachelor's thesis [136].

Sample	cps (²³² Th)	Δ cps (²³² Th)	cps (ISTD)	Δ cps (ISTD)	R_{korr}
0 ppt	100.11	32.94	10484.13	188.71	0.00
10 ppt	1458.39	128.34	10435.75	229.59	0.13
50 ppt	6352.04	317.60	10509.24	241.71	0.59
100 ppt	12890.94	257.82	10370.65	280.01	1.23
200 ppt	26958.47	350.46	10265.44	472.21	2.62
400 ppt	54766.38	1314.39	10374.06	248.98	5.27
600 ppt	84534.32	2028.82	9644.34	308.62	8.76

Table A43: Results of the ICP-MS measurement and the calculated parameters $S_{\%}$ and R_d determined using the calibration of Table A42 of the samples of the batch sorption experiment HCP / Th(IV) / ISA after a contact time of 72 h. The errors were calculated using the Gaussian error propagation. The samples and blanks were diluted 1:10 in 2 % HNO_3 . This measurement was performed as part of F. Schröders's bachelor's thesis [136].

Sample	cps (^{232}Th)	Δ cps (^{232}Th)	cps (ISTD)	Δ cps (ISTD)	R_{korr}	$S_{\%} / \%$	$\Delta S_{\%} / \%$	$R_d /$ $L\ kg^{-1}$	$\Delta R_d /$ $L\ kg^{-1}$
(HCP+Th(IV)) + ISA	9138.48	383.82	9507.35	133.10	9.52	72.57	1.42	5.29×10^2	3.17×10^2
(HCP+Th(IV)) + ISA	9118.52	200.61	9332.05	65.32	9.68	72.11	0.97	5.17×10^2	3.10×10^2
(HCP+ ISA) + Th(IV)	37959.81	607.36	9380.43	328.32	40.37	-	-	-	-
(HCP+ ISA) + Th(IV)	39740.68	834.55	9532.46	352.70	41.59	-	-	-	-
(HCP+ Th(IV)+ ISA)	26654.07	533.08	9803.03	284.29	27.09	21.91	3.42	5.61×10^1	3.37×10^1
(HCP+ Th(IV)+ ISA)	26386.66	659.67	9647.64	318.37	27.25	21.44	3.84	5.46×10^1	3.28×10^1
HCP+ Th(IV)	595.68	69.69	9672.63	338.54	0.52	98.50	0.43	1.31×10^4	7.88×10^3
HCP+ Th(IV)	752.53	60.20	9813.01	490.65	0.67	98.06	0.98	1.01×10^4	6.08×10^3
B I	30348.03	546.26	8916.30	240.74					
B II	33199.84	250.47	9340.42	364.28					

Table A44: Results of the ICP-MS measurement and the calculated parameters $S_{\%}$ and R_d using the calibration of Table A40 of the samples of the batch sorption experiment HCP / Th(IV) / ISA after a contact time of 39 d. The errors were calculated using the Gaussian error propagation. The samples and blanks were diluted 1:10 in 2% HNO_3 . This measurement was performed as part of S. Kissel's master's thesis [137].

Sample	cps (^{232}Th)	Δ cps (^{232}Th)	cps (ISTD)	Δ cps (ISTD)	R_{korr}	$S_{\%} / \%$	$\Delta S_{\%} / \%$	$R_d /$ $L\ kg^{-1}$	$\Delta R_d /$ $L\ kg^{-1}$
(HCP+Th(IV)) + ISA	11873.98	540.67	9417.28	255.47	12.50	59.21	1.25	2.90×10^2	6.09×10^1
(HCP+Th(IV)) + ISA	12650.50	465.39	9372.17	158.14	13.39	56.31	1.11	2.57×10^2	4.70×10^1
(HCP+ ISA) + Th(IV)	19832.73	715.32	9562.56	454.86	20.63	32.68	2.26	9.66×10^1	4.02×10^1
(HCP+ ISA) + Th(IV)	20337.63	1071.99	9435.74	354.07	21.45	30.02	2.51	8.56×10^1	4.13×10^1
(HCP+ Th(IV)+ ISA)	14558.01	600.53	9739.53	664.32	14.84	51.58	2.07	2.13×10^2	7.14×10^1
(HCP+ Th(IV)+ ISA)	14850.45	578.08	9290.34	501.94	15.88	48.19	1.90	1.85×10^2	5.71×10^1
B I	30037.60	1228.91	9317.14	620.57					
B II	27950.39	1206.04	9549.22	840.41					

Table A45: Results of the ICP-MS measurement of the calibration with ^{232}Th concentrations of 0-600 in 2% HNO_3 with 1:10 ACW and ^{193}Ir as internal standard for the batch sorption experiment HCP / Th(IV) / ISA after a contact time of 138 d. The ratio was determined. The limit of detection for ^{232}Th was calculated to be $\text{LOD} = 266.61 \text{ cps}$ and the limit of quantitation was calculated to be $\text{LOQ} = 311.30 \text{ cps}$. This measurement was performed as part of S. Kissel's master's thesis [137].

Sample	cps (^{232}Th)	Δcps (^{232}Th)	cps (ISTD)	Δcps (ISTD)	R_{korr}
0 ppt	221.92	75.83	7590.69	462.93	0.00
1000 ppt	172337.86	2477.91	7627.45	445.63	22.57
5000 ppt	922602.81	6926.51	7619.08	193.10	121.06
20000 ppt	3806204.36	29120.26	7580.65	280.94	502.07
40000 ppt	7547954.67	42937.05	7689.18	418.69	981.60
60000 ppt	11435333.53	54849.91	7438.76	153.05	1537.23

Table A46: Results of the ICP-MS measurement and the calculated parameters $S\%$ and R_d determined using the calibration of Table A45 of the samples of the batch sorption experiment HCP / Th(IV) / ISA after a contact time of 138 d. The errors were calculated using the Gaussian error propagation. The samples and blanks were diluted 1:10 in 2% HNO_3 . This measurement was performed as part of S. Kissel's master's thesis [137].

Sample	cps (^{232}Th)	Δcps (^{232}Th)	cps (ISTD)	Δcps (ISTD)	R_{korr}	$S\% / \%$	$\Delta S\% / \%$	$R_d /$ L kg^{-1}	$\Delta R_d /$ L kg^{-1}
(HCP+Th(IV)) + ISA	8148.35	205.29	22691.96	490.75	27.56	36.72	4.43	1.16×10^2	2.21×10^1
(HCP+Th(IV)) + ISA	7523.90	369.16	19952.84	593.88	26.23	39.77	5.33	1.31×10^2	2.93×10^1
(HCP+ ISA) + Th(IV)	7784.35	210.78	28104.03	464.53	35.81	17.76	5.69	4.30×10^1	1.68×10^1
(HCP+ ISA) + Th(IV)	7450.47	265.99	26675.97	518.73	35.51	18.45	6.39	4.51×10^1	1.92×10^1
(HCP+ Th(IV)+ ISA)	7468.81	454.11	19934.55	587.45	26.40	39.38	5.41	1.30×10^2	2.94×10^1
(HCP+ Th(IV)+ ISA)	7171.66	191.73	21222.99	455.20	29.30	32.71	4.90	9.68×10^1	2.61×10^1
B I	32030.83	334.02	7397	384.67					
B II	33660.10	855.65	7596	204.57					

Table A47: Results of the ICP-MS measurement of the calibration with ^{232}Th concentrations of 0-600 ppt in ACW acidified with conc. HNO_3 and ^{193}Ir as internal standard for the batch sorption experiment HCP / Th(IV) / ISA after a contact time of 194 d. The ratio was determined. The limit of detection for ^{232}Th was calculated to be $\text{LOD} = 213.05$ cps and the limit of quantitation was calculated to be $\text{LOQ} = 252.57$ cps.

Sample	cps (^{232}Th)	Δ cps (^{232}Th)	cps (ISTD)	Δ cps (ISTD)	R_{korr}
0 ppt	173.53	1.74	2985.37	34.49	0.00
10 ppt	1229.78	24.60	2930.27	159.62	0.36
20 ppt	2206.00	66.18	2870.19	90.38	0.71
50 ppt	6146.73	245.87	2980.35	96.00	2.00
100 ppt	11634.97	581.75	3043.78	271.37	3.76
200 ppt	26498.53	1589.91	3107.18	506.05	8.47
500 ppt	76398.23	5347.88	3150.59	744.78	24.19
1000 ppt	173321.76	13865.74	3320.79	2260.20	52.13

Table A48: Results of the ICP-MS measurement and the calculated parameters $S\%$ and R_d determined using the calibration of Table A47 of the samples of the batch sorption experiment HCP / Th(IV) / ISA after a contact time of 194 d. The errors were calculated using the Gaussian error propagation. The samples were measured undiluted acidified with conc. HNO_3 , the blanks were diluted 1:10 in 2 % HNO_3 .

Sample	cps (^{232}Th)	Δ cps (^{232}Th)	cps (ISTD)	Δ cps (ISTD)	R_{korr}	$S\% / \%$	$\Delta S\% / \%$	$R_d / \text{L kg}^{-1}$	$\Delta R_d / \text{L kg}^{-1}$
(HCP+Th(IV)) + ISA	85478.34	1.74	3200.63	34.49	26.65	43.49	33.83	1.54×10^2	2.12×10^2
(HCP+Th(IV)) + ISA	89431.62	24.60	3279.07	159.62	27.22	42.28	34.63	1.46×10^2	2.07×10^2
(HCP+ ISA) + Th(IV)	123224.09	66.18	3165.61	90.38	38.87	17.57	48.79	4.24×10^1	1.43×10^2
(HCP+ ISA) + Th(IV)	117416.84	245.87	3170.60	96.00	36.97	21.59	46.47	5.49×10^1	1.51×10^2
(HCP+ Th(IV)+ ISA)	90908.48	581.75	3100.51	271.37	29.26	37.94	37.40	1.22×10^2	1.94×10^2
(HCP+ Th(IV)+ ISA)	100979.29	1589.91	3113.85	506.05	32.37	31.35	42.30	9.10×10^1	1.79×10^2
B I	14230.38	2598.08	2835.13	740.74					
B II	12224.49	3606.24	2699.95	975.42					

Table A49: Results of the γ -spectroscopic measurement of ^{234}Th in the experiment of the sorption isotherm of HCP / Th(IV) / ISA. The peak area of the 63.3 keV γ ray was used for the calculation. The indicated activity, which was calculated, refers to the total volume of the stock solution.

Sample	A / Bq (^{234}Th)	$\Delta A / \text{Bq}$ (^{234}Th)	$S\% /$ %	$\Delta S\% /$ %	$[\text{Th}]_{\text{eq}} / \text{mM}$	$[\text{Th}]_{\text{sorb}} /$ mM
BG	1.97	0.75				
HCP/Th (10^{-6} M)	3.68	0.15	98.84	0.97	7.89×10^{-9}	9.94×10^{-3}
HCP/Th (10^{-7} M)	0.74	0.21	99.77	0.20	1.61×10^{-10}	1.00×10^{-3}
HCP/Th (10^{-8} M)	1.00	0.21	99.68	0.20	2.19×10^{-11}	1.01×10^{-4}
HCP/Th (10^{-9} M)	1.04	0.09	99.62	0.27	2.68×10^{-12}	1.02×10^{-5}
HCP/Th (10^{-10} M)	0.40	0.09	99.86	0.10	1.01×10^{-13}	1.01×10^{-6}
HCP/Th (10^{-11} M)	0.43	0.08	99.56	0.78	5.32×10^{-14}	1.64×10^{-7}
HCP/Th (10^{-12} M)	0.38	188.30	99.35	1.29	4.69×10^{-14}	9.81×10^{-8}
B I (1-4)	273.15	166.42				
B II (5)	96.15	113.49				
B III (6)	57.76	0.75				
B IV (7)	318.50	0.15				

Table A50: Results of the γ -spectroscopic measurement of ^{234}Th in the experiment of the sorption isotherm of HCP / Th(IV). The peak area of the 63.3 keV γ ray was used for the calculation. The indicated activity, which was calculated according to equations, refers to the total volume of the stock solution.

Sample	A / Bq (^{234}Th)	$\Delta A / \text{Bq}$ (^{234}Th)	$S\% /$ %	$\Delta S\% /$ %	$[\text{Th}]_{\text{eq}} / \text{mM}$	$[\text{Th}]_{\text{sorb}} /$ mM
BG	1.97	0.75				
HCP/Th (10^{-6} M)	232.28	5.88	1.4	6.1	9.86×10^{-7}	1.69×10^{-4}
HCP/Th (10^{-7} M)	231.10	5.68	1.9	6.0	9.81×10^{-8}	2.32×10^{-5}
HCP/Th (10^{-8} M)	221.14	5.87	6.1	5.8	9.39×10^{-9}	7.60×10^{-6}
HCP/Th (10^{-9} M)	230.91	5.69	1.9	6.0	9.81×10^{-10}	2.42×10^{-7}
HCP/Th (10^{-10} M)	99.56	2.53	6.4	5.8	9.36×10^{-11}	7.97×10^{-8}
HCP/Th (10^{-11} M)	10.48	0.27	-13.6	8.6	1.14×10^{-11}	
B I	235.47	5.80				
B II	106.34	2.63				
B III	9.23	0.47				

Table A51: Results of the ICP-MS measurement and the calculated parameters $S\%$ and R_d determined for the samples of the batch sorption experiment HCP / Pu(IV) / ISA after a contact time of 72 h. The errors were calculated using the Gaussian error propagation. The samples were measured undiluted, acidified with conc. HNO_3 and the blanks were diluted 1:50 in 2% HNO_3 . The limit of detection for ^{239}Pu was calculated to be $LOD = 24.22$ cps and the limit of quantitation was calculated to be $LOQ = 48.42$ cps. This measurement was performed as part of S. Kissel's master's thesis [137].

Sample	cps (^{239}Pu)	Δ cps (^{239}Pu)	cps (ISTD)	Δ cps (ISTD)	R_{korr}	$S\%$ / %	$\Delta S\%$ / %	R_d / L kg $^{-1}$	ΔR_d / L kg $^{-1}$
0 ppt	65.07	24.34	4425.71	150.47					
(HCP+ Pu(IV)) + ISA	9651.09	386.04	5485.61	230.40	16.77	71.50	1.88	5.01×10^2	4.63×10^1
(HCP+ Pu(IV)) + ISA	9758.03	361.05	5667.57	209.70	16.41	72.11	1.69	5.17×10^2	4.35×10^1
(HCP+ ISA) + Pu(IV)	15137.60	378.44	5585.74	189.92	51.83	11.93	4.49	2.70×10^1	1.15×10^1
(HCP+ ISA) + Pu(IV)	16633.02	249.50	5507.32	302.90	57.80	1.80	6.36	3.65×10^0	1.31×10^1
(HCP+ Pu(IV)+ ISA)	34291.04	480.07	5654.21	237.48	58.17	1.16	5.21	2.36×10^0	1.07×10^1
(HCP+ Pu(IV)+ ISA)	35293.17	529.40	6068.16	297.34	55.78	5.22	5.61	1.10×10^1	1.25×10^1
HCP+Pu(IV)	477.21	75.10	4504.16	269.18	0.09	99.85	0.03	1.34×10^5	2.87×10^4
HCP+Pu(IV)	323.70	99.04	2417.93	230.41	0.11	99.81	0.07	1.03×10^5	3.89×10^4
B I	37066.73	444.80	6552.30	209.67					
B II	40354.70	766.74	6568.94	210.21					

Table A52: Results of the ICP-MS measurement and the calculated parameters $S\%$ and R_d determined for the samples of the batch sorption experiment HCP / Pu(IV) / ISA after a contact time of 72 h. The errors were calculated using the Gaussian error propagation. The samples were measured undiluted, acidified with conc. HNO_3 and the blanks were diluted 1:50 in 2% HNO_3 . The limit of detection for ^{239}Pu was calculated to be $LOD = 71.29$ cps and the limit of quantitation was calculated to be $LOQ = 92.51$ cps. This measurement was performed as part of F. Schröders's bachelor's thesis [136].

Sample	cps (^{239}Pu)	Δ cps (^{239}Pu)	cps (ISTD)	Δ cps (ISTD)	R_{korr}	$S\%$ / %	$\Delta S\%$ / %	R_d / L kg $^{-1}$	ΔR_d / L kg $^{-1}$
0 ppt	50.06	8.96	11070.29	287.83					
(HCP+ Pu(IV)) + ISA	2836.83	252.48	10831.47	346.61	2.57	87.23	1.06	1.75×10^3	2.00×10^2
(HCP+ Pu(IV)) + ISA	4203.73	277.45	11098.73	321.86	3.74	80.08	1.22	1.14×10^3	1.09×10^2
(HCP+ ISA) + Pu(IV)	26399.98	844.80	11048.62	353.56	23.85	4.91	5.52	1.03×10^1	1.22×10^1
(HCP+ ISA) + Pu(IV)	24390.90	2829.34	10237.27	1617.49	23.78	5.19	18.93	1.09×10^1	4.21×10^1
(HCP+ Pu(IV)+ ISA)	22946.55	2042.24	10833.31	823.33	21.14	15.73	10.34	3.73×10^1	2.91×10^1
(HCP+ Pu(IV)+ ISA)	17743.78	656.52	11110.42	266.65	15.93	15.24	3.63	1.15×10^2	1.80×10^1

HCP+Pu(IV)	450.51	62.17	9893.17	544.12	0.41	97.82	0.28	1.20×10^4	2.08×10^3
HCP+Pu(IV)	216.92	39.91	10723.05	343.14	0.16	99.16	0.16	3.17×10^4	7.94×10^3
B I	3342.50	150.41	12019.00	360.57					
B II	2820.14	112.81	12125.79	206.14					

Table A53: Results of the ICP-MS measurement and the calculated parameters $S\%$ and R_d determined for the samples of the batch sorption experiment HCP / Pu(IV) / ISA after a contact time of 119 d. The errors were calculated using the Gaussian error propagation. The and the blanks were diluted 1:10 in 2% HNO₃. The limit of detection for ²³⁹Pu was calculated to be LOD = 52.07 cps and the limit of quantitation was calculated to be LOQ = 78.01 cps.

Sample	cps (²³⁹ Pu)	Δ cps (²³⁹ Pu)	cps (ISTD)	Δ cps (ISTD)	R_{korr}	$S\% / \%$	$\Delta S\% / \%$	$R_d /$ $L\ kg^{-1}$	$\Delta R_d /$ $L\ kg^{-1}$
0 ppt	40.04	26.11	10940.13	536.066	0.00				
(HCP+ Pu(IV)) + ISA	4590.95	146.91	8438.78	405.06	5.40	76.26	1.58	6.42×10^2	5.60×10^1
(HCP+ Pu(IV)) + ISA	6325.29	189.76	8645.78	198.85	7.28	68.01	1.59	4.25×10^2	3.11×10^1
(HCP+ ISA) + Pu(IV)	21425.07	214.25	8857.90	416.32	24.15	-6.12	6.13	-1.15×10^1	1.09×10^1
(HCP+ ISA) + Pu(IV)	21644.03	627.68	8804.44	343.37	24.55	-7.86	6.28	-1.46×10^1	1.08×10^1
(HCP+ Pu(IV)+ ISA)	20601.30	576.84	8734.36	270.77	23.55	-3.48	5.45	-6.73×10^0	1.02×10^1
(HCP+ Pu(IV)+ ISA)	16449.05	641.51	8610.73	189.44	19.07	16.22	4.62	3.87×10^1	1.32×10^1
HCP+Pu(IV)	380.43	63.15	8732.75	497.77	0.40	98.25	0.36	6.12×10^4	2.32×10^3
HCP+Pu(IV)	100.11	31.63	8625.82	405.41	0.08	99.65	0.19	5.71×10^4	3.19×10^4
B I	19743.91	454.11	8570.68	111.42					
B II	19291.14	327.95	8554.02	479.03					

Table A54: Measured pH and E_h values after a contact time of 72 h of the samples from the batch sorption experiment HCP / Pu(IV) / ISA.

Sample	pH (72 h)	E_h (SHE) / V (72 h)	pH (119 d)	E_h (SHE) / V (119 d)
(HCP+ Pu(IV)) + ISA	13.1	-0.57	13.1	-0.54
(HCP+ Pu(IV)) + ISA	13.2	-0.54	13.1	-0.52
(HCP+ ISA) + Pu(IV)	13.1	-0.52	13.1	-0.55
(HCP+ ISA) + Pu(IV)	13.1	-0.50	13.1	-0.49
(HCP+ Pu(IV)+ ISA)	13.1	-0.49	13.1	-0.56
(HCP+ Pu(IV)+ ISA)	13.2	-0.65	13.1	-0.46

Table A55: Time of sampling t and t_{akk} , counts cpm, determined activity A_i and efficiency TDCR from the LSC measurement, the corrected activity $A_i(korr)$, accumulated activity A_{cum} and the calculated flux J_i for the experiment HTO through-diffusion of the cell I.

Sampling	t_{akk} / d	cpm	A_i / Bq	TDCR	cpm(korr)	$A_i(korr) / Bq$	A_{cum} / Bq	$J_i / Bq (cm^2d)^{-1}$
7.12.21 18:15	0.29	2.38	0.10	0.41	23.80	0.98	0.98	0.68
8.12.21 10:45	0.97	18.25	0.75	0.40	182.50	7.53	8.51	2.18
8.12.21 17:00	1.24	23.42	0.99	0.39	234.20	9.93	18.44	7.59
9.12.21 10:40	1.97	135.44	5.82	0.39	1354.40	58.18	76.62	15.72
9.12.21 17:13	2.24	68.89	2.97	0.39	688.90	29.67	106.29	21.62
10.12.21 11:37	3.01	250.54	11.05	0.38	2505.40	110.47	216.75	28.66
10.12.21 18:23	3.29	108.48	4.62	0.39	1084.80	46.24	263.00	32.62
11.12.21 13:26	4.09	309.95	13.81	0.37	3099.50	138.12	401.12	34.61
12.12.21 11:18	5.00	381.01	17.16	0.37	3810.10	171.63	572.75	37.47
13.12.21 10:15	5.95	435.91	19.02	0.38	4359.10	190.19	762.93	39.56
13.12.21 16:07	6.20	113.10	4.86	0.39	1131.00	48.58	811.52	39.53
14.12.21 10:30	6.96	339.73	15.18	0.37	3397.30	151.80	963.32	39.42
14.12.21 16:10	7.20	118.90	5.17	0.38	1189.00	51.74	1015.06	43.59
15.12.21 10:35	7.97	352.32	15.29	0.38	3523.20	152.92	1167.97	39.64
15.12.21 17:29	8.26	145.71	6.31	0.39	1457.10	63.08	1231.05	43.64
16.12.21 10:44	8.97	339.55	15.13	0.37	3395.50	151.31	1382.37	41.88
16.12.21 15:35	9.18	101.22	4.30	0.39	1012.20	43.04	1425.40	42.36
17.12.21 10:03	9.95	356.48	16.06	0.37	3564.80	160.58	1585.98	41.51
18.12.21 11:13	10.99	495.55	22.14	0.37	4955.50	221.43	1807.40	42.00
19.12.21 13:36	12.09	524.23	23.11	0.38	5242.30	231.14	2038.55	41.82
20.12.21 10:40	12.97	424.68	18.82	0.38	4246.80	188.24	2226.79	42.66
21.12.21 9:55	13.94	450.45	19.50	0.39	4504.50	195.00	2421.79	40.04
22.12.21 11:31	15.01	508.05	22.28	0.38	5080.50	222.83	2644.62	41.55
23.12.21 12:50	16.06	482.59	21.51	0.37	4825.89	215.06	2859.68	40.55
25.12.21 11:21	18.00	901.99	40.09	0.38	9019.90	400.88	3260.56	41.14
26.12.21 11:50	19.02	521.81	22.71	0.38	5218.10	227.07	3487.63	44.28
27.12.21 15:13	20.16	558.39	24.62	0.38	5583.90	246.20	3733.84	42.92
28.12.21 11:22	21.00	422.81	18.50	0.38	4228.10	184.96	3918.79	43.82
29.12.21 11:18	22.00	469.64	21.04	0.37	4696.40	210.41	4129.20	41.97
30.12.21 15:43	23.18	577.77	25.14	0.38	5777.70	251.42	4380.63	42.24
31.12.21 12:19	24.04	421.41	18.58	0.38	4214.10	185.81	4566.43	43.06
3.1.22 15:32	27.17	1465.46	65.13	0.38	14654.60	651.32	5217.75	41.34
4.1.22 12:24	28.04	455.91	19.69	0.39	4559.10	196.85	5414.60	45.04
5.1.22 14:34	29.13	571.98	25.42	0.38	5719.80	254.21	5668.82	46.38
6.1.22 15:28	30.17	556.24	24.72	0.38	5562.40	247.22	5916.03	47.40
10.1.22 10:12	33.95	1838.94	82.84	0.37	18389.40	828.35	6744.38	43.58
11.1.22 11:06	34.99	567.76	25.93	0.37	5677.60	259.25	7003.64	49.71
12.1.22 10:57	35.98	514.72	23.25	0.37	5147.20	232.48	7236.12	46.54
13.1.22 10:50	36.98	511.38	23.35	0.37	5113.80	233.51	7469.63	46.68
14.1.22 12:16	38.04	520.98	22.85	0.38	5209.80	228.50	7698.13	42.89

Table A56: Time of sampling t and t_{akk} , counts cpm, determined activity A_i and efficiency TDCR from the LSC measurement, the corrected activity $A_i(korr)$, accumulated activity A_{cum} and the calculated flux J_i for the experiment HTO through-diffusion of the cell II.

Sampling	t_{akk} / d	cpm	A_i / Bq	TDCR	cpm(korr)	$A_i(korr) / Bq$	A_{cum} / Bq	$J_L / Bq (cm^2d)^{-1}$
7.12.21 18:20	0.30	4.69	0.20	0.39	46.90	2.00	2.00	1.30
8.12.21 10:50	0.99	14.86	0.63	0.39	148.60	6.33	8.33	1.80
8.12.21 16:52	1.24	21.21	0.90	0.39	212.10	9.04	17.37	7.04
9.12.21 10:45	1.98	123.83	5.45	0.38	1238.30	54.45	71.83	14.31
9.12.21 17:22	2.26	63.59	2.76	0.38	635.90	27.60	99.43	19.60
10.12.21 11:43	3.02	223.67	10.02	0.37	2236.70	100.21	199.64	25.66
10.12.21 18:28	3.31	97.26	4.30	0.38	972.60	43.00	242.64	29.93
11.12.21 13:32	4.10	299.00	13.11	0.38	2990.00	131.14	373.78	32.32
12.12.21 11:13	5.00	383.82	16.88	0.38	3838.20	168.79	542.56	36.58
13.12.21 10:21	5.97	426.55	18.96	0.38	4265.50	189.58	732.14	38.51
13.12.21 16:07	6.21	119.41	5.32	0.37	1194.10	53.21	785.35	43.36
14.12.21 10:26	6.97	340.68	15.26	0.37	3406.80	152.63	937.99	39.16
14.12.21 16:14	7.21	117.47	5.02	0.39	1174.70	50.20	988.19	40.67
15.12.21 10:30	7.97	357.69	15.65	0.38	3576.90	156.47	1144.66	40.25
15.12.21 17:24	8.26	140.01	6.06	0.39	1400.10	60.61	1205.27	41.28
16.12.21 10:50	8.99	327.56	14.68	0.37	3275.60	146.76	1352.03	39.56
16.12.21 15:30	9.18	96.22	4.21	0.38	962.20	42.09	1394.12	42.39
17.12.21 10:08	9.96	354.41	15.50	0.38	3544.10	155.03	1549.15	39.10
18.12.21 11:08	11.00	487.94	21.63	0.38	4879.40	216.29	1765.44	40.66
19.12.21 13:41	12.11	514.77	23.00	0.37	5147.70	230.01	1995.45	40.71
20.12.21 10:35	12.98	418.73	18.13	0.39	4187.30	181.27	2176.72	40.76
21.12.21 9:50	13.95	467.29	20.94	0.37	4672.90	209.36	2386.08	42.32
22.12.21 11:25	15.01	509.67	22.84	0.37	5096.70	228.35	2614.43	41.94
23.12.21 13:00	16.08	502.39	21.81	0.38	5023.90	218.05	2832.48	40.05
25.12.21 11:15	18.00	915.39	40.26	0.38	9153.90	402.55	3235.02	40.90
26.12.21 11:58	19.03	507.51	22.44	0.38	5075.10	224.36	3459.39	42.66
27.12.21 15:04	20.16	546.65	24.30	0.38	5466.50	242.96	3702.34	42.13
28.12.21 11:26	21.01	417.28	18.45	0.38	4172.80	184.47	3886.82	42.57
29.12.21 11:13	22.00	496.43	21.95	0.38	4964.30	219.47	4106.28	43.36
30.12.21 15:46	23.19	587.63	25.77	0.38	5876.30	257.73	4364.01	42.42
31.12.21 12:15	24.05	438.85	19.56	0.37	4388.50	195.57	4559.58	44.87
3.1.22 15:29	27.18	1491.22	66.10	0.38	14912.20	661.00	5220.58	41.29
4.1.22 12:32	28.06	418.41	18.70	0.37	4184.10	186.96	5407.54	41.74
5.1.22 14:38	29.15	571.74	25.21	0.38	5717.40	252.09	5659.63	45.39
6.1.22 15:32	30.18	529.96	22.88	0.39	5299.60	228.83	5888.45	43.19
10.1.22 10:07	33.96	1927.54	84.99	0.38	19275.40	849.89	6738.34	44.09
11.1.22 11:12	35.00	571.98	26.12	0.37	5719.80	261.18	6999.52	48.93
12.1.22 10:52	35.99	521.59	22.82	0.38	5215.90	228.17	7227.68	45.31
13.1.22 10:55	36.99	514.83	22.82	0.38	5148.30	228.20	7455.89	44.59
14.1.22 12:11	38.04	549.25	24.48	0.37	5492.50	244.76	7700.65	45.52

Table A57: Time of sampling t and t_{akk} , counts cpm, determined activity A_i and efficiency TDCR from the LSC measurement, the corrected activity $A_i(korr)$, for the experiment HTO out-diffusion of cell I in the primary compartment.

Sampling	t_{akk} / d	cpm	A_i / Bq	TDCR	cpm(korr)	$A_i(korr) / Bq$
24.1.22 11:40	0.00	77739.20	3559.49	0.38	8162616.00	373746.15
3.2.22 10:00	9.93	483.67	21.047	0.36	50785.35	2209.98
14.2.22 10:10	20.94	47.39	2.046	0.38	4975.95	214.85
24.2.22 9:50	30.92	31.89	1.381	0.39	3348.45	144.95
7.3.22 10:10	41.94	22.03	0.961	0.39	2313.15	100.92
14.3.22 13:49	49.09	12.50	0.521	0.38	1312.5	54.69
24.3.22 11:25	58.99	15.23	0.635	0.40	1599.15	66.63
4.4.22 11:20	69.99	12.12	0.505	0.40	1272.6	53.03
19.4.22 11:20	84.99	15.85	0.659	0.40	1664.25	69.17
21.4.22 11:51	87.01	1.64	0.067	0.41	172.2	7.00

Table A58: Time of sampling t and t_{akk} , counts cpm, determined activity A_i and efficiency TDCR from the LSC measurement, the corrected activity $A_i(korr)$, for the experiment HTO out-diffusion of cell I in the secondary compartment.

Sampling	t_{akk} / d	cpm	A_i / Bq	TDCR	cpm(korr)	$A_i(korr) / Bq$
24.1.22 11:40	0.00	3186.17	136.16	0.39	31861.70	1361.61
28.1.22 12:00	4.01	1021.43	44.80	0.38	10214.30	448.00
31.1.22 10:25	6.95	123.71	5.44	0.38	1237.10	54.40
3.2.22 10:00	9.93	31.97	1.38	0.39	319.70	13.80
7.2.22 10:35	13.95	14.51	0.64	0.38	145.10	6.35
10.2.22 9:45	16.92	4.06	0.17	0.40	40.60	1.67
14.2.22 10:10	20.94	4.34	0.19	0.39	43.40	1.86
17.2.22 10:16	23.94	2.31	0.10	0.40	23.10	0.97
21.2.22 13:45	28.09	2.44	0.10	0.40	24.40	1.01
24.2.22 9:50	30.92	-0.62	-0.03	0.41	-6.20	-0.25
28.2.22 11:00	34.97	1.29	0.05	0.40	12.90	0.53
2.3.22 11:55	37.01	-1.42	-0.06	0.40	-14.20	-0.59
7.3.22 10:10	41.94	1.67	0.07	0.40	16.70	0.70
14.3.22 13:49	49.09	150.30	3.12	0.80	1503.00	31.16
24.3.22 11:25	58.99	5.30	0.22	0.40	53.00	2.20
4.4.22 11:20	69.99	4.92	0.20	0.41	49.20	2.00
19.4.22 11:20	84.99	8.31	0.34	0.41	83.10	3.42
21.4.22 11:51	87.01	-0.04	0.00	0.40	-0.40	-0.02

Table A59: Time of sampling t and t_{akk} , counts cpm, determined activity A_i and efficiency TDCR from the LSC measurement, the corrected activity $A_i(korr)$, for the experiment HTO out-diffusion of cell II in the primary compartment.

Sampling	t_{akk} / d	cpm	A_i / Bq	TDCR	cpm(korr)	$A_i(korr) / Bq$
24.1.22 12:05	0.00	75640.50	3335.12	0.38	7942252.50	350187.50
3.2.22 10:24	9.93	461.05	20.49	0.38	48410.25	2151.57
14.2.22 11:00	20.95	59.97	2.58	0.39	6296.85	270.48
24.2.22 12:15	31.01	31.14	1.34	0.39	3269.70	140.45
7.3.22 10:27	41.93	21.87	0.94	0.39	2296.35	98.39
14.3.22 14:04	49.08	9.24	0.39	0.40	970.20	40.43
24.3.22 11:25	58.97	14.48	0.61	0.40	1520.40	64.15
4.4.22 11:20	69.97	12.39	0.52	0.40	1300.95	54.34
19.4.22 11:55	84.99	11.02	0.45	0.41	1157.10	47.38
21.4.22 12:07	87.00	1.57	0.06	0.41	164.85	6.72

Table A60: Time of sampling t and t_{akk} , counts cpm, determined activity A_i and efficiency TDCR from the LSC measurement, the corrected activity $A_i(korr)$, for the experiment HTO out-diffusion of cell II in the secondary compartment.

Sampling	t_{akk} / d	cpm	A_i / Bq	TDCR	cpm(korr)	$A_i(korr) / Bq$
24.1.22 12:05	0.00	4738.42	218.76	0.36	47384.20	2187.64
28.1.22 12:05	4.00	1140.28	50.95	0.37	11402.80	509.51
31.1.22 10:30	6.93	119.29	5.36	0.37	1192.90	53.59
3.2.22 10:24	9.93	30.54	1.29	0.40	305.40	12.89
7.2.22 10:40	13.94	14.73	0.62	0.40	147.30	6.15
10.2.22 9:50	16.91	2.11	0.09	0.40	21.10	0.87
14.2.22 11:00	20.95	5.61	0.24	0.40	56.10	2.36
17.2.22 10:09	23.92	0.91	0.04	0.41	9.10	0.37
21.2.22 13:48	28.07	1.08	0.04	0.41	10.80	0.44
24.2.22 12:15	31.01	0.29	0.01	0.40	2.90	0.12
28.2.22 10:55	34.95	0.62	0.03	0.40	6.20	0.26
2.3.22 12:00	37.00	-2.68	-0.11	0.39	-26.80	-1.13
7.3.22 10:27	41.93	1.01	0.04	0.40	10.10	0.42
14.3.22 14:04	49.08	7.16	0.30	0.40	71.60	3.01
24.3.22 11:25	58.97	6.53	0.26	0.41	65.30	2.64
4.4.22 11:20	69.97	4.80	0.19	0.41	48.00	1.93
19.4.22 11:55	84.99	9.89	0.42	0.39	98.90	4.23
21.4.22 12:07	87.00	0.35	0.01	0.40	3.50	0.14

Table A61: V_{sample} and A of the α -spectroscopy of 50 ml 2% HNO_3 and determined activity A_{wall} in the primary compartment of $^{238}Pu(IV)$ (wall sorption) for the $^{238}Pu(IV)$ in-diffusion of cell I and cell II.

	$V_{sample} / \mu l$	A / Bq	A_{wall} / Bq
Cell I	10	2.24	2666.67
Cell II	10	0.04	51.19

Table A62: Time t and V_{sample} of sampling, t_{akk} peak area and t_{Mess} of the α -spectroscopy, determined activity A and concentration of $^{238}\text{Pu(IV)}$ in solution in the primary compartment for the $^{238}\text{Pu(IV)}$ in-diffusion of cell I in absence of ISA. A value of 30% was assumed for the errors.

Sampling	$V_{\text{Sample}} / \mu\text{l}$	$t_{\text{akk}} / \text{d}$	Peak area	$t_{\text{Mess}} / \text{s}$	A / Bq	$c(^{238}\text{Pu}) / \text{M}$
12.7.22 16:00	10	0.00	10544	58620	1.03	6.82×10^{-10}
13.7.22 11:35	10	0.82	6669	74261	0.51	3.39×10^{-10}
14.7.22 10:45	20	1.78	9927	57600	0.99	3.26×10^{-10}
15.7.22 10:40	20	2.78	13345	81299	0.94	3.11×10^{-10}
16.7.22 10:35	20	3.77	7963	85141	0.53	1.76×10^{-10}
18.7.22 11:15	30	5.80	2432	46068	0.30	6.59×10^{-11}
19.7.22 10:25	30	6.77	4217	63463	0.38	8.32×10^{-11}
20.7.22 11:15	30	7.80	4155	79322	0.30	6.54×10^{-11}
21.7.22 11:10	30	8.80	6659	114473	0.33	7.27×10^{-11}
22.7.22 11:35	30	9.82	6230	92579	0.38	8.43×10^{-11}
26.7.22 16:30	50	14.02	18367	216000	0.48	6.41×10^{-11}
2.8.22 14:20	50	20.93	18594	216000	0.49	6.49×10^{-11}
5.8.22 11:00	50	23.79	12833	194268	0.37	4.96×10^{-11}
10.8.22 15:20	50	28.97	19254	216000	0.51	6.72×10^{-11}
15.8.22 10:30	50	33.77	22981	216003	0.61	8.04×10^{-11}
18.8.22 14:08	50	36.92	8131	190606	0.24	3.18×10^{-11}
24.8.22 15:13	50	42.97	12890	216001	0.34	4.48×10^{-11}
29.8.22 10:25	50	47.77	9091	216001	0.24	3.14×10^{-11}
5.9.22 10:55	50	54.79	6425	169572	0.21	2.82×10^{-11}
12.9.22 10:50	50	61.78	7958	168059	0.27	3.54×10^{-11}
19.9.22 14:09	50	68.92	9169	410265	0.12	1.63×10^{-11}
28.9.22 16:30	50	78.02	4457	266200	0.09	1.21×10^{-11}
7.10.22 10:50	60	86.78	10657	285310	0.21	2.31×10^{-11}
11.10.22 11:25	50	90.81	6657	244366	0.15	2.01×10^{-11}
19.10.22 14:10	50	98.92	6050	167602	0.20	2.68×10^{-11}
7.11.22 13:40	50	117.90	4117	244144	0.09	1.22×10^{-11}

Table A63: Time t and V_{sample} of sampling, t_{akk} , peak area and t_{Mess} of the α -spectroscopy, determined activity A and concentration c of $^{238}\text{Pu(IV)}$ in solution in the primary compartment for the $^{238}\text{Pu(IV)}$ in-diffusion of cell II in presence of ISA. A value of 30% was assumed for the errors.

Sampling	$V_{\text{Sample}} / \mu\text{l}$	$t_{\text{akk}} / \text{d}$	Peak area	$t_{\text{Mess}} / \text{s}$	A / Bq	c / M
12.7.22 15:30	10	0.00	731	3789	1.10	7.31×10^{-10}
13.7.22 11:35	10	0.84	1734	9198	1.08	7.15×10^{-10}
14.7.22 10:30	20	1.79	32889	88569	2.13	7.05×10^{-10}
15.7.22 11:00	20	2.81	17737	57600	2.10	6.96×10^{-10}
16.7.22 10:25	20	3.79	29589	85004	2.38	7.87×10^{-10}
18.7.22 11:25	30	5.83	19829	45092	3.01	6.65×10^{-10}
19.7.22 10:40	30	6.80	27983	62812	3.05	6.73×10^{-10}
20.7.22 11:25	30	7.83	24217	87359	1.89	4.17×10^{-10}
21.7.22 11:20	30	8.83	30275	114566	1.80	3.97×10^{-10}
22.7.22 11:40	30	9.84	23719	92688	1.74	3.84×10^{-10}
26.7.22 16:45	50	14.05	119744	259788	3.15	4.18×10^{-10}
29.7.22 11:20	50	16.83	102892	179780	3.92	5.20×10^{-10}
2.8.22 14:20	50	20.95	207396	321410	4.43	5.87×10^{-10}
10.8.22 15:30	50	29.00	57547	79722	4.95	6.57×10^{-10}
15.8.22 10:40	50	33.80	63532	95247	4.58	6.06×10^{-10}
18.8.22 14:15	50	36.95	113872	190707	4.09	5.43×10^{-10}
24.8.22 15:23	50	43.00	103966	261477	2.72	3.60×10^{-10}
29.8.22 10:50	50	47.81	84847	146087	3.98	5.28×10^{-10}
5.9.22 11:00	50	54.81	108552	169472	4.39	5.82×10^{-10}
12.9.22 11:05	50	61.82	118402	168138	4.83	6.40×10^{-10}
19.9.22 14:00	50	68.94	195027	248913	5.38	7.13×10^{-10}
28.9.22 16:40	50	78.05	50707	90656	3.83	5.08×10^{-10}
7.10.22 11:05	50	86.82	187955	285308	4.52	5.99×10^{-10}
11.10.22 11:28	50	90.83	187011	244367	5.25	6.96×10^{-10}
19.10.22 14:20	50	98.95	37270	76271	3.56	4.72×10^{-10}
7.11.22 14:09	50	117.94	120970	244144	3.39	4.50×10^{-10}

Table A64: Measured pH and E_h values of the samples from the Pu in-diffusion experiment HCP / Pu(IV) in absence and presence of ISA.

Sampling	pH	E_h (SHE) / V	pH	E_h (SHE) / V
12.7.22 16:00	13.00	-0.13	13.00	-0.28
15.7.22 10:40	13.30	-0.16	12.93	-0.24
19.7.22 10:25	12.90	-0.14	12.90	0.10
22.7.22 11:35	13.03	-0.26	12.96	-0.06
29.8.22 10:25	12.67	-0.44	12.49	-0.27
7.11.22 13:40	13.34	-0.21	12.97	0.07

Table A65: Samples of the abrasive peeling with the ground length x_{Sample} and weight m_{Sample} , peak area and t_{Mess} of the α -spectroscopy, determined activity AC_r and ΔAC_r of $^{238}\text{Pu(IV)}$ in HCP for the $^{238}\text{Pu(IV)}$ in-diffusion of cell I in absence of ISA. The efficiency of the α -detector is $\varepsilon = 0.078$ and background is $A = 0.13 \text{ Bq}$. The grey values are not shown.

Sample	$m_{\text{Sample}} / \text{mg}$	$x_{\text{Sample}} / \mu\text{m}$	Peak area	$t_{\text{Mess}} / \text{s}$	$x / \mu\text{m}$	$AC_r / \text{Bq g}^{-1}$	$\Delta AC_r / \text{Bq g}^{-1}$
1	14.6	29.00	16762	60	29.00	245310.03	2532.46
2	11.1	27.75	14226	496	56.75	33118.33	407.63
3	9.6	36.00	11807	1256	92.75	12543.90	174.42
4	6.9	37.25	28779	3208	130.00	16654.42	260.60
5	18.9	38.50	10879	112	168.50	65884.09	721.51
6	11.9	37.75	14998	606	206.25	26655.43	312.37
7	12.6	4.75	15623	5999	211.00	2642.11	29.82
8	10.8	45.50	47306	5178	256.50	10836.13	112.04
9	10.9	42.75	5975	2644	299.25	2649.06	42.11
10	13.9	31.50	6132	5997	330.75	936.09	13.80
11	13.3	10.00	10958	59143	340.75	171.27	2.14
12	11.2	20.25	1623	26302	361.00	61.93	1.84
13	23.4	17.25	17675	80746	378.25	115.76	1.03
14	5.8	11.50	1263	39587	389.75	53.72	2.19
15	13.0	17.25	2153	52046	407.00	33.30	0.92
16	14.4	31.75	4814	28570	438.75	143.25	2.38
17	15.1	22.00	2113	47212	460.75	31.54	0.85
18	9.3	21.50	1600	65644	482.25	23.12	0.88
19	8.3	17.75	3764	176863	500.00	21.13	0.59
20	7.9	36.50	4775	111123	536.50	57.40	1.24
21	14.9	14.00	2513	14275	550.50	144.93	3.17
22	21.0	31.50	1247	21850	582.00	28.89	1.00
23	15.7	44.75	3914	154800	626.75	12.68	0.34
24	11.9	10.50	889	86118	637.25	0.61	0.37
25	14.8	18.75	645	53272	656.00	2.04	0.41
26	15.3	8.25	847	68415	664.25	2.20	0.36
27	11.2	23.00	2753	258493	687.25	1.02	0.23
28	18.0	22.25	367	32352	709.50	1.13	0.42
29	18.7	16.00	549	49526	725.50	0.91	0.32
30	17.2	18.00	371	32395	743.50	1.26	0.44
31	12.6	6.75	456	46800	750.25	-0.01	0.46
32	18.4	17.50	325	29804	767.75	0.80	0.42
33	15.3	15.00	308	32393	782.75	-0.21	0.45
34	17.6	20.50	267	27912	803.25	-0.14	0.43
35	16.2	27.25	267	30523	830.50	-0.80	0.42
36	22.9	15.25	513	46800	845.75	0.67	0.27
37	14.9	41.00	500	46800	886.75	0.80	0.41
38	17.3	13.25	360	50400	900.00	-1.94	0.28
39	18.4	35.25	212	27792	935.25	-1.48	0.37
40	20.8	21.50	348	46800	956.75	-1.43	0.25

Table A66: Samples of the abrasive peeling with the ground length x_{Sample} and weight m_{Sample} , peak area and t_{Mess} of the α -spectroscopy, determined activity AC_r and ΔAC_r of $^{238}\text{Pu(IV)}$ in HCP for the $^{238}\text{Pu(IV)}$ in-diffusion of cell II in presence of ISA. The efficiency of the α -detector is $\varepsilon = 0.069$ and background is $A = 0.18 \text{ Bq}$.

Sample	$m_{\text{Sample}} / \text{mg}$	$x_{\text{Sample}} / \mu\text{m}$	Peak area	$t_{\text{Mess}} / \text{s}$	$x / \mu\text{m}$	$AC_r / \text{Bq g}^{-1}$	$\Delta AC_r / \text{Bq g}^{-1}$
1	13.5	30.25	8017	2432	30.25	3527.98	47.38
2	7.0	27.50	4471	3685	57.75	2490.98	51.75
3	9.5	23.00	13841	6999	80.75	3001.40	40.69
4	14.3	7.50	17399	6000	88.25	2928.63	30.26
5	8.2	25.00	8735	5233	113.25	2932.24	47.70
6	26.1	30.00	28565	5000	143.25	3166.67	22.35
7	12.8	49.50	10772	4355	192.75	2789.09	34.68
8	7.7	1.50	9941	4775	194.25	3899.36	64.10
9	6.7	31.50	7947	6000	225.75	2843.06	53.23
10	18.3	31.50	19412	5999	257.25	2554.62	23.09
11	10.2	12.50	10194	4587	269.75	3143.24	43.91
12	11.7	24.75	78761	49734	294.50	1949.08	18.07
13	13.2	24.25	7405	3871	318.75	2089.14	29.09
14	12.1	20.25	9835	5997	339.00	1952.13	25.55
15	9.5	13.50	12151	3421	352.50	51.329	5403.10
16	15.6	3.50	10022	5279	356.00	1754.29	20.90
17	10.9	28.00	109301	61455	384.00	2351.28	22.73
18	9.7	5.50	17532	21038	389.50	1229.94	15.79
19	6.7	9.00	63776	51885	398.50	2636.88	40.74
20	19.0	42.25	4507	1821	440.75	1880.14	29.81
21	15.8	35.00	14621	7200	475.75	1853.37	19.36
22	16.2	7.00	5450	3927	482.75	1232.49	18.46
23	13.5	5.25	6656	3694	488.00	1923.44	27.66
24	17.4	4.50	6665	4059	492.50	1359.22	18.48
25	14.7	4.50	9296	7200	497.00	1262.90	15.75
26	18.5	7.75	13125	6826	504.75	1498.35	15.44
27	16.1	15.75	7495	5068	520.50	1322.11	17.43
28	17.0	12.75	8252	4600	533.25	1520.68	19.06
29	19.6	23.75	8965	4623	557.00	1426.40	16.80
30	18.7	32.75	9632	6432	589.75	1152.72	13.34
31	20.9	19.75	9655	5395	609.50	1233.94	13.94
32	17.4	13.50	10059	7000	623.00	1188.45	13.75
33	12.7	27.00	8622	5872	650.00	1664.01	22.30
34	15.2	11.50	6464	6000	661.50	1017.53	14.42
35	19.4	16.50	8899	5953	678.00	1109.16	13.15
36	11.7	16.50	5999	4157	694.50	1775.00	27.62
37	14.9	16.75	58420	53099	711.25	1060.26	8.38
38	17.2	13.25	56408	50092	724.50	940.29	6.77
39	18.2	32.50	17599	16759	757.00	828.13	7.77
40	20.4	28.50	75996	57579	785.50	930.45	5.69
41	10.6	29.50	4789	7200	815.00	892.19	15.61
42	13.2	12.25	5000	7199	827.25	748.74	12.19
43	20.6	21.25	7486	7200	848.50	722.62	9.15
44	17.6	26.25	5407	5965	874.75	736.05	10.98
45	12.0	18.50	3574	6560	893.25	642.78	12.24
46	14.4	20.75	5257	6560	914.00	793.86	12.41
47	14.9	21.50	4394	5882	935.50	714.36	10.61

48	14.1	24.50	5089	6745	960.00	762.56	10.99
49	22.4	19.00	5783	6317	979.00	584.16	9.69
50	17.1	41.25	4829	5955	1020.25	676.60	8.19
51	22.4	18.00	6656	7200	1038.25	589.97	9.22
52	17.7	34.00	5520	7200	1072.25	617.44	9.49
53	17.7	37.50	5284	7017	1109.75	606.27	8.26
54	19.0	27.00	5966	8000	1136.75	559.24	9.53
55	14.2	27.75	4847	7199	1164.50	674.32	9.27
56	17.2	10.75	6013	8224	1175.25	605.46	10.78
57	17.9	21.50	4691	6268	1196.75	595.75	9.17
58	18.6	21.25	4859	6781	1218.00	548.52	7.87
59	17.1	16.00	5334	7531	1234.00	589.61	13.94
60	11.0	14.00	3245	6378	1248.00	653.74	11.38
61	10.3	14.75	3935	10000	1262.75	535.96	9.63
62	14.9	22.75	4288	7456	1285.50	547.14	7.38
63	13.8	14.50	5725	10000	1300.00	588.02	10.72
64	15.5	9.50	4626	8090	1309.50	522.89	9.68
65	13.6	9.25	4008	7813	1318.75	533.25	8.52
66	13.9	8.75	4574	8748	1327.50	532.03	10.96
67	11.9	16.50	3590	8271	1344.00	513.28	12.48
68	13.4	14.75	2705	5414	1358.75	526.76	8.83
69	14.1	14.50	3555	6969	1373.25	511.38	9.51
70	17.7	25.00	4365	6500	1398.25	539.55	8.86
71	13.8	15.50	3517	7013	1413.75	513.45	9.63
72	17.0	17.00	2649	5772	1430.75	404.60	8.41
73	16.2	21.25	3343	6818	1452.00	427.38	8.03
74	15.1	13.75	2767	6834	1465.75	400.43	8.28
75	16.1	20.00	3584	7201	1485.75	436.69	7.96
76	17.7	15.50	3295	7200	1501.25	387.46	7.27
77	21.2	18.75	3964	7043	1520.00	376.15	6.36
78	16.7	26.00	2985	7091	1546.00	376.87	7.45
79	13.5	13.50	1816	4344	1559.50	435.27	11.01
80	17.2	16.00	1882	4333	1575.50	377.89	9.22
81	14.4	14.75	2462	5981	1590.25	401.62	8.80
82	14.1	14.00	1984	5942	1604.25	351.37	8.55
83	17.9	23.50	3022	7047	1627.75	337.01	6.59
84	15.5	15.50	2596	7017	1643.25	355.43	7.56
85	13.8	18.50	2552	7201	1661.75	358.96	7.81
86	16.6	21.25	2793	7200	1683.00	348.52	7.12
87	15.4	17.25	2446	7054	1700.25	314.48	6.91
88	15.7	9.00	2249	7053	1709.25	300.84	6.86
89	15.2	22.00	7330	12285	1731.25	556.89	7.59
90	14.6	10.00	2050	7200	1741.25	287.52	6.91
91	16.8	18.50	2400	6782	1759.75	294.42	6.47
92	15.4	15.50	1998	6815	1775.25	281.03	6.80
93	12.1	27.25	1371	4705	1802.50	333.93	9.82
94	11.5	14.00	1748	7198	1816.50	309.01	8.22
95	20.9	9.00	2211	6542	1825.50	225.63	5.10
96	15.6	16.00	1586	6573	1841.50	226.26	6.15
97	11.3	12.75	1545	6026	1854.25	312.68	8.81
98	13.5	11.25	1509	6027	1865.50	271.81	7.62
99	14.9	6.50	1952	7201	1872.00	251.42	6.20
100	14.9	12.00	58196	246116	1884.00	217.75	1.74

101	18.1	30.75	2058	7200	1914.75	232.87	5.51
102	13.8	14.25	26127	100000	1929.00	261.16	2.54
103	10.4	21.25	4267	20000	1950.25	298.06	5.62
104	16.1	12.00	5526	12242	1962.25	395.00	5.99
105	14.6	25.75	10476	59141	1988.00	174.16	2.18
106	14.0	22.25	13164	57825	2010.25	222.63	2.60
107	11.7	20.00	4851	26323	2030.25	212.68	3.75
108	15.8	36.50	4434	22155	2066.75	183.32	3.15
109	14.3	19.00	15343	80708	2085.75	179.91	2.00
110	10.4	27.75	12873	80687	2113.50	218.46	2.96
111	16.1	18.50	9796	52351	2132.00	167.47	2.08
112	12.4	24.75	6409	48331	2156.75	149.81	2.38
113	15.0	20.00	7772	52434	2176.75	131.05	1.84
114	16.3	25.50	7865	50400	2202.25	136.09	1.86
115	14.2	18.75	8189	50400	2221.00	152.98	2.13
116	18.2	18.00	8092	46801	2239.00	127.66	1.68
117	23.9	8.75	6723	46800	2247.75	79.48	1.11
118	12.9	28.50	5585	46801	2276.25	119.92	2.02
119	10.4	25.25	5291	46801	2301.50	140.00	2.55
120	14.9	15.75	6602	49553	2317.25	117.34	1.78

Results and discussion – Screening experiments

Table A67: Results of the ICP-MS measurement of the calibration with ^{232}Th concentrations of 0-600 ppt in ACW acidified with conc. HNO_3 and ^{193}Ir as internal standard for the batch sorption experiment HCP / Th(IV) / Oxalate. The ratio was determined. The limit of detection for ^{232}Th was calculated to be $\text{LOD} = 439.70$ cps and the limit of quantitation was calculated to be $\text{LOQ} = 498.27$ cps.

Sample	cps (^{232}Th)	Δ cps (^{232}Th)	cps (ISTD)	Δ cps (ISTD)	R_{korr}
0 ppt	381.13	25.92	2978.25	80.41	0.00
10 ppt	837.29	19.26	2961.57	106.62	0.15
50 ppt	2537.59	71.05	2815.43	115.43	0.77
100 ppt	4647.72	162.67	2882.66	60.54	1.48
200 ppt	8406.48	193.35	2766.52	107.89	2.91
400 ppt	17210.71	344.21	2758.19	79.99	6.11
600 ppt	26270.61	1050.82	2789.31	111.57	9.29

Table A68: Results of the ICP-MS measurement and the calculated parameters $S\%$ and R_d determined using the calibration of Table A67 of the samples of the batch sorption experiment HCP / Th(IV) / Oxalate. The errors were calculated using the Gaussian error propagation. The samples were measured undiluted, acidified with conc. HNO_3 and the blanks were diluted 1:10 in 2% HNO_3 .

Sample	cps (^{232}Th)	Δ cps (^{232}Th)	cps (ISTD)	Δ cps (ISTD)	R_{korr}	$S\% / \%$	$\Delta S\% / \%$	$R_d / \text{L kg}^{-1}$	$\Delta R_d / \text{L kg}^{-1}$
(HCP+Th(IV)) + Oxalate	556.15	37.26	2703.74	162.22	0.08	99.77	0.06	8.78×10^4	2.40×10^4
(HCP+Th(IV)) + Oxalate	1137.32	63.69	2547.59	63.69	0.32	99.07	0.10	2.13×10^4	2.31×10^3
(HCP+Oxalate) + Th(IV)	820.06	59.04	2870.44	97.59	0.16	99.54	0.08	4.32×10^4	7.21×10^3
(HCP+Oxalate) + Th(IV)	821.73	49.30	2724.30	100.80	0.17	99.49	0.07	3.92×10^4	5.74×10^3
(HCP+ Th(IV)+ Oxalate)	679.50	44.85	2897.12	75.33	0.11	99.69	0.06	6.40×10^4	1.21×10^4
(HCP+ Th(IV)+ Oxalate)	685.60	41.14	2912.12	136.87	0.11	99.69	0.06	6.35×10^4	1.25×10^4
B I	2221.41	135.51	2587.04	119.00					
B II	1908.01	72.50	2492.01	97.19					

Table A69: Results of the ICP-MS measurement of the calibration with ^{232}Th concentrations of 0-600 ppt in ACW acidified with conc. HNO_3 and ^{193}Ir as internal standard for the batch sorption experiment HCP / Th(IV) / Citrate. The ratio was determined. The limit of detection for ^{232}Th was calculated to be $\text{LOD} = 351.37$ cps and the limit of quantitation was calculated to be $\text{LOQ} = 403.29$ cps.

Sample	cps (^{232}Th)	Δ cps (^{232}Th)	cps (ISTD)	Δ cps (ISTD)	R_{korr}
0 ppt	299.46	20.66	2185.84	78.69	0.00
10 ppt	641.16	50.65	2289.19	82.41	0.14
50 ppt	2051.92	77.97	2318.08	51.00	0.75
100 ppt	4104.18	73.88	2355.32	108.34	1.61
200 ppt	8123.51	268.08	2388.65	138.54	3.26
400 ppt	15737.08	361.95	2383.10	123.92	6.47
600 ppt	24375.48	975.02	2422.00	123.52	9.93

Table A70: Results of the ICP-MS measurement and the calculated parameters $S\%$ and R_d determined according to equations (14) and (15) using the calibration of Table A69 of the samples of the batch sorption experiment HCP / Th(IV) / Oxalate. The errors were calculated using the Gaussian error propagation. The samples were measured undiluted, acidified with conc. HNO_3 and the blanks were diluted 1:10 in 2% HNO_3 .

Sample	cps (^{232}Th)	Δ cps (^{232}Th)	cps (ISTD)	Δ cps (ISTD)	R_{korr}	$S\% / \%$	$\Delta S\% / \%$	$R_d / \text{L kg}^{-1}$	$\Delta R_d / \text{L kg}^{-1}$
(HCP+Th(IV)) + Citrate	996.20	30.88	2459.78	63.95	0.27	99.11	0.08	2.23×10^4	2.00×10^3
(HCP+Th(IV)) + Citrate	1365.70	64.19	2440.33	112.26	0.42	98.60	0.15	1.40×10^4	1.48×10^3
(HCP+ Citrate) + Th(IV)	942.86	58.46	2435.89	99.87	0.25	99.17	0.11	2.39×10^4	3.20×10^3
(HCP+ Citrate) + Th(IV)	1317.35	56.65	2388.66	54.94	0.41	98.62	0.12	1.43×10^4	1.26×10^3
(HCP+ Th(IV)+ Citrate)	1214.00	63.13	2365.87	59.15	0.38	98.75	0.12	1.58×10^4	1.57×10^3
(HCP+ Th(IV)+ Citrate)	1316.23	67.13	2441.45	117.19	0.40	98.66	0.15	1.48×10^4	1.65×10^3
B I	7904.95	450.58	2446.45	78.29					
B II	7586.23	477.93	2478.12	89.21					

Table A71: Results of the ICP-MS measurement and the calculated parameters $S\%$ and R_d determined according to equations (14) and (15) using the calibration of Table A69 of the samples of the batch sorption experiment HCP / Th(IV) / Phthalate. The errors were calculated using the Gaussian error propagation. The samples were measured undiluted, acidified with conc. HNO_3 and the blanks were diluted 1:10 in 2% HNO_3 .

Sample	cps (^{232}Th)	Δ cps (^{232}Th)	cps (ISTD)	Δ cps (ISTD)	R_{korr}	$S\%$ / %	$\Delta S\%$ / %	R_d / L kg^{-1}	ΔR_d / L kg^{-1}
HCP+Th(IV)	442.81	80.21	2403.10	4.52	0.05	99.81	0.28	1.27×10^5	2.14×10^4
HCP+Th(IV)	747.28	42.14	2467.57	3.84	0.17	99.45	0.15	3.61×10^5	1.94×10^4
(HCP+Th(IV)) + Phthalate	4038.05	117.10	2554.25	38.31	1.44	94.99	0.30	3.79×10^3	2.41×10^2
(HCP+Th(IV)) + Phthalate	697.83	27.22	2359.76	117.99	0.16	99.45	0.08	3.61×10^4	5.23×10^3
(HCP+ Phthalate) + Th(IV)	673.94	43.13	2308.64	138.52	0.15	99.46	0.10	3.70×10^4	6.89×10^3
(HCP+ Phthalate) + Th(IV)	585.04	31.59	2568.14	71.91	0.09	99.68	0.06	6.32×10^4	1.26×10^4
(HCP+ Th(IV)+ Phthalate)	530.04	24.91	2617.60	86.38	0.07	99.77	0.06	8.77×10^4	2.16×10^4
(HCP+ Th(IV)+ Phthalate)	562.26	24.18	2429.22	145.75	0.09	99.67	0.07	6.08×10^4	1.33×10^4
B I	7348.27	301.28	2398.10	100.72					
B II	7267.80	465.14	2448.11	75.89					

Appendix A5 Figures of experiments

Introduction – Speciation

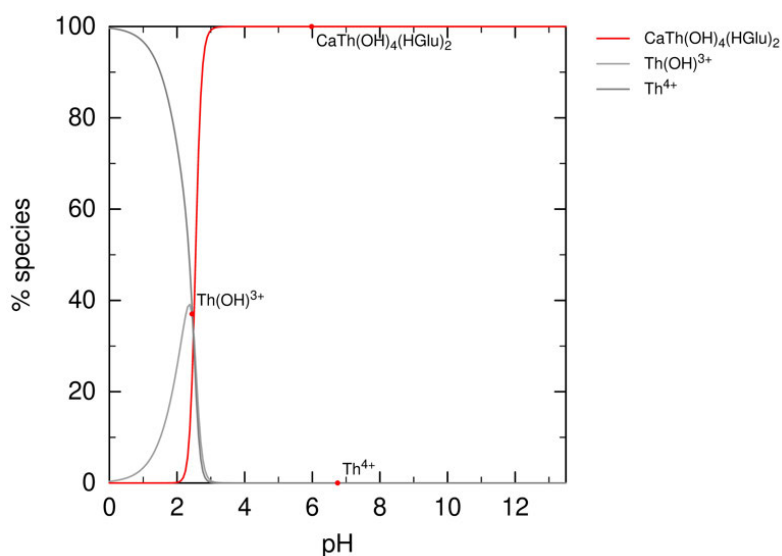


Figure A1: Speciation calculation for an equilibrium concentration of 1×10^{-8} M Th, 1×10^{-2} M GLU and 2×10^{-2} M Ca (Graphic generated by PhreePlot (version 1.0 [53]) using PHREEQC and the ThermoChimie database 11a, 2022 [54] and the complex formation constant of Gaona et al. [33]).

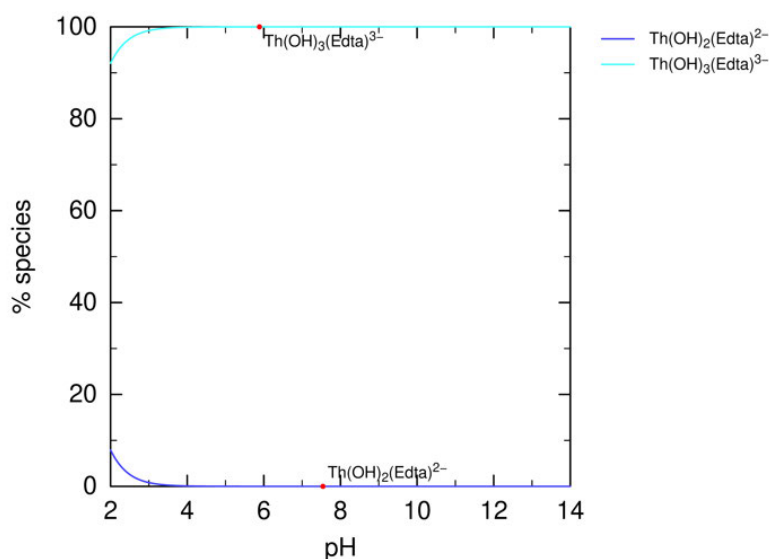


Figure A2: Speciation calculation for an equilibrium concentration of 1×10^{-8} M Th, 1×10^{-2} M EDTA and 2×10^{-2} M Ca (Graphic generated by PhreePlot (version 1.0 [53]) using PHREEQC and the ThermoChimie database 11a, 2022 [54] and the complex formation constant of Xia et al. [91]).

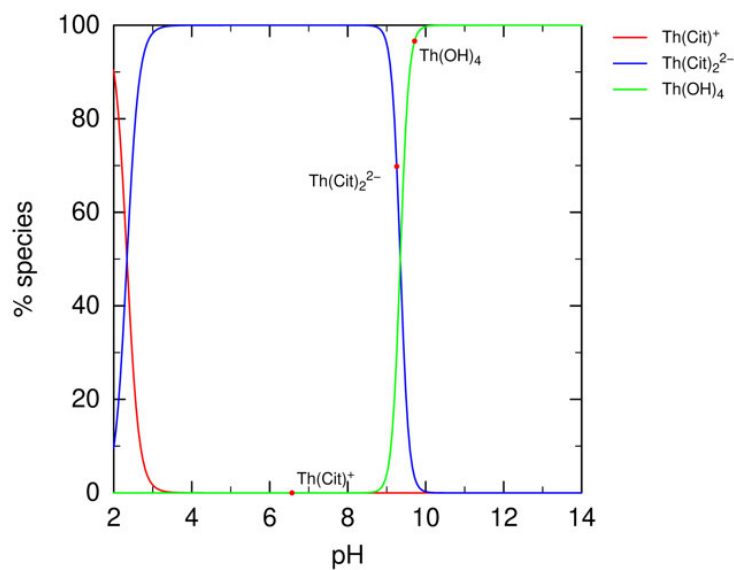


Figure A3: Speciation calculation for an equilibrium concentration of 1×10^{-8} M Th, 1×10^{-2} M citrate and 2×10^{-2} M Ca (Graphic generated by PhreePlot (version 1.0 [53]) using PHREEQC and the ThermoChimie database 11a, 2022 [54]).

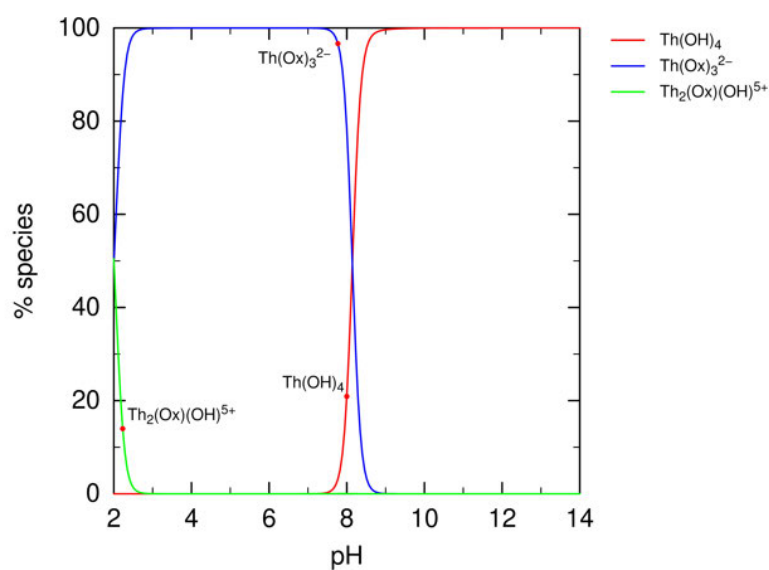
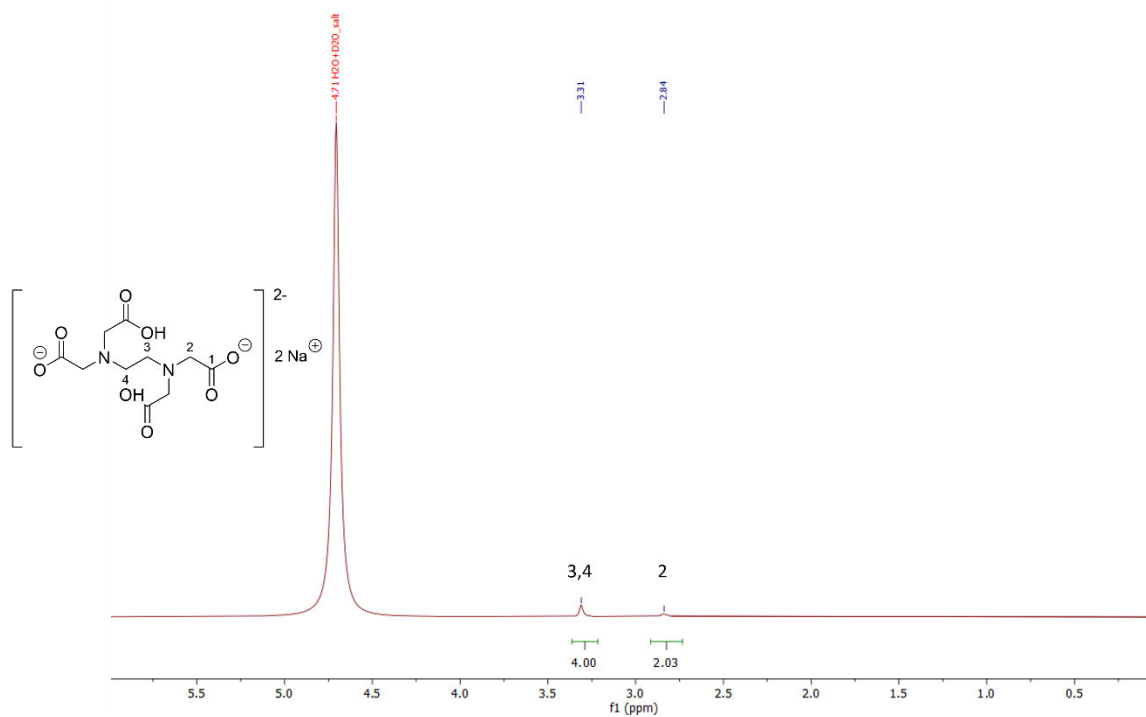


Figure A4: Speciation calculation for an equilibrium concentration of 1×10^{-8} M Th, 1×10^{-2} M oxalate and 2×10^{-2} M Ca (Graphic generated by PhreePlot (version 1.0 [53]) using PHREEQC and the ThermoChimie database 11a, 2022 [54]).

Experimental description – stock solution



$^1\text{H-NMR}$ (300 MHz, D_2O , COSY): δ (ppm): 2.84 (d, 1H, H-2), 3.31 (m, 1H, H-3, H-4)

Figure A5: $^1\text{H-NMR}$ spectrum of $\text{Na}_4\text{EDTA} \times 2 \text{H}_2\text{O}$ in ACW (pH = 13) in deuterium oxide and assignment of signals based on structural formula.

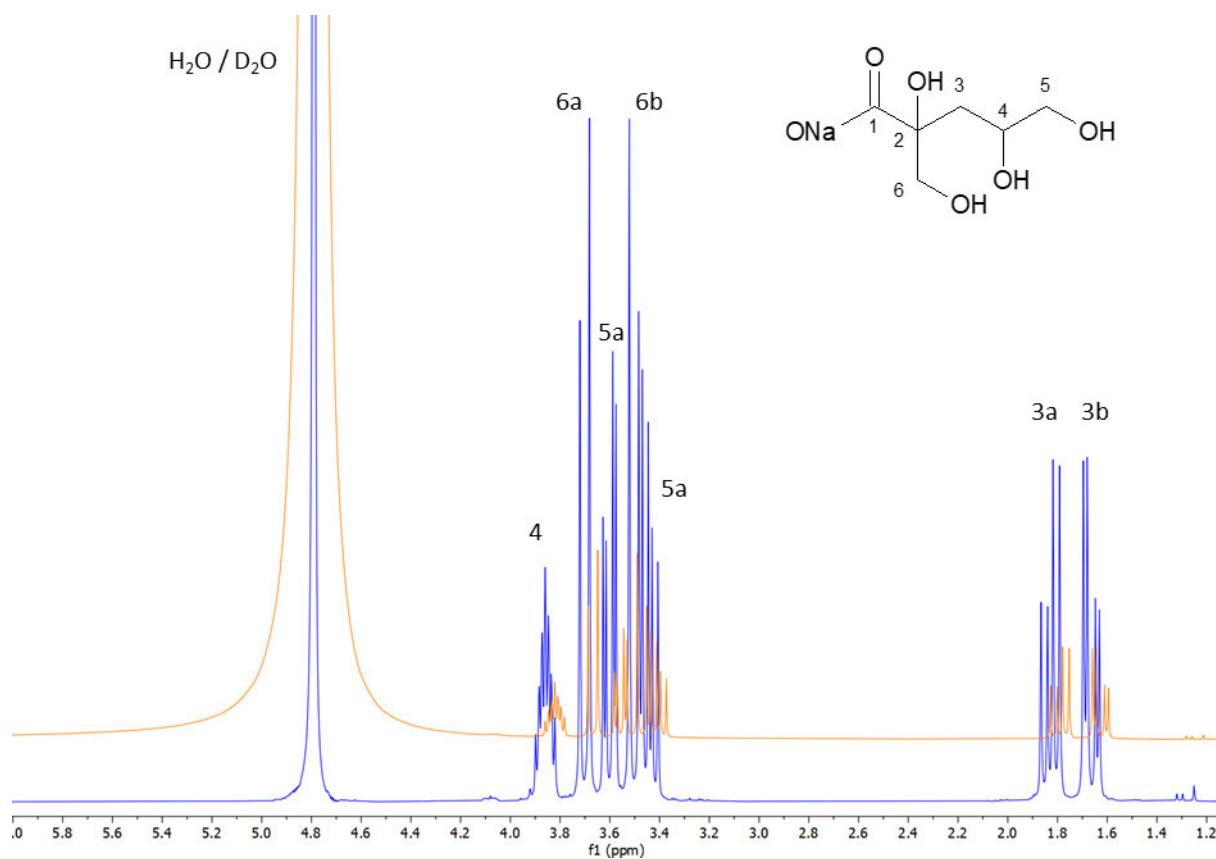


Figure A7: ^{13}C -NMR spectrum of NaISA in ACW (pH = 13) (yellow) and in in Milli-Q (pH = 10.1) (blue) in deuterium oxide and assignment of signals based on structural formula.

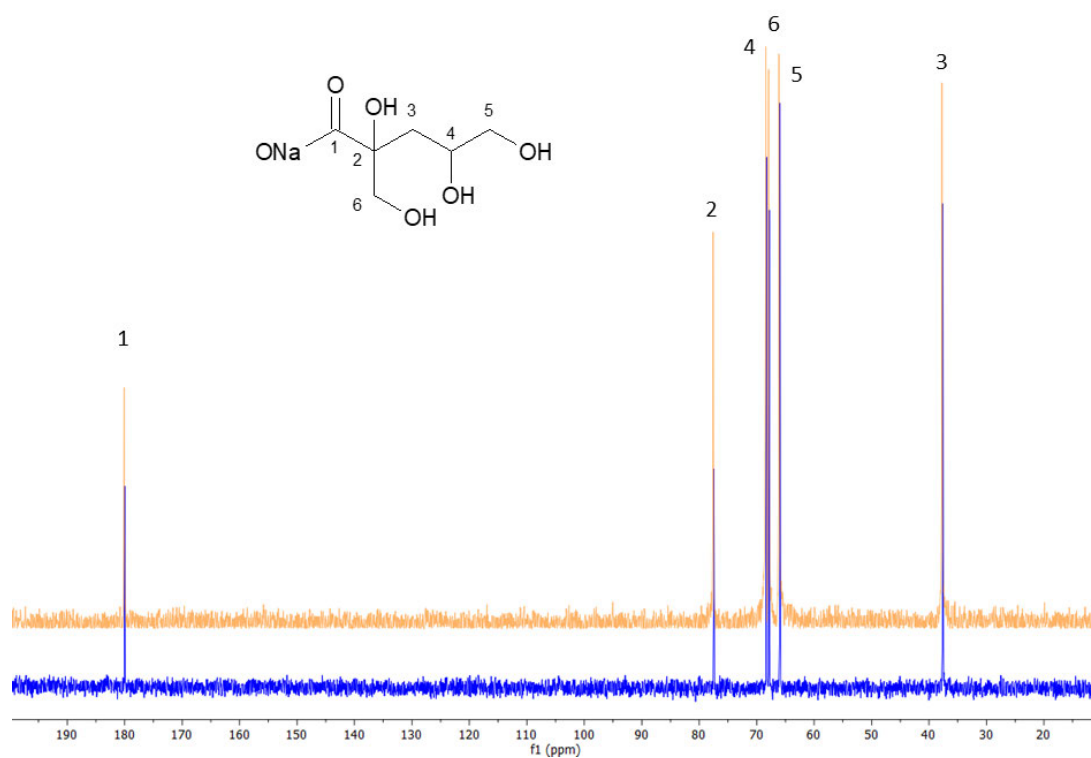


Figure A8: ^1H -NMR spectrum of NaISA in ACW (pH = 13) (yellow) and in in Milli-Q (pH = 10.1) (blue) in deuterium oxide and assignment of signals based on structural formula.

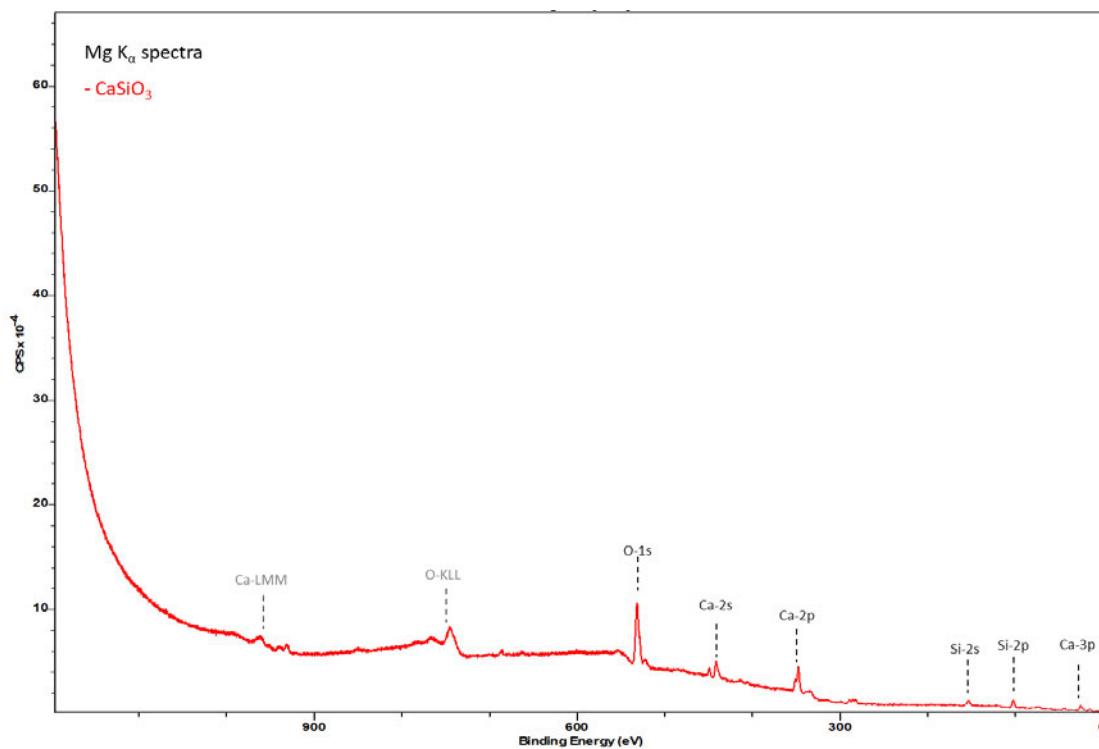


Figure A9: XPS overview spectra of CaSiO_3 measured with Mg K_α at an anode excitation energy of 1253.6 eV. The surface charge was corrected by normalizing the Ca 2p peak ($\Delta E_b = + 1.0$ eV). Ca-LMM and O-KLL denote Auger transitions and can be assigned the signals of the Auger electrons of Ca and O. The other signals were assigned to the photoelectrons from the different layers of the contained elements.

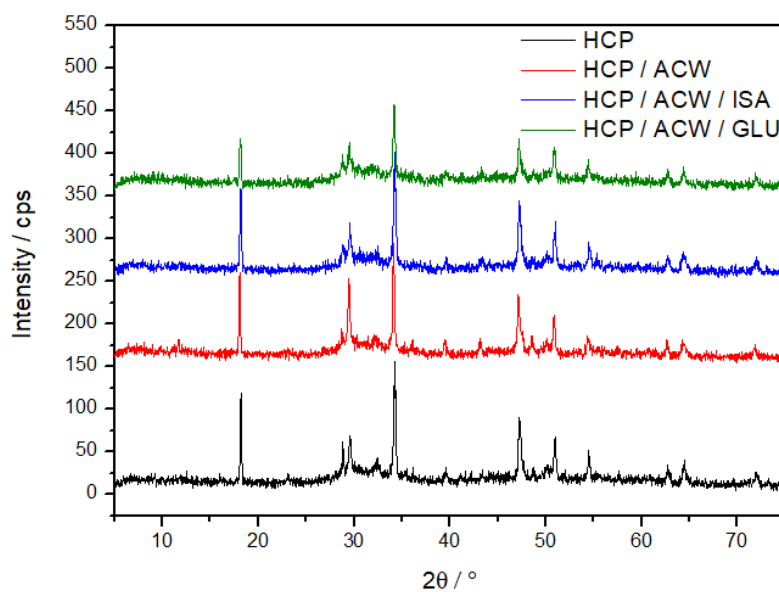


Figure A10: XRD patterns of crushed HCP (black), HCP / ACW (red), HCP / ACW / ISA (blue) and HCP / ACW / GLU (green) after a contact time of 124 h.

Results and discussion - GLU

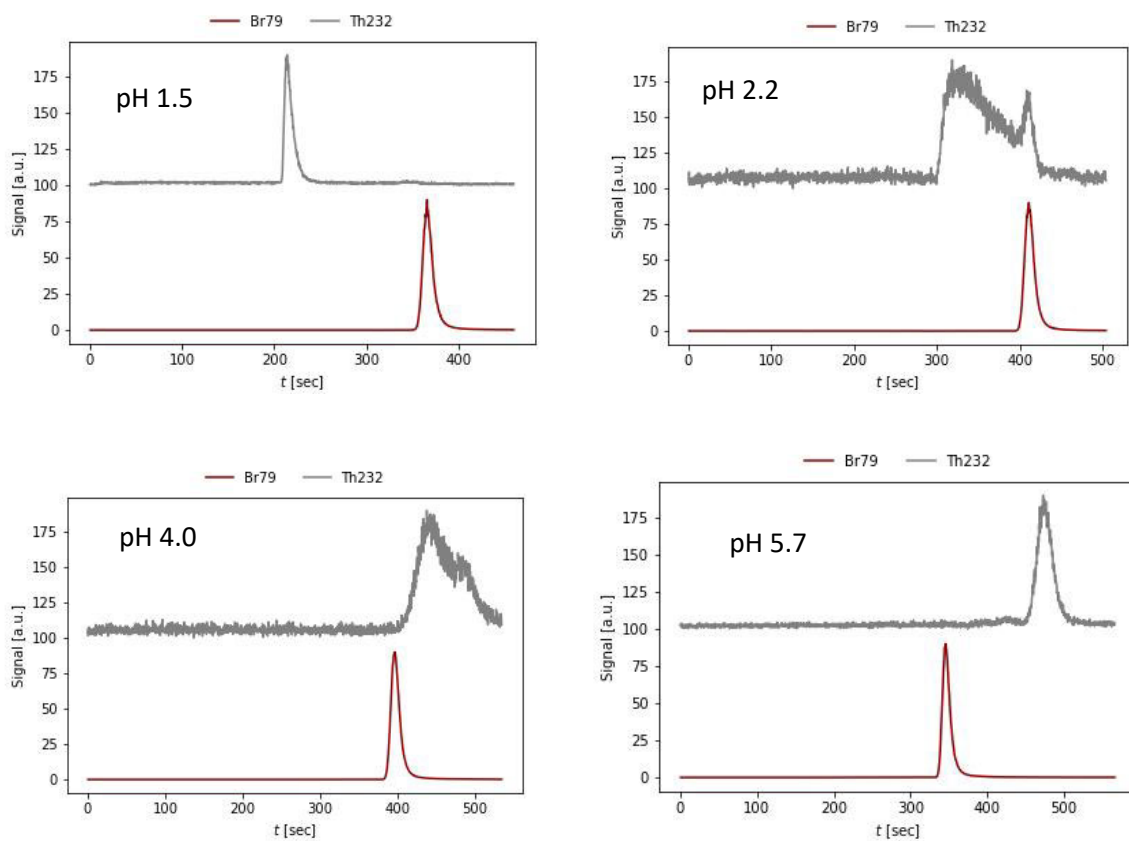


Figure A11: Normalized electropherogram of the CE-ICP-MS measurement of the samples Th-OH-GLU with $[GLU]_0/M = 1 \times 10^{-2}$. There is no GLU in the sample at pH = 1.5.

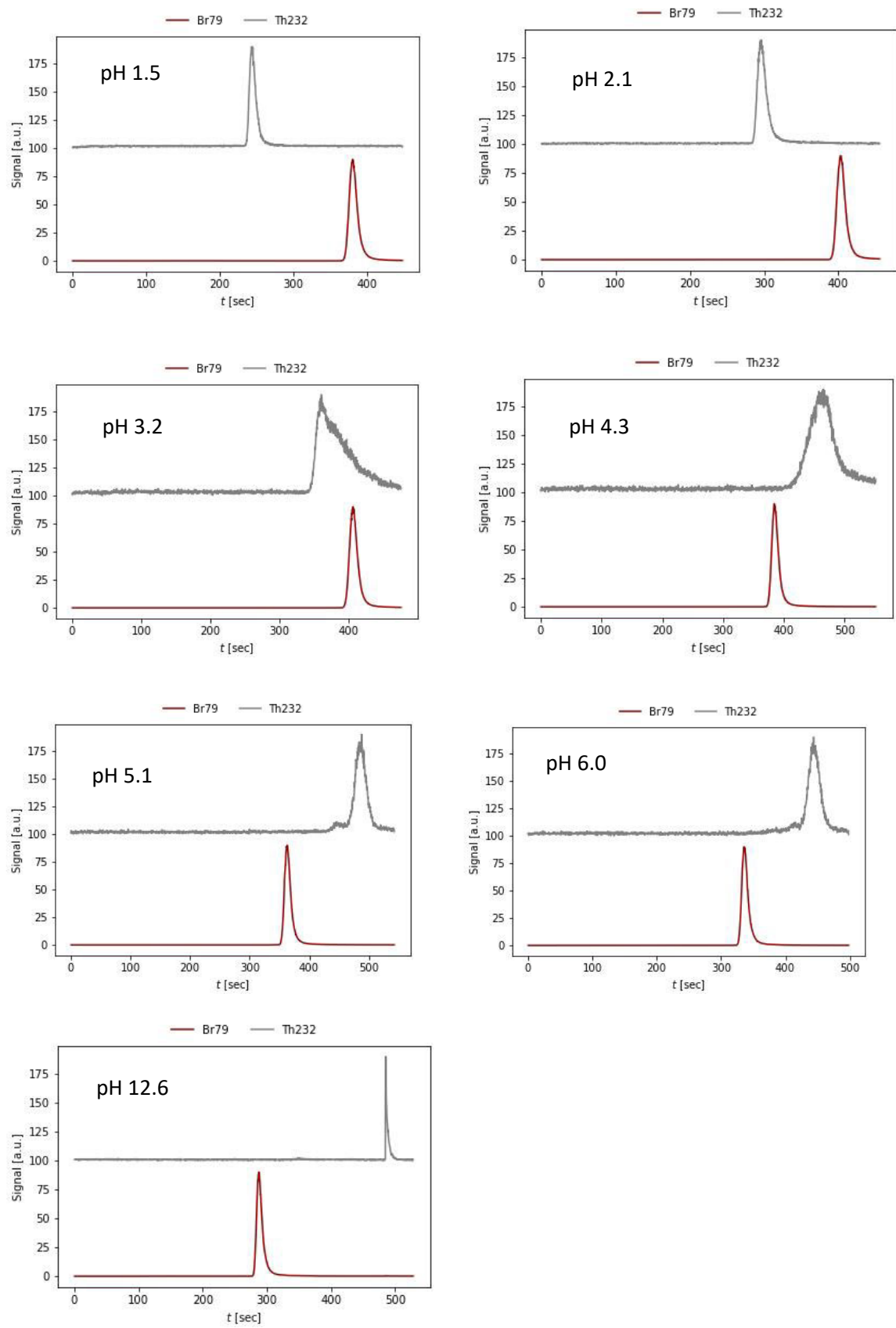


Figure A12: Normalized electropherogram of the CE-ICP-MS measurement of the samples Ca-Th-OH-GLU with $[GLU]_0/M = 1 \times 10^{-2}$ and $[Ca]_0/M = 1.7 \times 10^{-3}$ at different pH values.

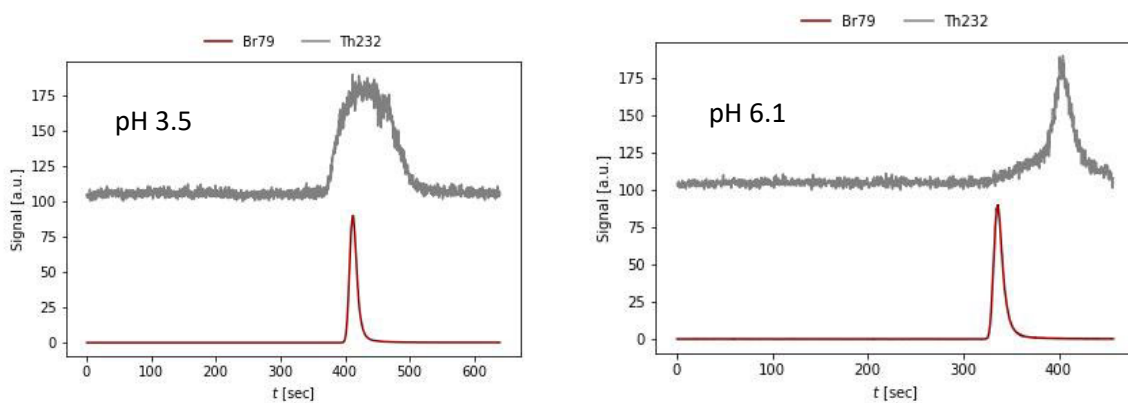


Figure A13: Normalized electropherogram of the CE-ICP-MS measurement of the samples Ca-Th-OH-GLU with $[GLU]_0/M = 1 \times 10^{-2}$ and $[Ca]_0/M = 1 \times 10^{-2}$ at different pH values.

Results and discussion – EDTA

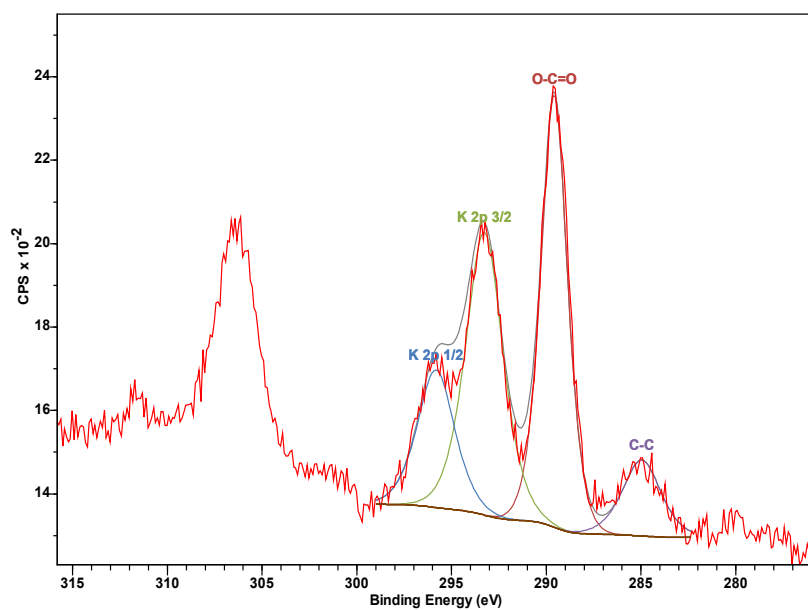


Figure A14: Gauss-Lorentz fit of the potassium signal and the different carbon components in the C 1s signal of the sample HCP / EDTA / ACW.

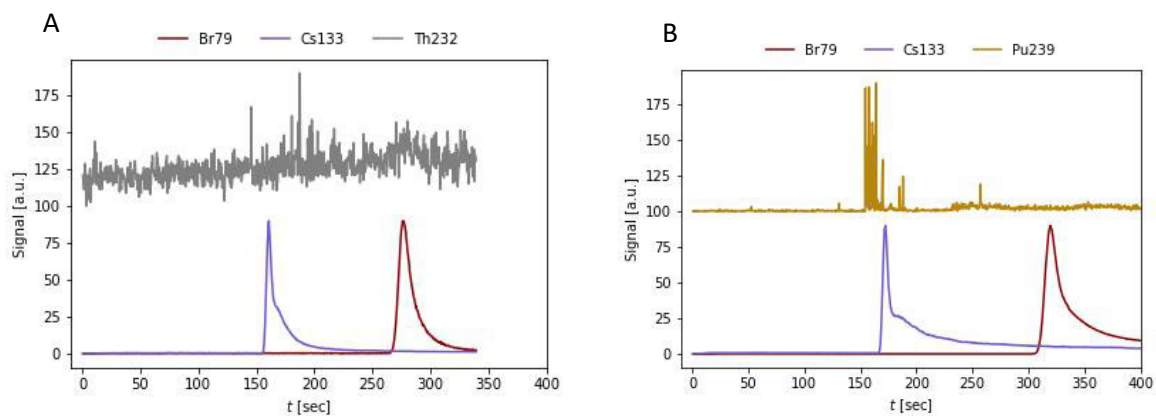


Figure A15: Normalized electropherogram of the CE-ICP-MS measurement of the samples Th(IV) (A) and Pu(IV) (B) at pH = 10.

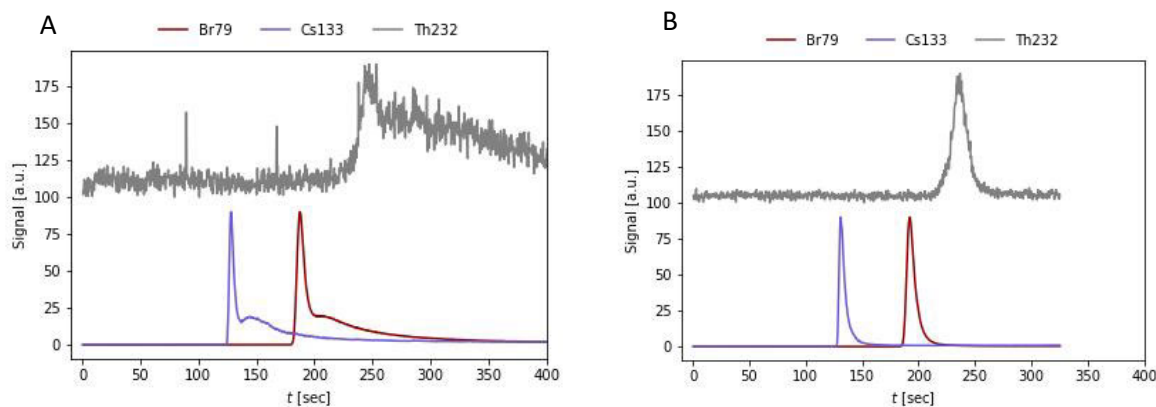


Figure A16: Normalized electropherogram of the CE-ICP-MS measurement of samples Th-OH-EDTA (A) and Ca-Th-OH-EDTA (B) with $[EDTA]_0/M = 1 \times 10^{-2}$ and $[Ca]_0/M = 1 \times 10^{-2}$ at pH = 10.

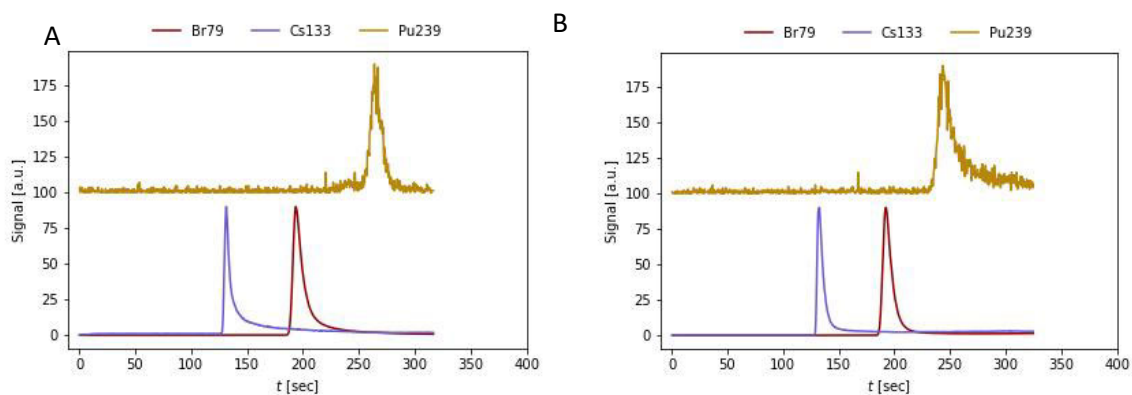


Figure A17: Normalized electropherogram of the CE-ICP-MS measurement of samples Pu-OH-EDTA (A) and Ca-Pu-OH-EDTA (B) with $[EDTA]_0/M = 1 \times 10^{-2}$ and $[Ca]_0/M = 1 \times 10^{-2}$ at pH = 10.

Results and discussion - ISA

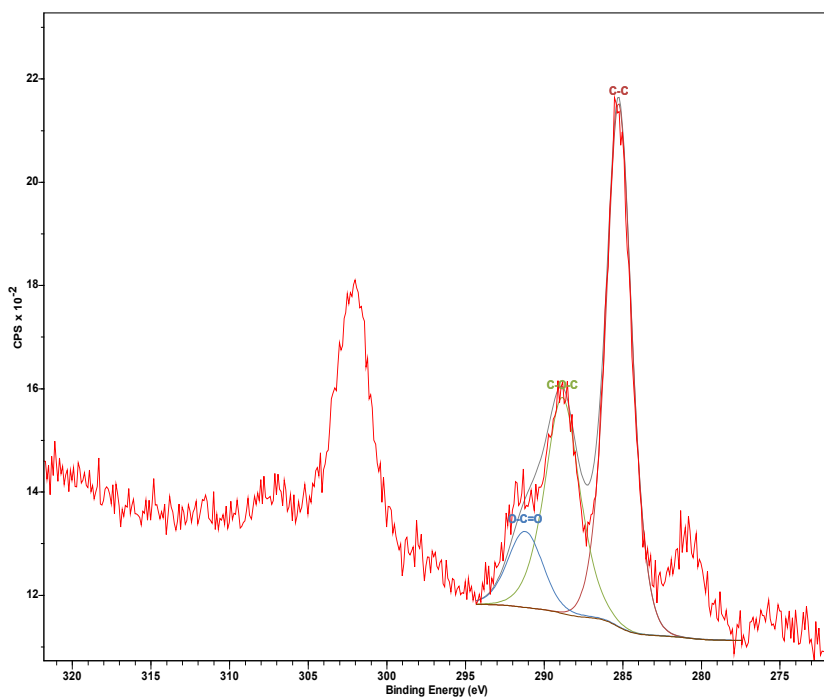


Figure A18: Gauss-Lorentz fit of the potassium signal and the different carbon components in the C 1s signal of the sample HCP / ISA / ACW.

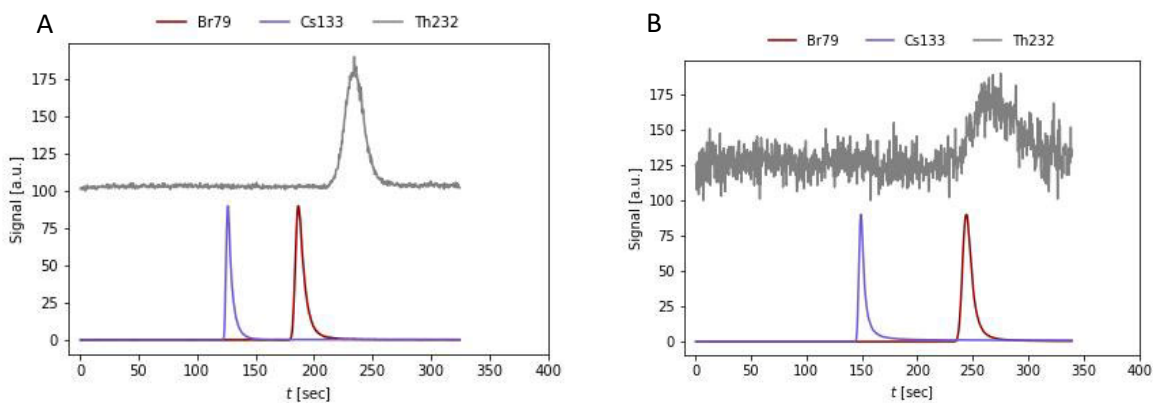


Figure A19: Normalized electropherogram of the CE-ICP-MS measurement of the samples Th-OH-ISA (A) and Ca-Th-OH-ISA (B) with $[ISA]_0/M = 1 \times 10^{-2}$ and $[Ca]_0/M = 1 \times 10^{-2}$ at pH = 10.

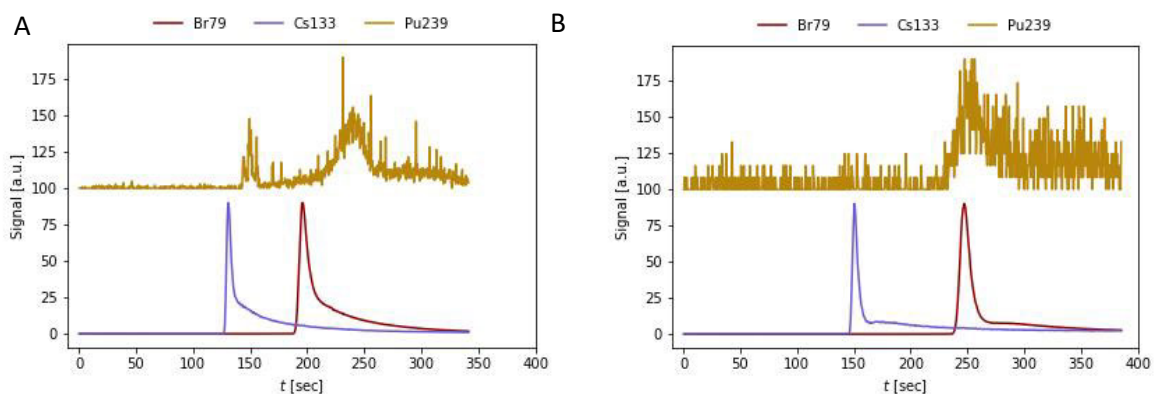


Figure A20: Normalized electropherogram of the CE-ICP-MS measurement of the samples Pu-OH-ISA (A) and Ca-Pu-OH-ISA (B) with $[ISA]_0/M = 1 \times 10^{-2}$ and $[Ca]_0/M = 1 \times 10^{-2}$ at $pH = 10$.

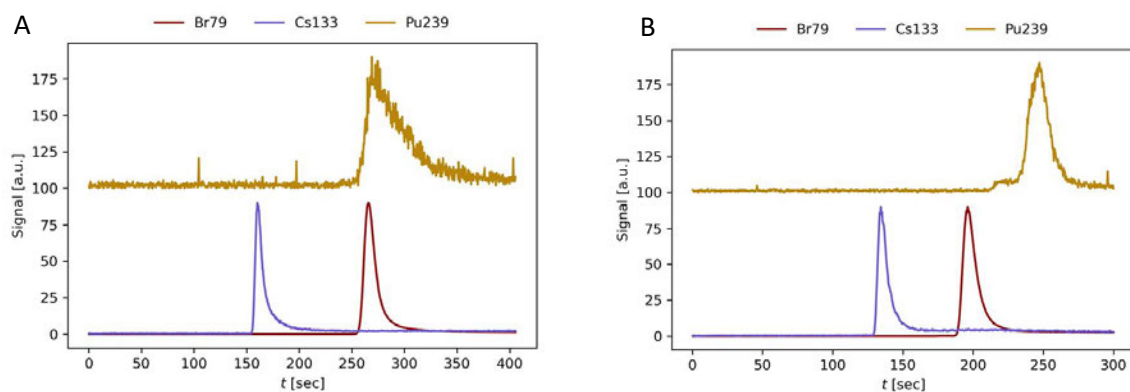


Figure A21: Normalized electropherogram of the CE-ICP-MS measurement of the samples Pu-OH-ISA (A) and Ca-Pu-OH-ISA (B) with $[ISA]_0/M = 1 \times 10^{-2}$ and $[Ca]_0/M = 3 \times 10^{-2}$ at $pH = 10$.

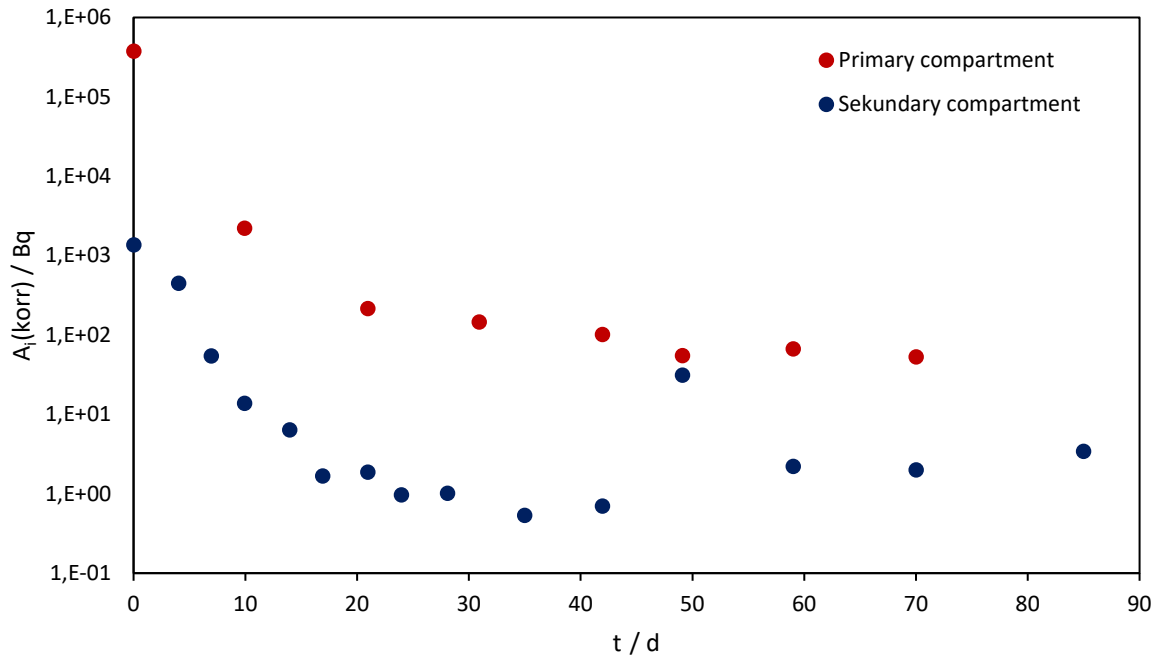


Figure A22: HTO differentiation of cell I with time and activity determined from the LSC measurement. The corresponding measured values can be found in Table A57 and Table A58.

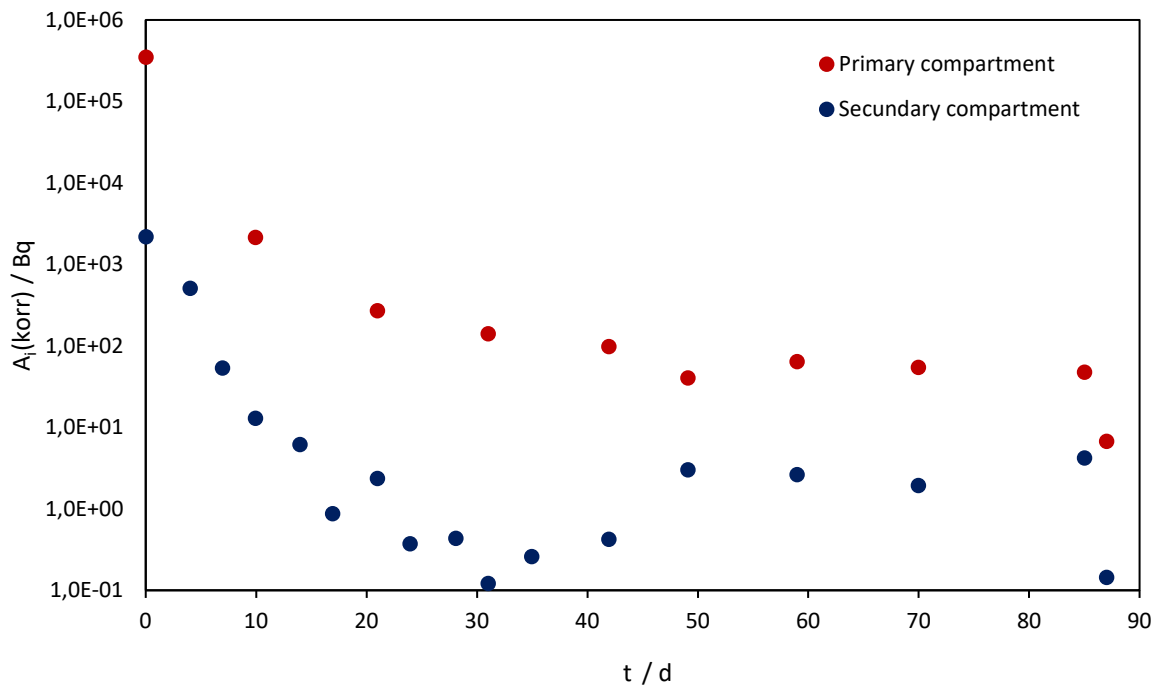


Figure A23: HTO differentiation of cell I with time and activity determined from the LSC measurement. The corresponding measured values can be found in Table A59 and Table A60.

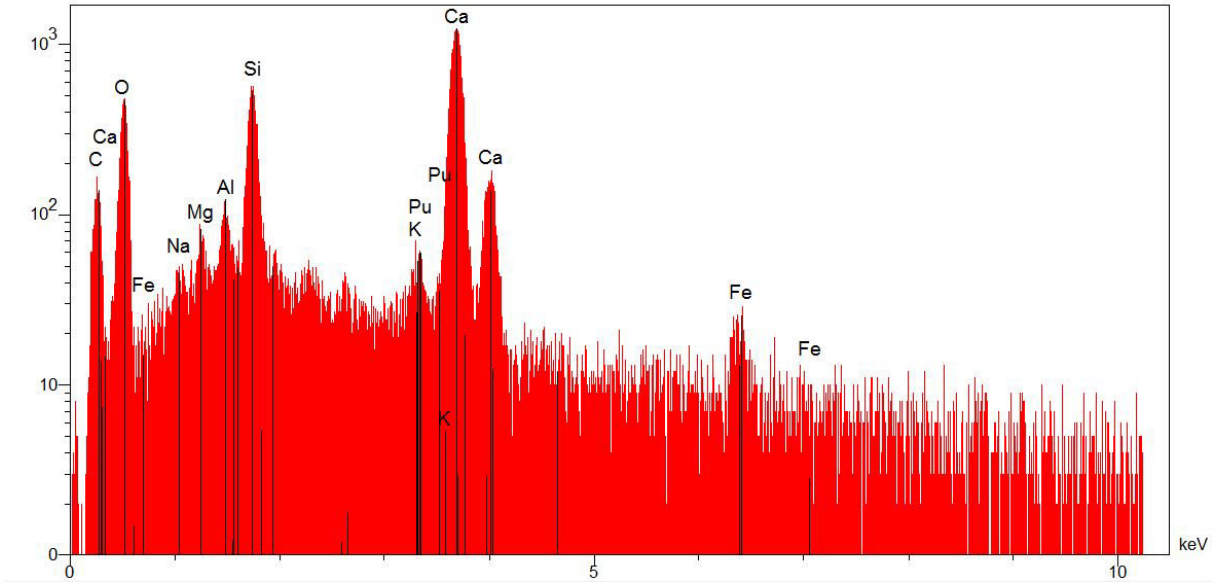


Figure A24: Example of a SEM/EDX spectra of the core from cell I (without ISA). The signals of C, O, Na, Mg, Al, Si, K, Ca, Fe, and Pu were detected.

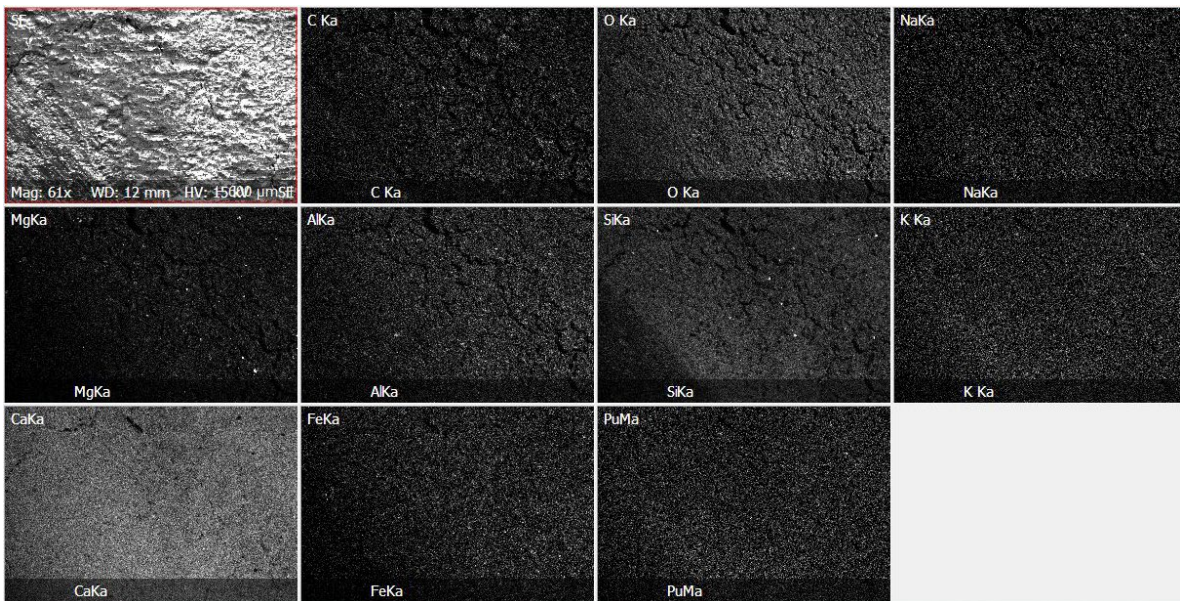


Figure A25: Example of a SEM/EDX mapping of the core from cell I (without ISA). The signals of C, O, Na, Mg, Al, Si, K, Ca, Fe, and Pu shows no different allocation.

Appendix A6 Error calculation

For the error calculation, errors of $\Delta V = 1 \times 10^{-5}$ L and $\Delta m = 5 \cdot 10^{-7}$ kg were assumed. For the measured pH values, an error of $\Delta pH = 0.1$ and for high pH values (~ 13) $\Delta pH = 0.2$ can be assumed.

ICP-MS

$$\Delta R = \pm \sqrt{\left(\frac{\partial R_{Sample}}{\partial CPS_{ISTD}} \cdot \Delta CPS_{Sample}\right)^2 + \left(\frac{\partial R_{Sample}}{\partial CPS_{ISTD}} \cdot \Delta CPS_{ISTD}\right)^2 + \left(\frac{\partial R_{BGE}}{\partial CPS_{ISTD BGE}} \cdot \Delta CPS_{BGE}\right)^2 + \left(\frac{\partial R_{BGE}}{\partial (CPS_{ISTD BGE})^2} \cdot \Delta CPS_{ISTD BGE}\right)^2} \quad (2)$$

$$\Delta S_{\%} = \pm \sqrt{\left(\frac{\partial R_{S\%}}{\partial R_{Sample}} \cdot \Delta R_{Sample}\right)^2 + \left(\frac{\partial R_{S\%}}{\partial R_{Blank}} \cdot \Delta \bar{R}_{Blank}\right)^2} \quad (3)$$

$$\Delta R_d = \pm \sqrt{\left(-\frac{\partial R_d}{\partial CPS_{ISTD}} \cdot \Delta CPS_{Sample}\right)^2 + \left(\frac{V}{\partial CPS_{Sample} \cdot m} \cdot \Delta CPS_{ISTD}\right)^2 + \left(\left(\frac{\partial CPS_{ISTD}}{\partial CPS_{Sample} \cdot m} - \frac{1}{m}\right) \cdot \Delta V\right)^2 + \left(\left(-\frac{\partial CPS_{ISTD} \cdot V}{\partial CPS_{Sample} \cdot m^2} + \frac{V}{m^2}\right) \cdot \Delta V\right)^2} \quad (4)$$

$$\Delta c_{eq} = \pm \sqrt{\left(\frac{\partial c_{eq}}{\partial R_{korr}} \cdot \Delta R_{korr}\right)^2 + \left(\frac{\partial c_{eq}}{\partial b} \cdot \Delta b\right)^2 + \left(\frac{\partial c_{eq}}{\partial m} \cdot \Delta m\right)^2} \quad (5)$$

LSC measurements

$$\Delta c_{eq} = \pm \sqrt{\left(c_0 \cdot \frac{1}{A(Blank)} \cdot \Delta A_{Sample}\right)^2 + \left(-c_0 \cdot \frac{A_{Sample}}{A(Blank)} \cdot \Delta A(Blank)\right)^2} \quad (6)$$

$$\Delta S_{\%} = \pm \sqrt{\left(\frac{\partial S_{\%}}{\partial c_{eq,Sample}} \cdot \Delta c_{eq,Sample}\right)^2 + \left(\frac{\partial S_{\%}}{\partial c_{eq}(Blank)} \cdot \Delta \bar{c}_{eq}(Blank)\right)^2} \quad (7)$$

$$\Delta R_d = \pm \sqrt{\left(\frac{\partial R_d}{\partial V} \cdot \Delta V\right)^2 + \left(\frac{\partial R_d}{\partial m} \cdot \Delta m\right)^2 + \left(\frac{\partial R_D}{\partial c_{eq}(Blank)} \cdot m \cdot \Delta \bar{c}_{eq, (Blank)}\right)^2 + \left(\frac{\partial R_D}{\partial c_{eq, Sample}} \cdot m \cdot \Delta \bar{c}_{eq, Sample}\right)^2} \quad (8)$$

γ -spectroscopy

$$\Delta A = \pm \sqrt{\left(\frac{1}{t \cdot PE \cdot EW} \cdot \Delta PF\right)^2 + \left(-\frac{PF}{t \cdot PE^2 \cdot EW} \cdot \Delta PE\right)^2} \quad (9)$$

$$\Delta A_o = \pm \frac{1}{\exp(-\lambda t)} \cdot \Delta A \quad (10)$$

$$\Delta A = \pm \sqrt{\left(\frac{1}{A_{spez} \cdot V \cdot M} \cdot \Delta A_o\right)^2 + \left(-\frac{A_o}{A_{spez} \cdot V^2 \cdot M} \cdot \Delta V\right)^2} \quad (11)$$

CE-ICP-MS measurements

The error of electrophoretic mobility $\Delta\mu_e$ was also calculated according to Gauss, assuming errors of $\Delta l = 0,3 \text{ cm}$, $\Delta U = 100 \text{ V}$ and $\Delta t_{R.EOF} = \Delta t_{R.Probe} = 10 \text{ s}$.

$$\Delta\mu_e = \pm \sqrt{\left(\frac{\partial\mu_e}{\partial l} \cdot \Delta l\right)^2 + \left(\frac{\partial\mu_e}{\partial U} \cdot \Delta U\right)^2 + \left(\frac{\partial\mu_e}{\partial t_{R,EOF}} \cdot \Delta t_{R,EOF}\right)^2 + \left(\frac{\partial\mu_e}{\partial t_{R,Probe}} \cdot \Delta t_{R,Probe}\right)^2} \quad (12)$$

Diffusion

The error values for diffusion through are calculated according to the following equations, $\Delta d = 0.1 \text{ mm}$.

$$\Delta N_{dif}^{\Delta t_i} = \pm \sqrt{\left(\frac{N_s^{t_i}}{V_{sample}} \cdot \Delta V_{low}\right)^2 + \left(\frac{N_s^{t_i} \cdot V_{low}}{V_{sample}^2} \cdot \Delta V_{Isample}\right)^2}. \quad (13)$$

$$\Delta A_{dif}^{\Delta t_i} = \frac{\Delta N_{dif}^{\Delta t_i}}{60 \cdot TCCR}. \quad (14)$$

$$\Delta O = \frac{d}{2} \cdot \pi \cdot \Delta d. \quad (15)$$

$$\Delta J_L^{t_i} = \sqrt{\left(\frac{\Delta A_{dif}^{\Delta t_i}}{O \cdot \Delta t_i}\right)^2 + \left(\frac{\Delta A_{dif}^{\Delta t_i}}{O^2 \cdot \Delta t_i} \cdot \Delta O\right)^2}. \quad (16)$$

List of Abbreviation

Abbreviation	Full name
ACW	Artificial cement pore water
ACW-VGL	Diluted caprock solution with artificial cement pore water (ger.: Verdünnte Gipshutlösung mit künstlichem Zementporenwasser)
Ar	Argon
An	Actinide
AtG	Atomgesetz
BET	Brunauer-Emmet-Teller
BG	Background
BGE	Background electrolyte
CE	Capillary electrophoresis
CEC	Cation exchange capacity
CE-ICP-MS	Capillary electrophoresis with inductively coupled plasma mass spectrometer
C-S-H	Calcium silicate hydrates
C/S	Calcium-to-silicon ratio
DCM	Double crystal monochromator
EDX	Energy-dispersive X-ray
EOF	Electroosmotic flux
EXAFS	Extended X-ray absorption fine structure
HCP	Hardened cement paste
HPGe	High purity Germanium
ICP-MS	Inductively coupled plasma mass spectrometer
JGU	Johannes Gutenberg-University
LOD	Limit of detection
LOQ	Limit of quantification
LSC	Liquid scintillation counting
OPC	Ordinary Portland Cement
PSL	Photostimulated luminescence
PMMA	Polymethylmethacrylat
PZC	Point of zero charge

SEM	Scanning electron microscope
SHE	Standard hydrogen electrode
StandAG	Standortauswahlgesetz
TRIGA	Training, Research, Isotopes, General Atomic
VGL	Diluted caprock solution (ger.: Verdünnte Gipshutlösung)
XANES	X-ray absorption near edge structure
XAS	X-ray absorption spectroscopy
XPS	X-ray photoelectron spectroscopy
XRD	X-ray powder diffraction

List of Chemicals

Chemical	Supplier
[1- ¹⁴ C]-D-Gluconacid	Hartmann Analytic GmbH, Braunschweig, Germany
[1- ¹⁴ C]-EDTA	Hartmann Analytic GmbH, Braunschweig, Germany
2-Brompropan	Merck, Darmstadt, Deutschland
Acetone	Fisher Scientific, Loughborough, UK
Aerosil® 300 (SiO ₂)	Evonik Industries, Essen, Germany
Argon gas (4.6)	Westfalen AG, Münster, Germany
Calcium hydroxide	VWR International GmbH, Darmstadt, Germany
Ca-isosaccharinic acid	Sigma Aldrich, St. Louis, Missouri, USA
Calcium oxide	ThermoFisher Scientific, Waltham, Massachusetts, USA
Calcium silicate	Sigma Aldrich, St. Louis, Missouri, USA
Chelex 100-200 mesh Resin	Bio-Rad, Hercules, California, USA
Citric acid monohydrate	Merck, Darmstadt, Germany
Dibutyl phthalate	Merck, Darmstadt, Germany
Diethylether (extra dry, MS, stab.)	Acros Organics (ThermoFisher Scientific), Waltham, Massachusetts, USA
Deuterium oxide, D ₂ O 99,5%	Deutero GmbH, Kastellaun, Germany
DOWEX® 1X8	Alfa Aesar, Haverhill, Massachusetts, USA
Ethylenediaminetetraacetate (EDTA)	VWR International GmbH, Darmstadt, Germany
Ethanol	Merck, Darmstadt, Germany
Hydrochloric acid (36%)	Fisher Scientific, Loughborough, UK
HTO	Perkin Elmer, Waltham, Massachusetts, USA
Ir-ICP-MS Standard (1000 ppm)	Accu Trace™, Accu Standard, New Haven, CT, USA
Lactose monohydrate, Normapur	VWR International GmbH, Darmstadt, Germany
Methanol	Acros Organics (ThermoFisher Scientific), Waltham, Massachusetts, USA
Milli-Q water (18.2 MΩ)	Synergy™ Millipore water system, Millipore GmbH, Schwalbach, Germany
Nitric acid	Merck, Darmstadt, Germany
Oxalic acid dihydrate	Merck, Darmstadt, Germany
Nitric acid (Suprapur)	Merck, Darmstadt, Germany

Perchloric acid (70%)	Riedel-de Haën, Seelze, Germany
Potassium chloride, 3M	Mettler-Toledo AG, Columbus, Ohio, USA
Potassium hydroxide	Merck, Darmstadt, Germany
Sodium Chloride	Merck, Darmstadt, Germany
Sodium hydroxide (30%, Suprapure®)	Merck, Darmstadt, Germany
Sodium hydroxide (CO ₂ -free)	VWR Chemicals BDH Proabo®, VWR Int., Radnor, Pasadena, USA
Sodium gluconate	Sigma Aldrich, St. Louis, Missouri, USA
Sodium perchlorate monohydrate	Merck, Darmstadt, Germany
Ultima Gold™ XR	Perkin Elmer, Waltham, Massachusetts, USA
Th-ICP-MS Standard (1000 ppm)	Peak Performance, CPI International, Santa Rosa, CA, USA
U-ICP-MS Standard (1000 ppm)	Peak Performance, CPI International, Santa Rosa, CA, USA

List of Units

Unit	Full name (and the respective definition in SI-units)
A	Ampere
a	Year
Å	Angstrom (1 Å = 10 ⁻¹⁰ m)
Bq	Becquerel
C	Coulomb (1 C = 1 A s)
cps	Counts per second (1 cps = 1 s ⁻¹)
d	Ds
eV	Electron-volt
g	Gram
h	Hours
Hz	Hertz (1 Hz = 1 s ⁻¹)
J	Joule (1 J = 1 kg m ² s ⁻²)
K	Kelvin
kg	Kilogram
L	Liter
m	Meter
min	Minute
mol	Mole
µl	Microliter
µm	Micrometer
M	Mole per liter (1 M = 1 mol L ⁻¹)
ppb	Parts per billion
ppm	Parts per million
ppt	Parts per trillion
rpm	Rounds per minute (min ⁻¹)
s	Second
V	Volt (1 V = 1 kg m ² A ⁻¹ s ⁻³)
wt%	Weight percent

W	Watt ($1 \text{ W} = 1 \text{ kg m}^2 \text{ s}^{-3}$)
Ω	Ohm ($1 \Omega = 1 \text{ kg m}^2 \text{ A}^{-2} \text{ s}^{-3}$)

List of Variables and Constants

Variable/constant	Definition (Units are given in brackets)
α	Capacitance factor of the rock (α is used for diffusion of HTO called ε and in this case indicates porosity).
A	Activity [Bq]
A_{cum}	Accumulated activity [Bq]
A_{spec}	Specific activity [Bq g ⁻¹]
c	Concentration [M]
c_o	Initial concentration [M]
c_{eq}	Equilibrium concentration [M]
\emptyset	Diameter [mm]
ε	Porosity
E_h	Redox potential
h	High of the diffusion core [mm]
I	Ionic strength [M]
ISTD	Internal standard
J_i	Flow [Bq (cm ² d) ⁻¹]
k	Boltzmann constant ($k = 1.38065 \cdot 10^{-23} \text{ J mol}^{-1}$)
K_d	Distribution coefficient [L kg ⁻¹]
l	Capillary length [cm]
LOD	Limit of detection
LOQ	Limit of quantification
m	Mass [kg]
μ	Electrophoretic mobility [cm ² V ⁻¹ s ⁻¹]
μ_0	Electrophoretic mobility for zero ionic strength [cm ² V ⁻¹ s ⁻¹]
μ_{eff}	Effective electrophoretic mobility [cm ² V ⁻¹ s ⁻¹]
N	Avogadro constant ($N = 6.022 \cdot 10^{23} \text{ mol}^{-1}$)
r	Radius [mm]
ρ	Density [kg m ⁻³]
R_d	Distribution coefficient [L kg ⁻¹]
RSD	Relative standard deviation [%]

$S_{\%}$	Sorption [%]
S/L	Solid-liquid-ratio [g L ⁻¹]
S_A	Signal of the analyte
S_{ISTD}	Signal of the internal standard
σ	Standard deviation
t	Time [s]
$t_{1/2}$	Half-life
t_{akk}	Past time from the beginning of the experiment
t_{EOF}	Time of EOF [s]
t_{mess}	Time of measurements
T	Temperature [K]
U	Voltage [V]
V	Volume [m ³]
w/z	Water-to-cement-ratio
x	Mole fraction

List of Figures

Figure 1: Tobermorite-based structure of the C-S-H phases at C/S ratios of 1.5 (A) and 0.67 (B) due to ageing of the cement [27].	3
Figure 2: The different retention mechanisms; according to Charlet and Manceau [45]. Adsorption (1) in the form of an outer-sphere complex (a); loss of hydration sphere (2) and formation of an inner-sphere complex (b); diffusion into the crystal lattice (3) and isomorphic substitution (c); rapid lateral diffusion (4,5) and formation of a surface polymer (d); adsorption on a mineral growth front (e and e'); formation of surface polymer and incorporation into the host matrix after crystal growth (f). The adsorbed ion can eventually return to solution, for example, due to surface redox reactions or dynamic equilibrium (g). (7) Organic-mineral complexation [46].	5
Figure 3: Schematic representation of the sorption isotherms with the loading of the sorbent $\log(q)$ and concentration of the sorbate in solution $\log([C])$ adopted according to [48].	6
Figure 4: Speciation calculation of 1×10^{-2} M GLU and 2×10^{-3} M Ca (Graphic generated by PhreePlot (version 1.0 [53]) using PHREEQC and the ThermoChimie database 11a, 2022 [54]).	10
Figure 5: Speciation calculation of 1×10^{-2} M EDTA and (A): for the system HCP / ACW calculated with 1.14×10^{-1} M Na, 2×10^{-3} M Ca, 1.8×10^{-1} M K and (B): for the system C-S-H / Milli-Q calculated with 1×10^{-2} M Na, 2×10^{-3} M Ca (Graphic generated by PhreePlot (version 1.0 [53]) using PHREEQC and the ThermoChimie database 11a, 2022 [54]).	11
Figure 6: Repository-related decomposition of cellulose by $\text{Ca}(\text{OH})_2$ by benzylic acid rearrangement to alpha-D-isosaccharinic acid (2S,4S) [77].	12
Figure 7: Speciation calculation of 1×10^{-2} M ISA and 2×10^{-3} M Ca (Graphic generated by PhreePlot (version 1.0 [53]) using PHREEQC and the ThermoChimie database 11a, 2022 [54]).	14
Figure 8: Speciation calculation of 1×10^{-8} M Am, 1×10^{-2} M EDTA and 2×10^{-3} M Ca (Graphic generated by PhreePlot (version 1.0 [53]) using PHREEQC and the ThermoChimie database 11a, 2022 [54]).	15
Figure 9: Speciation calculation of 1×10^{-8} M Th, 1×10^{-2} M GLU and 2×10^{-3} M Ca (Graphic generated by PhreePlot (version 1.0 [53]) using PHREEQC and the ThermoChimie database 11a, 2022 [54]).	16
Figure 10: Speciation calculation of 1×10^{-8} M Th, 1×10^{-2} M EDTA and 2×10^{-3} M Ca (Graphic generated by PhreePlot (version 1.0 [53]) using PHREEQC and the ThermoChimie database 11a, 2022 [54]).	17
Figure 11: Speciation calculation of 1×10^{-8} M Th, 1×10^{-2} M ISA and 2×10^{-3} M Ca (Graphic generated by PhreePlot (version 1.0 [53]) using PHREEQC and the ThermoChimie database 11a, 2022 [54]).	18
Figure 12: Speciation calculation of 1×10^{-8} M Pu(IV), 1×10^{-2} M GLU and 2×10^{-3} M Ca (Graphic generated by PhreePlot (version 1.0 [53]) using PHREEQC and the ThermoChimie database 11a, 2022 [54]).	19

Figure 13: Speciation calculation of 1×10^{-8} M Pu(IV), 1×10^{-2} M EDTA and 2×10^{-3} M Ca (Graphic generated by PhreePlot (version 1.0 [53]) using PHREEQC and (A): the ThermoChimie database 11a, 2022 [54] and (B): complex formation constants determined by DiBlasi et al.[39].....	20
Figure 14: Speciation calculation of 1×10^{-8} M Pu(IV), 1×10^{-2} M ISA and 2×10^{-3} M Ca (Graphic generated by PhreePlot (version 1.0 [53]) using PHREEQC and (A): the ThermoChimie database 11a, 2022 [54] and (B): complex formation constants determined by Tasi et al. [93,94].....	21
Figure 15: Change in color of HCP after batch experiments with ISA and GLU after a contact time of 124 d, with the effect being more evident with GLU.....	76
Figure 16: Average value from a double determination of the distribution coefficients R_d ($L\ kg^{-1}$) determined for Th(IV) uptake on C-S-H phase ($C/S = 1.0$) in presence and absence of GLU ($[Th(IV)]_0/M = 1 \times 10^{-8}$, $[GLU]_0/M = 1 \times 10^{-2}$, $S/L = 5\ g\ L^{-1}$, pH 11.4) after a contact time of 72 h. The dashed line represents an uptake of 99%.....	78
Figure 17: Results of the CE-ICP-MS measurement in the system Ca-Th(IV)-OH-GLU. Charge distribution determined from speciation calculations (solid lines) described in Section 1.4.2 and the electrophoretic mobilities μ_{eff} of Th(IV) ($[Th(IV)]_0 = 4 \times 10^{-7}$) in absence and presence of GLU ($[GLU]_0/M = 1 \times 10^{-2}$) and Ca(II) ($[Ca(II)]/M = 1.7 \times 10^{-3}$ and 1×10^{-2}) at different pH values ($I = 0.1\ M$).	80
Figure 18: Average value from a double determination of the distribution coefficients R_d ($L\ kg^{-1}$) determined for Th(IV) uptake on HCP in presence of the organic ligands oxalate, citrate and phthalate ($[Th(IV)]_0/M = 1 \times 10^{-8}$, $[OL]_0/M = 1 \times 10^{-2}$, $S/L = 5\ g\ L^{-1}$, pH 13.3) after a contact time of 72 h.....	152

List of Tables

Table 1: Results of the semiquantitative analysis mode in ICP-MS for ACW and after leaching of HCP in absence in presence of the organic ligands GLU, EDTA and ISA. All values are given in M and the comparison to the literature at the cement degradation state I [22].	74
Table 2: Results of the semiquantitative analysis mode in ICP-MS for the Milli-Q water after leaching of C-S-H phases (C/S = 0.8) in absence in presence of the organic ligands GLU, EDTA and ISA. All values are given in M and the comparison to the literature at the cement degradation state III [22]....	75
Table 3: Determined concentrations as a mean value from the double determination of ²³² Th in the samples of the batch sorption experiment HCP / Th(IV) / GLU after a contact time of 72 h along the values of the binary system HCP / Th(IV) and HCP / GLU determined with ICP-MS measurements.	77
Table 4: The determined values from the ICP-MS measurement of the batch sorption experiment HCP / GLU after a contact time of 72 h and the calculated concentrations of ²³² Th when the ordinary Portland cement contains 2.8 ppm ²³² Th.....	77
Table 5: Summary of complexation constants from the master's thesis of Tamara Kutyma [129] and values from the literature [33,66].	81